L-Università ta' Malta
Faculty of Engineering

DOCTOR OF PHILOSOPHY IN ENGINEERING DISSERTATION

Sensorless Control in Steer-by-Wire Application

KRIS SCICLUNA

Supervised by:

PROF. ING. CYRIL SPITERI STAINES

Co-supervised by:

DR. ING. REIKO RAUTE

A dissertation submitted in partial fulfilment of the requirements for the degree of Doctor of Philosophy in Engineering

by the

Faculty of Engineering

July 2020

Copyright Notice

Dedicated to my parents and my fiancée Claire

Acknowledgements

I would like to express my sincere gratitude to my thesis supervisors Prof. Ing. Cyril Spiteri Staines *(Professor)* and Dr Ing. Reiko Raute *(Senior Lecturer)* at the Department of Industrial Electrical Power Conversion, University of Malta. This research initiative would not have been possible without the constant guidance, support and encouragement they have shown throughout this project.

Specials thanks to the technical staff at the Department of Industrial Electrical Power Conversion, Ing. Daniel Zammit *(Senior Systems Engineer)*, Mr John Camilleri *(Lab Officer)* and Mr Kevin Camilleri *(Lab Officer)* for their assistance with the hardware aspects of this research project.

I would like to acknowledge my colleagues and the management at the Malta College for Arts, Science and Technology for the support provided in this project during my employment.

Abstract

This dissertation presents Sensorless Control as applied to the Steer-by-Wire Application. The steer-by-wire is an integral part of the electrification of automotive vehicles whereby mechanical components are replaced by electronic sensors and electrical actuators. In this by-wire application, the column linking the handwheel and the steered wheel sides is removed and replaced by an electrical machine at each end of the arrangement. The fundamental aim of steer-by-wire is to replicate the input at the handwheel given by the driver to the steered wheels with the minimum delay possible. In order for this to be implemented, robust position measurements at both ends of the system are required. Traditionally, position sensors have been identified as being more prone to failure than other types of electronic transducers. Hence, backup position measurements are typically included in steer-by-wire to ensure the necessary safety levels.

In this dissertation, it is proposed that redundant position sensors are replaced by a sensorless algorithm. The algorithm is to be used for the detection of sensor failures and possible changeover to sensorless operation. The steering wheel in an automotive vehicle is typically at rest at the initial position with fast transients while steering. Therefore, a sensorless algorithm for zero speed operation and with sufficient bandwidth to track the position transients is required. From literature, High Frequency-based Sensorless Control was identified as being the most suitable for this application.

The magnetic signatures of the Surface-Mounted Permanent Magnet Synchronous Machines used for sensorless control in this dissertation were investigated under different operating conditions, including different transient injection angles, load current and rotor speed. The deviation of the signatures of the experimental machines from the fundamental theoretical models was identified and results for different machine geometries compared. Due to the presence of significant saliency harmonics, an innovative search-based sensorless algorithm was proposed to estimate the speed and position of the experimental machines.

The search-based sensorless method was tested in sensorless current, speed and position control systems under dynamic load conditions. The sensorless operation was extended to the steer-by-wire application with typical scenarios investigated for the current-controlled handwheel and the position-controlled steered wheel side.

Table of Contents

List of Figures

List of Tables

List of Abbreviations

ADC	Analogue to Digital Converter
ANN	Artificial Neural Network
BOM	Bill of Materials
DSP	Digital Signal Processor
EKF	Extended Kalman Filter
EMC	Electromagnetic Compatibility
EPAS	Electrically Power Assisted Steering
FDA	Filter Design and Analysis
FFT	Fast Fourier Transfer
FPGA	Field Programmable Gate Array
HF	High Frequency
HFI	High-Frequency Injection
IIR	Infinite Impulse Response
INFORM	Indirect Flux Detection by Online Reactance Measurement
IPM	Integrated Power Module
IPMSM	Interior buried Permanent Magnet Synchronous Machine
LF	Low Frequency
LUT	Look-Up Table
MRAS	Model Reference Adaptive System
MSOA	Multi-Stage Op-Amp
OBD	On-Board Diagnostics
P	Proportional
PCB	Printed Circuit Board
PI	Proportional-Integral
PLL	Phased Locked Loop
PMSM	Permanent Magnet Synchronous Machine
PWM	Pulse Width Modulation
RFO	Rotor Flux Oriented
RMSE	Root Mean Square Error
SBF	Sideband Filter
SBO	Search-Based Observer
SMO	Sliding Mode Observer
SMP	Space Modulation Profiling
SM-PMSM	Surface-mounted Permanent Magnet Synchronous Machine
SNN	Structured Neural Network
SNR	Signal-to-Noise Ratio
SP	Single Pole
SPWM	Sinusoidal Pulse Width Modulation
SSI	Serial Synchronous Interface
SVPWM	Space Vector Pulse Width Modulation

Chapter 1 – Project Introduction

1.1 Steer-by-Wire Application

Steer-by-wire is an innovative approach which aims to replace mechanical linkage components in the steering arrangement with alternative systems based on electronic systems and electrical actuators. The resulting by-wire applications result in more mechanically flexible designs, adjustable steering 'feel' and additional safety. By-wire systems have been introduced in several forms, including the steering in automobiles which is mainly investigated in this dissertation.

The steering system in cars is typically built around a rack and pinion arrangement, through which the driver can position the angle of the wheels through a handwheel and a physical column link to the rack and pinion. Advances in steering arrangement have included the introduction of power steering through hydraulic or electrical based mechanical gain. Although power steering reduces the torque required at the handwheel, there is still a direct mechanical link from the handwheel side to the steered wheel side of the vehicle.

Modern electric-based power steering uses an electrical machine coupled to the handwheel to provide Electrically Power Assisted Steering (EPAS). The EPAS system requires sensors and electronic drivers to operate the electrical machine in such a way that the opposing torque felt by the driver at the handwheel is reduced to comfortable levels. The use of electrical machines for improved steering can be extended to steer-by-wire, where the steering column is removed and replaced by two electrical machines. One of the machines is used at the handwheel to replace the steering 'feel' which would be felt by the driver, and the other machine is used at the steering wheel side to position the wheels.

While the automotive steer-by-wire conceptually provides significant advantages over traditional power steering arrangement, it poses substantial challenges which have limited its use in commercial vehicles. To obtain the required functional safety by the automotive industry, researchers have included redundancy in the form of backup sensors and mechanical fail safes. The inclusion of such devices increases the cost of the steer-by-wire system to the extent that commercial viability becomes questionable.

One of the critical components in steer-by-wire is the position sensor at both the handwheel and steered wheel side of the arrangement. This dissertation proposes the use of sensorless algorithms for the estimation and control of the position at the shafts of the machines used in steer-by-wire. These algorithms have the advantage of operating on electronic-based transducers which are still required for fundamental control of the machine. Such electronic sensors are soldered directly onto the electronic Printed Circuit Boards (PCBs) and tend to be more robust than electromechanical transducers such as encoders used for position measurement.

1.2 Sensorless Control at Low to Zero Speed

Sensorless algorithms within electrical drives aim to estimate and control the speed and position of electrical machines without having a dedicated sensor measuring these parameters. Typically, the algorithms calculate estimates based on current and voltage measurements from sensors which are still required for fundamental control of the machine thus having the advantage of not requiring additional sensors.

For this dissertation, AC machines were considered for the designated steer-by-wire application since these are generally considered to offer optimum performance-price characteristics for industrial applications. Sensorless algorithms have been widely used on AC machines prominently at medium to high speed. When operating in such a speed range, the position and speed of the machine can be estimated using model-based observers which tend to be simple to implement and provide robust measurements suitable for closed-loop control.

In the steer-by-wire application, the electrical machines are predominantly stationary with changes in position from the initial position. The application of sensorless algorithms for AC machines at zero speed is particularly challenging as the back-emf used in model-based observers is negligible, thus requiring a different approach. Zero sensorless speed control typically involves the tracking of high-frequency transients or continuous components, which are position-dependent. In this dissertation an innovative Search-Based Observer (SBO) is proposed which was tested with several continuous High-Frequency Injection (HFI) techniques.

1.3 Project Objectives

The main aim of this dissertation was to achieve robust sensorless control for a Permanent Magnet Synchronous Machine (PMSM) at low to zero speed. The PMSM

type chosen for this dissertation was found to have a magnetic signature which does not follow the fundamental single saliency model. The sensorless observers reviewed from literature are mainly based on single saliency tracking, thus they would fail at tracking the position for such a machine. Hence, the development of the SBO was required for use in the designated speed region.

For this project, High Frequency (HF) injection was used for saliency-based position detection. The SBO developed uses an innovative approach were the magnetic signature obtained from the amplitude of the resulting HF currents of the PMSM are mapped to a Look-up Table (LUT) with respect to rotor position, machine current, and rotor speed. The rotor position estimation is obtained by comparing the instantaneous HF currents with those previously commissioned in the LUT table. This approach is shown to be applicable for sensorless control of machines with multiple harmonic saliencies besides the fundamental component.

The magnetic signature of the machine was investigated under both continuous rotating and pulsating HF injection. An analysis was carried out, which shows that pulsating injection is more suitable for the SBO because it offers several injection angles in the stationary frame from which a suitable one for sensorless control can be chosen. The selection of a suitable injection angle for sensorless control was based on statistical parameters such as Signal-to-Noise (SNR) ratio and sensitivity which differentiate between magnetic signatures.

Experimental results for different operating load and speed conditions are presented for sensorless current, speed and position control. Different reference inputs are used for both generic machine control and the steer-by-wire application. The dissertation layout and the contents of each chapter in the dissertation are presented in Section 1.4.

1.4 Novel Contributions

This dissertation investigates the performance of sensorless low to zero speed control for both steer-by-wire and general industrial applications. The main novel contributions are:

- The use of sensorless speed/position control and estimation algorithms applied to the steer-by-wire application is an original concept. The use of sensorless methods in this particular application has not been previously reported in literature. The results reported and discussed in this dissertation show that the

proposed methods can be used for both open-loop estimation and also closed-loop control in case of an encoder fault.

- The search-based observer method proposed is a novel approach which allows for sensorless control of the electrical machine by using additional HF signal injection. The resulting HF position-dependent current amplitudes are distorted by multiple saliencies. The method uses all the saliencies present to derive a distinct fingerprint for each machine to achieve position estimation, rather than filtering or selecting a limited amount of saliency components.
- Furthermore, the search-based method is commissioned in such a way to integrate the saliency of both the rotor and stator under different operating conditions. This differs from most sensorless methods available in literature which predominantly investigate the effects of the stator saliency.

1.5 Dissertation Layout

Chapter 1 gives an introduction to the steer-by-wire application and outlines the proposed solution of using a sensorless low to zero speed observer for position estimation. A short review of sensorless algorithms normally adopted in this operating range is given, and the challenges of obtaining a robust position estimate are discussed. A brief overview of the innovative SBO proposed in this dissertation is provided with the critical objectives in this dissertation identified.

Chapter 2 presents a literature review on steer-by-wire technology, applications and characteristics. The generation of suitable force feedback and safety requirements within the system are discussed. Experimental tests were carried out on a test vehicle and steering results for various vehicle speeds and turning conditions are shown. The formulation of a simplified torque reference characteristic is discussed with respect to the handwheel position.

Chapter 3 discusses the selection of a suitable machine for the steer-by-wire application by comparing several types of machines, mainly those of AC construction. The mathematical modelling for the PMSM chosen is shown with derivations for current, speed and position transfer functions as required within a Rotor Flux Oriented (RFO) control topology. Experimental results for sensored current, speed and position control of the PMSM are given under dynamic load conditions.

Chapter 4 presents a literature review on sensorless algorithms, which are sub-divided into those algorithms based on fundamental frequency signals and those based on frequencies higher than the fundamental. Various model-based estimation techniques are briefly discussed. However, these were not considered for steer-by-wire since they are intended mainly for high-speed operation. An overview of non model-based estimation techniques was given with an emphasis on commonly used methods such as transient injection, PWM transient tracking, and continuous HF Injection. The mathematical modelling for each of these approaches is given with reference to position estimation.

Chapter 5 describes the experimental system and sub-systems used in this dissertation. The experimental setup of the two PMSMs used to investigate sensorless control is described, and its practical limitations are discussed. The microcontroller firmware used for the sensorless implementation is also briefly explained. The custom-designed PCBs for this dissertation are also shown. These boards mainly include the STM32 shield, gate drivers, saliency measurement, power inverters and encoder interface.

Chapter 6 discusses the magnetic saliency of the PMSMs chosen for the experimental system in this dissertation. Experimental measurements with continuous rotating injection have shown that multiple harmonics exist in the saliency. The magnetic signature is investigated in further detail with a continuous pulsating injection, at different current and speed operating points. The compensation of the identified harmonics with Space Modulation Profiling (SMP) was discussed and shown to pose significant limitations to real-time commissioning of the sensorless observer.

Chapter 7 presents the innovative SBO technique and the selection of suitable magnetic signatures for sensorless control. Deviation and gradient parameters are defined, which are based on statistical calculations which measure SNR and sensitivity of the different magnetic signatures obtained through pulsating injection. The SBO was consists of three processes: commissioning, search and Speed LUT selection Phased-Locked Loop (PLL).

Chapter 8 introduces the sensorless current control of the PMSM with the SBO. The performance of the sensorless drive was tested under four quadrants of operation with results obtained for mechanical and electrical rotor position, position estimation error,

rotor speed, synchronous frame current and HF current amplitudes. Sensorless current operation is investigated from no-load to full load condition.

Chapter 9 extends sensorless operation with the SBO to speed and position control. Sensorless speed operation is investigated at low and zero speed, for forward and reverse rotation. The various current operating points were tested from no-load to full load condition. Sensorless position control was tested with step-type inputs in both no-load and loaded conditions. Experimental measurements for mechanical and electrical rotor position, position estimation error, rotor speed, synchronous frame current and HF current amplitudes are given for both sensorless speed and position states.

Chapter 10 shows the application of the SBO applied to the steer-by-wire application. Sensorless control is shown for both current control at the handwheel and position control at the steered wheel side. Tests are carried out for different current gains through which the torque in the system is adjusted. The position demands used in this chapter reflect the experimental measurement obtained on the test vehicle in Chapter 2.

Chapter 11 summarizes the main results obtained in this dissertation and conclusions for the project are given. Comparisons with the steering measurements obtained from the test vehicle are presented, and possible improvements in both control algorithms as system hardware are provided.

Chapter 2 – Steer-by-Wire Application

2.1 Introduction

The steer-by-wire application is introduced in this chapter and its advantages and disadvantages over conventional steering arrangements presented. The force feedback at the handwheel, which is necessary to provide an authentic driving feel is also discussed. The safety requirements for the steer-by-wire application are identified from literature, and the relevance to this research is highlighted. Given the complexity associated with modelling steering arrangements, an experimental system characterization of the steering system at the driver side is presented which was carried out on a test vehicle.

2.2 Steer-by-Wire Technology

The proposition of control-by-wire systems in automotive applications came about with the improvement and acceptance of electrical/electronic technology in the automotive sector. The embedding of signal and power electronics has already resulted in the development and utilization of throttle-by-wire and brake-by-wire. This has led to the idea of an all electronically controlled car where all the driver's inputs such as throttle, brake and steering are not directly mechanically coupled but measured through sensors and driven electrically through the use of appropriate drive mechanisms [1-3].

By-wire technologies have been shown to offer significant advantages over their traditional counterparts found in previous-generation automobiles; these include [4, 5]:

- Throttle-by-wire offers a better fuel economy and reduced gas emissions.
- Brake-by-wire reduces the risk of skidding and loss of control.
- Steer-by-wire decreases the volume required for the steering arrangement, and the placement of the handwheel is not restricted.

Of all the aforementioned 'by-wire' systems, steer-by-wire is the most challenging to implement due to the various components needed and due to the critical safety nature of the application. In order to guarantee the widespread use of the technology, the resultant steer-by-wire systems must be both fault-tolerant and have a response which is comparable to traditional power steering arrangements already available on the market [6]. The basic principle of the steer-by-wire system is that the traditional column

connecting the handwheel to the rack and pinion arrangement which drives the wheels is eliminated. This is replaced by a system of sensors and electric drives which replicate the feel of a mechanically coupled system. The dynamic response, according to the steering capabilities of a driver for different production vehicles, was researched in [7]. Sensors, actuators and controllers must be chosen and designed in order to track rates of change in the steering position typical of steer-by-wire.

2.3 Steer-by-Wire in Automotive Applications

Although the steer-by-wire system aims to eliminate some of the mechanical linkages within the traditional steering mechanism; it still attempts to replicate the steering feel, especially at the driver's end. Conventional steering equipment consists of a kinematic chain with various components [1]: the handwheel, the column, the shaft, the pinion, the rack, the tie rods, the arms and finally the steered wheels (Figure 2.1). This linearized steering arrangement can be represented with transfer functions in the s-domain (Figure 2.2).

Relevant mechanical parameters within a conventional steering arrangement are the moments of inertia of the handwheel and steered wheel (J_h and J_s), viscous friction coefficients (B_h and B_s), shaft torsional friction K_f and damping coefficient C_f. The effect of the road surface on the steered wheel is modelled by a torque component T_e which is commonly referred to as the environment torque. The input torque applied by the driver on the handwheel is denoted as T_d. In order to position the wheels at the desired setpoint a steering torque, T_s is applied while a reaction torque T_r is exerted by the steering arrangement at the handwheel. The handwheel position is denoted as θ_h while the steered wheel position is denoted as θ_s. The torque ratio denoted as $1/N_{Th}$ is the ratio of T_r / T_s while the angle ratio $1/N_{\theta h}$ is the ratio θ_s / θ_h. The value of the two ratios is equal and is determined by the rack and pinion, tie rod and arm leverage arrangement.

In a steer-by-wire system, the mechanical arrangement is simplified (Figure 2.3) by the introduction of two electrical machines at the handwheel and steered wheel side. Machine M1 is typically current-controlled to provide the reaction torque T_r. Machine M2 is typically position-controlled to provide the steering torque T_s. The steering torque T_s is significantly higher than the reaction torque T_r (through the ratio N_{Th}), such that for a direct drive system, the power rating of machine M2 is higher than M1.

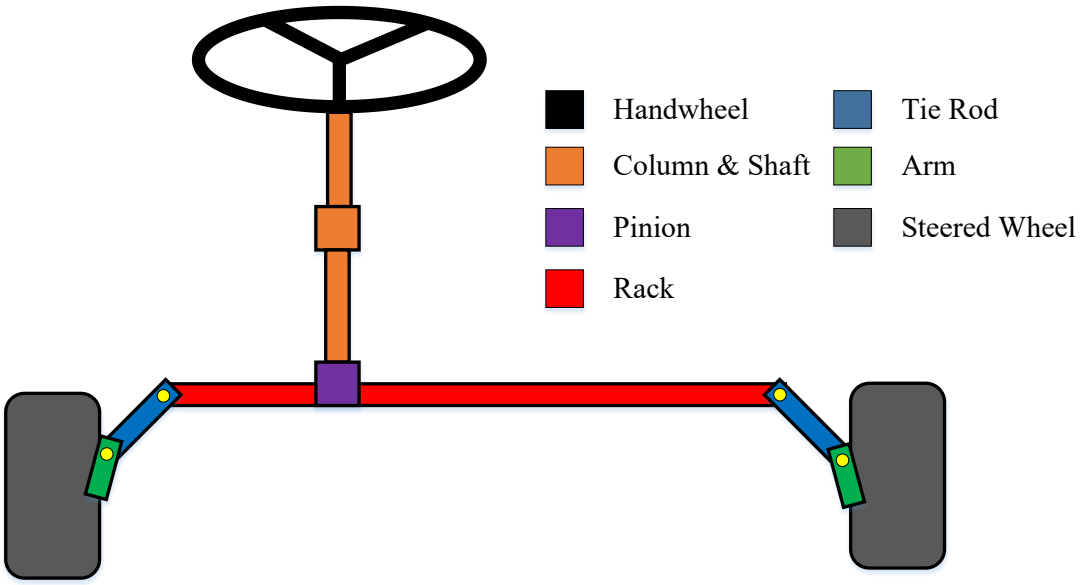

Figure 2.1 – Conventional Steering Arrangement

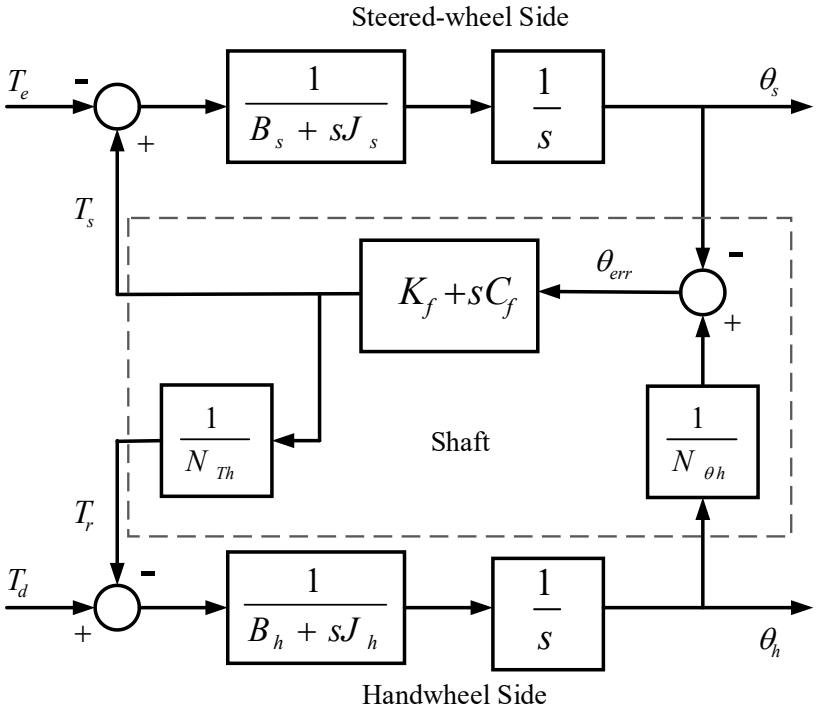

Figure 2.2 - Transfer Function Model for Conventional Steering Arrangement

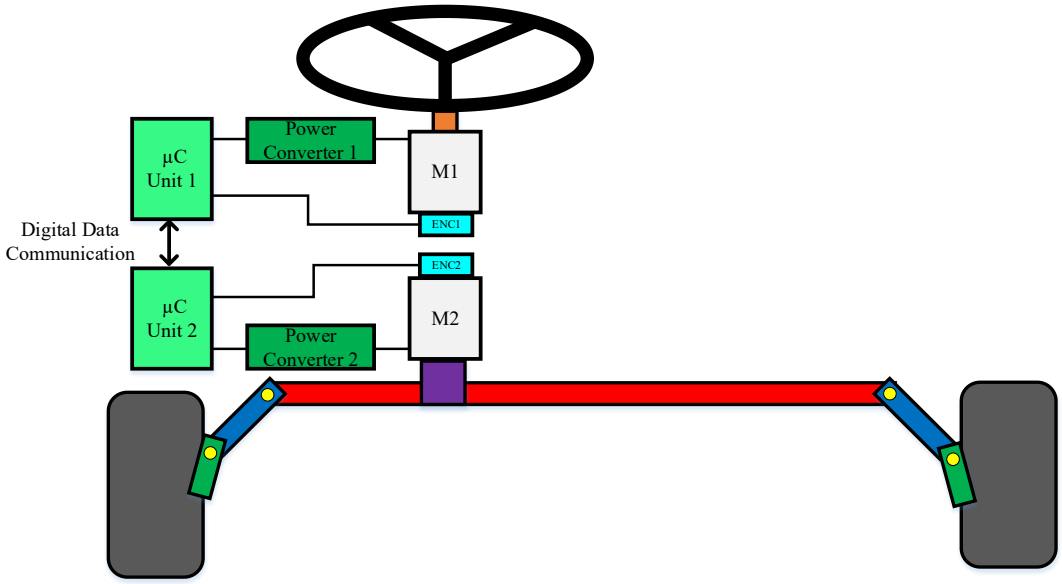

Figure 2.3 - Steer-by-Wire System

2.4 Steer-by-Wire Characteristics

Steer-by-wire technology is an active area of research in the field of automotive electronics. The advantages and disadvantages of implementing the system in production vehicles are listed in Sections 2.4.1 and 2.4.2 respectively.

2.4.1 Steer-by-Wire System Advantages

- The absence of the steering column simplifies the interior car design and allows car designers more creative freedom. Since signals are transferred electronically and not mechanically, the handwheel does not necessarily have to be fixed on the dashboard [4, 8-10].
- The absence of the steering shaft, column and gear reduction mechanism allows for better utilization of the engine compartment. Significant reductions in the volume required by the steering mechanism have been shown [4, 8-11].
- Without the mechanical, physical connection between the handwheel and the steered wheel arrangement, it is less likely that the impact produced by a frontal crash will cause the steering wheel to invade the driver's space. This significantly reduces the occurrence and seriousness of injury to the driver [8-12].
- The steer-by-wire system dynamics can be easily adjusted to optimize steering response and driver comfort. This is possible by modifying the force feedback

being generated through the controller unit and having independent handwheel and road wheel arrangements [1, 8, 11, 13, 14].

- The steer-by-wire system eliminates the need for hydraulic fluid in the steering arrangement system, and hence it is a cleaner alternative. The risk of hydraulic fluid leaking in the steering section is completely eliminated [1, 9, 10, 13, 15].
- Reduction of noise and vibration through the elimination of the hydraulic pump [11, 16].

2.4.2 Steer-by-Wire System Disadvantages

- In the steer-by-wire system, there is a complexity in generating authentic force feedback at the handwheel which emulates that of a mechanically coupled system and which has the same effects on the driver [9, 15, 17].
- In order for the widespread implementation of steer-by-wire in production cars, the system must have the same performance or preferably outperform conventional mechanical coupled systems [1, 6].
- Steer-by-wire without any mechanical backup is the most complex of the by-wire systems. Comparably other by-wire systems such as shift-by-wire, throttle-by-wire and brake-by-wire are at an advanced integration stage in production cars; while steer-by-wire is still in its preliminary stages [13, 18].

2.5 Force Feedback

In the steer-by-wire context, one of the most challenging issues is that of generating realistic force feedback at the handwheel which gives an authentic driving feeling to the driver when compared to conventional hydraulic or electrically assisted steering systems [10, 19]. Hence given the importance of this area in steer-by-wire; the generation of realistic forces is a popular topic of research in literature [20-24].

There are various methodologies in which a reference for the force feedback can be generated. This force feedback replicates the forces generated by the column and rack and pinion at the handwheel. In a steer-by-wire system, the force feedback or reaction torque is generated by machine M1 (Figure 2.3), which is typically in a current-controlled mode. One of the most common approaches to generate force

feedback is through model-based systems [13, 25, 26]. Given that the mechanical constants of a system such as the moment of inertia and coefficients of friction can be approximated, the force feedback can be calculated using mathematical models. Models for creating artificial steering feel with high fidelity to traditional steering systems requires modelling for complex effects such as alignment torque and jacking torque [13, 19, 27]. The complexity of such mathematical models requires the use of a high-end controller unit which increases the overall system cost.

In order to possibly use a less powerful controller unit, researchers have also suggested the use of a torque-map based method to eliminate the need for real-time calculation [21, 28]. The torque-map is basically a Look-Up Table (LUT) where the torque value is selected from a range of pre-set values depending on a number of independent variables; mainly vehicle velocity and handwheel angle. For a more accurate emulation of the forces at the road wheel, it has also been proposed to include a torque sensor at the steered wheel side of the steer-by-wire setup [28, 29]. The advantage of having an actual sensor measuring the torque at the output of the system eliminates the need for mathematically modelling the different forces. However, there are a number of disadvantages which include the cost of the torque sensor which will significantly increase the cost of implementation of the steer-by-wire system and the harsh operating automotive environment in which the sensor will be used. Researchers have attempted to replicate the benefits of having a torque measurement by estimating the torque via a direct current measurement at the steered wheel side motor (machine M2 in Figure 2.3). The advantage of this approach is that the complexity of mathematical modelling is still reduced while there is no need for additional sensors since the current sensors will still be required for typical motor control operations.

Model-based feedback estimation includes a number of parameters associated with the steering system which are not typically considered when using other methods such as the torque map-based approach. As with any model-based estimation system, the numerous system constants are assumed constant while they are susceptible to real-time variations. Typically, the errors introduced by these variations are not significant; however, they still deteriorate system performance and are difficult to quantify or compensate for in real-time.

2.6 Safety Analysis in Steer-by-wire System

Since the aim of steer-by-wire research was to develop systems robust enough for production purposes, it is not surprising that safety is one of the top priorities in related technical literature [30-35]. An error in the overall system can have severe effects. Due to the increased safety-critical dependence of automotive vehicles on hardware and software integrity governmental institutions and automotive awarding bodies have set up strict standards which need to be adhered to such as MISRA, MIL-STD-882B, IE661508 and DO-178B.

While denoting safety in the steer-by-wire system, it is essential to distinguish between safety and reliability. System reliability is a measure of whether a particular task is performed within a specific target such as time; while system safety is about ensuring that an accident does not occur. The overall safety-critical requirements for the steer-by-wire application were identified by Pimentel [30] as follows:

1) *Failure mode requirements* which involve reducing the occurrence of a set of identified failure modes.
2) *Safety goal requirements* which involve using specific procedures to ensure safety in terms of recoverability and fault tolerance.
3) *Value domain requirements* which involve the verification of the expected ranges for physical system variables such as the handwheel angle θ_h and the steering angle θ_s.
4) *Development environment requirements* which are a unique set of requirements which are not intended for consumer end safety but at the development and testing stage.

The failure modes for the steer-by-wire system are:

1) The steered wheel does not follow the handwheel
2) The steered wheel turns without a command from the driver
3) No force feedback is given to the handwheel

The above failure modes can be a result of a number of underlying principles; however, the most common sources are:

1) Failure of the encoder measuring the handwheel angle θ_h or steered wheel angle θ_s.

2) Failure of the current/torque sensors at the handwheel side motor or steered wheel side motor.

In order to reduce the possibility of system failure, the introduction of redundant measurement systems is recommended. The main aim of this dissertation is to research the application of sensorless algorithms as a redundant measurement system. Sensorless algorithms are aimed at the estimation of the motor positions θ_h and θ_s without the use of an encoder. While it is unlikely that the position estimates $\hat{\theta}_h$ and $\hat{\theta}_s$ will be more accurate than the angles θ_h and θ_s produced by a high-resolution encoder; the estimates can provide an expected range of values for the encoder measurements which can be used for validation. When the discrepancy between the values of the encoder and the estimation algorithm is more than a specified amount of degrees, a fault condition is triggered. The sensorless algorithms developed as part of this dissertation should allow for the complete changeover to a sensorless control mode once detection of a fault occurs; without significant degradation in both steering dynamics and torque/force feedback to the driver.

2.7 Experimental Force Feedback Characterisation

The complexity of modelling force feedback in such a way to replicate an authentic feeling at the driver's end was highlighted in Section 2.5. In this dissertation, a simplified position-dependent force feedback model is proposed based on experimental data logging which was carried out on a test vehicle. The data was logged through the diagnostics port of a vehicle fitted with an electrical-based power steering arrangement as described in Section 2.7.1.

2.7.1 Road Vehicle Steering Experiments

The characterization of the steering arrangement was carried out on a Kia Sportage 2014 test vehicle (Figure 2.4) which has embedded Electrically Power Assisted Steering (EPAS). The control of the EPAS requires a number of sensors such as position sensors, torque sensors and vehicle velocity sensors. The data from these sensors amongst others can be accessed through an On-Board Diagnostics (OBD) II port (Figure 2.5).

Figure 2.4 – Kia Sportage 2014 Test Vehicle

Figure 2.5 – Kia Sportage 2014 OBD-II port connection

The test vehicle was driven from 10 km/h to 40 km/h in steps of 10 km/h with varying handwheel angles θ_h from 10° to 40° in both clockwise and anti-clockwise directions. Higher velocity and steering angles were not possible due to safety considerations as these tests were carried out on in normal driving conditions. The setting of the vehicle speed and handwheel tilt angle varies between experiments as these were set manually by the driver. The experimental data logged for vehicle velocity, steering wheel angle and steering wheel torque by the on-board diagnostics unit at a sampling rate of 13.3 Hz are shown in Figures 2.6 – 2.9. A test with the same road vehicle while steering in a roundabout with approximate vehicle velocity setpoints of 10 km/h and 20 km/h is shown in Figures 2.10 – 2.13.

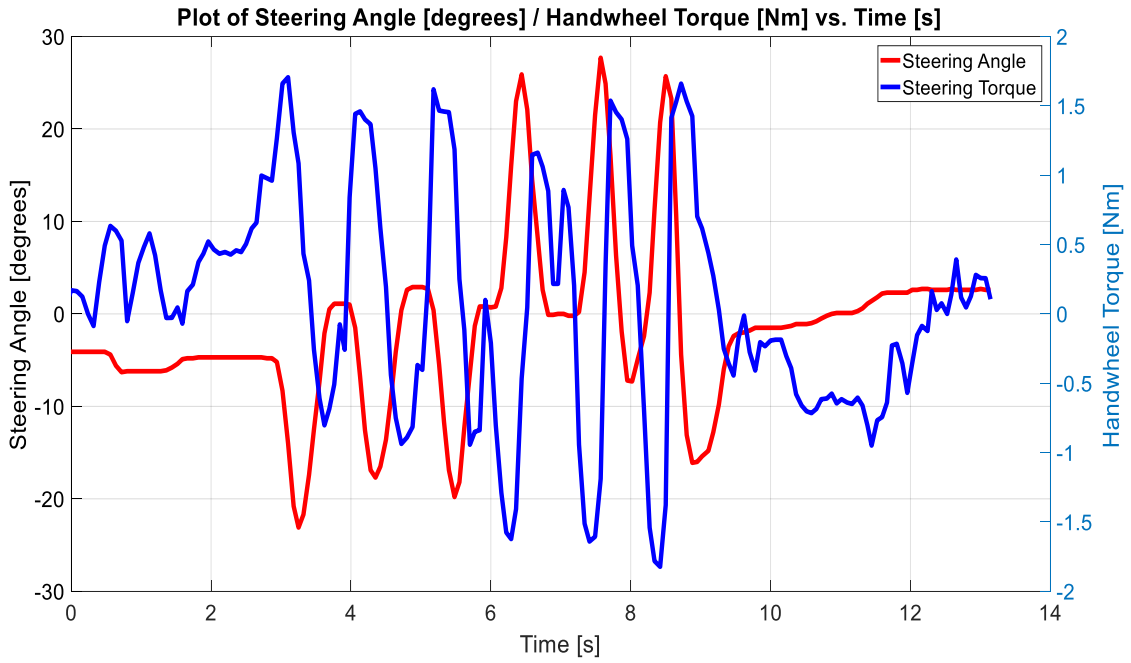

Figure 2.6 – Plot Steering Angle [degrees] / Handwheel Torque [Nm] vs. Time [s], with a vehicle speed of approx. 10 km/h and angle tilt approx. 20 degrees.

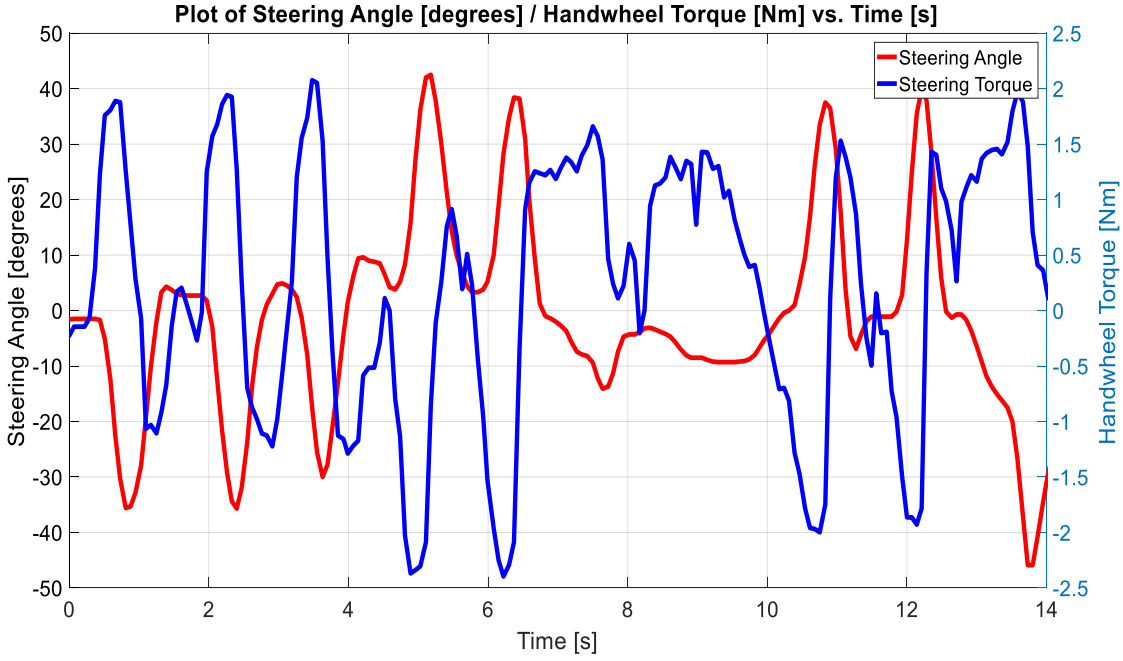

Figure 2.7 – Plot Steering Angle [degrees] / Handwheel Torque [Nm] vs. Time [s], with a vehicle speed of approx. 20 km/h and angle tilt approx. 40 degrees.

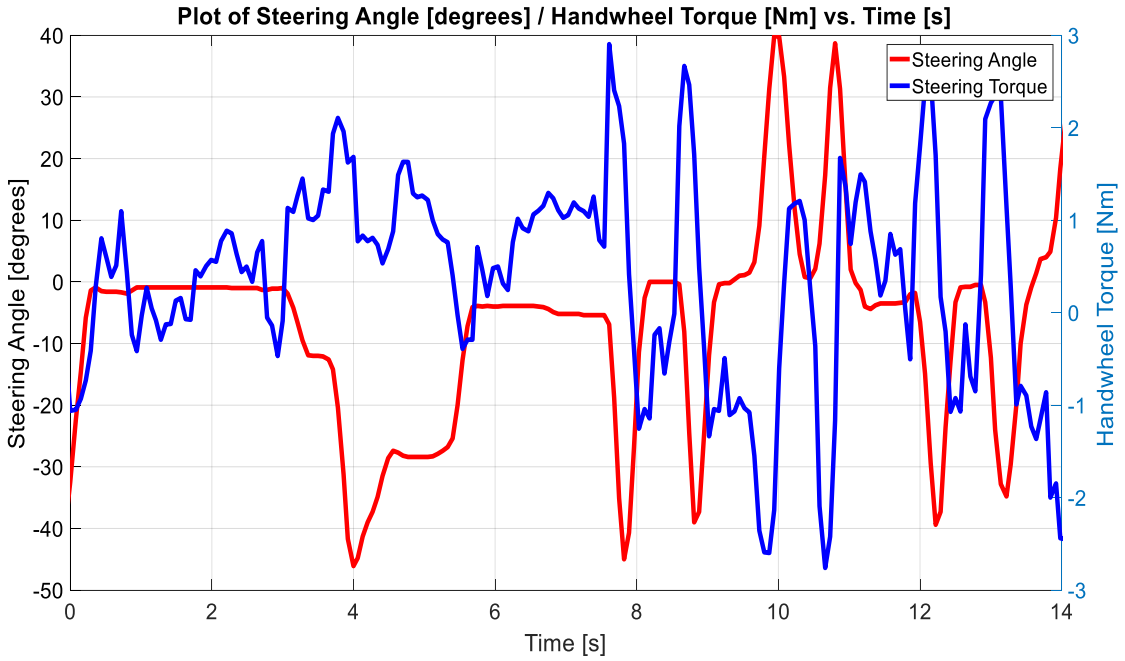

Figure 2.8 – Plot Steering Angle [degrees] / Handwheel Torque [Nm] vs. Time [s], with a vehicle speed of approx. 30 km/h and angle tilt approx. 40 degrees

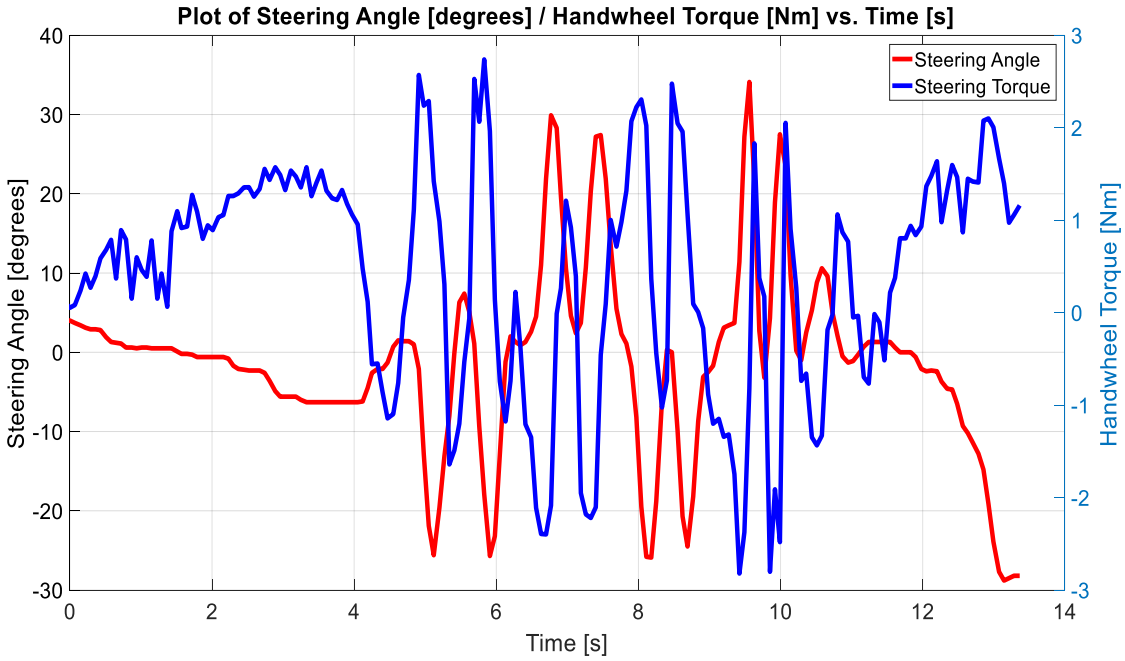

Figure 2.9 – Plot Steering Angle [degrees] / Handwheel Torque [Nm] vs. Time [s], with a vehicle speed of approx. 30 km/h, and angle tilt approx. 30 degrees.

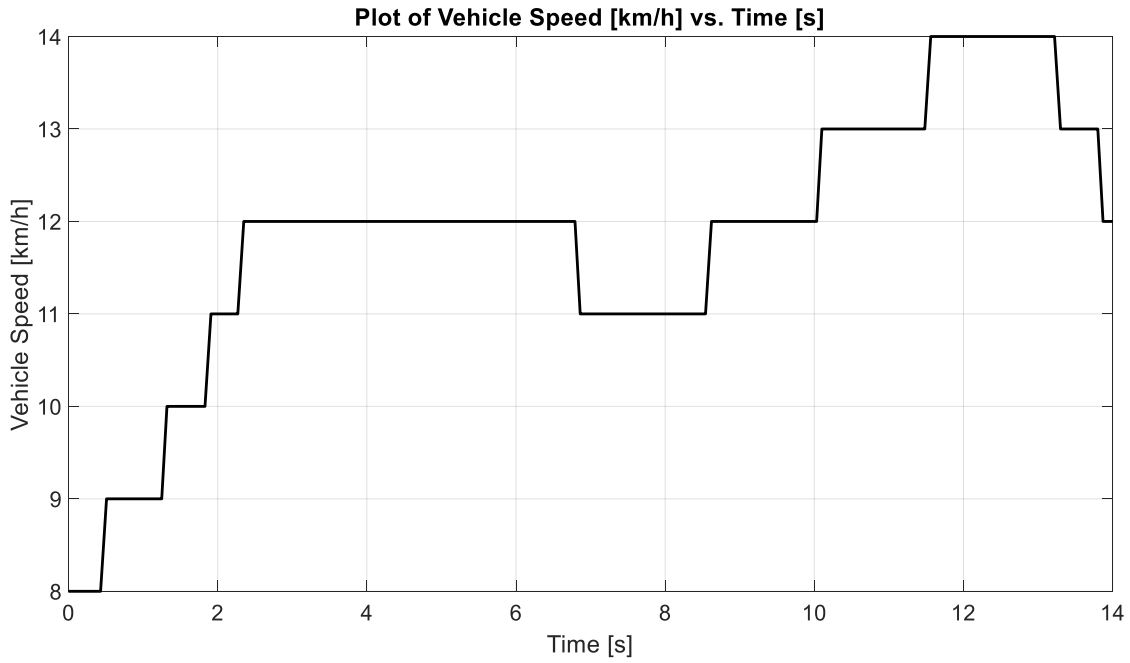

Figure 2.10 – Plot Vehicle Speed [km/h] vs. Time [s], with a vehicle speed setpoint of approx. 10 km/h and angle tilt for roundabout turn.

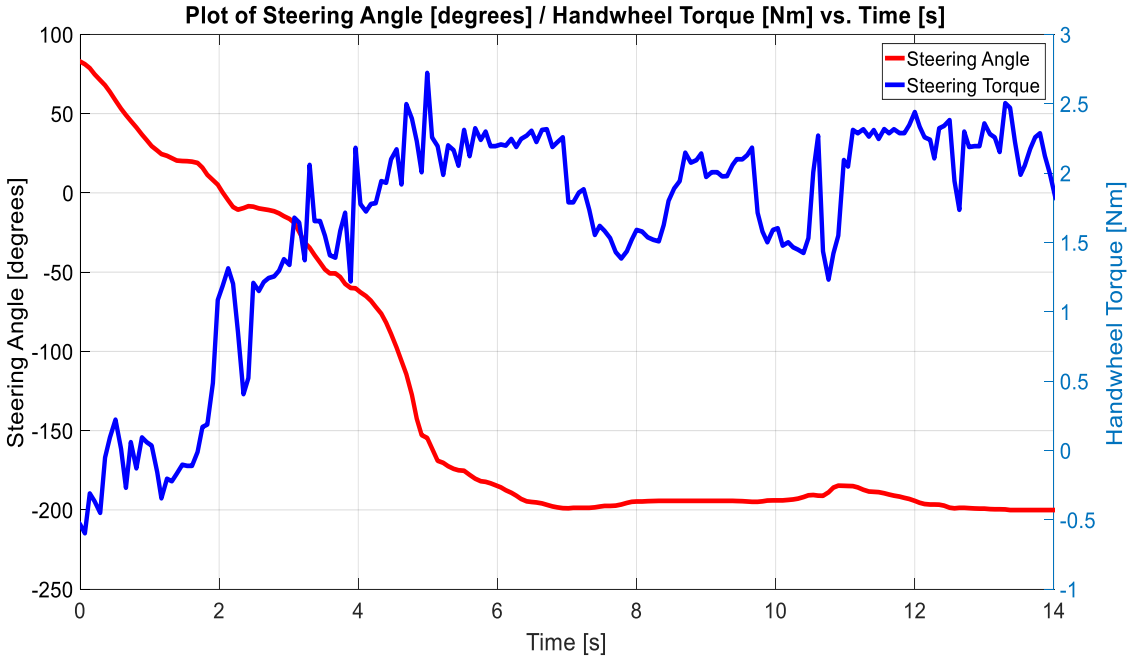

Figure 2.11 – Plot Steering Angle [degrees] / Handwheel Torque [Nm] vs. Time [s], with a vehicle speed setpoint of approx. 10 km/h and angle tilt for roundabout turn.

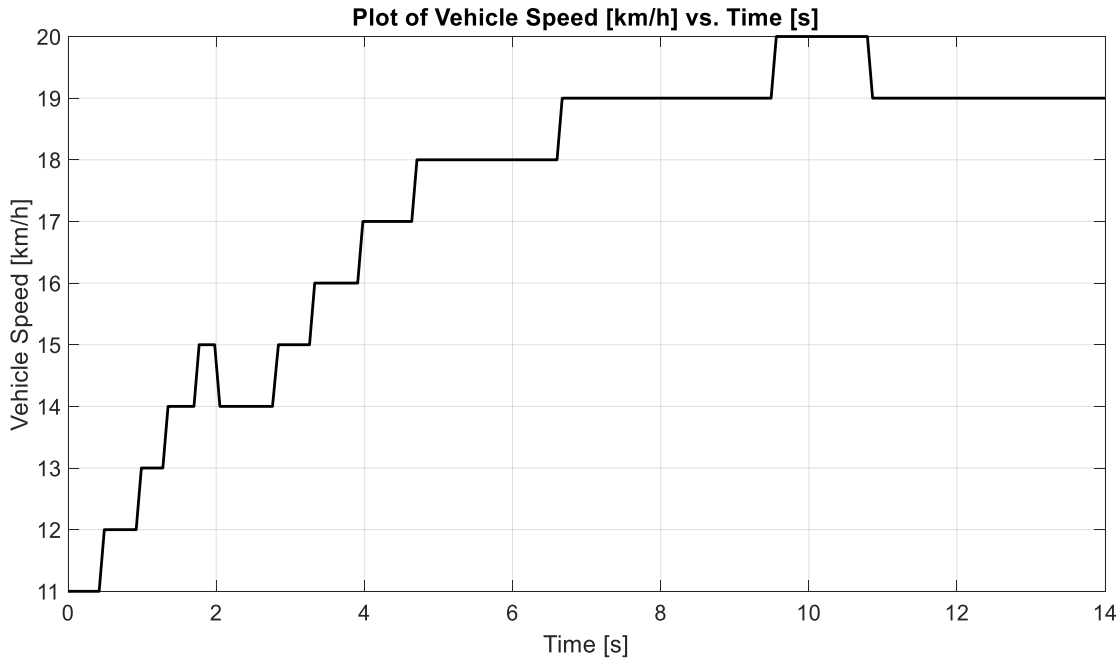

Figure 2.12 – Plot Vehicle Speed [km/h] vs. Time [s], with a vehicle speed setpoint of approx. 20 km/h and angle tilt for roundabout turn

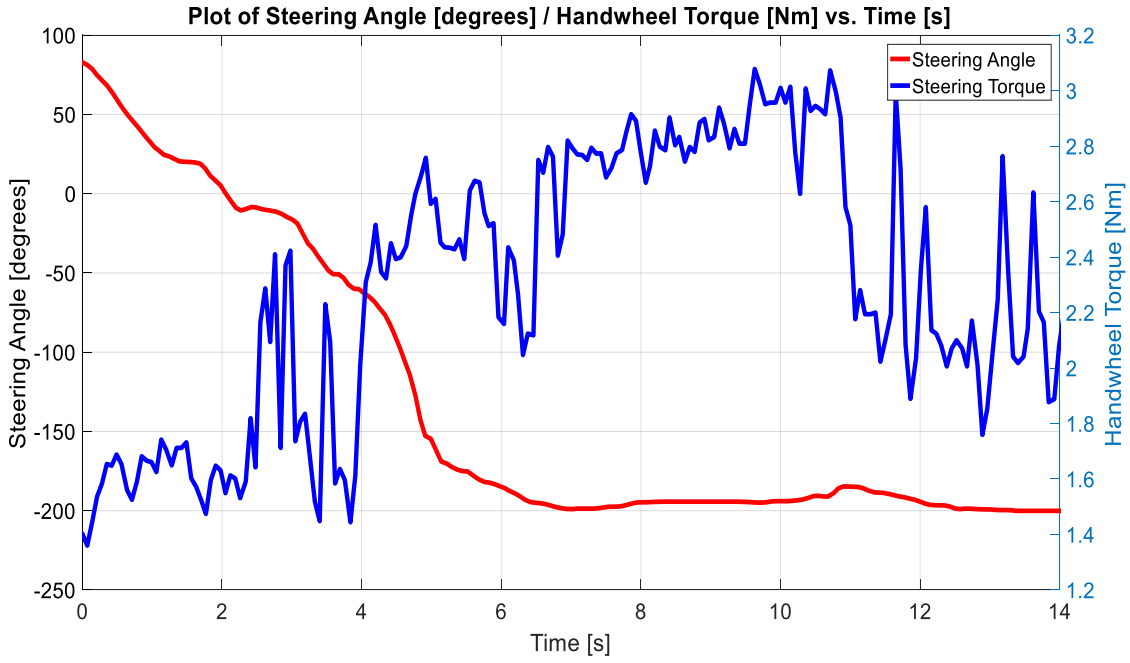

Figure 2.13 – Plot Steering Angle [degrees] / Handwheel Torque [Nm] vs. Time [s], with a vehicle speed setpoint of approx. 20 km/h, and angle tilt for roundabout turn.

2.7.2 Force Feedback Characterization

From the experimental results presented in Figures 2.6 – 2.9 it was observed that the torque produced by the EPAS motor always opposes the direction of motion of the handwheel such that it returns to a centre zero position if no torque is applied by the driver. The exact model for the torque output is not linear and is multi-variable as described in Section 2.5 dependent on steering position, rate of change of steering position and vehicle velocity. From the experiments carried out in this research the maximum torque for each set of experiments was found to vary linearly at low steering angles; while being limited to a value of 2-3 Nm for angles approximately larger than ±20°. This was also observed while steering in a roundabout, as shown in Figures 2.10 – 2.13. The maximum steering rate for the test vehicle was found to be 286 degrees/s.

For the purposes of this research, a simplified model for the torque-handwheel position characteristic is proposed, as shown in Figure 2.14 to generate the force feedback as a function of the handwheel angle θ_h. The torque reference used on the current-controlled machine M1 in the steer-by-wire system is proportional to the handwheel angle θ_h for the range ±20°. For larger angles, the torque is limited to ±2 Nm opposing the direction of the handwheel angle. This torque model can be easily implemented in a vector controlled PMSM as the torque reference just has to be linearly scaled to the synchronous frame reference current i_q^*. The main advantage of this model is that it offers power on demand since stator currents are only applied to generate torque when a change from the initial position is detected. While the proposed model is not intended to replace more sophisticated mathematical models of the steering arrangement, it provides a more realistic testbench for the sensorless control in this dissertation.

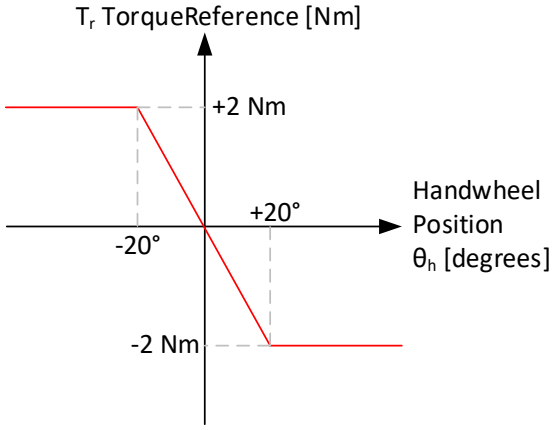

Figure 2.14 - Torque Reference–Position Generation Characteristic.

2.8 Summary

A review of steer-by-wire technology applied to automotive applications was reviewed in this chapter. The advantages and disadvantages compared to the conventional steering arrangement were also highlighted. An s-domain model of the steering system of a vehicle was shown in Figure 2.2. The reaction torque T_r is generated by the handwheel machine (M1 in Figure 2.3) and the steering torque T_s is generated by the steered wheel machine (M2 in Figure 2.3). The operation of the steer-by-wire system was identified as being dependent on position measurements at both ends of the system such that the integrity of the encoders is safety-critical to the application.

The methods in literature used to improve the functional safety of steer-by-wire were found to rely mostly on redundant hardware. Overcoming the cost and complexity of this additional hardware is one of the aims of this dissertation. Hence, it was proposed to provide additional independent measurements through sensorless algorithms. Such algorithms estimate the position and speed using data from sensors which are already integrated into the electric drive for fundamental sensored operation.

Experimental steering results for the vehicle velocity, steering angle and steering torque were shown for a Kia Sportage 2014 test vehicle; these were obtained through data logging through the OBD-II interface. The maximum steering rate was found to be 286 degrees/s while the torque generated by the EPAS electric motor is typically within the range ± 2 Nm with peaks at ± 3 Nm. From these experimental results**,** a simplified model was proposed to generate a torque reference as a function of the handwheel position.

The measurements obtained from the experimental vehicle were used to generate references at both sides of the steer-by-wire system. This allows for a more realistic analysis of the transient and steady-state performance of the sensorless algorithms within a steering scenario. The accuracy of sensorless estimates is typically dependent on the load of the machine under test. Therefore the simplified torque-reference position model was used to also provide more representative load conditions.

Chapter 3 – Sensored Control of Permanent Magnet Synchronous Machine

3.1 Introduction

This chapter is dedicated to the control technique used for the current, speed and position control of the Permanent Magnet Synchronous Machine (PMSM). The selection of the PMSM for steer-by-wire systems is also presented. The characteristics of PMSMs are compared to other types of commonly used electrical machines. The electrical and mechanical dynamic equations of a general PMSM are derived. These equations are the basis for Rotor Flux Oriented Control (RFO). The design of a cascaded control system consisting of cascaded current, speed and position loops is shown with suitable dynamics for the steer-by-wire application. Experimental results demonstrating the performance of each of the closed-loop controllers within the cascaded RFO architecture are presented.

3.2 Permanent Magnet Synchronous Machine Modelling

3.2.1 Selection of Machines for Steer-by-Wire systems

In several steer-by-wire implementations, researchers have opted to use brushed DC motors or brushed DC-based servo drives for providing the force feedback at the handwheel and position control at the steered wheel side [9, 10, 22]. The main aim of these studies was to investigate the performance of tracking and steering algorithms rather than to develop practical industry-grade solutions. Hence, the drawbacks of having a DC machine-based drive in automotive applications were not considered.

Brushed DC machines are still common in control and robotic applications as they do not require complex control algorithms. The speed of DC machines of the permanent magnet type in motoring mode can be easily controlled through the voltage applied to the motor's armature. High torque and low current profiles can also be obtained. However, there are also disadvantages which make the brushed DC machines unsuitable for the steer-by-wire system, which include [36]:

- A bulky construction compared to similarly rated motors of the induction or synchronous type. This is a significant drawback in steer-by-wire as one of the targets is to reduce the volume required for the steering arrangement to improve cabin space.

- Low efficiency and reliability.
- The requirement for regular maintenance due to the commutator and brushes.

Given the numerous drawbacks identified for the integration of DC machines in the steer-by-wire system, researchers have considered systems which use PMSMs for handwheel force feedback and roadside actuation [37-39]. In the quoted work, two types of permanent magnet synchronous motors have been used [40]:

- Surface-Mounted Permanent Magnet Synchronous Machine (SM-PMSM) where the permanent magnets are mounted on the rotor surface with a high strength adhesive (Figure 3.1).
- Interior buried Permanent Magnet Synchronous Machine (IPMSM) where the permanent magnets are embedded inside the rotor, unlike the SM-PMSM type. The IPMSM motor is more robust at high operating speeds than the SM-PMSM (Figure 3.2).

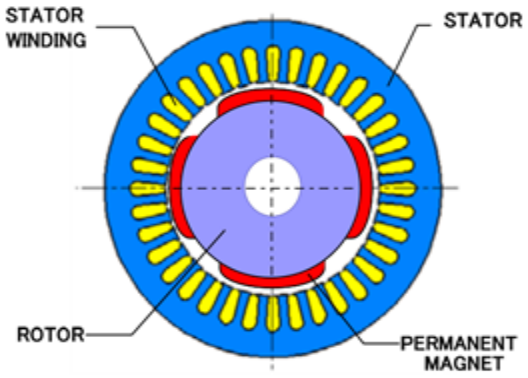

Figure 3.1 - SM-PMSM motor cross-section [40]

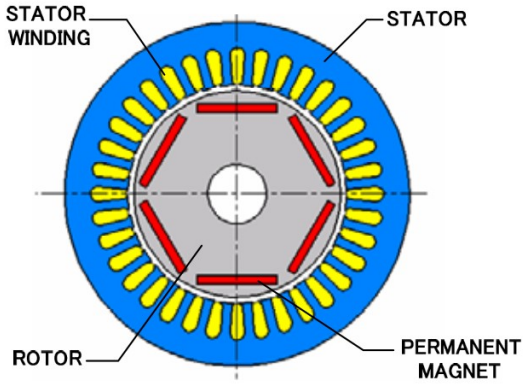

Figure 3.2 - IPMSM motor cross-section [40]

The increase in popularity of permanent magnet motors in industrial applications, in general, was brought about through the improvement in rare earth magnet material technology and reduction in cost. For the steer-by-wire application, permanent magnet synchronous machines offer the following advantages [36]:

- Higher efficiency and higher power density.
- Better heat dissipation characteristics than brushed DC and induction motors.
- No maintenance of commutator and brushes required.

Although the PMSM is more suitable for steer-by-wire applications than other motors, the design of the control algorithms and hardware is more complicated due to:

- PMSMs being multi-phase machines, where a current sensor is required per phase. This increases the cost and complexity of the power electronic circuitry necessary to drive the machine.
- While the speed of a DC brushed motor is generally proportional to the magnitude of the DC voltage applied to the motor; in a PMSM the speed of the rotor is a function of the stator flux frequency which is controlled by the frequency of the AC stator phase voltages.
- Sensing of multiple sensors and computation of algorithms such as vector control to operate the PMSM requires the use of an advanced microcontroller or DSP unit with sufficient computational power.

3.2.2 PMSM Dynamic Equations

In Section 3.2.1, the advantages of the PMSM for the steer-by-wire application were discussed. In this section, the mathematical model for a PMSM is derived. The mathematical model used for this dissertation is based on the typical modelling used in literature for PMSMs [41, 42]. The model for the PMSM is derived from the equation for the stator flux linkage in the dq-frame [43]:

$$\Psi_{sd} + j\Psi_{sq} = (L_d i_d + \Psi_{rd}) + jL_q i_q \quad (3.1)$$

Where:

Ψ_{sd} Stator flux linkage on the d-axis [Wb],

Ψ_{sq} Stator flux linkage on the q-axis [Wb],

L_d Stator inductance on the d-axis [H],

L_q Stator inductance on the q-axis [H],

i_q Stator current on the d-axis [A],

i_d Stator current on the q-axis [A],

Ψ_{rd} Stator flux linkage due to permanent magnets aligned to the rotor d-axis [Wb].

Consider the typical stator equation in the αβ-frame:

$$v_{\alpha\beta} = \mathrm{R}i_{\alpha\beta} + \frac{\mathrm{d}\,\Psi_{s_{\alpha\beta}}}{\mathrm{dt}} \tag{3.2}$$

Where:

$v_{\alpha\beta}$	Stator voltage in the αβ-frame	[V],
R	Stator resistance	[Ω],
$i_{\alpha\beta}$	Stator current in the αβ-frame	[A],
$\Psi_{s_{\alpha\beta}}$	Stator flux linkage in the αβ-frame	[Wb].

Equation (3.2) can be transformed into the dq-frame:

$$v_{dq} = \mathrm{R}i_{dq} + \mathrm{j}\omega_r\Psi_{s_{dq}} + \frac{\mathrm{d}\,\Psi_{s_{dq}}}{\mathrm{dt}} \tag{3.3}$$

Where:

v_{dq}	Stator voltage in the dq-frame	[V],
R	Stator resistance	[Ω],
i_{dq}	Stator current in the dq-frame	[A],
$\Psi_{s_{dq}}$	Stator flux linkage in the dq-frame	[Wb],
ω_r	Rotor Electrical Frequency	[rad/s].

Resolving (3.3) into d and q components results in (3.4-3.5).

$$v_d = \mathrm{R}i_d - \omega_r\Psi_{s_q} + \frac{\mathrm{d}\,\Psi_{s_d}}{\mathrm{dt}} \tag{3.4}$$

$$v_q = \mathrm{R}i_q + \omega_r\Psi_{s_d} + \frac{\mathrm{d}\,\Psi_{s_q}}{\mathrm{dt}} \tag{3.5}$$

Resolving (3.1) into d and q components results in (3.6-3.7).

$$\Psi_{s_d} = \left(\mathrm{L_d}i_d + \Psi_{r_d}\right) \tag{3.6}$$

$$\Psi_{sq} = \mathrm{L_q}i_q \tag{3.7}$$

Substituting (3.6) and (3.7) in (3.4)

$$v_d = \mathrm{R}i_d - \omega_\mathrm{r}\mathrm{L_q}i_q + \frac{\mathrm{d}\left(\mathrm{L_d}i_d + \Psi_{\mathrm{r_d}}\right)}{\mathrm{dt}} \tag{3.8}$$

$$v_d = \mathrm{R}i_d + \mathrm{L_d}\frac{\mathrm{d}\,i_{s_d}}{\mathrm{dt}} - + \frac{\mathrm{d}\,\Psi_{\mathrm{r_d}}}{\mathrm{dt}}\ \omega_\mathrm{r}\mathrm{L_q}i_q \tag{3.9}$$

Assuming $\frac{\mathrm{d}\,\Psi_{\mathrm{r_d}}}{\mathrm{dt}} = 0$ for the permanent magnet flux,

$$v_d = \mathrm{R}i_d + \mathrm{L_d}\frac{\mathrm{d}\,i_d}{\mathrm{dt}} - \omega_\mathrm{r}\mathrm{L_q}i_q \tag{3.10}$$

Substituting (3.6) and (3.7) in (3.5)

$$v_q = \mathrm{R}i_q + \omega_\mathrm{r}\left(\mathrm{L_d}i_{s_d} + \Psi_{\mathrm{r_d}}\right) + \frac{\mathrm{d}\,\mathrm{L_q}i_q}{\mathrm{dt}} \tag{3.11}$$

$$v_q = \mathrm{R}i_q + \mathrm{L_q}\frac{\mathrm{d}\,i_q}{\mathrm{dt}} + \omega_\mathrm{r}\mathrm{L_d}i_d + \omega_\mathrm{r}\Psi_{\mathrm{r_d}} \tag{3.12}$$

The equivalent circuit of the PMSM based on (3.10) and (3.12) is shown in Figure 3.3 [43].

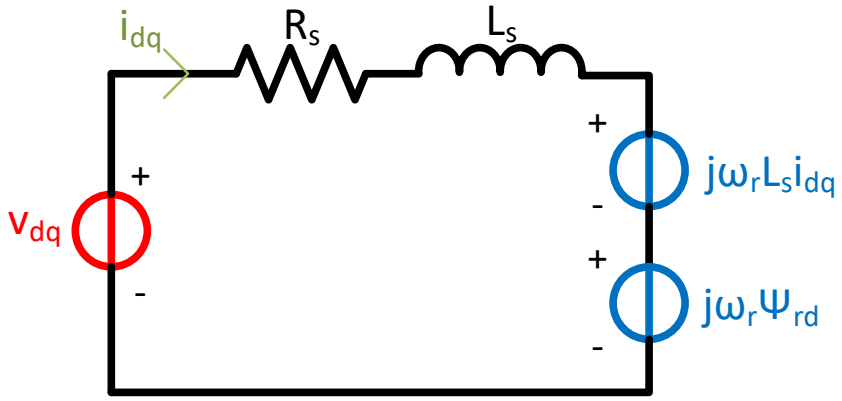

Figure 3.3 – PMSM dq-frame equivalent circuit [40]

3.2.3 Rotor Flux Orientated Control of the PMSM

In this research, Rotor Flux Orientated (RFO) vector control was used to control the PMSM due to its robustness over a wide operating range [44-46]. A typical position control topology using RFO is shown in Figure 3.4. This topology uses a cascaded controller approach with inner current control loops and outer speed and position loops. During speed control, only the speed control loop is used whilst for position control, both speed and position control loops are used. The controllers must be tuned and implemented in such a way that the inner loops are significantly faster than the outer loop.

In sensored mode, the ***mechanical*** rotor position, ***mechanical*** rotor speed and ***electrical*** rotor position from the encoder are used as feedback for each of the cascaded control loops. In sensorless mode, these measurements are obtained from the sensorless observer. Proportional-Integral (PI) controllers are used for the dq-frame current loops and the speed loop. A Proportional (P) controller is typically used to obtain the desired position control dynamics. Since the dq-frame electric transfer function derived in Section 3.2.4 removes cross-coupling terms, these can be added as feedforward terms to the PI current controller outputs. The stationary frame voltages (v_a, v_b, v_c) and current (i_a, i_b, i_c) require transformation between the stationary and synchronous frames, which is a function of the ***electrical*** rotor position. This accentuates the requirement for accurate position information to have a correctly oriented system with respect to the rotor magnets' flux.

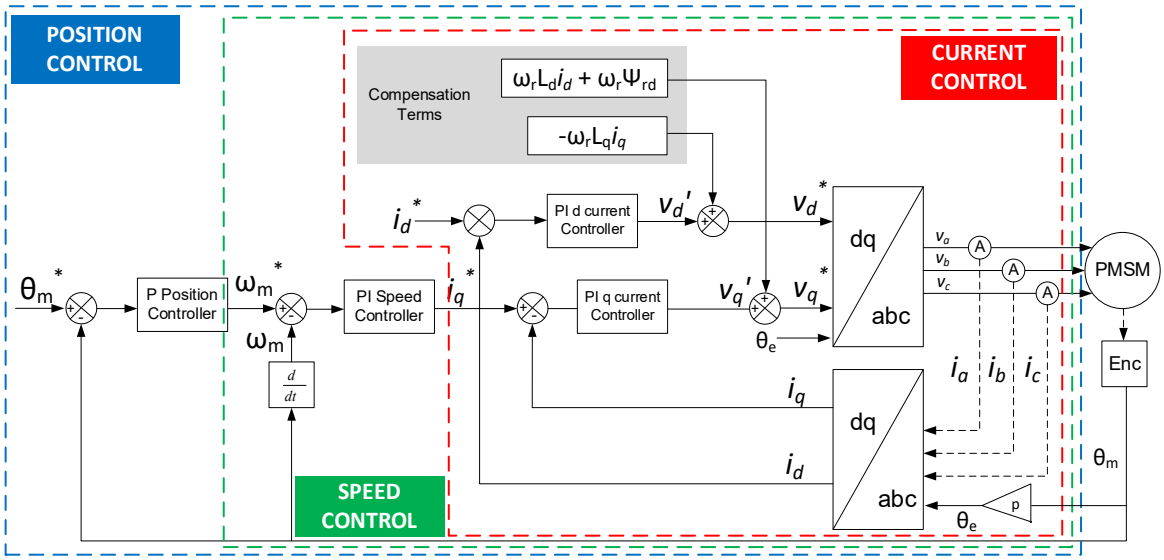

Figure 3.4 - Rotor Flux Orientated Position Control of PMSM

3.2.4 Current Controller Design

In order to tune the PI current controllers shown in Figure 3.4, the current transfer functions in the dq-frame of the PMSM were derived. These transfer functions can be obtained from the system equations derived previously in (3.10) and (3.12).

$$v_d = \mathrm{R}i_d + \mathrm{L_d}\frac{\mathrm{d}\,i_d}{\mathrm{dt}} - \omega_\mathrm{r}\mathrm{L_q}i_q \tag{3.10}$$

$$v_q = \mathrm{R}i_q + \mathrm{L_q}\frac{\mathrm{d}\,i_\mathrm{q}}{\mathrm{dt}} + \omega_\mathrm{r}\mathrm{L_d}i_d + \omega_\mathrm{r}\Psi_{\mathrm{r_d}} \tag{3.12}$$

These terms are eliminated from (3.10) and (3.12) to be eventually compensated for as feed-forward terms in the actual control system (Figure 3.4). Hence (3.10) and (3.12) can be written as:

$$v_d = \mathrm{R}i_d + \mathrm{L_d}\frac{\mathrm{d}\,i_d}{\mathrm{dt}} \tag{3.13}$$

$$v_q = \mathrm{R}i_q + \mathrm{L_q}\frac{\mathrm{d}\,i_q}{\mathrm{dt}} \tag{3.14}$$

Applying Laplace transformation to (3.13) and (3.14) results in:

$$\frac{I_d(s)}{V_d(s)} = \frac{1}{s\mathrm{L_d}+\mathrm{R}} \tag{3.15}$$

$$\frac{I_q(s)}{V_q(s)} = \frac{1}{s\mathrm{L_q}+\mathrm{R}} \tag{3.16}$$

The electrical machine parameters were determined from measurements on the drive since they were not provided with the technical dataset of the machine. R, L_d and L_q were calculated from the steady-state and transient responses in the synchronous dq-frame in locked-rotor conditions. Consider the application of a step reference in v_d^* = 1 V (4.2 % rated machine voltage) as shown in Figure 3.5. After the transient, the steady-state current i_d was measured at 4.07 A. The resistance was calculated to be R = 246 mΩ. Since the bandwidth was measured at f_{3dB} =92.0 Hz (assuming $f_{3dB} = \frac{0.35}{t_r}$, where t_r is the rise time from 10% to 90% of the steady-state value), the d-axis inductance was calculated at L_d = 426 µH.

To determine the value of the synchronous q-axis inductance L_q a similar approach was used by applying a step-input v_q^* = 1 V (4.2 % rated machine voltage) as shown in Figure 3.6. The value of R was assumed to be identical to that found in the d-axis. The resulting bandwidth was found to be f_{3dB} = 57.6 Hz such that the synchronous inductance L_q = 679 µH. From the resultant machine parameters listed in Table 3.1, a significant difference between the d and q axis inductances was noted. Although the experimental determination of parameters has limited accuracy, a factor of 1.6 was observed between L_q and L_d, which indicates that saliency is present on the test machine.

Parameter	Value
R	246 mΩ
L_d	426 µH
L_q	679 µH

Table 3.1 - PMSM Electrical l Parameters

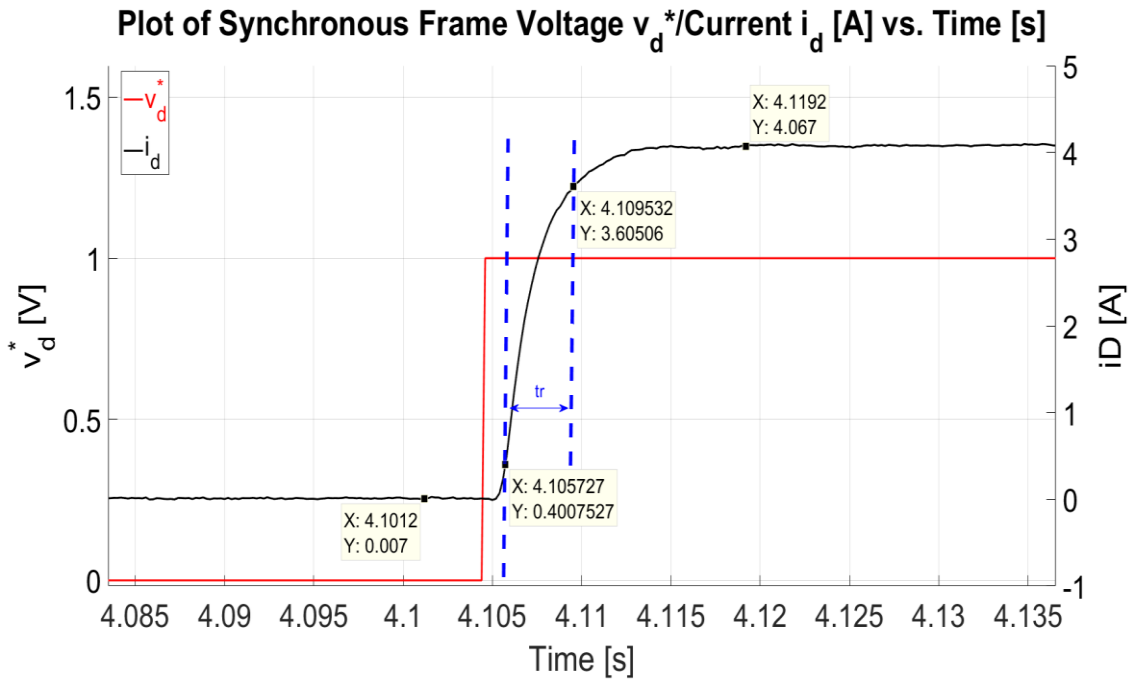

Figure 3.5 - Plot of v_d^* [V] and i_d [A] vs. Time [s] for step input in v_d^*=1 V with locked rotor conditions.

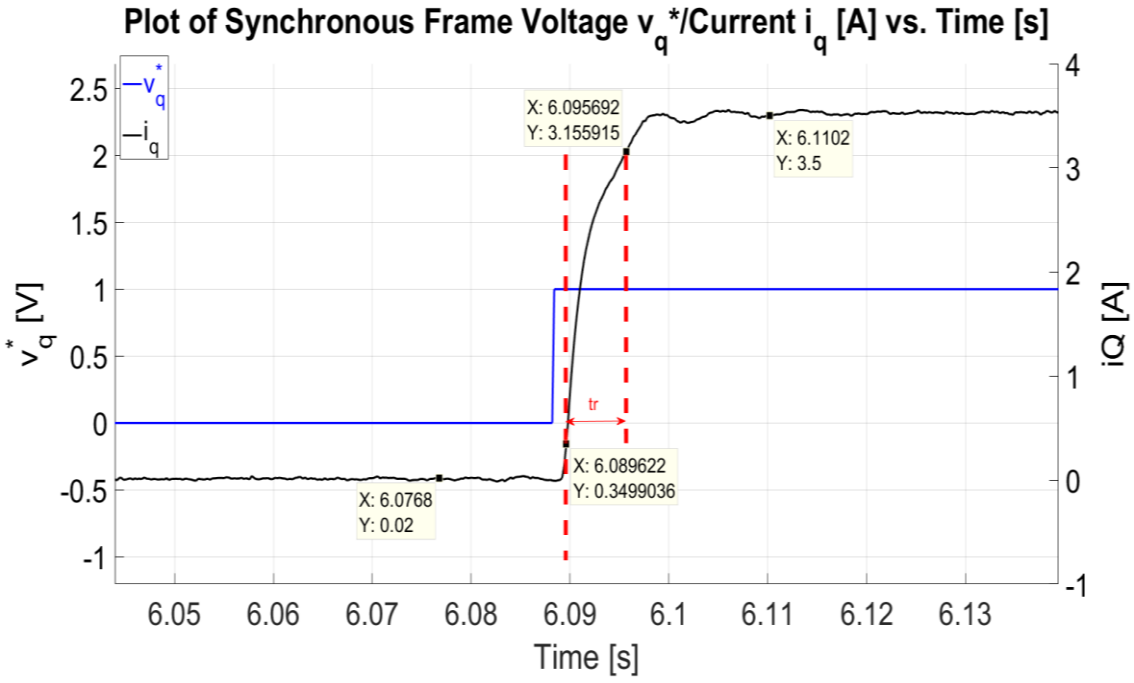

Figure 3.6 - Plot of v_q^* [V] and i_q [A] vs. Time [s] for step input in v_q^*=1 V with locked rotor conditions.

The resultant dq-frame current loops can be controlled through a traditional PI controlled closed-loop with unity feedback, as shown in Figure 3.7. The PI controller can be designed using frequency-domain tools, however, since the values from the electrical parameters R, L_d and L_q are only approximated, experimental tuning of the PI gains was also done with the resultant performance shown in Section 3.4.

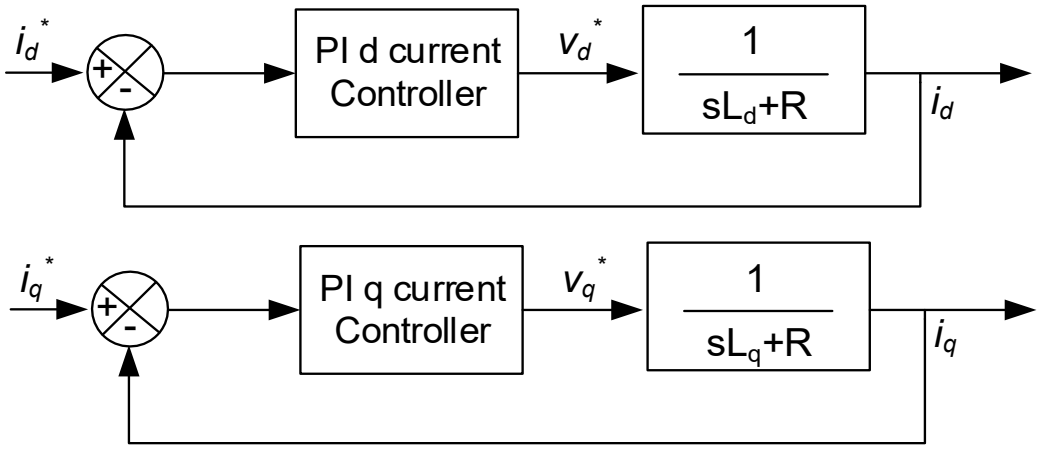

Figure 3.7 - Closed-loop current controller in the dq-frame

3.2.5 Speed Controller Design

The reference input to the current loop i_q^* is generated from the speed controller loop. In order to tune the speed PI controller, the transfer function relating the mechanical rotor speed ω_m of the PMSM to electrical torque of the machine is required. The equation of motion of the PMSM is given by:

$$T_e - T_L = \mathrm{J}\dot{\omega}_m + \mathrm{B}\omega_m \qquad (3.17)$$

Where:

T_e	Electrical torque generated by the PMSM	[Nm],
T_L	Load torque applied at the PMSM shaft	[Nm],
ω	Rotational speed of the machine shaft	[rad/s],
J	Moment of inertia of the shaft	[kgm^2],
B	Coefficient of friction of the shaft	[Nms/rad].

Assuming no-load torque and applying the Laplace transformation to (3.17) the following transfer function is obtained:

$$\frac{\omega_{m(s)}}{T_e(s)} = \frac{1}{sJ+B} \tag{3.18}$$

Given that $T_e = K_t i_q$ where K_t is the torque constant, the transfer function in (3.18) can be written as:

$$\frac{\omega_{m(s)}}{I_q(s)} = \frac{K_t}{sJ+B} \tag{3.19}$$

The mechanical parameters were estimated using experimental results similar to those used for the calculation of the electrical parameters in Section 3.2.4. The torque constant was found from the datasheet to be K_t = 0.643 Nm/A. A step reference in the synchronous current i_q^*= 1 A was applied in RFO current control and the rotor speed observed is shown in Figure 3.8. This test was carried out with the test machine coupled to the loading machine. As can be seen when a torque current component is applied the resultant speed has an oscillatory component. The oscillations are predominantly a result of cogging torque, mechanical tolerances and low encoder resolution. For the purpose of this experiment to determine the components J and B the average of the steady-state rotational speed response was found to be ω_{m0}=12.45 rad/s. The coefficient of friction component was found to be B = 51.65 x 10^{-3} Nms/rad from B=$\frac{K_t}{\omega_{m0}}$. The experimental bandwidth of the mechanical transfer function was found to be 0.752 Hz with a resultant moment of inertia of J = 10.93 x 10^{-3} kg m^2. The mechanical parameters derived in this section are listed in Table 3.2.

The speed control system consists of a PI controller tuned to work with the plant shown in Figure 3.9. Similarly, to the electrical plants, the PI controller for the mechanical plant can be designed using frequency-domain tools. However, since the values of the mechanical parameters, J and B are once again approximated, experimental tuning of the PI gain was done with the resultant performance shown in Section 3.5.

Parameter	Value
K_t	0.643 Nm/A
J	10.93 x 10^{-3} kg m^2
B	51.65 x 10^{-3} Nms/rad

Table 3.2 - PMSM Mechanical Parameters

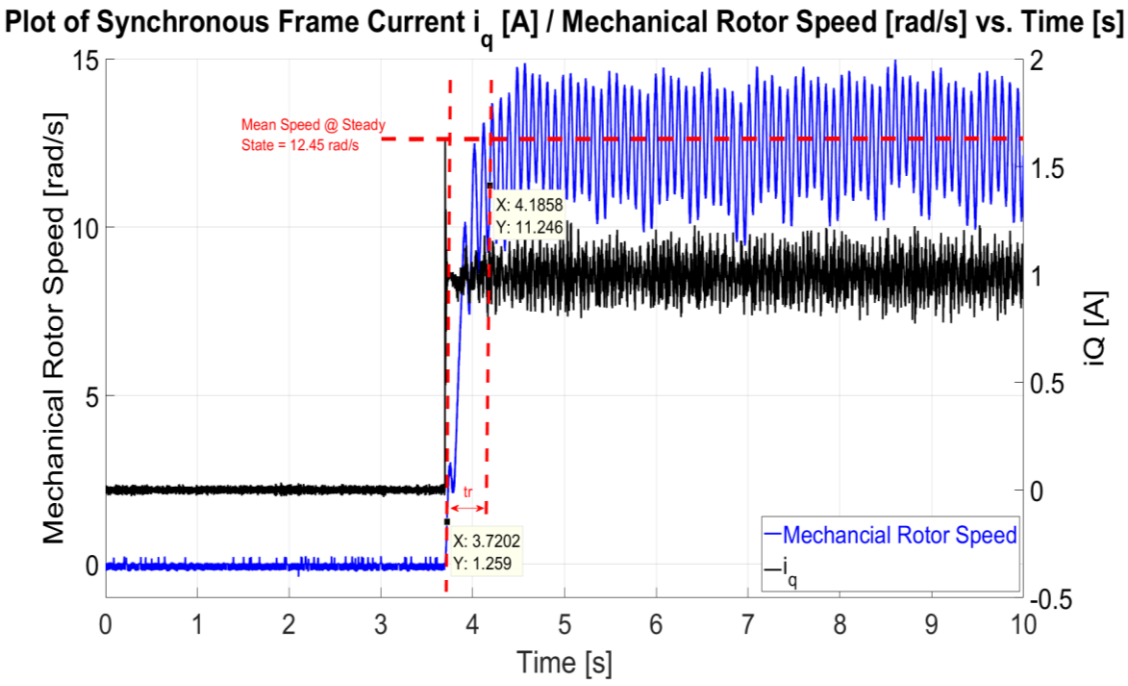

Figure 3.8 – Plot of i_q [A] and Mechanical Rotor Speed ω_m [rad/s] vs. Time [s] for step input in i_q^*=1 A.

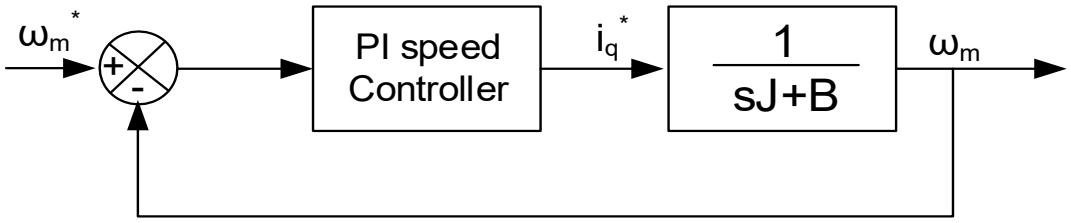

Figure 3.9 - Closed-loop speed controller

3.2.6 Position Controller Design

The reference input to the speed loop is generated from the position loop. In order to tune the position controller a transfer function relating the machine position θ_m to the machine rotational speed ω_m is required. The differential equation which relates these two parameters is:

$$\omega_m = \frac{d\theta_m}{dt} \tag{3.20}$$

By applying a Laplace transformation on (3.20), the following characteristic equation is obtained:

$$\frac{\theta_m(s)}{\omega_m(s)} = \frac{1}{s} \tag{3.21}$$

Since the transfer function (3.21) is a pure integrator, typically a Proportional (P) Controller is used for the position closed-loop, as shown in Figure 3.10. The tuning of the proportional gain for the position controller was also carried out on the experimental setup.

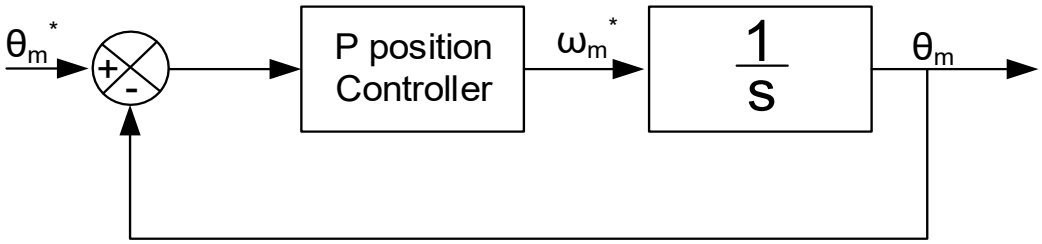

Figure 3.10 - Closed-loop position control

3.4 Sensored Current Control

The current controller topology presented in Section 3.2.4 was tested on the experimental setup by setting the test machine M3 in current control mode and the setpoint machine M4 in speed control mode, as shown in Figure 3.11. Since the machines are assumed to be identical; the performance of the current controllers in machine M4 is expected to be similar to that on M3. The speed reference on M4 was set to ω_{m4}^{*}=-2 rad/s.

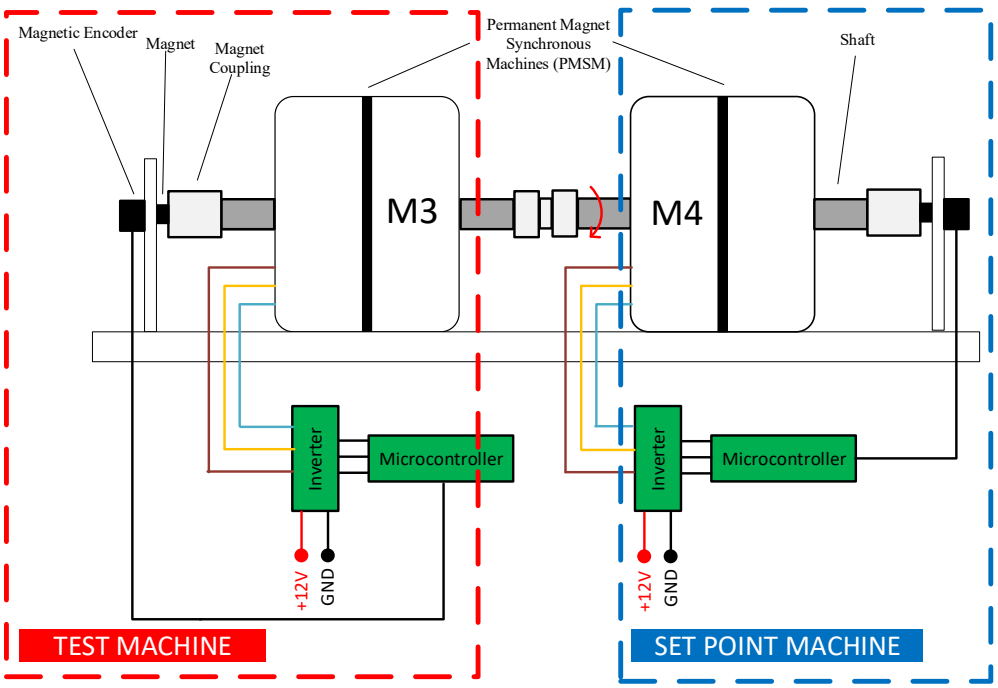

Figure 3.11 – Experimental Setup with Test Machine M3 and Set Point Machine M4

The performance of the current controlled machine M3, for a mean rotor ***mechanical*** speed of 2 rad/s, i_{d3}^* = 0 A and with a step-change in i_{q3}^* = 10 A is shown in Figures 3.12 – 3.15. The current controller was designed using the root locus technique via the MATLAB SISO tool and then tuned experimentally on the setup. The current controller PI gains were set to $K_{p\_I3} = 0.3$ and $K_{i\ I3} = 350$. The actual rotor speed is shown in Figure 3.12, with an overshoot of 6.197 rad/s observed at the instant of application of a step reference in i_{q3}^*=10 A (100 % of rated value). Both the ***mechanical*** and ***electrical*** rotor positions are shown in Figure 3.13. The ***electrical*** rotor position is based on the ***mechanical*** position scaled by the number of pole pairs (6 for PMSM under test). The reference and actual synchronous frame currents i_{d3}, i_{q3} are shown in Figure 3.14. From Figure 3.14 (b) for the synchronous current i_{q3}, the closed-loop current bandwidth was found to be 281 Hz with a percentage overshoot of 57.4 %. The three-phase stator currents are shown in Figure 3.15. The peak of the three-phase stator currents corresponds to the value of i_{q3}^*.

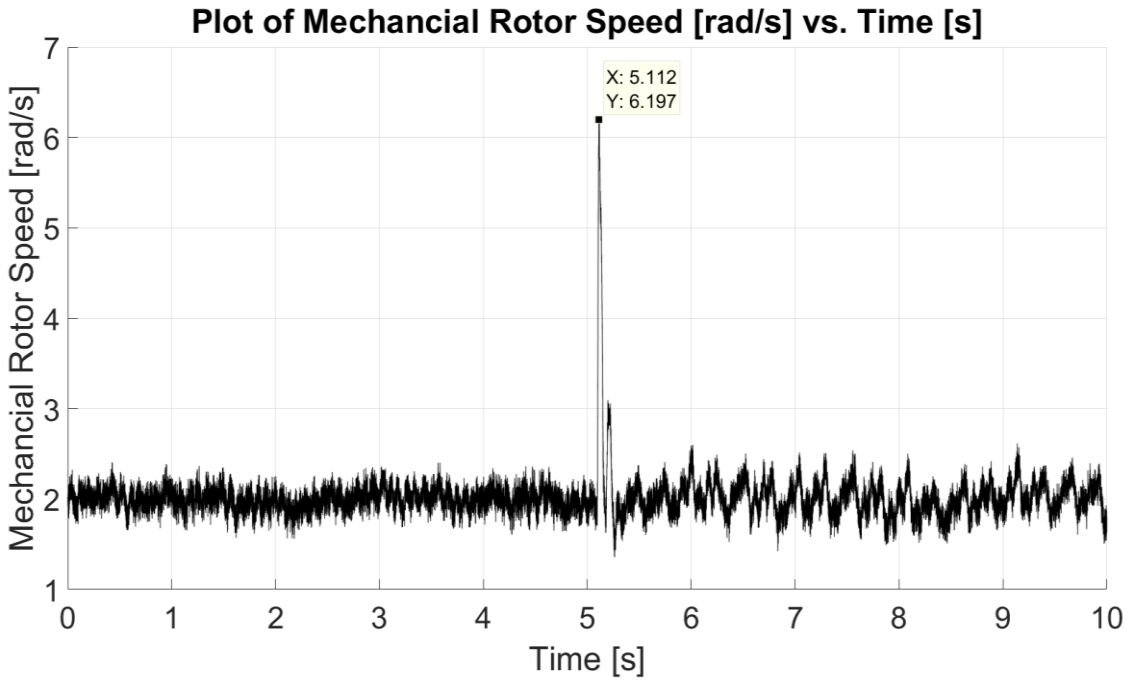

Figure 3.12 – Plot of Mechanical Rotor Speed ω_m [rad/s] vs. Time [s] with ω_{m4}^* = -2 rad/s on M4, i_{d3}^*= 0 A and step in i_{q3}^*=10 A at t = 5 s on M3 in sensored current control.

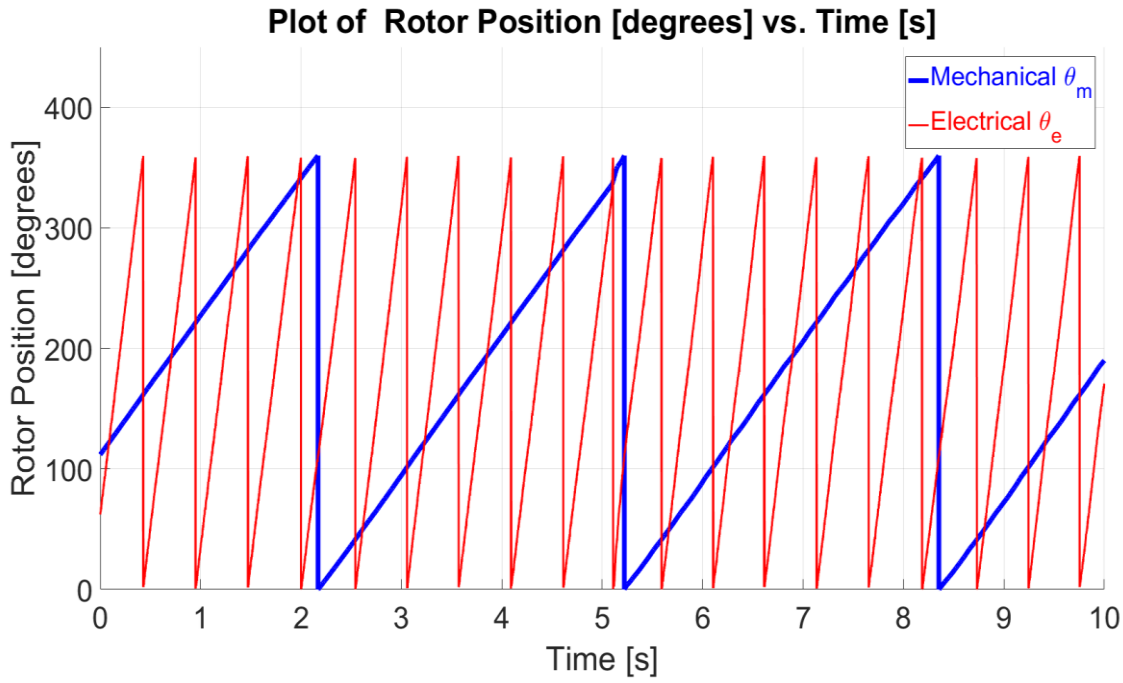

Figure 3.13 – Plot of Mechanical/Electrical Rotor Position [degrees] vs. Time [s] with $\omega_{m4}^* = -2$ rad/s on M4, $i_{d3}^* = 0$ A and step in $i_{q3}^* = 10$ A at t = 5 s on M3 in sensored current control.

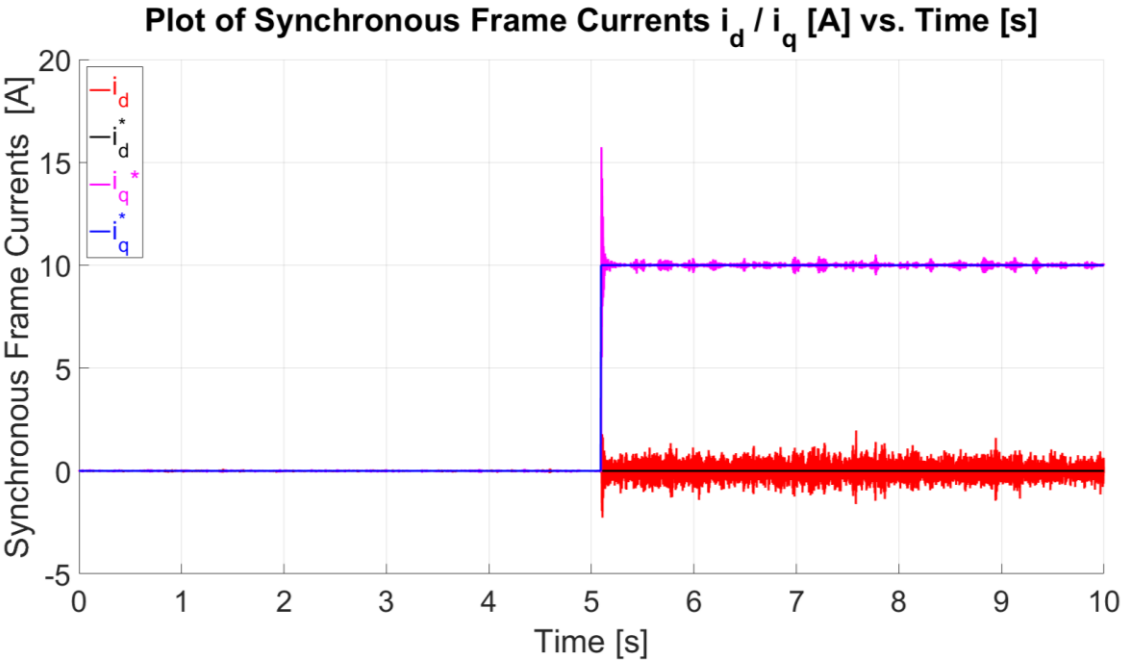

Figure 3.14 (a) – Plot of Synchronous Stator Frame Currents i_d, i_q [A] vs. Time [s] with $\omega_{m4}^* = -2$ rad/s on M4, $i_{d3}^* = 0$ A and step in $i_{q3}^* = 10$ A at t = 5 s on M3 in sensored current control.

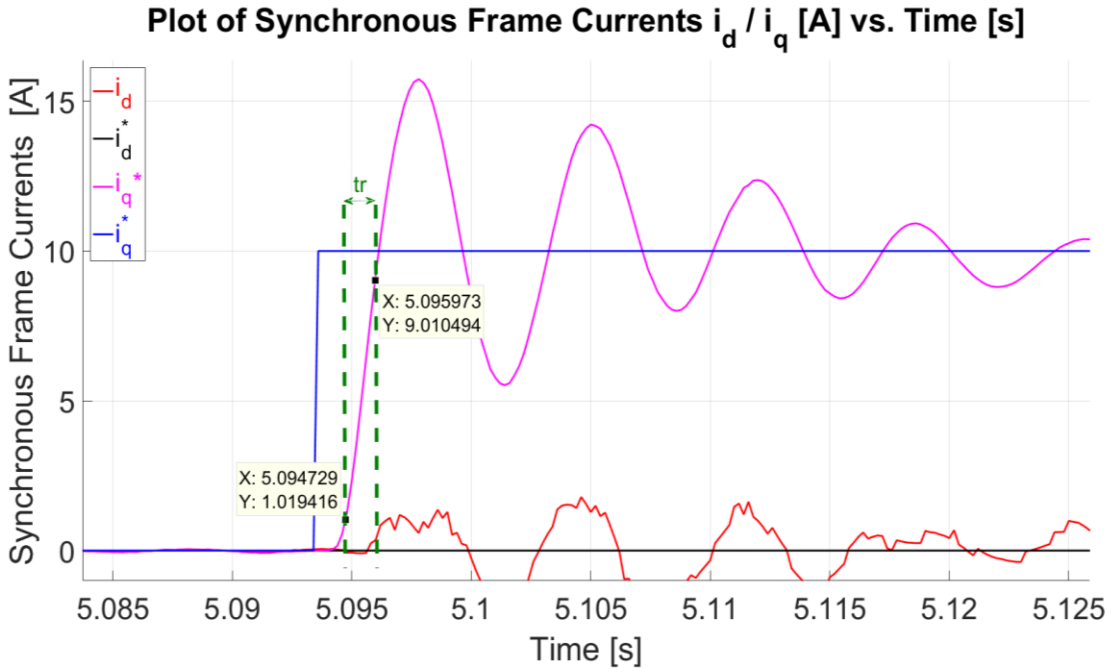

Figure 3.14 (b) – Plot of Synchronous Stator Frame Currents i_d, i_q [A] vs. Time [s] with ω_{m4}^* = -2 rad/s on M4, i_{d3}^*= 0 A and step in i_{q3}^*=10 A at t = 5 s on M3 in sensored current control at t = 5 s.

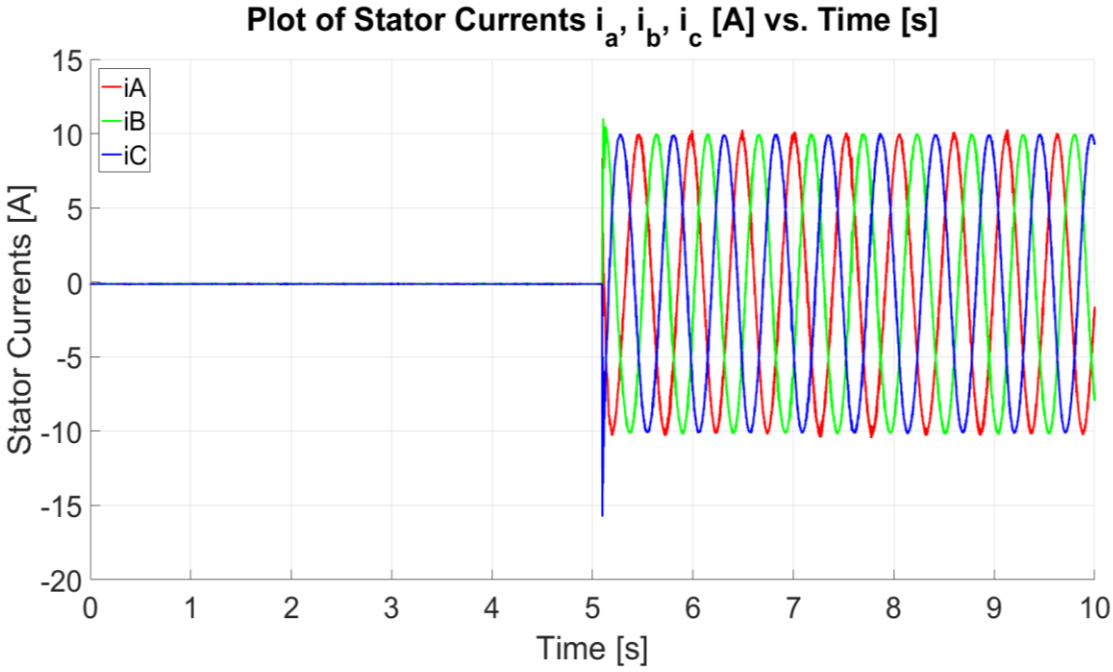

Figure 3.15 – Plot of Three Phase Stator Currents i_a, i_b, i_c [A] vs. Time [s] with ω_{m4}^* = -2 rad/s on M4, i_{d3}^*= 0 A and step in i_{q3}^*=10 A at t = 5 s on M3 in sensored current control.

The performance of the current controllers in M3 for an operating point of 2 rad/s but with a step in i_{q3}^* = -10 A, with all other parameters constant is shown in Figures 3.16 – 3.18. The performance is similar to what was observed for the positive i_{q3}^*. In this case, since the rotor speed is kept in the same direction of rotation but the polarity of i_{q3} was reversed, the machine acts as a generator instead of a motor since the flow of power is reversed. The actual rotor speed is shown in Figure 3.16, with an overshoot to -1.863 rad/s observed at the instant of application of a step reference in i_{q3}^*=-10 A (-100 % of rated value). Both the ***mechanical*** and ***electrical*** rotor positions are shown in Figure 3.17. The reference and actual synchronous frame currents i_{d3}, i_{q3} are shown in Figure 3.18. The percentage overshoot in i_{q3} is of 64.4 %.

The experiments shown for sensored current control with i_{q3} were repeated for the d-axis current controller, and similar results were obtained. However, since the use of the d-axis controller is not used in transient conditions with the reference being set to i_{d3}^* = 0 A for all test conditions such results were not included in this dissertation.

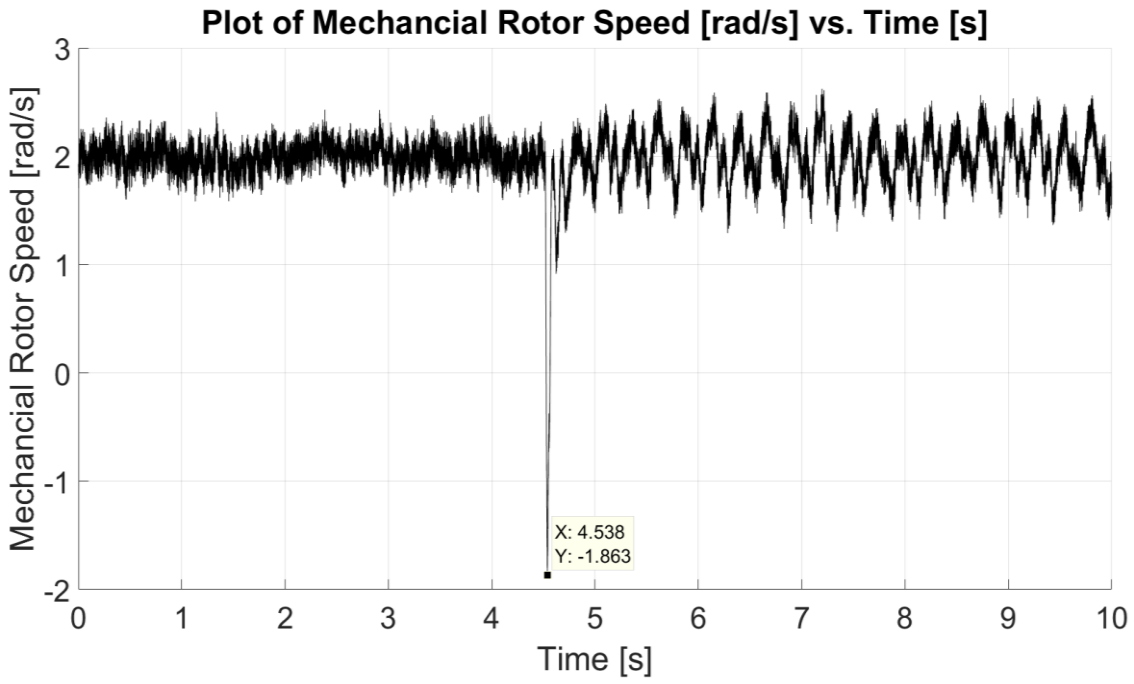

Figure 3.16 – Plot of Mechanical Rotor Speed ω_m [rad/s] vs. Time [s] with ω_{m4}^* = -2 rad/s on M4, i_{d3}^*= 0 A and step in i_{q3}^*=-10 A at t = 4.5 s on M3 in sensored current control.

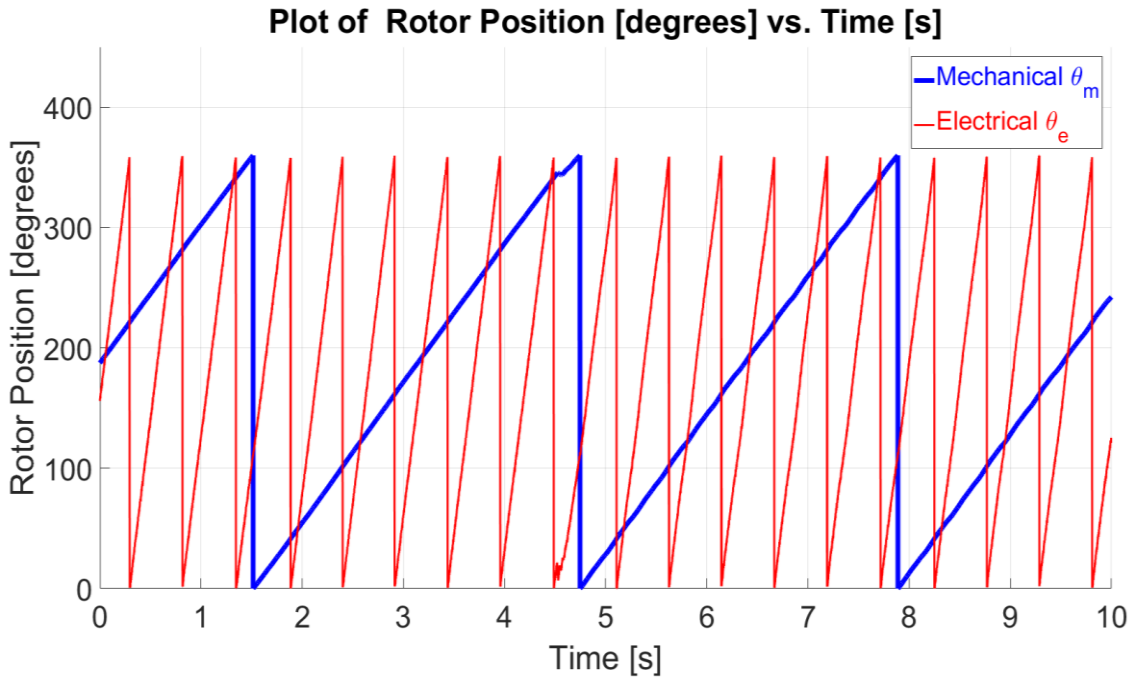

Figure 3.17 – Plot of Mechanical/Electrical Rotor Position [degrees] vs. Time [s] with $\omega_{m4}^* = -2$ rad/s on M4, $i_{d3}^* = 0$ A and step in $i_{q3}^* = -10$ A at t = 4.5 s on M3 in sensored current control.

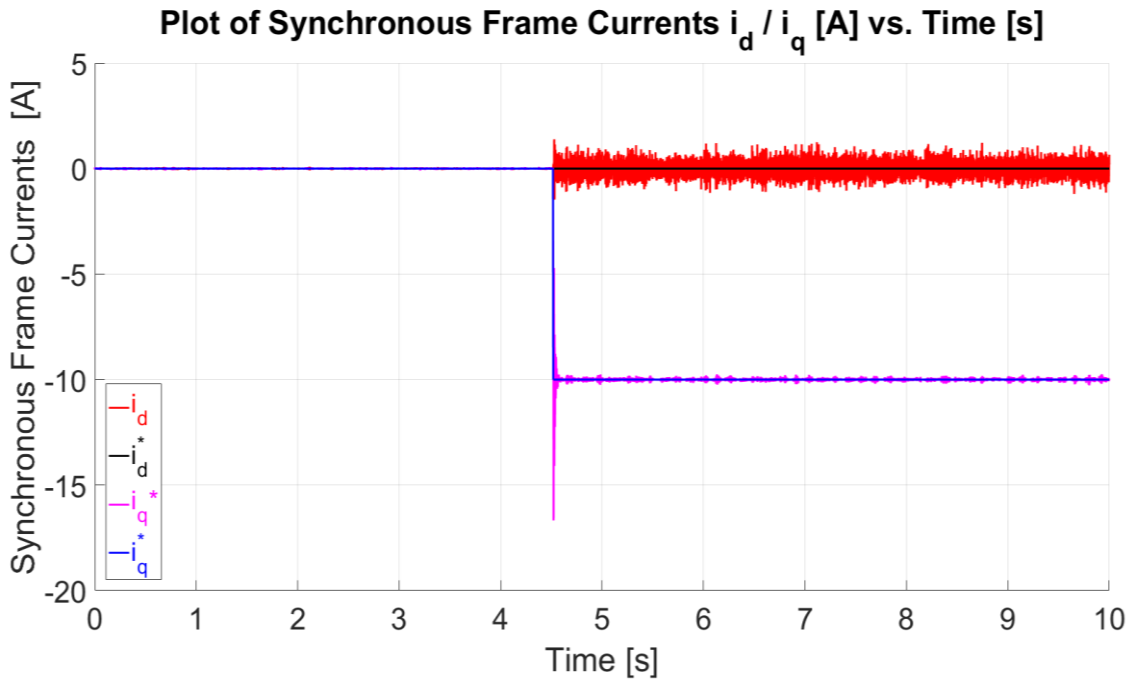

Figure 3.18 – Plot of Synchronous Stator Frame Currents i_d, i_q [A] vs. Time [s] with $\omega_{m4}^* = -2$ rad/s on M4, $i_{d3}^* = 0$ A and step in $i_{q3}^* = -10$ A at t = 4.5 s on M3 in sensored current control.

3.5 Sensored Speed Control

The speed controller presented in Section 3.2.5 was implemented on the experimental setup by setting the test machine M3 in speed control mode and the reference machine M4 in current control mode. Since the machines are assumed to be identical; the performance of the speed controller in machine M4 is expected to be similar to that of the test machine M3.

The mechanical rotor speed measurement ω_m is obtained from the encoder and filtered through a quadrature PLL with PI gains $K_{p\_PLL1} = 30$ and $K_{i\_PLL1} = 5000$. A PLL is used instead of numerical differentiation to reduce the high-frequency transient which arises from differentiating discrete-time signals. The speed controller was designed using the root locus technique via the MATLAB SISO tool and then tuned experimentally on the setup. The cascaded speed control loop used a PI speed controller with $K_{p\_W3} = 0.3$ and $K_{i\_W3} = 60$. The current controller gains within the cascaded speed control loop are identical to those used in Section 3.4 ($K_{p\_I4} = 0.3$, $K_{i\_I4} = 350$). The work presented in this research concentrated on the low-speed operation of the steer-by-wire system. Thus operation at low speeds is investigated, namely with the reference for the mechanical rotor speed in M3 varied from 5 rad/s to 0 rad/s and then -5 rad/s at approximately 10 s intervals. Current references on machine M4 are $i_{d4}^* = 0$ A and $i_{q4}^* = 5$ A.

The reference and actual ***mechanical*** rotor speeds are shown in Figures 3.19 (a)-(b). For this research, a 12-bit digital position encoder was used. In order to obtain a robust speed measurement with sufficient SNR, a PLL-based filter was used as described in Section 7.5. The SNR can be improved by reducing the bandwidth of the PLL. However, this limits the transient response of the control loops. Therefore, the bandwidth cannot be reduced indefinitely such that oscillations due to discretization are still observed throughout the speed measurements in this dissertation. While speed measurements can be improved with higher resolution encoders, these would not be economically viable for an automotive application. The ***mechanical*** and ***electrical*** rotor position are shown in Figure 3.20. The synchronous frame reference and actual currents are shown in Figure 3.21.

The bandwidth of the closed-loop speed controller is calculated experimentally from Figure 3.19 (b) to be 15.93 Hz. The actual speed has an overshoot of 27.6%. The current reference i_{q3}^* generated by the speed controller is shown to be tracked adequately by the

controller in Figure 3.19. This is to be expected since the current controller bandwidth (281 Hz) is a factor of 17.6 times larger than that of the speed controller. The current i_{q3} required for rotation can also be noted to vary between the forward and reverse directions from Figure 3.21 (while i_{q4}^* is kept constant) with a larger current required for forward rotation due different frictional forces.

Testing with a negative value of i_{q4}^* on the loading machine M4 was also carried out under similar conditions. The current references on machine M3 are set to $i_{d3}^* = 0$ A and $i_{q3}^* = -5$ A. The reference and actual ***mechanical*** rotor speeds are shown in Figures 3.22. The ***mechanical*** and ***electrical*** rotor positions are shown in Figure 3.23. The synchronous frame reference and actual currents are shown in Figure 3.24.

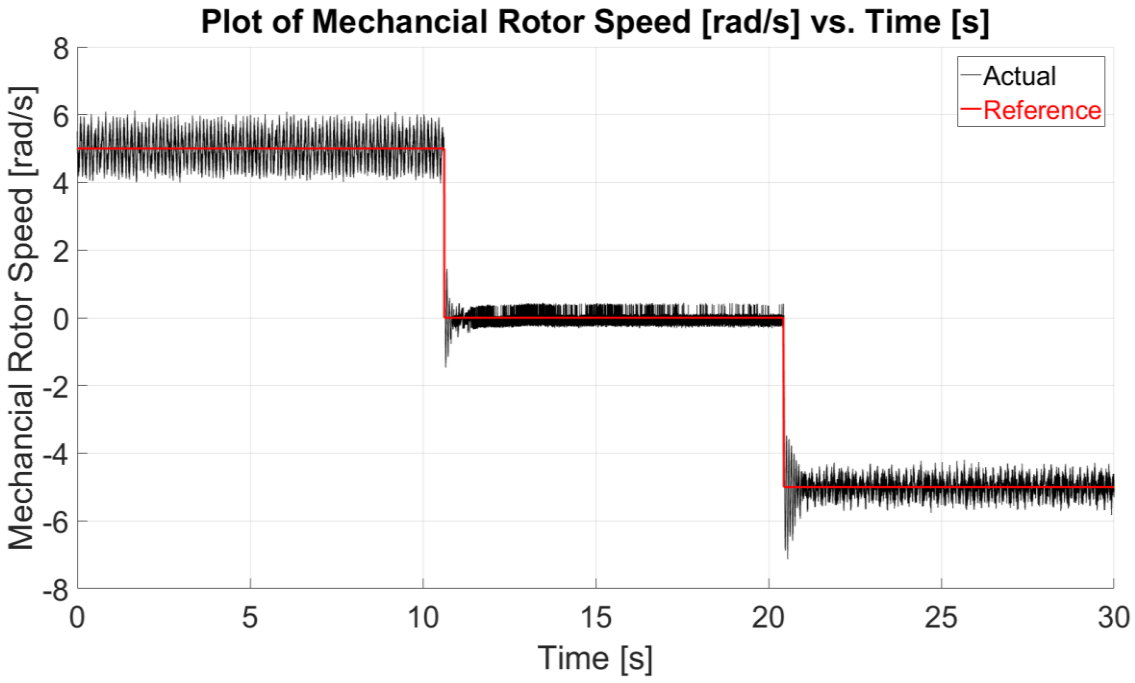

Figure 3.19 (a) – Plot of Reference/Actual Mechanical Rotor Speed ω_m [rad/s] vs. Time [s] with $\omega_{m3}^* = 5$, 0 and -5 rad/s on M3, $i_{d4}^* = 0$ A and $i_{q4}^* = 5$ A on M4, in sensored speed control.

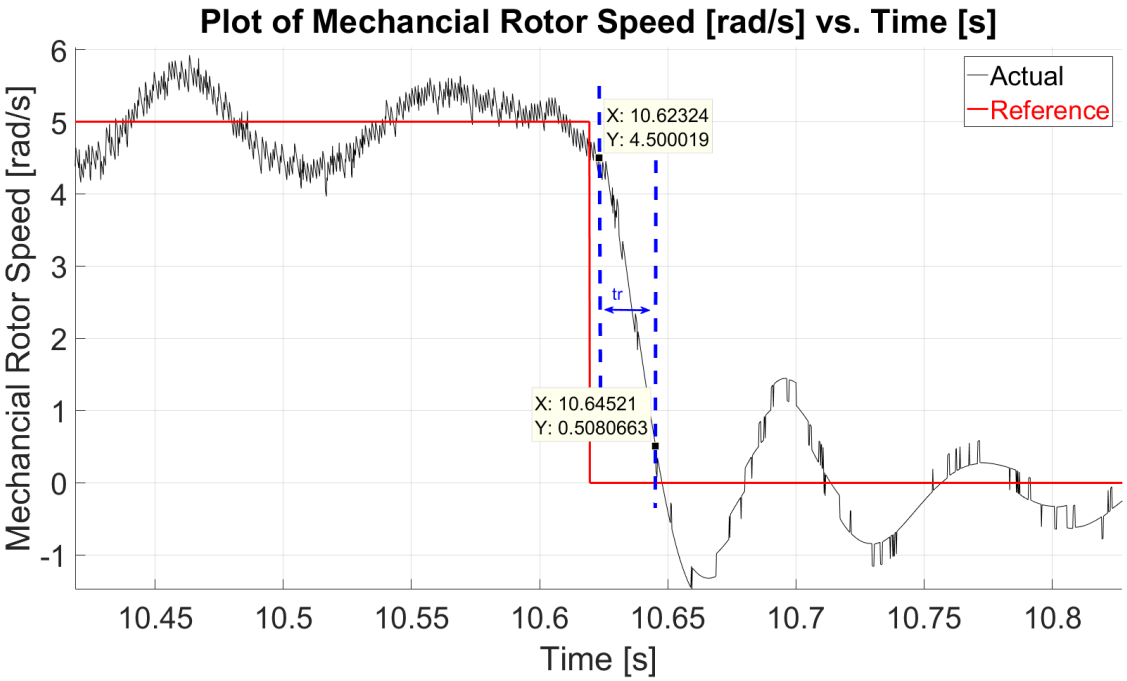

Figure 3.19 (b) – Plot of Reference/Actual Mechanical Rotor Speed ω_m [rad/s] vs. Time [s] with $\omega_{m3}^* = 5$, 0 and -5 rad/s on M3, $i_{d4}^* = 0$ A and $i_{q4}^* = 5$ A on M4, in sensored speed control in at transient from 5 to 0 rad/s.

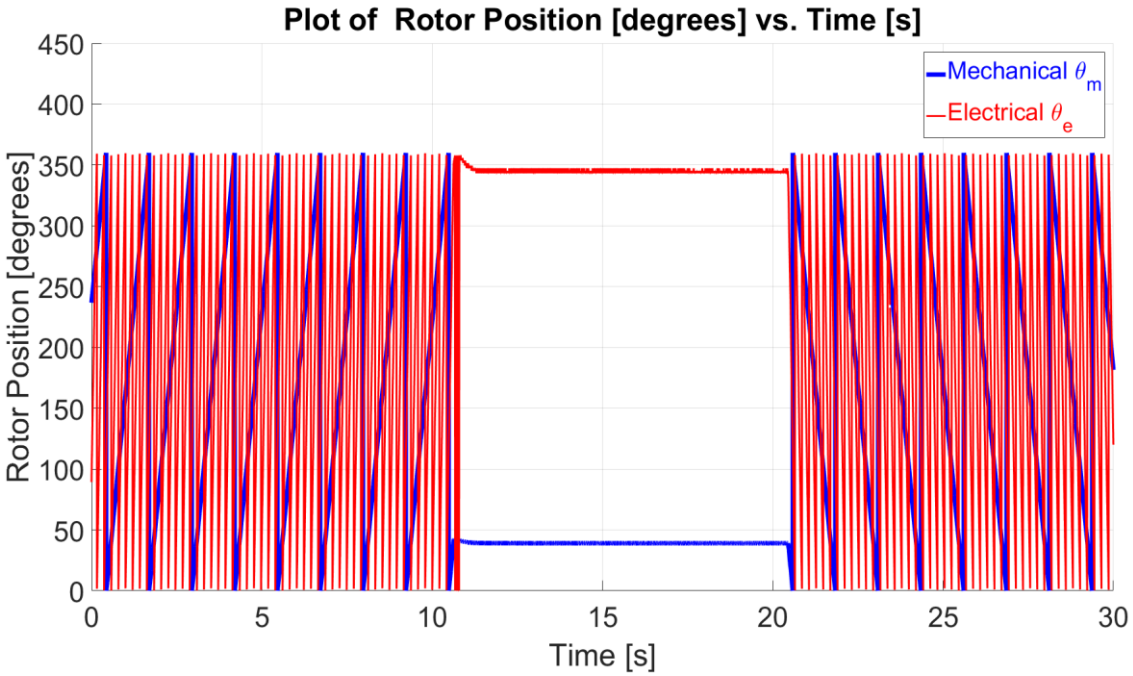

Figure 3.20 – Plot of Mechanical/Electrical Rotor Position [degrees] vs. Time [s] with $\omega_{m3}^* = 5$, 0 and -5 rad/s on M3, $i_{d4}^* = 0$ A and $i_{q4}^* = 5$ A on M4, in sensored speed control.

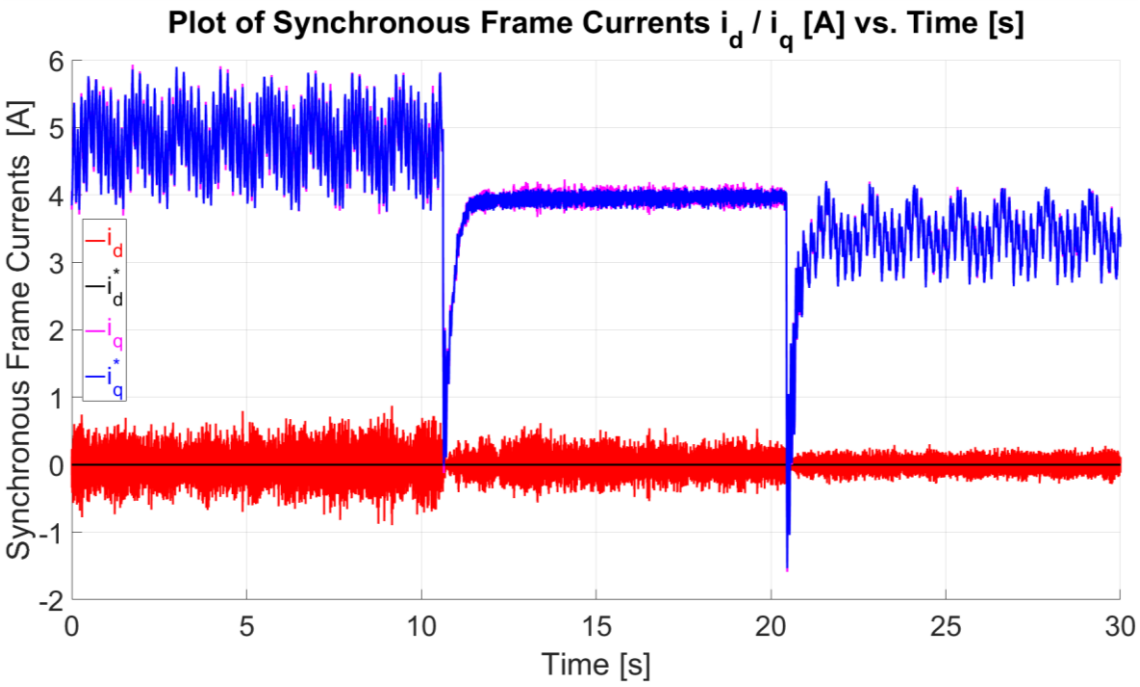

Figure 3.21 – Plot of Synchronous Stator Frame Currents i_d, i_q [A] vs. Time [s] with $\omega_{m3}^* = 5$, 0 and -5 rad/s on M3, $i_{d4}^* = 0$ A and $i_{q4}^* = 5$ A on M4, in sensored speed control.

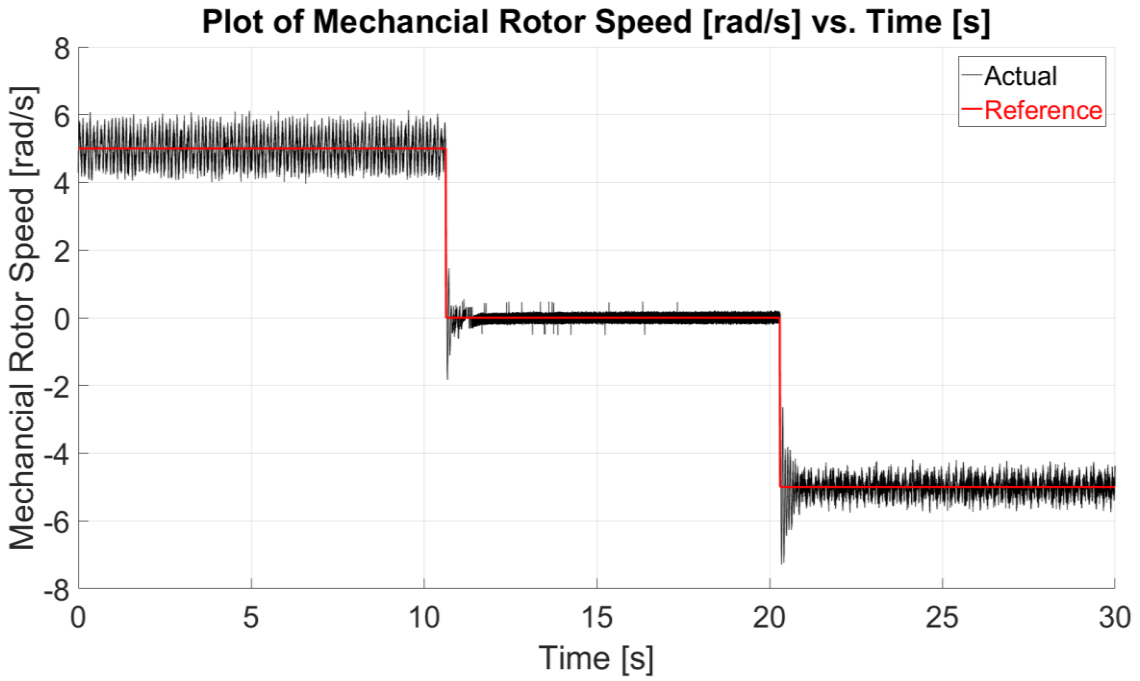

Figure 3.22 – Plot of Reference/Actual Mechanical Rotor Speed ω_m [rad/s] vs. Time [s] with $\omega_{m3}^* = 5$,0 and -5 rad/s on M3, $i_{d4}^* = 0$ A and $i_{q4}^* = -5$ A on M4, in sensored speed control.

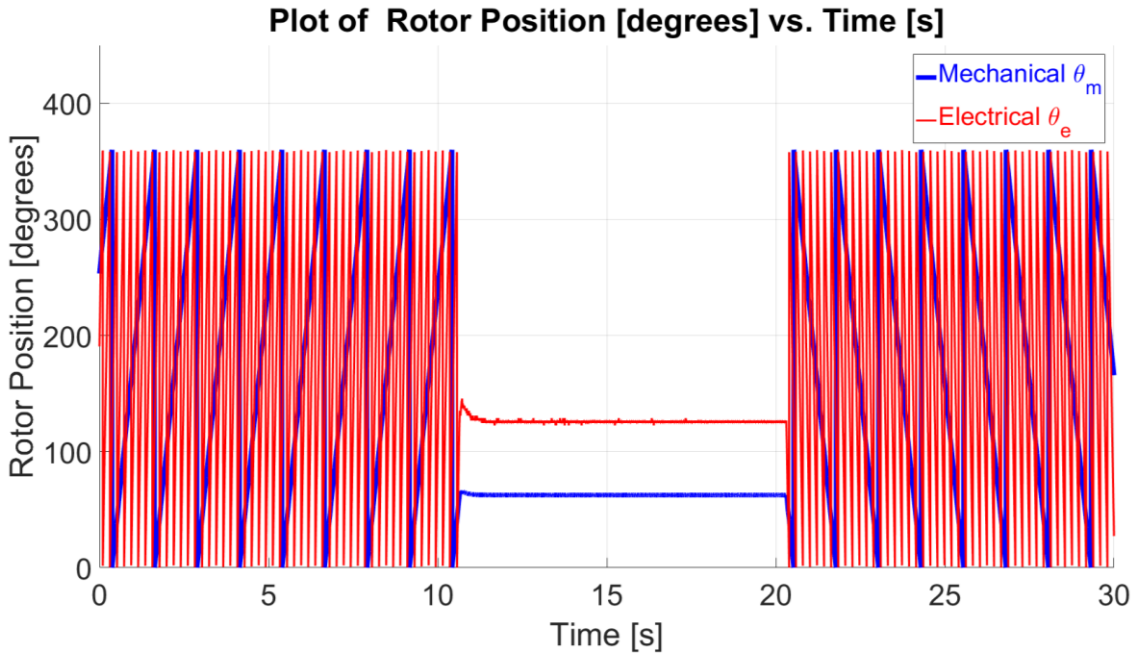

Figure 3.23 – Plot of Mechanical/Electrical Rotor Position [degrees] vs. Time [s] with $\omega_{m3}^* = 5{,}0$ and -5 rad/s on M3, $i_{d4}^* = 0$ A and $i_{q4}^* = -5$ A on M4, in sensored speed control.

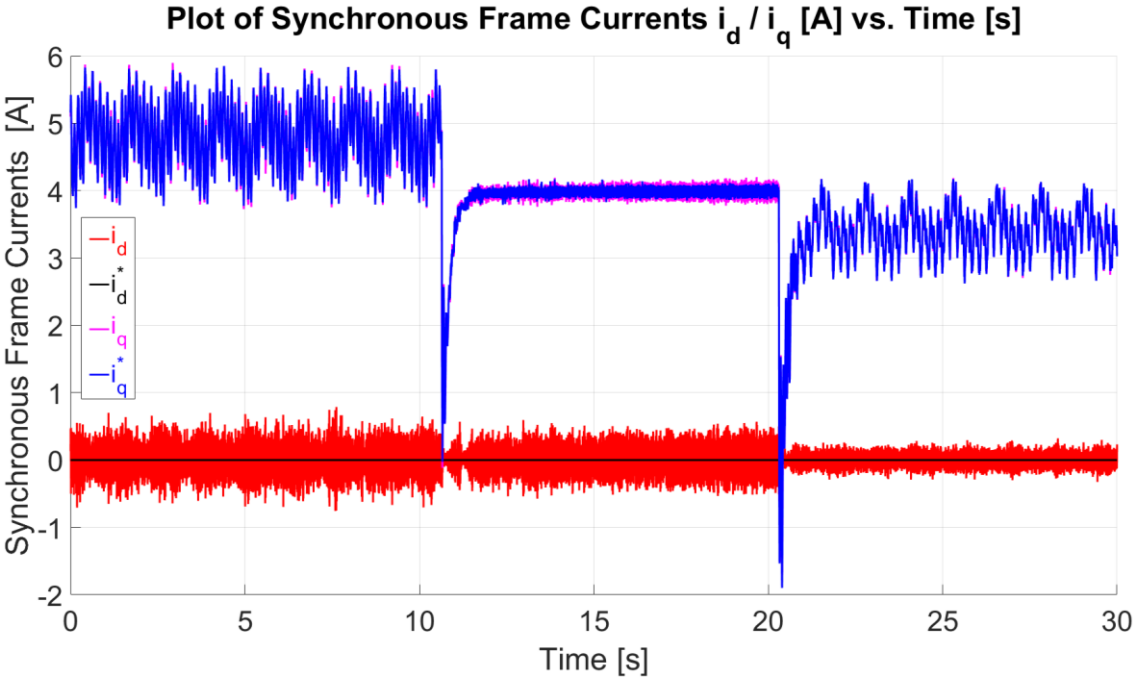

Figure 3.24 – Plot of Synchronous Stator Frame Currents i_d, i_q [A] vs. Time [s] with $\omega_{m3}^* = 5{,}0$ and -5 rad/s on M3, $i_{d4}^* = 0$ A and $i_{q4}^* = -5$ A on M4, in sensored speed control.

3.6 Sensored Position Control

3.6.1 Sensored Position Control for step-input reference

The sensored position control of machine M3 was also tested with machine M4 operating in current control as a load. In this sub-section, the performance of the closed-loop position-controlled loop with a step input $\theta_m^* = 3$ rad (172°) is shown. The position controller was designed using the root locus technique via the MATLAB SISO tool and then tuned experimentally on the setup. The position control architecture consists of three cascaded loops for current ($K_{p\_I3} = 0.3$, $K_{i\_I3} = 350$), speed ($K_{p\_W3} = 0.3$, $K_{i\_W3} = 50$) and position ($K_{p\_P3} = 5.75$) as shown in Figure 3.4. The current controller on the loading machine M4 is set to a lower bandwidth than M3 ($K_{p\_I4} = 0.1$, $K_{i\_I4} = 1$) to limit oscillations on the shaft. The synchronous current references on M4 are set to $i_{d4}^* = 0$ A and $i_{q4}^* = 5$ A.

The reference and actual ***mechanical*** positions are shown in Figure 3.25, while the reference and actual ***mechanical*** rotor speeds are shown in Figure 3.26. The ***electrical*** rotor position is shown in Figure 3.27. The reference and actual synchronous frame currents are shown in Figure 3.28, while the three-phase stator stationary frame currents are shown in Figure 3.29. From Figure 3.25 (b) the bandwidth of the position controller was found to be 1 Hz. While the bandwidth of the position controller can theoretically be increased further, there is a limitation on the amount of current i_{q3} which can be sourced at the instant when the step input is applied. For the purposes of this experiment, the synchronous i_q-current i_{q3}^* was limited to 15 A (150 % rated value). This can be increased in the case where a low-impedance source, such as an automotive battery is used. The high demand in current is a result of the steep gradient in i_{q3}^* at the instant the step reference input is applied. The current requirement can be reduced by using a sigmoid reference instead of the step as described in Section 3.6.2.

An identical test was carried out with a change in $i_{q4}^* = -5$ A. The reference and actual ***mechanical*** positions are shown in Figure 3.30 while the reference and actual ***mechanical*** rotor speeds are shown in Figure 3.31. The ***electrical*** rotor position is shown in Figure 3.32. The reference and actual synchronous frame currents are shown in Figure 3.33, while the three-phase stator stationary frame currents are shown in Figure 3.34. The results shown in this section show the complete operation of the

cascaded RFO position control architecture, as discussed in Section 3.2.3 for both positive and negative load values on i_{q4}^*.

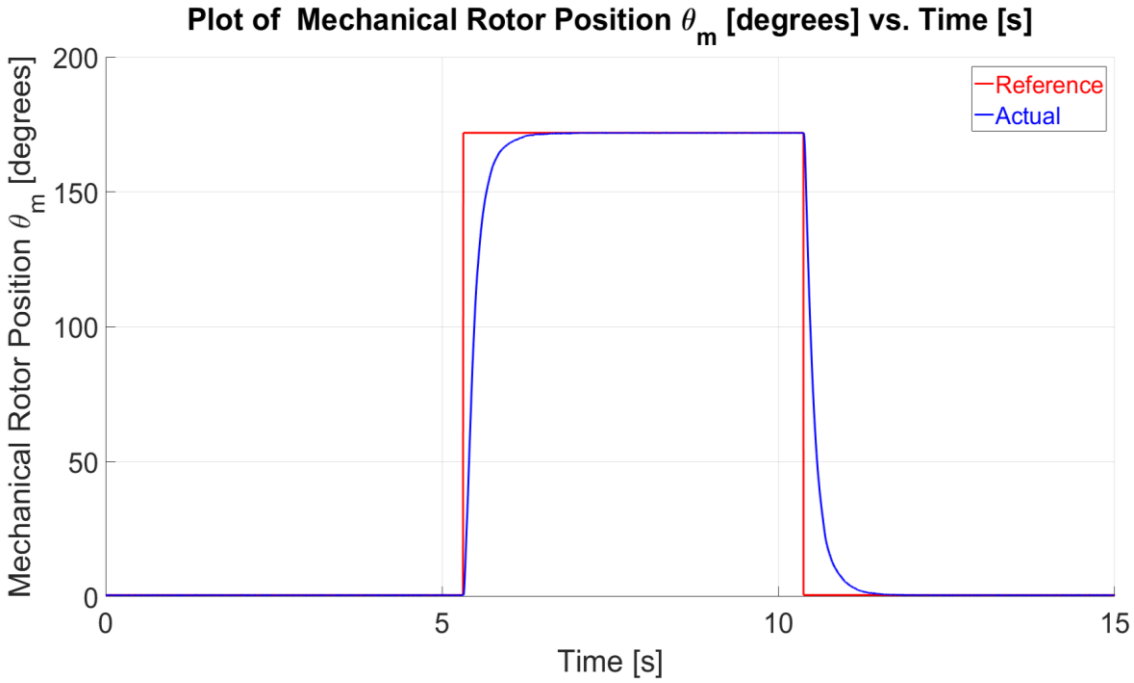

Figure 3.25 (a) - Plot of Reference/Actual Mechanical Rotor Position θ_m [degrees] vs. Time [s] with step position references of 0 rad to 3 rad (0° to 172°) and 3 rad to 0 rad (172° to 0°) on M3, i_{d4}^*= 0 A and i_{q4}^*=5 A on M4, in sensored position control.

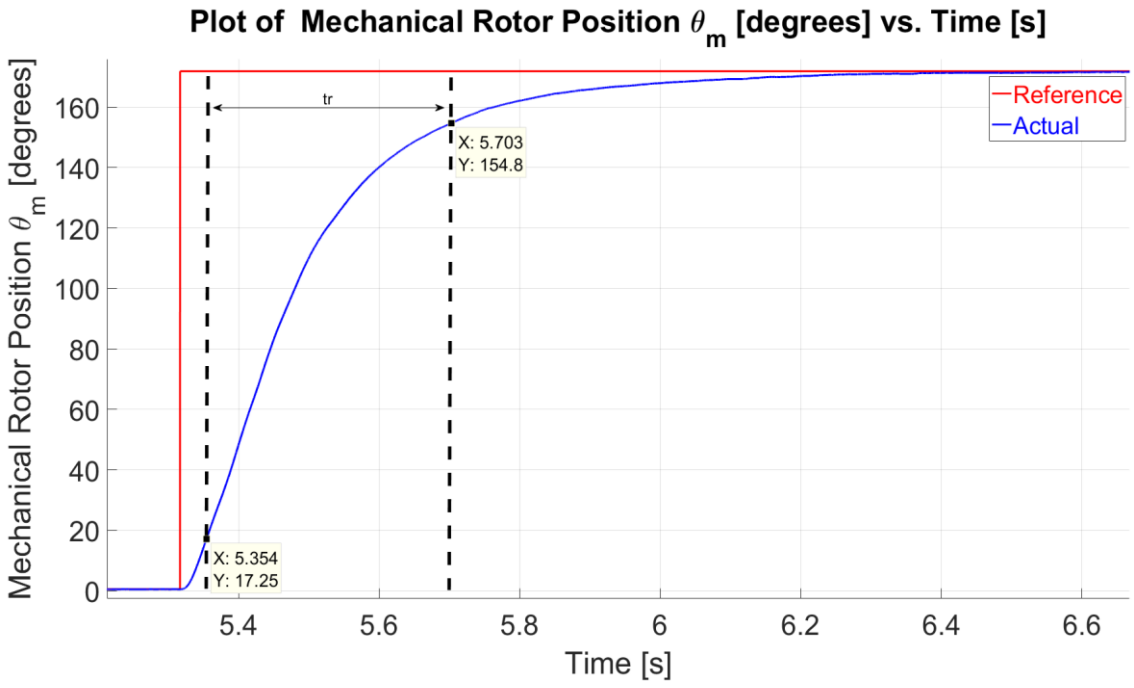

Figure 3.25 (b) - Plot of Reference/Actual Mechanical Rotor Position θ_m [degrees] vs. Time [s] with step position references of 0 rad to 3 rad (0° to 172°) and 3 rad to 0 rad (172° to 0°) on M3, i_{d4}^*= 0 A and i_{q4}^*=5 A on M4, in sensored position control at first position transient.

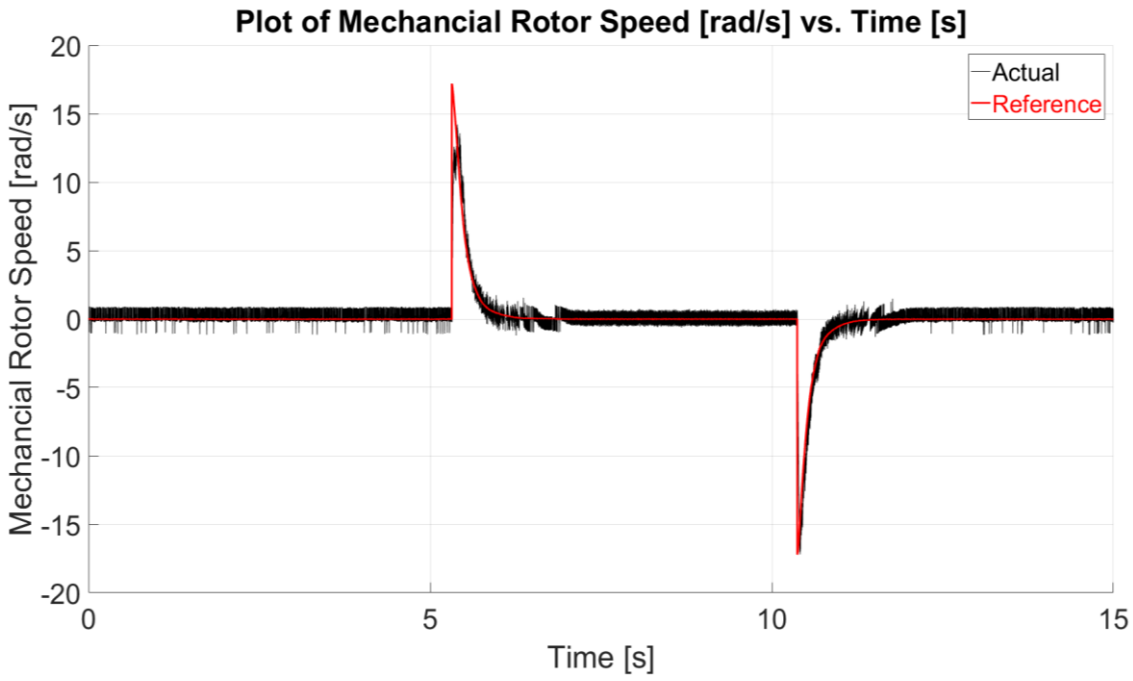

Figure 3.26 – Plot of Reference/Actual Mechanical Rotor Speed ω_m [rad/s] vs. Time [s] with step position references of 0 rad to 3 rad (0° to 172°) and 3 rad to 0 rad (172° to 0°) on M3, i_{d4}^*= 0 A and i_{q4}^*=5 A on M4, in sensored position control.

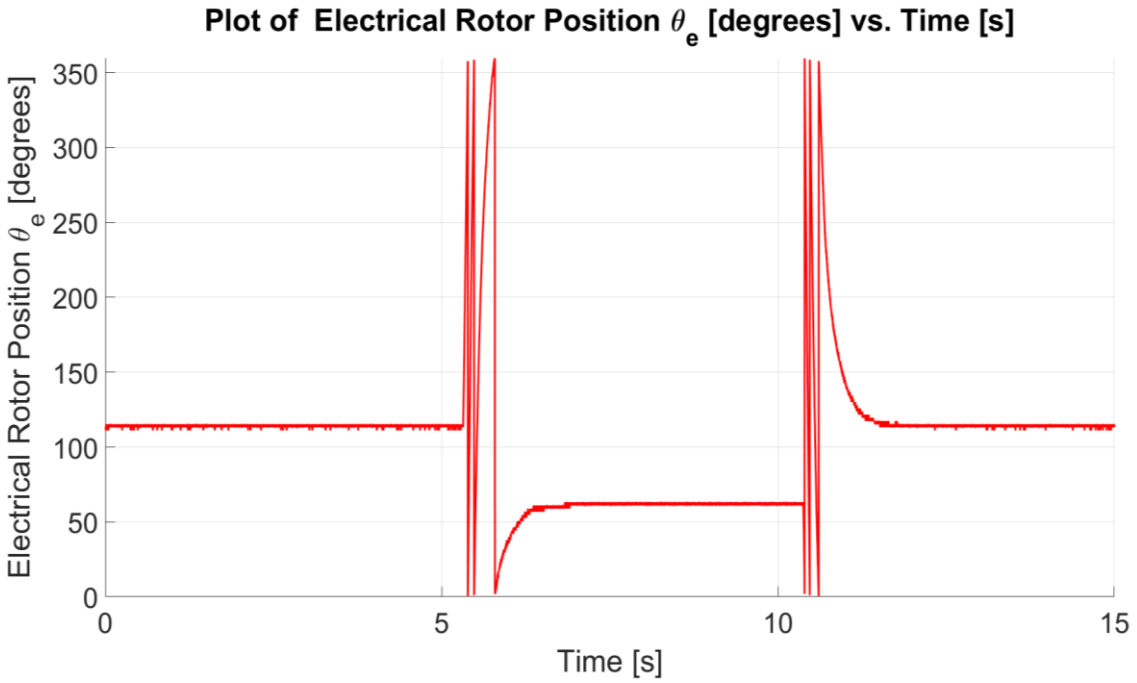

Figure 3.27 - Plot of Electrical Rotor Position θ_e [degrees] vs. Time [s] with step position references of 0 rad to 3 rad (0° to 172°) and 3 rad to 0 rad (172° to 0°) on M3, i_{d4}^*= 0 A and i_{q4}^*=5 A on M4, in sensored position control.

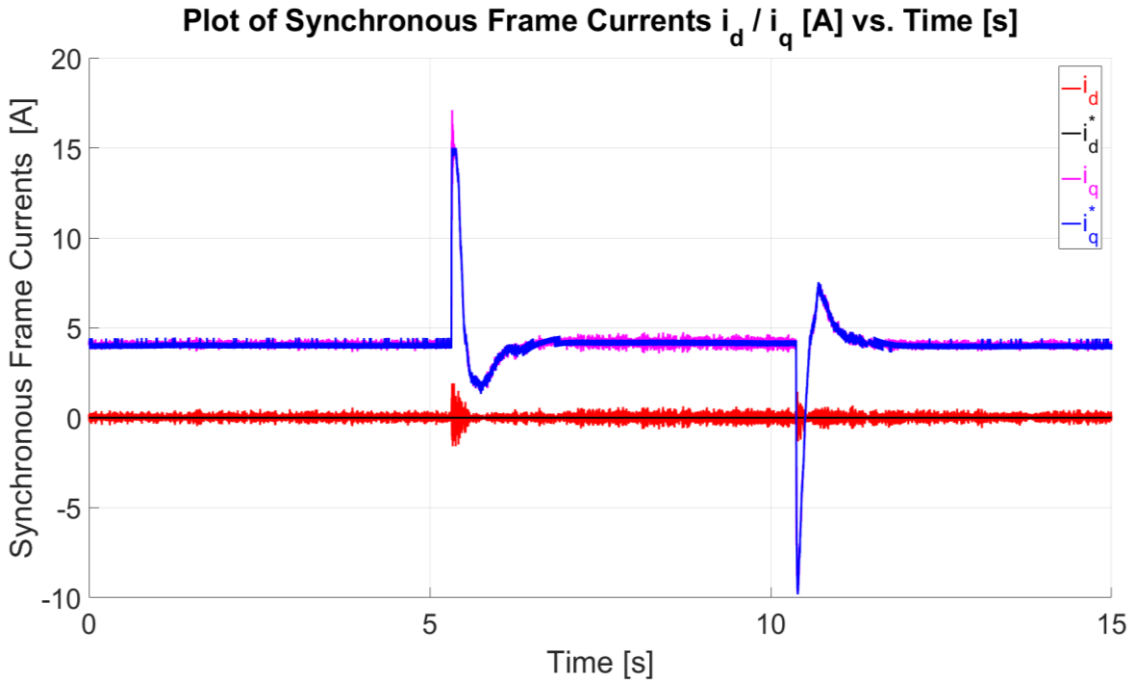

Figure 3.28 – Plot of Synchronous Stator Frame Currents i_d, i_q [A] vs. Time [s] with step position references of 0 rad to 3 rad (0° to 172°) and 3 rad to 0 rad (172° to 0°) on M3, i_{d4}^*= 0 A and i_{q4}^*=5 A on M4, in sensored position control.

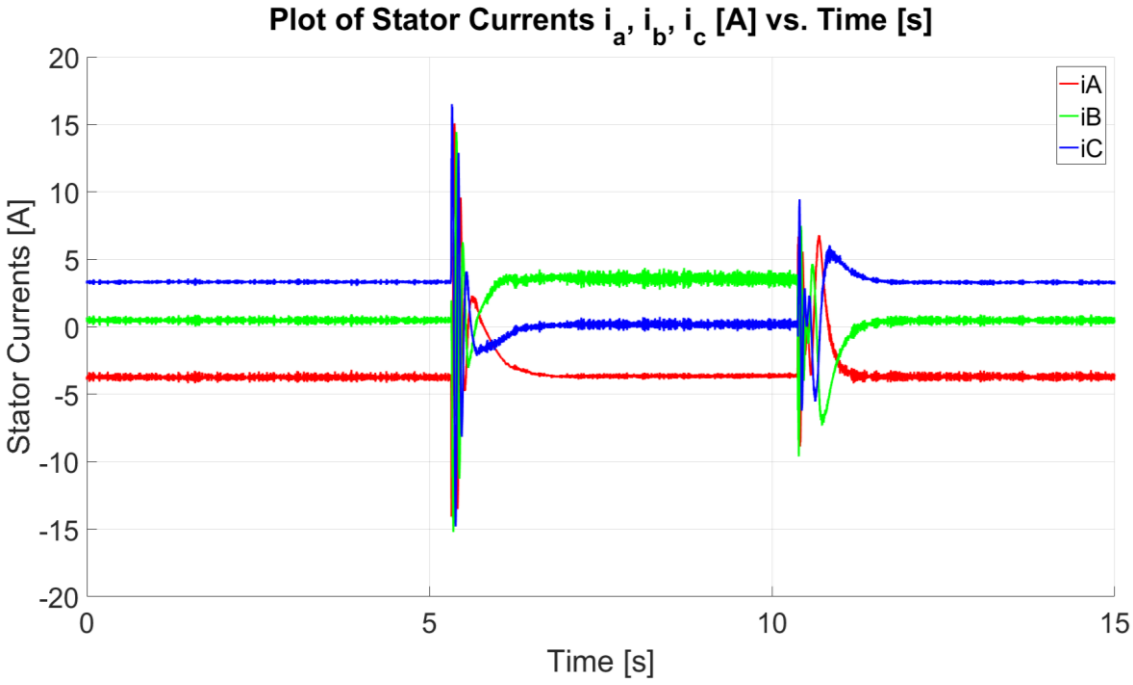

Figure 3.29 - Plot of Three-Phase Stator Currents i_a, i_b, i_c [A] vs. Time [s] with step position references of 0 rad to 3 rad (0° to 172°) and 3 rad to 0 rad (172° to 0°) on M3, i_{d4}^*= 0 A and i_{q4}^*=5 A on M4, in sensored position control.

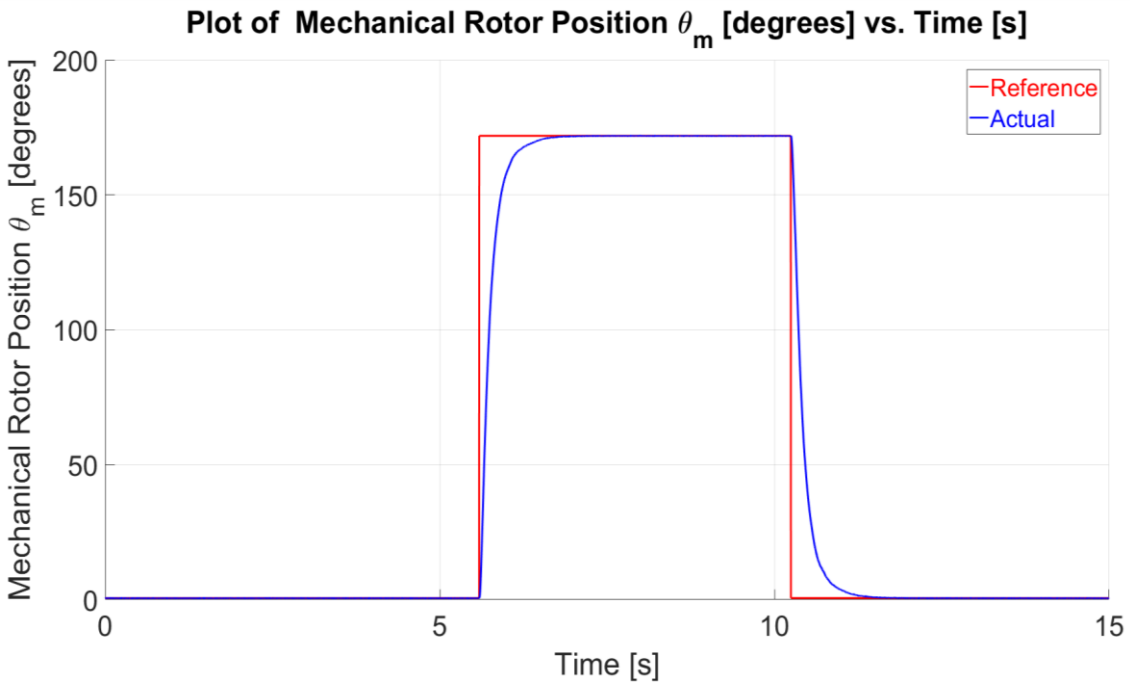

Figure 3.30 - Plot of Reference/Actual Mechanical Rotor Position θ_m [degrees] vs. Time [s] with step position references of 0 rad to 3 rad (0° to 172°) and 3 rad to 0 rad (172° to 0°) on M3, $i_{d4}^* = 0$ A and $i_{q4}^* = -5$ A on M4, in sensored position control.

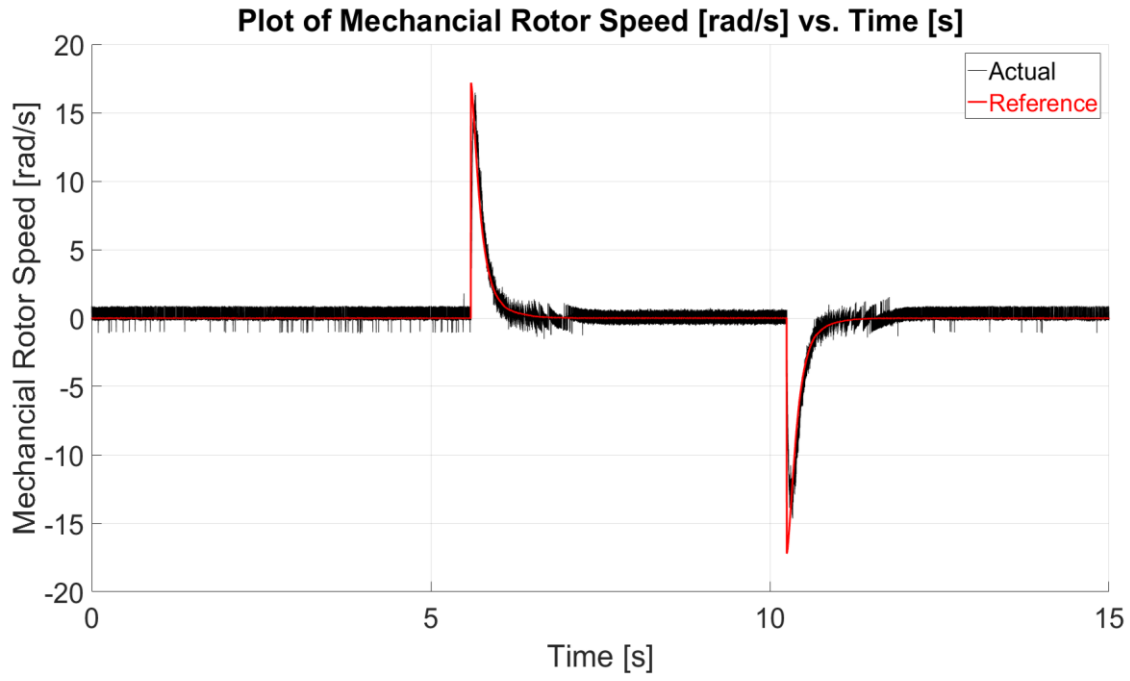

Figure 3.31 – Plot of Reference/Actual Mechanical Rotor Speed ω_m [rad/s] vs. Time [s] with step position references of 0 rad to 3 rad (0° to 172°) and 3 rad to 0 rad (172° to 0°) on M3, $i_{d4}^* = 0$ A and $i_{q4}^* = -5$ A on M4, in sensored position control.

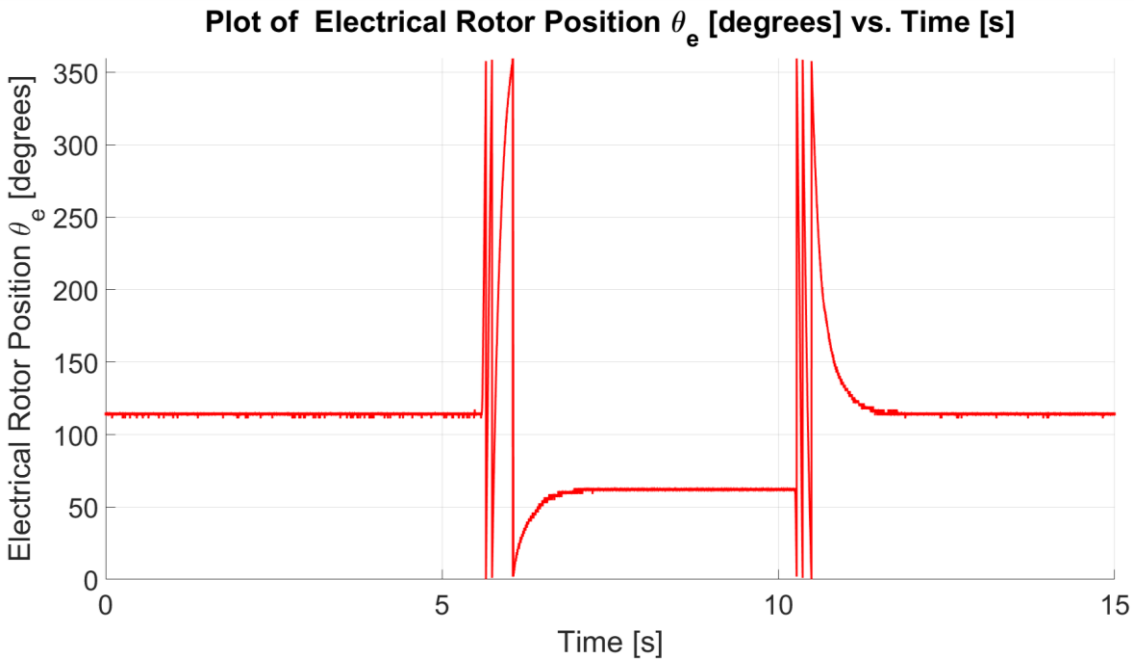

Figure 3.32 - Plot of Electrical Rotor Position θ_e [degrees] vs. Time [s] with step position references of 0 rad to 3 rad (0° to 172°) and 3 rad to 0 rad (172° to 0°) on M3, i_{d4}^*= 0 A and i_{q4}^*=-5 A on M4, in sensored position control.

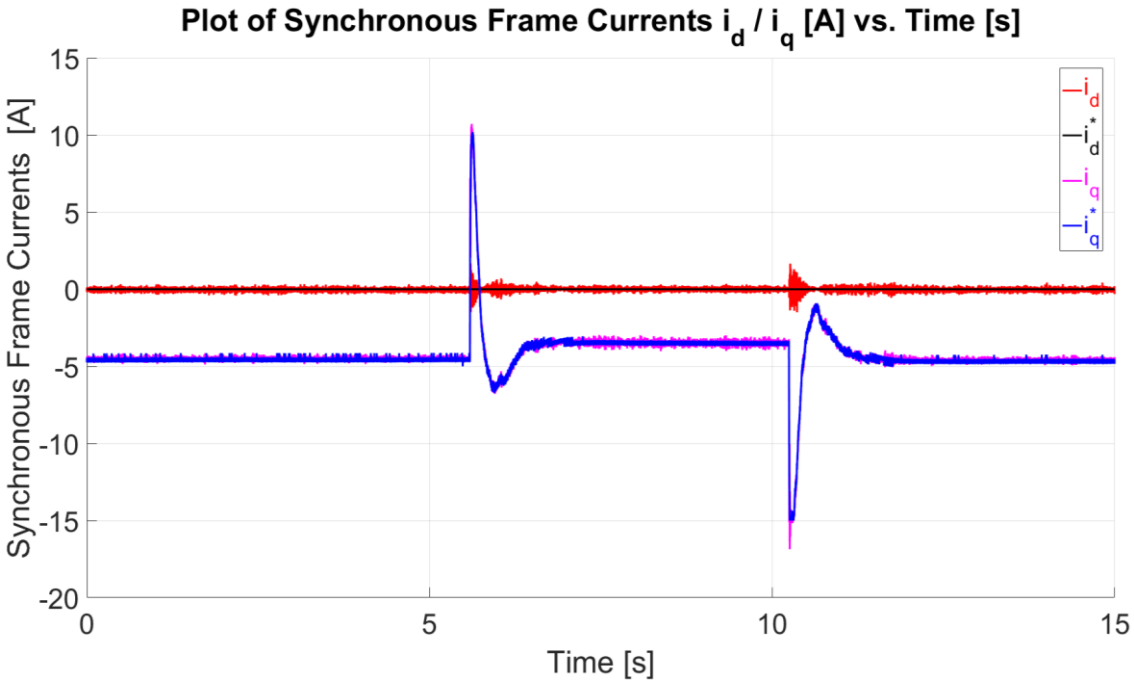

Figure 3.33 – Plot of Synchronous Stator Frame Currents i_d, i_q [A] vs. Time [s] with step position references of 0 rad to 3 rad (0° to 172°) and 3 rad to 0 rad (172° to 0°) on M3, i_{d4}^*= 0 A and i_{q4}^*=-5 A on M4, in sensored position control.

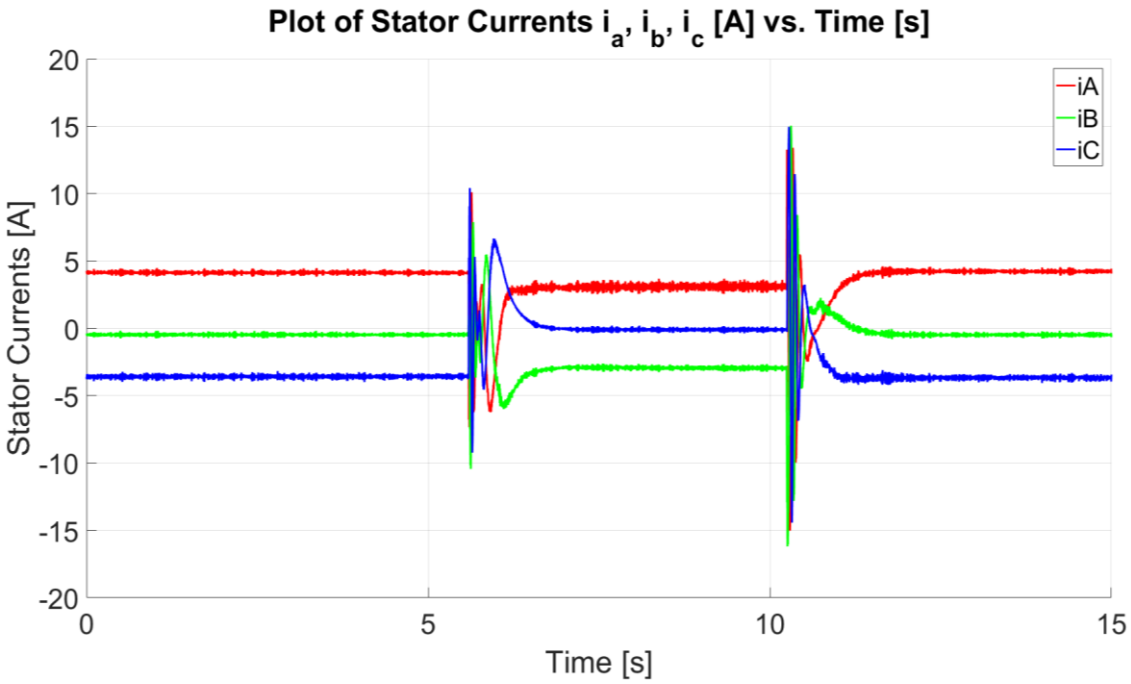

Figure 3.34 - Plot of Three-Phase Stator Currents i_a, i_b, i_c [A] vs. Time [s] with step position references of 0 rad to 3 rad (0° to 172°) and 3 rad to 0 rad (172° to 0°) on M3, i_{d4}^*= 0 A and i_{q4}^*=-5 A on M4, in sensored position control.

3.6.2 Sensored Position Control for sigmoid-function reference

In the steer-by-wire system, the steered wheel side is required to be in position-controlled mode. While the performance for the operation of the position-controlled PMSM drive under a step reference was shown in Section 3.6.1; the typical steering requirements in steer-by-wire do not to typically require such step transients. From the experimental data logged in Chapter 2 from the test vehicle in this dissertation, it is being proposed that a sigmoid function is used instead of a step reference. This can be justified by the fact that steering is actuated by the driver and thus transitions from a stationary position typically involve a delay associated with the driver's reaction times, as shown in Section 2.7. The mathematical formulation of the sigmoid functions used in this dissertation is presented in Appendix B.

The sigmoid-based position reference function is set to turn left and right by 146.6 degrees by configuring the sigmoid function parameters as described in Appendix B. The transient from start to end of the sigmoid function is approximately 189 degrees/s. The closed-loop position control system was tested with the same controller settings for speed and current as described in Section 3.6.1 but with an increased position controller

gain K_{p_P3} = 7.5. The increase in the position controller is possible since the initial position gradient is reduced with respect to a step input. The current references on the loading machine M4 are set to i_{d4}^{*} = 0 A, i_{q4}^{*} = 5 A. The reference and actual ***mechanical*** rotor position is shown in Figure 3.35 while the reference and actual ***mechanical*** rotor speed is shown in Figure 3.36. The ***electrical*** rotor position is shown in Figure 3.37. The synchronous frame reference and actual currents are shown in Figure 3.38, while the stator stationary frame currents are shown in Figure 3.39. The proposed position control results in a satisfactory steady-state response with zero steady-state error, however a velocity error (the difference between reference and output during ramp part of the signal) of 44.4° exists in the actual ***mechanical*** rotor position during the ramp part of the reference. This is not an issue for automotive steer-by-wire applications since such a lag shall not be experienced by a human driver.

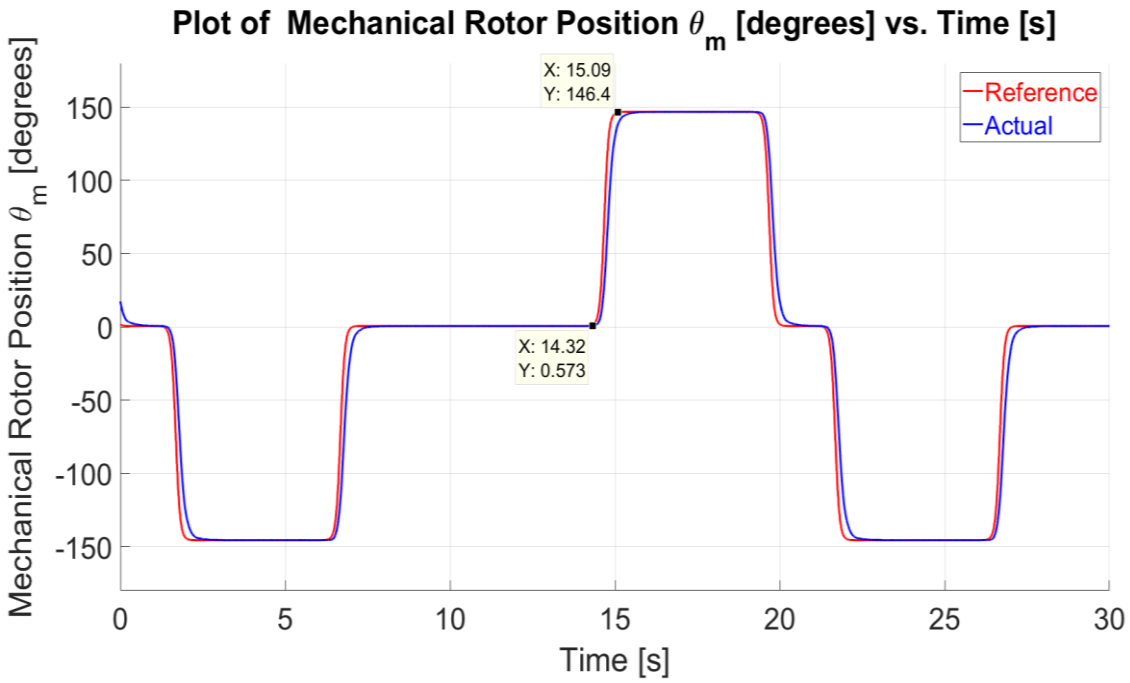

Figure 3.35 (a) - Plot of Reference/Actual Mechanical Rotor Position θ_m [degrees] vs. Time [s] with sigmoid position references on M3, i_{d4}^{*}= 0 A and i_{q4}^{*}=5 A on M4, in sensored position control.

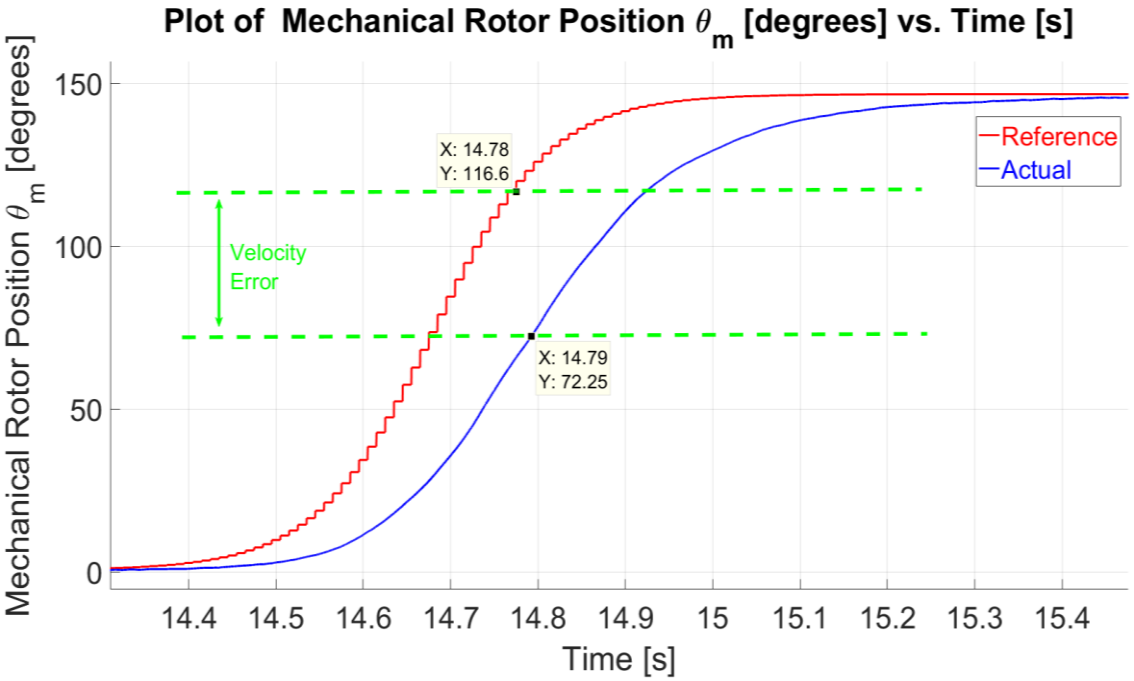

Figure 3.35 (b) - Plot of Reference/Actual Mechanical Rotor Position θ_m [degrees] vs. Time [s] with sigmoid position references on M3, i_d^*= 0 A and i_q^*=5 A on M4, in sensored position control at t = 15 s.

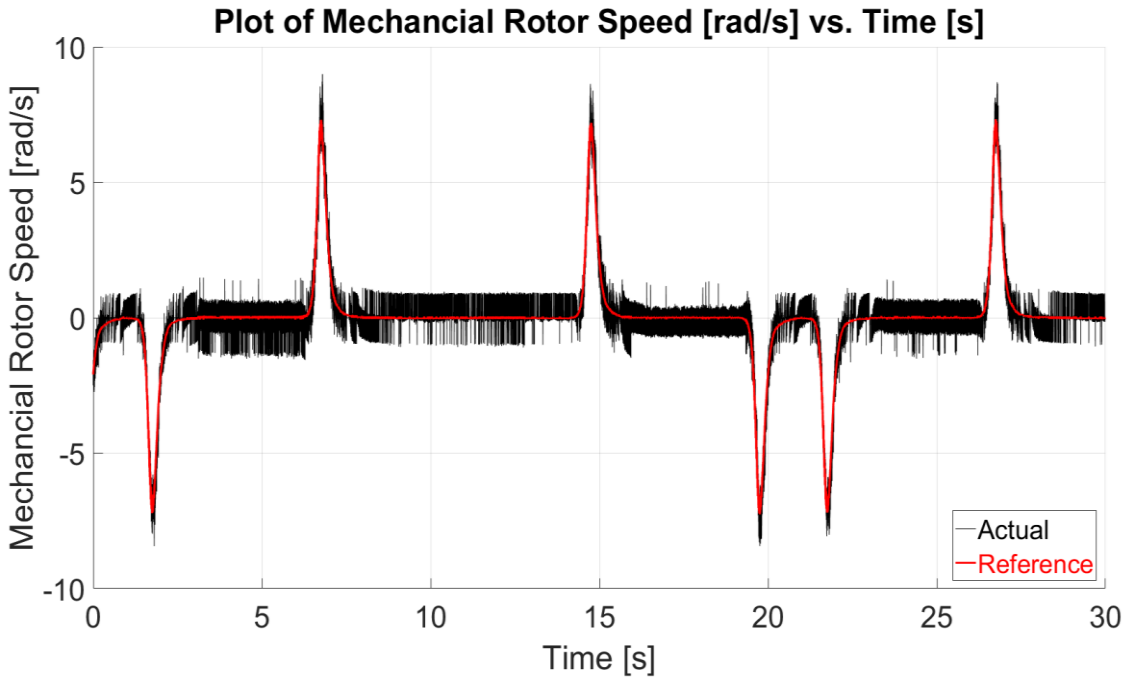

Figure 3.36 - Plot of Reference/Actual Mechanical Rotor Speed ω_m [rad/s] vs. Time [s] with sigmoid position references on M3, i_{d4}^*= 0 A and i_{q4}^*=5 A on M4, in sensored position control.

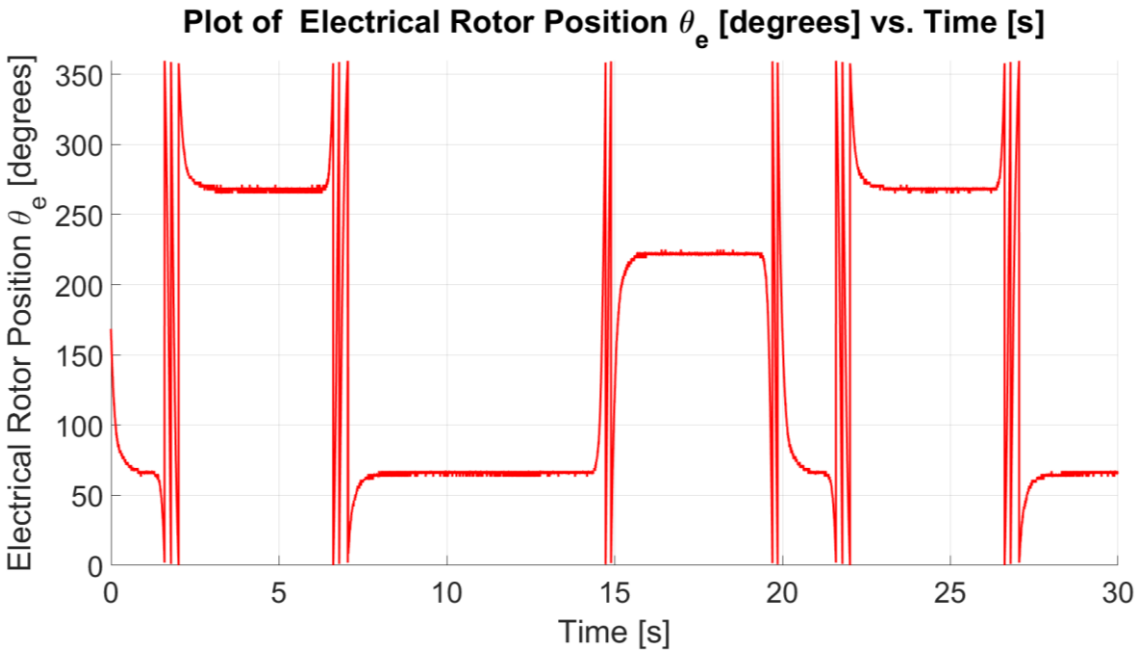

Figure 3.37 - Plot of Electrical Rotor Position θ_e [degrees] vs. Time [s] with sigmoid position references on M3, $i_{d4}^* = 0$ A and $i_{q4}^* = 5$ A on M4, in sensored position control.

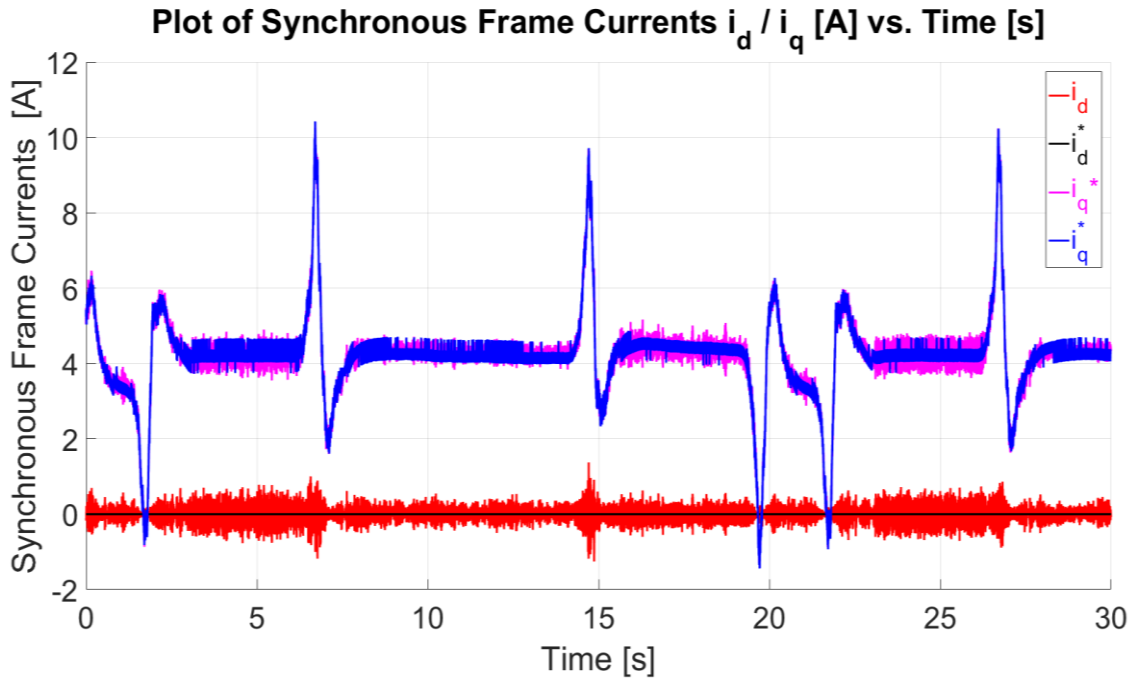

Figure 3.38 - Plot of Synchronous Stator Frame Currents i_d/i_q [A] vs. Time [s] with sigmoid position references on M3, $i_{d4}^* = 0$ A and $i_{q4}^* = 5$ A on M4, in sensored position control.

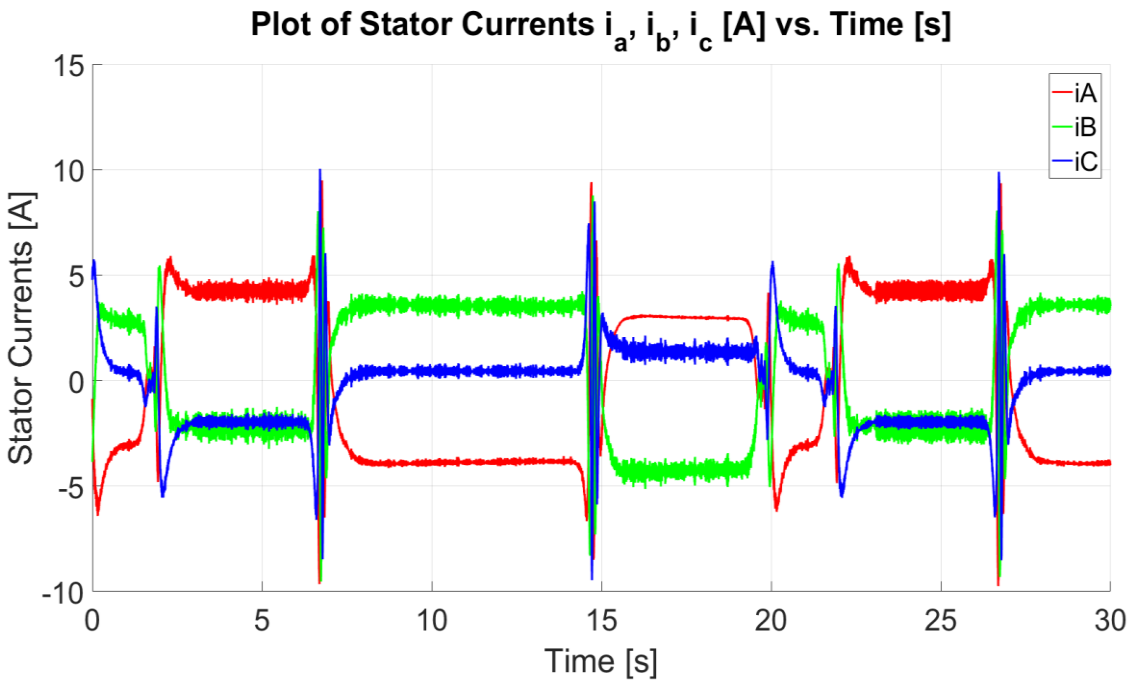

Figure 3.39 - Plot of Three-Phase Stator Currents i_a, i_b, i_c [A] vs. Time [s] with sigmoid position references on M3, i_{d4}^*= 0 A and i_{q4}^*=5 A on M4, in sensored position control.

The sigmoid-based position-controlled experiment was repeated with the current references on the loading machine M4 set to i_{d4}^* = 0 A, i_{q4}^* = -5 A. The reference and actual positions and speeds are shown in Figures 3.40 to 3.42 whilst the synchronous and stationary frame currents are shown in Figures 3.43 to 3.44.

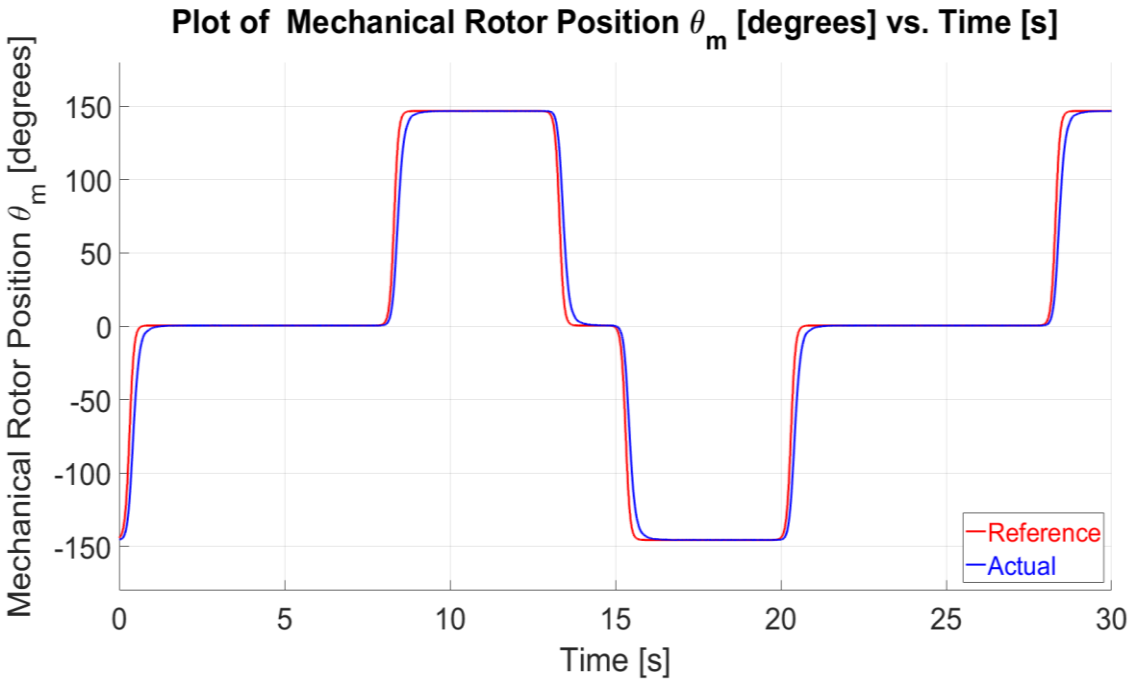

Figure 3.40 - Plot of Reference/Actual Mechanical Rotor Position θ_m [degrees] vs. Time [s] with sigmoid position references on M3, i_{d4}^*= 0 A and i_{q4}^*=-5 A on M4, in sensored position control.

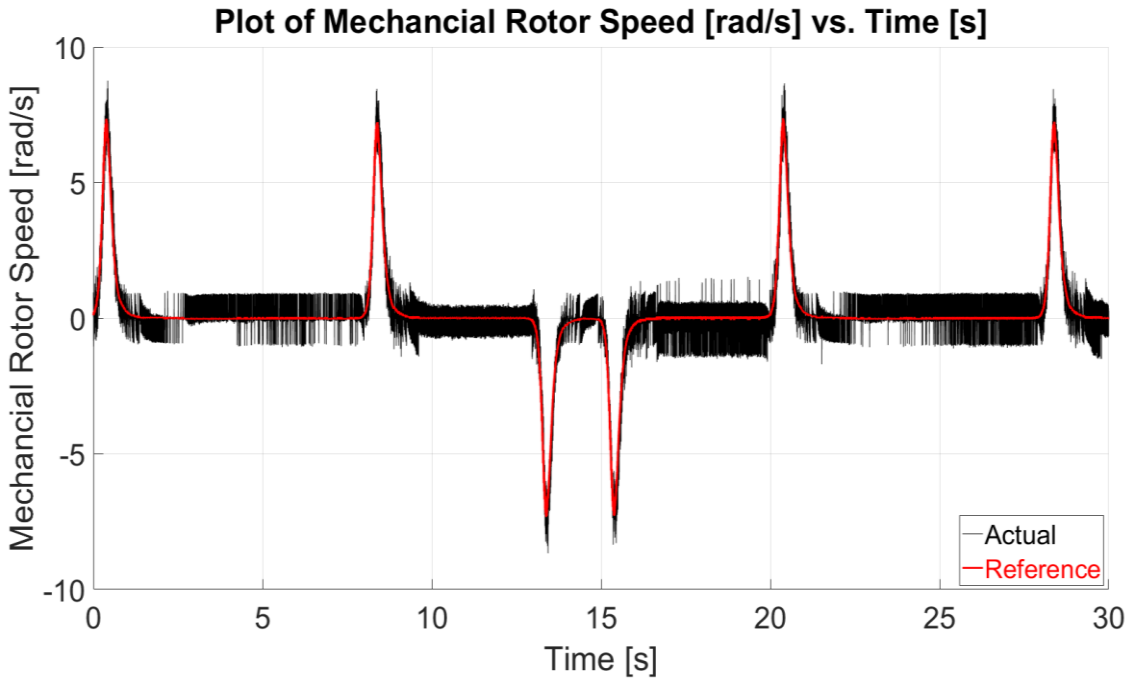

Figure 3.41 - Plot of Reference/Actual Mechanical Rotor Speed ω_m [rad/s] vs. Time [s] with sigmoid position references on M3, i_{d4}^*= 0 A and i_{q4}^*=-5 A on M4, in sensored position control.

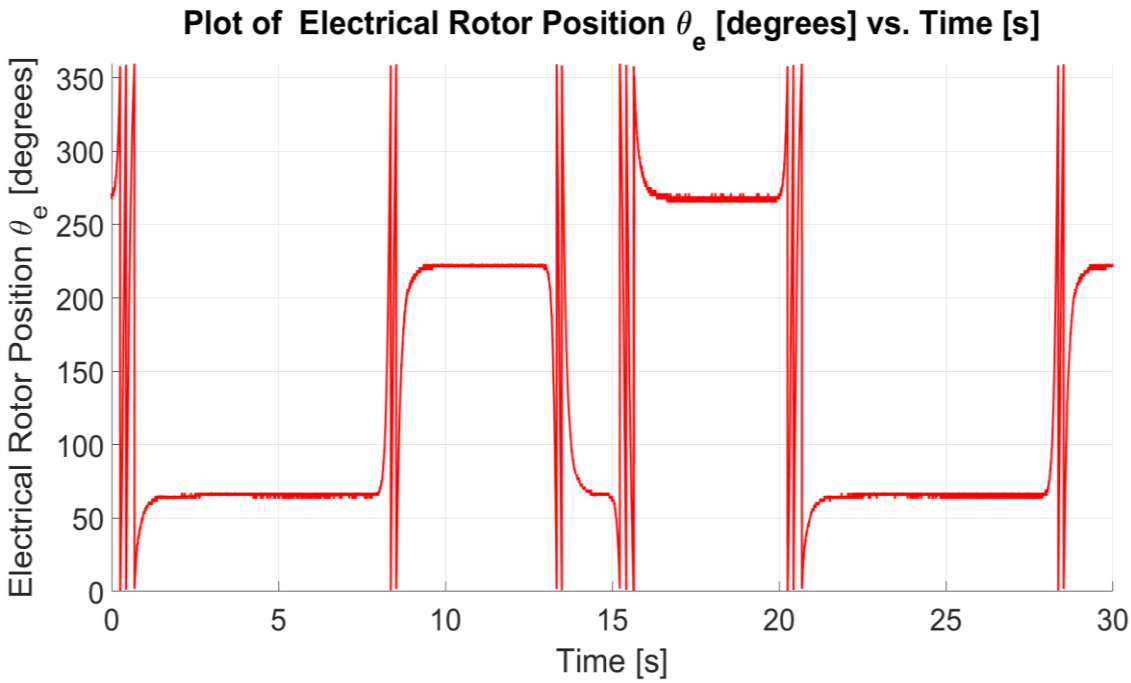

Figure 3.42 - Plot of Electrical Rotor Position θ_e [degrees] vs. Time [s] with sigmoid position references on M3, i_{d4}^*= 0 A and i_{q4}^*=-5 A on M4, in sensored position control.

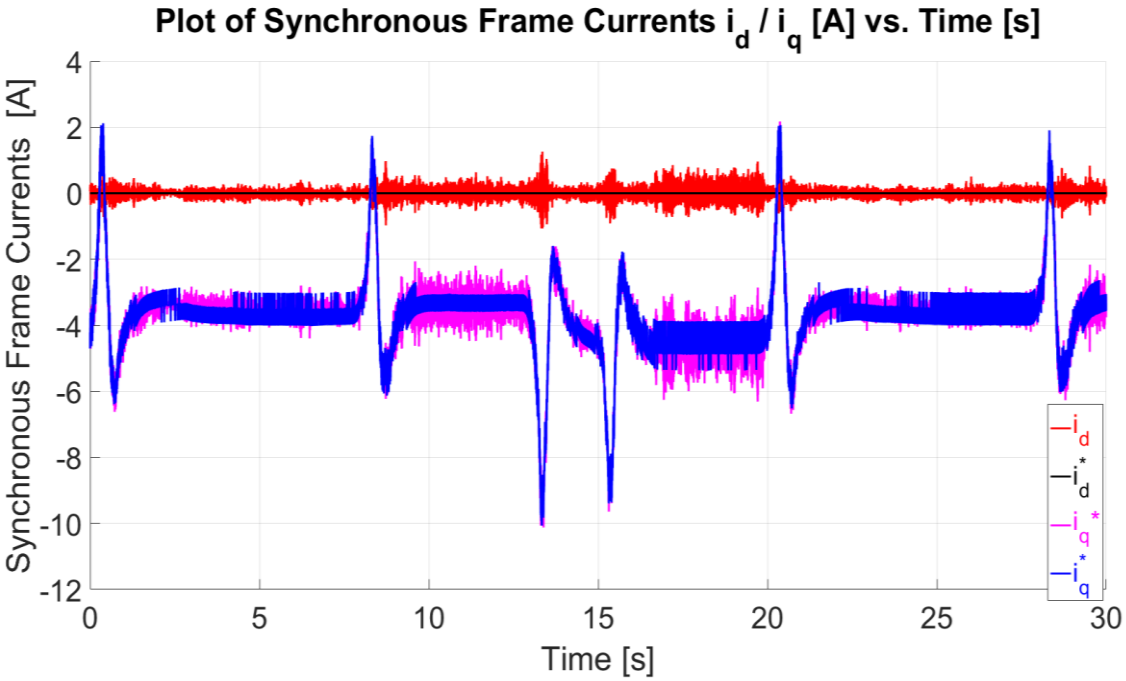

Figure 3.43 - Plot of Synchronous Stator Frame Currents i_d/i_q [A] vs. Time [s] with sigmoid position references on M3, i_{d4}^*= 0 A and i_{q4}^*=-5 A on M4, in sensored position control.

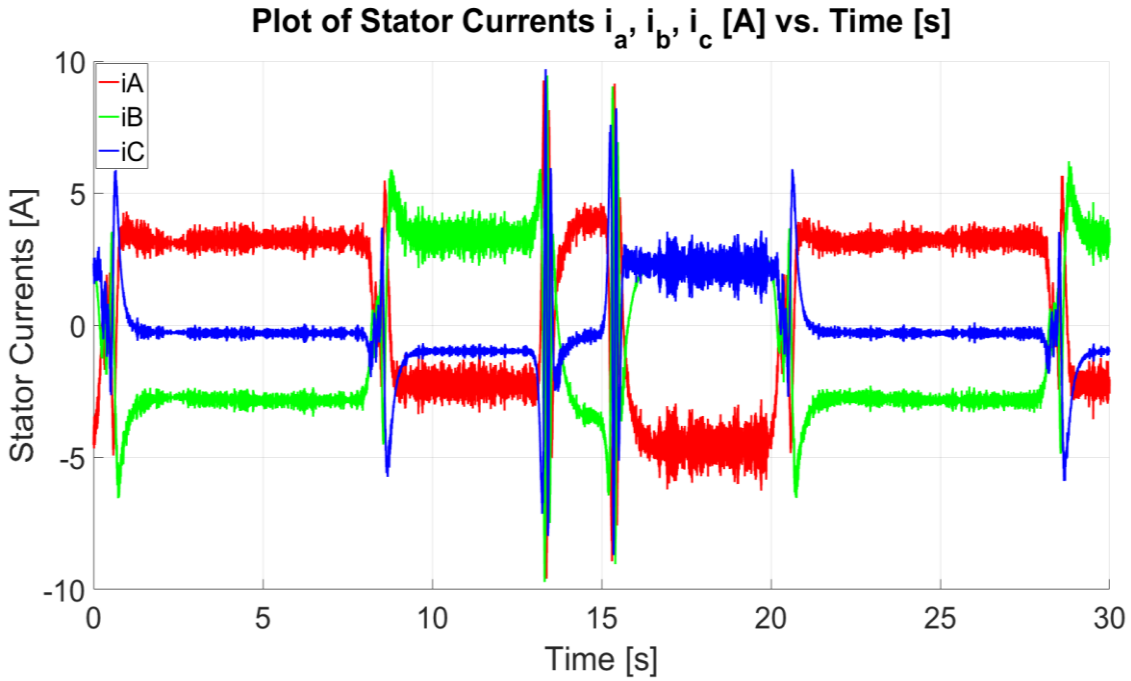

Figure 3.44 - Plot of Three-Phase Stator Currents i_a, i_b, i_c [A] vs. Time [s] with sigmoid position references on M3, i_{d4}^*= 0 A and i_{q4}^*=-5 A on M4, in sensored position control.

3.6.3 Sensored Position Control with Lead-Lag Compensator

The sensored position-controlled response shown in Section 3.6.2 is generally suitable for the steer-by-wire application since the steady-state error is zero. However, in a number of servo applications, it is required to reduce the velocity error to a minimum. The implementation of this was carried out by analysing the steady-state error of the position loop.

The type of a system is equal to the number of integrators in the open-loop transfer function, including both the controller and the plant [47]. If a simple proportional controller is used as described in Section 3.2.6, the type of the system is 1 since there is only one integrator. In general, the stator velocity error constant K_v for a unit ramp is (3.22).

$$\mathrm{K_v} = \lim_{s \to 0} s\, G(s) \tag{3.22}$$

Substituting the open-loop transfer function in (3.22) results in (3.23)

$$\mathrm{K_v} = \lim_{s \to 0} s\, \frac{\mathrm{K_p}}{s} \tag{3.23}$$

Therefore, the steady-state error for the unit ramp is (3.24).

$$e_{ss} = \frac{1}{\mathrm{K_v}} = \frac{1}{\mathrm{K_p}} \tag{3.24}$$

Since (3.30) is effectively a constant, the velocity error shown in Figure 3.35 results. If a PI controller is used instead of the proportional controller, the system would be increased to type 2, which has no velocity ramp error. However, having two integrators if often not a recommended approach due to stability concerns.

A similar performance can be achieved by using a lead-lag compensator. A lead-lag compensator-based controller was designed in MATLAB with a bandwidth of 5 Hz and a damping ratio $\zeta = 0.707$. The controller parameters were adjusted until a satisfactory tracking response was observed on a simulated model using the same position sigmoid reference as used in the previous sections in this chapter. The compensator transfer function in the s-domain is given in (3.25). The resulting position closed-loop control system is shown in Figure 3.45.

$$C_{leadlag(s)} = \frac{42.776(s+22.61)}{(s+1.204)} \tag{3.25}$$

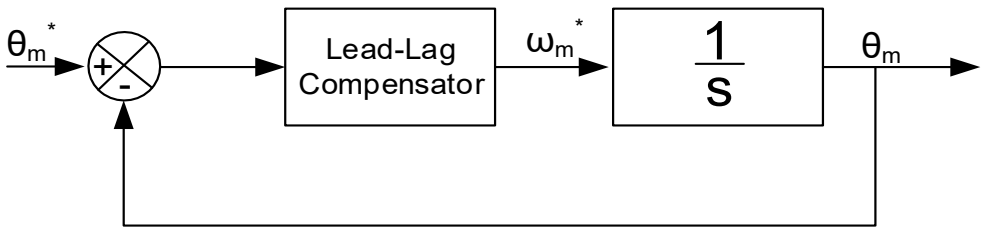

Figure 3.45 - Closed-loop position control with Lead-Lag Compensator

The performance of the lead-lag compensator as a position controller with the RFO cascaded architecture is shown with identical speed, and current controller settings on M3 as in Section 3.6.2 with the current references on the loading machine M4 set to $i_{d4}^* = 0$ A, $i_{q4}^* = 5$ A. The reference and actual positions and speeds are shown in Figures 3.46 to 3.48 whilst the synchronous and stationary frame currents are shown in Figures 3.49 to 3.50. The introduction of the lead-lag compensator reduces the velocity error to a negligible value with respect to when a proportional controller was used, as shown in Figure 3.46. The experiment was repeated with an $i_{d4}^* = 0$ A, $i_{q4}^* = -5$ A. The reference and actual positions and speeds are shown in Figures 3.51 to 3.53 whilst the synchronous and stationary frame currents are shown in Figures 3.54 to 3.55.

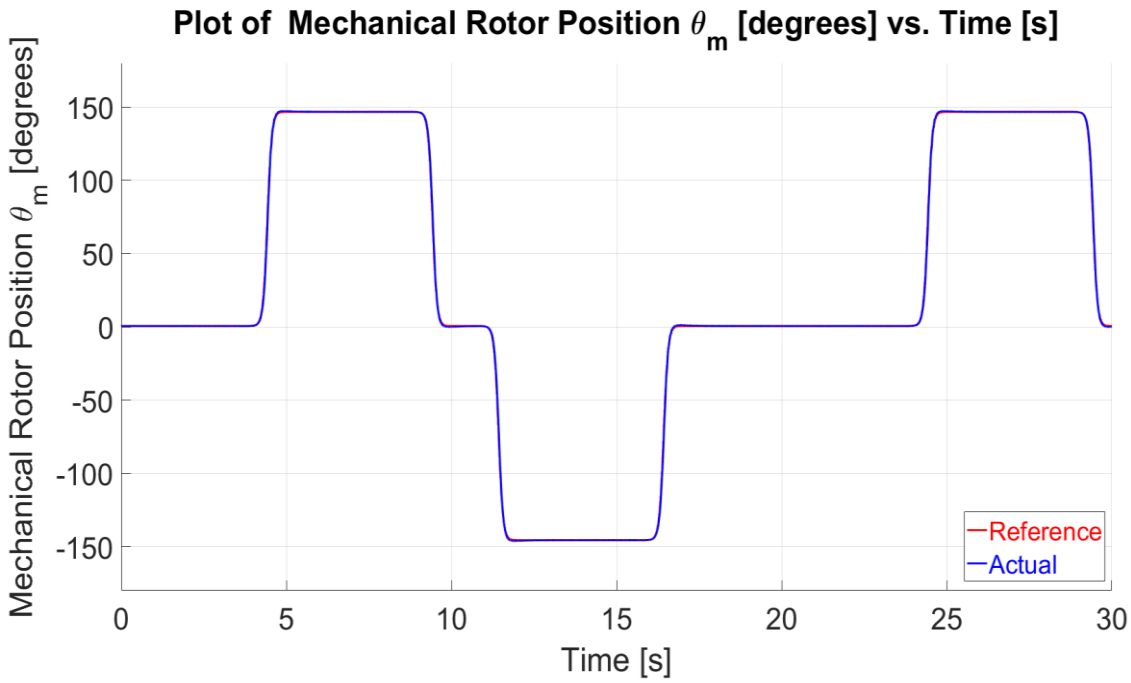

Figure 3.46 - Plot of Reference/Actual Mechanical Rotor Position θm [degrees] vs. Time [s] with sigmoid position and lead-lag compensator with references on M3, i_{d4}^*= 0 A and i_{q4}^*=5 A on M4, in sensored position control.

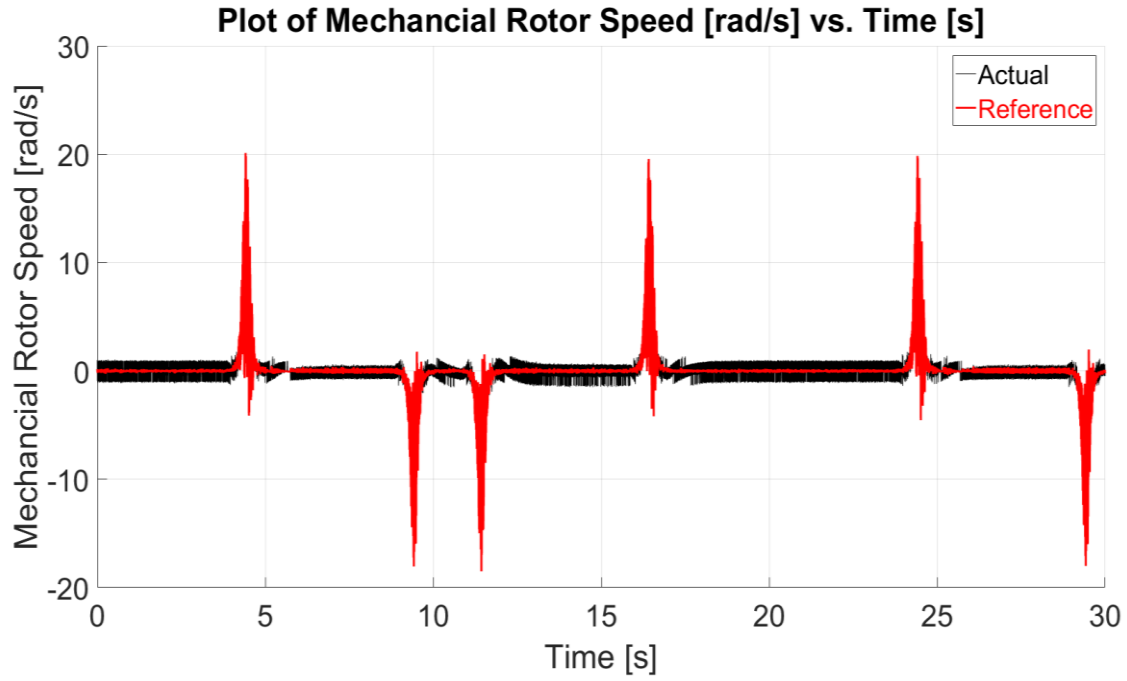

Figure 3.47 - Plot of Reference/Actual Mechanical Rotor Speed ω_m [rad/s] vs. Time [s] with sigmoid position and lead-lag compensator with references on M3, $i_{d4}^* = 0$ A and $i_{q4}^* = 5$ A on M4, in sensored position control.

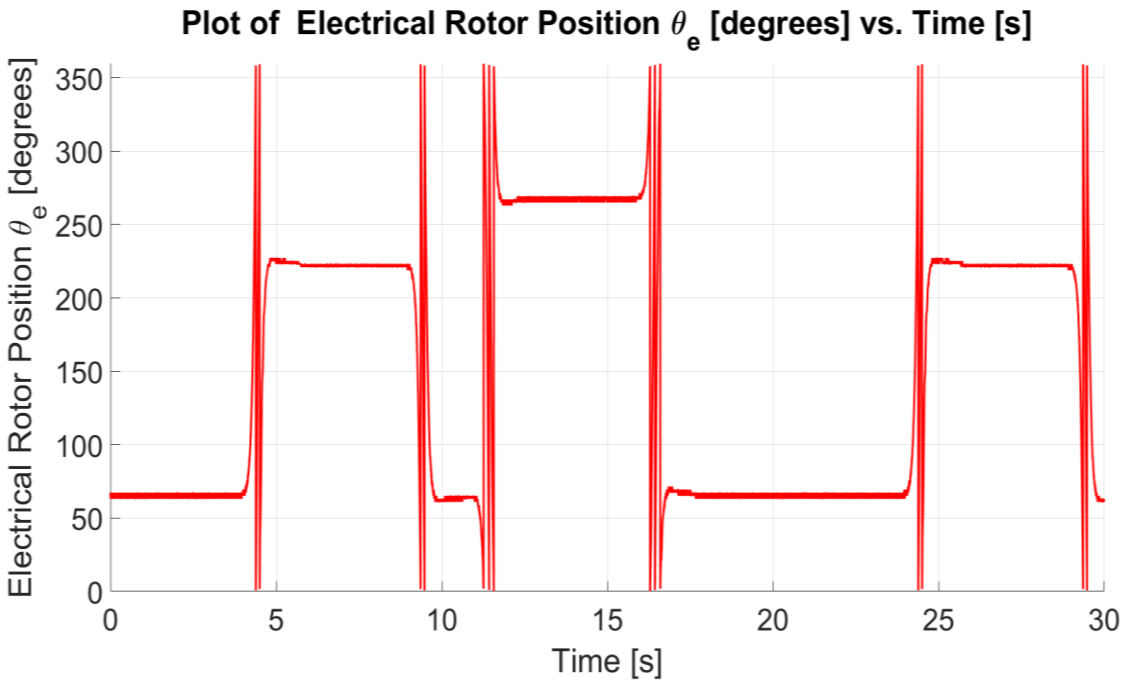

Figure 3.48 – Plot of Electrical Rotor Position θ_e [degrees] vs. Time [s] with sigmoid position and lead-lag compensator with references on M3, $i_{d4}^* = 0$ A and $i_{q4}^* = 5$ A on M4, in sensored position control.

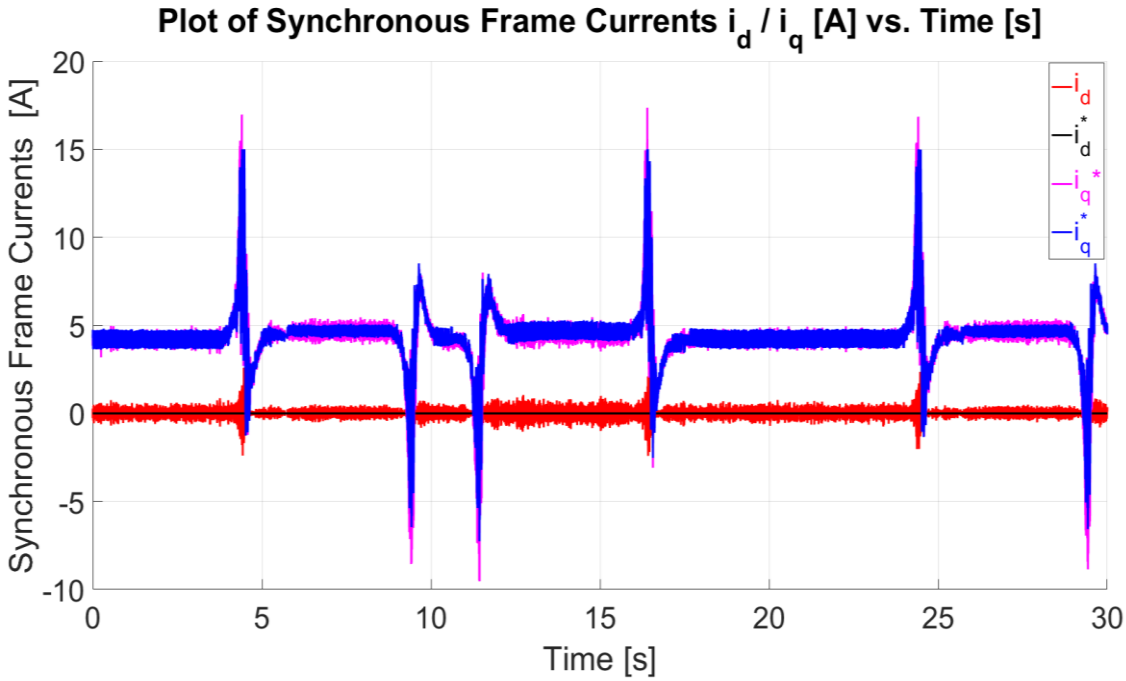

Figure 3.49 – Plot of Synchronous Stator Frame Currents i_d/i_q [A] vs. Time [s] with sigmoid position and lead-lag compensator with references on M3, i_{d4}^*= 0 A and i_{q4}^*=5 A on M4, in sensored position control.

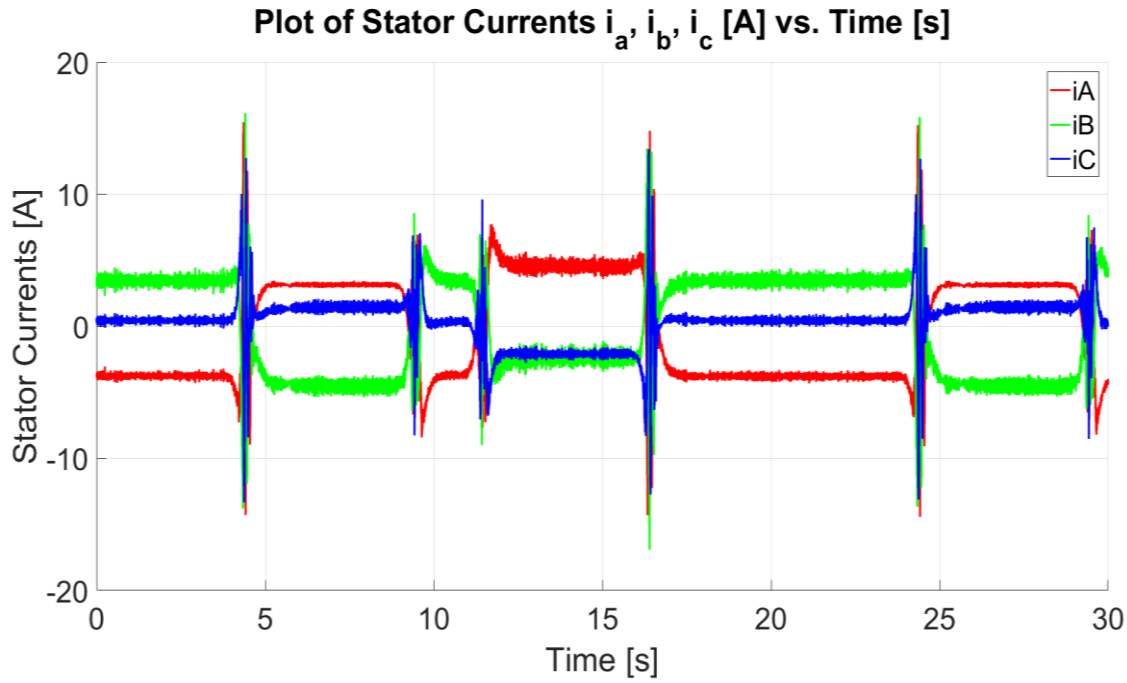

Figure 3.50 – Plot of Three-Phase Stator Currents i_a, i_b, i_c [A] vs. Time [s] with sigmoid position and lead-lag compensator with references on M3, i_d^*= 0 A and i_q^*=5 A on M4, in sensored position control.

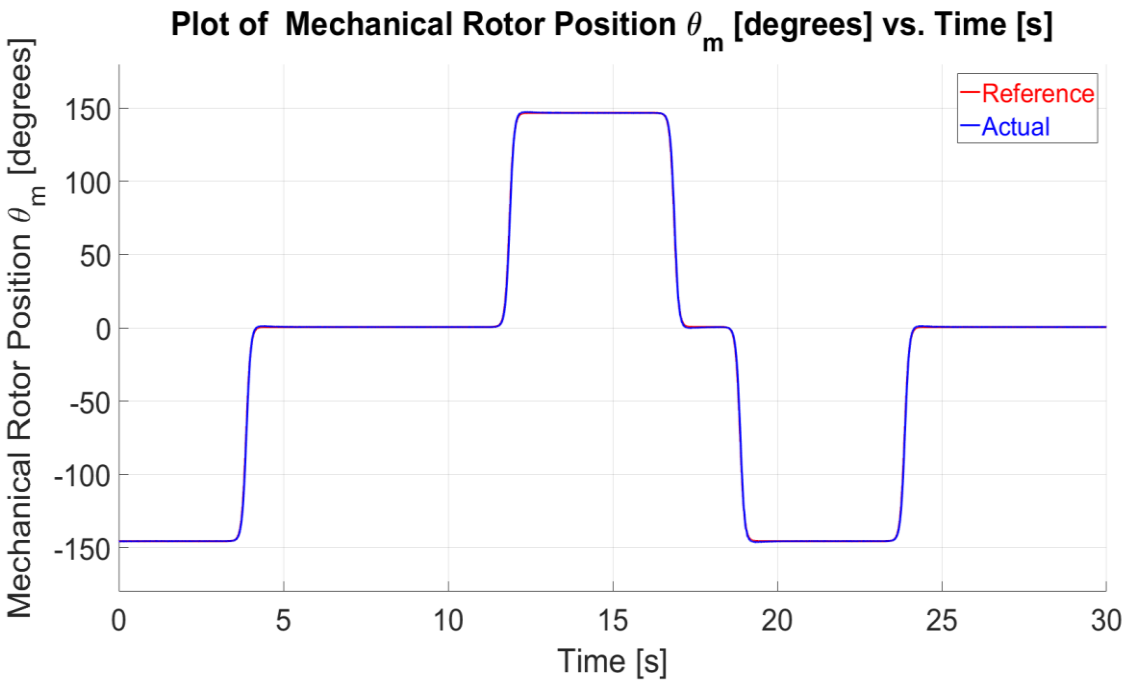

Figure 3.51 – Plot of Reference/Actual Mechanical Rotor Position θ_m [degrees] vs. Time [s] with sigmoid position and lead-lag compensator with references on M3, i_{d4}^*= 0 A and i_{q4}^*=-5 A on M4, in sensored position control.

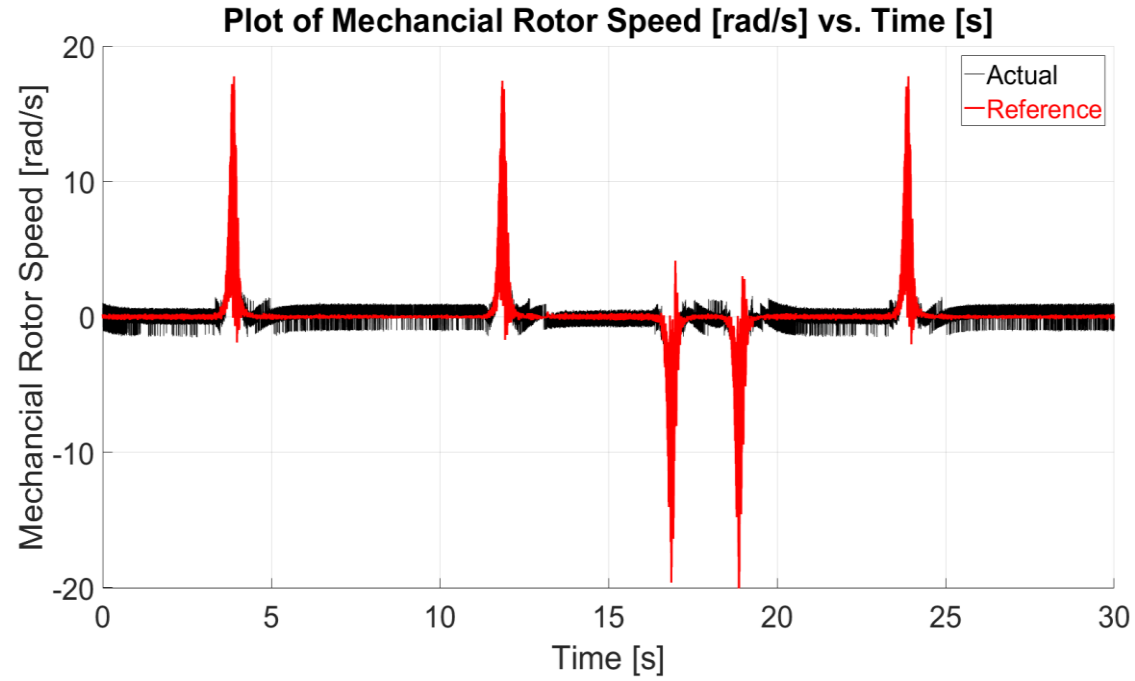

Figure 3.52 – Plot of Reference/Actual Mechanical Rotor Speed ω_m [rad/s] vs. Time [s] with sigmoid position and lead-lag compensator with references on M3, i_{d4}^*= 0 A and i_{q4}^*=-5 A on M4, in sensored position control.

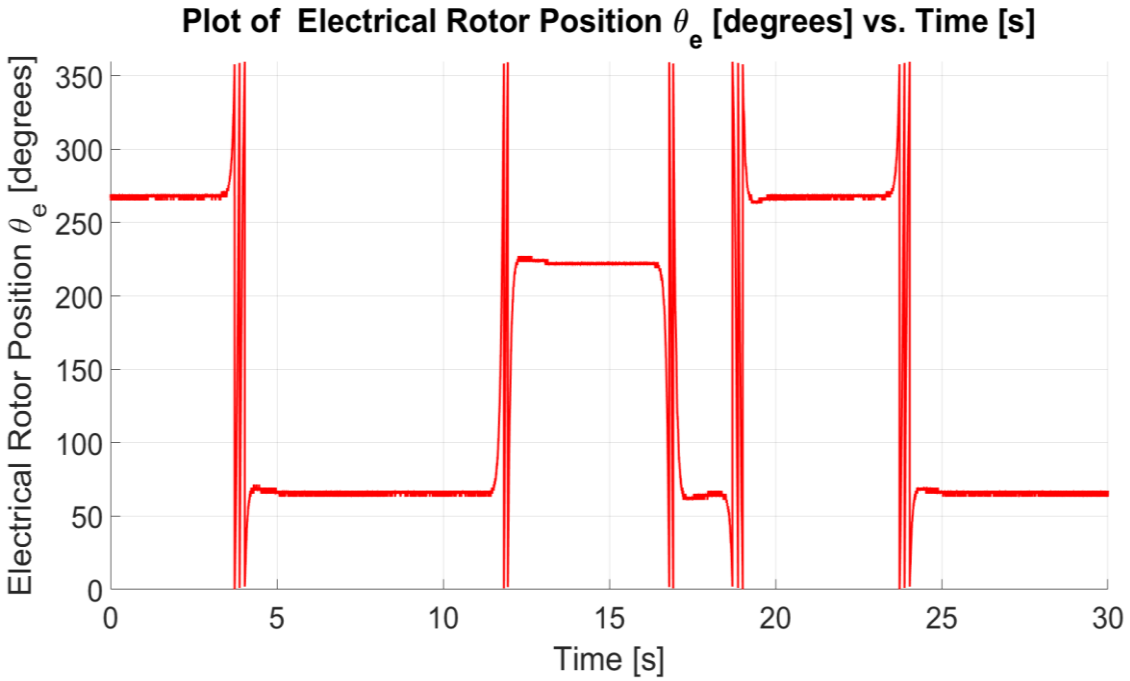

Figure 3.53 – Plot of Electrical Rotor Position θ_e [degrees] vs. Time [s] with sigmoid position and lead-lag compensator with references on M3, $i_{d4}^* = 0$ A and $i_{q4}^* = -5$ A on M4, in sensored position control.

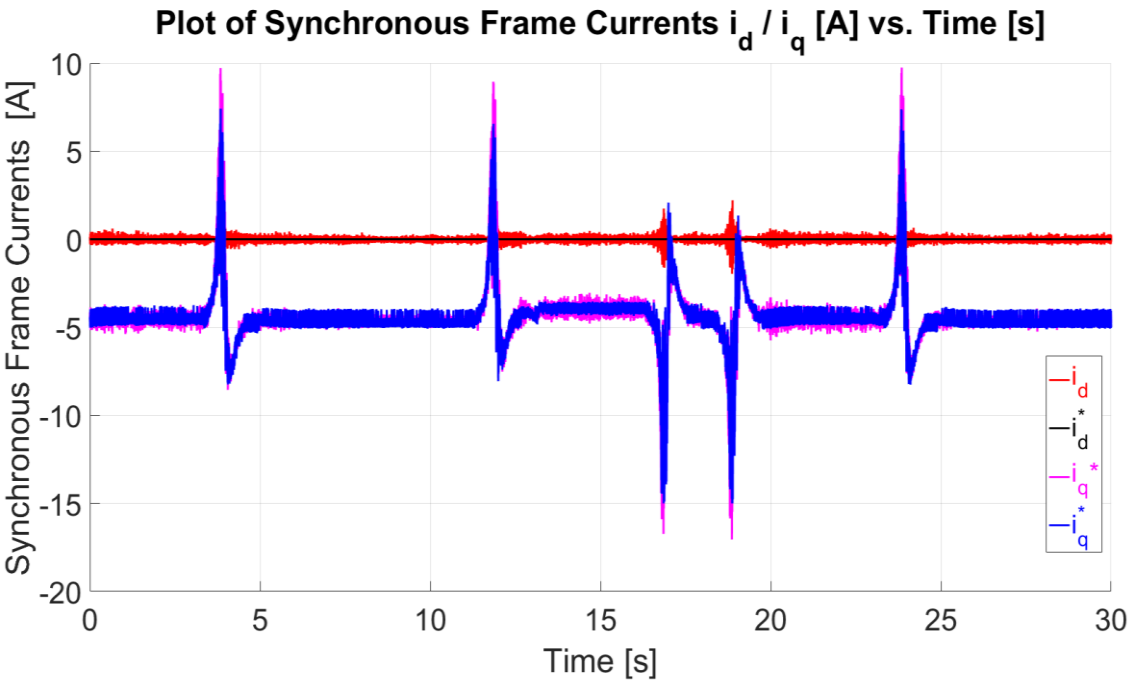

Figure 3.54 – Plot of Synchronous Stator Frame Currents i_d/i_q [A] vs. Time [s] with sigmoid position and lead-lag compensator with references on M3, $i_{d4}^* = 0$ A and $i_{q4}^* = -5$ A on M4, in sensored position control.

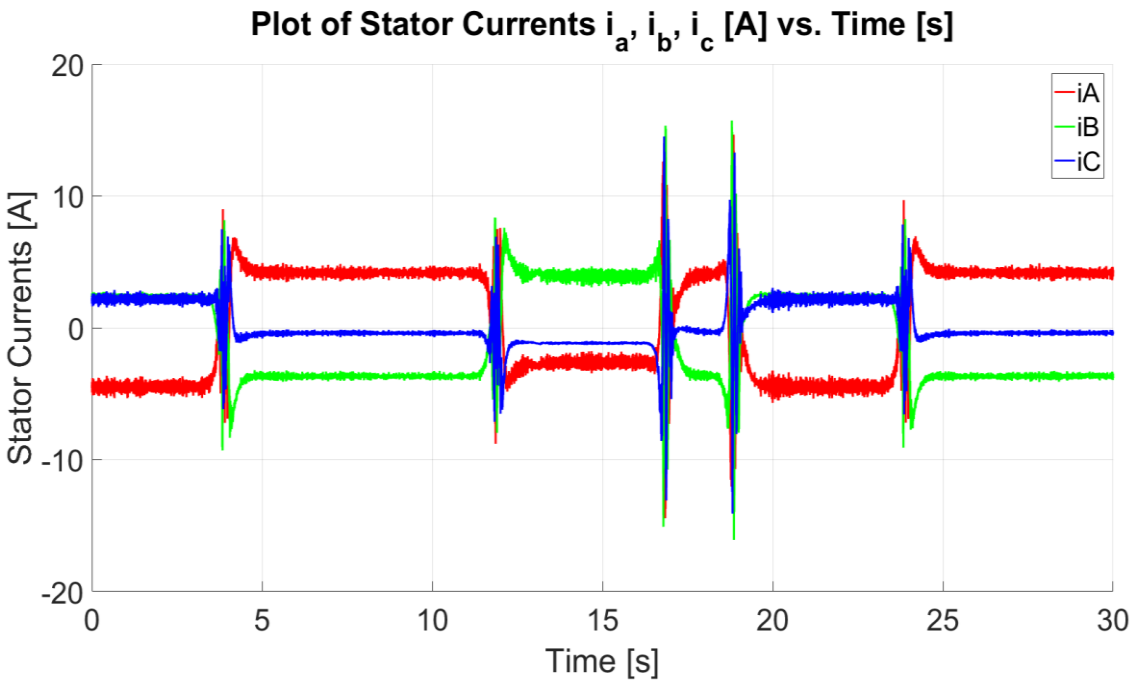

Figure 3.55 – Plot of Three-Phase Stator Currents i_a, i_b, i_c [A] vs. Time [s] with sigmoid position and lead-lag compensator with references on M3, $i_{d4}^* = 0$ A and $i_{q4}^* = -5$ A on M4, in sensored position control.

3.7 Summary

This chapter presented an overview of the PMSM and its advantages for the proposed steer-by-wire application in this dissertation. The dynamic equations of the PMSM machine were derived, and the current, speed and position loops for RFO control, as shown in Figure 3.4. The electrical and mechanical parameters of the PMSM were derived through experimental measurements from the drive itself since they were not listed in the technical datasheet. The electrical parameters R, L_d and L_q were found through locked rotor tests and application of step voltage references v_d^* and v_q^*. The open-loop bandwidths of the d and q-axis electrical plants were found to be 92 Hz and 57.6 Hz respectively. The difference in the bandwidth (assuming an equal resistance R) is a result of L_q being a factor of 1.6 times larger than the L_d. This is an indication that the machine under test has a significant amount of rotor position-dependent saliency. The mechanical parameters were also found through the application of a step i_q-current reference. The moment of inertia, J, was calculated from the steady-state of the resultant speed while the coefficient of friction B was obtained from the rotor speed transient, assuming a first-order system.

Sensored current control operation was mainly shown for different i_q-current values with the i_d-current reference set to 0 A since field weakening operation was not considered in this dissertation. For current controller gains of $K_{p\_I3} = 0.3$ and $K_{i\_I3} = 350$, the current loop bandwidth was determined experimentally to be 281 Hz with an overshoot of 57.4%. Sensored speed operation was tested on M3 with machine M4 acting as a load. For speed controller gains of $K_{p\_W3} = 0.3$ and $K_{i\_W3} = 60$ in speed-controlled mode the speed loop bandwidth was experimentally determined to be 15.93 Hz with an overshoot of 27.6 %. The sensored position operation was tested by introducing a proportional gain of $K_{p\_P3} = 5.75$ outside the speed control loops. For this setting, the bandwidth was found experimentally to be equal to 1 Hz. The proportional gain in the position loop is limited when using a step-reference due to the high current demanded at the initial step transient. The current demanded for the current loop is proportional to the position control gain. In order to reduce such a demand, sigmoid based functions are introduced instead of step references.

The sigmoid references are particularly suited for steer-by-wire operation since they better approximate the steering movements actuated by the driver. The proportional controller within the position loop results in a type 1 system which has a velocity error for ramp inputs. Since a significant part of the sigmoid function is of the ramp type a significant velocity error of 44° was observed between the reference and actual rotor position. Mitigation of this velocity error was proposed through the use of a lead-lag compensator which was shown to reduce the velocity error to a negligible value.

Chapter 4 – Review of Sensorless Control Algorithms

4.1 Introduction to Sensorless Control

Sensorless control algorithms have been widely used to estimate the position and speed of electrical machines without having a dedicated sensor. Typically encoders or tachogenerators are used to obtain these measurements in sensored closed-loop control of electrical drives. However, these sensors usually are mechanically coupled to the rotor shaft and tend to be more susceptible to failure than other electronic-based transducers due to mechanical vibrations and the harshness of the surrounding environment. Sensorless control is aimed at the estimation of the rotor position and speed as a function of other measurable electrical quantities such as the stator currents and voltages which are still measured for the fundamental position or speed control of the electrical machine.

In this dissertation, the sensorless position estimation of the rotor position at low to zero speed of a Surface-Mounted Permanent Magnet Synchronous Machine (SM-PMSM) is investigated. The rotor electrical position θ_e is required for the Rotor Flux Oriented (RFO) vector control algorithm in order to ensure a precise torque control. The position and speed estimates can be used for the validation of encoder measurements in sensored operation or for complete sensorless operation. This chapter reviews the main sensorless control methods which can be classified into the following categories [48, 49]:

- Methods based on signals at the fundamental motor frequency.
- Methods based on the injection of signals at a higher frequency than the fundamental.
- Methods based on the detection of inherent high-frequency signals.

In general, sensorless algorithms using signals at the fundamental motor frequency are used for medium to rated operating speed. When the speed is reduced close to the standstill, techniques which operate at a higher frequency than the fundamental are used. The different categories are described in this chapter and suitable methods for the steer-by-wire application are outlined.

4.2 Sensorless Control with Fundamental Frequency Signals.

Methods based on signals at the fundamental motor frequency can operate over a wide range of speeds [50, 51]. The main drawback of these sensorless control methods is that most are based on the measurement or estimation of the rotational back-emf, which decreases significantly at low speeds. Hence, the accuracy of estimates at this operating point is severely affected by sensor offsets, power semiconductor nonlinearities and noise. Model-based sensorless observers can be further sub-divided into open-loop and closed-loop methods [48].

Open-loop methods estimate the rotor position from a direct voltage measurement across the stator terminals. The direct measurement is used in a number of medium to high speed, low starting torque applications such as unmanned vehicles [52, 53], automotive [54, 55] and aerospace [56, 57]. The direct measurement method is mostly used with a six-step type commutation where the back-emf can be read from the voltage of the non-conducting phase at each step of the commutation cycle [55, 58-61]. When a non-conducting phase is not available such as with Sinusoidal Pulse Width Modulation (SPWM) or Space Vector Pulse Width Modulation (SVPWM), the measurements can be replaced through a machine voltage model [62]. Both measurement and model-based techniques have a restricted minimum operating frequency [48] due to the low back-emf close to zero speed.

Closed-loop methods use internal compensation schemes in order to improve upon the performance of open-loop methods. One of the most commonly used closed-loop sensorless methods is the Model Reference Adaptive System (MRAS) [63, 64]. The MRAS method uses a parallel combination of a reference model and an adjustable model from which a back-emf based error is calculated. The error is then compensated for by the closed-loop feedback system. The Extended Kalman Filter (EKF) is a stochastic type filter which has also been used for closed-loop estimation purposes in permanent magnet machines [65, 66]. The EKF operates on a least square variance estimation to calculate the state of the estimated system. The EKF has the advantage of higher immunity to measurement noise and parameter variation [67]. Although the use of the EKF has been reported to lower the speed threshold at which estimation is still accurate, its performance is still inadequate for sensorless closed-loop operation in the zero speed region [68]. Similarly to the EKF, the Sliding Mode Observer (SMO) is also used to reduce the dependency of estimates on parameter variations [69, 70]. A sliding

hyperplane is defined and chosen through error vectorial calculations. The hyperplane is used to make the system slide until minimum error is achieved. The conventional SMO uses a signum function as the switching function and is known to suffer from chattering. An improved version was proposed in [71], which uses a sigmoid function instead. Since the SMO is still dependent on the rotational back-emf, it is not sufficiently accurate for closed-loop sensorless control at low speeds.

The application considered in this work is related to vehicle steering and is characterized by extended periods at the initial handwheel position with transients during vehicle steering. Since at steady-state the application is at zero speed, the methods based on the fundamental frequency signals are not recommended due to the low back-emf voltages which would be available for estimation. Hence, for this dissertation, such methods were not considered any further. The next sections 4.3-4.8 shall conduct an overview of High Frequency (HF) based sensorless control techniques which are more suitable for the steer-by-wire application proposed in this dissertation.

4.3 High Frequency-based Sensorless Control techniques

Algorithms for tracking position-dependent machine parameter variations have been widely reported in literature. In the case of asynchronous machines, such variations could be present due to a number of sources such as the rotating flux itself [72], rotor slots [73-76] or magnetic asymmetries embedded in the rotor [77-81]. In the case of synchronous machines, the saliencies are mainly due to the magnetic saturation in the SM-PMSMs [76, 82-84] and geometric asymmetries in interior permanent magnet synchronous machines (IPMSMs) [85, 86].

There are different methods in which position-dependent machine parameter variations can be detected in a PMSM. These can be sub-divided into four categories:

1. Transient Injection Tracking
2. PWM Transient Tracking
3. Continuous Injection Tracking
4. PWM Harmonics Tracking

The first transient injection method was proposed by Schroedl [87, 88] and is also known as the "INFORM" method, which stands for **I**Ndirect **F**lux Detection by **O**nline **R**eactance **M**easurement. In this approach, the flux angle is estimated by applying a transient test voltage through which real-time inductance measurements are carried out.

The INFORM method has been used in highly dynamic speed/torque sensorless drives and simple position control applications with limited accuracy. The tracking of inductance variation using the INFORM method has been reported to be dependent on the flux and load state of the electrical machine [89]. Different techniques have been implemented in order to eliminate the dependence on the flux and load state which are typically based on filtering [90], function approximation and LUTs [91], spatial and Kalman filtering [92], modulation profiling [73] and Structured Neural Networks (SNNs) [93]. Besides the flux-load dependences, additional disturbances arise from inter-modulation of saliencies which have been demodulated using Sideband Filters (SBFs) [90], SNNs and artificial neural networks (ANNs) [89]

Other researchers [94-97] have proposed a transient saliency detection method which does not necessitate the injection of an additional test voltage vector on the machine. This sensorless technique is suitable for high end modern electrical machines which are designed and manufactured to have a low level of geometric asymmetry. These methods analyse the derivative of the current during inverter switching. The rapid change in voltage which occurs during inverter switching results in a current transient which can be used for position estimation purposes. The method generally does not require particular modification to the Pulse Width Modulation (PWM) or sequence in switching but requires current derivative sensors such as the Rogowski type along with oversampling in the digital controller's Analogue to Digital Converters (ADCs) for accurate derivative current measurements.

The continuous signal injection methods typically consist of a HF voltage injection with an observer for saliency tracking [78-80, 93, 98, 99]. The type of saliency present in an electrical machine will affect whether or not rotor or flux position-dependent harmonics will result. Through the use of appropriate signal processing techniques, the harmonics can be used to obtain the required rotor position and speed. The observer can be implemented to track either magnetic flux [78, 98] or physical saliencies [73, 79, 80]. Such observers estimate the rotor position and speed without requiring exact values for the machine parameters. The type of saliencies which exist in PMSMs and which can be tracked by such observers depends on whether the machine is of the IPMSM or the SM-PMSM type. In IPMSMs, it is typically attributed to the geometric saliency while on SM-PMSMs, it is mainly associated with magnetic saturation [100].

The basic approach in continuous HF signal injection is to superimpose an additional HF component to the fundamental reference voltage of the inverter. This HF injection results in a HF current component which is superimposed on the fundamental frequency currents. The HF currents can be isolated through the use of a suitable band-pass filter which removes the fundamental component in the current signals. The current component containing useful rotor position information can be obtained through demodulation [78, 80, 101-104] and filtering [73, 82].

Although the estimates based on saliency tracking sensorless control algorithms have been proven to work at low-speeds, some challenges still arise when such algorithms are implemented in practice. For instance, the SM-PMSM was reported in [82] to have a saliency that does not correspond only to the rotor position but is affected by a phase shift that is load dependent. Another effect which could be a source of error is the presence of saturation dependent harmonics which exist at twice the electrical frequency and its multiples [100]. Various techniques have been used to mitigate the effects of these harmonics, such as the 'Harmonic Compensation' technique reported in [73]. This technique has proven valid only to mitigate the effects of a small number of harmonics. Since the number of harmonics in an inverter-based drive is typically more than what can be handled by this technique, other methods were proposed. One method, known as 'Space Modulation Profiling' (SMP) [105] carries out real-time compensation using a pre-determined set of compensation factors generated off-line through a zero phase shift filter. Besides the continuous voltage signal injection in the stationary reference frame, the injection can also be carried out in the synchronous dq-frame [85]. This method was reported to generate less torque ripple as the injection can be carried out as a pulsating vector in the estimated d-axis.

Continouos injection methods have been shown to provide robust sensorless control in the zero speed region, however this sensorless methodology has the drawback that it introduces additional acoustic noise and torque ripple. Both these factors are related to the amplitude of the HF voltage injection. The attenuation of both noise and ripple components are research areas which are being actively investigated. Researchers have proposed the reduction of the injection amplitude, and the use of signal processing techniques for compensation of the reduced SNR in the HF current amplitudes [106-108]. Another method which could be possibly used is to inject at a frequency beyond the audible range (> 20 kHz), however this is limited by the switching frequency losses

[102, 109]. State of the art techniques have successfully used pseudo-random HF voltage injection with square wave injection [110, 111] at a fixed switching frequency to spread the HF current spectrum over a wider range and thus attenuate the noise level and torque ripple at specific frequency components. Pseudo-random injection based methods have been further extended use random PWM switching frequency [112] which spreads the sprectrum of both the injected component and the PWM.

Although both transient and continuous voltage injection methods have been proven to provide accurate position and speed estimates, both of these approaches require an injection of additional signals on the fundamental. PWM-based techniques were developed to carry out sensorless control without additional injection. The first reported use of such techniques was in [113, 114] where the current of the machine windings was separated into two components: fundamental and transient component. This technique requires the use of a PWM generation method which uses zero voltage vectors [100]. By measuring the derivative component in the stator currents, a rotor position estimate can be computed at each PWM period. Other similar PWM-based methods use a slightly modified PWM excitation such as Edge Shifting of Standard SVPWM [34, 84, 86, 90, 115]. Similar to the INFORM method, this approach requires the measurement of the current derivative. In order to take appropriate current derivative measurements, the common mode and high-frequency oscillations present must settle with the requirement of a minimum duration of one voltage vector. The minimum vector duration is catered for through extended modulation [115]. Although edge shifting has the advantage of reducing the switching losses associated with the additional signal injection, it has the drawback that it disrupts the symmetry of the fundamental PWM waveform. This requires compensation when using synchronized sampling with the PWM period [100]. Another method which also uses the current derivative is the Zero Sequence Carrier Injection proposed in [84]. Measurement is taken during zero-sequence voltage vectors that occur two times in each PWM cycle. In order to have a measurable zero-sequence current, the motor star point is connected to the midpoint of a split DC link. The current flowing between these two points is regulated by a limiting inductance and capacitance which are tuned to filter low-frequency current components. The main disadvantage of this method is that it requires additional passive components.

The use of the PWM harmonics for saliency-based sensorless control has also been proposed in [116]. The switching harmonics in the inverter PWM voltages can be used

for position and speed estimation purposes without the requirement of further injection. The saliencies in this method are detected in a similar manner as other high-frequency injection methods. Current and voltage measurements are required on a particular PWM harmonic in order to calculate a rotor position-dependent impedance component. In order to minimize the error in the estimates, compensation for offset, saturation modulation and inverter disturbances were included in the form of a look-up table (LUT). The use of inherent PWM harmonics is a viable method for obtaining estimates at low or zero speeds however it has the disadvantage that it requires a complex multi-parameter dependent LUT which is specific to the electrical machine being controlled.

4.4 Transient Injection Tracking

Transient voltage injection sensorless control was first introduced by Schroedl's [87, 88, 117-119] and was based on magnetic anisotropy detection. This can be done through the measurement of the change in the stator current space vector $\bar{i}_s$ as a result of a stator voltage space vector $\bar{v}_s$ during a time interval τ. The complex INFORM reactance is given in (4.1). For the purposes of sensorless estimation in PMSMs, it is assumed that the machine is driven by a six switch three-phase inverter such that test vectors can be applied in the stationary frame in steps of $\frac{\pi}{3}$. The INFORM reference frame uses a real axis ζ (aligned to the direction of maximum magnetic conductivity) and an imaginary axis η, as shown in Figure 4.1. The angle between the stationary axis α and the voltage space vector $\bar{v}_s$ is defined as γ_v while the angle between the stationary axis α and the INFORM real axis ζ is defined as γ_{INFORM}.

$$\bar{x}_{INFORM} = \frac{\bar{v}_s}{\bar{i}_s / d\tau} \tag{4.1}$$

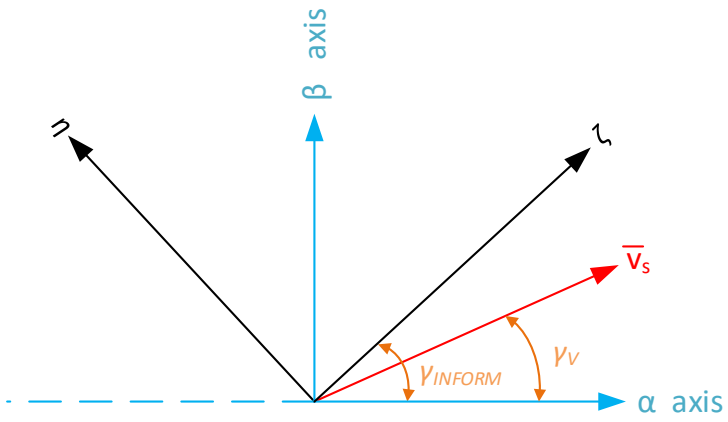

Figure 4.1 – Stationary and INFORM frames

Since both geometric and saturation effects have a periodicity of 180 electrical degrees, $\bar{x}_{INFORM}$ is also a periodic function of γ_{INFORM} and γ_{v} as shown in (4.2).

$$\bar{x}_{INFORM} = f(2\gamma_{\mathrm{INFORM}} - 2\gamma_{\mathrm{v}}) \tag{4.2}$$

To minimize the computational load of digital processors, it is more convenient to work with the inverse of $\bar{x}_{INFORM}$ as in (4.3).

$$\bar{y}_{INFORM} = (\bar{x}_{INFORM})^{-1} \tag{4.3}$$

The real and imaginary parts of $\bar{y}_{INFORM}$ shown in (4.4-4.5) contain rotor position information and can be used for sensorless estimation.

$$y_{RE,INFORM} = Re\{\bar{y}_{\mathrm{INFORM}}\} = y_0 - \Delta y.\cos(2\gamma_{\mathrm{INFORM}} - 2\gamma_{\mathrm{v}}) \tag{4.4}$$

$$y_{IM,INFORM} = Im\{\bar{y}_{\mathrm{INFORM}}\} = -\Delta y.\sin(2\gamma_{\mathrm{INFORM}} - 2\gamma_{\mathrm{v}}) \tag{4.5}$$

Using multiple INFORM measurements the INFORM angle γ_{INFORM} can be calculated. The INFORM method operates in ζ-η frame of reference and the resulting angle also has an ambiguity of 180°. The INFORM axis is superimposed on the flux axis ('d'-axis) in the case of PMSM with buried magnets where reluctance effects are dominant or perpendicular to the flux axis for PMs with surface mounted magnets where the saturation effect dominates. The detection of the direction can be determined by the appropriate application of a flux stator current component and monitoring of the change in the current change per unit time [87].

Methods based on INFORM measurements have been known to produce an excellent dynamic response in low speed-controlled and basic position-controlled applications. The drawback of the conventional method as presented in this section is that a particular measuring sequence is required to eliminate the back-EMF which is assumed negligible in the derivation of the $\bar{y}_{INFORM}$ component. A Kalman filter implementation is also generally required to improve the estimation results [87] for this method. The position information also has an angular displacement which is a function of the stator current and which results from a variation of the magnetic operating point of the machine.

4.5 PWM Transient Tracking

The transient injection techniques presented in Section 4.4 have been shown to produce a suitable dynamic response for low-speed sensorless control in AC machines. The drawback of this approach was that although not continuous, additional transient signals are still required to detect position-dependent variations in machine parameters. Researchers have attempted to replicate similar results by using the transients inherent in PWM switching. Such a method was described in [120] for AC machines in general and applied to PMSMs in [76]. The variation of the stator inductance under the effect of main flux saturation is modelled in (4.6-4.8).

$$L_{sa} = \mathrm{L_{s0}} + \Delta \mathrm{L_{s,sat}} \cos(2\theta_e) \tag{4.6}$$

$$L_{sb} = \mathrm{L_{s0}} + \Delta \mathrm{L_{s,sat}} \cos(2\theta_e - \tfrac{2\pi}{3}) \tag{4.7}$$

$$L_{sc} = \mathrm{L_{s0}} + \Delta \mathrm{L_{s,sat}} \cos(2\theta_e - \tfrac{4\pi}{3}) \tag{4.8}$$

Where:

L_{sa}, L_{sb}, L_{sc} are the three-phase stator inductances,

$\mathrm{L_{s0}}$ is the average phase inductance,

$\Delta \mathrm{L_{s,sat}}$ is the amplitude of the rotor position-dependent inductance.

The SVPWM for a six switch inverter has 6 active states (“100”, “110”, “010”, “011”, “001”, “101”) and 2 null states (“000”, “111”). The current transient response to the application of voltage vectors can be measured and used for rotor position estimation. For this purpose, a position vector (4.9) is defined, which can also be expressed, as shown in (4.10).

$$\overline{p_s} = \frac{\Delta \mathrm{L_{S,sat}}}{\mathrm{L_{s0}}} \left(p_a + p_b e^{\frac{j2\pi}{3}} + p_c e^{\frac{j4\pi}{3}} \right) \tag{4.9}$$

$$\overline{p_s} = \frac{\Delta \mathrm{L_{S,sat}}}{\mathrm{L_{s0}}} \left(\cos 2\theta_e + \cos\left(2\left(\theta_e - \tfrac{2\pi}{3}\right)\right) e^{\frac{j2\pi}{3}} + \cos\left(2\left(\theta_e - \tfrac{4\pi}{3}\right)\right) e^{\frac{j4\pi}{3}} \right) \tag{4.10}$$

For the case of switching V_1 (vector “100”) and V_0, the scalar quantities can be calculated from (4.11-4.13).

$$p_a = 2 - g\frac{d\,i_a{}^{(u10)}}{dt} \tag{4.11}$$

$$p_b = -1 - g\frac{d\,i_c{}^{(u10)}}{dt} \tag{4.12}$$

$$p_c = -1 - g\frac{d\,i_b{}^{(u10)}}{dt} \tag{4.13}$$

Where $g = \frac{3L_0\left(1-\left(\frac{\Delta L_{S,sat}}{2L_{S0}}\right)^2\right)}{V_{DC}}$

$$\frac{d\,i_a{}^{(u10)}}{dt} = \frac{d\,i_a{}^{(u1)}}{dt} - \frac{d\,i_a{}^{(u0)}}{dt}$$

$$\frac{d\,i_b{}^{(u10)}}{dt} = \frac{d\,i_b{}^{(u1)}}{dt} - \frac{d\,i_b{}^{(u0)}}{dt}$$

$$\frac{d\,i_c{}^{(u10)}}{dt} = \frac{d\,i_c{}^{(u1)}}{dt} - \frac{d\,i_c{}^{(u0)}}{dt}$$

The values of the scalar quantities given in (4.11-4.13) for voltage vectors V_1 and V_0 can be found tabulated for all other switching vectors for both star and delta machines in [120]. Since the calculations for this method requires measurement of the current derivative, a minimum duration for the voltage vector is required to allow for high-frequency oscillations associated with the transient response of the sensor [100] and effective HF machine capacitance [72] to decay. The duration of test vectors is shortest at low-speed operation and at the transitions between different voltage sectors. In order to extend the duration of voltage vectors, for instance, V_1 and V_2, which are below the minimum duration; new opposing vectors (V_4 and V_7 for this case) of the same duration of the required increment are introduced such that the fundamental PWM waveform is unchanged. This can be carried out by edge shifting of the PWM signals. The only drawback of this technique is that the PWM waveform does not remain symmetrical, which would require further compensation in the case synchronized sampling is used.

The method presented in this section is based on (4.6-4.8) in which it is assumed that the phase inductances are modulated by a single sinusoidal component; however, this is not necessarily the case in experimental machines as other unwanted saliencies introduce harmonics into the signals used for estimation purposes. Filtering has been used in order to eliminate harmonics, as described in [73, 121, 122]. At low speed, the useful and corrupting components, however, are close to each other in the frequency spectrum and

therefore difficult to filter. In [76] an adaptive disturbance identifier was used, which combines a synchronous filter with LUT compensation for low-speed operation.

4.6 Continuous Injection Tracking

In continuous injection tracking methods, a HF voltage signal is superimposed over the fundamental signals in order to detect position-dependent HF current amplitudes. Such methods have been shown to produce suitable estimates for closed-loop sensorless control at low and zero speeds. The injected signal can be of various types including rotating sinusoidal signal injection [78, 81, 123-125], pulsating sinusoidal injection [99, 126-128], square wave signal injection [129-133] and arbitrary injection [83, 115, 134-136]. The injection can be done either in the stationary αβ-frame or in the synchronous dq-frame. Theoretically injecting only in the d-axis would not produce significant additional torque ripple. However, in closed-loop sensorless control, the d-axis can only be estimated, and therefore increased torque noise would still be introduced to some degree due to imperfect alignment resulting from the error in the rotor position estimate. Generally, given that there is a pronounced saliency, a small injection in the stationary frame is sufficient for estimation purposes which can be done in open-loop form, as shown in Figure 4.2. With such a method, the effects of nonlinearities in the semiconductor switches must be evaluated and compensated for if they are of the same order of magnitude as the injected component.

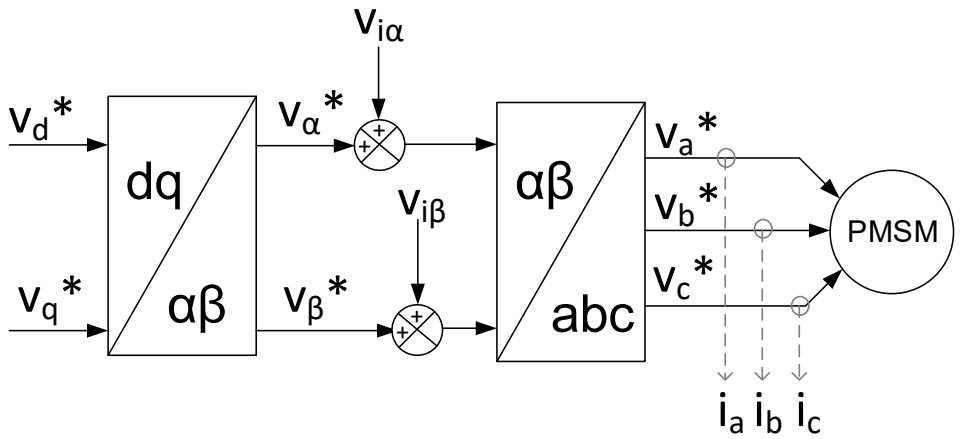

Figure 4.2 - High-Frequency Injection in the αβ stationary frame.

In rotating sinusoidal injection, a HF voltage signal is superimposed on the fundamental control voltages. The resulting HF current is amplitude modulated in the time domain, which translates to a frequency sideband to the injected component in the frequency domain. The amplitude modulation of the HF current is a function of the electrical rotor

position. Hence the rotor position can be extracted through suitable demodulation techniques such as homodyning, heterodyning and synchronous filtering [137].

4.6.1 Rotating Sinusoidal Signal Injection

The saliency detected is typically represented as the synchronous frame inductances being different from each other. Consider the stator flux linkage in the synchronous frame shown in (4.14).

$$\Psi_{\mathrm{sdq}} = \begin{bmatrix} L_d & 0 \\ 0 & L_q \end{bmatrix} i_{dq} + \Psi_{\mathrm{rd}} \tag{4.14}$$

Where Ψ_{sdq} is the total flux linkage in the stator in the synchronous dq-frame,

L_d, L_q are the stator inductances in the synchronous dq-frame,

i_{dq} is the matrix for the stator currents in the synchronous dq-frame,

Ψ_{rd} is the total rotor permanent magnet flux aligned with the d-axis.

Consider the matrix T in (4.15) which is the transformation matrix from the synchronous dq-frame to the stationary αβ-frame.

$$T = \begin{bmatrix} \cos\theta_{\mathrm{e}} & -\sin\theta_{\mathrm{e}} \\ \sin\theta_{\mathrm{e}} & \cos\theta_{\mathrm{e}} \end{bmatrix} \tag{4.15}$$

Multiplying both by sides in (4.16) by T:

$$T\Psi_{\mathrm{sdq}} = TL_{dq} i_{dq} + T\Psi_{\mathrm{rd}}$$

$$T\Psi_{\mathrm{sdq}} = TL_{dq} T^{-1} T i_{dq} + T\Psi_{\mathrm{rd}}$$

$$\Psi_{\mathrm{s}\alpha\beta} = TL_{dq} T^{-1} i_{\alpha\beta} + T\Psi_{\mathrm{rd}} \tag{4.16}$$

From (4.16) the stator inductance $L_{\alpha\beta}$ is given by (4.17).

$$L_{\alpha\beta} = TL_{dq}T^{-1} = \begin{bmatrix} \cos\theta_{\mathrm{e}} & -\sin\theta_{\mathrm{e}} \\ \sin\theta_{\mathrm{e}} & \cos\theta_{\mathrm{e}} \end{bmatrix} \begin{bmatrix} L_d & 0 \\ 0 & L_q \end{bmatrix} \begin{bmatrix} \cos\theta_{\mathrm{e}} & \sin\theta_{\mathrm{e}} \\ -\sin\theta_{\mathrm{e}} & \cos\theta_{\mathrm{e}} \end{bmatrix} \tag{4.17}$$

Using trigonometric identities (4.17) can be simplified into (4.18).

$$L_{\alpha\beta} = \begin{bmatrix} \frac{L_d + L_q}{2} - \frac{L_q - L_d}{2}\cos 2\theta_e & -\frac{L_q - L_d}{2}\sin 2\theta_e \\ -\frac{L_q - L_d}{2}\sin 2\theta_e & \frac{L_d + L_q}{2} + \frac{L_q - L_d}{2}\cos 2\theta_e \end{bmatrix} \quad (4.18)$$

The stator inductance matrix (4.18) is a function depending on twice the electrical rotor position. When the machine is of the salient type, L_d and L_q are not equal resulting in cross-coupling inductance terms between the α and β axes. When L_d and L_q are equal for a non-salient machine, the stator inductance matrix becomes a diagonal matrix (4.19) with no cross-coupling effects and position-dependent modulation.

$$L_{\alpha\beta} = \begin{bmatrix} L_{ns} & 0 \\ 0 & L_{ns} \end{bmatrix} \quad (4.19)$$

Where L_{ns} is the stator inductance for a non-salient type machine.

For simplification, the general stator inductance matrix in (4.18) is written as (4.20).

$$L_{\alpha\beta} = \begin{bmatrix} L + \Delta L\cos 2\theta_e & \Delta L\sin 2\theta_e \\ \Delta L\sin 2\theta_e & L - \Delta L\cos 2\theta_e \end{bmatrix} \quad (4.20)$$

Where: $L = \frac{L_d + L_q}{2}$

$$\Delta L = \frac{L_d - L_q}{2}$$

The injection rotation voltage is generally applied in the stationary frame in the form of (4.21).

$$v_{i\alpha\beta} = V_i \begin{bmatrix} \cos \omega_i t \\ \sin \omega_i t \end{bmatrix} \quad (4.21)$$

Where: $v_{i\alpha\beta}$ is the injected voltage in the stationary αβ-frame,

V_i is the voltage injection amplitude,

ω_i is the voltage injection frequency.

Assuming that at the injection frequency, the inductive reactance is significantly larger than the resistance, the injection voltage can also be written as (4.22).

$$v_{i\alpha\beta} = \mathrm{j}\omega_\mathrm{i} L_{\alpha\beta}\, i_{i\alpha\beta} \tag{4.22}$$

The injected current component can be expressed as (4.23) by re-arranging terms in (4.22).

$$i_{i\alpha\beta} = -\frac{\mathrm{j}{L_{\alpha\beta}}^{-1} v_{i\alpha\beta}}{\omega_\mathrm{i}} \tag{4.23}$$

The inverse of the stator inductance matrix can be expressed as in (4.24).

$${L_{\alpha\beta}}^{-1} = \frac{1}{L^2 - \Delta L^2}\begin{bmatrix} L - \Delta L\cos 2\theta_\mathrm{e} & -\Delta L \sin 2\theta_\mathrm{e} \\ -\Delta L \sin 2\theta_\mathrm{e} & L + \Delta L\cos 2\theta_\mathrm{e} \end{bmatrix} \tag{4.24}$$

Substituting (4.22) in (4.23) results in the injected current in terms of the rotor position given in (4.25).

$$i_{i\alpha\beta} = \frac{-V_i}{\omega_\mathrm{i}(L^2 - \Delta L^2)}\begin{bmatrix} L - \Delta L\cos 2\theta_\mathrm{e} & -\Delta L \sin 2\theta_\mathrm{e} \\ -\Delta L \sin 2\theta_\mathrm{e} & L + \Delta L\cos 2\theta_\mathrm{e} \end{bmatrix}\begin{bmatrix} \cos\omega_\mathrm{i} t \\ \sin\omega_\mathrm{i} t \end{bmatrix} \tag{4.25}$$

Simplifying (4.25) using trigonometric identities results in (4.26)

$$i_{i\alpha\beta} = \frac{V_i}{\omega_\mathrm{i}(L^2 - \Delta L^2)}\begin{bmatrix} L\sin\omega_\mathrm{i} t + \Delta L\sin(2\theta_\mathrm{e} - \omega_\mathrm{i} t) \\ -L\cos\omega_\mathrm{i} t + \Delta L\cos(2\theta_\mathrm{e} - \omega_\mathrm{i} t) \end{bmatrix} \tag{4.26}$$

Which can be also written as (4.27):

$$i_{i\alpha\beta} = \begin{bmatrix} \mathrm{I}_1\sin\omega_\mathrm{i} t + \mathrm{I}_2\sin(2\theta_\mathrm{e} - \omega_\mathrm{i} t) \\ -\mathrm{I}_1\cos\omega_\mathrm{i} t - \mathrm{I}_2\cos(2\theta_\mathrm{e} - \omega_\mathrm{i} t) \end{bmatrix} \tag{4.27}$$

Where $\mathrm{I}_1 = \frac{V_i L}{\omega_\mathrm{i}(L^2 - \Delta L^2)}$

$\mathrm{I}_2 = \frac{V_i \Delta L}{\omega_\mathrm{i}(L^2 - \Delta L^2)}$

4.6.2 Rotating Sinusoidal Injection Detection using Heterodyning

The injected frequency current shown in (4.27) has a frequency component at the injected frequency ω_i and a rotor position amplitude-modulated sideband at $2\theta_e - \omega_i t$. This is often referred to as the negative sequence component since it is rotating at $-\omega_i t$ in the opposing direction of the injected component. The frequency spectra of the high-frequency voltage and currents are shown in Figures 4.3 and 4.4, respectively.

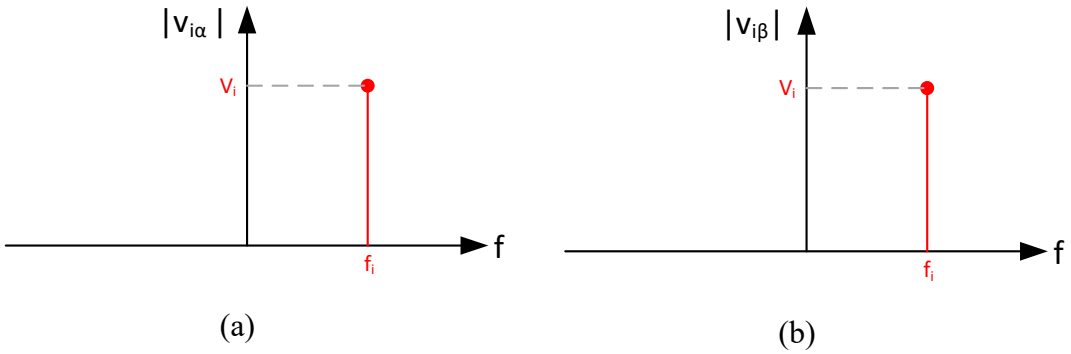

Figure 4.3 – Frequency spectrum of the injected voltage $v_{i\alpha}$ (a) and $v_{i\beta}$ (b)

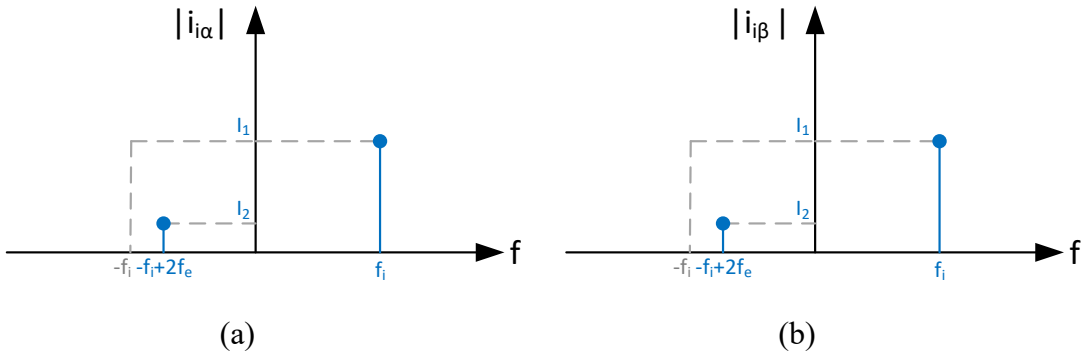

Figure 4.4 – Frequency spectrum current resulting from the injection $i_{i\alpha}$ (a) and $i_{i\beta}$ (b)

The rotor position information can be extracted from the stationary frame HF currents (4.27) using a variety of methods such as the PLL observer [137, 138] with a heterodyning section as shown in Figure 4.5.

The error output term ε derived from heterodyning is expressed in terms of the HF currents $i_{i\alpha\beta}$, estimated electrical rotor position $\hat{\theta}_e$ and HF injection frequency ω_i in (4.28).

$$\varepsilon = i_{i\alpha}\cos\left(2\hat{\theta}_e - \omega_i t\right) + i_{i\beta}\sin\left(2\hat{\theta}_e - \omega_i t\right) \tag{4.28}$$

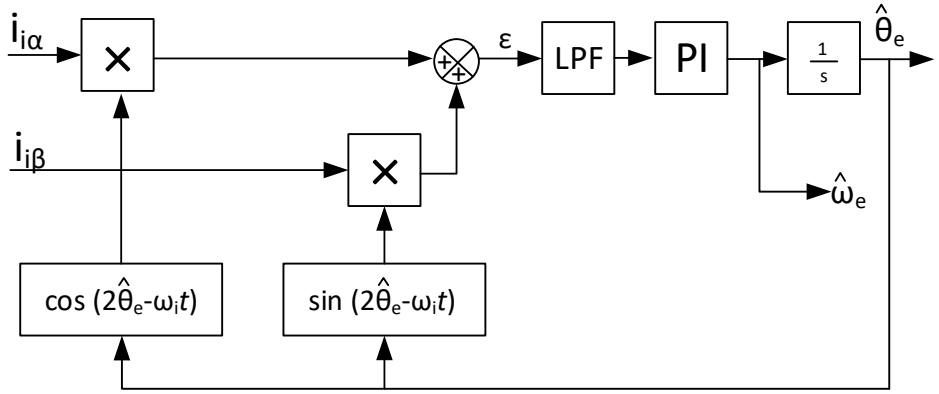

Figure 4.5 - PLL rotor position/speed estimator with heterodyning.

Expanding the HF current terms in (4.28) the error term ε can also be written, as shown in (4.29).

$$\varepsilon = \mathrm{I}_1 \sin\left(2\left(\omega_\mathrm{i} t - \hat{\theta}_\mathrm{e}\right)\right) + \mathrm{I}_2 \sin\left(2\left(\theta_\mathrm{e} - \hat{\theta}_\mathrm{e}\right)\right) \tag{4.29}$$

The error term ε in (4.29) consists of a HF component with an amplitude I_1 and a low-frequency component with an amplitude I_2. The error term can be filtered with a first-order low-pass filter resulting in (4.30).

$$\varepsilon_f \approx \mathrm{I}_2 \sin\left(2\left(\theta_\mathrm{e} - \hat{\theta}_\mathrm{e}\right)\right) \tag{4.30}$$

Hence, the error term fed into the PI controller in the PLL is proportional to the error between the actual and estimated rotor positions for small values of $2\left(\theta_\mathrm{e}\text{-}\hat{\theta}_\mathrm{e}\right)$ as shown in (4.31).

$$\varepsilon_f \approx \mathrm{I}_2 \; 2\left(\theta_\mathrm{e} - \hat{\theta}_\mathrm{e}\right) \tag{4.31}$$

Since the estimated rotor position is fed back to the heterodyning section, the PLL tracks the estimated rotor position in order to reduce the error term to zero. An integrator is introduced after the PI controller such that a value for the estimated electrical rotor frequency is also obtained within the same loop.

The PLL with heterodyning consists of a number of sections; not all of which are linear. In order to tune the PI controller using frequency-domain tools, a linearized transfer function is required. The difference between the actual and estimated rotor angles can be written from (4.31), as shown in (4.32). This can be used to linearize the input part of the PLL loop such that a linear model of the approximated system is obtained, as shown in Figure 4.6.

$$\theta_e - \hat{\theta}_e \approx \frac{\varepsilon_f}{2I_2} \tag{4.32}$$

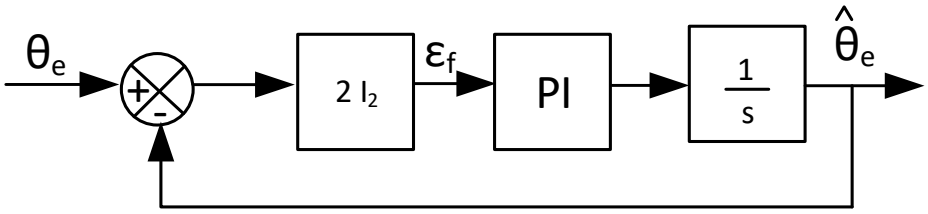

Figure 4.6 - Linearized PLL Estimation Loop.

Since the term I_2 consists of constants a linearized open-loop transfer function can be obtained (4.33) which can be used for tuning PI controller gains using frequency-domain tools.

$$G(s) \approx \frac{2I_2}{s} \tag{4.33}$$

4.6.3 Rotating Sinusoidal Injection Detection using Synchronous Frame Transformation

Another method to obtain the rotor position information from the HF currents in (4.27) is to use a frame transformation filter [137] as shown in Figure 4.7. The amplitude modulated sidebands differ from the injected components not only in magnitude and phase but also in the direction of rotation. By transforming the stationary frame currents with a transformation $e^{-j\omega_i t}$ the injected components are shifted to DC components (Figure 4.8). These DC components do not contain rotor position information, so they are filtered out (Figure 4.9). The relevant components containing the position information are shifted by $e^{j2\omega_i t}$ such that the components at the rotor frequency $2f_e$ should theoretically remain (Figure 4.10). If any remaining offsets are removed from the saliency dependent currents (i_{sal} in Figure 4.7), the rotor position can be simply estimated through an inverse tangent operation.

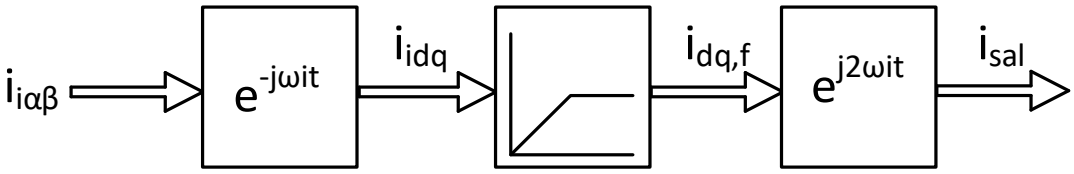

Figure 4.7 – Synchronous Filtering of High-Frequency Currents

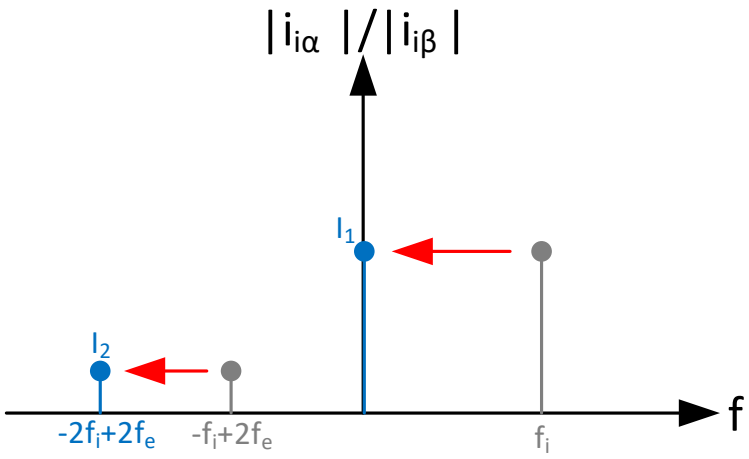

Figure 4.8 – Shifting of High-Frequency Currents into Synchronous Frame

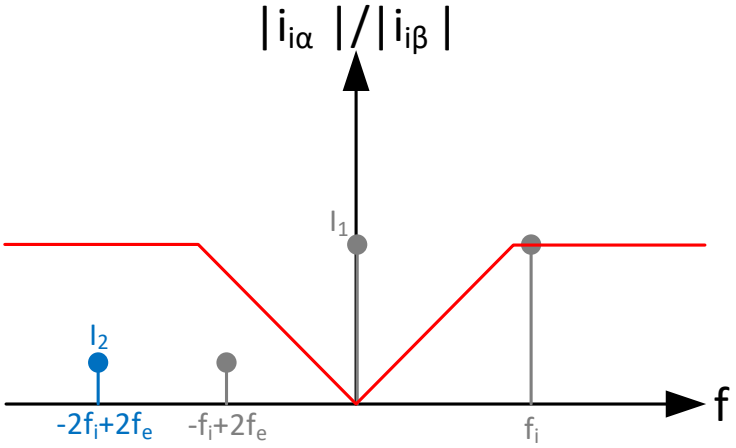

Figure 4.9 – Filtering of DC component in Synchronous Frame

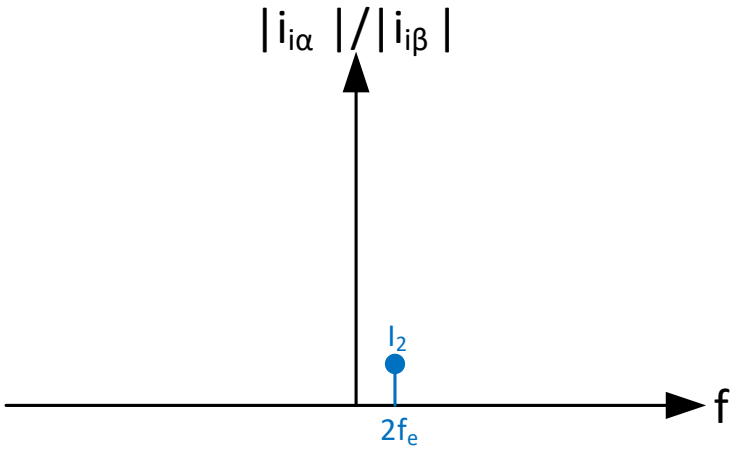

Figure 4.10 – Shifting of Rotor Position Component to Rotor Frequency

4.6.4 Pulsating Signal Injection

The rotating sinusoidal signal injection in (4.21) can be replaced by a pulsating sinusoidal signal injection in the form of (4.34) as shown in Figure 4.11. While the rotating injection has a circular locus in the stationary αβ-frame a pulsating vector will alternate between opposing quadrants at a fixed angle γ with the α-axis. The terms A_1 and A_2 are introduced since the sinusoidal injection in each of the axes does not necessarily have equal amplitude and is dependent on the angle of injection. The resulting pulsating vector has a magnitude of V_i and an angle with respect to the stationary α axis of γ.

$$v_{i\alpha\beta} = \begin{bmatrix} A_1 \cos \omega_i t \\ A_2 \cos \omega_i t \end{bmatrix} \tag{4.34}$$

The magnitude of the pulsating vector and the angle γ can be set through (4.35-4.36).

$$A_1 = V_i \cos \gamma \tag{4.35}$$

$$A_2 = V_i \sin \gamma \tag{4.36}$$

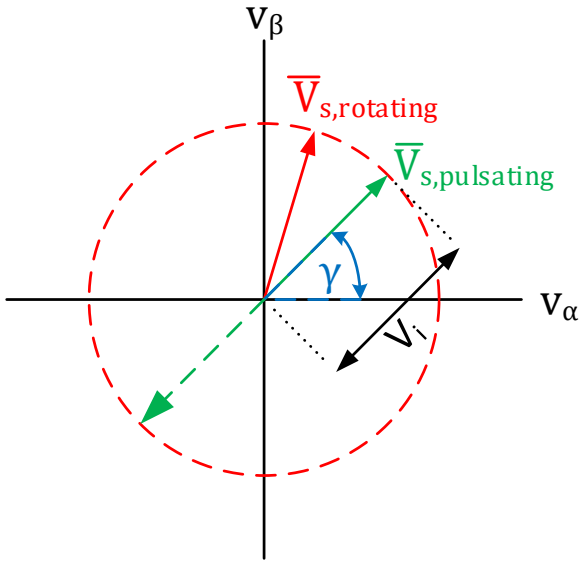

Figure 4.11 – Stationary frame continuous injection with rotating / pulsating vectors.

With a similar analysis to that carried out in Section 4.6.1, the HF current components for pulsating voltage injection are given in (4.37).

$$\begin{bmatrix} i_{i_\alpha} \\ i_{i_\beta} \end{bmatrix} = \begin{bmatrix} \mathrm{I_1 A_1}\sin(\omega_\mathrm{i} t) - \mathrm{I_2 A_1}\cos(2\theta_\mathrm{e})\sin(\omega_\mathrm{i} t) - \mathrm{I_2\, A_2}\sin(2\theta_\mathrm{e})\sin(\omega_\mathrm{i} t) \\ \mathrm{I_1 A_2}\sin(\omega_\mathrm{i} t) + \mathrm{I_2 A_2}\cos(2\theta_\mathrm{e})\sin(\omega_\mathrm{i} t) + \mathrm{I_2\, A_1}\sin(2\theta_\mathrm{e})\sin(\omega_\mathrm{i} t) \end{bmatrix} \quad (4.37)$$

The HF currents in (4.37) can be demodulated by multiplying by $2\sin(\omega_i t)$. The product results in distinct HF components which contain no useful rotor position information and low frequency (LF) components, which are a function of the electrical rotor position. The LF rotor position dependent components can be extracted by low-pass filtering the product of (4.37) with the HF injection component resulting in the HF current amplitudes $A_{i\alpha}$, $A_{i\beta}$ in (4.38).

$$\begin{bmatrix} \mathrm{A_{i\alpha}} \\ \mathrm{A_{i\beta}} \end{bmatrix} = \begin{bmatrix} \mathrm{I_1 A_1} - \mathrm{I_2 A_1}\cos(2\theta_\mathrm{e}) - \mathrm{I_2\, A_2}\sin(2\theta_\mathrm{e}) \\ \mathrm{I_1 A_2} + \mathrm{I_2 A_2}\cos(2\theta_\mathrm{e}) + \mathrm{I_2\, A_1}\sin(2\theta_\mathrm{e}) \end{bmatrix} \quad (4.38)$$

By substituting (4.35-4.36) in (4.38) the resulting HF rotor positon dependent current amplitudes can be expressed in terms of the pulsating voltage amplitude and angle (4.39).

$$\begin{bmatrix} \mathrm{A_{i\alpha}} \\ \mathrm{A_{i\beta}} \end{bmatrix} = \begin{bmatrix} \mathrm{I_1 A_1} - \mathrm{I_2 V_i}\cos(\gamma - 2\theta_\mathrm{e}) \\ \mathrm{I_1 A_2} + \mathrm{I_2 V_i}\sin(\gamma - 2\theta_\mathrm{e}) \end{bmatrix} \quad (4.39)$$

The equations for the pulsating voltage injection are visibly more complex compared to the ones for the rotating voltage injection. In [139], the application of a pulsating vector in either the α (γ=0°) or β (γ=90°) axis only is recommended to simplify (4.38). The case for injection into the α axis only results in (4.40).

$$\begin{bmatrix} \mathrm{A_{i\alpha}} \\ \mathrm{A_{i\beta}} \end{bmatrix} = \begin{bmatrix} \mathrm{I_1 V_i} - \mathrm{I_2 V_i}\cos(2\theta_\mathrm{e}) \\ -\mathrm{I_2 V_i}\sin(2\theta_\mathrm{e}) \end{bmatrix} \quad (4.40)$$

Injecting on one stationary axis only however has two main practical limitations. The first was noticed while carrying out the experimental testing for this research. The magnetic signature is dependent on the orientation angle of injection γ. Limiting the injection to only two directions would limit the selection of signature profiles which could be used for sensorless estimation. The second limitation is that since the voltage injection (4.34) in the experimental drive is carried out in open-loop form (no dedicated voltage controller with voltage feedback), the actual voltage at the output of the inverter will not follow precisely the reference. Hence the actual A_1 or A_2 components will not be regulated to the setpoint values. The demodulation and sensorless estimation, as proposed in this dissertation, is done in an innovative way based on synchronized

sampling and aliasing of unwanted components as described in Section 6.3.2. This method is not affected by the additional complexity in the HF current amplitudes in (4.38) associated with injecting pulsating vectors in both the α and β axes. Pulsating voltage injection also has the advantage that it intrinsically cancels external phase distortions and does not require additional compensation as opposed to rotating injection [123].

4.7 Arbitrary Signal Injection Tracking

The arbitrary signal injection tracking is based on the current derivative rather than the injection of a specific injection signal [83, 140]. Recall that the stator voltage in the stationary frame can be written as (4.41) and the flux in the synchronous frame as (4.42).

$$v_{\alpha\beta} = \mathrm{R_s} i_{s\alpha\beta} + \frac{d}{dt}\Psi_{s\alpha\beta} \tag{4.41}$$

$$\Psi_{s\alpha\beta} = L_{\alpha\beta}\, i_{s\alpha\beta} + T\Psi_{rd} \tag{4.42}$$

Substituting (4.42) in (4.41):

$$v_{\alpha\beta} = \mathrm{R_s} i_{s\alpha\beta} + \frac{d}{dt}\left(L_{\alpha\beta}\, i_{s\alpha\beta} + T\Psi_{rd}\right)$$

$$v_{\alpha\beta} = \mathrm{R_s} i_{s\alpha\beta} + L_{\alpha\beta}\frac{\mathrm{d\, i_{s\alpha\beta}}}{\mathrm{dt}} + \omega_e \dot{L_{\alpha\beta}}\, i_{\alpha\beta} + \omega_e \dot{T}\Psi_{rd} \tag{4.43}$$

From (4.43) the current derivative can be expressed as in (4.44).

$$\frac{d\, i_{s\alpha\beta}}{dt} = (\mathrm{Y_\Sigma I} + \mathrm{Y_\Delta} S(\theta_e))\left(v_{\alpha\beta} - \mathrm{R_s} i_{s\alpha\beta} - \omega_e(\dot{L_{\alpha\beta}}\, \mathrm{i_{s\alpha\beta}} + \dot{T}\Psi_{rd})\right) \tag{4.44}$$

Where: $\mathrm{Y_d} = \frac{1}{\mathrm{L_d}}$, $\mathrm{Y_q} = \frac{1}{\mathrm{L_q}}$,

$\mathrm{Y_\Sigma} = \frac{\mathrm{Y_d + Y_q}}{2}$, $\mathrm{Y_\Delta} = \frac{\mathrm{Y_d - Y_q}}{2}$,

I is the identity matrix,

$$S(\theta_e) = \begin{bmatrix} \cos(2\theta_e) & \sin(2\theta_e) \\ \sin(2\theta_e) & -\cos(2\theta_e) \end{bmatrix}$$

The term $\mathrm{Y_\Sigma}$ denotes the average part of the admittance while $\mathrm{Y_\Delta}$ denotes the salient part of the admittance generating the rotor position-dependent current response. If an

isotropic (non-salient) machine model is assumed the change in current in the discrete domain can be computed from (4.45) with (4.46).

$$\Delta i_{\alpha\beta\Sigma}[n] = (\mathrm{Y_\Sigma})\big(v_{\alpha\beta}[n] - \mathrm{R_s i_{\alpha\beta}[n]} - \omega_\mathrm{e}[n-1]v_L[n-1]\big)\mathrm{t_s} \quad (4.45)$$

$$v_L[n] = \mathrm{L\dot{}_{\alpha\beta}}[n]\, i_{s\alpha\beta}[n] + \dot{\mathrm{T}}[n]\Psi_\mathrm{rd}[n] \quad (4.46)$$

Where:

$\Delta i_{\alpha\beta\Sigma}[n]$ is the change in current over one sample with the isotropic model

$\mathrm{t_s}$ is the sampling time

The difference in the actual current over one sample can be found through the difference of two consecutive samples (4.47).

$$\Delta i_{\alpha\beta}[n] = i_{\alpha\beta}[n] - i_{\alpha\beta}[n-1] \quad (4.47)$$

The error between the change in current calculated with the isotropic model and the actual change in current is given by (4.48).

$$e_i = \Delta i_{\alpha\beta}[n] - \Delta i_{\alpha\beta\Sigma}[n] \quad (4.48)$$

In [140], it is shown that the error between the two current change quantities is a function of the rotor position estimate as given in (4.49). Hence, the rotor position can be derived using trigonometry, as shown in (4.50). A PLL observer similarly to that proposed for the rotating injection tracking can also be used instead of the inverse tangent.

$$e_i = \mathrm{Y_\Delta} S(\theta_\mathrm{e}) v_L[n]\mathrm{t_s} \quad (4.49)$$

$$\theta_\mathrm{e} = \frac{1}{2}\tan^{-1}\left(\frac{v_{L\alpha}e_{i\beta} + v_{L\beta}e_{i\alpha}}{v_{L\alpha}e_{i\alpha} + v_{L\beta}e_{i\beta}}\right) \quad (4.50)$$

The arbitrary injection method presented in this section is a more general approach based on the current derivative rather than on the injection of a particular HF waveform. In [83] successful zero to low-speed sensorless control was shown for a SM-PMSM. An advantage of arbitrary injection-based methods includes the direct estimation of the rotor position. A filter is used only for parameter estimations and noise cancellation. This results in a sensorless drive with high bandwidth and robust precision position control.

4.8 PWM Harmonics Tracking

Most three-phase electrical machines are operated by means of a PWM inverter whereby the fundamental voltage demand is met by switching between the positive and negative potentials of the dc-link voltage at HF. Besides the fundamental voltages, a number of high-frequency components are created as a result of the HF switching. These higher frequency harmonics are mostly attenuated in the machine's currents due to the increased reactance at higher frequencies. In [116], it was proposed that the PWM current harmonics are used for sensorless estimation; similarly to what is done in other continuous injection methods but without the need for additional injection signals. The Fourier series for the PWM voltage of a typical inverter is given in (4.51) [116].

$$v_x(t) = \frac{a_{PWM0x}}{2} + \sum_{n=1}^{\infty}(a_{PWMnx}\cos n\omega_{\mathrm{PWM}}t + b_{PWMnx}\sin n\omega_{\mathrm{PWM}}t) \quad (4.51)$$

Where:

$\frac{a_{PWM0x}}{2}$	is the desired fundamental output voltage of the PWM,
$a_{PWMnx},\ b_{PWMnx}$	are the Fourier amplitudes of the n th harmonic,
n	is the harmonic number,
ω_{PWM}	is the fundamental PWM frequency,
x	refers to any of the phases a, b and c.

In [116], it was found that for an induction machine, the second PWM harmonic shown in (4.52) has the largest amplitude and therefore, it is the most suitable for sensorless control.

$$v_{PWM2\alpha\beta} = \frac{2}{3}\frac{\mathrm{V_{DC}}}{\pi}\left(\sin(\pi \mathrm{m_A}) + \sin(\pi \mathrm{m_B})\, e^{\mathrm{j}\frac{2\pi}{3}} + \sin(\pi \mathrm{m_C})\, \mathrm{e}^{\mathrm{j}\frac{4\pi}{3}}\right)\cos\left(2\omega_{\mathrm{PWM}}t\right) \quad (4.52)$$

Where $\mathrm{m_A}, \mathrm{m_B}, \mathrm{m_C}$ are the modulation indices of the respective phases.

In order to compensate for switching non-linearities introduced by the switching power semiconductors on the inverter output voltages; an impedance calculation was proposed instead of just using the high-frequency currents. This is shown in Figure 4.12.

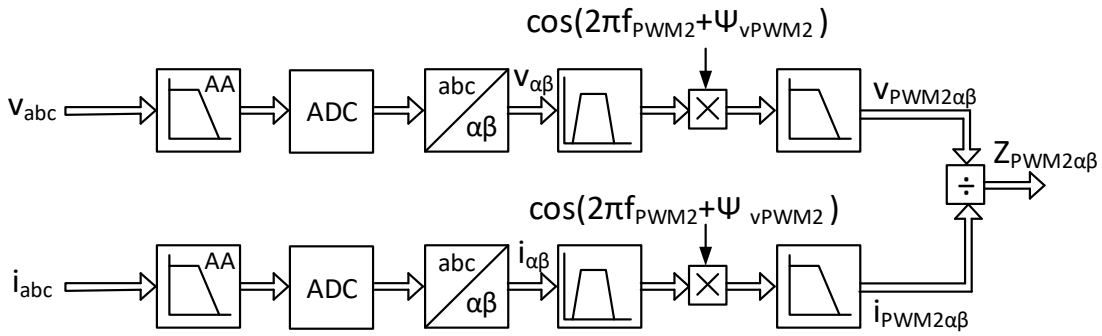

Figure 4.12 – PLL observer for PWM Harmonics Tracking.

The phase voltages and currents are filtered for anti-aliasing effects through the use of an analogue low-pass filter and sampled using an ADC. The sampled phase quantities are transformed in the stationary reference frame αβ components. The HF components are then separated from the fundamental ones through a band-pass filter and demodulated by multiplying by a sinusoidal component at twice the PWM frequency. The demodulated components can be further low pass filtered before a phasor division is carried out to obtain the impedance. After compensating for any offsets in $Z_{PWM2\alpha\beta}$ and possible loading effects the rotor position angle can be deduced with either an inverse tangent or PLL observer.

The practical implementation of PWM harmonics tracking sensorless method was shown in [116, 141] for sensorless speed and position control applications. Even with minor position-dependent modulation on the machine, successful sensorless operation at zero speed was shown. The main advantage of the method is that it does use any additional signals and that switch nonlinearities are compensated for through the impedance calculation. In this particular implementation is that the PWM frequency is set to 1.818 kHz, which is relatively low, especially for modern drives.

While modern microcontrollers support higher PWM frequencies, the resulting harmonic currents will be significantly attenuated by the increased impedance in higher frequencies ranges. This would possibly require the use of further signal analogue conditioning circuitry to ensure ADC measurements with sufficient Signal-to-Noise ratio.

4.9 Summary

In this chapter, various sensorless techniques applicable to different speed ranges of AC machines are discussed. Model-based sensorless techniques based on the measurement

and estimation of back-emf quantities were reviewed. These methods were noted to produce a satisfactory dynamic response in sensorless closed-loop operation at high speeds where the back-emf is significantly large. Since the steer-by-wire operation mostly operates at zero speed with high transients from this set point, model-based algorithms were not considered to be suitable for the application.

Hence, various sensorless techniques based on higher frequency signals rather than the fundamental were reviewed. Transient injection tracking based on both the INFORM method and PWM tracking were noted to be dependent on the current derivative produced by the transient signal. While these algorithms are known for producing excellent results in low-speed control applications, further enhancements to the basic algorithms are required for precision position control applications. In these methods, the inclusion of current derivative sensors is typically required, which would increase the electric drive cost above of the requirements for basic vector control operation. The continuous injection was reviewed for various types of injected signals such as rotating sinusoidal, pulsating sinusoidal, square-wave and also arbitrary injection. The injection can be applied in both the stationary frame and in the estimated reference frame. Injection in the stationary frame, however, is considered to be more robust since it is not dependent on the rotor position being estimated. Square wave and arbitrary injection have been shown to produce good results for position estimation; however, their performance on PMSMs with magnetic signatures similar to the ones used in this dissertation was not investigated in the literature.

Given the sensorless review presented in this chapter, the use of a continuous rotating and pulsating sinusoidal injection will be considered for the steer-by-wire application in this dissertation. Such methods have been shown to provide robust sensorless control in the zero-speed region for a wide range of machine constructions while requiring a relatively simple HF injection added to the fundamental control voltages.

Chapter 5 – Experimental Setup

5.1 Introduction

In this chapter, the hardware and firmware components used in the experimental setup of this dissertation are presented. The sensorless low/zero speed investigation was carried out on 400 W Surface Mounted Permanent Magnet Synchronous Machines (SM-PMSMs). The magnetic signature of SM-PMSMs with different stator/rotor dimensions was investigated in Chapter 6. The magnetic signatures of all machines tested contain significant saliency harmonics. Although the search-based sensorless method proposed in this dissertation can be applied to all machines, machine M3 was chosen for sensorless control as it was the closest to the fundamental saliency model. The sensored and sensorless control of SM-PMSMs requires a three-phase inverter with feedback for rotor position (sensored) and stator currents (sensored/sensorless). The electronic circuits required for High Frequency (HF) injection-based sensorless control were custom designed and implemented as part of the project itself. Numerous modular circuit designs are presented including the gate driver board, inverter boards, saliency measurement board and encoder interface board.

A microcontroller unit is required for: the generation of the gate drive board Pulse Width Modulated (PWM) signals, the sampling of the various sensor measurements and the calculations for the chosen Rotor Flux Oriented (RFO) control topology. An STM32F4 microcontroller board was used for the drive control, which offers a trade-off between cost and performance. The chosen microcontroller unit also offers the possibility of high-speed communication with MATLAB via an embedded serial port emulator.

5.2 PMSM Experimental Setup

The sensored/sensorless investigation at low to zero speed was carried out with two SM-PMSMs of similar construction referred to as M3 and M4 (Figure 5.1). The sensored and sensorless operation were investigated on machine M3 while machine M4 was used in sensored mode for setting the speed or current operating points. The electrical and mechanical parameters of M3 are given in Table 5.1, with those for M4 being assumed identical. The parameters R, L_d, L_q, J and B were determined experimentally in Section 3.2.

The selection of the PMSMs M3 and M4 was based on the torque determined experimentally at the handwheel on a Kia Sportage test vehicle through the OBD unit

(Section 2.7) which was found to be in the range ± 3 Nm. The rated torque of the experimental PMSMs was calculated to be 6.36 Nm which is higher but of the same order of magnitude of that observed while steering. The machines used in this dissertation could not be used in a direct drive at the steered wheel side as a gearbox would be required to produce the additional torque. However, the methods proposed in this dissertation are not limited to specific machines and therefore they are also applicable to machines with a higher rated torque output as would be required for a direct-drive steered wheeled side in steer-by-wire.

The machine shafts are coupled with a high damping rubber-type flexible coupling (NBK XGS-39C-17-17) which is designed explicitly for servo-controlled applications, as shown in Figure 5.1. This type of coupling compensates for both angular and axial misalignment. This was required since the alignment was carried out manually with a dial gauge, as shown in Figures 5.2 (a) – (b). When the individual uncoupled shafts were tested for axial eccentricity, a variation of approximately 0.05 mm was measured. This is a result of the off-centric oscillations of the shaft due to the manufacturing tolerances on these low-cost PMSMs. When the coupling was introduced between the two shafts, an axial eccentricity of 0.08 mm was measured. This variation is a result of both machine tolerances and shaft misalignment.

Symbol	Description	Value	Unit
P	Rated Power	400	W
N_{rated}	Rated Speed	600	RPM
T_{rated}	Rated Torque	6.36	Nm
V_{rms}	Rated RMS Voltage	24	V
I_{rms}	Rated RMS Current	7	A
L_d	d-axis stator inductance	426	µH
L_q	q-axis stator inductance	679	µH
R	Stator resistance	246	mΩ
J	Moment of Inertia	10.93×10^{-3}	kg m^2
B	Coefficient of Friction	51.65×10^{-3}	Nms/rad
p	Number of Pole Pairs	6	-

Table 5.1 – PMSM Machine Parameters

The consideration of non-ideal mechanical motion components is relevant as this differs from the ideal mechanical modelling presented for the PMSM in Chapter 3. In both sensored and sensorless operation, it was observed that unmodelled mechanical components result in different currents components required to rotate in forward or reverse directions for the same speed reference. The alignment using dial gauges can be improved by using two dial gauges to measure both vertical and horizontal axis axial oscillations simultaneously. Furthermore, dedicated precision instruments based on laser

alignment technology such as the Fluke 830 exist. However, this is specially designed for larger machines which generally require fixed couplings.

In Figure 5.1, it can be observed that an encoder is fitted on each of the machine shafts M3 and M4. A single encoder is sufficient since the shaft is assumed to be a rigid body from end to end. However, two encoders were used on the experimental setup for two main reasons:

- Since a flexible coupling was used and axial oscillations exist on both M3 and M4, having an encoder closer to the rotor being controlled was considered to be a more robust solution.
- If a single encoder was used, it would have to be read on one microcontroller board and transferred via an SPI/I2C protocol to the microcontroller unit controlling the other machine. These protocols are designed for onboard communication between the microcontroller and peripheral devices. When transmission from one microcontroller to the other was attempted in this dissertation, the data received at the slave end had a low Signal-to-Noise Ratio (SNR) which was insufficient for vector control purposes.

Given the aforementioned reasons it was felt that more robust measurements would be obtained using two encoders with the encoder isolation boards as discussed in Section 5.7.

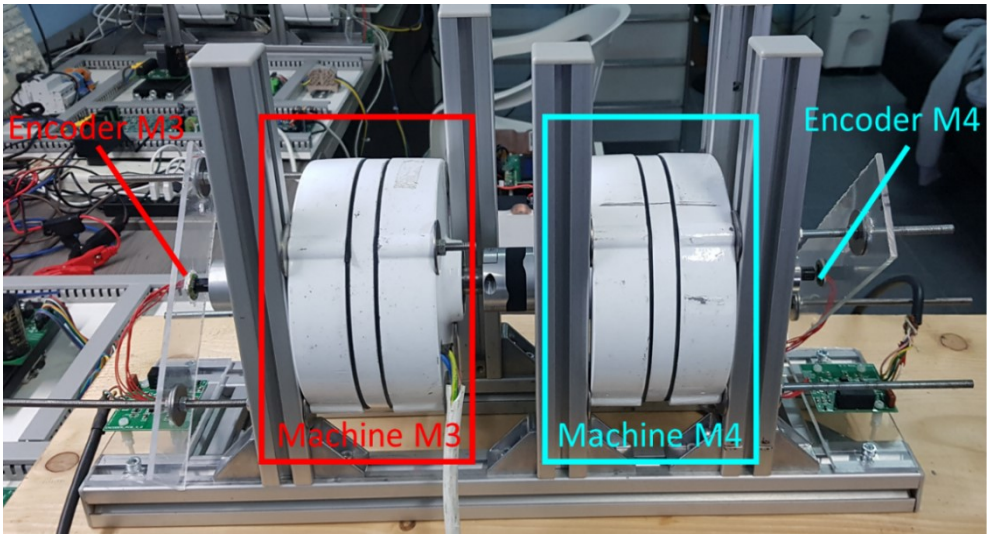

Figure 5.1 – PMSM Experimental Setup

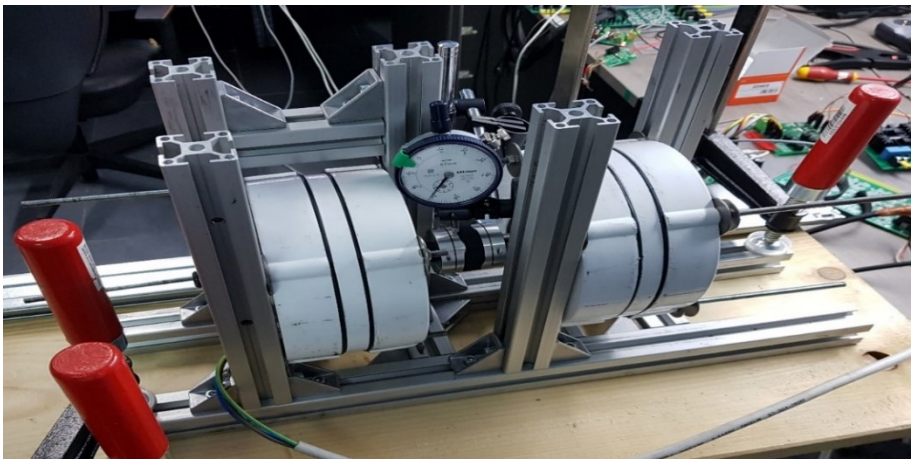

Figure 5.2 (a) – Shaft Alignment using Dial Gauge (front view)

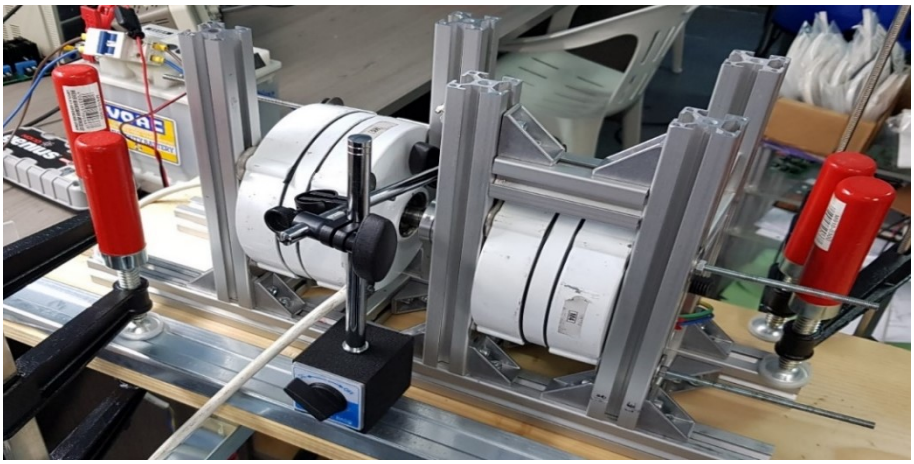

Figure 5.2 (b) – Shaft Alignment using Dial Gauge (rear view)

5.3 STM32 Microcontroller

5.3.1 STM32 Microcontroller Firmware

The control operation of the inverter drive in this dissertation is carried out through an STM32F407VGT6 microcontroller which is integrated within the STM32F407G-DISC1 development board. The microcontroller has a 32-bit ARM Cortex M4 architecture with a floating-point unit. The main clock frequency can be increased up to 168 MHz through a PLL architecture supplied by an on-board crystal oscillator. The firmware operation for generic sensored and sensorless control is shown in the flowchart in Figure 5.3. At start-up, the required registers are set up with the main timers used setup as follows: ADC DMA timer interrupt at 40 kHz, Control loop timer interrupt at 5 kHz, and PWM Timer at 20 kHz.

In order to improve the SNR of the measurements used for both fundamental control and sensorless estimation, the ADCs on the microcontroller are sampled at a frequency of

40 kHz which results in 8 samples for each 5 kHz control loop. The 8 samples are combined with an averaging filter for usage in the microcontroller. Various measurements can be obtained through the microcontroller ADCs including fundamental currents (i_a, i_b, i_c), fundamental voltages (v_a, v_b, v_c), DC link voltage (v_{dc}) and HF current amplitudes (A_{ia}, A_{ib}, A_{ic}).

In a sensored mode of operation, the mechanical rotor position θ_m is obtained from a 12-bit magnetic encoder (Broadcom AEAT-6012-A06) through a Synchronous Serial Interface (SSI). An encoder interface board was introduced to isolate the encoder circuit from the low signal electronics, as discussed in Section 5.7. The RFO control topology requires a measurement of the electrical rotor position θ_e, which is obtained by scaling the mechanical rotor position θ_m by the number of pole pairs (p = 6 for M3/M4). Since the encoder produces a discretized measurement, a quadrature PLL [138] is used to obtain filtered values of the mechanical rotor speed ω_{mf} and θ_{mf}. A detailed analysis of PLLs used for sensored and sensorless operation is given in Section 7.5. The discrete differentiation of the encoder measurement results in low SNR due to the encoder output data being a digital signal. The sensorless algorithm within the main timer interrupt is operated at a frequency of 2.5 kHz. The operating frequency of the observer was reduced from the 5 kHz of the main control loop mainly to improve the SNR of the measurements used for sensorless control since two measurements of the HF current amplitude components are available to calculate one sensorless estimate.

In this dissertation, the main sensorless algorithm which was investigated is the Search-Based Observer (SBO) with real-time commissioning, which is presented in Section 7.4. This sensorless method compares the HF current amplitudes in the stationary αβ frame to the previously commissioning LUTs. Besides the HF current amplitudes, $A_{i\alpha}$ and $A_{i\beta}$, the SBO also requires measurements for the synchronous frame current i_q and the estimated rotor speed for Look-Up Table (LUT) Selection. The SBO uses the previously estimated mechanical rotor position to iterate the search part of the algorithm to a limited number of elements within the LUT.

The high-frequency injection components are superimposed on the fundamental stationary αβ components which are converted into the three-phase stationary frame abc components. Sine Pulse Width Modulation (SPWM) is used to obtain the duty cycles for the three phases D_a, D_b and D_c. The high-side and low-side switching signals are

generated automatically by the microcontroller PWM timer with a dead-time of 1 μs introduced in the dedicated Peripheral unit. The variables which necessitate monitoring are in a 2-byte format transferred to MATLAB through a virtual COM port interface.

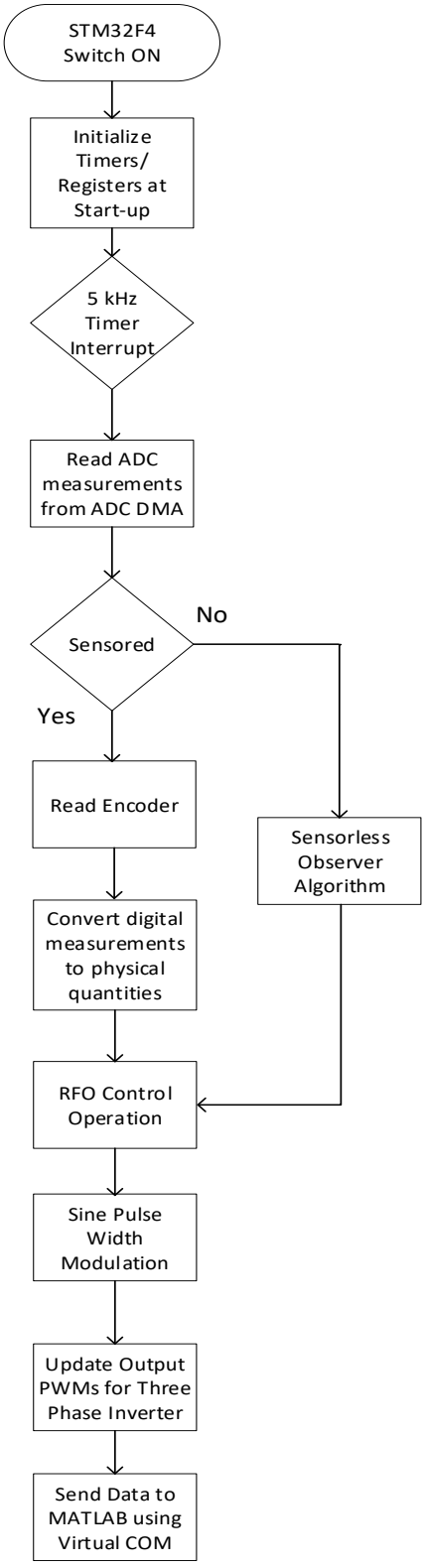

Figure 5.3 – STM32 Firmware Flowchart

5.3.2 STM32 Shield Board

In this dissertation, the STM32F407G-DISC1 development board was used to reduce development time and cost as compared to developing a custom microcontroller board. The development of an improved solution in terms of EMC and board-to-board communication was researched in [142]. A shield board was designed for the development board, as shown in Figure 5.4 (Schematic in Appendix A.1). The shield board provides additional capacitance to the 3 V and 5 V lines on the embedded board and provides a more convenient distribution of pins according to the designated function as used in this dissertation.

Figure 5.4 – STM32 Shield Board

The most relevant pinout connections and their designate functionalities are given in Table 5.2. The STM32 shield board connects to the encoder interface board, saliency measurement board and the gate drive board. The pins which are designated as ADC pins have a preceding first-order low-pass filter with a bandwidth of 5 kHz for anti-aliasing purposes. The bandwidth of the filter can be easily adjusted by modifying the value of the resistance in the filter of the respective ADC pin.

Microcontroller Pin	Microcontroller Function	Inverter Function
PE9	PWM Timer	PWM_a
PE8	PWM Timer	PWM_an
PE11	PWM Timer	PWM_b
PE10	PWM Timer	PWM_bn
PE13	PWM Timer	PWM_c
PE12	PWM Timer	PWM_cn
PB12	Digital I/O	ENC_CS
PB14	Digital I/O	ENC_DO
PB13	Digital I/O	ENC_CLK
PA1	ADC	i_a
PC4	ADC	i_b
PC1	ADC	i_c
PC5	ADC	v_a
PA2	ADC	v_b
PB1	ADC	v_c
PA4	ADC	A_{ia}
PA3	ADC	A_{ib}
PA0	ADC	A_{ic}

Table 5.2 – STM32 Microcontroller Pin Designations

5.4 Gate Driver Board

The six switch three-phase inverter topologies used in this dissertation were designed to use all N-channel MOSFETs. Historically, such designs were necessary because of the low availability of high current rated P-channel MOSFETs which is generally not the case at the time of writing. However, having identical MOSFETs allows for lower component variations. In order to operate the high side N-channel MOSFETs in the ohmic and cut-off regions, a gate-driver circuit is required to ensure that the gate-to-source voltage V_{GS} is much higher than the thermal voltage V_T required to switch on the MOSFET. In order to ensure that the voltage at the gate is always higher than that at the source, an isolated power supply or charge pump configuration is required at the output of the isolated gate driver stage.

The charge pump configuration is a cost-effective solution as it only requires an additional capacitor and diode to level shift the voltage when the high side transistor is on. However, this technique poses limitations on the switching frequency and is not as robust as having an isolated power source for the MOSFET. For the purposes of this dissertation, a total of six isolated supplies are used in the gate driver board in Figure 5.5 (Schematic in Appendix A.2). The isolated supplies at the low side MOSFETs are not required; however, an identical layout was kept for both high and low sides to minimize the discrepancy in turning on and off the MOSFETs associated with stray parasitic components. The isolated supplies are boost DC-DC converters (RECOM RI-0512S) which step up the main 5 V rail to six isolated 12 V supplies. The output of each DC-DC converter is clamped by a 15 V 1N5245B Zener diode to protect the MOSFET

input against converter overshoot during startup. MOSFETs within the power rating range as those used in this dissertation have a typical maximum $V_{GS} = \pm 20$ V. Therefore, clamping at 15 V protects the input of the MOSFETs from exceeding the maximum Gate-Source voltage. The actual gate driver ICs are the ADuM3223 which provide dual isolated channel outputs (up to 3000 V RMS) from the isolated boost DC-DC converter supplies. The primary function of the gate driver board is to level shift the 3 V microcontroller PWM outputs PWM_a, PWM_an, PWM_b, PWM_bn, PWM_c, and PWM_cn to isolated 12 V voltage levels supplying the gate resistors on the inverter power boards.

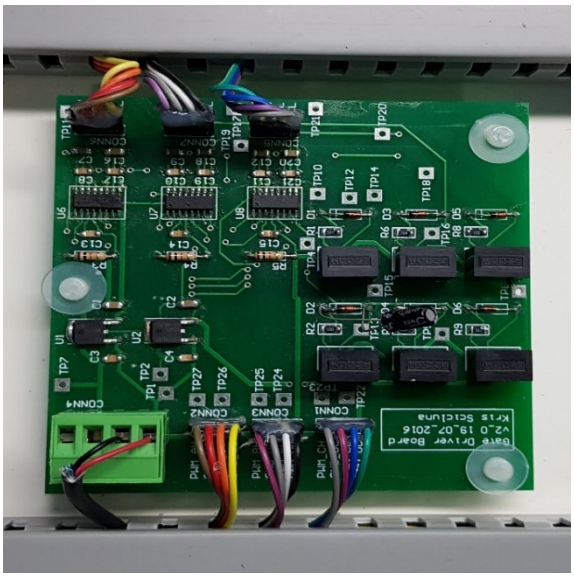

Figure 5.5 – Gate Driver Board

5.5 Saliency Measurement Board

The sensorless control presented in this dissertation is based on the detection of saliency modulated parameters as a function of the rotor position. In order to optimize both fundamental control and detection of HF components, the Multi-Stage Op-Amp (MSOA) circuit board shown in Figure 5.6 was designed (Schematic in Appendix A.3). The measurement board is equipped with three S22P015S0 hall effect current sensors for the measurement of stator currents and four TL082 op-amp based buffer circuits for the voltage measurement of the stator voltages and the DC link voltage.

The fundamental stator current measurements are obtained from the current sensor outputs with appropriate signal conditioning for maximum use of ADC input voltage levels and a Butterworth 4th order filter with a bandwidth of 750 Hz to remove the high-frequency current component. The HF current components at 2.5 kHz are obtained from

the current sensor output with a Butterworth 2nd order high-pass filter with a bandwidth of 500 Hz followed by a 1st order low-pass filter with a bandwidth of 10 kHz. Since the injection frequency is of 2.5 kHz and the sampling frequency is of 5 kHz, an op-amp based rectifier circuit was introduced to rectify the HF current components before measurement with the ADC. The rectified HF voltage components were obtained in an identical way with the source being provided by the op-amp based voltage measurement circuits.

The design of this circuit board was originally intended to provide both rectified HF current and voltage measurements using the same filter designs to minimize the phase shifts introduced. However, the first-order low pass filter at 10 kHz used for the current measurement signal did not provide sufficient attenuation to remove the 20 kHz component in the voltage measurement due to the PWM switching. As a result of this, the HF voltage measurements were not used as the resultant admittance signals (HF current divided by HF voltage) showed a lower SNR than when using the HF currents only ($A_{i\alpha}$, $A_{i\beta}$). The saliency measurements and sensorless control presented in this dissertation are based on the rectified HF current measurements sampled with the 12-bit ADC on the STM32 microcontroller. The detection, filtering and rectification of these HF currents is done through op-amp based signal conditioning techniques.

The op-amp based functions were mostly implemented with the TL082 dual op-amp amplifier IC which is a low-cost solution suitable for general signal conditioning applications. The rectification circuit used to produce the rectified HF component was based on the OPA2211 amplifier, which has a slew rate of 27 V/µs and is suitable for precision amplifier applications.

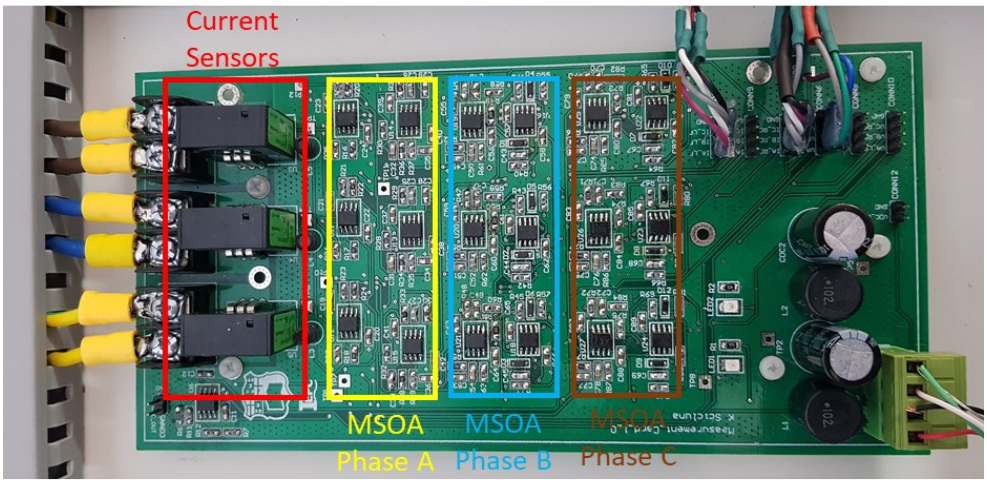

Figure 5.6 – Saliency Measurement Board

5.6 Inverter Power Boards

5.6.1 Discrete Inverter Power Board Implementation

The main inverter power board uses discrete MOSFETs, as shown in Figure 5.8 (Schematic in Appendix A.4). The MOSFETs are N-channel MOSFETs IRFP7718PBF which have a maximum drain to source voltage V_{DSmax} = 75 V and rated continuous drain current I_d = 195 A. These transistors were mainly chosen due to the low drain-source on-resistance R_{DSon} = 1.8 mΩ. The low on-state resistance minimizes the voltage drops across the inverter switches, which are considered as a non-linearity. Such non-linearities affect the HF components injected which are used for sensorless control. The on-state resistance at a rated current of i_q = 10 A results in a voltage drop of 18 mV which is 0.6 % of the maximum pulsating voltage of 3 V. This was considered negligible and further compensation schemes for inverter non-linearities were not considered.

This board includes a number of capacitors with Bill of Materials (BOM) listed in Table 5.3 to minimize both low-frequency variations and switching transients associated with parasitic inductances. All capacitors are electrically connected across the DC link (Figure 5.7); however, their location on the Printed Circuit Board (PCB) varies according to the type of the dielectric. The aluminium electrolytic capacitors are used to maintain a stable DC link without low-frequency variations. Since the Equivalent Series Resistance (ESR) and Equivalent Series Inductance (ESL) of electrolytic capacitors are still relatively high, they can be located at any point on the PCB. Typically they are located near the power connected input connectors. The polyester metal film capacitors are used to minimize transient voltage oscillations resulting during the PWM transient edges. Metal film capacitors are used for their low ESR and ESL, and therefore it is critical that they are placed as close as possible on the PCB to the individual half-bridges (MOSFETS Q1 and Q2 in Figure 5.7). This board was also used for HF injection on M3 as a more stable DC link and lower disturbances were observed compared to other inverter design (Section 5.6.2) due to the additional capacitance used.

Part No.	Value	Quantity	Dielectric
ALP22A103CD063	10 mF	3	Aluminium
MKT1820710065	100 µF	3	Polyester
PEH200KC5150MB2	15 mF	2	Aluminium

Table 5.3 – Capacitor BOM in Discrete Power Board Implementation

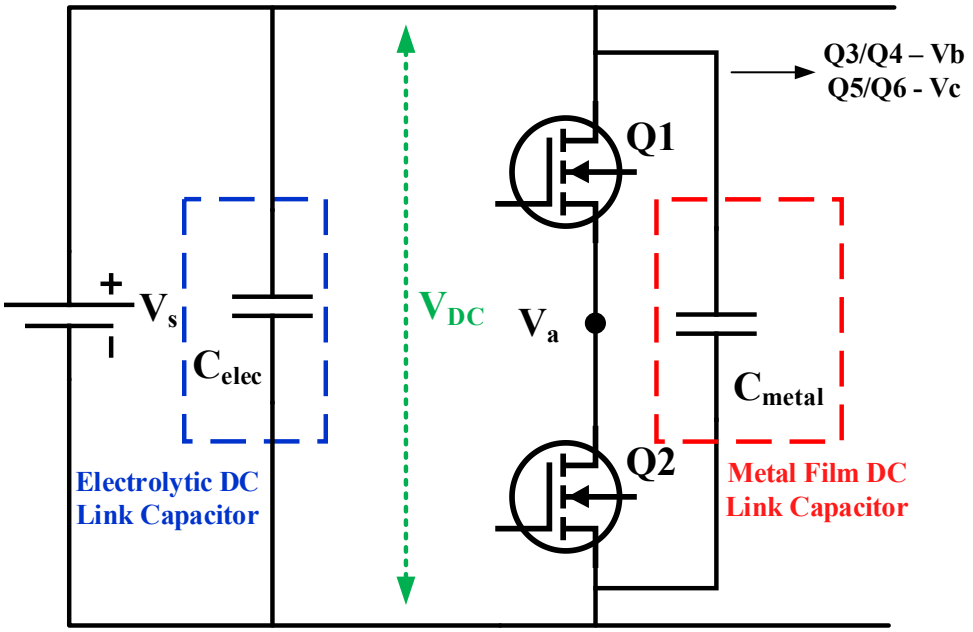

Figure 5.7 – Practical DC-Link Capacitances

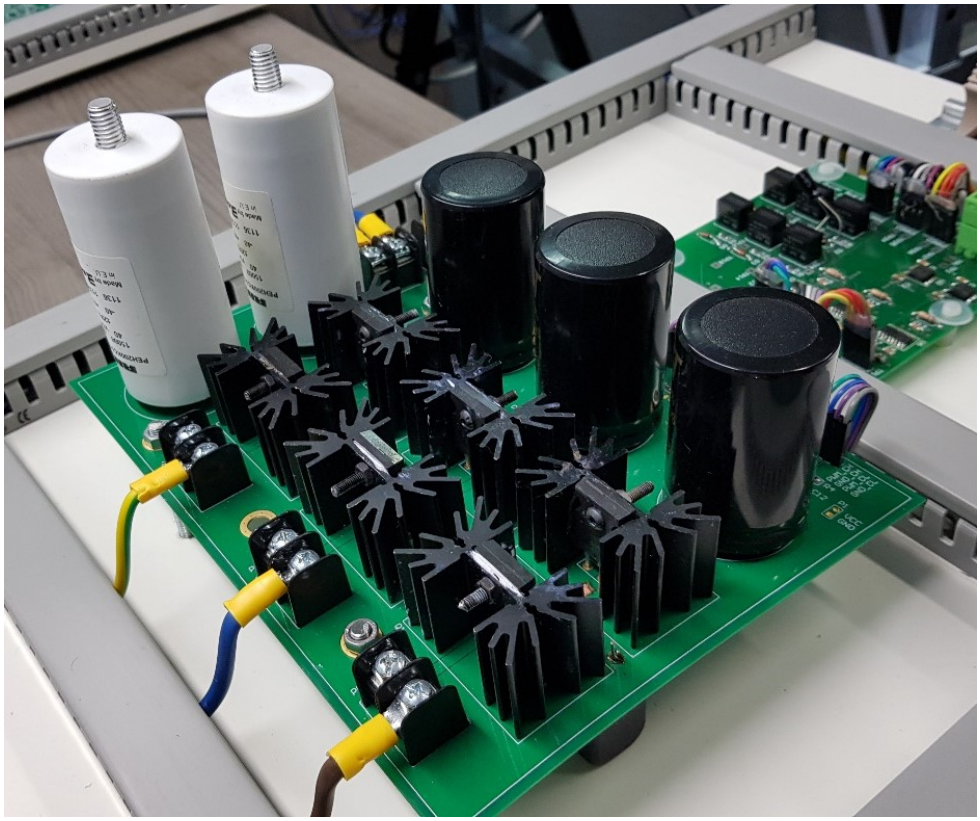

Figure 5.8 – Discrete Inverter Power Board Implementation

5.6.2 Integrated Inverter Power Board Implementation

The inverter power board implementation proposed in Section 5.6.1 was a suitable prototyping solution for the purposes of this dissertation however the layout area and volume required for the implementation would not be suitable for a number of applications where volume is constrained including the steer-by-wire implementation. At the time of writing, a number of Integrated Power Modules (IPM) were available on the market through which a three-phase inverter topology is implemented on a single integrated circuit at a fraction of the cost of having six discrete transistors. The reduced form factor also results in lower stray inductances between the high side and low side MOSFETs to a level which cannot be achieved with discrete components.

An alternative solution to that proposed in Section 5.6.1 was developed around the FTCO3V455A1, which is a dedicated automotive IPM. This module was convenient as it has a sufficient rating (40 V 150 A) for the PMSM used in this dissertation, and it could be used directly with the gate driver circuitry described in Section 5.4. There are also IPM modules specially designed for higher DC link values which also integrate the gate driver circuitry within the IPM to further reduce the footprint of the designed solution. The Integrated Inverter Power Board Implementation developed as part of this dissertation is shown in Figure 5.9 (Schematic in Appendix A.5).

The PCB was laid out on a 4-layer design in order to increase the plane capacitance to minimize the transients associated with parasitic inductances. An ALP22A103CD063 10 mF aluminium electrolytic capacitor and an MKT1820710065 100 µF Polyester Film Capacitance were introduced to reduce the effects of inductances further and stabilize the DC link. This inverter implementation had similar performance to the discrete implementation (Section 5.6.1) for fundamental control operation. However, when HF injection was introduced, the DC Link had higher variations than those observed in the discrete implementation. This is mainly attributed to the discrete implementation having 300 µF of film-based capacitance while the integrated board had 100 µF. As a result of this, the integrated IPM-based inverter drive was only used for the sensored operation of machine M4 without the HF injection. PCB via stitching was used in this design so as to provide a low resistance path between multiple power planes at the same potential.

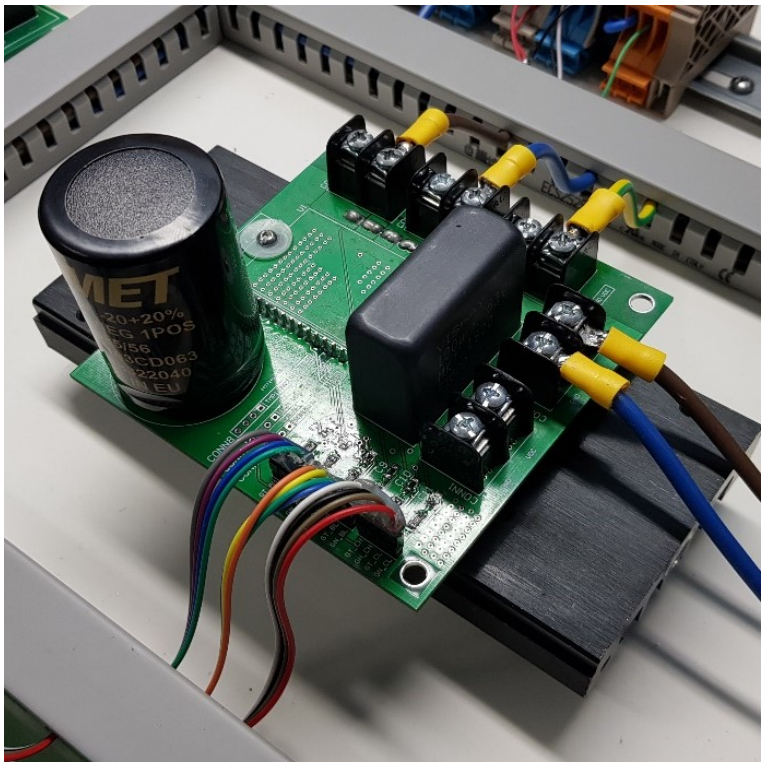

Figure 5.9 – Integrated Inverter Power Board Implementation

5.7 Encoder Interface Board

In this dissertation, the Broadcom AEAT-6012-A06 12-bit magnetic encoder was used for the measurement of the mechanical rotor position θ_m. The encoder operated on an SSI interface protocol which requires the encoder to be clocked with a frequency of up to 1 MHz at which a data signal is transmitted back to the originating device of the clock frequency.

In order to improve the Electromagnetic Compatability (EMC) robustness of the encoder, the circuit was isolated through the interface board shown in Figure 5.10 (Schematic in Appendix A.6). The clock (CLKUC) and chip select (CSUC) signals are output from the microcontroller and passed through TLP2361 photo-isolators. Since the isolators operate on an inverted logic, a 74LVC1G04 inverter IC was introduced. Once the encoder is clocked and enabled, it provides a serial data signal (DOISO) which is transferred similarly through the photo-isolators and inverter for correct logic operation. The transferred serial data signal (DOUC) is read serially by the STM32 microcontroller.

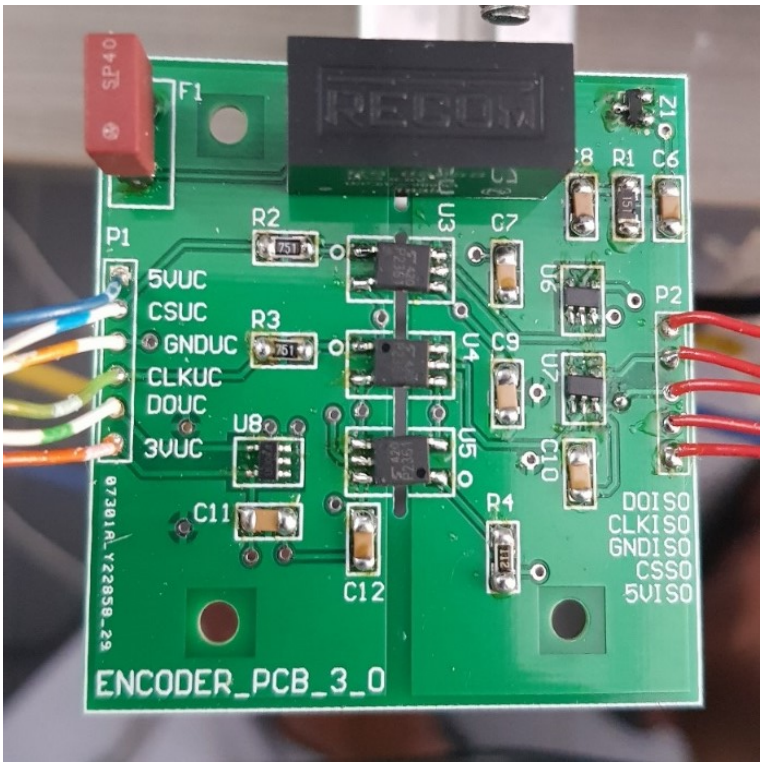

Figure 5.10 – Encoder Interface Board

5.8 Final Experimental Setup

The various modular circuit boards presented in this chapter were assembled in panel form to facilitate inspection and testing, as shown in Figure 5.11 (with discrete MOSFETs inverter) and Figure 5.12 (with IPM inverter). The input terminal distribution provides an arrangement of single-pole (SP) MCBs which enables a DC power supply to be connected in parallel with a 12 V Lead-Acid battery. Low-signal electronics are supplied from an additional bench power supply providing ± 9 V which is then regulated through on-board linear regulators within the PCBs themselves. The three-phases of the machine are connected to the three-phase machine terminals at the bottom of the panel.

The panels shown in Figures 5.10 and 5.11 are very similar except for the power board used in each panel. The discrete inverter implementation (Figure 5.11) is used for sensorless control of machine M3 while the integrated implementation (Figure 5.12) is used for sensored control of the machine M4.

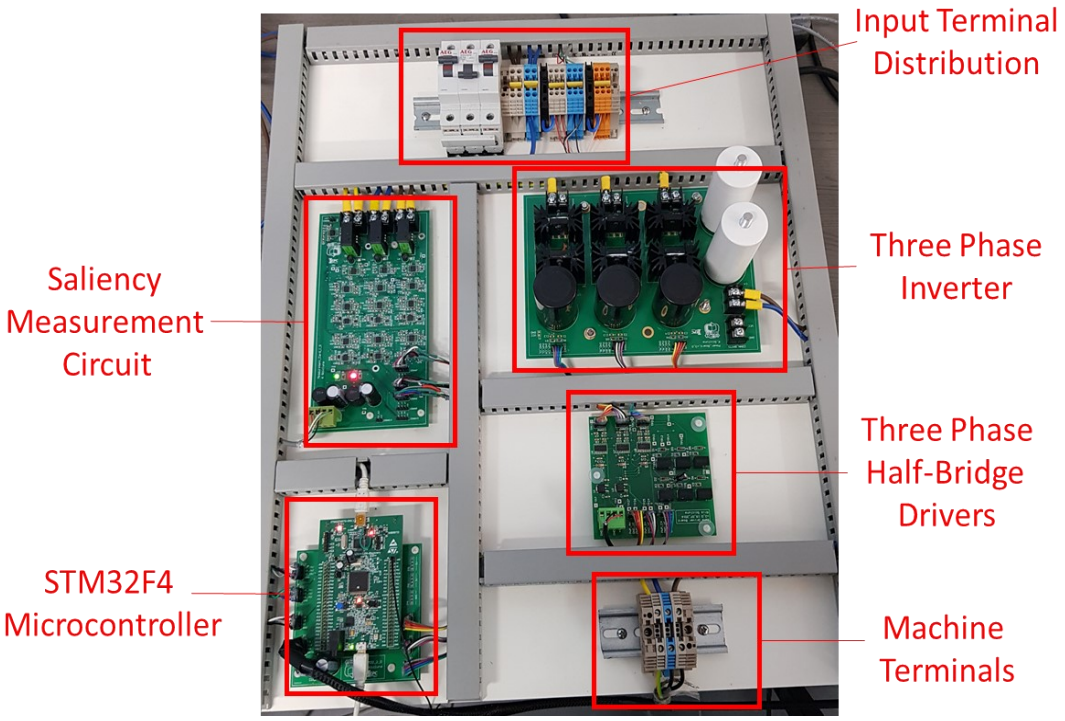

Figure 5.11 – Final Inverter with Discrete Inverter Power Board Implementation

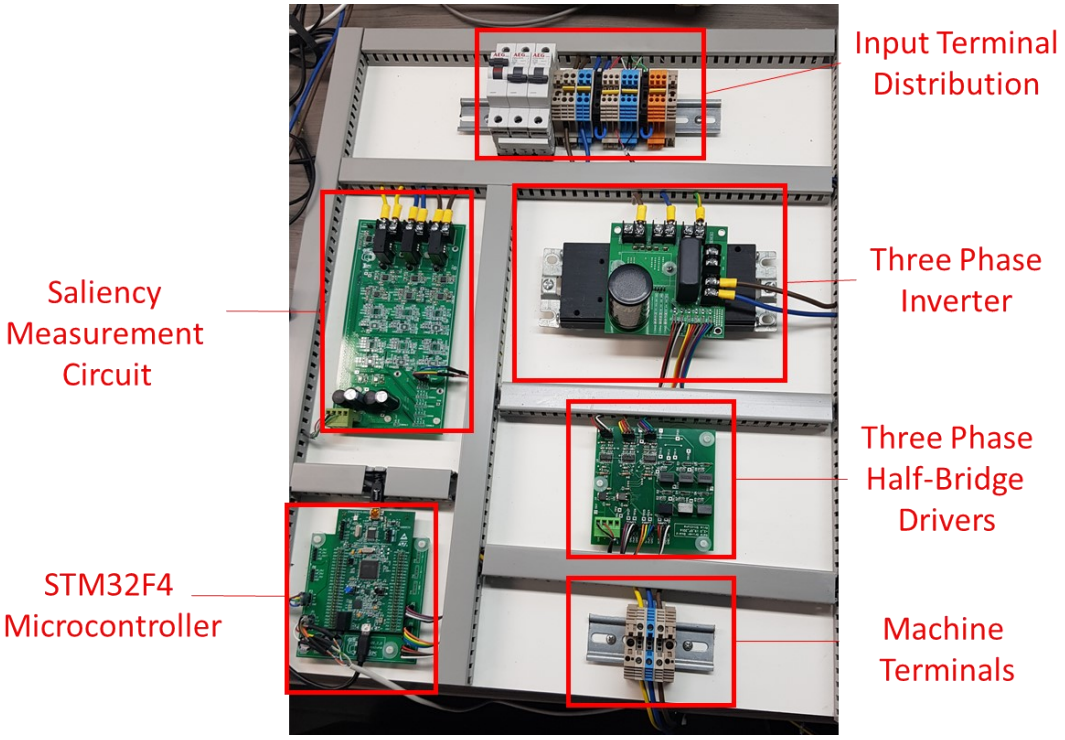

Figure 5.12 – Final Inverter with Integrated Inverter Power Board Implementation

5.9 Summary

In this chapter, the experimental setup used for sensorless investigation in this dissertation consisting of two mechanically coupled PMSMs was presented. The machine parameters obtained from the datasheet and experimentally were presented in Table 5.1. From the values of L_d and L_q, it can be deduced that the machines exhibit significant saliency suitable for saliency-based sensorless control. The practical limitations in the mechanical arrangement of the drives were identified and their effects of machine control considered.

The STM32 firmware routine was shown in the form of a flowchart in Figure 5.3, which identifies the critical processes for both sensored and sensorless operation. It was explained that the ADCs were oversampled at a frequency of 40 kHz with respect to the control loop of 5 kHz. Oversampling was used to increase the SNR of the measurements being used for control by averaging 8 samples. The sensorless observer loop is operating at a frequency of 2.5 kHz such that 2 HF current samples are available within the 5 kHz control loop. New rotor speed/position estimates are available at the 2.5 kHz rate.

The design and operation of various modular PCBs was discussed, including the STM32 shield board and gate driver board. The saliency measurement board was shown to provide both fundamental and HF measurements form the machines. While the board provided measurements for both HF currents and voltages, only the currents are used for saliency detection. Two inverter designs were considered with the discrete implementation found to have a better performance for HF injection due to the additional capacitance on the board. The encoder board which isolates the microcontroller pins from the actual magnetic encoder IC was also shown. The experimental setup presented in this dissertation is used for determination of the magnetic signatures of the SM-PMSMs (Chapter 6), sensorless current control (Chapter 8), sensorless speed/position control for generic applications (Chapter 9) and steer-by-wire (Chapter 10).

Chapter 6 – High Frequency Based Sensorless Estimation in PMSMs

6.1 Introduction

This chapter presents an outline for saliency-based low/zero speed sensorless control. Machine saliency models for both the ideal case with a dominant single fundamental saliency and also for machines with multiple harmonic saliencies are discussed. The HF current amplitudes for the test machine M3 (Figure 3.11, Section 3.4) are shown for both continuous rotating and pulsating injection HF signals.

The resulting HF saliency is investigated at different operating points, including different load currents, voltage injection amplitudes and voltage injection angles in the stationary αβ frame. Compensation of saliency harmonics using the SMP technique is also shown.

6.2 Magnetic Saliency

6.2.1 Introduction to Magnetic Saliency in PMSMs

Magnetic saliency in an electrical machine is defined as the variation of the stator inductance as a function of the rotor position. This difference is typically expressed as the difference between the synchronous frame stators inductances L_d and L_q. In general, various sources can contribute to magnetic saliency such as [143, 144]:

1. geometric saliency
2. magnetic saturation due to varying magnetic flux in the iron parts
3. saturation due to the mechanical eccentricity of the rotor
4. eddy-current-loss-reflected resistance-based saliency

In the case of Internal PMSMs (IPMSMs), the magnetic saliency is mainly due to the geometric construction while in Surface Mounted PMSMs (SM-PMSMs) it is predominantly due to the saturation caused by the magnetic flux from the permanent magnets on the rotor [100, 105, 143]. The saliency in PMSMs can be represented as a variation in either the leakage or magnetizing inductances in the dq-frame as expressed in (6.1) and (6.2).

$$L_d = L_{ld} + L_{md} \tag{6.1}$$

$$L_q = L_{lq} + L_{mq} \tag{6.2}$$

Where

L_{ld}/L_{lq} are the stator leakage inductances representing unlinked flux in the d/q axes

L_{md}/L_{mq} are the magnetising inductances representing the fundamental flux crossing the air-gap in the dq axes

6.2.2 Geometric Saliency

While geometric saliency is usually predominant in IPMSMs, it could possibly also contribute to SM-PMSMs due to stator and rotor eccentricities resulting from manufacturing tolerances. The rotor of the experimental SM-PMSMs used in this dissertation is of the partially inset type (Figure 6.1). The magnets are mounted onto the partially inset rotor slot opening with high strength adhesive. The assembly tolerances in magnet placement and slot machining are expected to result in a varying air gap due to different magnet positioning above the rotor lamination edge. The stator windings on the steel laminations are shown in Figure 6.2. When inspecting the experimental machine, it was noticed that the internal stator core was not perfectly circular with a certain amount of eccentricity, which results in an elliptical stator. This would also contribute to variations in the air-gap. The construction of both the rotor and stator is expected to affect the machine saliency and result in deviation from the ideal theoretical models.

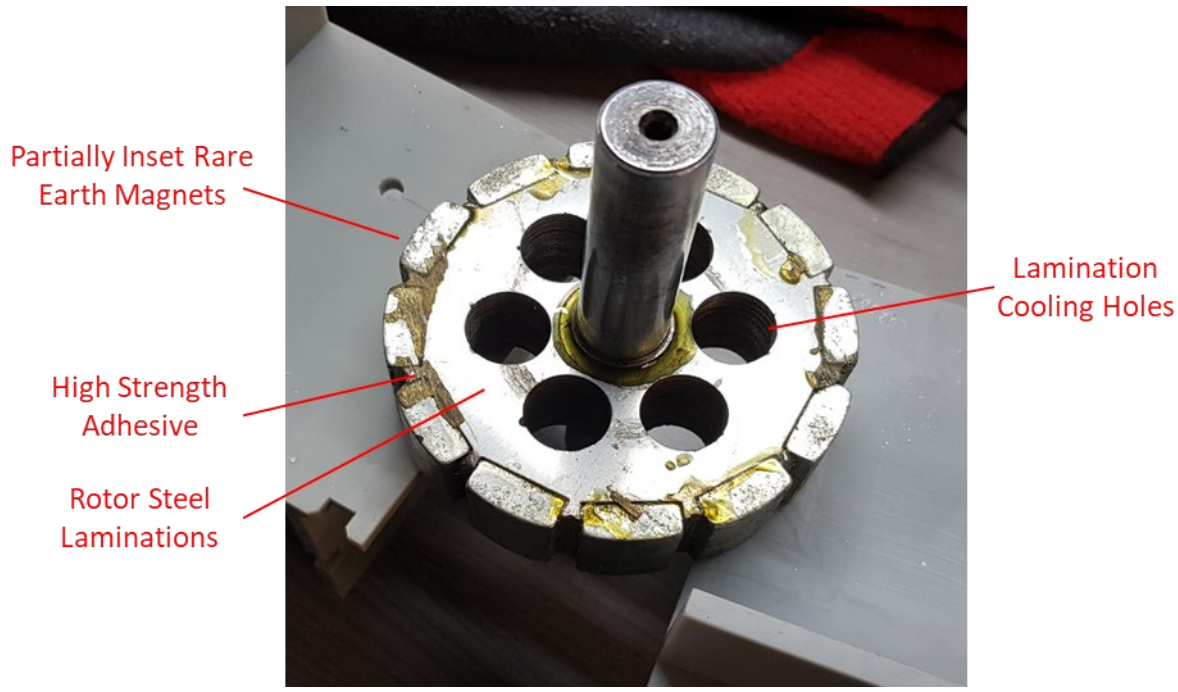

Figure 6.1 – SM-PMSM rotor with partially inset magnets.

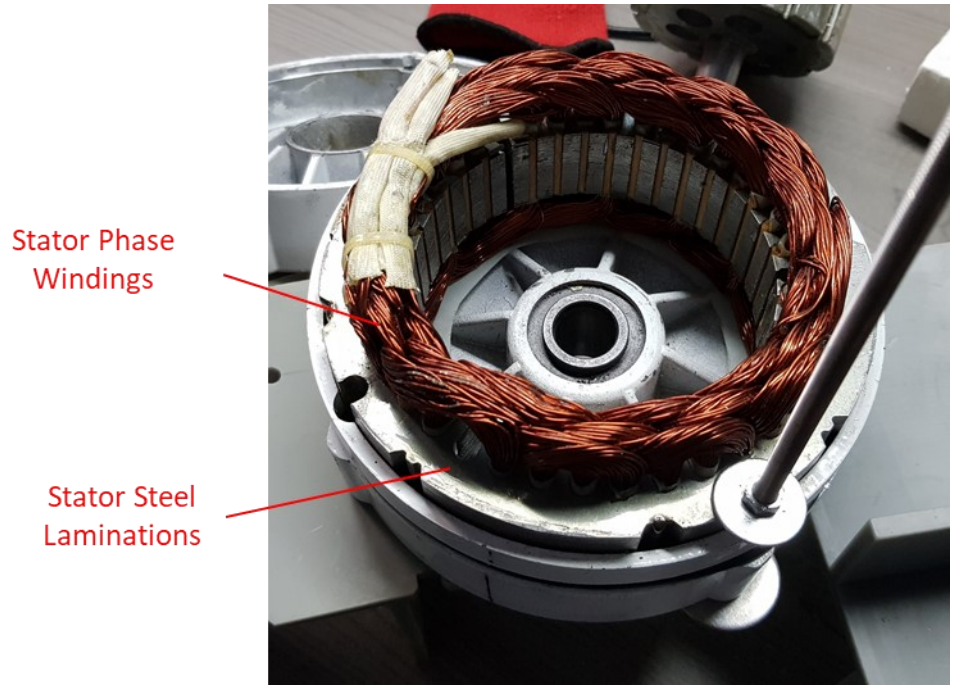

Figure 6.2 – SM-PMSM stator with elliptical laminations.

6.2.3 Saturation Saliency

The effects of saturation on both the magnetizing and leakage inductances have been analysed in terms of synchronous dq components in [105]. Saturation mainly results due to the high air gap flux densities attributed to surface-mounted magnets interacting with the stator and effectively decreasing the magnetizing inductance component.

If a RFO system is used, the maximum of the air gap flux density will be aligned with the d-axis while the minimum is at the q-axis. The high flux density about the d-axis results in a concentration of flux which produces saturation at the stator teeth and tooth tips. This saturation can be modelled as an increase in the effective air-gap length of the d-axis flux path reducing the magnetizing d-axis inductance L_{md}. Since there is no flux concentration in the q-axis, the magnetizing q-axis inductance L_{mq} is unaffected. When this saturation effect is dominant $L_{mq} > L_{md}$.

When an electromagnetic torque is required from the machine, a q-axis current i_q is applied. This creates an additional flux component $L_m i_q$ which introduces a phase shift in the unloaded air gap flux profile. Since the saturation saliency is a function of the airgap flux; the magnetic saliency signature is expected to also be a function of i_q.

6.2.4 Multiple Saliencies Model

While possible sources for saliency in PMSMs were outlined in Sections 6.2.2 and 6.2.3, in practice, it is difficult to differentiate between the saliency components which are a result of geometric eccentricities and saturation effects. Furthermore, the interactions between different segments in the machine will result in a magnetic signature which generally cannot be modelled by the ideal single saliency model expressed in (4.27). While such a model for saliency has been used in literature [74, 78, 79, 145], it is only applicable to a limited range of AC machines.

$$i_{i\alpha\beta} = \begin{bmatrix} \mathrm{I}_1 \sin \omega_\mathrm{i} t + \mathrm{I}_2 \sin(2\theta_\mathrm{e} - \omega_\mathrm{i} t) \\ -\mathrm{I}_1 \cos \omega_\mathrm{i} t - \mathrm{I}_2 \cos(2\theta_\mathrm{e} - \omega_\mathrm{i} t) \end{bmatrix} \tag{4.27}$$

Where $\mathrm{I}_1 = \frac{V_i L}{\omega_\mathrm{i}(L^2 - \Delta L^2)}$

$$\mathrm{I}_2 = \frac{V_i \Delta L}{\omega_\mathrm{i}(L^2 - \Delta L^2)}$$

The model in (4.27) also assumes that the demodulated negative sequence components (terms with magnitude I_2) are perfect sinusoidal functions of the electrical rotor position θ_e with a phase shift between the α and β components of 90°. For basic trigonometric observers without additional compensation schemes deviation from this ideal single saliency model will result in significant estimation errors.

In most machines, such as the case of the experimental machines used in this dissertation, the ideal saliency profile was not observed. The various sources of saliency, including geometric and saturation effects, will contribute to multiple harmonic saliencies which can be of the same order of magnitude of the fundamental saliency. In [81] a more detailed model is presented for a PMSM with multiple saliencies which extends the result in (4.24) through a Fourier series summation for sinusoidally distributed saliencies and a balanced three-phase sinusoidal injection.

Similarly, to what was observed for the single saliency model; the extended Fourier series-based model has both a positive and negative sequence component. The positive sequence component contains no information regarding the rotor position θ_e. Although the multiple saliency model takes into consideration the various harmonics in the magnetic signature, it still does not distinguish between different sources of saliencies.

6.3 Experimental Saliency Determination

6.3.1 Rotating Voltage Injection Saliency with Homodyne Demodulation

If a balanced three-phase rotating injection is used in the form of (6.3) the resultant HF currents were shown to be equal to (4.27). In order to extract the saliency dependent signals from the HF currents demodulation must be applied. This can be carried out by Homodyne Demodulation, that is multiplying the input signal by the high-frequency carrier to obtain a Low Frequency (LF) signal which contains information about the amplitude modulation and a High Frequency (HF) signal which is to be filtered out. The resulting HF current amplitudes after demodulating with a $2\sin\omega_i t$ carrier signal and filtering the HF components results in (6.4-6.5). The HF current amplitudes $A_{i\alpha}$, $A_{i\beta}$ are functions of $2\theta_e$ since an ideal single saliency model was assumed in the derivation of (4.24).

$$v_{i\alpha\beta} = V_i \begin{bmatrix} \cos\omega_i t \\ \sin\omega_i t \end{bmatrix} \tag{6.3}$$

$$i_{i\alpha\beta} = \begin{bmatrix} -I_1 \sin\omega_i t - I_2 \sin(2\theta_e - \omega_i t) \\ I_1 \cos\omega_i t + I_2 \cos(2\theta_e - \omega_i t) \end{bmatrix} \tag{4.27}$$

$$A_{i\alpha} = -I_1 + I_2 \cos(2\theta_e) \tag{6.4}$$

$$A_{i\beta} = I_2 \sin(2\theta_e) \tag{6.5}$$

Where $A_{i\alpha}$, $A_{i\beta}$ are the rotor position-dependent demodulated HF current amplitudes in the stationary α/β axes.

6.3.2 Rotating Voltage Injection Saliency with Aliasing-based Demodulation

From basic sampling theory, it is known that if a signal is sampled at less than twice every period, it cannot be reconstructed effectively. In particular, if the frequency of the signal to be sampled is equal or multiple to the sampling frequency; those frequency components will become effectively signals at 0 Hz. Consider a simple rectified sinusoidal signal with a fundamental frequency f_m which is equal to the sampling frequency f_s (Figure 6.3). If $f_m = f_s$ the sampling will always occur at the same instance and will appear to be a constant 0 Hz signal after sampling.

If the signal of frequency f_m is amplitude modulated, the frequency component at f_m will be shifted to 0 Hz while its amplitude will result in sidebands to the 0 Hz component.

This effectively demodulates the amplitude modulated signal without any additional processing.

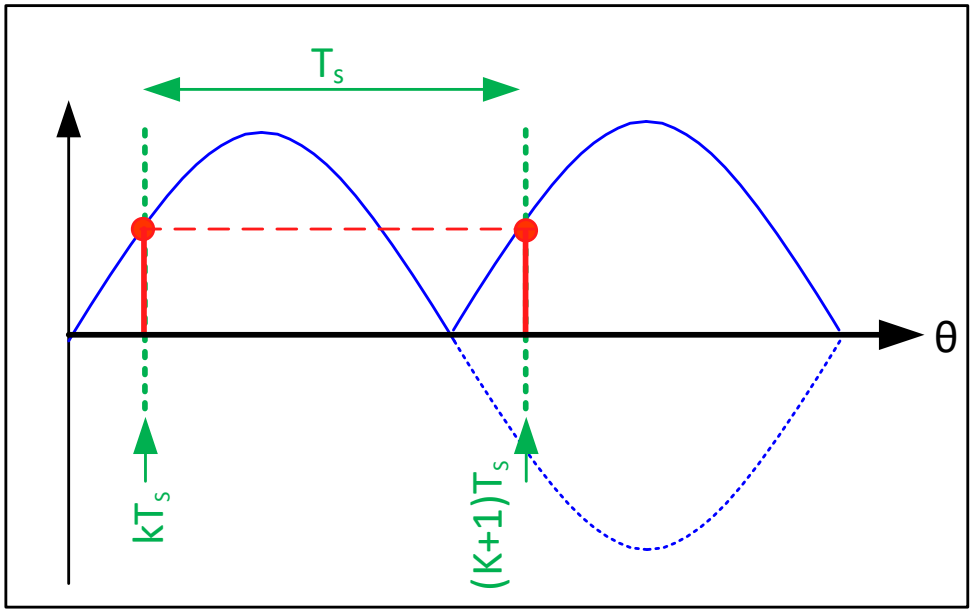

Figure 6.3 – Aliasing effect when $f_m = f_s$

This technique can be effectively used to obtain the HF current amplitudes from the amplitude modulated HF current signals instead of using homodyne or heterodyne techniques. The HF current signals have a centre frequency f_i, thus sampling at this same frequency will result in an aliasing effect. This will shift the injection frequency and its multiples to 0 Hz while the amplitude modulation due to saliency will be shifted to a sideband about the 0 Hz as required for sensorless estimation. This approach is a simplified demodulation technique since there is no useful rotor position-dependent information at the injection frequency and its multiples. The resultant HF current rotor position dependent components after sampling and aliasing are given in (6.6-6.7).

$$A_{i\alpha} = A_{\alpha 0} + f_{\alpha}(2\theta_e) \tag{6.6}$$

$$A_{i\beta} = A_{\beta 0} + f_{\beta}(2\theta_e) \tag{6.7}$$

Where

$A_{\alpha 0}$, $A_{\beta 0}$ are the DC offsets in the demodulated HF current amplitudes due to both saliency and aliasing in the α/β axis.

$f_{\alpha}(2\theta_e)$, $f_{\beta}(2\theta_e)$ are the saliency-based rotor position-dependent functions.

The aliasing dependent demodulation has various advantages compared to the approach presented in Section 6.3.1, which include:

- No trigonometric operations are required on the digital controller for demodulation.
- No particular saliency model is assumed.

Furthermore, if the PWM frequency used in the electric drive is also a multiple of the sampling frequency, this will also be shifted to 0 Hz through the aliasing process. The functions $f_\alpha(2\theta_e)$, $f_\beta(2\theta_e)$ can be used to represent both ideal SM-PMSMs and also those with multiple saliencies. The components aliased to 0 Hz are inherently integrated into the Look-Up Tables (LUTs) when using the search-based method proposed in this dissertation such that no further compensation is required for the DC offset components $A_{\alpha 0}$, $A_{\beta 0}$. The analogue hardware presented in this dissertation was designed to operate at an injection frequency of f_i = 2.5 kHz. Since the HF signals are rectified, the input signals at the ADC have a fundamental frequency of 5 kHz. The ADC sampling frequency is 40 kHz averaged out over 8 samples which gives a synchronized sampling frequency f_s = 5 kHz. The PWM frequency was set to f_{PWM} = 20 kHz, which is also a multiple of the f_s such that the PWM components and its multiple harmonics are also aliased to DC.

6.3.3 Rotating Voltage Injection Saliency Experimental Results

The HF current amplitudes $A_{i\alpha}$, $A_{i\beta}$ were monitored for SM-PMSM M3 in RFO control at an unloaded operating point (i_{q3}^* = 0 A, i_{d3}^* = 0 A) while it was being driven at a reference rotor speed ω_{m4}^* = 1 rad/s by the a similar SM-PMSM machine M4 in RFO speed-controlled mode. A rotating voltage injection of the form (6.3) was used.

The amplitude of the voltage injection V_i = 3 V with f_i = 2.5 kHz. The test was carried out over a 60 s period during which continuous rotating carrier voltage injection was applied. The rotor speed of M3 is shown in Figure 6.4, while the rotor mechanical position is shown in Figure 6.5. The HF current amplitudes after demodulation by aliasing are shown in Figure 6.6. The peak-to-peak current amplitudes of the demodulated HF current amplitudes are approximately equal to $A_{i\alpha\_pp}$ = 71.3 mA and $A_{i\beta\_pp}$ = 83.8 mA.

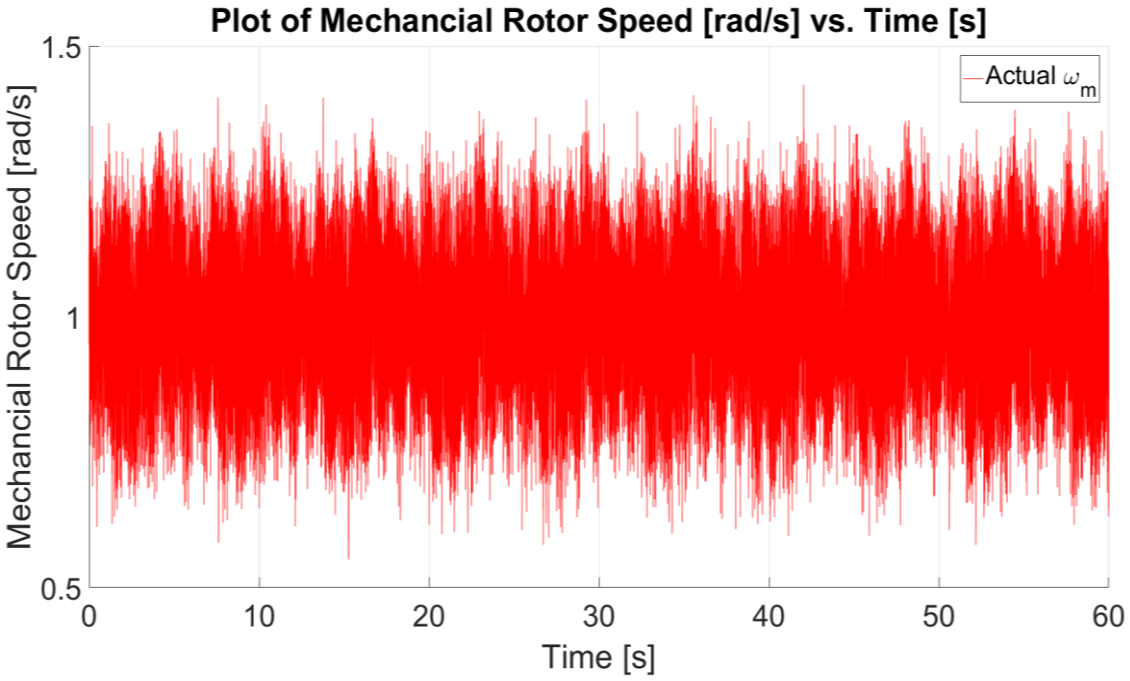

Figure 6.4 – Plot of Rotor Mechanical Speed [rad/s] vs. Time [s] with ω_{m4}^{*} = 1 rad/s on M4, i_{d3}^{*}= 0 A and i_{q3}^{*}= 0 A on M3 during continuous rotating injection.

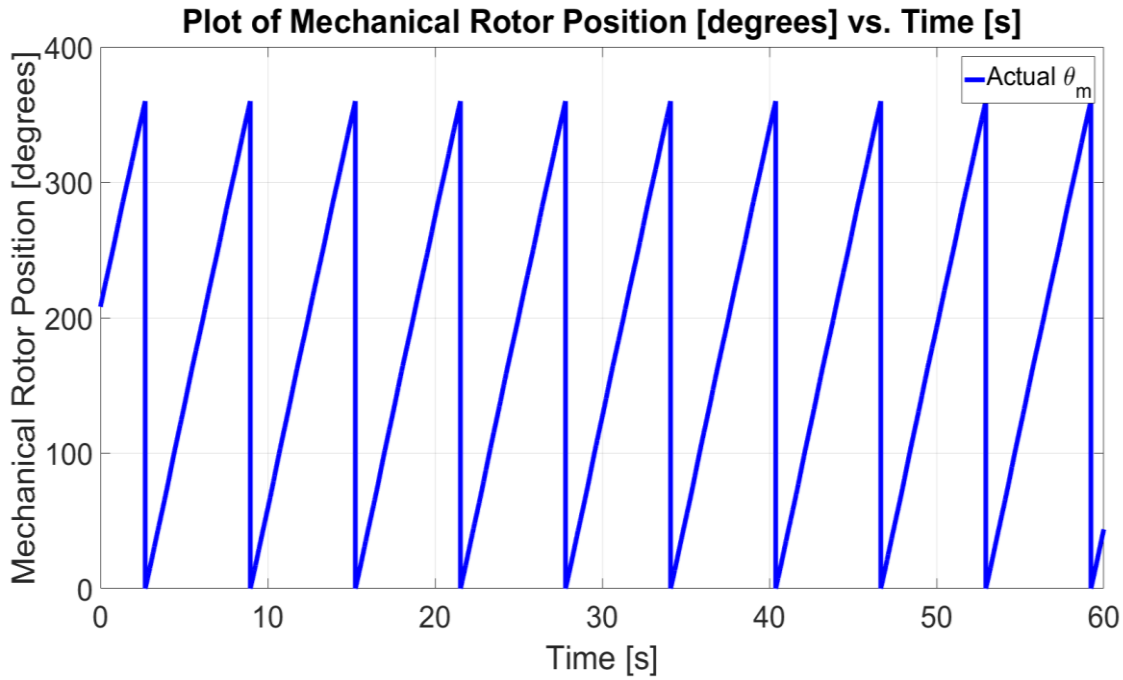

Figure 6.5 – Plot of Rotor Mechanical Position [°] vs. Time [s] ω_{m4}^{*} = 1 rad/s on M4, i_{d3}^{*}= 0 A and i_{q3}^{*}= 0 A on M3 during continuous rotating injection.

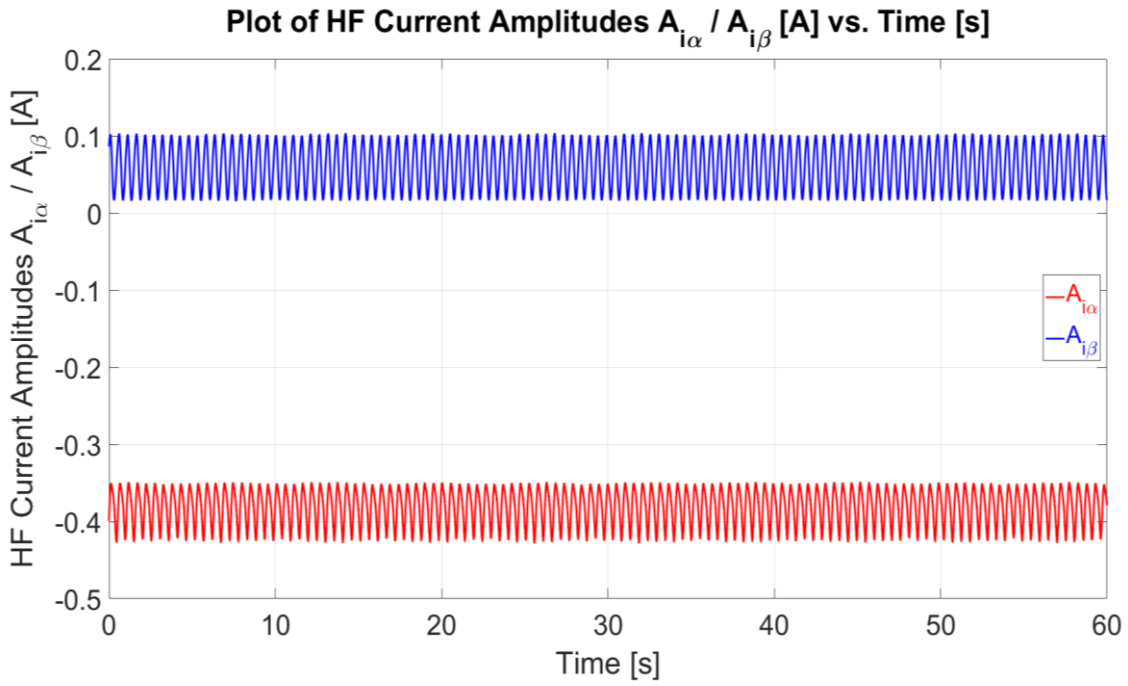

Figure 6.6 (a) – Plot of HF Current Amplitudes $A_{i\alpha}$, $A_{i\beta}$ [°] vs. Time [s] with $\omega_{m4}^{*} = 1$ rad/s on M4, $i_{d3}^{*} = 0$ A and $i_{q3}^{*} = 0$ A on M3 during continuous rotating injection.

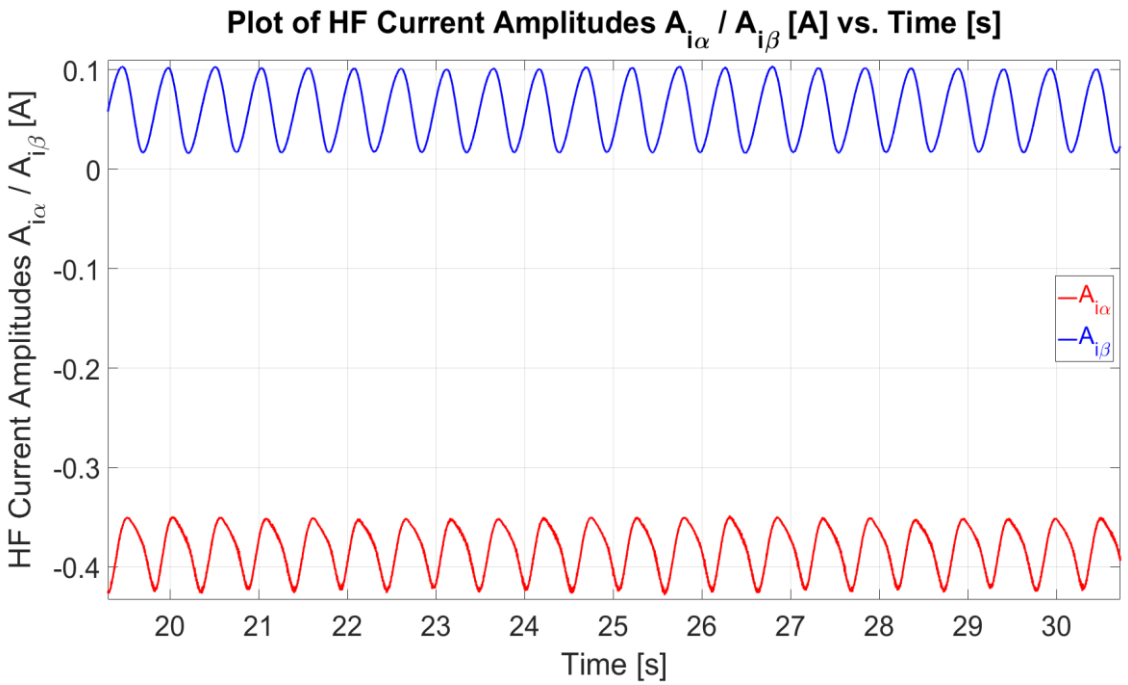

Figure 6.6 (b) – Plot of HF Current Amplitudes $A_{i\alpha}$, $A_{i\beta}$ [°] vs. Time [s] with $\omega_{m4}^{*} = 1$ rad/s on M4, $i_{d3}^{*} = 0$ A and $i_{q3}^{*} = 0$ A on M3 during continuous rotating injection (zoomed in between t = 20 – 30 s).

The magnetic signature of the SM-PMSM M3 for a continuous rotating injection can also be observed in the three-dimensional magnetic signature plot of Figure 6.7 (a). The saliency repeats itself as a function of $2\theta_e$ such that 12 cycles are observed for one mechanical revolution of θ_m for the 6-pole experimental machine under test. From the two-dimensional saliency plots in Figures 6.7 (b)-(c) the presence of harmonics can be observed since the resulting functions are not single sinusoidal components. The complex plot of $A_{i\alpha}$ and $A_{i\beta}$ in Figure 6.7 (d) shows that the variation in amplitude and phase shift in the αβ components distorts the ideal single saliency model complex plot from a circular locus into a more triangular shape. With this type of magnetic signature, traditional trigonometric based sensorless observers result in significant estimation errors not suitable for closed-loop sensorless control at low/zero speed.

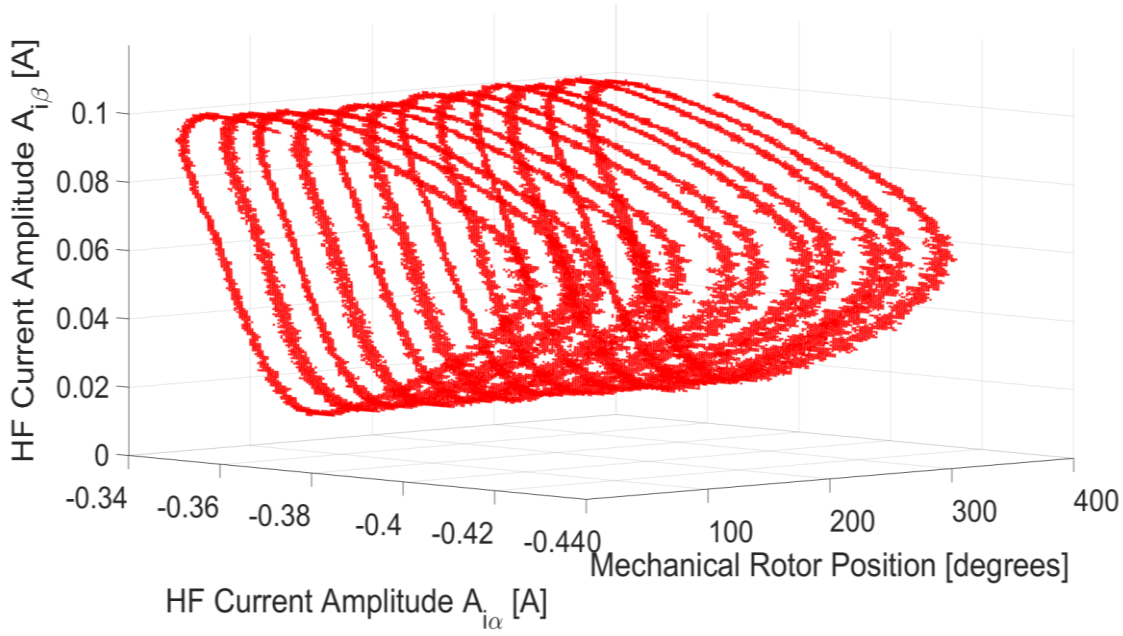

Figure 6.7 (a) – Three-Dimensional Plot of HF Current Amplitudes $A_{i\alpha}$ [A], $A_{i\beta}$ [A], θ_m [°] with $\omega_{m4}^* = 1$ rad/s on M4, $i_{d3}^* = 0$ A and $i_{q3}^* = 0$ A on M3 during continuous rotating injection.

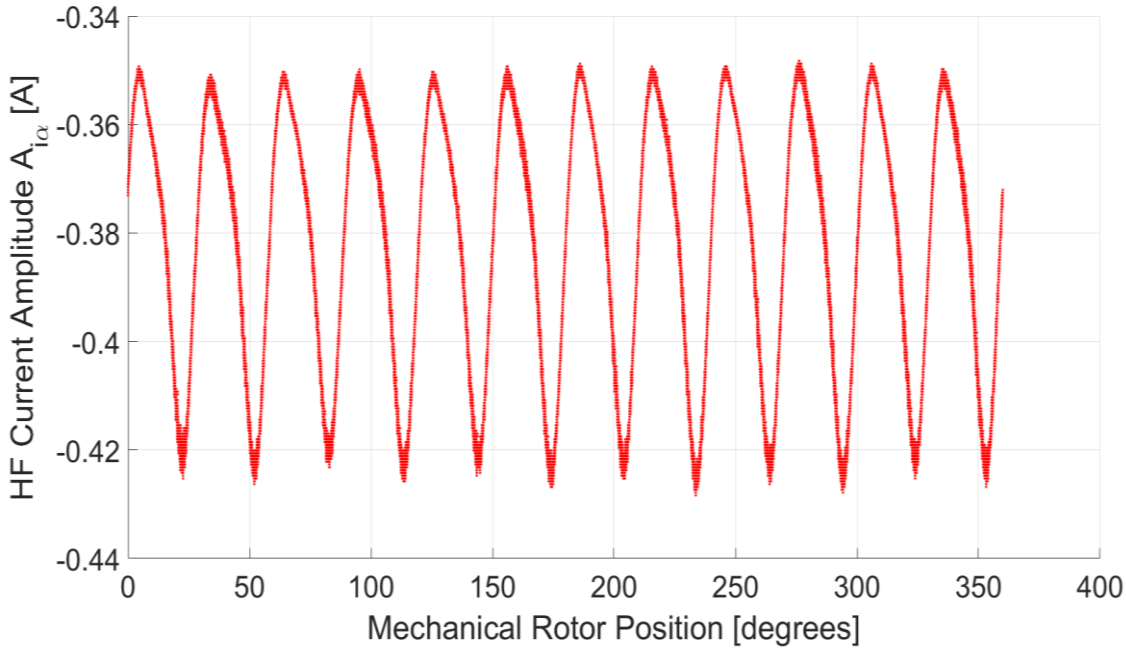

Figure 6.7 (b) – Plot of HF Current Amplitude $A_{i\alpha}$ [A] vs. θ_m [°] $\omega_{m4}^* = 1$ rad/s on M4, $i_{d3}^* = 0$ A and $i_{q3}^* = 0$ A on M3 during continuous rotating injection.

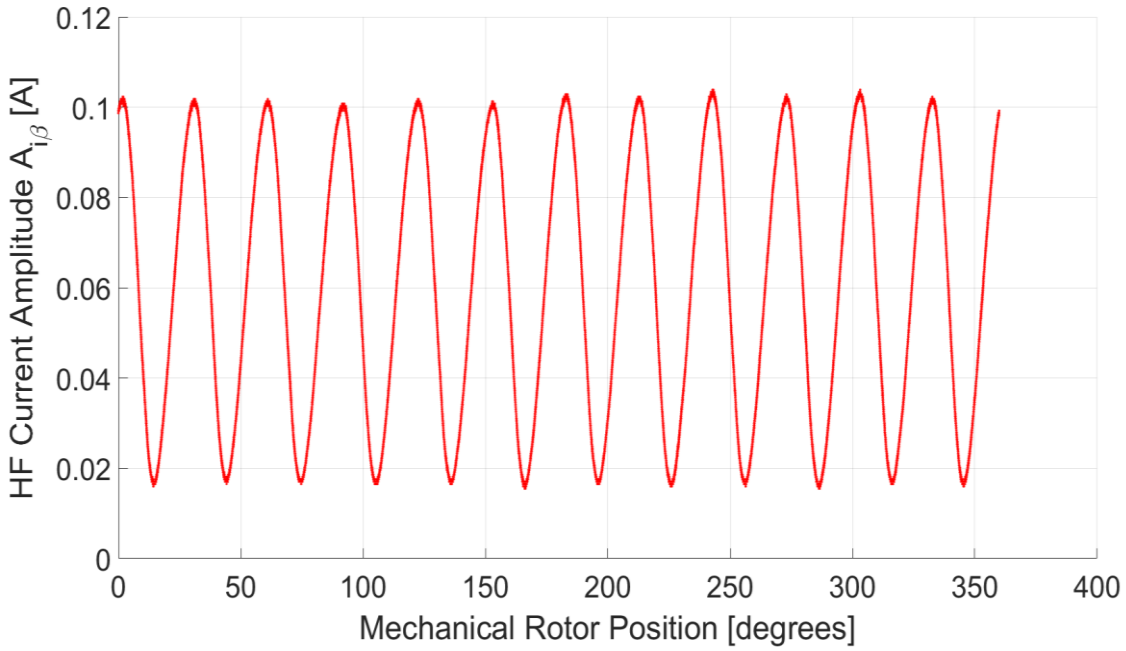

Figure 6.7 (c) – Plot of HF Current Amplitude $A_{i\beta}$ [A] vs. θ_m [°] with $\omega_{m4}^* = 1$ rad/s on M4, $i_{d3}^* = 0$ A and $i_{q3}^* = 0$ A on M3 during continuous rotating injection.

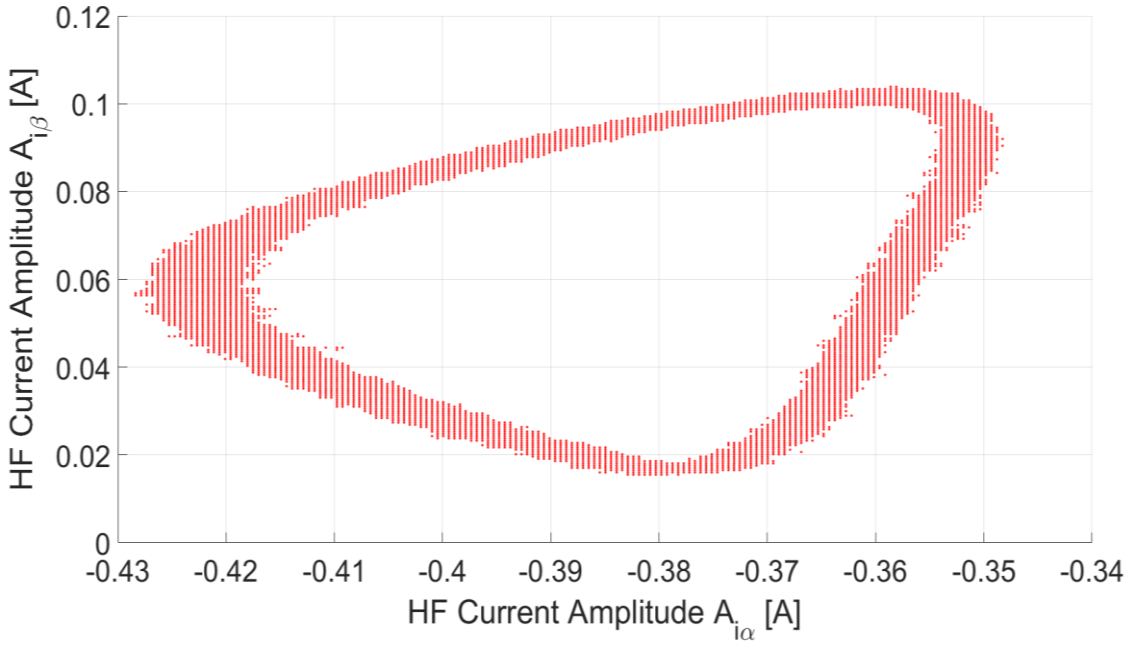

Figure 6.7 (d) – Plot of HF Current Amplitude $A_{i\alpha}$ [A] vs. $A_{i\beta}$ [A] with ω_{m4}^{*} = 1 rad/s on M4, i_{d3}^{*}= 0 A and i_{q3}^{*}= 0 A on M3 during continuous rotating injection.

Assuming that the mean mechanical rotor speed on M3 is 1 rad/s, the electrical rotor frequency ω_e = 6 rad/s (f_e= 0.95 Hz). Since the fundamental saliency was mathematically shown to occur at $2f_e$ the frequency of the fundamental saliency component occurs at 1.9 Hz. This can be observed from the frequency spectrum of the HF current amplitude components $A_{i\alpha}$, $A_{i\beta}$ (Figures 6.8-6.9). Besides the fundamental component, however other harmonic components are also present at f_e, $3f_e$ and $4f_e$. The significance of the harmonics can be deduced from Table 6.1. The harmonic components at multiples of the fundamental saliency are of the same order of magnitude as the fundamental with a predominant harmonic at $4f_e$ which has a magnitude of 31.14 % of the fundamental for $A_{i\alpha}$ and 11.25 % of the fundamental for $A_{i\beta}$.

f (Hz)	**$\lvert A_{i\alpha}(f)\rvert$ (A)**	**$\lvert A_{i\alpha}(f)\rvert/\lvert A_{i\alpha}(2f_e)\rvert$ (%)**	**$\lvert A_{i\beta}(f)\rvert$ (A)**	**$\lvert A_{i\beta}(f)\rvert/\lvert A_{i\beta}(2f_e)\rvert$ (%)**
f_e	0.0017	6.97	0.0017	5.47
$2f_e$	0.0244	-	0.0311	-
$3f_e$	0.0005	2.05	0.0021	6.75
$4f_e$	0.0076	31.14	0.0035	11.25

Table 6.1 – Harmonic Saliency Magnitude Comparison to Fundamental

From these practical measurements with continuous rotating voltage injection, it was determined that the single saliency model given in (4.27) does not apply to the SM-PMSM machine under test due to the significance of the harmonic saliency.

The results shown in Figure 6.8 – 6.9 can also be used to assess the injected component with respect to the rating machine current. After aliasing the injected component in the HF currents is shifted to DC level. These components possibly contain remnants of the PWM switching frequency after analogue filtering, but these should be negligible. The DC component in $A_{i\alpha}$ = 0.38 A and that in $A_{i\beta}$ = 0.06 A. These DC components are 3.8 % in the α-axis and 0.6 % with respect to to the rated peak current of the PMSM of 10 A. While these components will result in HF torque ripple and acoustic noise, they are considered negligible. Methods for mitigation of torque and acoustic effects from literature are discussed in Section 4.3.

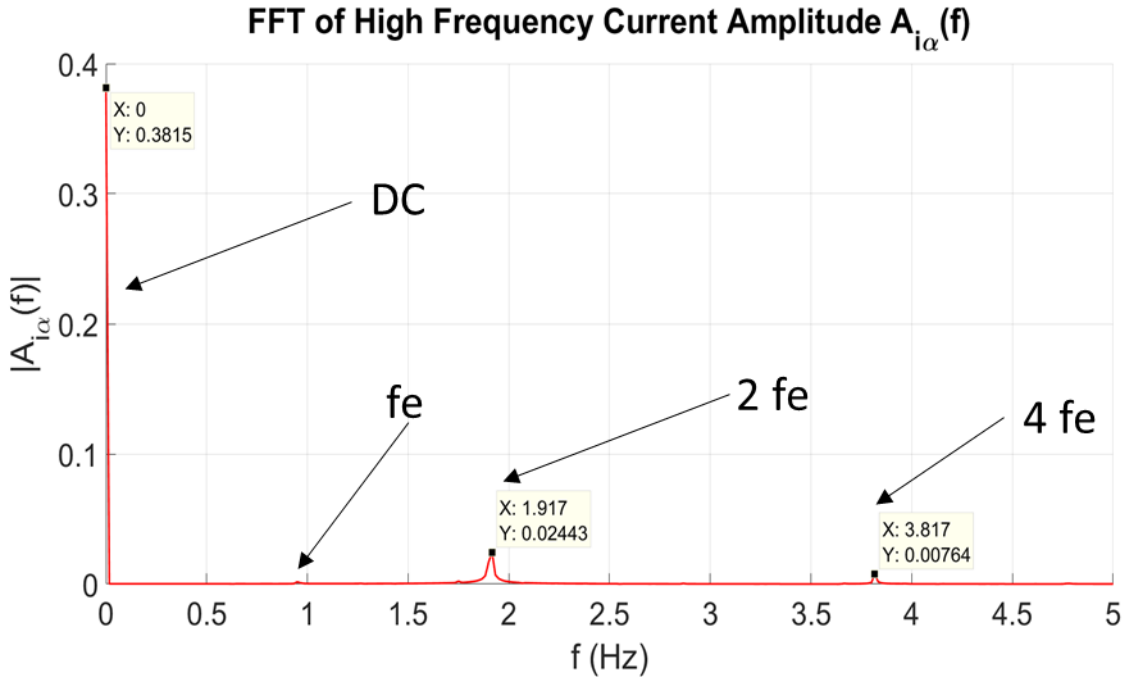

Figure 6.8 – FFT analysis of $A_{i\alpha}$ with i_{d3}^{*} = 0 A and i_{q3}^{*} = 0 A on M3 during continuous rotating injection.

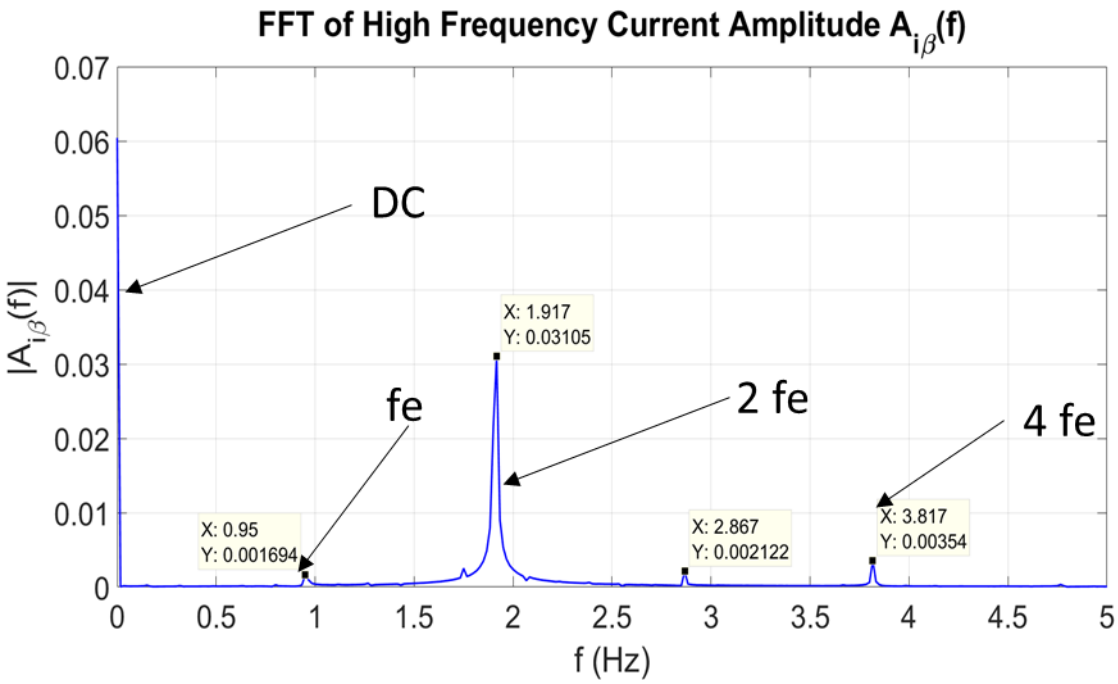

Figure 6.9 – FFT analysis of $A_{i\beta}$ with i_{d3}^{*}= 0 A and i_{q3}^{*}= 0 A on M3 during continuous rotating injection.

6.3.4 Rotating Voltage Injection Saliency at Different Amplitudes

The HF current amplitudes $A_{i\alpha}$, $A_{i\beta}$ were expressed in terms of the components I_1 and I_2 (6.4-6.5) for continuous rotating injection. Since both I_1 and I_2 and proportional to the input voltage amplitude V_i, the amplitudes of $A_{i\alpha}$, $A_{i\beta}$ are also expected to be proportional to V_i. For the ideal single saliency model, the DC offset of $A_{i\alpha}$ is also proportional to the input voltage amplitude V_i.

For the same operating point as in Section 6.3.3 (ω_{m4}^{*} = 1 rad/s, i_{q3}^{*}= 0 A, i_{d3}^{*}= 0 A) the saliency was investigated at different values of V_i while keeping all other test parameters constant. The variation in the HF current amplitudes for V_i = 1 V to 3 V in steps on 1 V can be observed in Figures 6.10 (a) – (d). The DC offsets and the peak-to-peak current of the HF amplitudes are given in Table 6.2. DC offset variation is observed in both α and β components; as opposed to the ideal single saliency representation which includes a DC offset component only in the α HF current term. This is possibly attributed to non-ideal open-loop inverter injection, inverter non-linearities and saliency harmonics which deviate the actual saliency measurement from what was derived in (6.4 – 6.5).

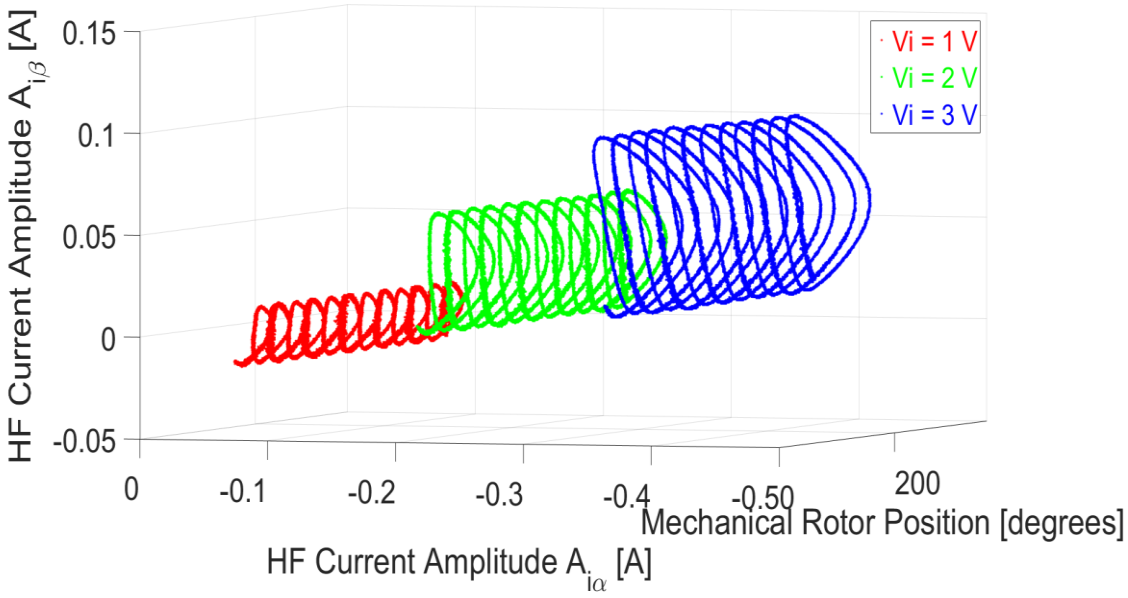

Figure 6.10 (a) – Three-Dimensional Plot of HF Current Amplitudes $A_{i\alpha}$ [A], $A_{i\beta}$ [A], θ_m [°] with $\omega_{m4}^* = 1$ rad/s on M4, $i_{d3}^* = 0$ A and $i_{q3}^* = 0$ A on M3 during continuous rotating injection for different V_i.

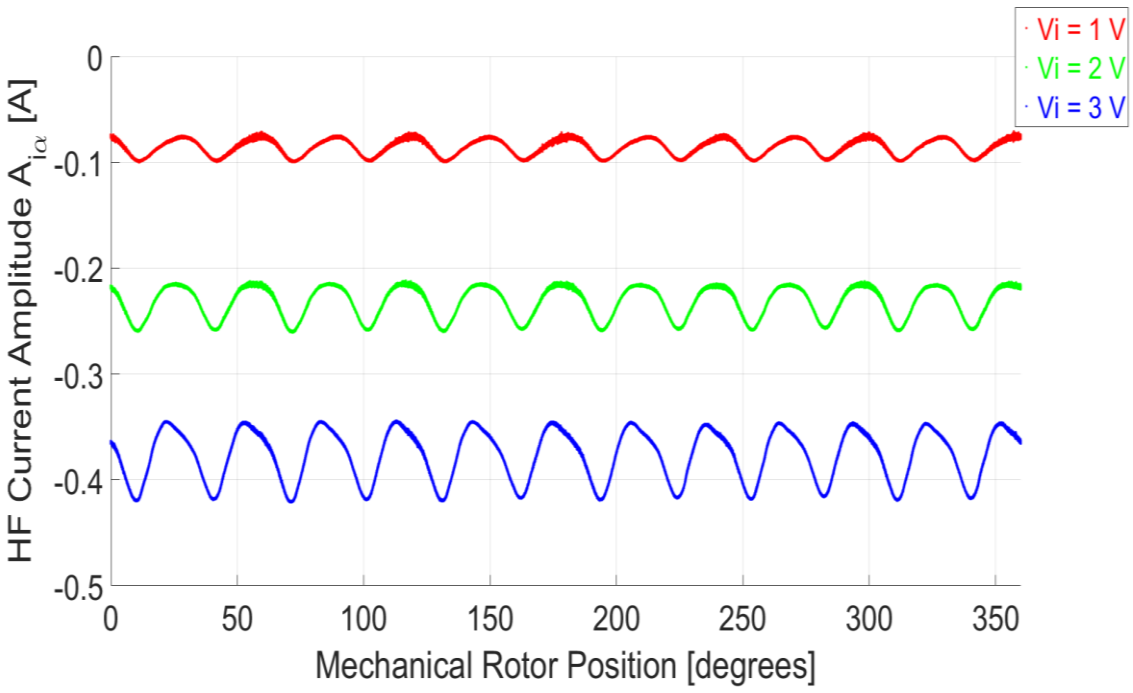

Figure 6.10 (b) – Plot of HF Current Amplitude $A_{i\alpha}$ [A] vs. θ_m [°] with $\omega_{m4}^* = 1$ rad/s on M4, $i_{d3}^* = 0$ A and $i_{q3}^* = 0$ A on M3 during continuous rotating injection for different V_i.

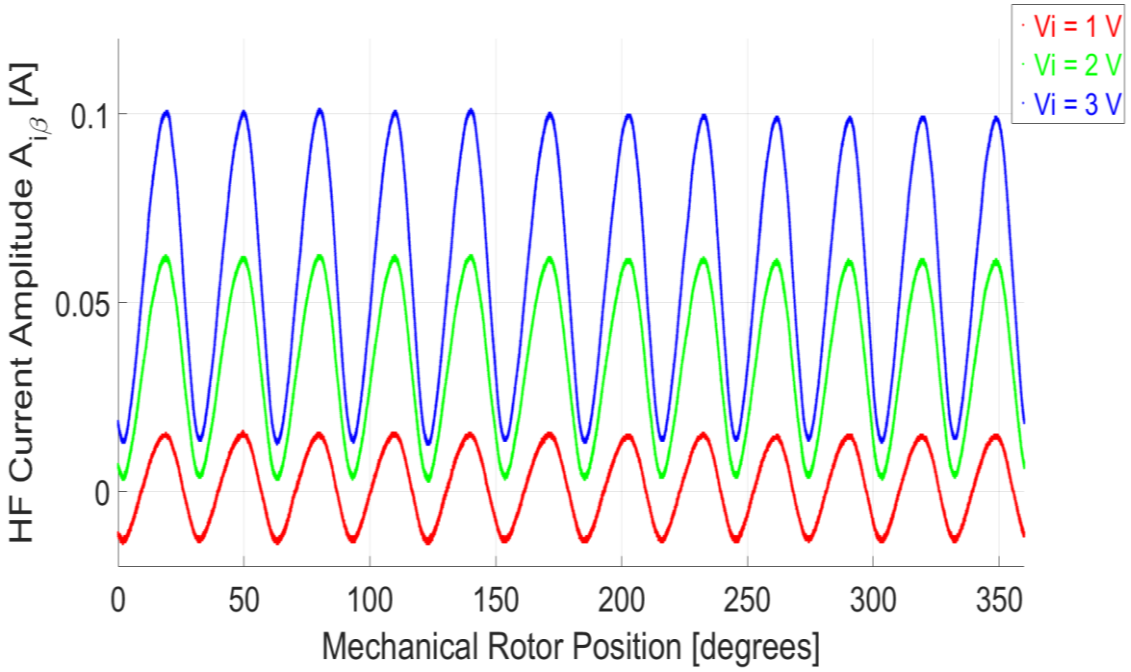

Figure 6.10 (c) – Plot of HF Current Amplitude $A_{i\beta}$ [A] vs. θ_m [°] with $\omega_{m4}^* = 1$ rad/s on M4, $i_{d3}^* = 0$ A and $i_{q3}^* = 0$ A on M3 during continuous rotating injection for different V_i.

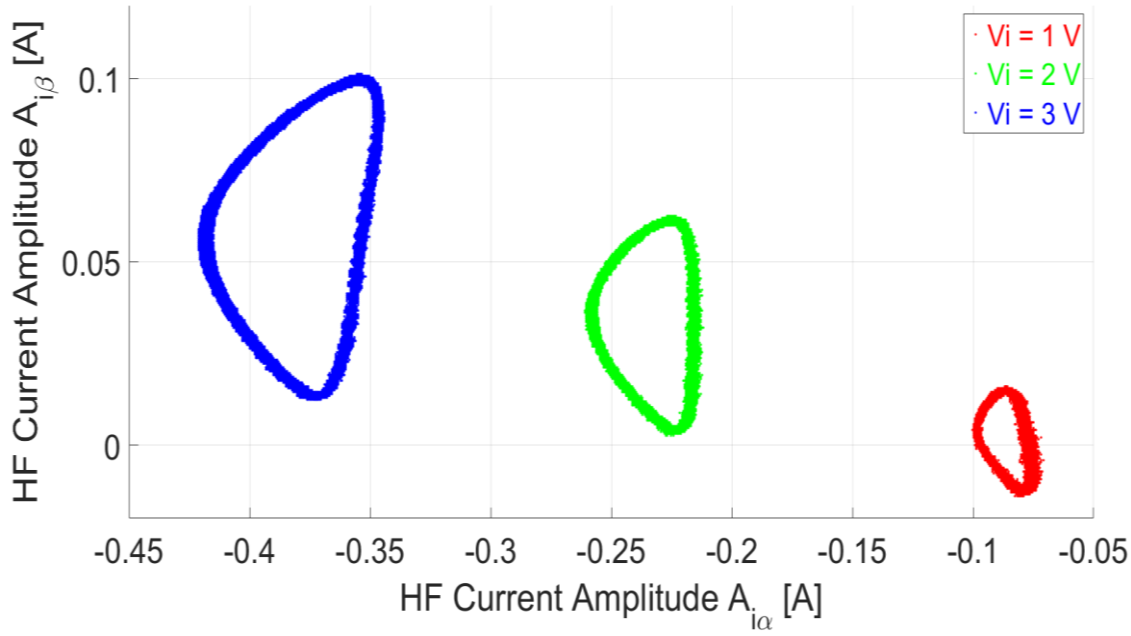

Figure 6.10 (d) – Plot of HF Current Amplitude $A_{i\alpha}$ [A] vs. $A_{i\beta}$ [A] with $\omega_{m4}^* = 1$ rad/s on M4, $i_{d3}^* = 0$ A and $i_{q3}^* = 0$ A on M3 during continuous rotating injection for different V_i.

Vi(V)	$A_{i\alpha\_DC}$ (A)	$A_{i\alpha\_pp}$ (A)	$A_{i\beta\_DC}$ (A)	$A_{i\beta\_pp}$ (A)
1	-86.2 x 10^{-3}	23.7 x 10^{-3}	19 x10^{-3}	28.93 x 10^{-3}
2	-232.7 x 10^{-3}	44 x 10^{-3}	34.6 x10^{-3}	59.42 x 10^{-3}
3	-377.4 x 10^{-3}	74.4 x 10^{-3}	59 x 10^{-3}	87.37 x 10^{-3}

Table 6.2 – HF Current Amplitudes DC Offsets and Peak-to-peak values for different V_i

For the purposes of sensorless control, saliencies with higher peak-to-peak amplitudes are generally better due to an improved Signal-to-Noise Ratio (SNR) of the signals being used for sensorless estimation. The voltage injection can be increased further. However, practical limitations include available DC link voltage, acoustic noise and torque ripple associated with higher amplitude current components.

6.3.5 Pulsating Voltage Injection Saliency with α/β axis injection only

The injection of a pulsating voltage vector was described in Section 4.6.4. Initially, a pulsating voltage vector on the α-axis only ($\gamma = 0°$) and on the β-axis only ($\gamma = 90°$) was considered. The pulsating vectors are at an injection frequency of f_i= 2.5 kHz. The test conditions are for an unloaded machine identical to those described for the rotating voltage injection in Section 6.3.3 (ω_{m4}^* = 1 rad/s, i_{q3}^*= 0 A, i_{d3}^*= 0 A). The pulsating voltage injection for $\gamma = 0°$ and $\gamma = 90°$is expressed in (6.8 – 6.9) respectively. The voltage injection amplitude is set to V_i = 3 V.

$$v_{i\alpha\beta} = V_i \begin{bmatrix} \cos \omega_i t \\ 0 \end{bmatrix} \qquad (\gamma = 0°) \tag{6.8}$$

$$v_{i\alpha\beta} = V_i \begin{bmatrix} 0 \\ \cos \omega_i t \end{bmatrix} \qquad (\gamma = 90°) \tag{6.9}$$

For a demodulated high-frequency signal with a pulsating voltage injection, the HF current amplitudes were shown in (4.39) for an ideal single saliency machine. When $\gamma = 0°$ the saliency currents are given in (6.10) while for $\gamma = 90°$ the HF saliency currents are given in (6.11).

$$\begin{bmatrix} A_{i\alpha} \\ A_{i\beta} \end{bmatrix} = \begin{bmatrix} I_1 A_1 + I_2 V_i \cos(\gamma - 2\theta_e) \\ I_1 A_2 + I_2 V_i \sin(\gamma - 2\theta_e) \end{bmatrix} \tag{4.39}$$

$$\begin{bmatrix} A_{i\alpha} \\ A_{i\beta} \end{bmatrix} = \begin{bmatrix} I_1 V_i + I_2 V_i \cos(2\theta_e) \\ -I_2 V_i \sin(2\theta_e) \end{bmatrix} \quad (\gamma = 0°) \tag{6.10}$$

$$\begin{bmatrix} A_{i\alpha} \\ A_{i\beta} \end{bmatrix} = \begin{bmatrix} I_2 V_i \sin(2\theta_e) \\ I_1 V_i + I_2 V_i \cos(2\theta_e) \end{bmatrix} \quad (\gamma = 90°) \tag{6.11}$$

The magnetic signature when injecting pulsating vectors at the aforementioned angles in the αβ frame is shown in Figure 6.11. The HF amplitudes $A_{i\alpha}$, $A_{i\beta}$ are shown as a function of the mechanical rotor position in Figures 6.11 (a) – (c). The complex polar plot of the $A_{i\alpha}$, $A_{i\beta}$ is shown in Figure 6.11 (d). From these results, it was observed that while the same magnitude of V_i = 3 V is injected; the variation in the angle γ from 0° to 90° significantly affects the shape and size of $A_{i\alpha}$, $A_{i\beta}$. This shows that the magnetic signature of the experimental machine under test is significantly different from that of an ideal single saliency machine described in (6.10 – 6.11).

From equations (6.10) and (6.11), it can be seen that the HF amplitude should have a DC offset which depends on the injection angle. Figure 6.11(b) shows the experimental case of γ = 90°, where it is expected that the α-component should have a zero-offset. It is clearly seen that this is not the case and the main reason for this is the affect of the multiple saliences present in the electrical machine which have not been taken into consideration in the derivation of (6.10-6.11).

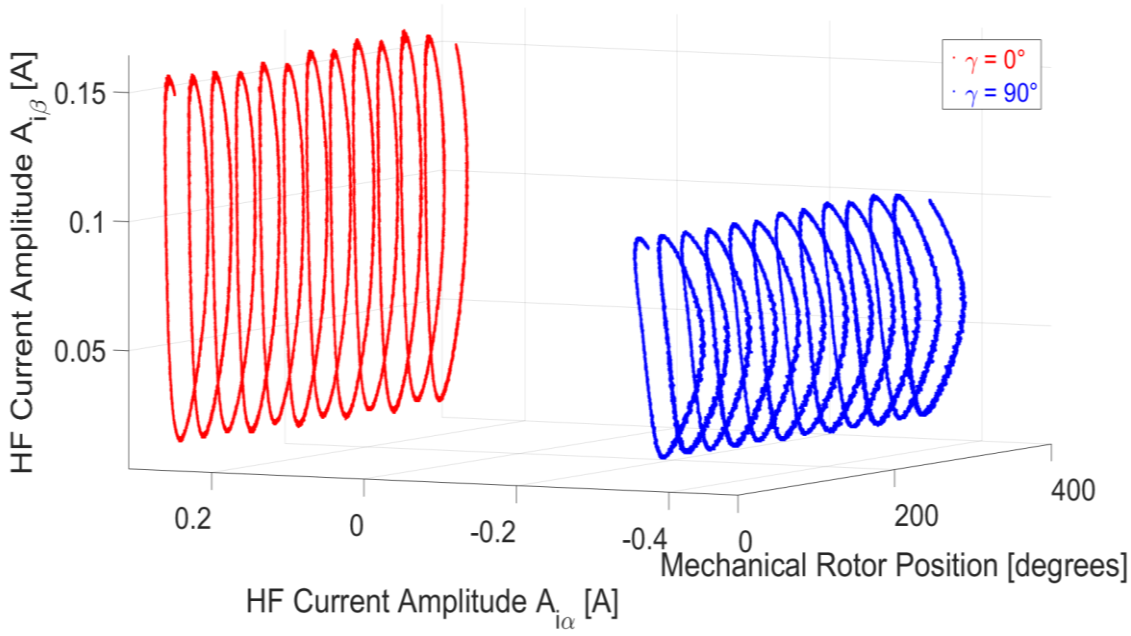

Figure 6.11 (a) – Three-Dimensional Plot of HF Current Amplitudes $A_{i\alpha}$ [A], $A_{i\beta}$ [A], θ_m [°] with ω_{m4}^* = 1 rad/s on M4, i_{d3}^*= 0 A and i_{q3}^*= 0 A on M3 during continuous pulsating injection for γ = 0/90°.

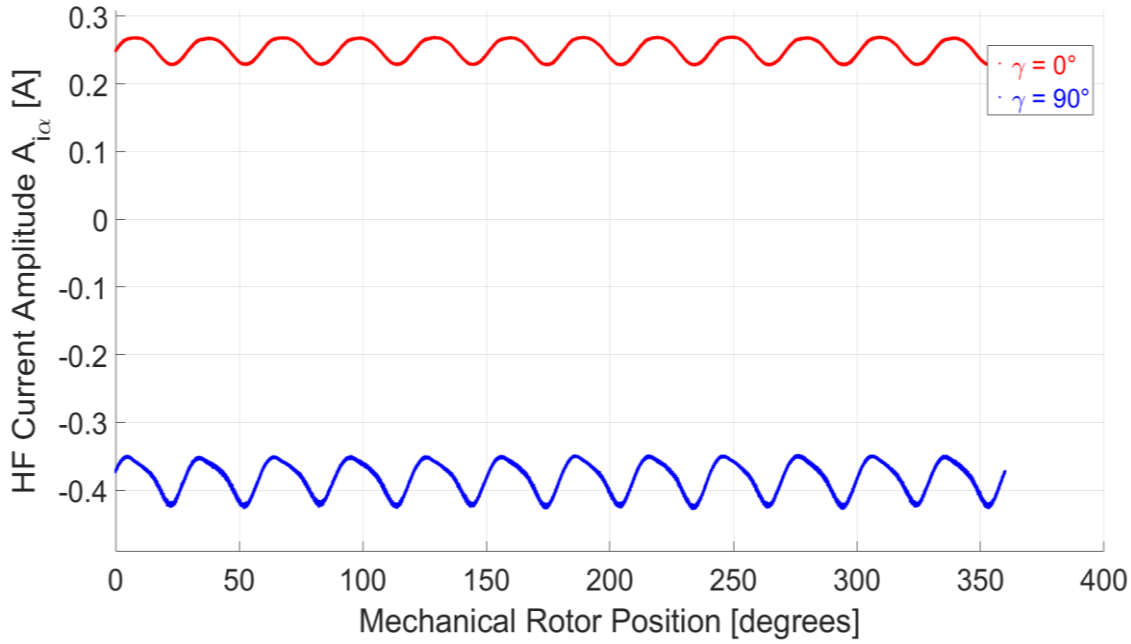

Figure 6.11 (b) – Plot of HF Current Amplitude $A_{i\alpha}$ [A] vs. θ_m [°] with $\omega_{m4}^* = 1$ rad/s on M4, $i_{d3}^* = 0$ A and $i_{q3}^* = 0$ A on M3 during continuous pulsating injection for $\gamma = 0/90°$.

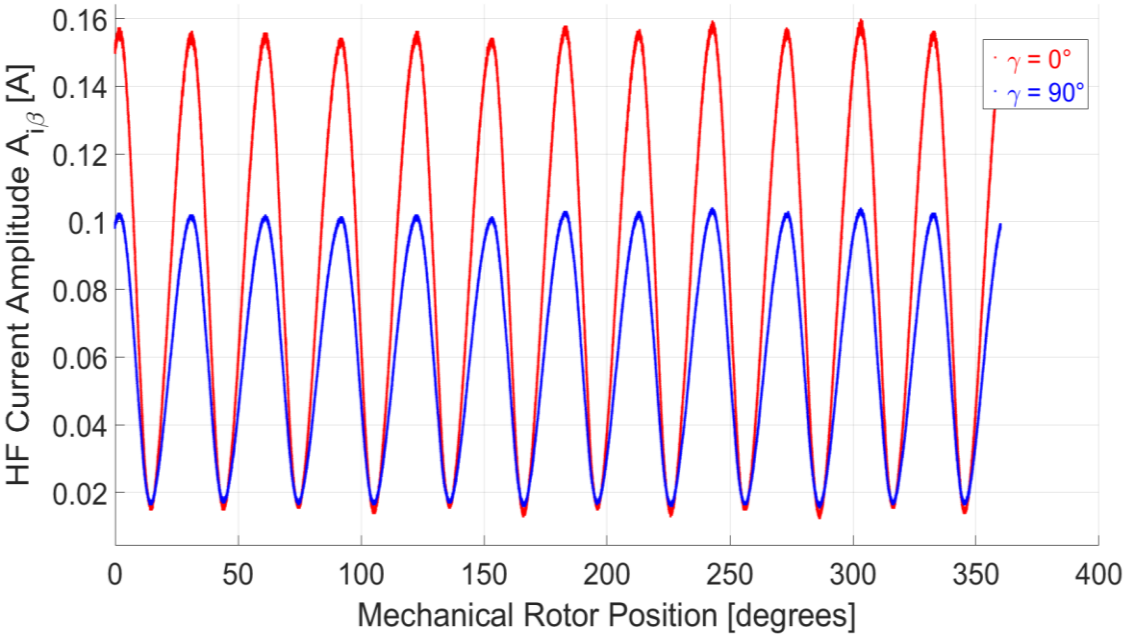

Figure 6.11 (c) – Plot of HF Current Amplitude $A_{i\beta}$ [A] vs. θ_m [°] with $\omega_{m4}^* = 1$ rad/s on M4, $i_{d3}^* = 0$ A and $i_{q3}^* = 0$ A on M3 during continuous pulsating injection for $\gamma = 0/90°$.

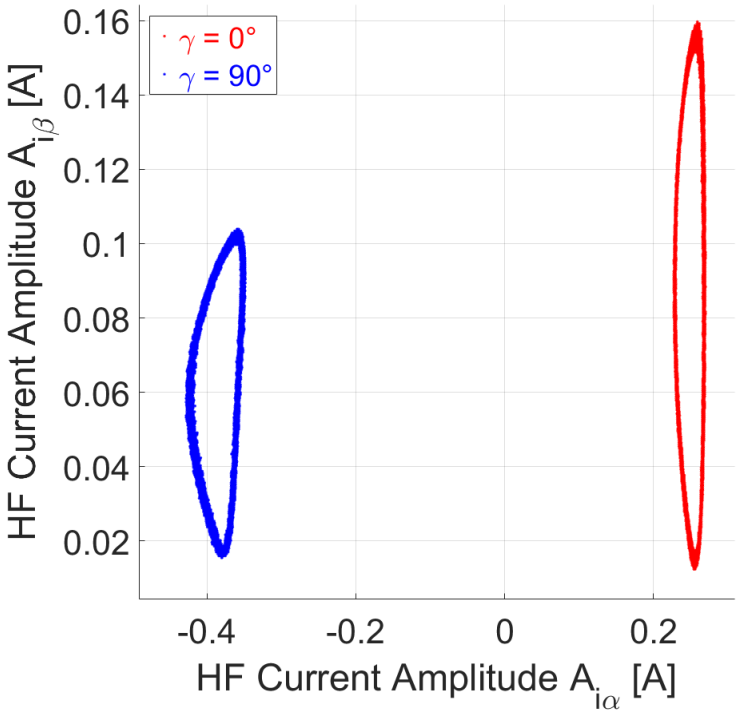

Figure 6.11 (d) –Plot of HF Current Amplitude $A_{i\alpha}$ [A] vs. $A_{i\beta}$ [A] with ω_{m4}^{*} = 1 rad/s on M4, i_{d3}^{*}= 0 A and i_{q3}^{*}= 0 A on M3 during continuous pulsating injection for γ = 0/90°.

γ (°)	$A_{i\alpha\_DC}$ (A)	$A_{i\alpha\_pp}$ (A)	$A_{i\beta\_DC}$ (A)	$A_{i\beta\_pp}$ (A)
0	247 x 10^{-3}	38.7 x 10^{-3}	85.2 x 10^{-3}	140 x 10^{-3}
90	-391 x 10^{-3}	72.3 x 10^{-3}	59.1 x 10^{-3}	84.2 x 10^{-3}

Table 6.3 – HF Current Amplitudes DC Offsets and Peak-to-peak values for γ = 0/90°

Theoretically from the equations derived in (6.10-6.11), the magnetic signature in the complex αβ frame should remain a constant circle at γ = 0/90° with only a different centre point due to the DC offset. From the results in Figure 6.11, it was observed that the saliency-dependent signals in the practical machine vary with the injection angle beyond what is modelled for a single saliency machine. Given the significant variation observed with γ at these two injection angles, the HF current amplitude variation at different values on the αβ axes was investigated.

6.3.6 Pulsating Voltage Injection Saliency with Arbitrary Angle Injection

In section 6.3.5, it was observed that the saliency varies significantly with γ and therefore the measurement at different values of γ could result in a wider selection of profiles for

sensorless control. The pulsating vectors are at an injection frequency of f_i =2.5 kHz. For this experiment the machine is kept in an unloaded condition (ω_{m4}^* = 1 rad/s, i_{q3}^*= 0 A, i_{d3}^*= 0 A). The pulsating voltage injection is applied in the form shown in (6.12). The maximum amplitude of the pulsating vector $V_i = 3$ V. The angle γ was varied for $0° \leq \gamma \leq 165°$ in steps of 15°.

$$v_{i\alpha\beta} = \begin{bmatrix} A_1 \cos \omega_i t \\ A_2 \cos \omega_i t \end{bmatrix} \tag{6.12}$$

Where

$$A_1 = V_i \cos \gamma \qquad A_2 = V_i \sin \gamma$$

The variation in the injection angle γ results in significantly different HF current amplitudes $A_{i\alpha}$, $A_{i\beta}$ with respect to the rotor mechanical position as shown in Figures 6.12 (a) – (c). The resulting magnetic signatures vary not only in the DC offset but also in shape and size as observed from the complex plot in Figure 6.12 (d). Considering different injection angles provides a wider range of saliencies from which an optimum one could be selected for sensorless control applications.

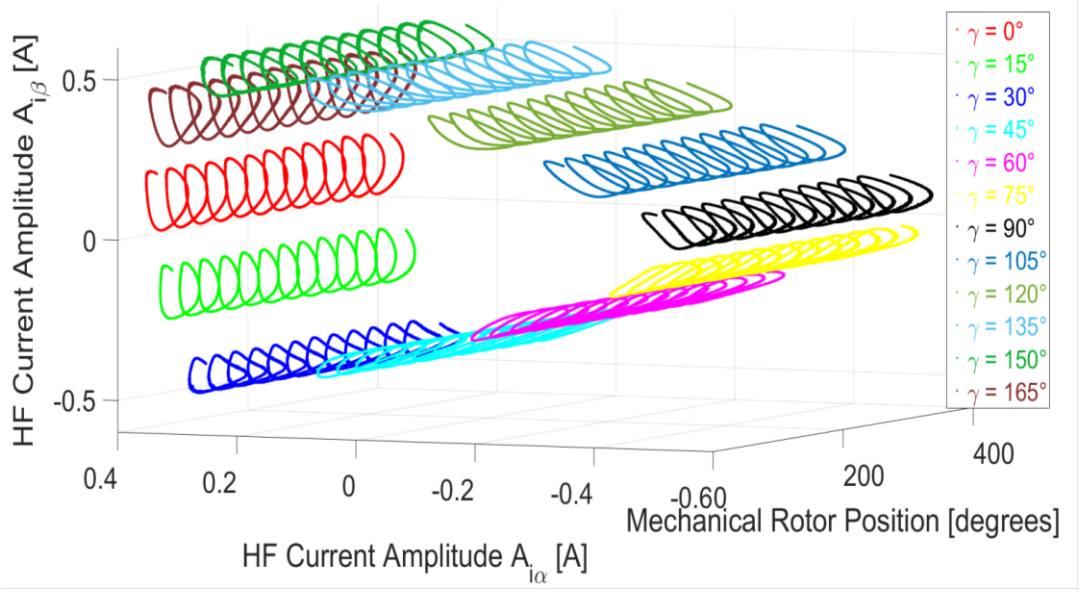

Figure 6.12 (a) – Three-Dimensional Plot of HF Current Amplitudes $A_{i\alpha}$ [A], $A_{i\beta}$ [A], θ_m [°] with ω_{m4}^* = 1 rad/s on M4, i_{d3}^*= 0 A and i_{q3}^*= 0 A on M3 during continuous pulsating injection for arbitrary γ.

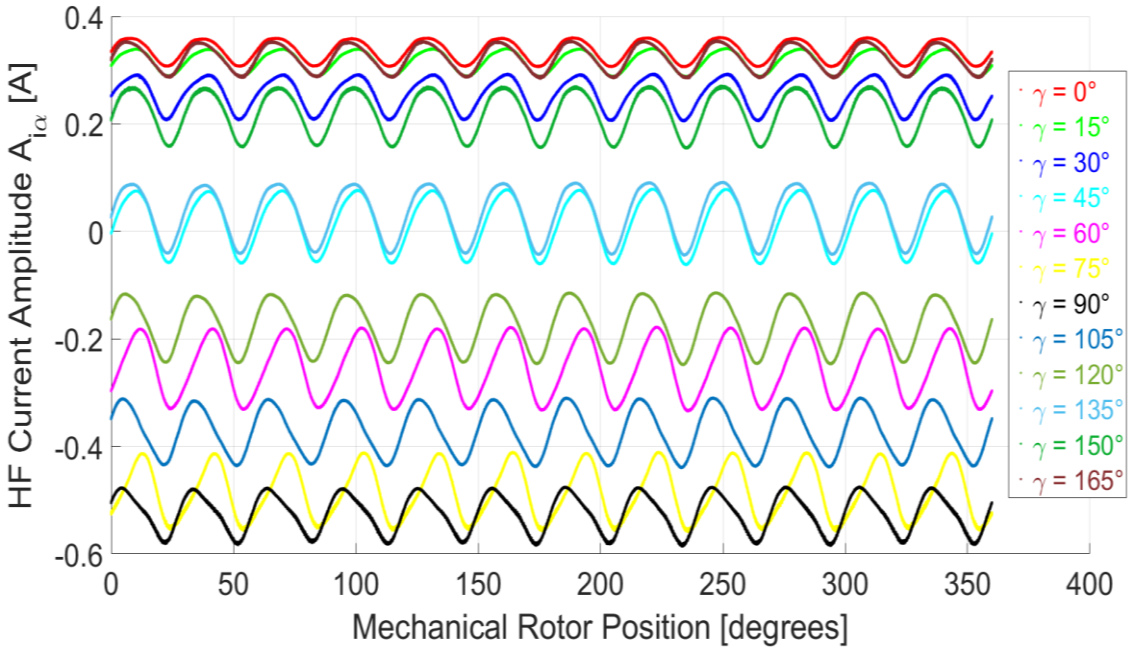

Figure 6.12 (b) – Plot of HF Current Amplitude $A_{i\alpha}$ [A] vs. θ_m [°] with ω_{m4}^* = 1 rad/s on M4, i_{d3}^* = 0 A and i_{q3}^* = 0 A on M3 during continuous pulsating injection for arbitrary γ.

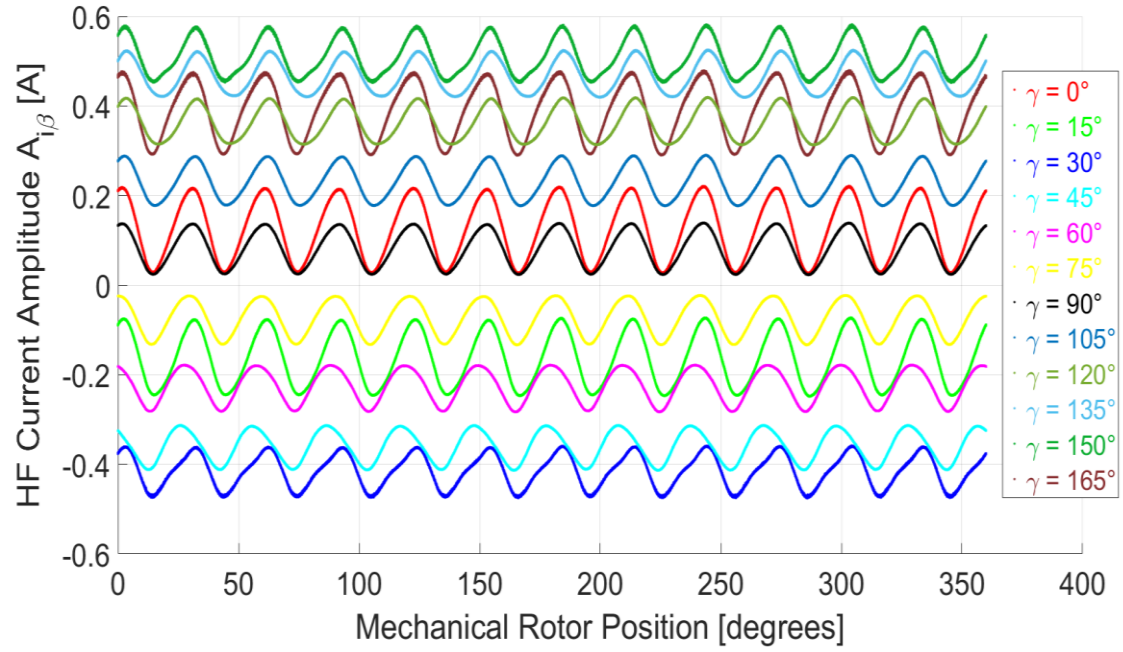

Figure 6.12 (c) – Plot of HF Current Amplitude $A_{i\beta}$ [A] vs. θ_m [°] with ω_{m4}^* = 1 rad/s on M4, i_{d3}^* = 0 A and i_{q3}^* = 0 A on M3 during continuous pulsating injection for arbitrary γ.

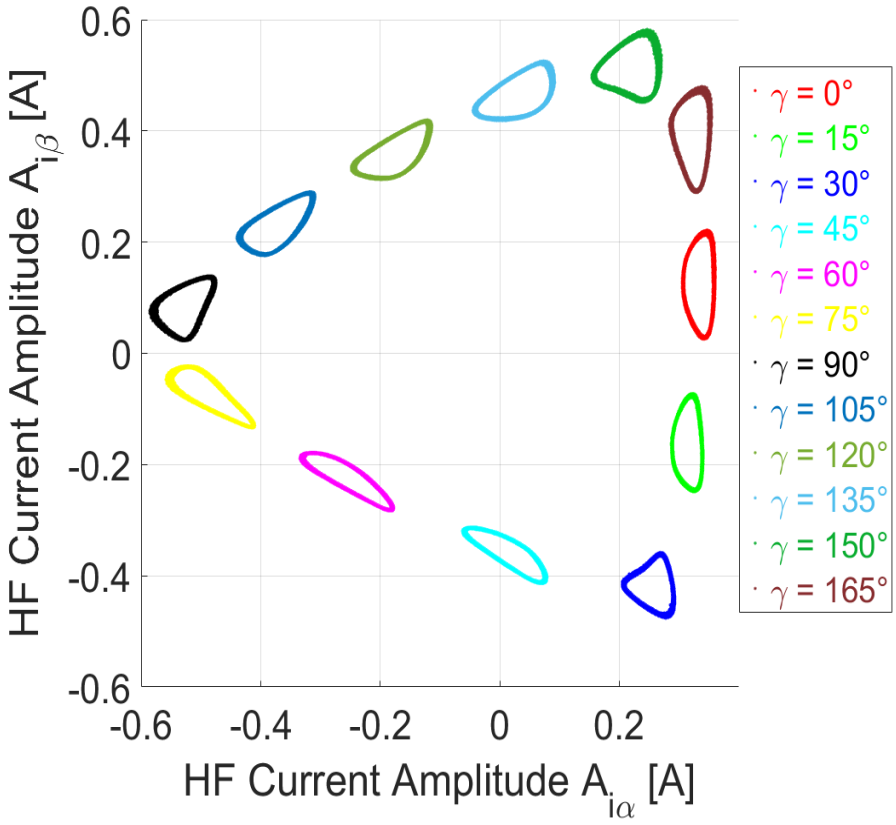

Figure 6.12 (d) – Plot of HF Current Amplitude $A_{i\alpha}$ [A] vs. $A_{i\beta}$ [A] with $\omega_{m4}^* = 1$ rad/s on M4, $i_{d3}^* = 0$ A and $i_{q3}^* = 0$ A on M3 during continuous pulsating injection for arbitrary γ.

6.3.7 Saliency Variation with Machine Loading

The HF current amplitude measurements carried out in Sections 6.3.3 – 6.3.6 were carried out for the operating point $i_{q3}^* = 0$ A. In general, the saliency of a PMSM changes at different values of the synchronous frame currents i_d and i_q. For the purposes of this research variation in i_d^* was not considered because the machine was not used in the field weakening region; however, similar effects to those obtained for variations in i_q^* are expected.

The HF current amplitude response of the machine was measured for V_i=3 V, f_i = 2.5 kHz and ω_{m4}^* = 1 rad/s. The synchronous current reference was varied from -10 A ≤ i_{q3}^* ≤ 10 A at intervals of 2.5 A. The HF current amplitudes for negative values of i_{q3}^* are given in Figure 6.13 and for positive values in Figure 6.14.

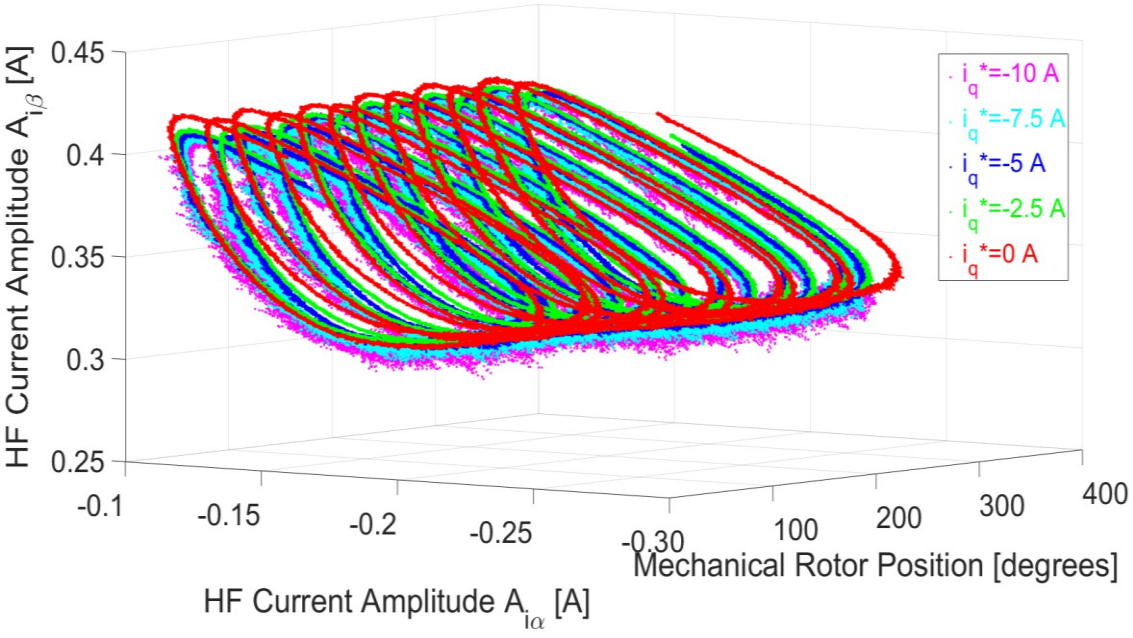

Figure 6.13 (a) – Three-Dimensional Plot of HF Current Amplitudes $A_{i\alpha}$ [A], $A_{i\beta}$ [A], θ_m [°] with $\omega_{m4}^* = 1$ rad/s on M4, $i_{d3}^* = 0$ A and -10 A $\leq i_{q3}^* \leq 0$ A on M3 during continuous pulsating injection γ=120°.

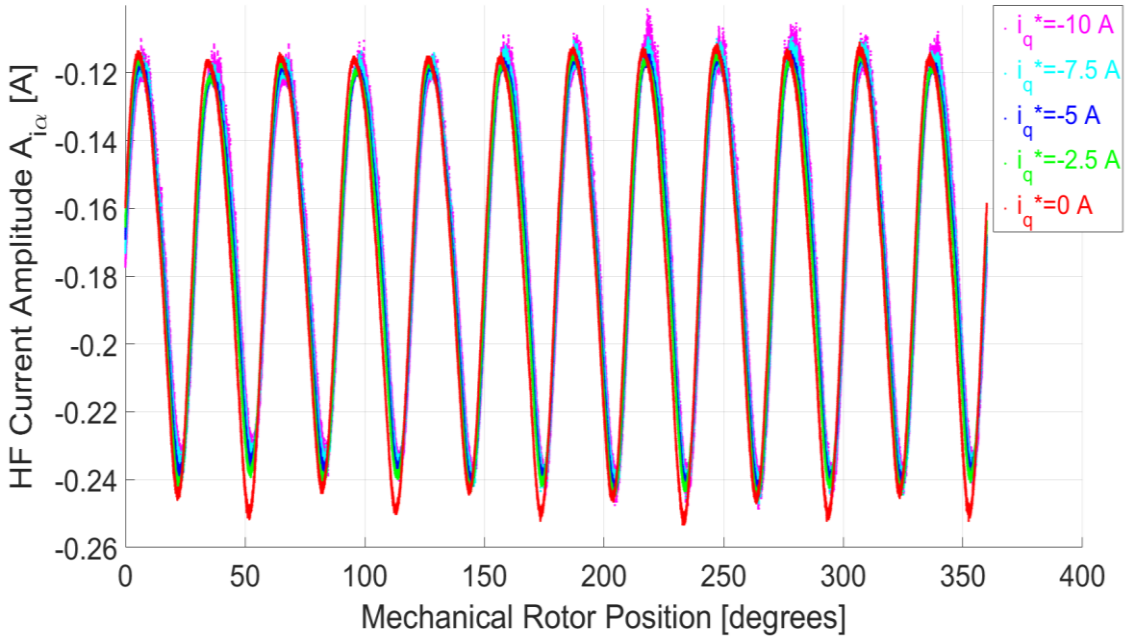

Figure 6.13 (b) – Plot of HF Current Amplitude $A_{i\alpha}$ [A] vs. θ_m [°] with $\omega_m^* = 1$ rad/s on M4, $i_{d3}^* = 0$ A and -10 A $\leq i_{q3}^* \leq 0$ A on M3 during continuous pulsating injection γ=120°.

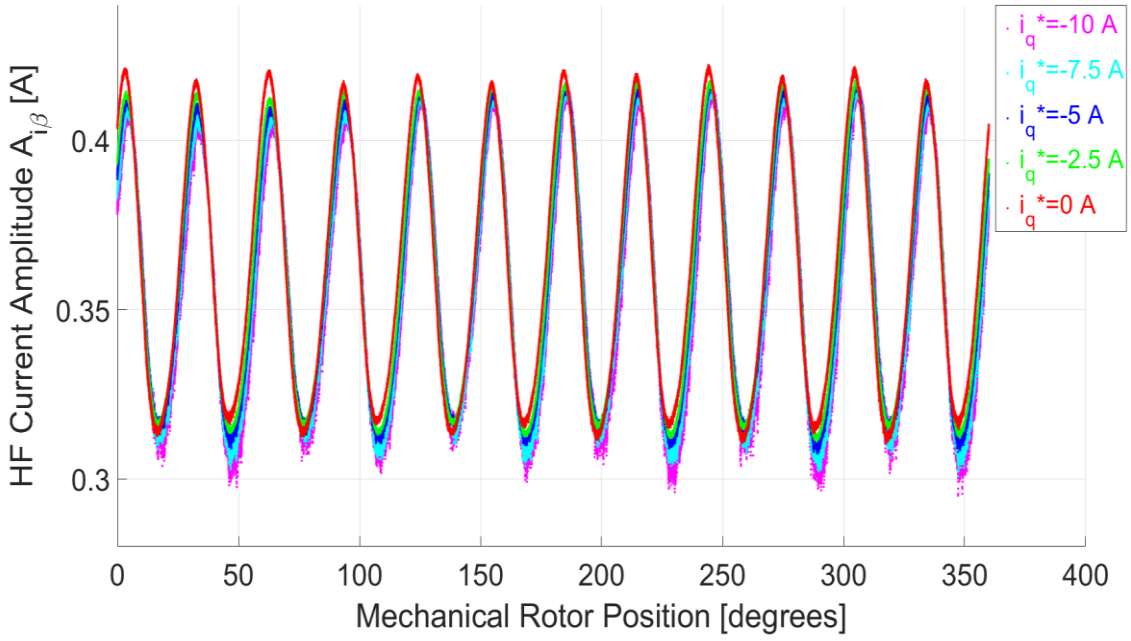

Figure 6.13 (c) – Plot of HF Current Amplitude $A_{i\beta}$ [A] vs. θ_m [°] with $\omega_{m4}^* = 1$ rad/s on M4, $i_{d3}^* = 0$ A and -10 A ≤ i_{q3}^* ≤ 0 A on M3 during continuous pulsating injection γ=120°.

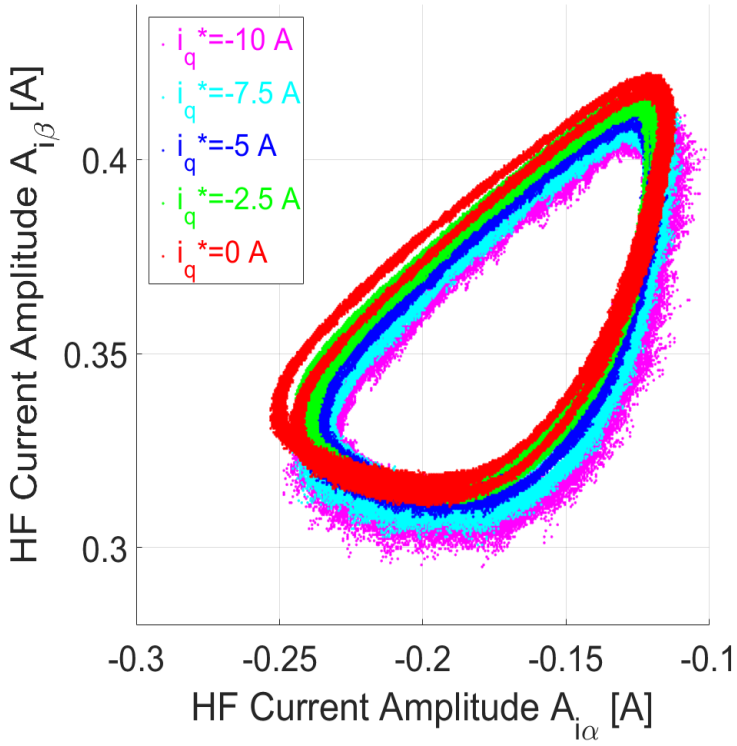

Figure 6.13 (d) – Plot of HF Current Amplitude $A_{i\alpha}$ [A] vs $A_{i\beta}$ [A] with $\omega_{m4}^* = 1$ rad/s on M4, $i_{d3}^* = 0$ A and -10 A ≤ i_{q3}^* ≤ 0 A on M3 during continuous pulsating injection γ=120°.

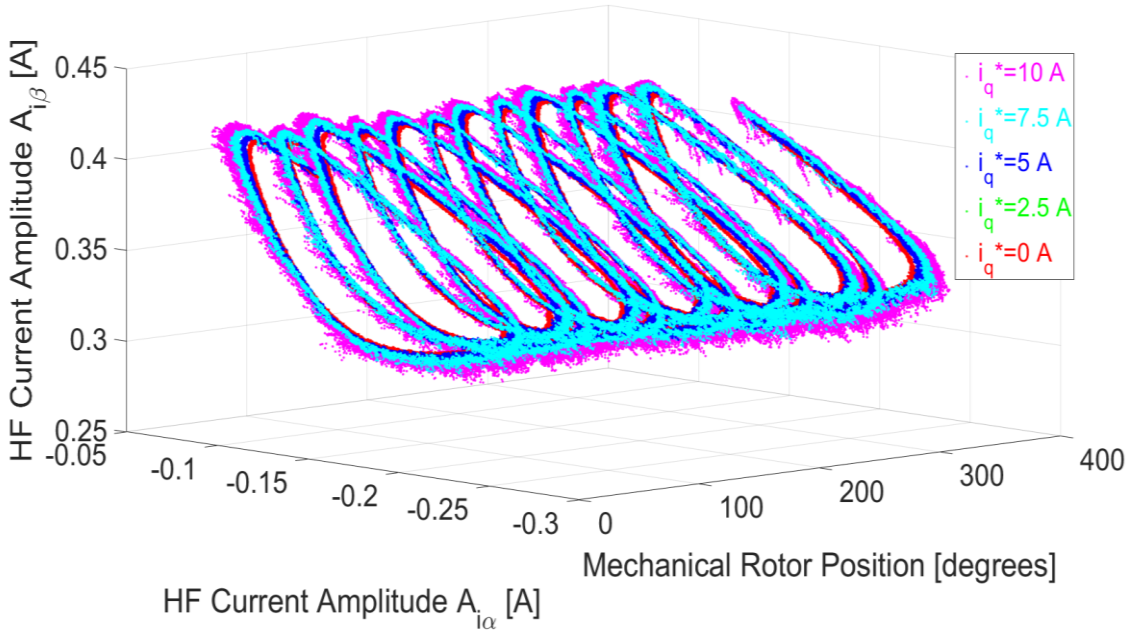

Figure 6.14 (a) – Three-Dimensional Plot of HF Current Amplitudes $A_{i\alpha}$ [A], $A_{i\beta}$ [A], θ_m [°] with $\omega_{m4}^* = 1$ rad/s on M4, $i_{d3}^* = 0$ A and 0 A ≤ i_{q3}^* ≤ 10 A on M3 during continuous pulsating injection γ=120°.

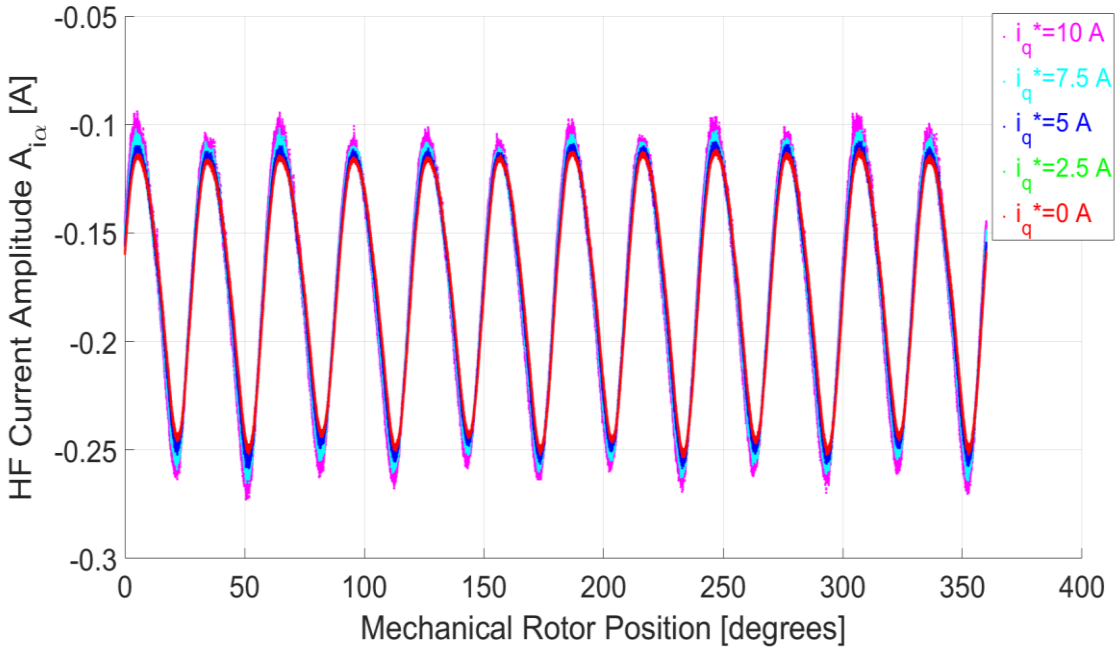

Figure 6.14 (b) – Plot of HF Current Amplitude $A_{i\alpha}$ [A] vs. θ_m [°] with $\omega_m^* = 1$ rad/s on M4, $i_{d3}^* = 0$ A and 0 A ≤ i_{q3}^* ≤ 10 A on M3 during continuous pulsating injection γ=120°.

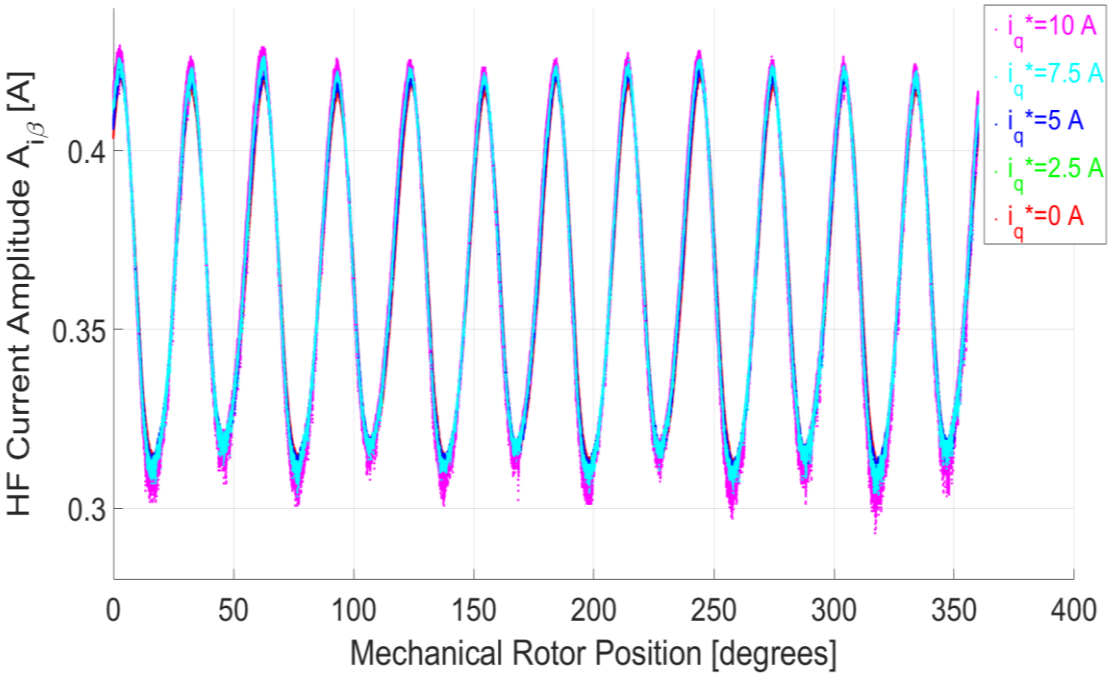

Figure 6.14 (c) – Plot of HF Current Amplitude $A_{i\beta}$ [A] vs. θ_m [°] with $\omega_{m4}^* = 1$ rad/s on M4, $i_{d3}^* = 0$ A and 0 A ≤ i_{q3}^* ≤ 10 A on M3 during continuous pulsating injection γ=120°.

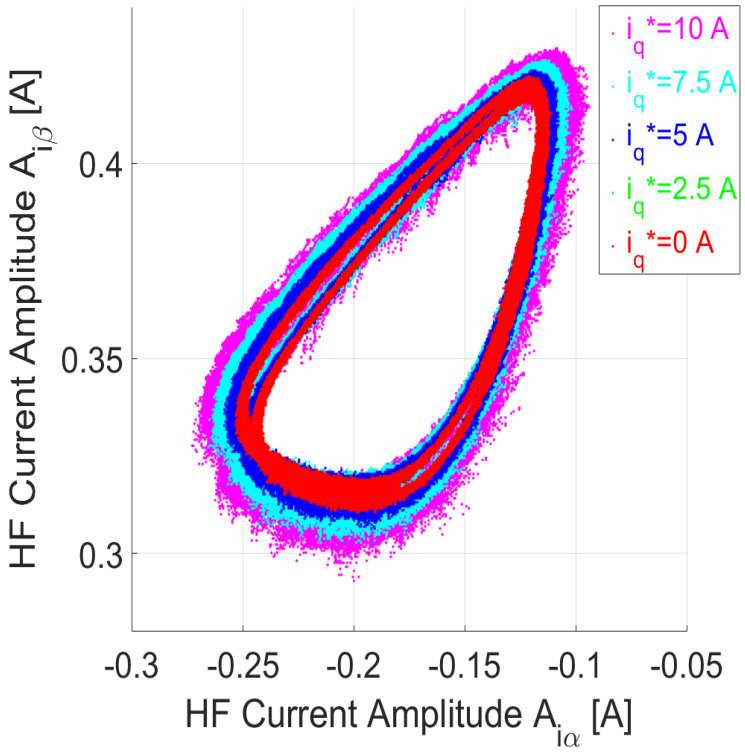

Figure 6.14 (d) – Plot of HF Current Amplitude $A_{i\alpha}$ [A] vs $A_{i\beta}$ [A] with $\omega_{m4}^* = 1$ rad/s on M4, $i_{d3}^* = 0$ A and 0 A ≤ i_{q3}^* ≤ 10 A on M3 during continuous pulsating injection γ=120°.

6.3.8 Saliency Variation with Machine Rotational Speed

In this dissertation, it was shown that due to the construction of the stator and rotor the saliency is also a function of the mechanical rotor position θ_m as the HF current amplitude response varies slightly depending on the absolute mechanical position of the rotor. Typically, sensorless control algorithms at low/zero speed only consider the saliency with respect to θ_e assuming that the saliency dependent functions $A_{i\alpha}$, $A_{i\beta}$ repeat themselves exactly between pairs of poles. The mapping of the HF current amplitudes with the rotor mechanical position θ_m also provides insight into the dependency of the saliency with the rotor speed ω_m.

The saliency was measured with $V_i = 3$ V, $f_i = 2.5$ kHz, $i_{d3}^* = 0$ A, $i_{q3}^* = 0$ A for different values of the rotor speed references ω_{m4}^*. The rotor speed was varied in the range -2 rad/s $\leq \omega_{m4}^* \leq 2$ rad/s as shown in Figures 6.15 – 6.16. From the mean values of the samples of $A_{i\alpha}$ and $A_{i\beta}$ (defined as $\overline{A_{i\alpha\_sort}}$, $\overline{A_{i\beta\_sort}}$ in Section 7.2) with respect to the mechanical position a phase shift was observed as a function of the rotor speed. Both $\overline{A_{i\alpha\_sort}}$, $\overline{A_{i\beta\_sort}}$ are subject to a phase shift to the left-hand side of the θ_m axis as the speed increases in the negative direction. This effect could possibly be attributed to the rate of change and direction of the flux producing saturation-based saliency. Given this rotor speed dependency, some form of compensation mechanism or inclusion of different magnetic signatures as a LUT is required for improved sensorless estimation.

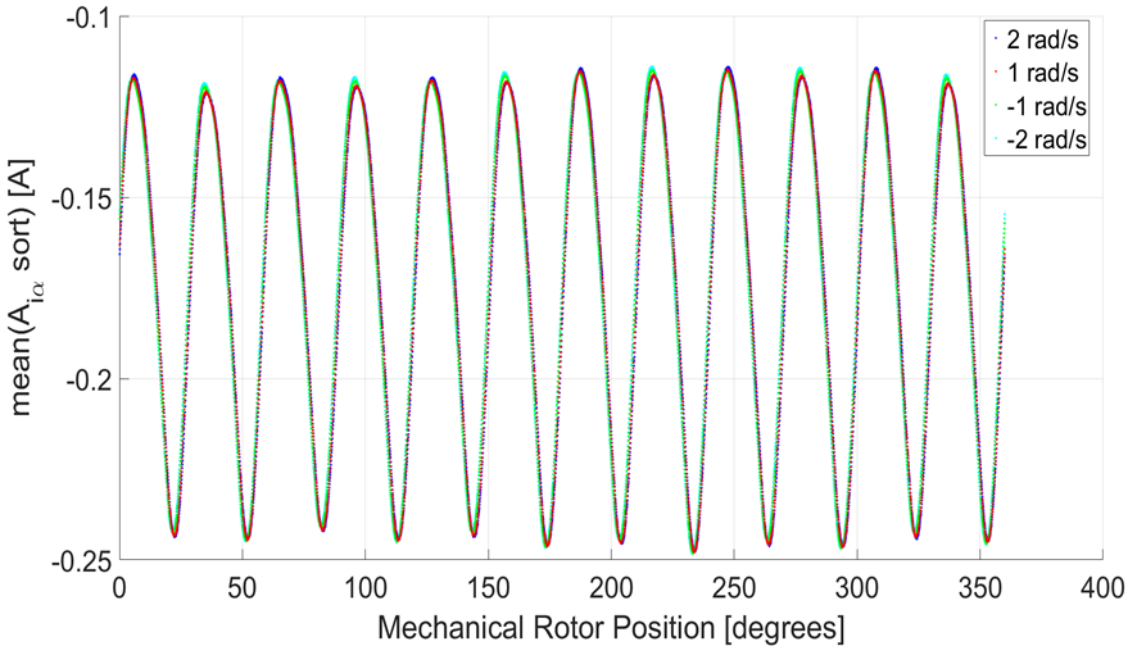

Figure 6.15 (a) – Plot of $\overline{A_{i\alpha\_sort}}$ [A] vs. θ_m [°] for $i_{d3}^* = 0$ A, $i_{q3}^* = 0$ A on M3 with -2 rad/s $\leq \omega_{m4}^* \leq 2$ rad/s on M4 and continuous pulsating injection γ=120°.

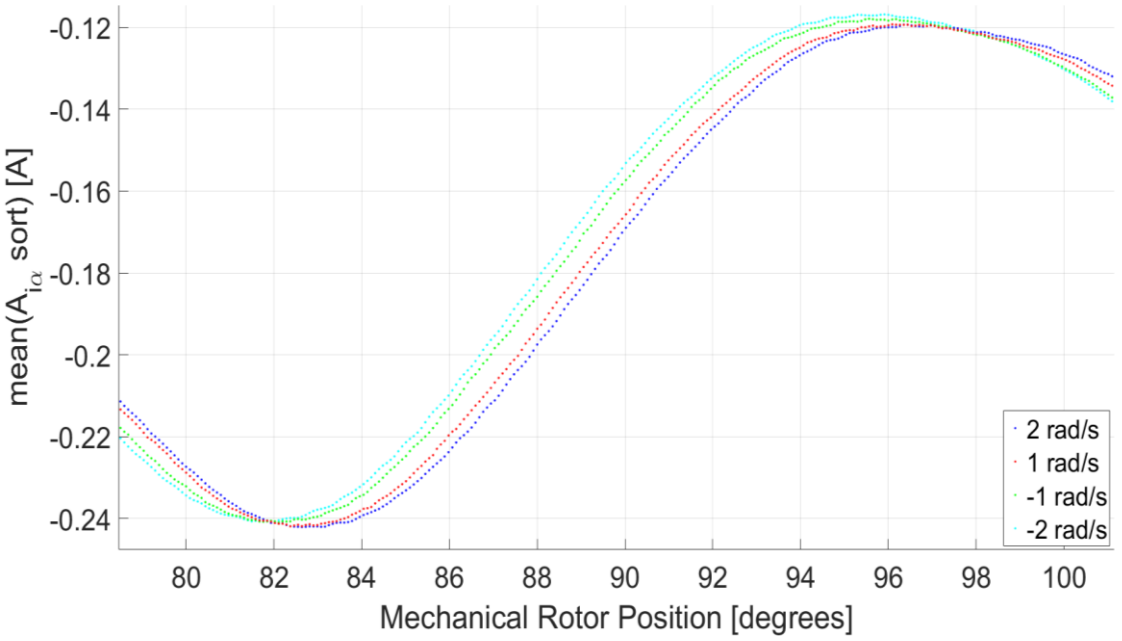

Figure 6.15 (b) – Plot of $\overline{A_{i\alpha\_sort}}$ [A] vs. θ_m [°] for $i_{d3}^* = 0$ A, $i_{q3}^* = 0$ A on M3 with -2 rad/s $\leq \omega_{m4}^* \leq 2$ rad/s on M4 and continuous pulsating injection γ=120° zoomed in for 80° $\leq \theta_m \leq$ 100°.

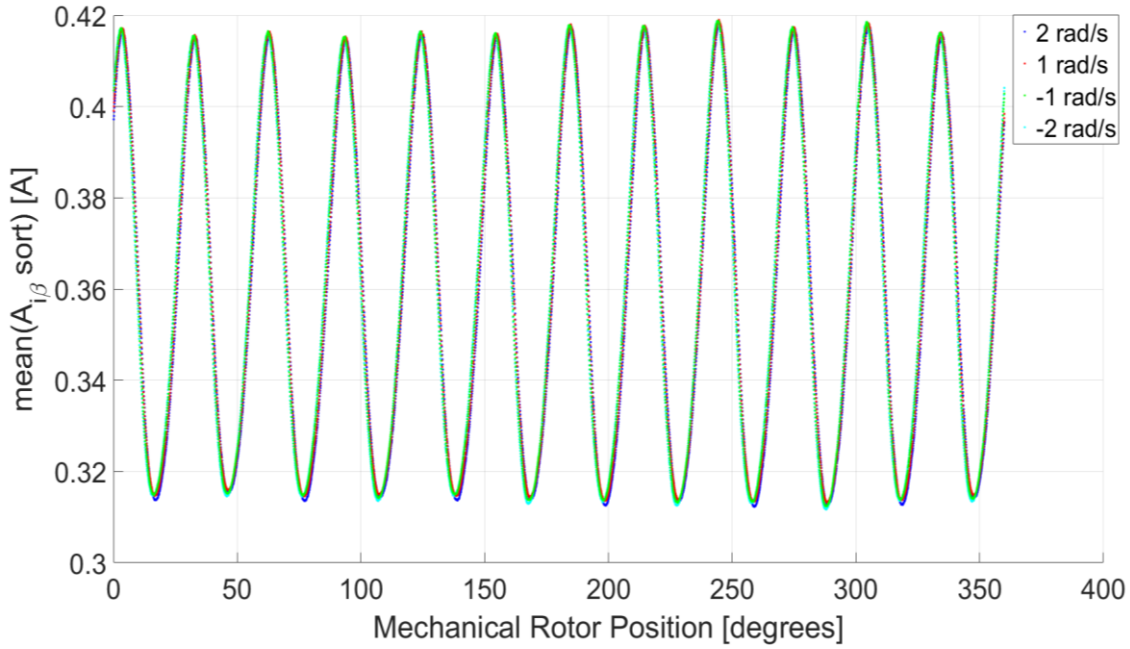

Figure 6.16 (a) – Plot of $\overline{A_{i\beta\_sort}}$ [A] vs. θ_m [°] for $i_{d3}^* = 0$ A, $i_{q3}^* = 0$ A on M3 with -2 rad/s $\leq \omega_{m4}^* \leq 2$ rad/s on M4 and continuous pulsating injection γ=120°.

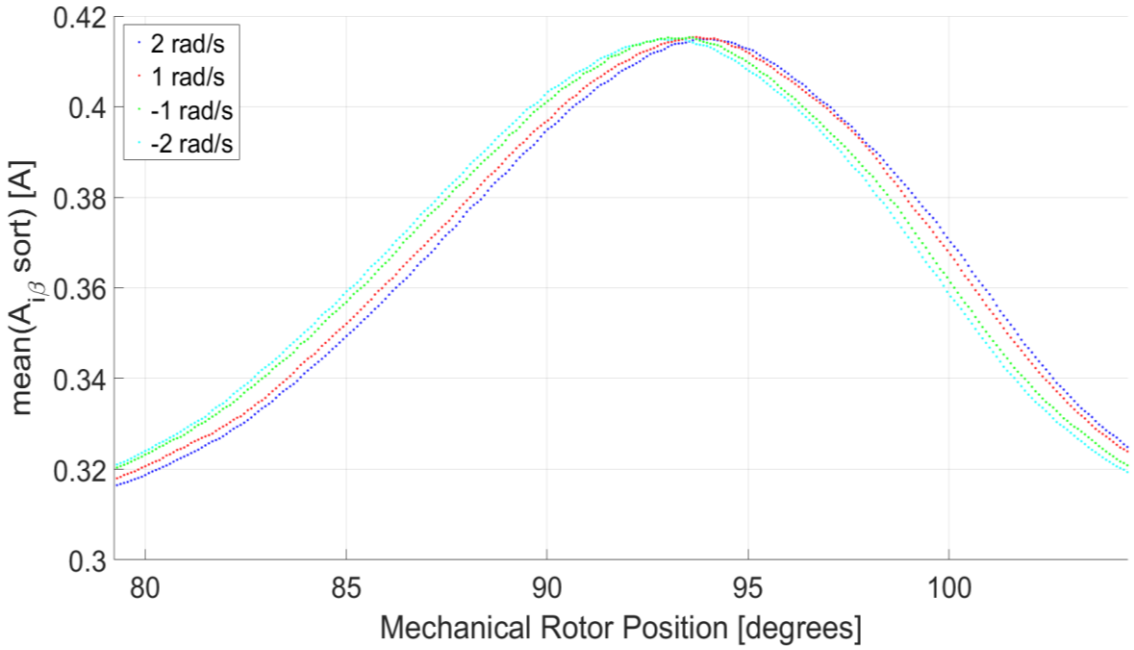

Figure 6.16 (b) – Plot of $\overline{A_{i\beta\_sort}}$ [A] vs. θ_m [°] for i_{d3}^*= 0 A, i_{q3}^* = 0 A on M3 with -2 rad/s ≤ ω_{m4}^* ≤ 2 rad/s on M4 and continuous pulsating injection γ=120° zoomed in for 80° ≤ θ_m ≤ 100°.

6.4 Saliency in Different SM-PMSMs

6.4.1 Alternative SM-PMSM construction

In this dissertation, various SM-PMSM constructions were investigated. While the innovative search-based observer proposed in this dissertation in Chapter 7 can operate on machine saliencies with significant harmonics besides the fundamental, the accuracy is improved as the saliency approaches the ideal one. Different machine constructions of the surface-mounted type result in different magnetic signatures as the stator, rotor and magnet dimensions are varied.

One of the machines whose saliency was measured is shown in Figure 6.17. This machine is of similar construction to the one presented in Section 6.2.2. The alternative SM-PMSM has a larger stator diameter, larger rotor diameter and thinner surface-mounted magnets. As described in Section 6.2, the resultant saliency in a machine can be a result of multiple physical effects, and the identification of the contribution of these effects can be complex. Such complex analysis was not carried out in this dissertation, but the magnetic signatures obtained for the different machines were considered with respect to their potential use in sensorless control applications.

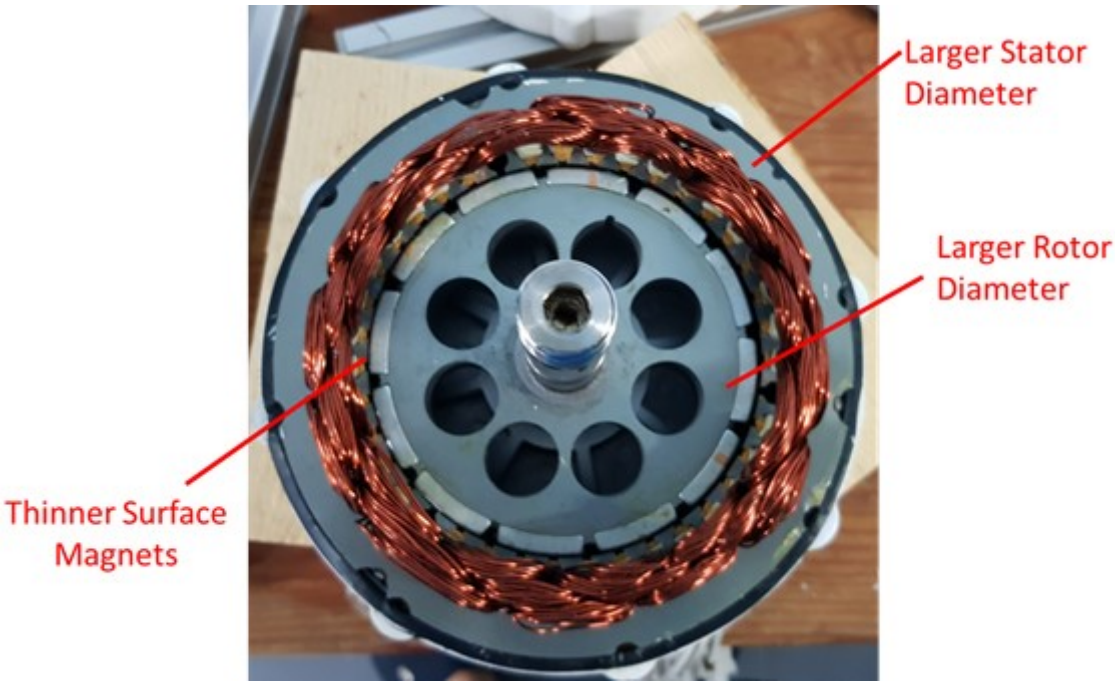

Figure 6.17 – SM-PMSM machine with larger diameter rotor construction.

6.4.2 Experimental Saliency for Alternative SM-PMSM construction

The saliency of the machine with larger stator/rotor diameters referred to as M1 shown in Figure 6.17 was determined using a pulsating voltage injection with arbitrary voltage injection angle γ. The machine M1 was driven by a similar machine in speed controller mode referred to as M2. The pulsating vectors are at an injection frequency of 2.5 kHz. The test conditions are for an unloaded machine (ω_{m2}^{*} = 2 rad/s, i_{q1}^{*}= 0 A, i_{d1}^{*}= 0 A). The maximum amplitude of the pulsating vector V_i= 2 V. The angle γ was varied for $0° \leq \gamma \leq 165°$ in steps of 15°. The variation in the injection angle γ results in significantly different HF current amplitudes $A_{i\alpha}$, $A_{i\beta}$ with respect to the rotor mechanical position, as shown in Figures 6.28 (a) – (c). The resulting magnetic signatures vary not only in the DC offset but also in shape and size (Figure 6.18 (d)).

Compared to the signature of the machine presented in Section 6.2, the response of this machine is more triangular in nature. Such a magnetic saliency tends to have reduced accuracy at the points of the triangle as a result of a low gradient in both $A_{i\alpha}$, $A_{i\beta}$. Similar results for this machine were obtained as observed in Section 6.3 when operating the machine at different values of i_q-current and different rotor speeds.

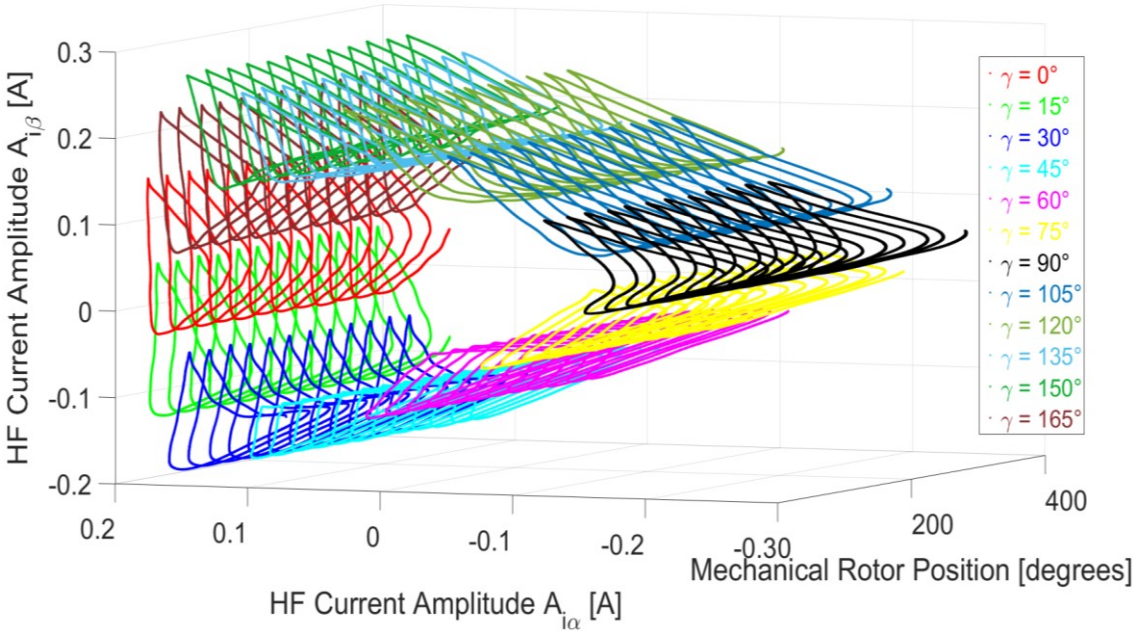

Figure 6.18 (a) – Three-Dimensional Plot of HF Current Amplitudes $A_{i\alpha}$ [A], $A_{i\beta}$ [A], θ_m [°] with ω_m^* = 2 rad/s on M2, i_{d1}^*= 0 A and i_{q1}^*= 0 A on M1 during continuous pulsating injection for arbitrary γ.

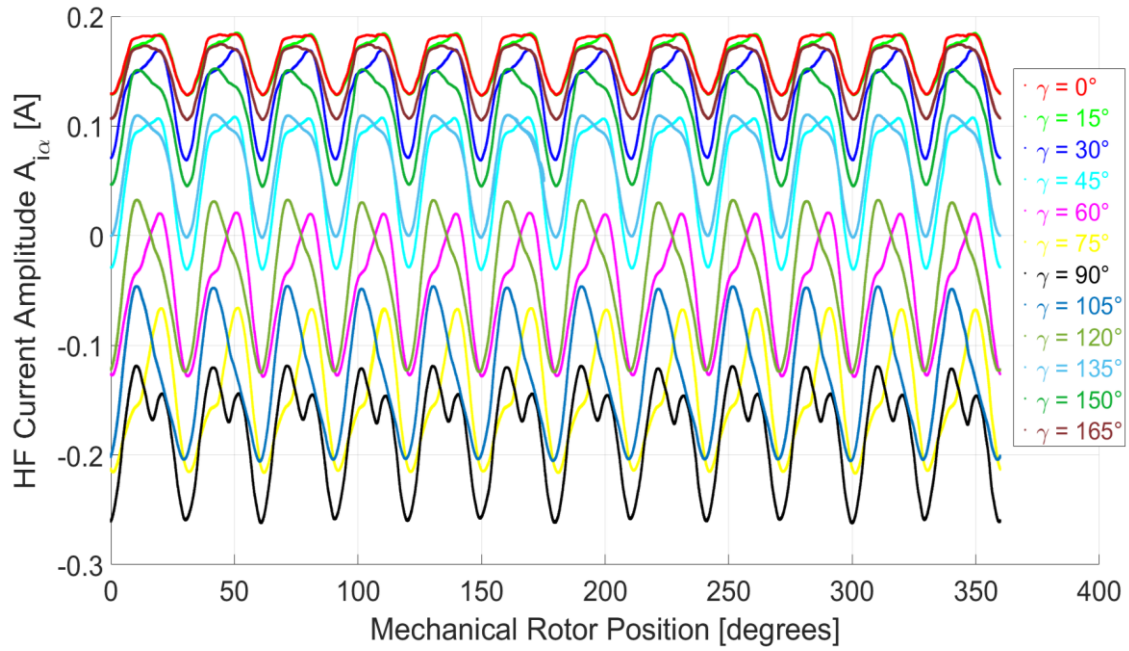

Figure 6.18 (b) – Plot of HF Current Amplitude $A_{i\alpha}$ [A] vs. θ_m [°] with ω_m^* = 2 rad/s on M2, i_{d1}^*= 0 A and i_{q1}^*= 0 A on M1 during continuous pulsating injection for arbitrary γ.

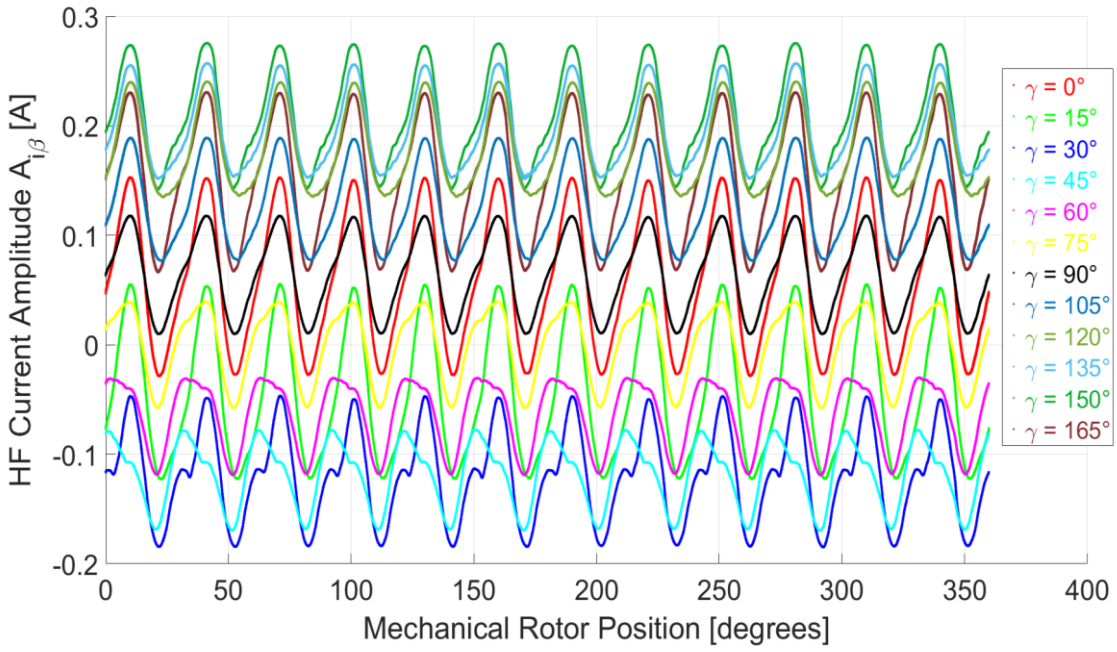

Figure 6.18 (c) – Plot of HF Current Amplitude $A_{i\beta}$ [A] vs. θ_m [°] with ω_m^* = 2 rad/s on M2 i_{d1}^*= 0 A and i_{q1}^*= 0 A on M1 during continuous pulsating injection for arbitrary γ.

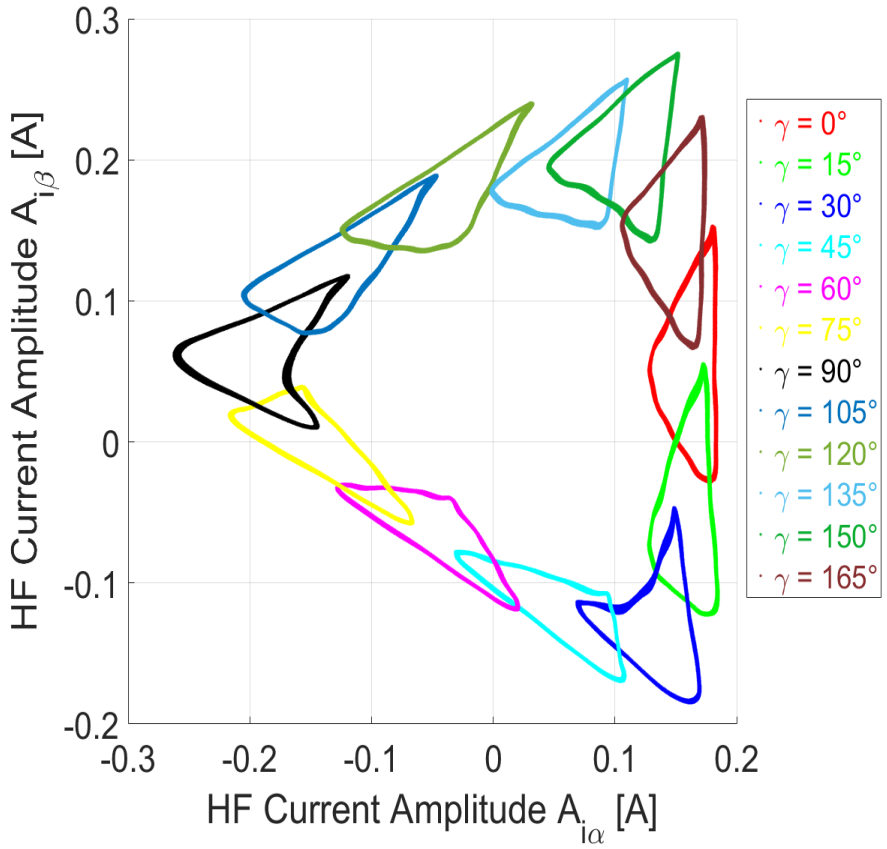

Figure 6.18 (d) – Plot of HF Current Amplitude $A_{i\alpha}$ [A] vs. $A_{i\beta}$ [A] with ω_m^* = 2 rad/s on M2, i_{d1}^*= 0 A and i_{q1}^*= 0 A on M1 during continuous pulsating injection for arbitrary γ.

6.5 Saliency Compensation using Space Modulation Profiling

6.5.1 Introduction to Space Modulation Profiling

The problem of having significant harmonics besides the fundamental saliency signature is a common problem with experimental AC machines. In Section 6.3.3, it was shown that the machine under test in this dissertation has significant harmonics in both $A_{i\alpha}$, $A_{i\beta}$ measurements (Figures 6.8 – 6.9). The harmonics are challenging for sensorless control because the signals being used have amplitude and phase distortion such that the typical observers based on a predominant fundamental saliency do not apply. A significant approach to compensate for such harmonics was proposed in [105] and is Space Modulation Profiling (SMP). The basis of SMP is to use a zero-phase filter to compute the difference between the ideal and actual saliency and to apply the resulting compensation terms in real-time. The zero-phase filter allows for the use of a high order filter with a sharp roll-off to filter out harmonics at low/zero speed without introducing a phase delay. This filtering technique can only be applied offline since it requires signal processing in both forward and reverse directions.

The fundamental component of the HF current amplitude response measured in Section 6.3.3 has a frequency of 1.917 Hz. In order to attenuate the harmonic content, a filter was designed in MATLAB using the Filter Design & Analysis (FDA) Tool. The filter was designed as an Infinite Impulse Response (IIR) Butterworth with a filter order of 20, a sampling frequency of 5 kHz and corner frequencies of f_{cl} = 1.5 Hz and f_{ch} = 2.5 Hz. The resultant magnitude response and phase response of the filter are shown in Figure 6.19 (a) – (b).

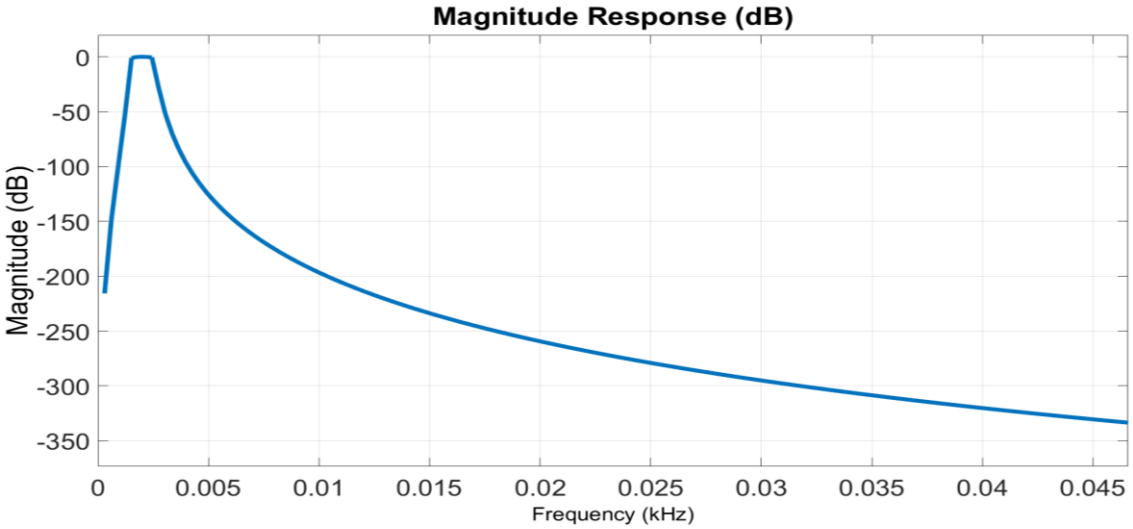

Figure 6.19 (a) – IIR Butterworth 20th order filter design for SMP
Magnitude Response [dB] vs. Frequency [kHz]

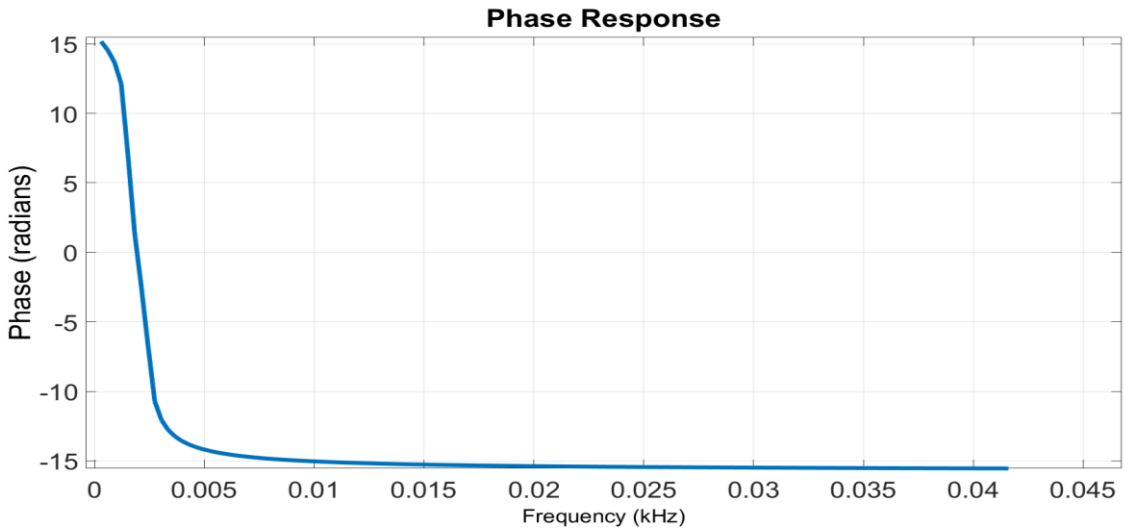

Figure 6.19 (b) – IIR Butterworth 20th order filter design for SMP
Phase Response (dB) vs. Frequency [kHz]

The FFT response of $A_{i\alpha}$, $A_{i\beta}$ for the operating point f_e=0.95 Hz, i_{d3}^* = 0 A and i_{q3}^* = 0 A before and after the application of the filter designed using the FDA tool and applied through the zero-phase filtering MATLAB function *filtfilt* is shown in Figures 6.20 – 6.21.

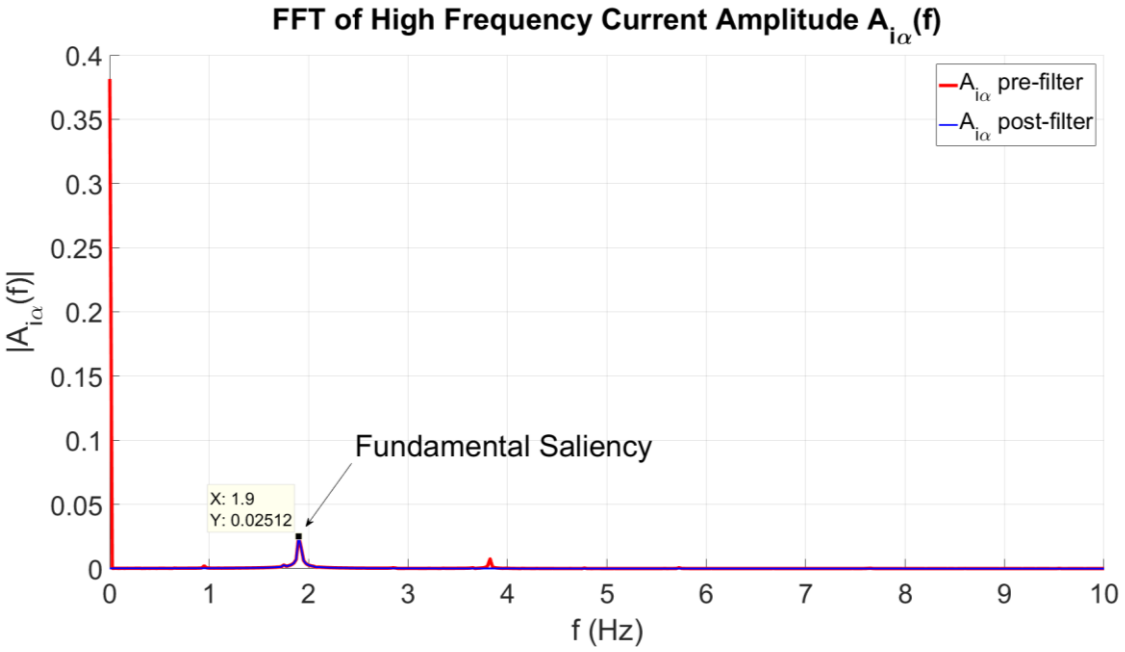

Figure 6.20 – FFT analysis of $A_{i\alpha}$ with i_d^*= 0 A and i_q^*= 0 A during continuous rotating injection pre and post zero-phase filtering.

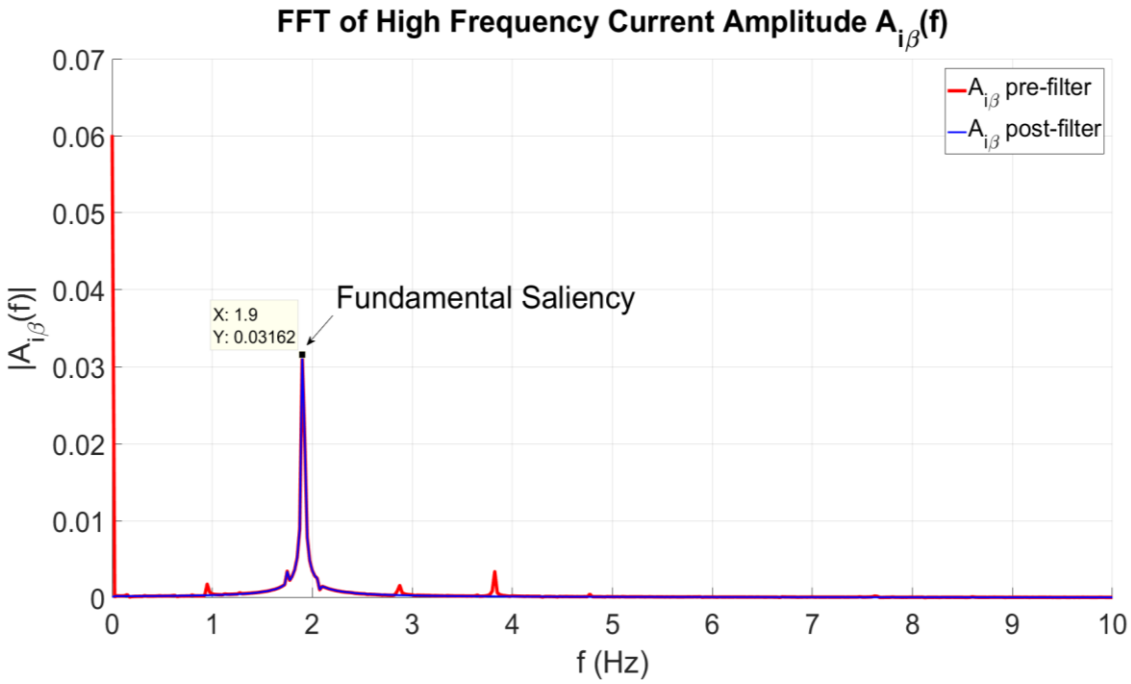

Figure 6.21 – FFT analysis of $A_{i\beta}$ with i_d^*= 0 A and i_q^*= 0 A during continuous rotating injection pre and post zero-phase filtering.

The application of the designed zero phase filter significantly reduces the harmonics outside the corner frequencies of the filter. Since the zero-phase filter cannot be applied in real-time, the compensation terms are calculated by subtracting the post-filtering signals from the actual HF current amplitude signals as shown in (6.13-6.14). The compensation signals $A_{i\alpha_{comp}}$, $A_{i\beta_{comp}}$ are compiled as SMP tables with respect to the mechanical rotor position θ_m, as shown in Figures 6.22 – 6.23. Both α and β SMP tables include all frequency components outside the bandwidth of the designed filter and are applied in real-time as a function of the estimated rotor position.

$$A_{i\alpha_{comp}} = A_{i\alpha} - A_{i\alpha\_zpf} \quad (6.13)$$

$$A_{i\beta_{comp}} = A_{i\beta} - A_{i\beta\_zpf} \quad (6.14)$$

Where $A_{i\alpha}$, $A_{i\beta}$ are the demodulated HF current amplitudes in the αβ axes

$A_{i\alpha\_zpf}$, $A_{i\beta\_zpf}$ are zero-phase filtered HF current amplitudes in the αβ axes

$A_{i\alpha_{comp}}$, $A_{i\beta_{comp}}$ are the resultant compensation terms in the αβ axes

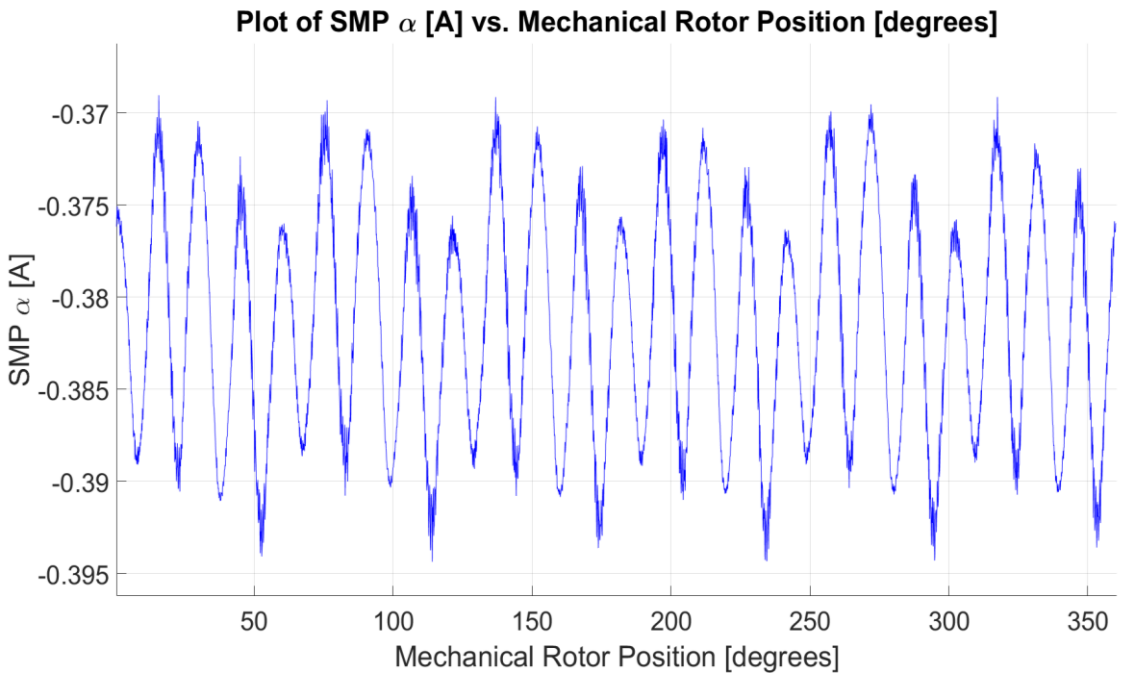

Figure 6.22 – Plot of SMP α Compensation Terms [A] vs. Mechanical Rotor Position θ_m [°] for f_e=0.95 Hz, i_{d3}^* = 0 A and i_{q3}^* = 0 A.

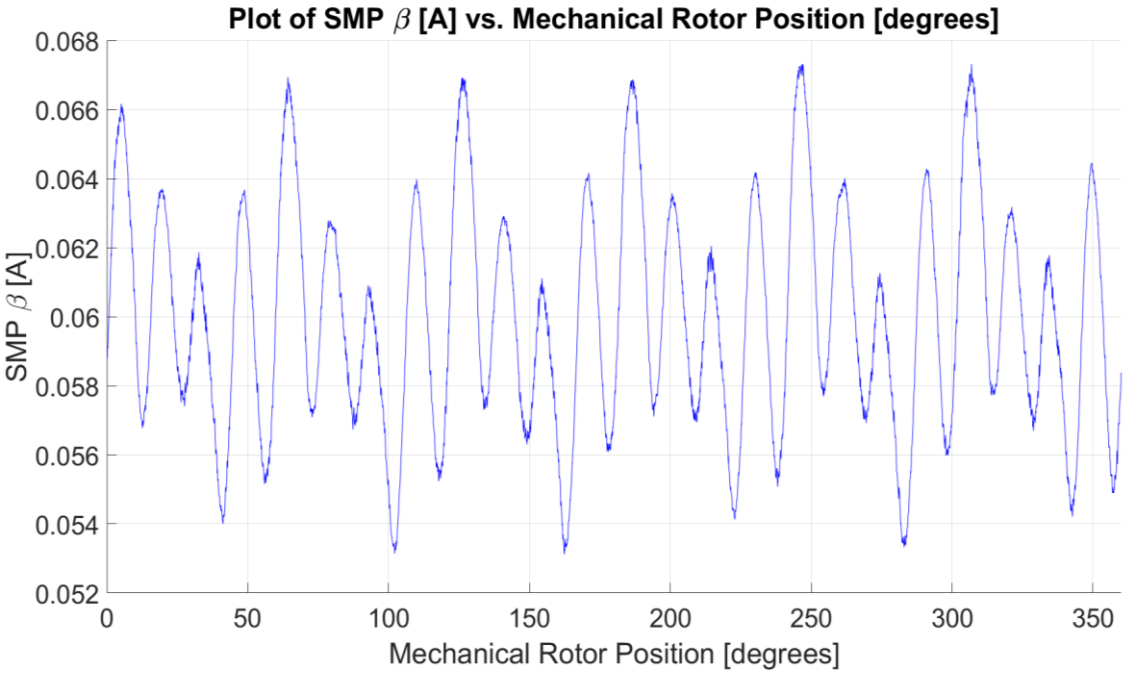

Figure 6.23 – Plot of SMP β Compensation Terms [A] vs. Mechanical Rotor Position θ_m [°] for f_e=0.95 Hz, i_{d3}^* = 0 A and i_{q3}^* = 0 A.

6.5.2 Space Modulation Profiling Based Observer

The sensorless estimation of the rotor position using SMP tables can be implemented through the SMP Based Observer shown in Figure 6.24. The HF current amplitudes

$A_{i\alpha}$, $A_{i\beta}$ are compensated by the SMP terms $A_{i\alpha_{comp}}$, $A_{i\beta_{comp}}$. The resultant components after applying the SMP compensation to $A_{i\alpha}$, $A_{i\beta}$ are shown in Figures 6.25 – 6.26 (DC component in $A_{i\alpha}$, $A_{i\beta}$ is removed in MATLAB plots for comparison purposes). The observer is based on a traditional PLL architecture [138] which produces estimates from the saliencies for $2\hat{\omega}_e$ and $2\hat{\theta}_e$.

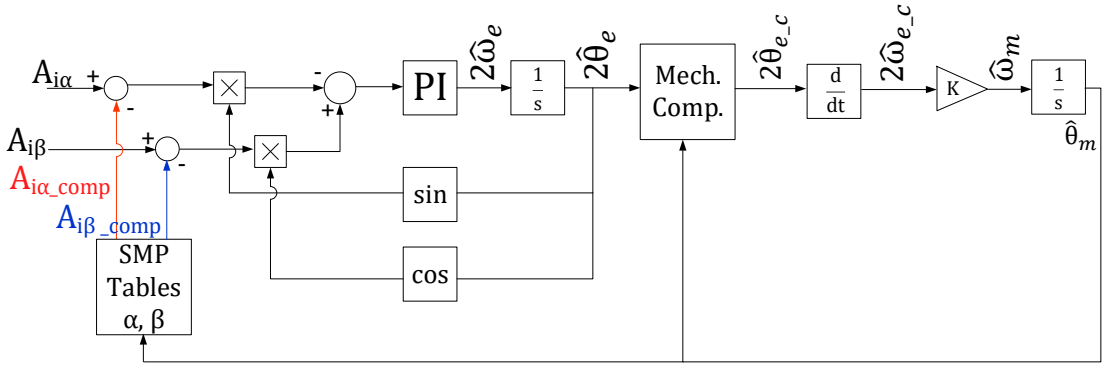

Figure 6.24 – SMP Based Sensorless Observer

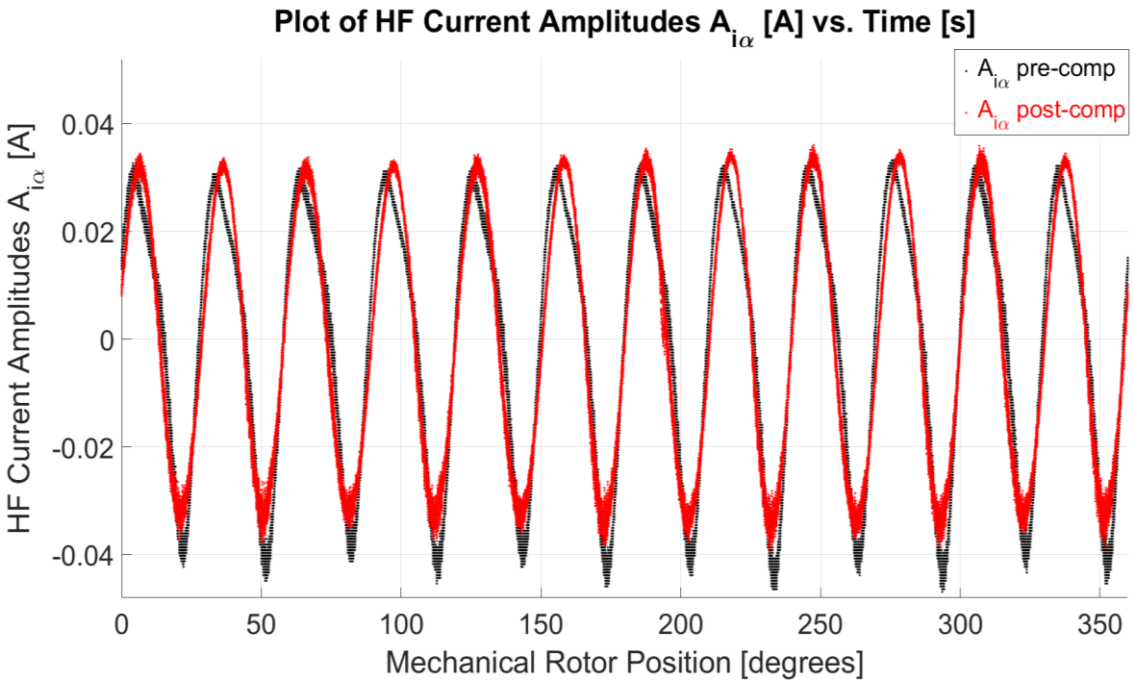

Figure 6.25 – Plot of HF Current Amplitude $A_{i\alpha}$ [A] vs. θ_m [°] for f_e=0.95 Hz, i_{d3}^* = 0 A and i_{q3}^* = 0 A with SMP compensation.

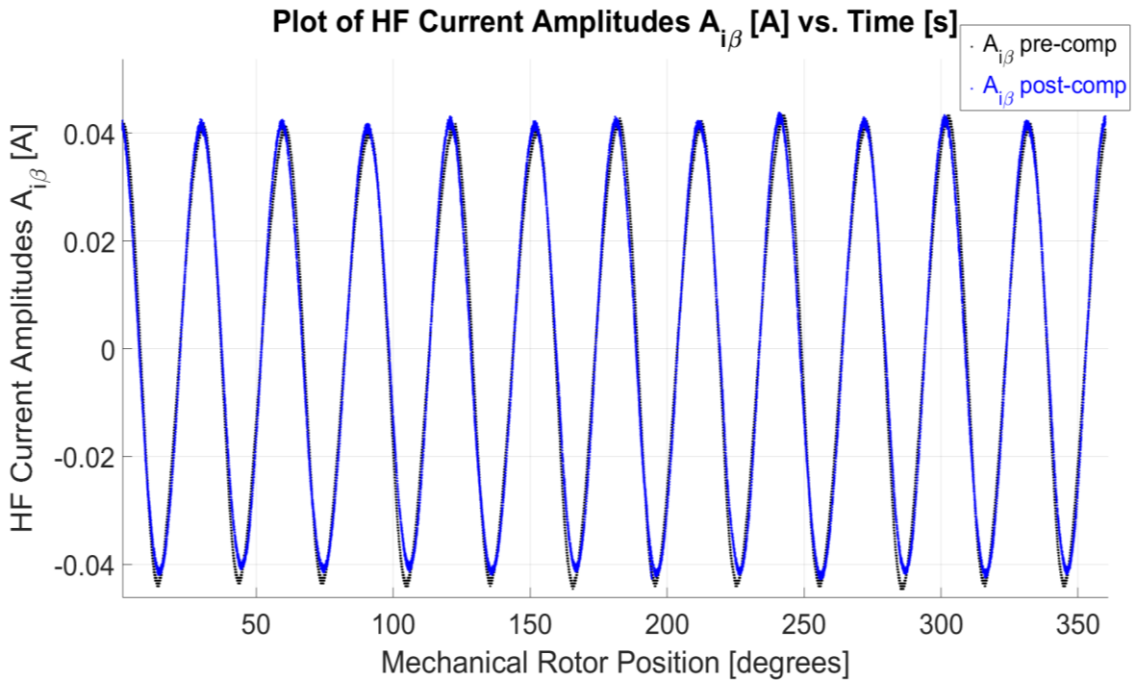

Figure 6.26 – Plot of HF Current Amplitude $A_{i\beta}$ [A] vs. θ_m [°] for f_e=0.95 Hz, i_{d3}^* = 0 A and i_{q3}^* = 0 A with SMP compensation.

The rotor position estimate $2\hat{\theta}_e$ from the saliency and the actual electrical rotor position at twice the fundamental frequency $2\theta_e$ are shown in Figure 6.27. It can be observed that for the machine under test, even though harmonic compensation with the SMP tables is applied a significant error exists between the actual and estimated quantities. The instantaneous error in the estimate $2\hat{\theta}_e$ is shown as a function of the mechanical rotor position in Figure 6.28. The error in the estimate is a function of the actual absolute mechanical position of the rotor and is attributed to the variation in saliency between different electrical sectors in the machine. The demodulated HF current amplitudes $A_{i\alpha}$, $A_{i\beta}$ which should have a constant amplitude at different electrical sectors in the machine are actually themselves amplitude modulated. Since this is a mechanical domain effect, it is not compensated for with the SMP tables as it is not filtered out by the designed zero-phase filter, as shown in Figure 6.29. The resultant HF current amplitudes after zero-phase filtering $A_{i\alpha\_zpf}$, $A_{i\beta\_zpf}$ still have some degree of amplitude modulation, which is not modelled for in the standard observer. This error is compensated for through the use of another LUT for the compensation term $2\hat{\theta}_{e\_c}$ which is further deducted from $2\hat{\theta}_e$. The DC offset in the error in the electrical rotor position shown in Figure 6.28 is

mainly attributed to the PLL estimation error due to the different amplitudes in $A_{i\alpha}$, $A_{i\beta}$ even after SMP has been applied.

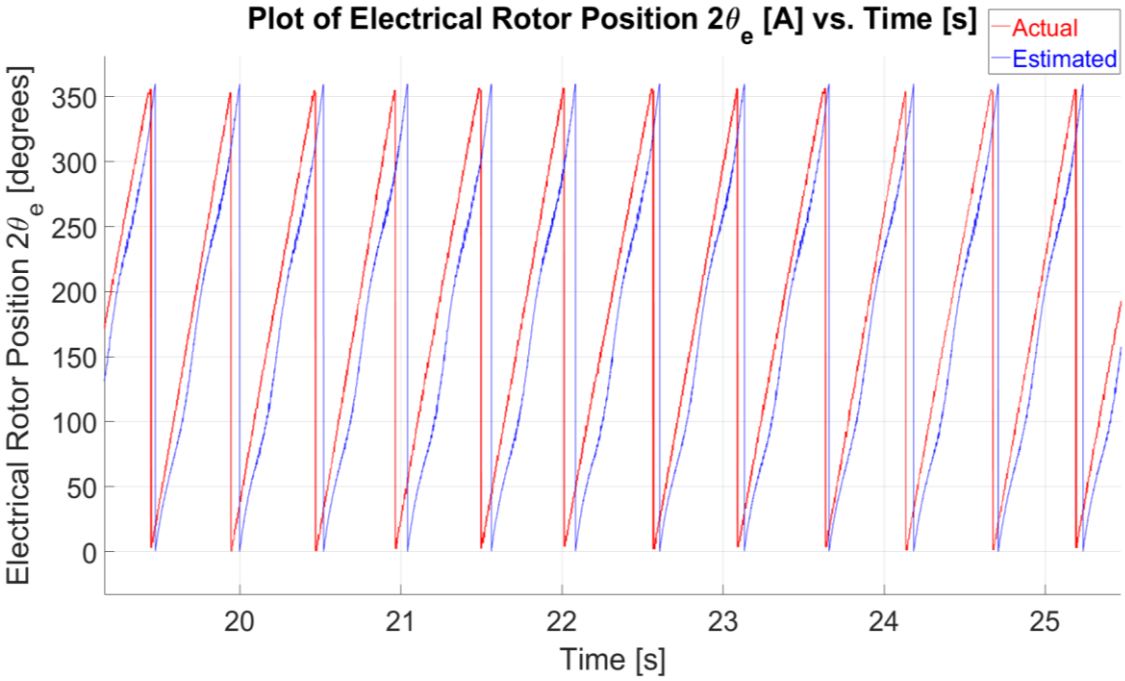

Figure 6.27 – Plot of Actual/Estimated Electrical Rotor Position $2\theta_e$ [°] vs. Time [s] without mechanical compensation zoomed in between 20 s ≤ t ≤ 25 s.

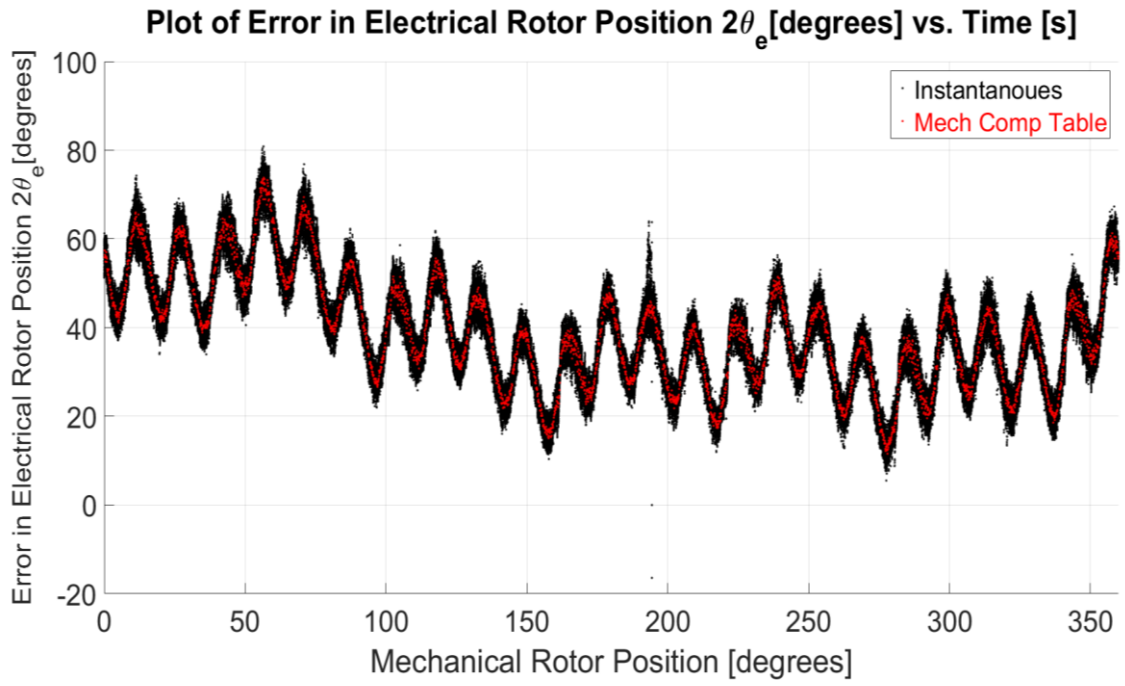

Figure 6.28 – Plot of Error in Electrical Rotor Position $2\theta_e$[°] vs. Mechanical Rotor Position θ_m [°].

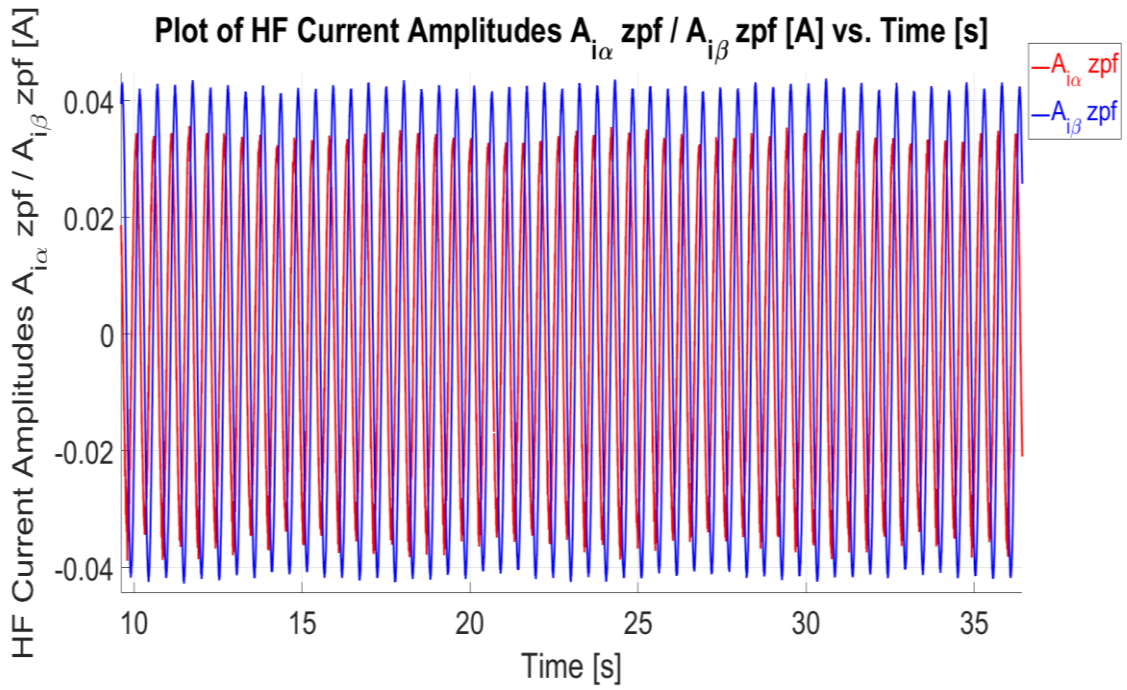

Figure 6.29 –Plot of HF Current Amplitudes post zero-phase filtering $A_{i\alpha\_zpf}$. $A_{i\beta\_zpf}$ [A] vs. Time [s] without mechanical compensation zoomed in between 10 s ≤ t ≤ 35 s.

The resultant electrical rotor position after compensation $2\hat{\theta}_{e\_c}$ is shown in Figure 6.30, while the actual/estimated mechanical rotor positions are shown in Figure 6.31. The error between the actual/estimation mechanical rotor positions is shown in Figure 6.32 to have an absolute maximum error of 5.05° and a RMSE of 1.83°.

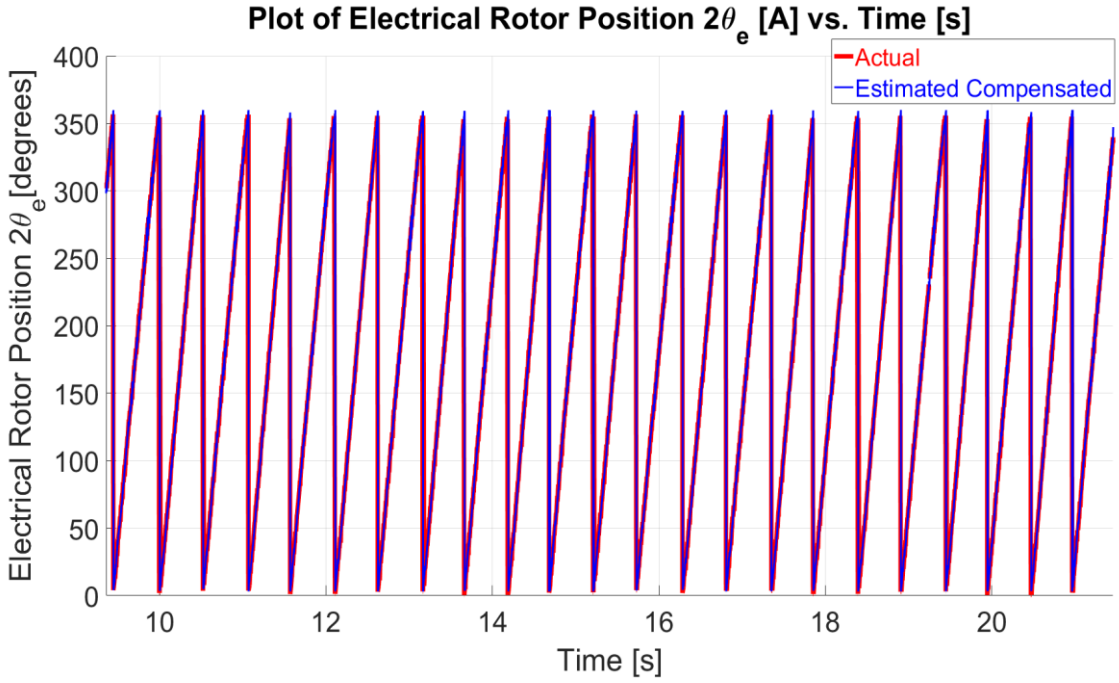

Figure 6.30 – Plot of Actual/Estimated Electrical Rotor Position $2\theta_e$ [°] vs. Time [s] with mechanical compensation zoomed in between 10 s ≤ t ≤ 25 s.

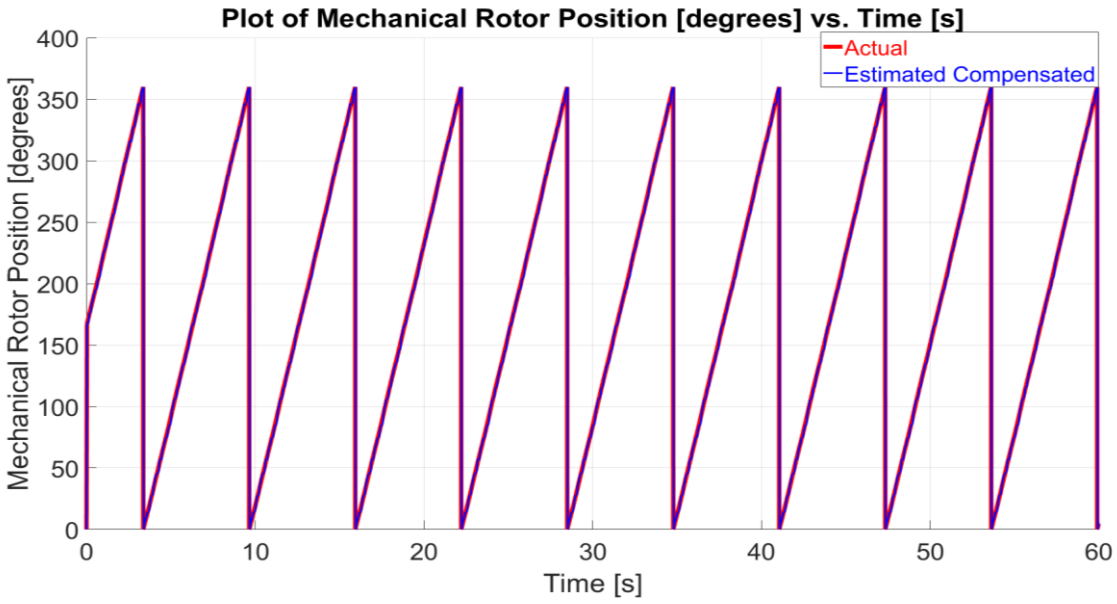

Figure 6.31 – Plot of Actual/Estimated Mechanical Rotor Position θ_m [°] vs. Time [s] with mechanical compensation.

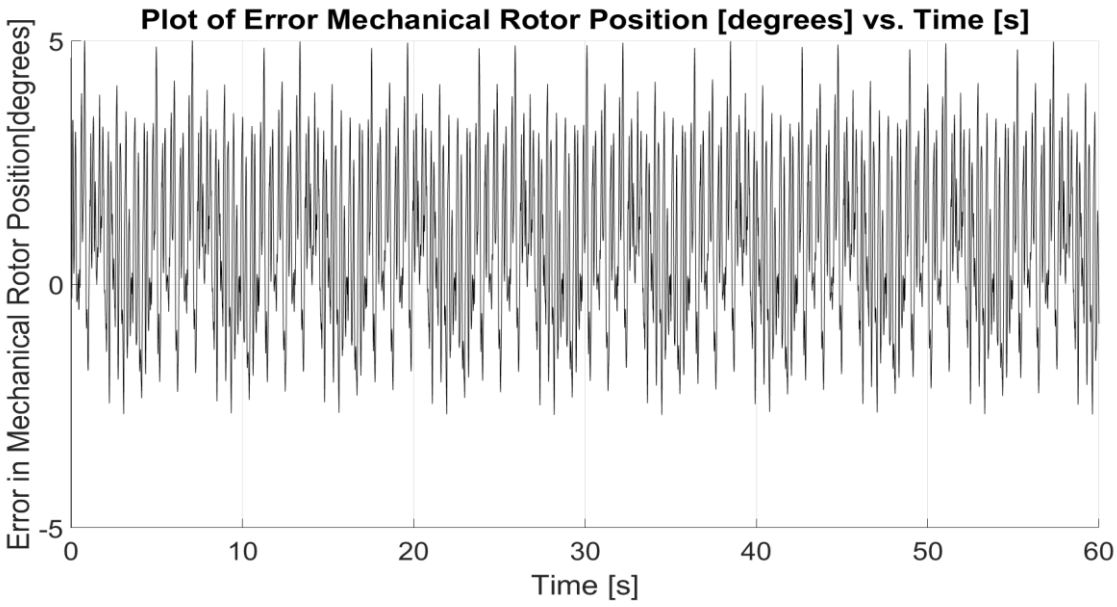

Figure 6.32 – Plot of Error in Mechanical Rotor Position θ_m [°] vs. Time [s] with mechanical compensation.

6.5.3 SMP Based Observer Limitations

The SMP Observer was shown to operate on the generation of compensation LUTs based on zero-phase filtering of the HF current amplitudes obtained from the measurement circuitry. This zero-phase filtering cannot be computed in real-time as it

requires forward and reverse samples in time to cancel the phase distortion attributed to high order filters. This limits the use of the SMP technique as it allows only for an offline calibration where the LUTs have to be generated offline on a software package such as MATLAB and included in the microcontroller memory before drive start-up.

For the machine under test it was observed that the HF current amplitudes are in themselves amplitude modulated as a function of the mechanical rotor position; this could possibly be a result of asymmetries in the stator and rotor along with varying magnet thickness. The SMP technique compensates only for harmonics in the electrical domain with no consideration for variations which exist in the mechanical domain. Hence it was required to introduce another compensation LUT for mechanical compensation, as shown in Figure 6.24 to obtain a more accurate estimate.

While the introduction of SMP tables significantly corrects for the distortion in the saliencies due to harmonic saliencies of significant magnitude the observers used in conjunction with this method to do not take into consideration the variations due to other physical machine properties which affect the HF current amplitude measurements. For the purposes of this dissertation it was felt that the practical implementation of a low/zero speed observer required an improved observer to the one based on SMP. The innovative Search Based Observer (SBO) integrates the non-ideal effects in the saliency as a LUT, instead of compensating for them. This was possible by using a search-based algorithm with the LUTs instead of the PLL observer.

6.6 Summary

This chapter has presented the various sources for saliency in PMSMs and outlined geometric and saturation components in Section 6.2. The use of synchronized sampling and aliasing for demodulation was shown to be a more effective way to obtain the HF current amplitudes with respect to other demodulation in Sections 6.3.1-6.3.2. Experimental saliency measurements were also presented for both rotating and pulsating HF injection in Sections 6.3.3-6.3.6. The variation in the magnetic signature when varying the i_q-current and the rotor speed were also analysed in Sections 6.3.7-6.3.8.

An alternative SM-PMSM machine with different stator and rotor dimensions was investigated in Section 6.4 to assess the suitability of their magnetic signature for sensorless control. The compensation of harmonic saliency and estimation using the SMP based observer was also presented in Section 6.5.

The variation of the pulsating injection shown in Section 6.3.6 for different angles γ indicates that the resulting HF current amplitudes $A_{i\alpha}$, $A_{i\beta}$ vary beyond what is predicted by the single saliency models. Hence, some injection angles are possibly more suitable for use with sensorless control than others as they work better closer to the ideal signature. In Chapter 7 an analysis is presented for the different HF current amplitudes (at different injection angles γ), in terms of Signal-to-Noise Ratio (SNR) and gradient sensitivity at different rotor positions (mA/°). The availability of distinct HF current signatures is considered to be an advantage of pulsating injection over rotating injection. For rotating injection, only one HF current signature is observed as shown in Section 6.3.3 and therefore no selection is possible.

Chapter 7 – Search-Based Sensorless Estimation

7.1 Introduction

This chapter presents the innovative Search-Based Observer (SBO) for sensorless estimation with HF injection for low to zero-speed applications on Permanent Magnet Synchronous Machines (PMSMs). Since the observer's accuracy is dependent on the deviation and sensitivity of the magnetic signature, numerical analysis for the selection of a suitable saliency signature is proposed. The three SBO sub-processes: commissioning, searching and speed LUT selection are presented.

7.2 Selection of Saliency for Sensorless Control

Traditional sensorless algorithms for low to zero speed sensorless control mostly rely on a single saliency model where the fundamental saliency is an order of magnitude higher than the harmonic saliencies. In practice, most Surface Mounted Permanent Magnet Synchronous Machines (SM-PMSMs) deviate from this model, such as the case with the experimental machines in this dissertation. In (4.39) it was shown that for an ideal machine with a pulsating injection γ the HF current amplitudes $A_{i\alpha}$ and $A_{i\beta}$ are two sinusoidal components which only differ in their DC offset and are always phase shifted by 90°. Such a saliency would result in a perfectly circular complex plot, which was not observed in Section 6.3.6 for different values of γ.

$$\begin{bmatrix} A_{i\alpha} \\ A_{i\beta} \end{bmatrix} = \begin{bmatrix} I_1 A_1 - I_2 V_i \cos(\gamma - 2\theta_e) \\ I_1 A_2 + I_2 V_i \sin(\gamma - 2\theta_e) \end{bmatrix} \tag{4.39}$$

$$\begin{bmatrix} \frac{dA_{i\alpha}}{d\theta_e} \\ \frac{dA_{i\beta}}{d\theta_e} \end{bmatrix} = \begin{bmatrix} -2I_2 V_i \sin(\gamma - 2\theta_e) \\ -2I_2 V_i \cos(\gamma - 2\theta_e) \end{bmatrix} \tag{7.1}$$

Considering the derivatives (7.1) of the HF current amplitudes, for a single-saliency machine the phase shift is in such a way that the maxima or minima of $A_{i\alpha}$, $A_{i\beta}$ $\left(\frac{dA_{i\alpha}}{d\theta_e} = 0, \frac{dA_{i\beta}}{d\theta_e} = 0\right)$ coincides with the maximum derivative in the other axis. This translates into a constant summed derivative for all values of θ_e. Since the phase shift in the machine under test between the $\alpha\beta$ components was observed not to be 90°, the derivative of the saliencies will not follow (7.1). Hence, the summed rate of change

between different rotor positions will vary. Different injection angles γ will also result in magnetic signatures with significantly different derivatives. For the purposes of sensorless control a higher derivative in $A_{i\alpha}$, $A_{i\beta}$ with respect to the rotor position is better because there is a higher distinction between different rotor positions. The derivates of the different magnetic signatures obtained through arbitrary injection of the angle γ should be analysed and injection angles which result in extremely low derivates simultaneously in both $A_{i\alpha}$ and $A_{i\beta}$ should not be used for sensorless control. At such points, the sensitivity of the observer would be extremely low and could result in unstable sensorless control.

The experimental measurements of $A_{i\alpha}$, $A_{i\beta}$ were carried out through the Saliency Measurement circuit board (Section 5.5) and sampled through the microcontroller ADC (Section 5.3). The noise component due to the measurement process coupled with non-ideal effects such as open-loop injection, inverter non-linearities and time-dependent variations in the machine saliency will result in a deviation of the instantaneous HF amplitudes with respect to the mean of the same measured sample. During this research, it was found that different machine i_q-current operating points result in significantly different deviations from the mean and this should also be factored in when selecting saliencies for sensorless control.

In this dissertation, a numerical analysis of the saliencies obtained in Section 6.3.6 is proposed to determine a suitable saliency signature for sensorless control based on finding optimum between:

1) The highest combined **gradient** in $A_{i\alpha}$, $A_{i\beta}$ (A/°) for all values of $\theta_{m.}$
2) The lowest **deviation** in $A_{i\alpha}$, $A_{i\beta}$ with respect to the mean of the sample.

The numerical analysis assumes that a sample for $A_{i\alpha}$, $A_{i\beta}$ has been measured for a period T s. The data collected in Section 6.3.6 was obtained over a period T = 120 s for each value of γ. All the samples were sorted with respect to an integer element number N which is a scaled quantity of the mechanical rotor position θ_m ($0° \leq \theta_m < 360° \rightarrow 0 \leq N < 4095$). The mapping was done for 4095 levels which coincide with the resolution of the 12-bit digital encoder used in this dissertation. The multiple samples collected over the period T and sorted with respect to each element N are

defined as $A_{i\alpha\_sort}$, $A_{i\beta\_sort}$. The mean value for the sorted values for each value of N are defined as $\overline{A_{i\alpha\_sort}}$, $\overline{A_{i\beta\_sort}}$ as shown in Figure 7.1.

The normalized deviation components D_α, D_β for $A_{i\alpha}$, $A_{i\beta}$ are given in (7.2-7.3).

$$D_\alpha = \frac{\sigma A_{i\alpha\_sort}}{\max|\overline{A_{i\alpha\_sort}}|} \tag{7.2}$$

$$D_\beta = \frac{\sigma A_{i\beta\_sort}}{\max|\overline{A_{i\beta\_sort}}|} \tag{7.3}$$

Where D_α, D_β is the normalized deviation in the HF current amplitudes $A_{i\alpha}$, $A_{i\beta}$

$\sigma A_{i\alpha\_sort}$, $\sigma A_{i\beta\_sort}$ is the standard deviation in $A_{i\alpha\_sort}$, $A_{i\beta\_sort}$

$\max|\overline{A_{i\alpha_{sort}}}|$, $\max|\overline{A_{i\beta\_sort}}|$ is the absolute peak value of $\overline{A_{i\alpha\_sort}}$, $|\overline{A_{i\beta\_sort}}|$

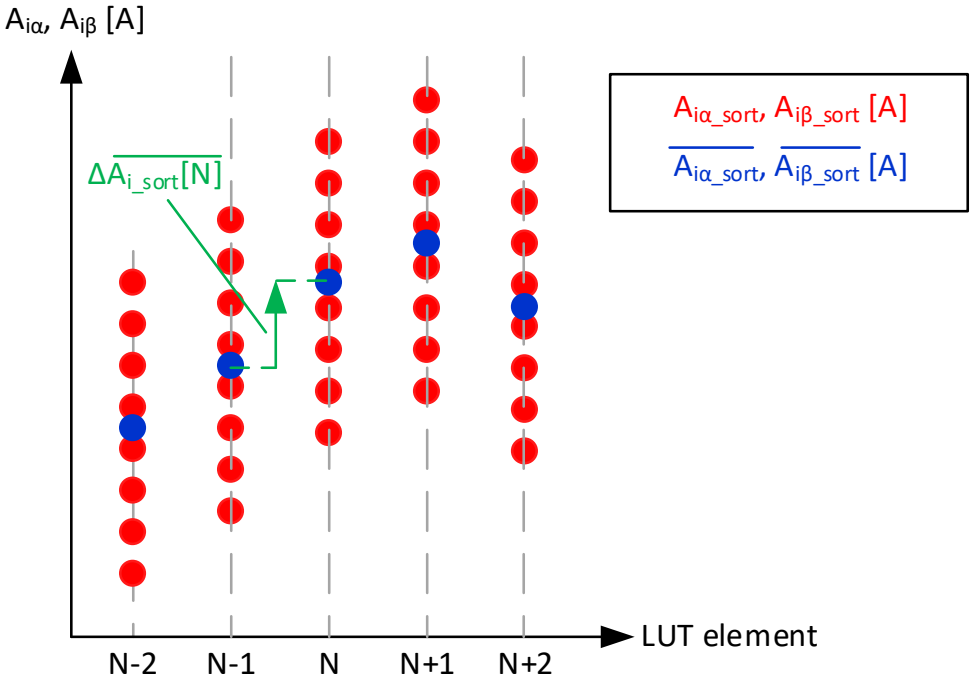

Figure 7.1 – Sorting and Averaging of $A_{i\alpha}$, $A_{i\beta}$ Measurements

The deviation components are normalized with respect to the peak of the mean sorted HF measurements in order for adequate comparison between different magnetic signatures. The mean of the deviation components (7.4-7.5) and the maxima (7.6-7.7) are used for numerical magnetic signature analysis and comparison.

$$\overline{D_\alpha} = \overline{\left|\frac{\sigma A_{1\alpha\_sort}}{\max|\overline{A_{1\alpha}}|}\right|} \tag{7.4}$$

$$\overline{D_\beta} = \overline{\left|\frac{\sigma A_{1\beta\_sort}}{\max|\overline{A_{1\beta}}|}\right|} \tag{7.5}$$

$$D_{\alpha max} = \max\left(\left|\frac{\sigma A_{i\alpha\_sort}}{\max|\overline{A_{1\alpha}}|}\right|\right) \tag{7.6}$$

$$D_{\beta max} = \max\left(\left|\frac{\sigma A_{i\beta\_sort}}{\max|\overline{A_{1\beta}}|}\right|\right) \tag{7.7}$$

The gradient which is the change between one element value and another as shown in Figure 7.1 is defined as $\Delta\overline{A_{i\alpha\_sort}}$, $\Delta\overline{A_{i\beta\_sort}}$. Two parameters dependent on the gradient of the saliency are defined in (7.8-7.9).

$$\min\_\Delta\alpha\beta = \min(|\Delta\overline{A_{i\alpha\_sort}}| + |\Delta\overline{A_{i\beta\_sort}}|) \tag{7.8}$$

$$\overline{\Delta\alpha\beta} = \overline{|\Delta\overline{A_{i\alpha\_sort}}| + |\Delta\overline{A_{i\beta\_sort}}|} \tag{7.9}$$

The minimum gradient defined in (7.8) represents the minimum summed gradient for all elements 0 to N. An extremely low min_Δαβ is not suitable for sensorless control as it reduces the sensorless observer accuracy at particular rotor positions. The average gradient defined in (7.9) represents the mean of the summed gradient in both the α and β saliencies for all elements 0 to N.

The parameters defined in (7.4 – 7.9) are used to analyse the magnetic signatures at different injection angles γ for different i_q-currents and rotor speeds. Magnetic signatures chosen for sensorless control should have low deviation ($\overline{D_\alpha}$, $\overline{D_\beta}$, $D_{\alpha max}$, $D_{\beta max}$) and high gradients ($\min\_\Delta\alpha\beta, \overline{\Delta\alpha\beta}$). The numerical analyses of $A_{i\alpha\_sort}$, $A_{i\beta\_sort}$ for $\gamma = 0°$ are shown in Figures 7.2 – 7.3 respectively. The absolute summation of the mean gradients $|\Delta\overline{A_{i\alpha\_sort}}|+|\Delta\overline{A_{i\beta\_sort}}|$ is shown in Figure 7.4. From Figures 7.2 and 7.3, it can be observed that the instantaneous HF current amplitude measurements (red markers) have a deviation from the mean (blue markers), this deviation represented as D_α and D_β is also shown (black marker). The summation of the gradients is shown in Figure 7.4 to have periodic low gradient points with respect to the element N (scaled mechanical rotor position). These points occur at 24 times per one mechanical revolution which corresponds to 4 times per one electrical revolution for the six-pole machine under test.

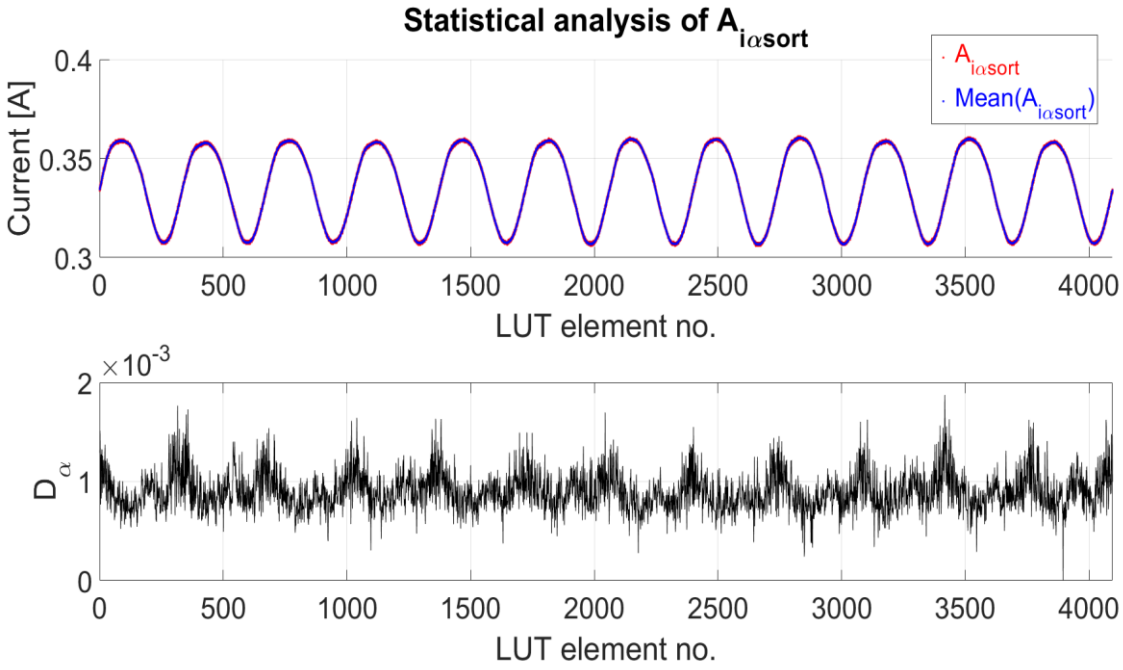

Figure 7.2 (a) – Plot of $A_{i\alpha\_sort}$ [A], $\overline{A_{i\alpha\_sort}}$ [A], D_α vs. element N for continuous pulsating injection for γ=0°.

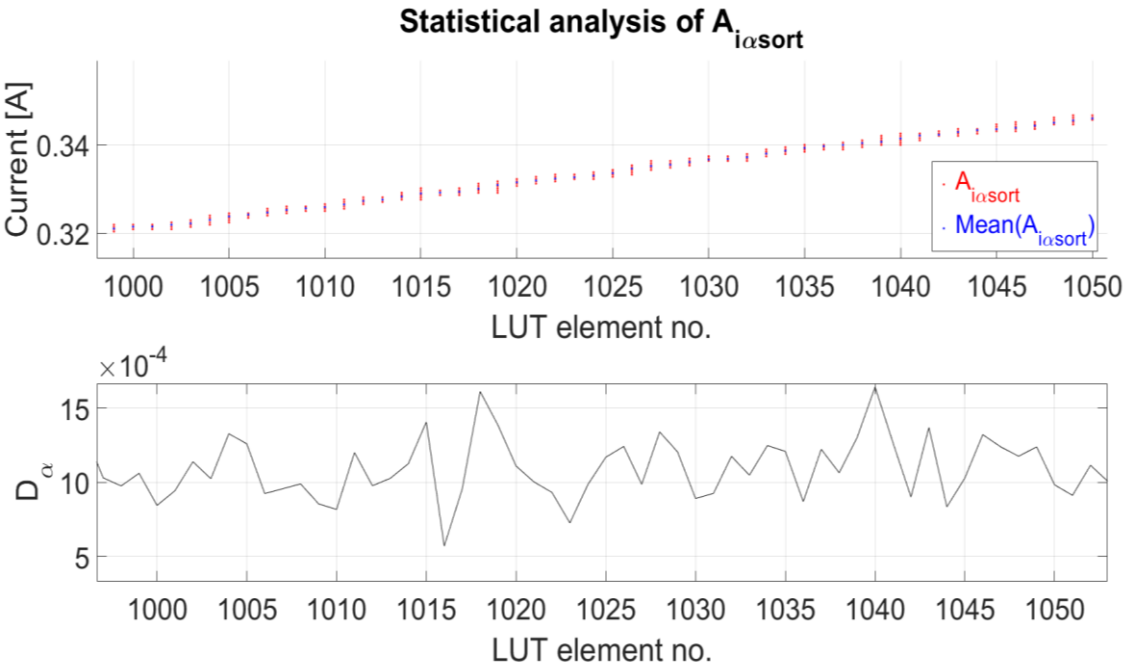

Figure 7.2 (b) – Plot of $A_{i\alpha\_sort}$ [A], $\overline{A_{i\alpha\_sort}}$ [A], D_α vs. element N for continuous pulsating injection for γ=0° zoomed between 1000 ≤ N ≤ 1050.

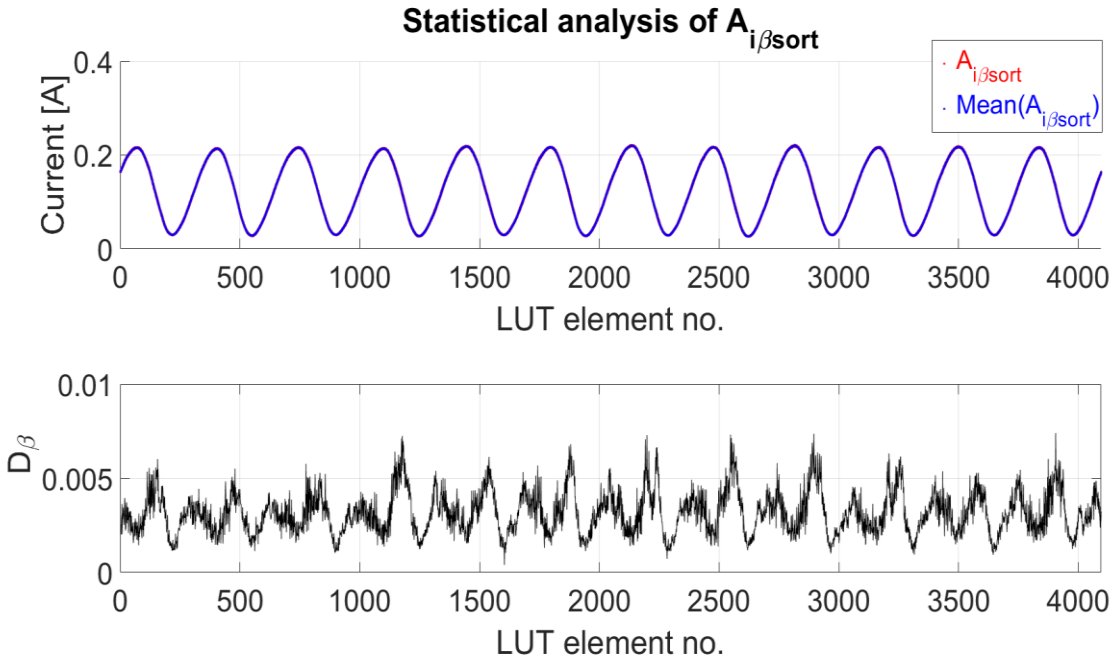

Figure 7.3 (a) – Plot of $A_{i\beta\_sort}$ [A], $\overline{A_{i\beta\_sort}}$ [A], D_β vs. element N for continuous pulsating injection for γ=0°.

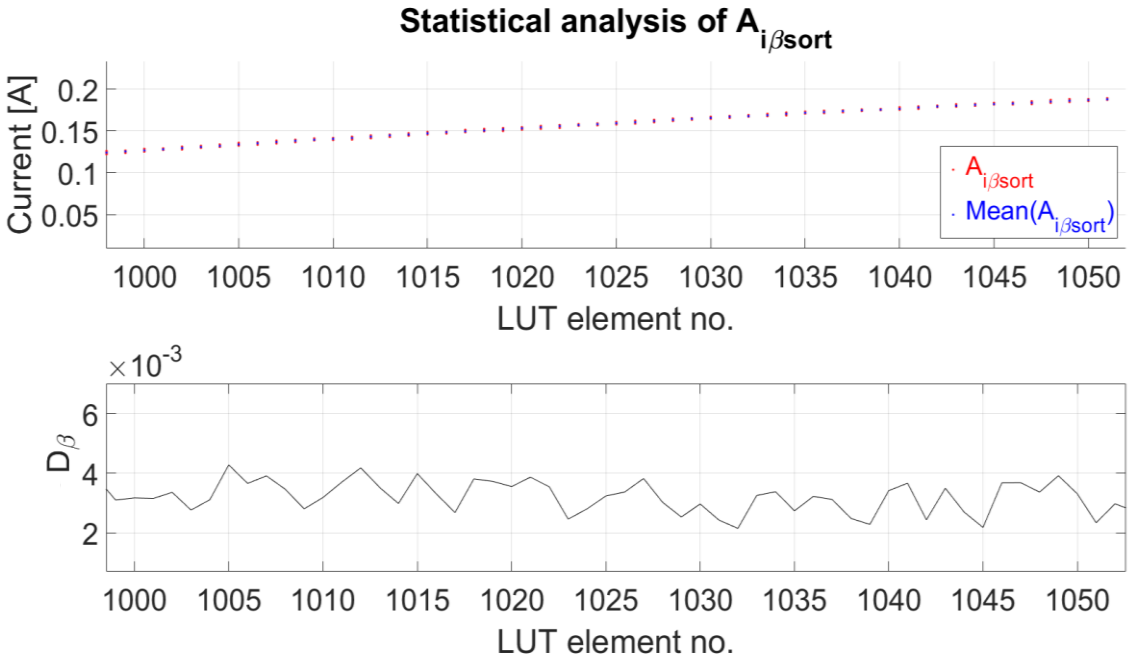

Figure 7.3 (b) – Plot of $A_{i\beta\_sort}$ [A], $\overline{A_{i\beta\_sort}}$ [A], D_β vs. element N for continuous pulsating injection for γ=0° zoomed between 1000 ≤ N ≤ 1050.

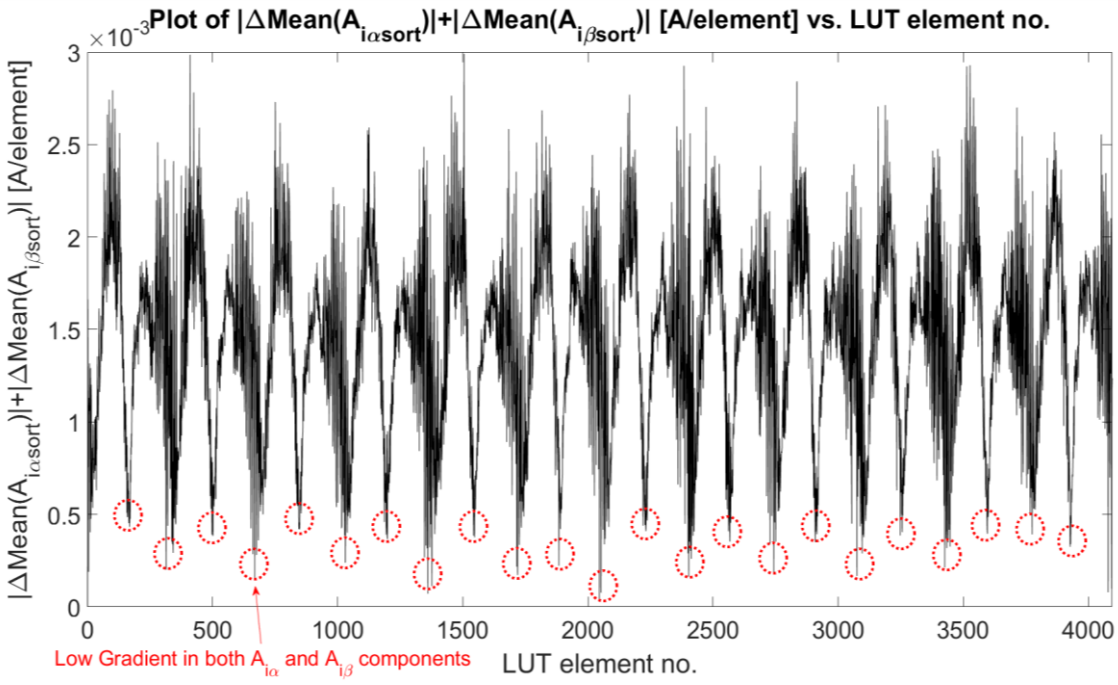

Figure 7.4 (a) – Plot of $|\Delta\overline{A_{i\alpha\_sort}}|+|\Delta\overline{A_{i\beta\_sort}}|$ [A/element] vs. element N for continuous pulsating injection for γ=0°.

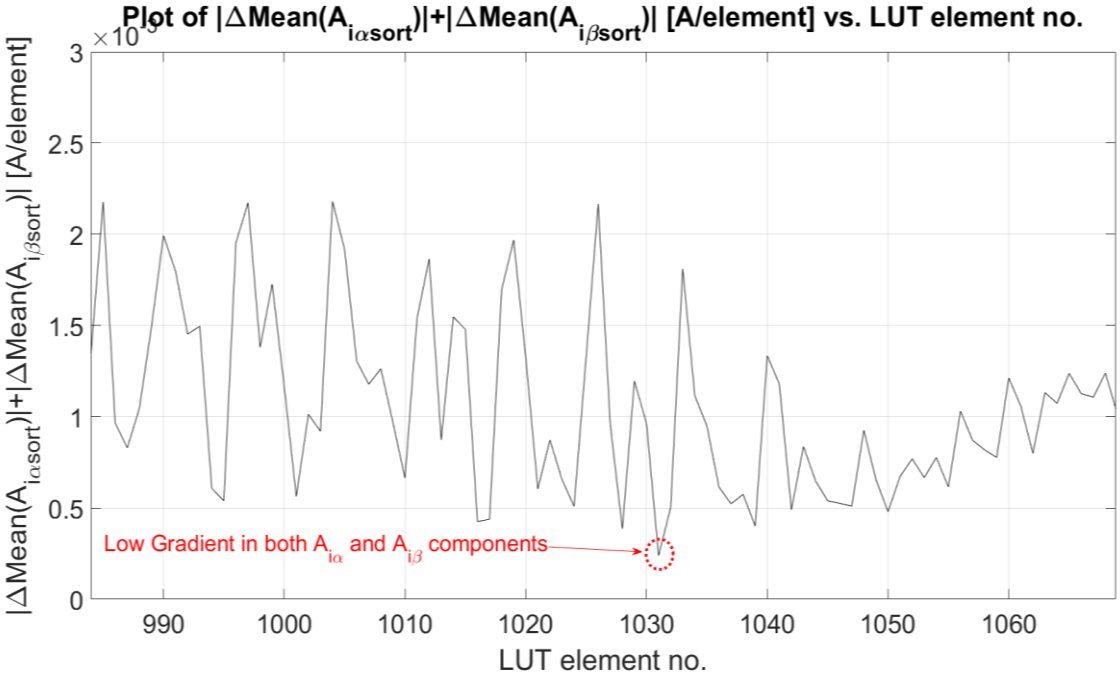

Figure 7.4 (b) – Plot of $|\Delta\overline{A_{i\alpha\_sort}}|+|\Delta\overline{A_{i\beta\_sort}}|$ [A/element] vs. element N for continuous pulsating injection for γ=0° zoomed between 1000 ≤ N ≤ 1050.

The numerical analysis for the values of γ tested in Section 6.3.6 is presented in Table 7.1. The parameters defined in (7.4-7.9) are shown to vary at different injection angles γ. For the purposes of this dissertation, the injection angle with the highest value of min_Δαβ was chosen as the most suitable signature for sensorless control as this parameter was observed to improve the robustness sensorless closed-loop estimation. The mean gradient $\overline{\Delta\alpha\beta}$ was found to be of the same order of magnitude for all values of γ tested.

While the deviation parameters in Table 7.1 were observed to vary their overall magnitude is generally of the same order of magnitude and therefore the selection based on min_Δαβ was preferred. The best signature from Table 7.1 was found to be at γ = 120° where the min_Δαβ component is a factor of 11.2 larger than that at γ = 0° and a factor of 5.24 larger than that at γ = 90°. This further shows the validity of considering multiple injection angles in the stationary αβ rather than those on the orthogonal axes only. The numerical analysis at the optimum injection angle γ = 120° is shown in Figures 7.5 – 7.7.

γ	$\overline{D_\alpha}$	$D_{\alpha max}$	$\overline{D_\beta}$	$D_{\beta max}$	min_Δαβ (A/element)	$\overline{\Delta\alpha\beta}$ (A/element)
0	8.98E-04	0.0019	0.0028	0.0063	3.31E-05	0.0014
15	9.28E-04	0.0018	0.0022	0.0049	9.88E-05	0.0013
30	0.0016	0.0041	0.0015	0.0038	2.27E-05	0.0013
45	0.0056	0.012	9.13E-04	0.0019	2.47E-04	0.0014
60	0.0015	0.0035	0.0013	0.0025	4.33E-05	0.0015
75	0.0014	0.0038	0.0027	0.0051	4.88E-05	0.0016
90	0.0012	0.0033	0.0027	0.0059	7.08E-05	0.0014
105	0.0011	0.0024	0.0013	0.0027	6.62E-05	0.0014
120	0.0018	0.0037	9.00E-04	0.002	3.71E-04	0.0014
135	0.005	0.0114	8.47E-04	0.0021	2.70E-04	0.0014
150	0.0022	0.0048	0.0013	0.0038	8.07E-05	0.0015
165	0.0014	0.0036	0.0017	0.004	7.01E-05	0.0016

Table 7.1 – Saliency Numerical Analysis for 0°≤ γ ≤165°, f_i = 2.5 kHz, V_i = 3 V.

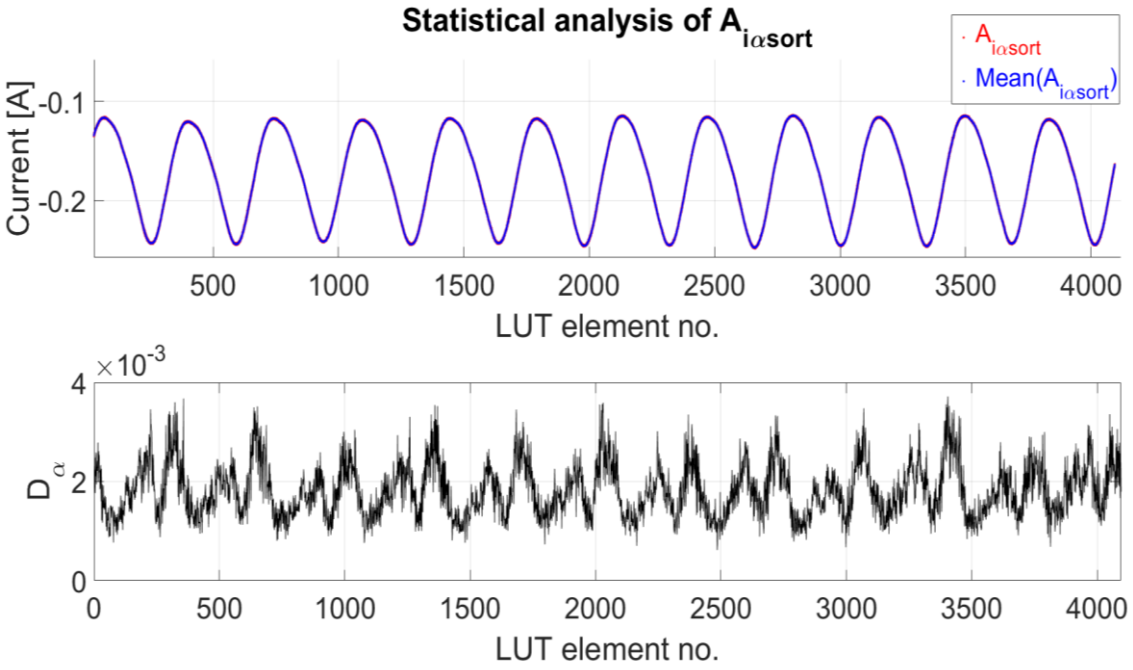

Figure 7.5 – Plot of $A_{i\alpha\_sort}$ [A], $\overline{A_{i\alpha\_sort}}$ [A], D_α vs. element N for continuous pulsating injection for γ=120°.

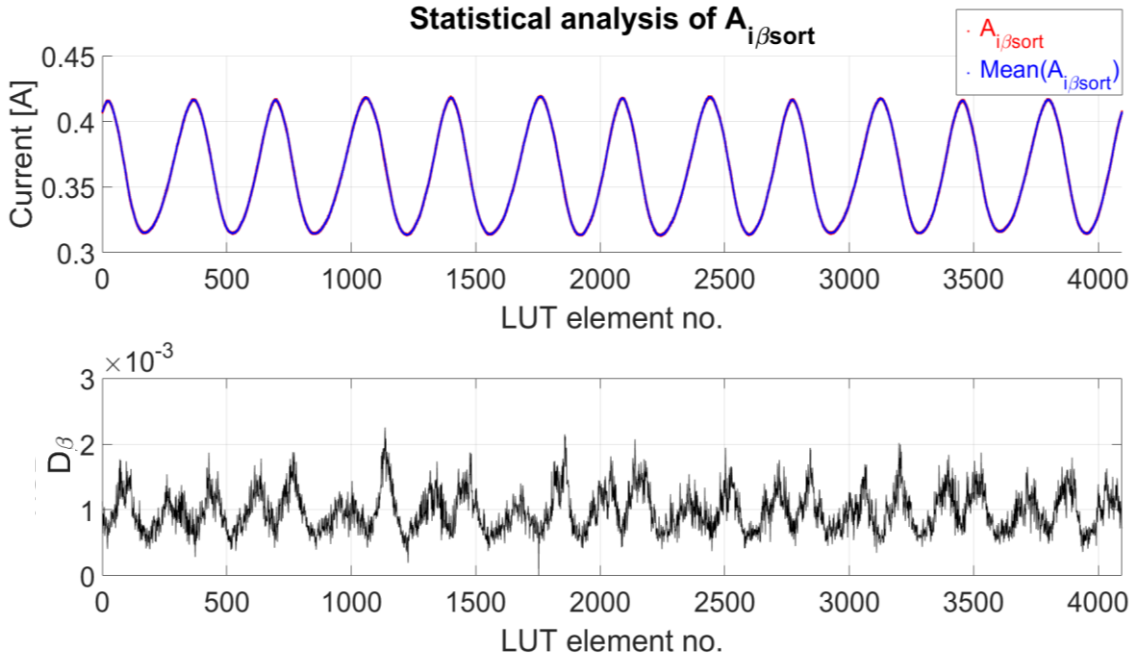

Figure 7.6 – Plot of $A_{i\beta\_sort}$ [A], $\overline{A_{i\beta\_sort}}$ [A], D_β vs. element N for continuous pulsating injection for γ=120°.

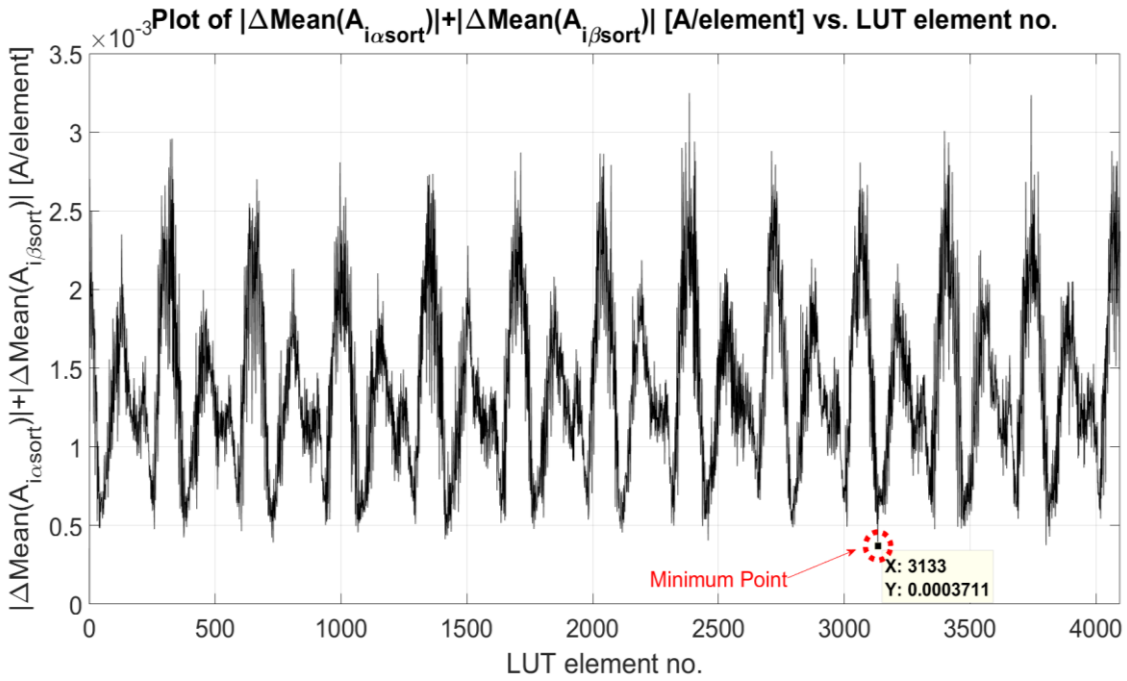

Figure 7.7 – Plot of $|\Delta\overline{A_{i\alpha\_sort}}|+|\Delta\overline{A_{i\beta\_sort}}|$[A/element] vs. element N for continuous pulsating injection for γ=120°.

The selection of the angle γ = 120° was carried out for the case of the unloaded machine with i_{q3}^{*} = 0 A. In Sections 6.3.7 and 6.3.8 the change in the magnetic signature was presented for variations in both load and rotor speed. Since the magnetic signature varies with both these parameters, a change in the optimum injection γ could be possible with respect to the unloaded operation point at an average rotor speed of 1 rad/s. The determination of the most suitable injection γ using the numerical based approach presented in this section was carried out with tables presented in Appendix A for the following additional operating points:

- $0° \leq \gamma \leq 165°$, i_{q3}^{*} = 0 A, 5 A, -5 A at ω_{m4}^{*} = 1 rad/s
- $0° \leq \gamma \leq 165°$, ω_{m4}^{*} = 1 rad/s, 2 rad/s, 3 rad/s at i_{q3}^{*} = 0 A

From these operating points, it was observed that the most suitable injection angle γ remains at 120° for different speeds close to the zero-speed point while it changes at different loading currents. Given this result, in order to obtain the best sensorless estimates possible, the injection angle γ should be adjusted according to the load of the machine. Furthermore, the most suitable injection angle is also expected to be dependent on the d-axis current.

Since the deviation of the HF current amplitudes in $A_{i\alpha}$, $A_{i\beta}$ tends to increase with increased values of i_q the uncertainty in the accuracy of the proposed numerical analysis for γ increases. Considering this and the constraints associated with this project the variation of the most suitable injection angle γ was not investigated for multi-parameter dependency and the injection angle $\gamma = 120°$ obtained for $i_{q3}^* = 0$ A was used for all the operating points of the machine. Performing the proposed analysis with a larger data set from experiments of longer duration could give more precise statistical results. While the preliminary investigation presented for finding a suitable γ for sensorless control does not necessarily prove that the optimum γ was found, it is a more structured alternative to a trial and approach. The sensorless operation of the machine at the proposed injection angle $\gamma = 120°$ was found to be suitable and shown to be stable over the full load operating range of the machine in Chapters 8 and 9.

7.3 Saliency Variation with Machine Loading

In this dissertation, the injection angle was kept constant $\gamma = 120°$ for all operating points as described in Section 7.2. The numerical analysis was carried out for $\gamma = 120°$ (Table 7.2) for the operating points described in Section 6.3.7 for $-10 \text{ A} \leq i_{q3}^* \leq 10$ A at V_i=3 V, f_i = 2.5 kHz and $\omega_{m4}^* = 1$ rad/s.

From the results presented in Table 7.2, it was observed that both the mean deviation $\overline{D_\alpha}$, $\overline{D_\beta}$ and the maximum deviation $D_{\alpha max}$, $D_{\beta max}$ increase with both positive/negative loading of i_{q3}^*. The variation of the deviation parameters in the signature is shown in Figures 7.8 – 7.9. Since the deviation increases with i_{q3}^* the accuracy of the sensorless algorithms is expected to decrease at such operating conditions.

i_q^* (A)	$\overline{D_\alpha}$	$D_{\alpha max}$	$\overline{D_\beta}$	$D_{\beta max}$	min_Δαβ (A/element)	$\overline{\Delta\alpha\beta}$ (A/element)
-10	0.0063	0.0178	0.0034	0.0121	4.38E-05	0.0016
-7.5	0.0049	0.013	0.0026	0.0067	1.53E-05	0.0015
-5	0.0031	0.0078	0.0015	0.0037	6.60E-05	0.0014
-2.5	0.0021	0.0047	0.0010	0.0021	7.6E-05	0.0013
0	0.0018	0.004	0.0009	0.002	3.88E-04	0.0014
2.5	0.0024	0.0052	0.0012	0.003	1.13E-04	0.0014
5	0.0036	0.0093	0.0018	0.0046	6.59E-05	0.0015
7.5	0.0047	0.0124	0.0025	0.0073	1.64E-05	0.0017
10	0.0063	0.0199	0.0037	0.0134	2.37E-05	0.0019

Table 7.2 – Saliency Numerical Analysis for $-10 \text{ A} \leq i_{q3}^* \leq 10$ A, f_i = 2.5 kHz, V_i = 3 V.

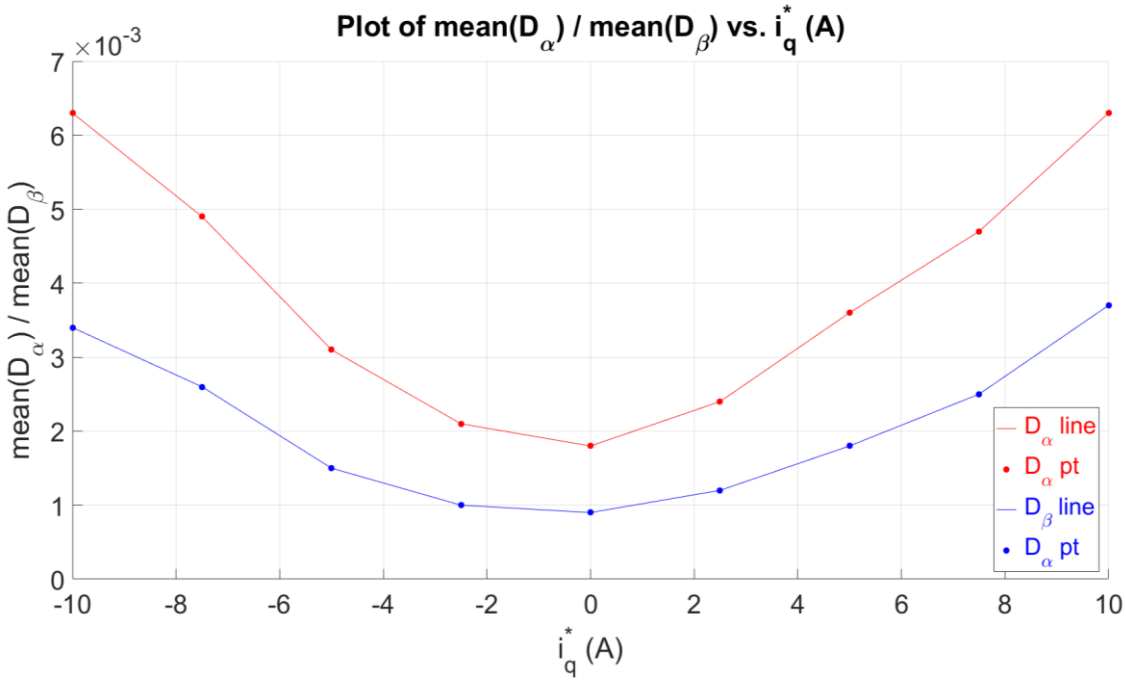

Figure 7.8 – Plot of $\overline{D_\alpha}, \overline{D_\beta}$ with $\omega_{m4}^* = 1$ rad/s on M4, $i_{d3}^* = 0$ A and -10 A ≤ i_{q3}^* ≤ 10 A on M3 during continuous pulsating injection γ=120°.

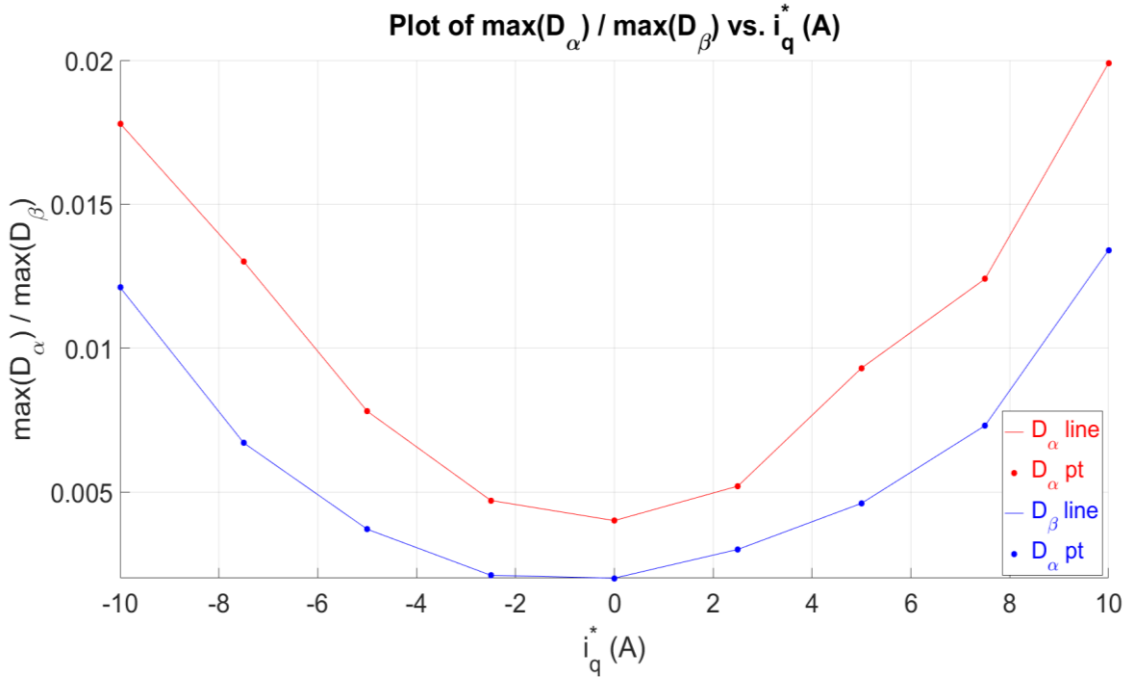

Figure 7.9 – Plot of $D_{\alpha max}, D_{\beta max}$ with $\omega_{m4}^* = 1$ rad/s on M4, $i_{d3}^* = 0$ A and -10 A ≤ i_{q3}^* ≤ 10 A on M3 during continuous pulsating injection γ=120°.

7.4 Search Based Observer with Real-time Commissioning

7.4.1 Introduction to the Sensorless Search-based Observer

The magnetic signature of the SM-PMSM under test in this dissertation was shown in Chapter 6 to have multiple saliencies which are a function of the mechanical rotor position. The use of traditional observers used with HF injection is not suitable since these typically assume a predominantly single saliency model. Although the harmonics can be compensated for through the SMP based observer, this technique was shown to have significant limitations in Section 6.5.2. These limitations include offline commissioning and additional position-dependent compensation for the mechanical domain.

In order to obtain accurate sensorless estimates from machines with magnetic signatures with high harmonic content, an innovative sensorless Search Based Observer (SBO) with Real-Time Commissioning is proposed in this dissertation. The observer is based on the comparison of real-time HF current amplitudes $A_{i\alpha}$, $A_{i\beta}$ in the αβ frame with previously-stored LUTs. The comparison produces an estimate dependent on the closest element in the LUT with respect to the instantaneous HF current measurement (equivalent to the mechanical rotor position). The SBO can also be commissioned on the experimental setup in real-time, offering the possibility of adaptive LUTs in applications where drift is expected due to time-varying parameters in the machine itself and the operating conditions. The SBO is subdivided into three distinct processes which include: commissioning, search and the speed LUT selection.

7.4.2 Commissioning Process

The commissioning process is required to generate LUTs which map the magnetic saliency signature of the SM-PMSM at varying load conditions with the mechanical rotor position. Since the saliency was observed to vary significantly with the i_q-current, the different signatures have to be mapped to their corresponding value of i_q as described in Section 6.3.7.

The commissioning process in the SBO is shown in the flowchart in Figure 7.10. When LUT commissioning is initiated the mechanical rotor position θ_m (where one revolution of the mechanical rotor position θ_m is mapped into 4095 LUT elements), the HF current amplitudes in the α axis ($A_{i\alpha}$) and in the β axis ($A_{i\beta}$) are measured at each sampling interval. The effective sampling frequency is of 5 kHz, which

is synchronized with the 2.5 kHz injection such that 2 samples are obtained at each HF injection cycle. At the first occurrence of each LUT element the value of the $A_{i\alpha}$, $A_{i\beta}$ is stored in the respective LUT element. From the second occurrence of the element onwards, the LUTs are adapted using an Infinite Impulse Response (IIR) discrete filter whose bandwidth is set through the gain G_{IIR}. The bandwidth of the filter allows filtering noise outside the natural frequency of the saliency profile and also the rate of change of adaptation of the LUTs. For the results presented in this dissertation, the IIR filter bandwidth was set to 75 Hz. In order to facilitate the commissioning, process the dataset in Section 6.3.7 was used for commissioning of the LUTs $A_{i\alpha}$_LUT, $A_{i\beta}$_LUT and processed in MATLAB. This process can also be carried out in real-time since it does not require the use of computationally intensive algorithms, as was the case for SMP table generation.

The commissioning process was carried out for V_i=3 V, f_i = 2.5 kHz, ω_{m4}^* = 1 rad/s and γ = 120°. The synchronous current reference was varied from -10 A≤ i_{q3}^* ≤ 10 A at intervals of 2.5 A. As discussed in Section 6.3.8 the saliency with respect to the mechanical rotor position is also a function of the rotational speed; hence either a calibration of additional LUTs at different speeds is required or the inclusion of the offset to compensate for the rotor speed-dependent phase shift.

7.4.3 Search Process

The estimation part of the SBO observer is shown in Figure 7.11. The search is in the form of a "for-loop" with an incremental counter *I*. The search element *J* is calculated through the multi-variable dependent function expressed in (7.10).

$$J = f_1\left(\hat{\theta}_m, I\right) = \frac{\hat{\theta}_m[n-1]\mathrm{N}}{360} + I - \frac{\mathrm{S}}{2} \tag{7.10}$$

Where

N is the total number of LUT elements in one mechanical rotor revolution,

I is the value of the "for-loop" counter which has a range from 0 to S,

S is the total number of elements to be searched.

The error between the instantaneous HF current amplitude measurements ($A_{i\alpha}$, $A_{i\beta}$) and the LUT elements ($A_{i\alpha}$_LUT, $A_{i\beta}$_LUT) are denoted as ε_α, ε_β. The vectoral sum of the errors is denoted as ε. The sensorless estimate $\hat{\theta}_m[n]$ is calculated as a function of the element *J* which has the least error ε at the end of the "for-loop" operation (J_{min}).

In sensorless estimation and control results presented in this dissertation, stable operation was achieved with a minimum of S=30 elements. The value of S does not require tuning in real-time. While a larger value of S will result in the comparison of a larger number of LUT elements, this requires a longer time to compute on the processor. If a minimum of 15 elements are searched at 2.5 kHz in each direction (S=30 elements), the detection capability of the observer is of ±15 elements every 400 µs. This translates into 3297 mechanical °/s, considering one mechanical revolution is mapped to 4095 LUT elements (N=4095).

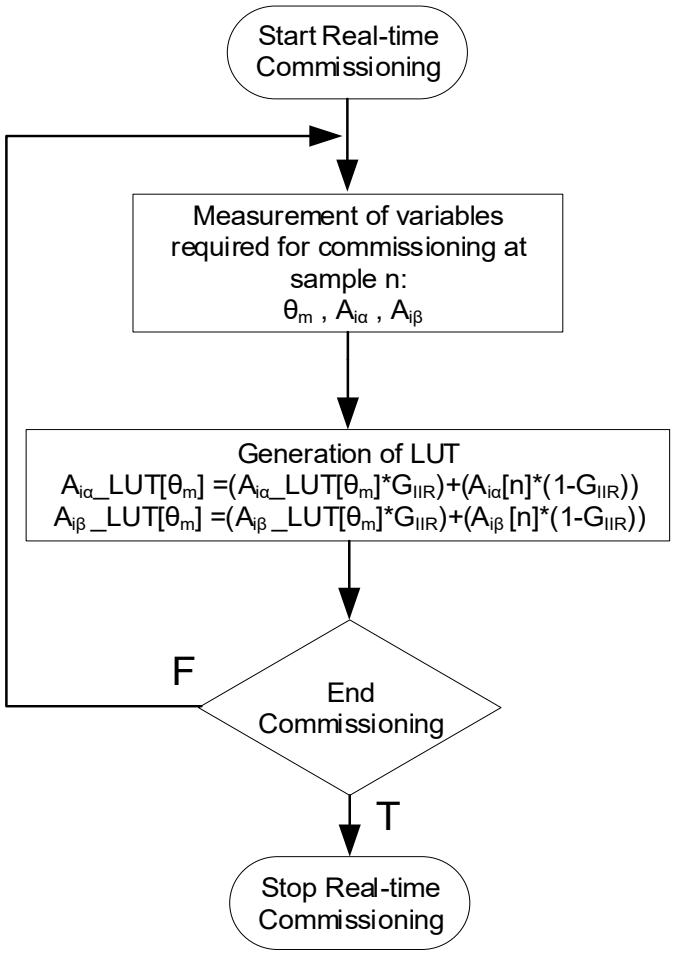

Figure 7.10 – Real-time LUT Commissioning Process

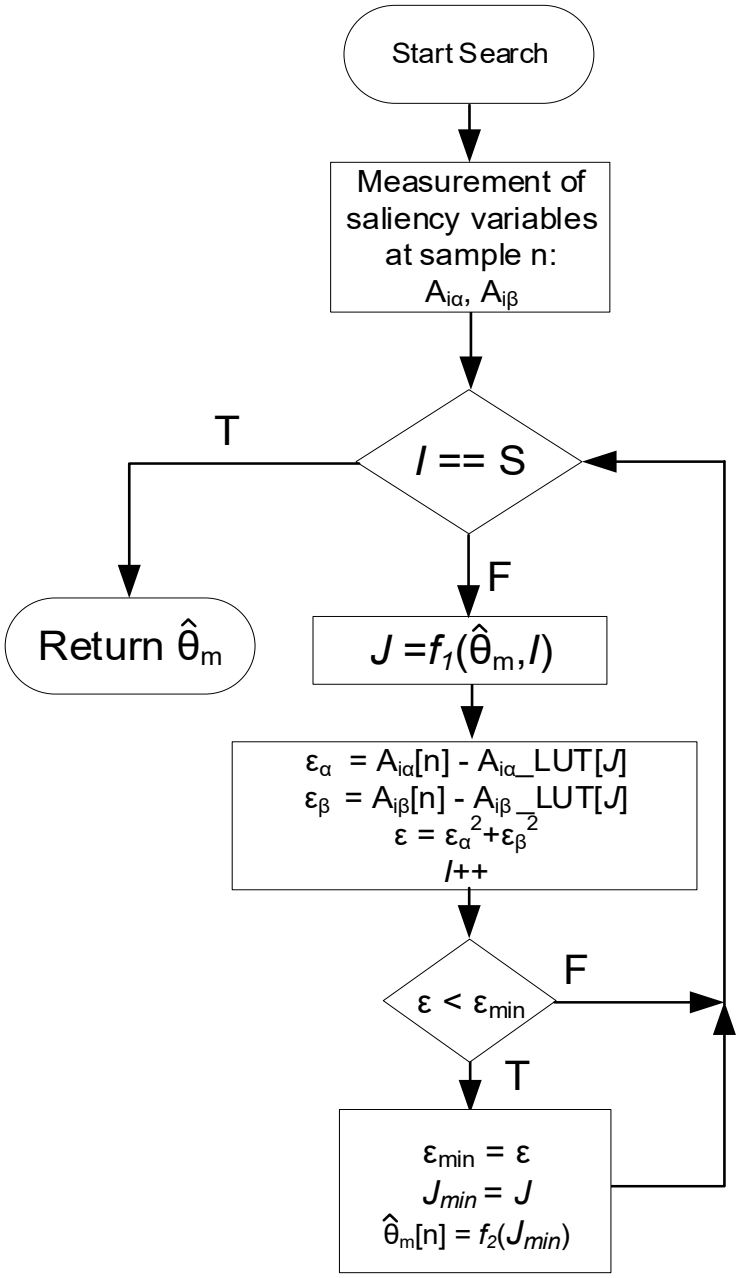

Figure 7.11 – Search Based Observer Estimation Process

The search-based method presented in this section requires the estimation error in the previous period to be within the search range S. Stability issues could arise if this is not the case. Such issues could be mitigated by increasing the search range S however this requires additional computational time to process the increased iterations within the loop. In this dissertation, stability issues where minimized by oversampling of the HF current amplitudes to eliminate erroneous ADC sample and by using the maximum search range possible S without compromising the overall microcontroller performance.

7.4.4 Speed LUT Selection PLL

In Chapter 6, the magnetic signature was shown to vary with both the i_q-current and the rotor speed. Although the saliency variation for different rotor speeds at no load was shown in Section 6.3.8 to be in the form of a phase shift, a significant amplitude distortion was noted for higher loading currents. Hence LUTs were calibrated for both forward and reverse rotations resulting in a four-quadrant LUT table with the following quadrants:

I. Positive i_q, Forward ω_m
II. Negative i_q, Forward ω_m
III. Positive i_q, Negative ω_m
IV. Negative i_q, Negative ω_m

Since the variation in the zero-speed region for different speeds was found to be minor, calibration at 1 rad/s (9.5 rpm) for forward rotation and -1 rad/s (-9.5 rpm) for reverse rotation was found to be sufficient for sensorless control in the designated range of operation in this dissertation. Possibly improved sensorless performance can be obtained by commissioning at different values of rotor speeds rather than a single point for forward and reverse rotation. Since an estimated rotor speed is required for LUT quadrant selection, a conventional quadrature Phase-Locked Loop (PLL) [29] shown in Figure 7.12 is used to calculate $\hat{\omega}_{mf\_SBO}$.

The error term *e* of the PLL is given in (7.11-7.12). For small values of *e* in (7.12), the error can be assumed to be linear such that the PI controller regulates *e* to zero. The PLL closed-loop system was designed to have a bandwidth of 1.13 Hz (K_{p_PLL3} = 50, K_{i_PLL3} = 300). The selection of such a low bandwidth was possible since this PLL (PLL3) was only used to select the LUT to be used in the SBO and the estimates are not used within the current/speed control loops. Measurements for these loops are generated from an additional PLL with higher closed-loop bandwidth.

$$e = \sin\hat{\theta}_m \cos\hat{\theta}_{mf} - \cos\hat{\theta}_m \sin\hat{\theta}_{mf} \tag{7.11}$$

$$e = \sin\left(\hat{\theta}_m - \hat{\theta}_{mf}\right) \tag{7.12}$$

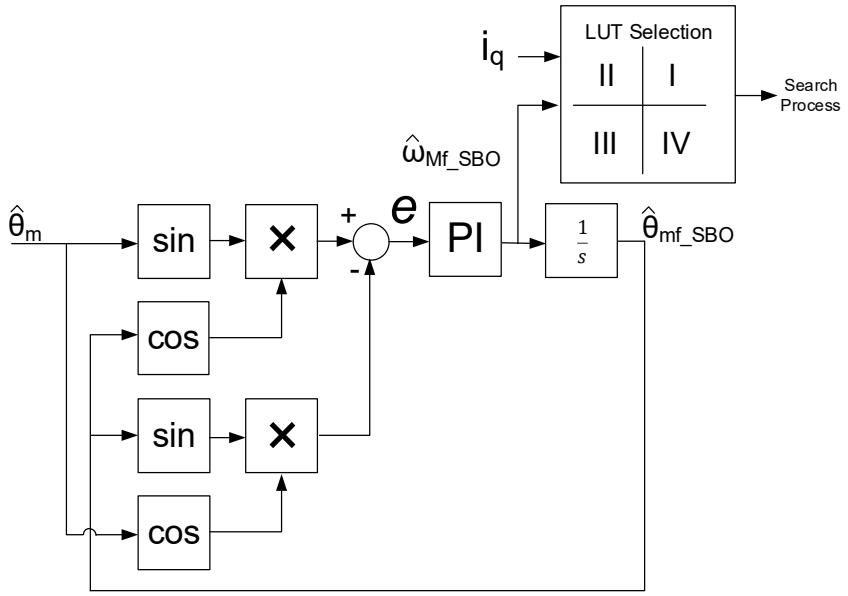

Figure 7.12 – PLL Based direction detection for LUT selection

7.5 Position and Speed Filtering for RFO Control

The RFO control of the PMSM requires various measurements as discussed in Chapter 3, mainly the three-phase stator currents (i_a, i_b, i_c) and the electrical rotor position (θ_e) for current control, the mechanical rotor speed (ω_m) for speed control, and the mechanical rotor position (θ_m) for position control. In sensorless mode, the position/speed measurements typically obtained for a dedicated sensor are to be obtained from a sensorless observer. In the low-speed range operation designated in this dissertation, the proposed SBO observer was found to produce satisfactory results when appropriate filtering is applied.

The position/speed measurements are obtained from the filtering topology shown in Figure 7.13. The topology shows the filtering applied in both sensored/sensorless modes. In sensored operation, the actual position measurement θ_m is obtained from a 12-bit digital encoder mounted on the rotor shaft as described in Section 5.2. Due to the limited discrete resolution of the encoder, a PLL (PLL1) was used to filter the encoder data and produce filtered measurements for the rotor position θ_{mf} and the rotor speed ω_{mf}. The controller gains of PLL1 were set in firmware to be $K_{p\_PLL1} = 30$ and $K_{i\_PLL1} = 5000$ for a designed bandwidth of 11.33 Hz. The main reason why PLL1 was used is in order to obtain a speed measurement with a suitable Signal-to-Noise Ratio (SNR). The rotor

speed could be obtained from the differentiation of the rotor position measurement; however, this results in a low SNR since the measurements are discretized. The electrical rotor position estimate used for sensored operation is obtained by multiplying θ_{mf} by the number of pole pairs on the machine (p=6).

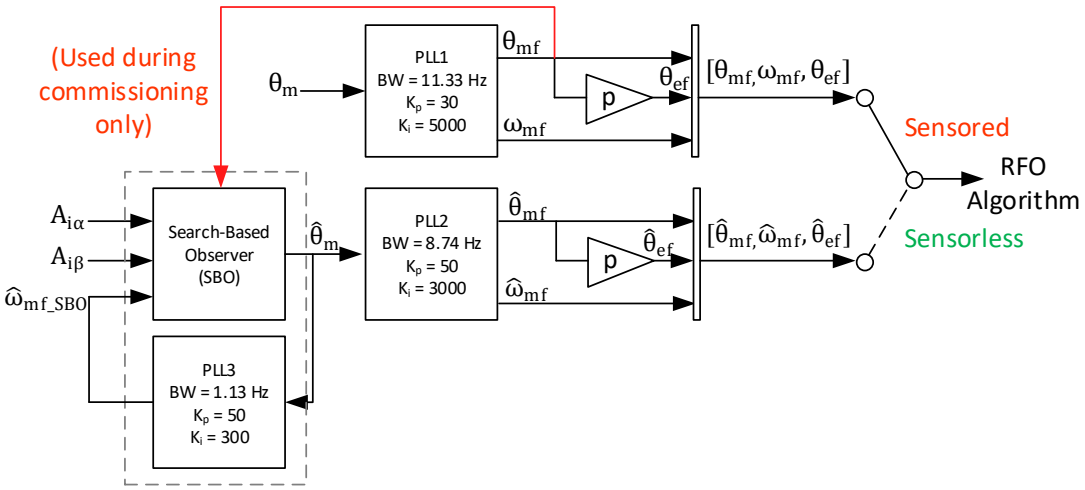

Figure 7.13 – Position and Speed Filtering Topology for Sensored/Sensorless Operation

The sensorless measurements are obtained from the SBO observer proposed in Section 7.4. The observer requires the HF current amplitudes $A_{i\alpha}$, $A_{i\beta}$ and also a filtered speed measurement $\hat{\omega}_{mf\_SBO}$ for the LUT selection (Section 7.4.4). The PLL used for the calculation of $\hat{\omega}_{mf\_SBO}$ (PLL3) has a low bandwidth of 1.13 Hz set through the controller gains $K_{p\_PLL3} = 50$, $K_{i\_PLL3} = 300$ on the microcontroller. The results of the PLL3 are only used for LUT selection to compensate for the variation of the magnetic signature with speed and not for the sensorless RFO control.

The sensorless observer outputs the estimated mechanical rotor position $\hat{\theta}_m$ from the search-based process. This estimate is discretized and requires filtering through another PLL (PLL2). In order to attenuate the discretization from the search process and transient estimation error, the bandwidth of PLL2 was set to 8.74 Hz by setting the controller gains on the microcontroller to $K_{p\_PLL2} = 50$, $K_{i\_PLL2} = 3000$. PLL2 operates in a similar way to PLL1 with only different controller gains. Hence, a single PLL could be used with adaptive gains; however, this would require a seamless transition between sensored and sensorless operation. It was found that more robust sensorless control was achieved with having two parallel paths, as shown in Figure 7.13 on the microcontroller. The required sensored or sensorless operation is simply chosen through a simple switch mechanism embedded in the microcontroller firmware.

7.6 Summary

This chapter mainly analyses the suitability of the magnetic signatures at different operating points with respect to sensorless control and SBO for sensorless estimation from HF current amplitudes. Gradient and deviation criteria were defined in Section 7.2 to differentiate between magnetic signatures at different injection angles γ. From the research carried out in this dissertation, it was found that the most suitable injection angle from the numerical analysis changes with the i_q-current of the machine. Although the magnetic signature was also found to be speed dependent the most suitable injected angle γ from the numerical analysis was not found to change for a limited speed range close to zero speed. Due to time constraints associated with mapping, the magnetic signature at γ=120° was used throughout the range of loading operating points of the machine. While the performance of the SBO at this injection angle was found to be stable for a wide range of operating points possible improvements could be obtained in the sensorless estimates if the injection angle is adapted to the optimum value during real-time operation following further investigation.

The SBO sub-processes were presented in Sections 7.4.2 – 7.4.4 and shown to be suitable for sensorless estimation in magnetic signatures with strong harmonic saliencies in the HF currents $A_{i\alpha}$, $A_{i\beta}$. While the observer can be used in highly distorted saliencies, the sensorless estimates tend to improve as the magnetic signature approximates that of the ideal single saliency machine due to more constant sensitivity along the various rotor positions. For the sensorless control experiments in this dissertation commissioning of LUTs in four quadrants was carried out (Section 7.4.4) in order to have a more detailed map of the magnetic signature.

The filtering of the various position/speed measurements in both sensored and sensorless operation as implemented in microcontroller firmware is shown in Section 7.5. Various PLL structures at different bandwidths are used for the different states in the RFO control algorithm. Sensorless current and position/speed control for various current/speed operating points using the proposed architecture in this chapter are presented in Chapters 8 and 9 respectively.

Chapter 8 – Sensorless Current Control Results

8.1 Introduction

The *dq*-frame current control loops within the RFO vector control structure are the inner cascaded loops required for speed and control applications. Since the current controllers require a transformation from the stationary frame to the *dq*-synchronous frame, an accurate estimate for the electrical rotor position is required for stable sensorless operation. In this chapter, the sensorless operation of the machine M3 on the experimental setup described in Section 5.2 is investigated in all four quadrants of operation. A search range of S=30 elements was used for all experimental results with the SBO observer proposed in this dissertation in Section 7.4.

8.2 Sensorless Current Control with Constant Forward Speed and Variable Load

The Search-Based Observer (SBO) was tested in sensorless current control, where the estimated electrical rotor position on machine M3 is used for RFO control. The speed of the drive is set to a reference value ω_{m4}^{*} = 1 rad/s by a sensored machine M4 in RFO speed-controlled mode, as shown in Figure 5.1. The SBO observer settings are as described in Section 7.4 (S=30 elements, K_{p_PLLB} = 50, K_{i_PLLB} = 300*)*. For successful sensorless implementation, the current controller gains were set to K_{p_I4} = 0.1 and K_{i_I4} = 100.

The actual/estimated ***mechanical*** rotor positions are shown in Figure 8.1 with a changeover to sensorless control at t=5.2 s. The error in the estimated mechanical rotor

position is shown in Figure 8.2, with the maximum absolute error being 2.55° and the Root Mean Square Error (RMSE) 0.63°. The actual/estimated ***electrical*** rotor position is shown in Figure 8.3. The mechanical rotor speed of the drive and the varying synchronous i_q-current are shown in Figures 8.4 – 8.5 respectively. The HF current amplitudes $A_{i\alpha}$, $A_{i\beta}$ are shown as a function of time in Figure 8.6 and as a function of the mechanical rotor position in Figure 8.7. The actual HF current amplitude measurements with respect to the commissioned LUTs can be observed in Figure 8.7.

The bandwidth of the current controllers was found experimentally to be 85.57 Hz from Figure 8.5 (b) which is less than for the sensored operation which was found to be 281 Hz in Section 3.4. The overshoot for the current control operation was found to be 6.7 % compared to 57.4 % for sensored operation. The reduction in bandwidth is a result of the reduced controller gains. This was required such that current controllers do not interfere with the signal injection at 2.5 kHz, as this would affect the instantaneous saliencies $A_{i\alpha}$, $A_{i\beta}$. Since the saliency differs significantly with i_q-current the reduction in the overshoot also limits the shifting between the different LUT elements. The bandwidth of the current controller could be possibly increased to that observed in sensored operation by increasing the injection frequency so as to minimize interference between the fundamental control and the open-loop injection. At a higher injection frequency, the impedance will be increased, and therefore a higher DC voltage will be required to keep the same HF current amplitudes required for a satisfactory Signal-to-Noise Ratio (SNR). Sampling at higher frequencies also requires improved ADC hardware and additional microcontroller processing power for running the algorithms with a faster cycle frequency. The sensorless current controller settings proposed have resulted in satisfactory operation when cascaded within the speed and position loops in this dissertation.

The changeover from sensored to sensorless current control on the Surface Mounted Permanent Magnet Synchronous Machines (SM-PMSM) under test occurs with stable operation throughout the period shown. As can be observed from the error between the actual/estimated positions, the SBO tracks both mechanical and electrical rotor positions without any drift with time. The synchronous frame current i_{q3} was successfully varied from 10 A (+100 % load) to -10 A (-100 % load). The variation in saliency as a result of the different loading points in the machine was also mapped to the corresponding LUTs resulting in stable sensorless operation for the different load operating points.

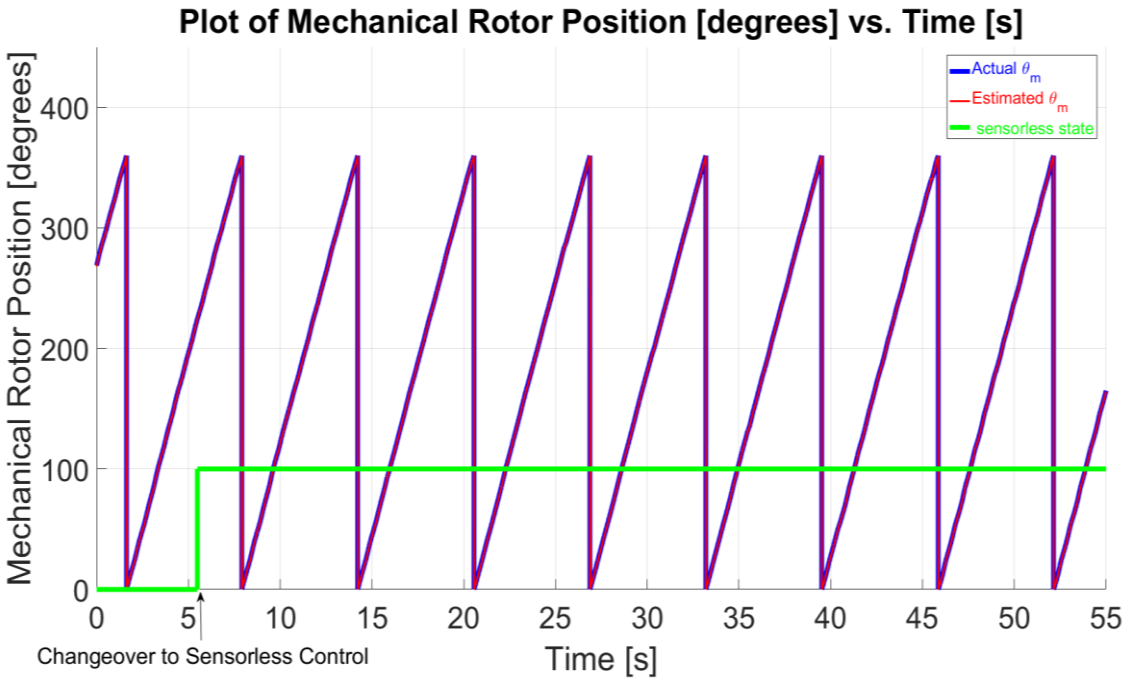

Figure 8.1 – Plot of Actual/Estimated Mechanical Rotor Position θ_m [°] vs. Time [s] with $\omega_{m4}^* = 1$ rad/s on M4, $i_{d3}^* = 0$ A and -10 A $\leq i_{q3}^* \leq$ 10 A in closed-loop sensorless current control.

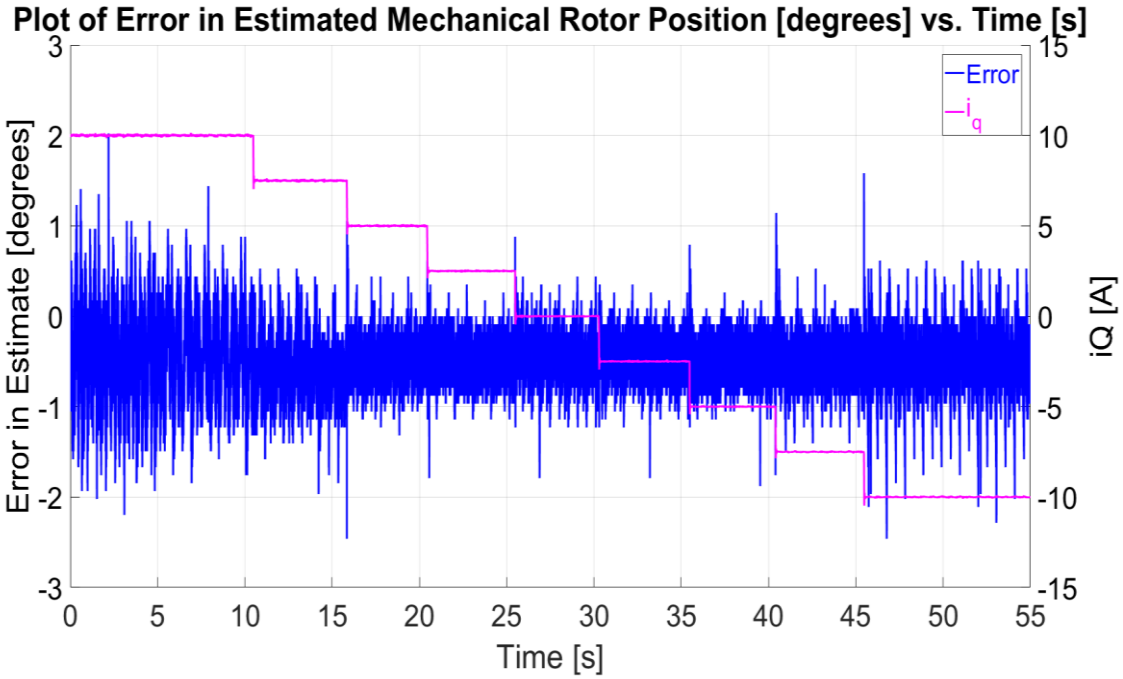

Figure 8.2 – Plot of Error in Estimated Mechanical Rotor Position θ_m [°] vs. Time [s] with $\omega_{m4}^* = 1$ rad/s on M4, $i_{d3}^* = 0$ A and -10 A $\leq i_{q3}^* \leq$ 10 A in closed-loop sensorless current control.

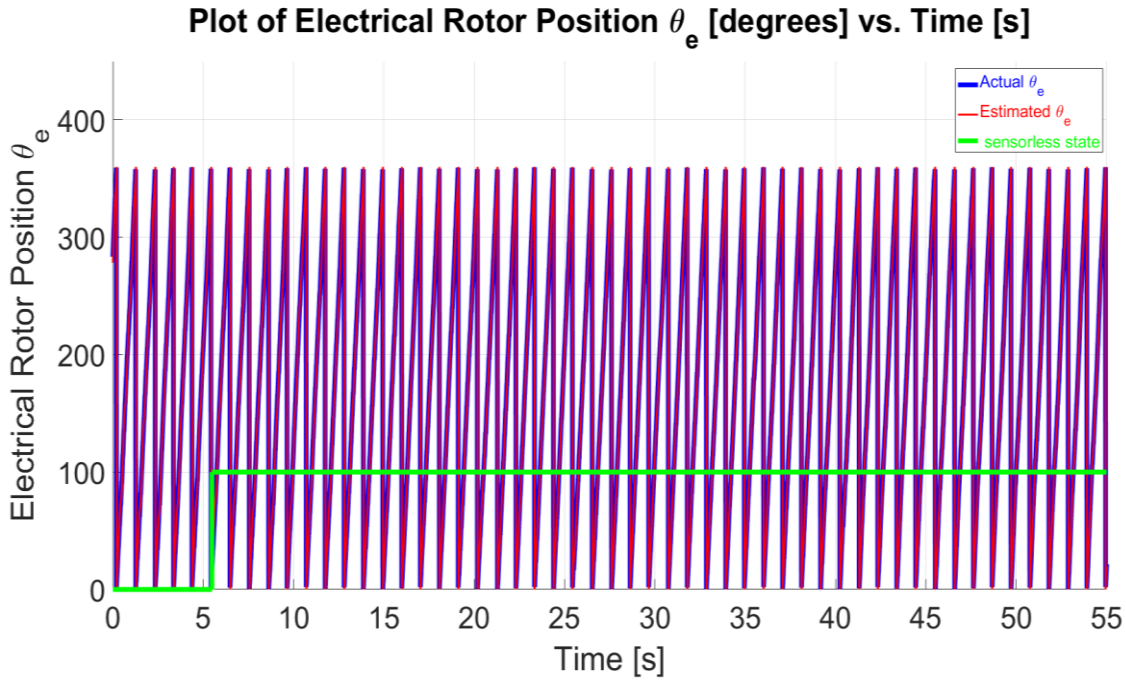

Figure 8.3 – Plot of Actual/Estimated Electrical Rotor Position θ_e [°] vs. Time [s] with $\omega_{m4}^* = 1$ rad/s on M4, $i_{d3}^* = 0$ A and -10 A $\leq i_{q3}^* \leq$ 10 A in closed-loop sensorless current control.

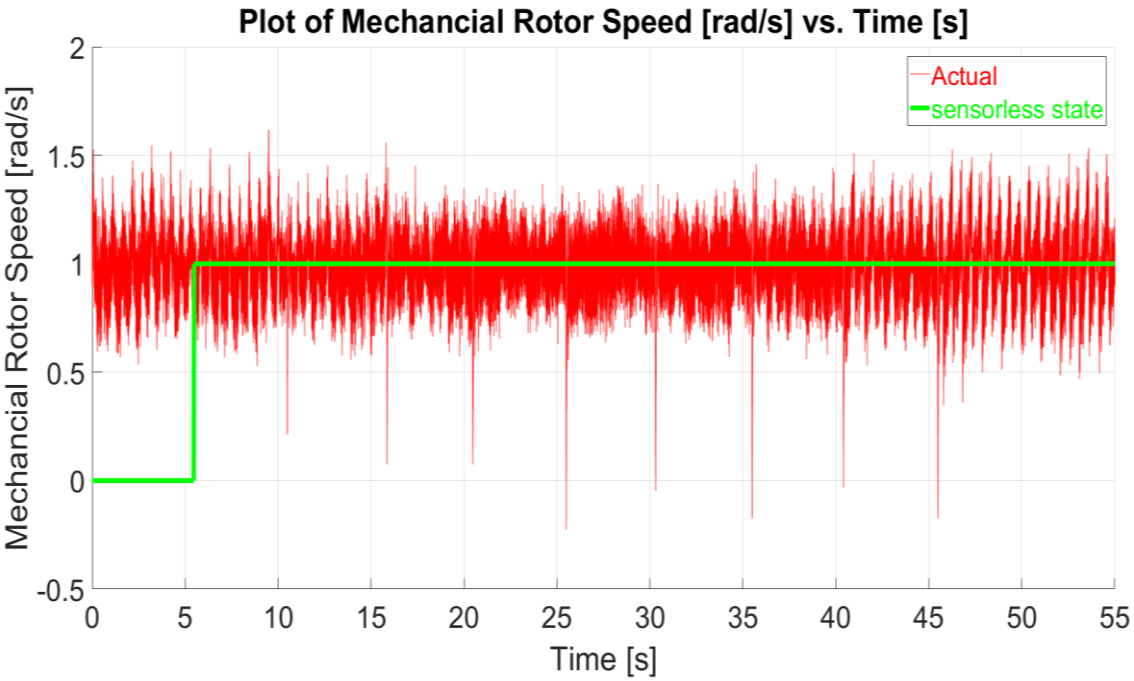

Figure 8.4 – Plot of Actual Rotor Speed ω_m [°] vs. Time [s] with $\omega_{m4}^* = 1$ rad/s on M4, $i_{d3}^* = 0$ A and -10 A$\leq i_{q3}^* \leq$ 10 A in closed-loop sensorless current control.

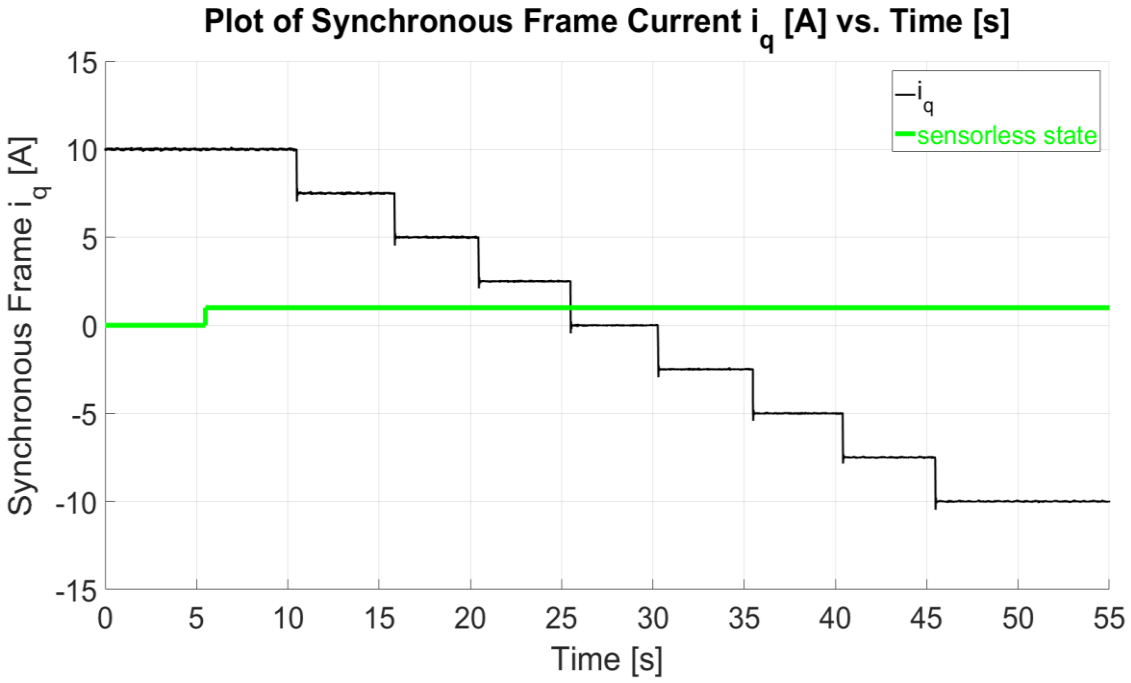

Figure 8.5 (a) – Plot of Synchronous Frame Current i_q [°] vs. Time [s] with $\omega_{m4}^* = 1$ rad/s on M4, $i_{d3}^* = 0$ A and -10 A ≤ i_{q3}^* ≤ 10 A in closed-loop sensorless current control.

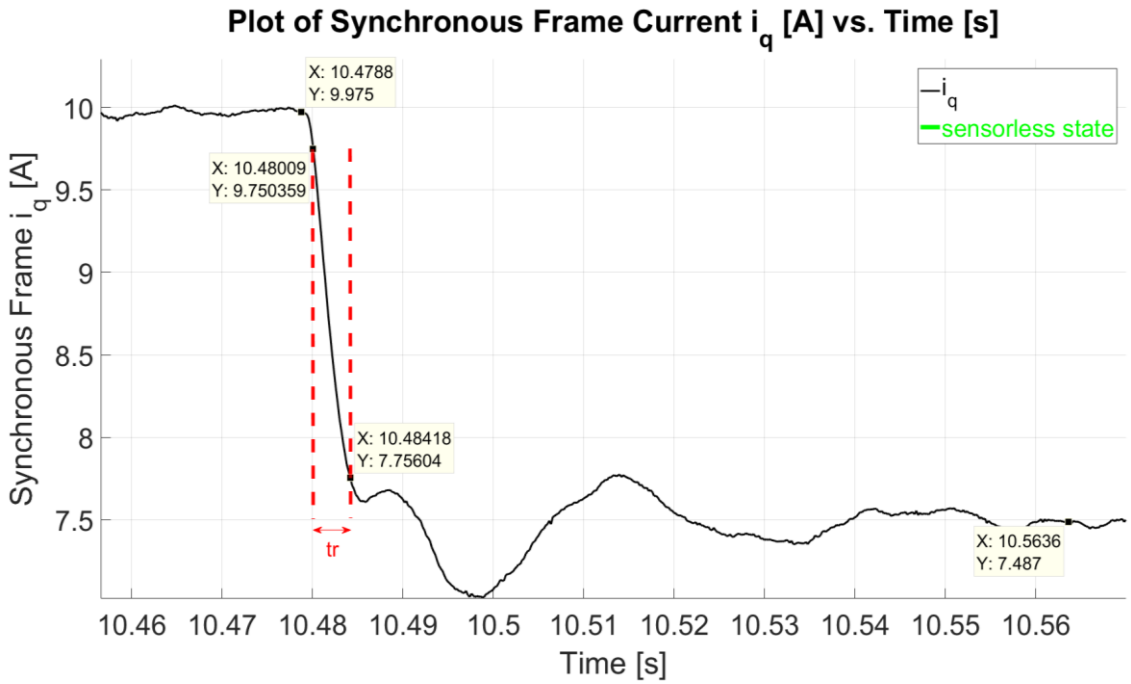

Figure 8.5 (b) – Plot of Synchronous Frame Current i_q [°] vs. Time [s] with $\omega_{m4}^* = 1$ rad/s on M4, $i_{d3}^* = 0$ A and -10 A≤ i_{q3}^* ≤ 10 A in closed-loop sensorless current control zoomed in at transient from 10 A to 7.5 A.

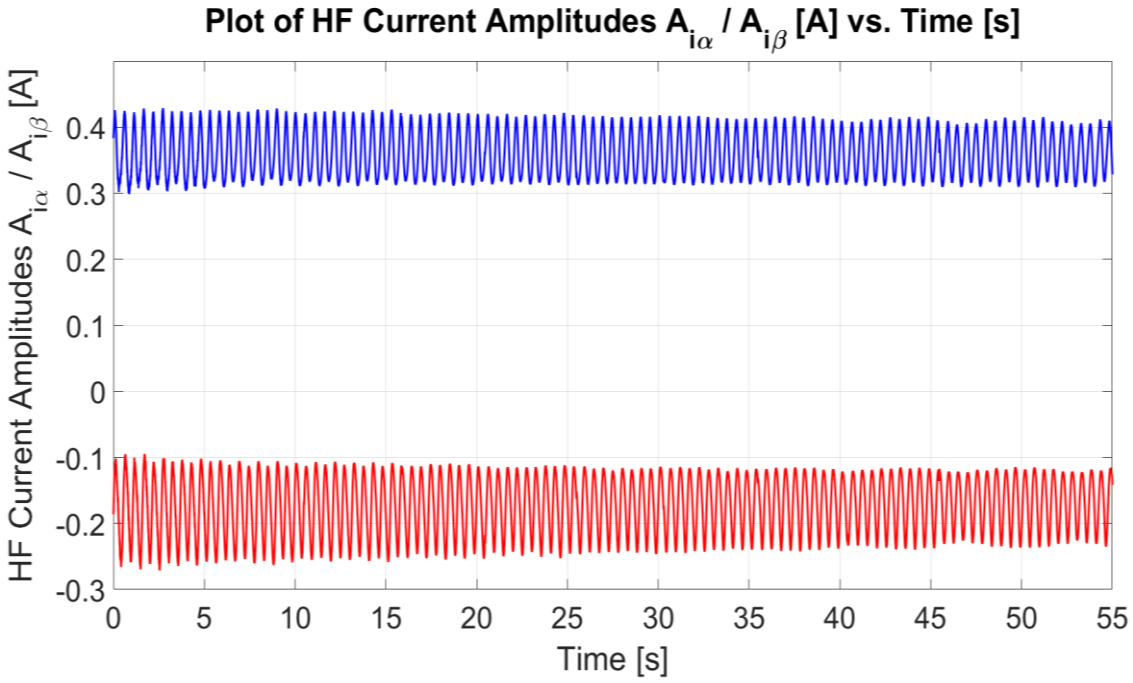

Figure 8.6 –Plot of HF Current Amplitudes $A_{i\alpha}$, $A_{i\beta}$ [A] vs. Time [s] with $\omega_{m4}^{*} = 1$ rad/s on M4, $i_{d3}^{*} = 0$ A and -10 A$\leq i_{q3}^{*} \leq 10$ A in closed-loop sensorless current control.

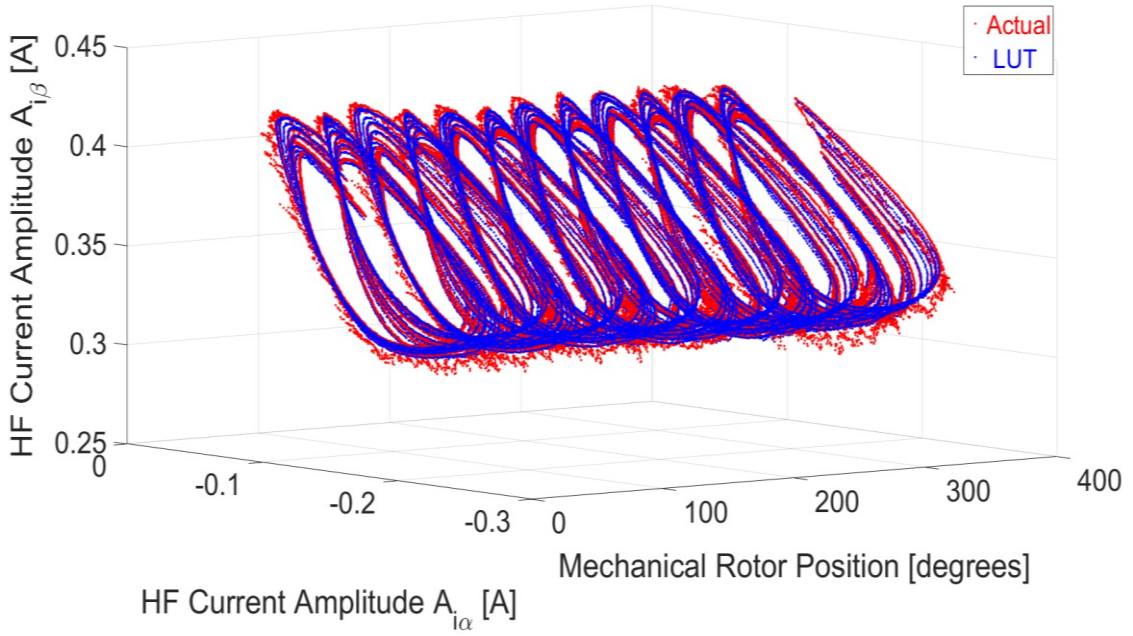

Figure 8.7 (a) – Three-Dimensional Plot of HF Current Amplitudes $A_{i\alpha}$ [A] , $A_{i\beta}$ [A] , θ_m [°] with $\omega_{m4}^{*} = 1$ rad/s on M2, $i_{d3}^{*} = 0$ A and -10 A$\leq i_{q3}^{*} \leq 10$ A in closed-loop sensorless current control.

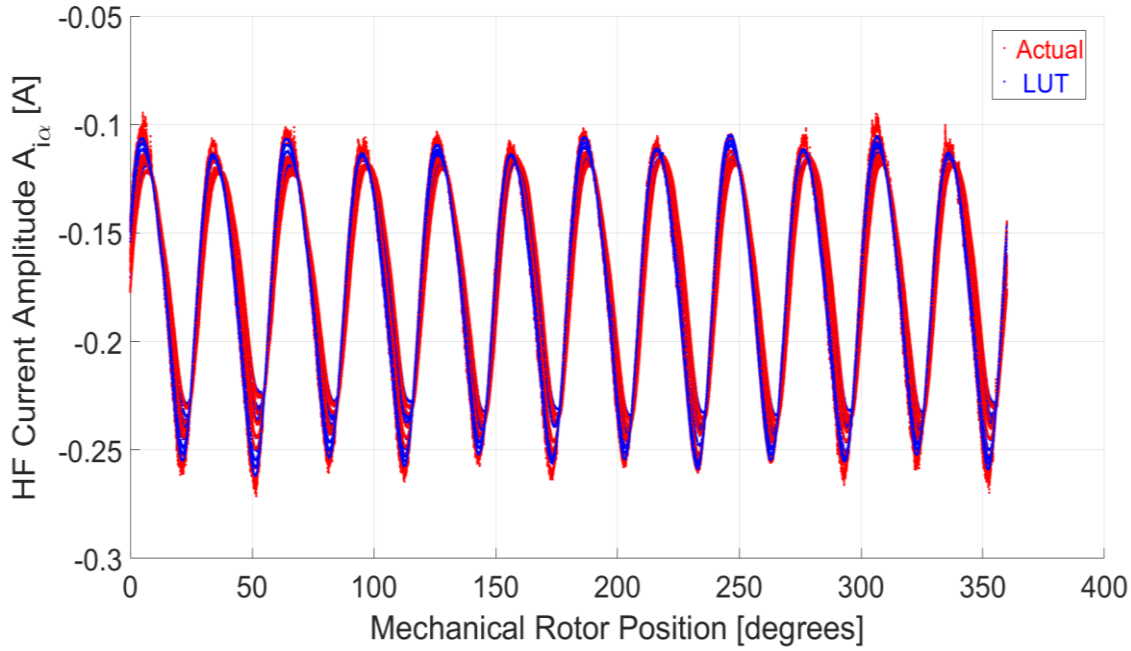

Figure 8.7 (b) –Plot of HF Current Amplitude $A_{i\alpha}$ [A] vs. θ_m [°] with $\omega_{m4}^* = 1$ rad/s on M4, $i_{d3}^* = 0$ A and -10 A$\leq i_{q3}^* \leq$ 10 A in closed-loop sensorless current control.

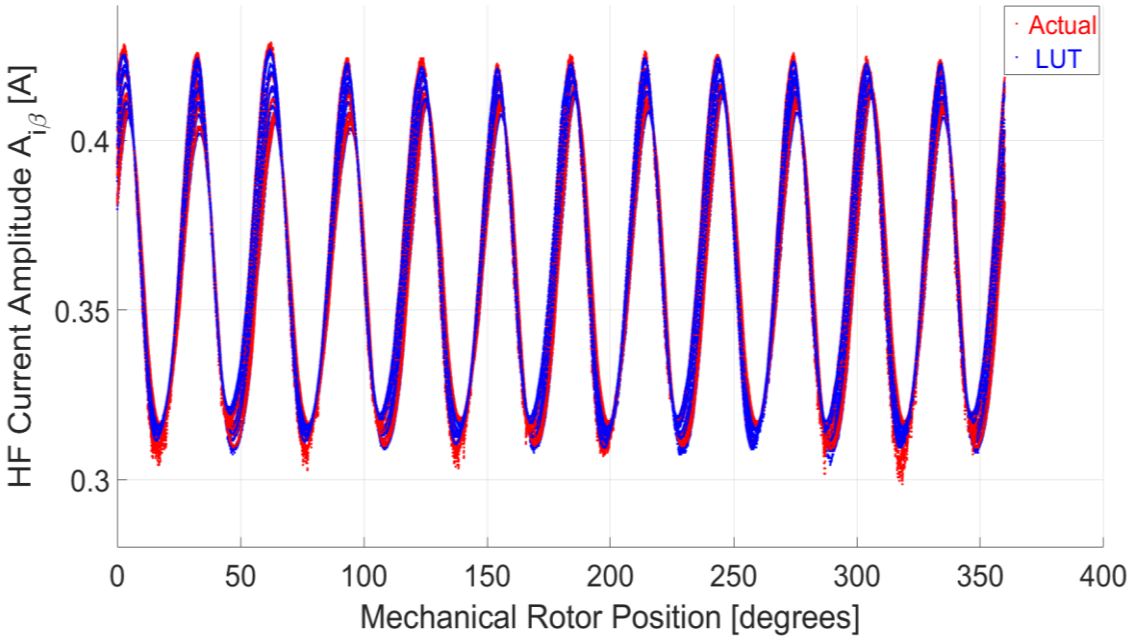

Figure 8.7 (c) –Plot of HF Current Amplitude $A_{i\beta}$ [A] vs. θ_m [°] with $\omega_{m4}^* = 1$ rad/s on M4, $i_{d3}^* = 0$ A and -10 A$\leq i_{q3}^* \leq$ 10 A in closed-loop sensorless current control.

8.3 Sensorless Current Control with Constant Reverse Speed and Variable Load

The SBO observer was tested in similar conditions to those in Section 8.2, but with the speed of the drive set to a reference value, ω_{m4}^{*} = -1 rad/s by the sensored machine M4. The SBO settings and sensorless current controller settings on machine M3 are identical to those indicated in Section 8.2.

The actual/estimated ***mechanical*** rotor positions are shown in Figure 8.8 with a changeover to sensorless control at t=5.2 s. The error in the estimated mechanical rotor position is shown in Figure 8.9, with the maximum absolute error being 2.90° and the RMSE 0.65°. The actual/estimated ***electrical*** rotor positions are shown in Figure 8.10. The mechanical rotor speed of the drive and the varying synchronous current i_{q3} are shown in Figures 8.11 – 8.12 respectively. The HF current amplitudes $A_{i\alpha}$, $A_{i\beta}$ are shown in Figures 8.13 as a function of time. The actual HF current amplitude superimposed on the commissioned LUTs can be observed in Figure 8.14 as a function of the mechanical rotor position.

From this test, it was observed that the changeover from sensored to sensorless current control on the SM-PMSM machine occurs with stable operation throughout the period shown. The results show seamless changeover from sensored to sensorless current control for the SM-PMSM, followed by continuous stable operation in sensorless control throughout the results. The synchronous frame current i_{q3} was varied from 10 A (+100 % load) to -10 A (-100 % load). It can be observed that the SBO tracks both mechanical and electrical rotor positions without any drift in the error between the actual/estimated positions.

The results which are shown in Sections 8.2 – 8.3 demonstrate successful sensorless current control in all four quadrants of operation at rated load. The SBO sensorless method is capable of providing robust position estimates during operation at constant rotor speed. In the next sections, 8.3 and 8.4, similar experimental results for sensorless current control whilst varying the speed at constant load shall be presented.

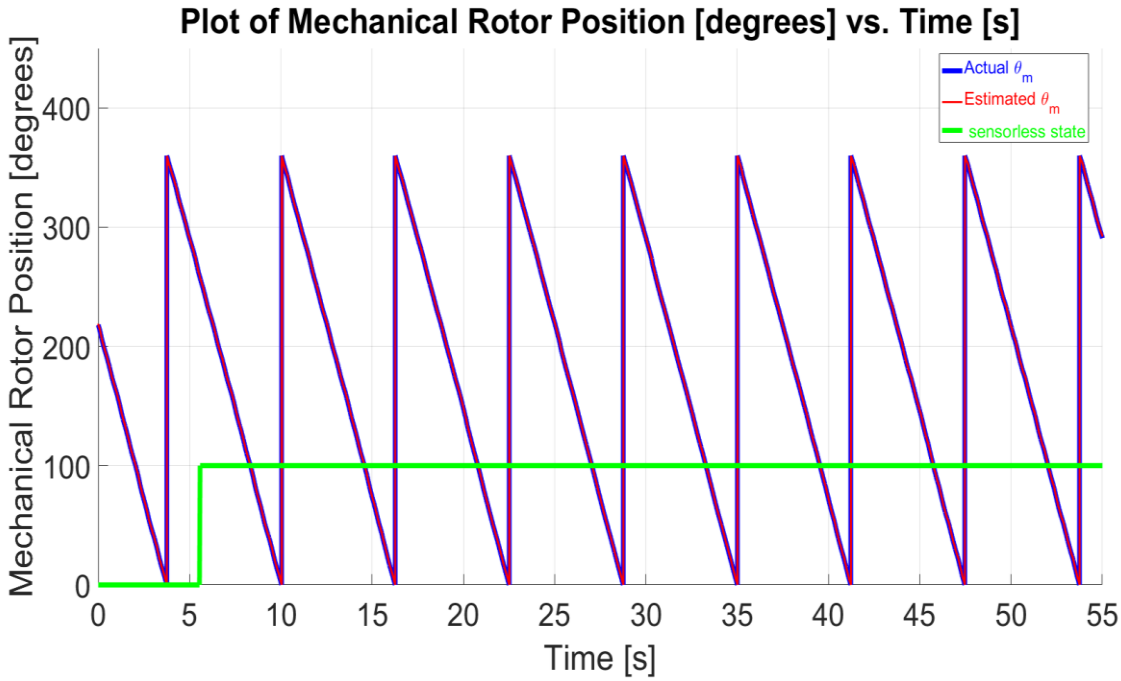

Figure 8.8 – Plot of Actual/Estimated Mechanical Rotor Position θ_m [°] vs. Time [s] with $\omega_{m4}^* = -1$ rad/s on M4, $i_{d3}^* = 0$ A and $-10\ A \leq i_{q3}^* \leq 10$ A in closed-loop sensorless current control.

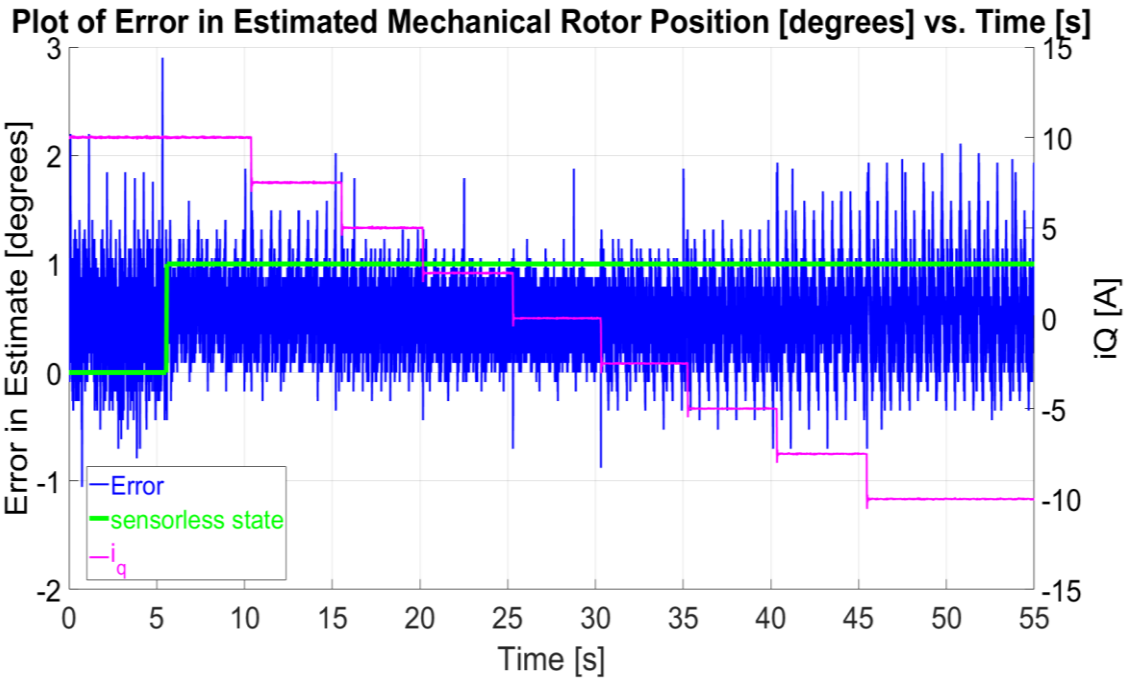

Figure 8.9 – Plot of Error in Estimated Mechanical Rotor Position θ_m [°] vs. Time [s] with $\omega_{m4}^* = -1$ rad/s on M4, $i_{d3}^* = 0$ A and $-10\ A \leq i_{q3}^* \leq 10$ A in closed-loop sensorless current control.

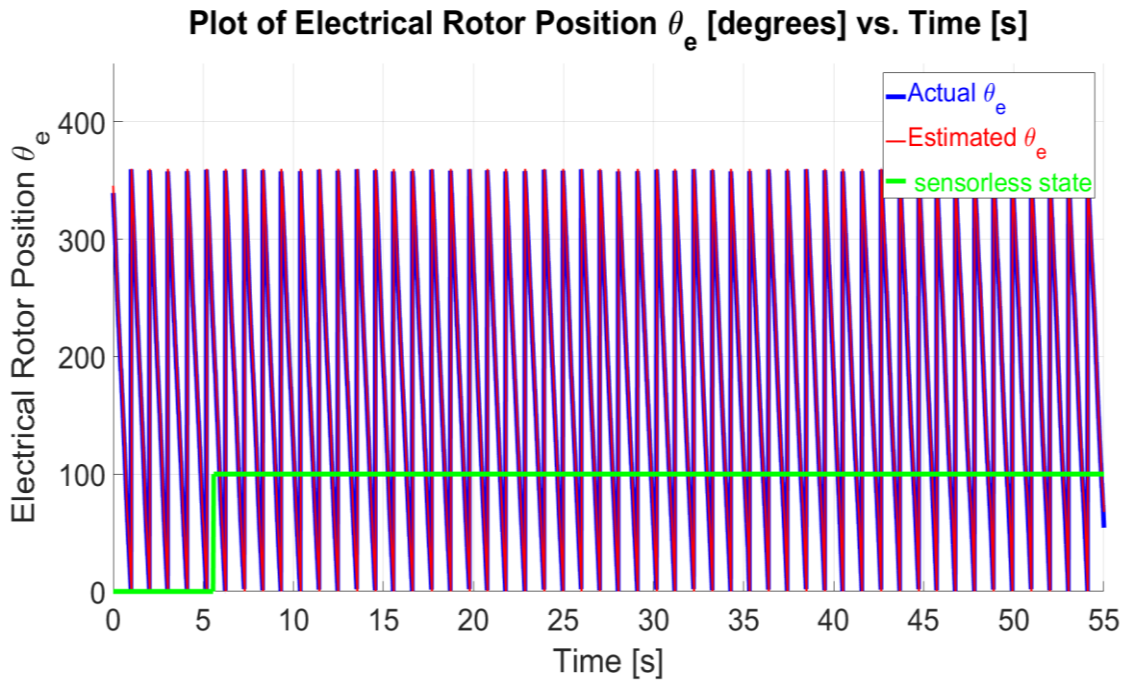

Figure 8.10 – Plot of Actual/Estimated Electrical Rotor Position θ_e [°] vs. Time [s] with $\omega_m^* = -1$ rad/s on M4, $i_{d3}^* = 0$ A and -10 A$\leq i_{q3}^* \leq$ 10 A in closed-loop sensorless current control.

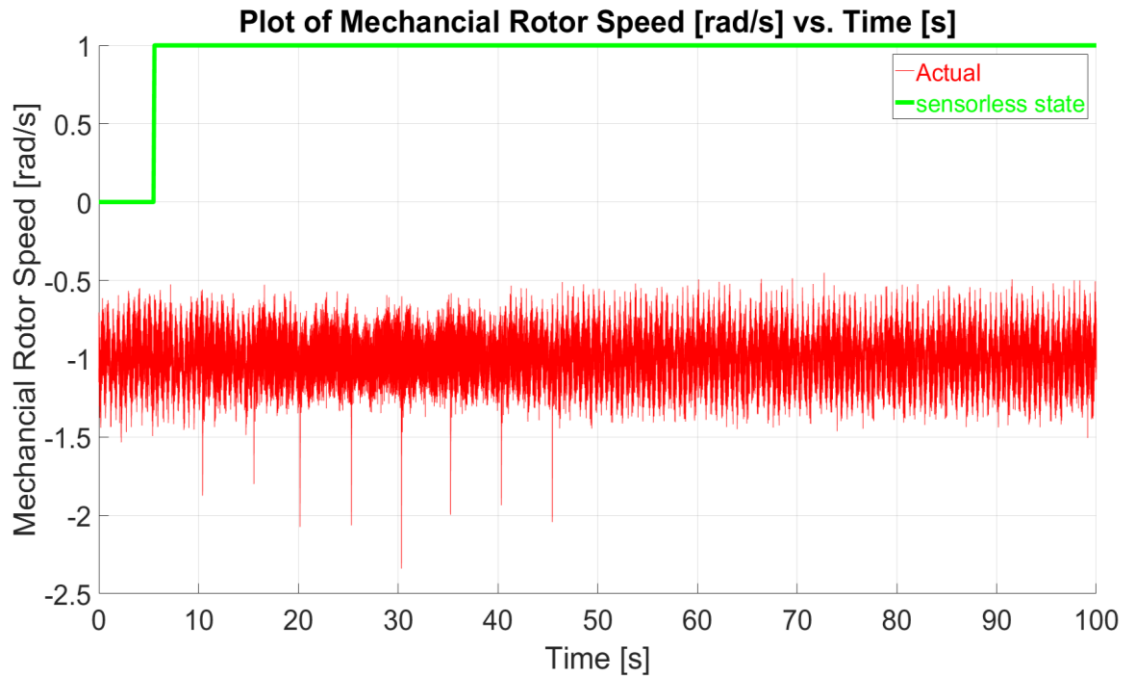

Figure 8.11 – Plot of Actual Rotor Speed ω_m [°] vs. Time [s] with $\omega_{m4}^* = -1$ rad/s on M4, $i_{d3}^* = 0$ A and -10 A$\leq i_{q3}^* \leq$ 10 A in closed-loop sensorless current control.

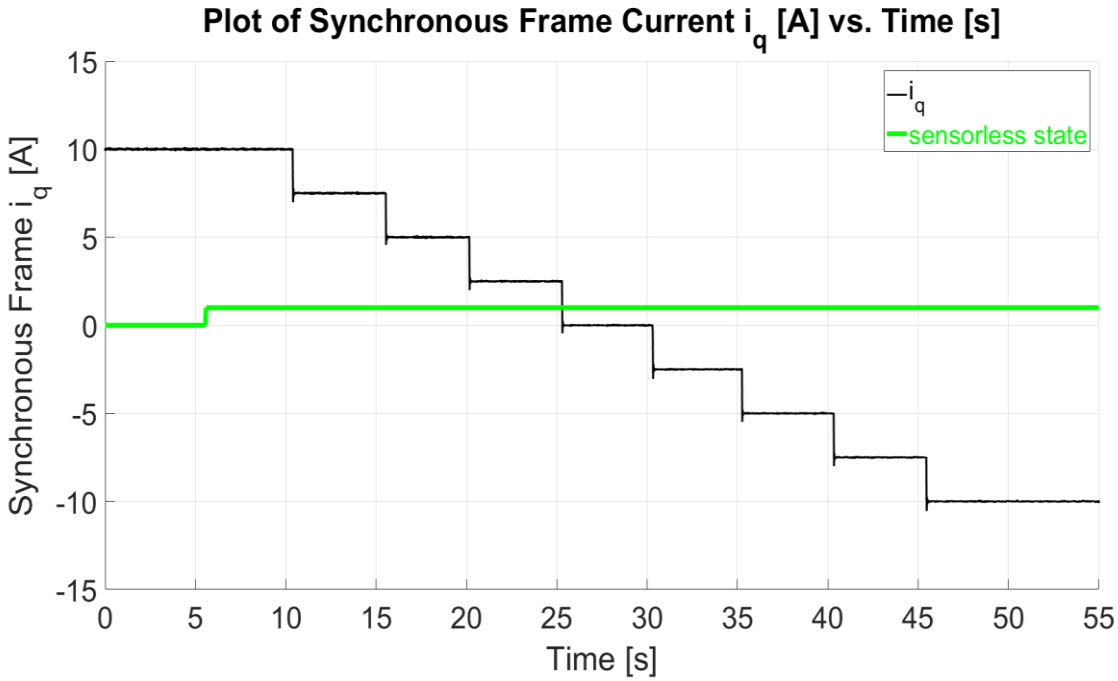

Figure 8.12 – Plot of Synchronous Frame Current i_q [°] vs. Time [s] with $\omega_{m4}^* = -1$ rad/s on M4, $i_{d3}^* = 0$ A and -10 A$\leq i_{q3}^* \leq 10$ A in closed-loop sensorless current control.

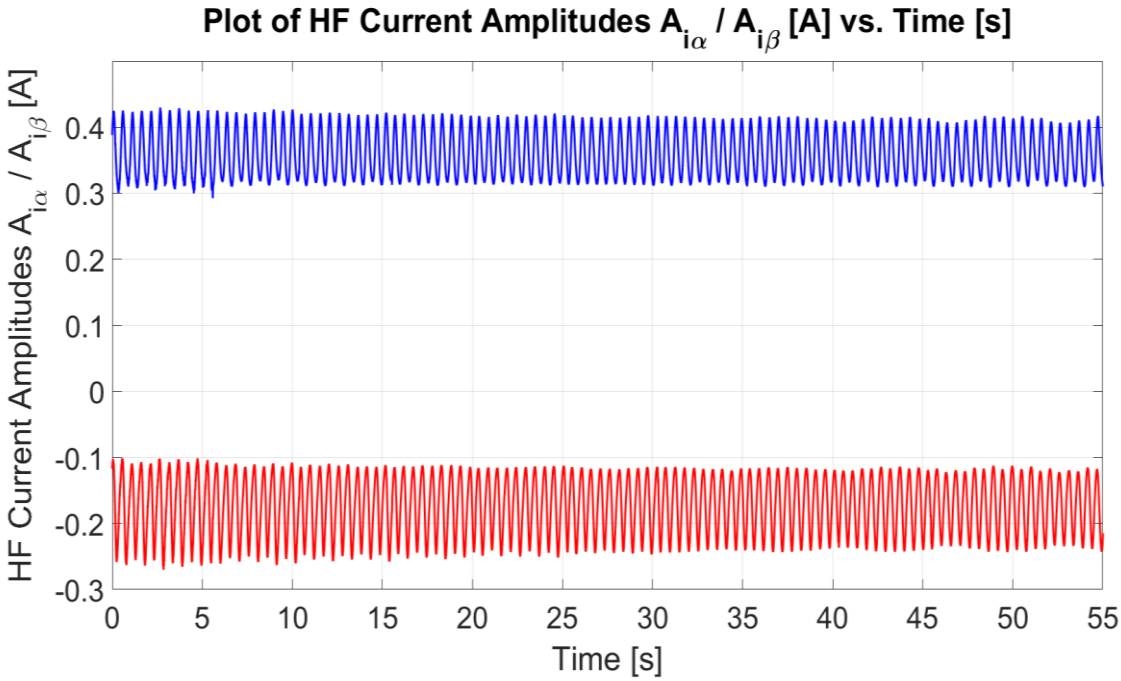

Figure 8.13 –Plot of HF Current Amplitudes $A_{i\alpha}$ / $A_{i\beta}$ [A] vs. Time [s] with $\omega_{m4}^* = -1$ rad/s on M4, $i_{d3}^* = 0$ A and -10 A$\leq i_{q3}^* \leq 10$ A in closed-loop sensorless current control.

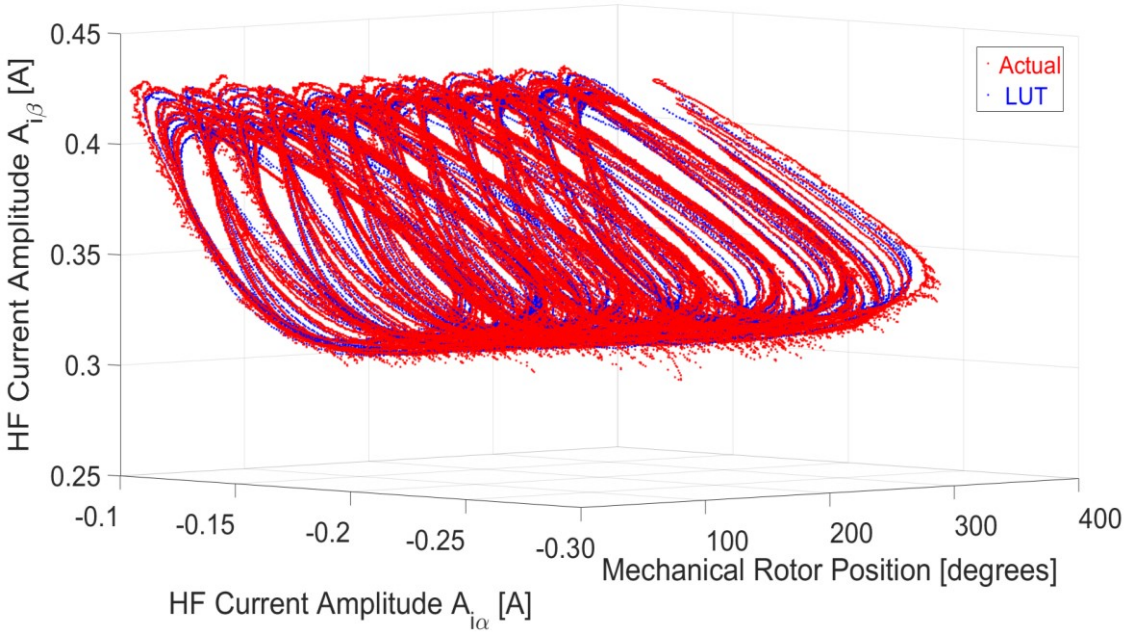

Figure 8.14 (a) – Three-Dimensional Plot of HF Current Amplitudes $A_{i\alpha}$ [A], $A_{i\beta}$ [A], θ_m [°] with $\omega_{m4}^* = 1$ rad/s on M4, $i_{d3}^* = 0$ A and -10 A$\leq i_{q3}^* \leq$ 10 A in closed-loop sensorless current control.

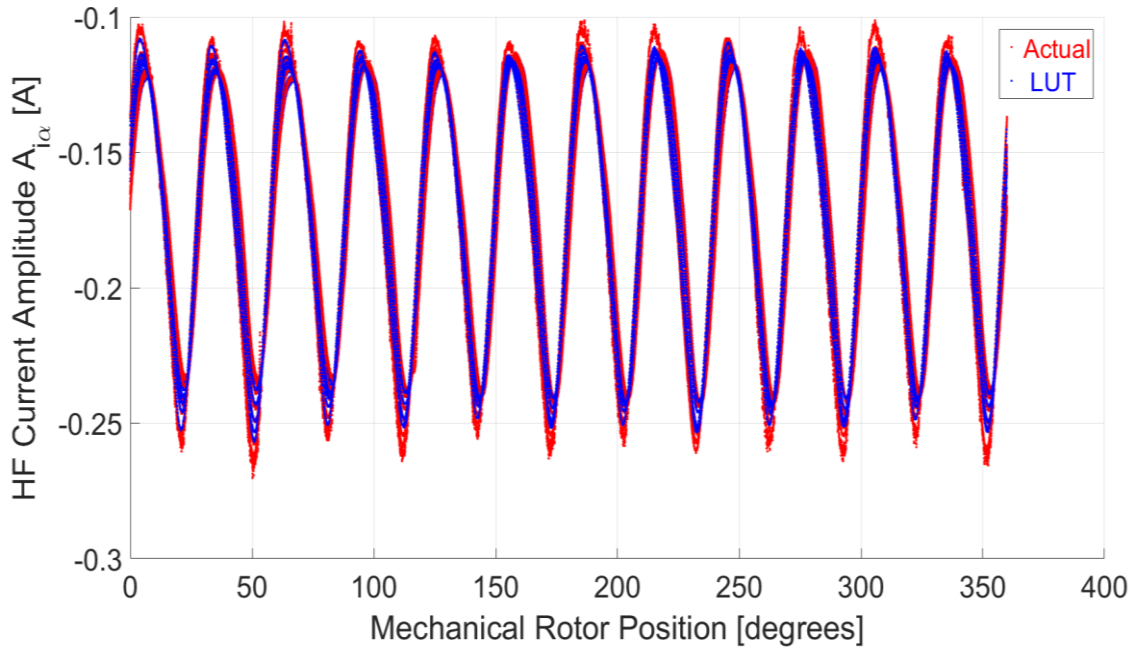

Figure 8.14 (b) –Plot of HF Current Amplitude $A_{i\alpha}$ [A] vs. θ_m [°] with $\omega_{m4}^* = 1$ rad/s on M4, $i_{d3}^* = 0$ A and -10 A$\leq i_{q3}^* \leq$ 10 A in closed-loop sensorless current control.

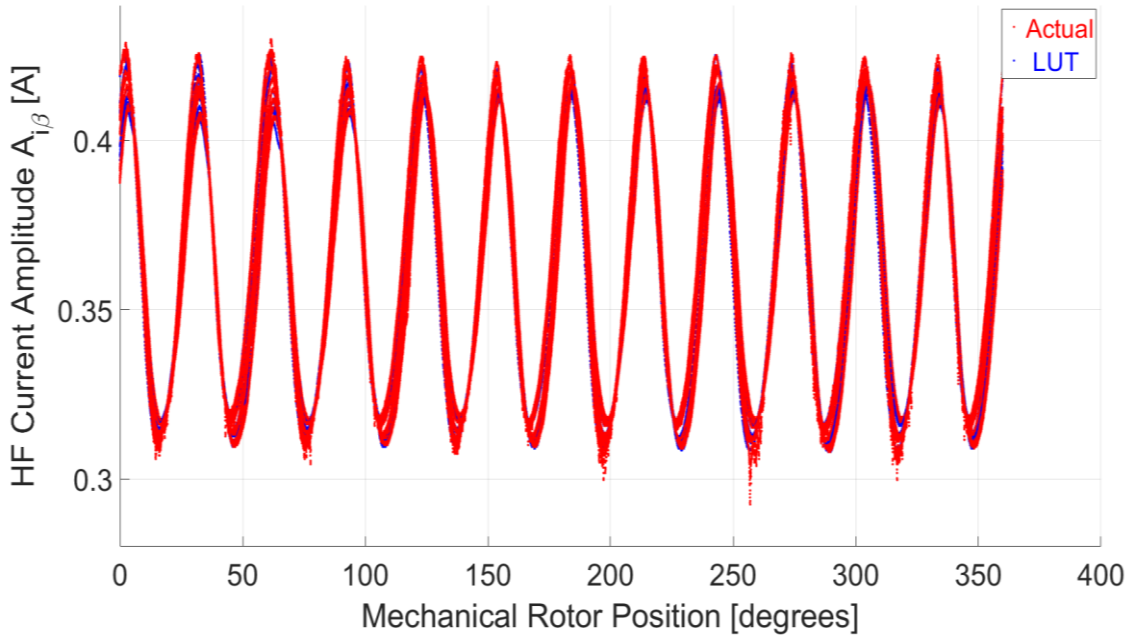

Figure 8.14 (c) –Plot of HF Current Amplitude $A_{i\alpha}$ [A] vs. θ_m [°] with $\omega_{m4}^* = 1$ rad/s on M4, $i_{d3}^* = 0$ A and -10 A ≤ i_{q3}^* ≤ 10 A in closed-loop sensorless current control.

8.4 Sensorless Current Control for Forward/Reverse Speed Operation and Constant Forward Torque

The SBO observer was tested at a speed of ω_{m4}^* = -1 rad/s (-9.5 rpm, -1.6 % rated), 0 rad/s and 1 rad/s (9.5 rpm, 1.6 % rated) controlled by the sensored machine M4 operating in RFO speed-controlled mode. The synchronous i_q-current of the sensorless machine under test, M3, was set to i_{q3}^*=10 A (100 % load). The actual/estimated ***mechanical*** rotor positions are shown in Figure 8.15 with a changeover to sensorless control at t = 6.5 s. The error in the estimated mechanical rotor position is shown in Figure 8.16, with the maximum absolute error being 2.99° and the RMSE 0.61°. The actual/estimated ***electrical*** rotor positions are shown in Figure 8.17. The mechanical rotor speed of the drive and the constant synchronous i_q-current are shown in Figures 8.18 – 8.19 respectively. The HF current amplitudes $A_{i\alpha}$, $A_{i\beta}$ are shown in Figure 8.20 as a function of time. The actual HF current amplitude measurements superimposed on the commissioned LUTs with respect to the mechanical rotor position can be observed in Figure 8.21 as a function of the mechanical rotor position.

Figure 8.16 shows how the DC offset and magnitude of the error of the mechanical rotor position estimation varies at -1 rad/s, zero speed, and 1 rad/s. The operation of the system in sensorless current control mode is still stable due to the four-quadrant LUT commissioning; however, the error tends to increase when operating in a region that was not explicitly calibrated for.

The error in the electrical rotor position is a scaled version of the error shown in Figure 8.16 multiplied by the number of pole pairs (p=6). Hence the maximum absolute error in the electrical rotor position is 18° with a RMSE of 3.66°. The error in the electrical rotor position should be kept as low as possible, as a higher error translates into a lower electromechanical torque per unit ampere drawn. While the RMSE indicates the overall validity of the proposed observer, potential issues could arise during transients of i_q at which the maximum error typically occurs. Possible ways to reduce the maximum error are to reduce the current controller bandwidth or commission the LUT at an increased number of intervals for the current i_q. The error in the estimates also depends on the number of elements searched (S=30 elements for the results shown).

For low-bandwidth systems reducing the search range could reduce the estimation error as the search is carried out within closer proximity of the previous estimate. For higher-bandwidth systems increasing the search range reduces the probability of having a position change outside the search capability of the observer. While modifying the search range could result in a lower error and an overall more stable system, the search range S=30 provided stable response within the full current operating range of the PMSM -10 A $\leq i_q \leq$ 10 A with the minimum number of elements.

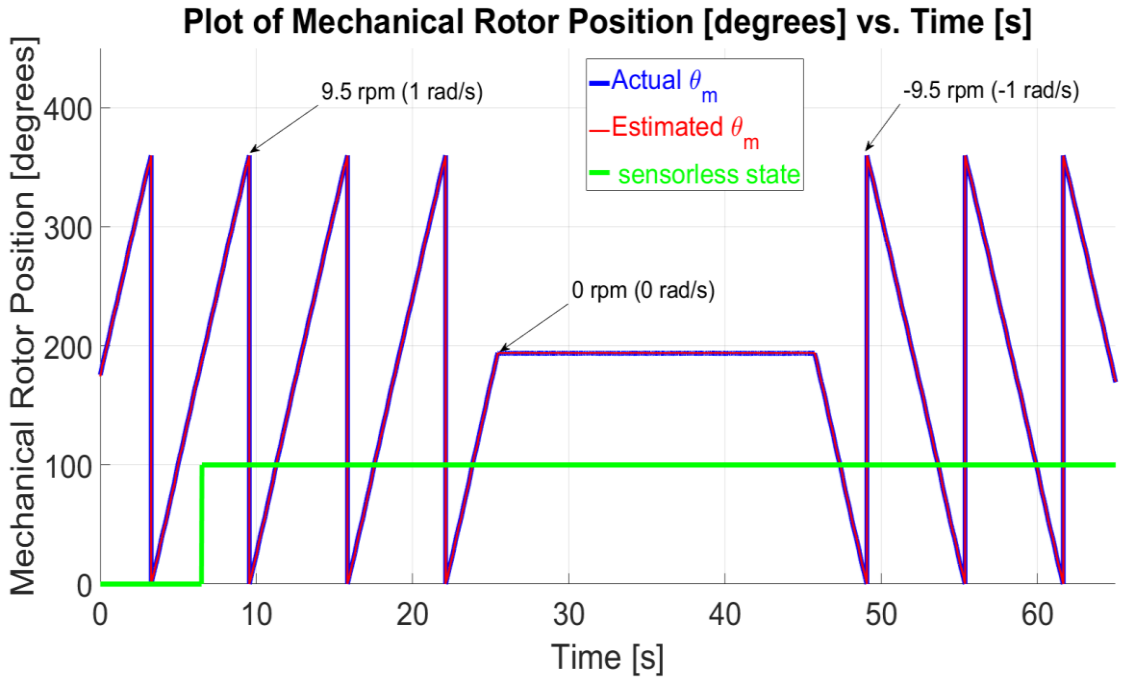

Figure 8.15 – Plot of Actual/Estimated Mechanical Rotor Position θ_m [°] vs. Time [s] with $\omega_{m4}^* = -1 / 0 / 1$ rad/s on M4, $i_{d3}^* = 0$ A and $i_{q3}^* = 10$ A in closed-loop sensorless current control.

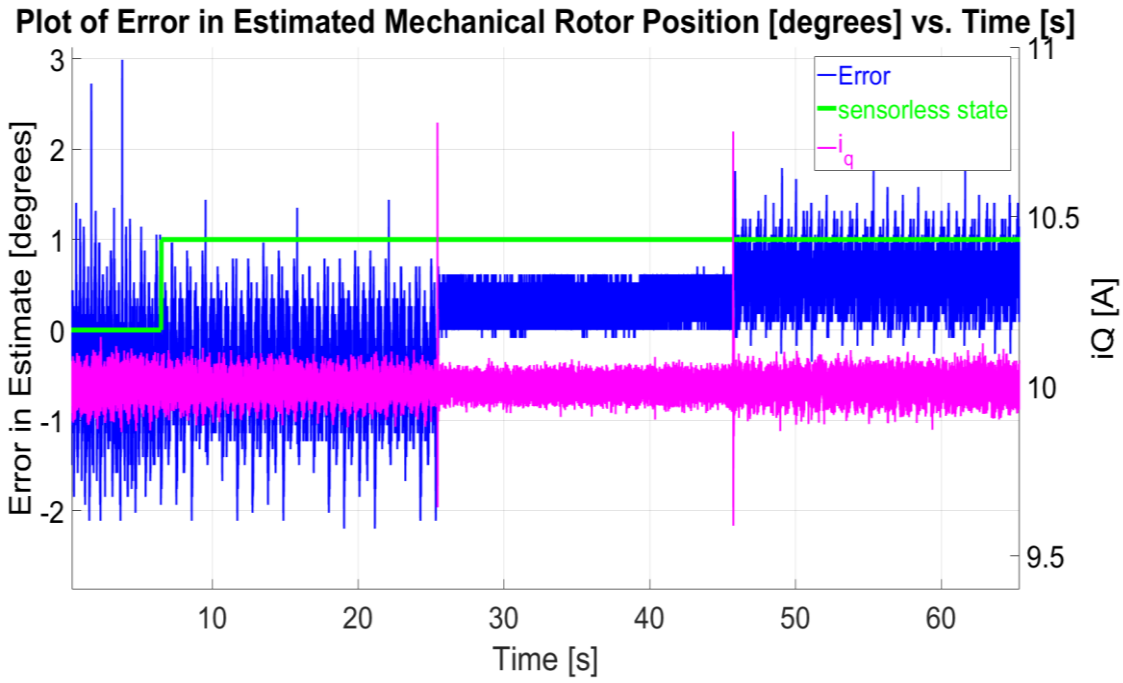

Figure 8.16 – Plot of Error in Estimated Mechanical Rotor Position θ_m [°] vs. Time [s] with $\omega_{m4}^* = -1 / 0 / 1$ rad/s on M4, $i_{d3}^* = 0$ A and $i_{q3}^* = 10$ A in closed-loop sensorless current control.

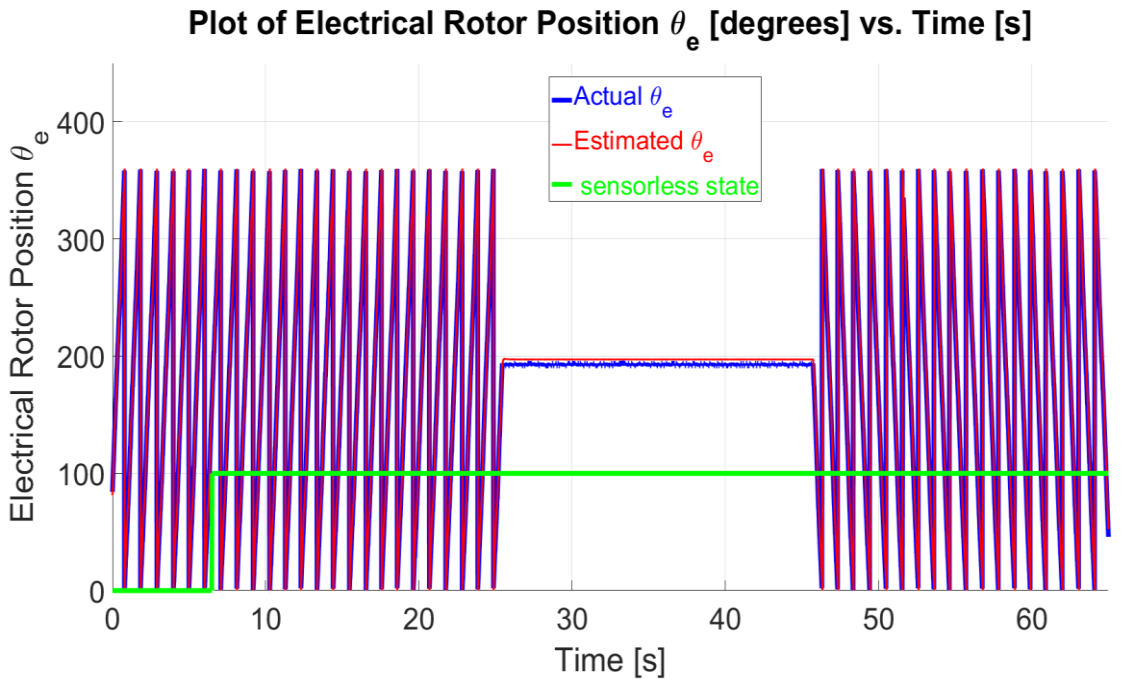

Figure 8.17 – Plot of Actual/Estimated Electrical Rotor Position θ_e [°] vs. Time [s] with $\omega_{m4}^* = -1 / 0 / 1$ rad/s on M4, $i_{d3}^* = 0$ A and $i_{q3}^* = 10$ A in closed-loop sensorless current control.

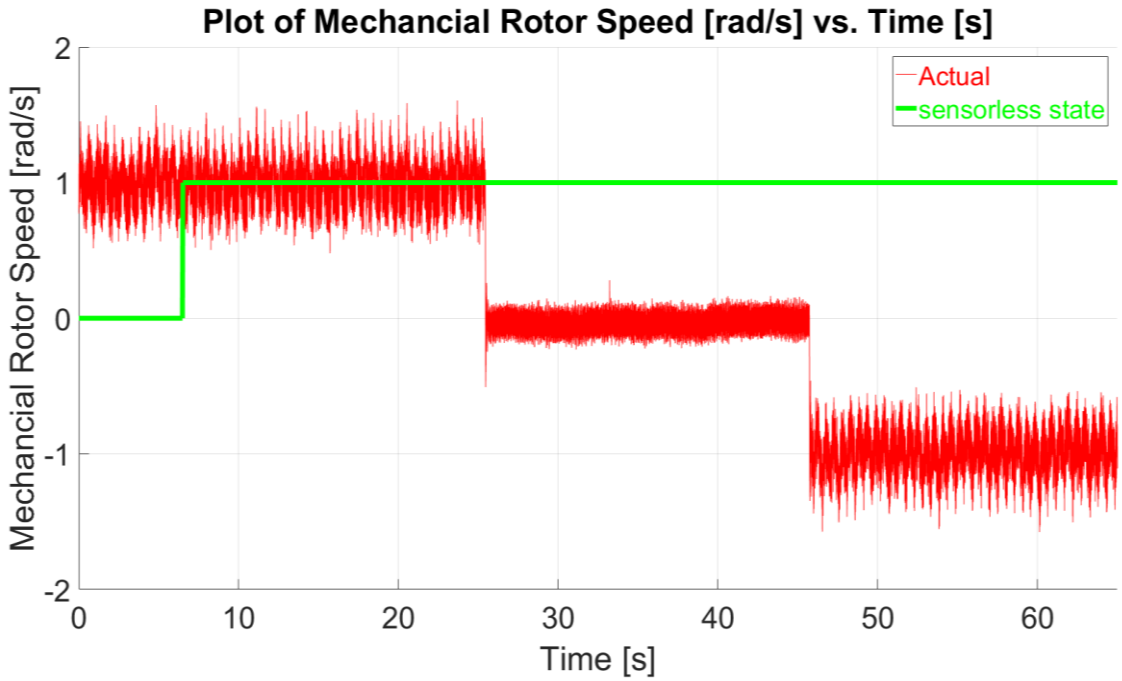

Figure 8.18 – Plot of Actual Rotor Speed ω_m [°] vs. Time [s] with $\omega_{m4}^* = -1 / 0 / 1$ rad/s on M4, $i_{d3}^* = 0$ A and $i_{q3}^* = 10$ A in closed-loop sensorless current control.

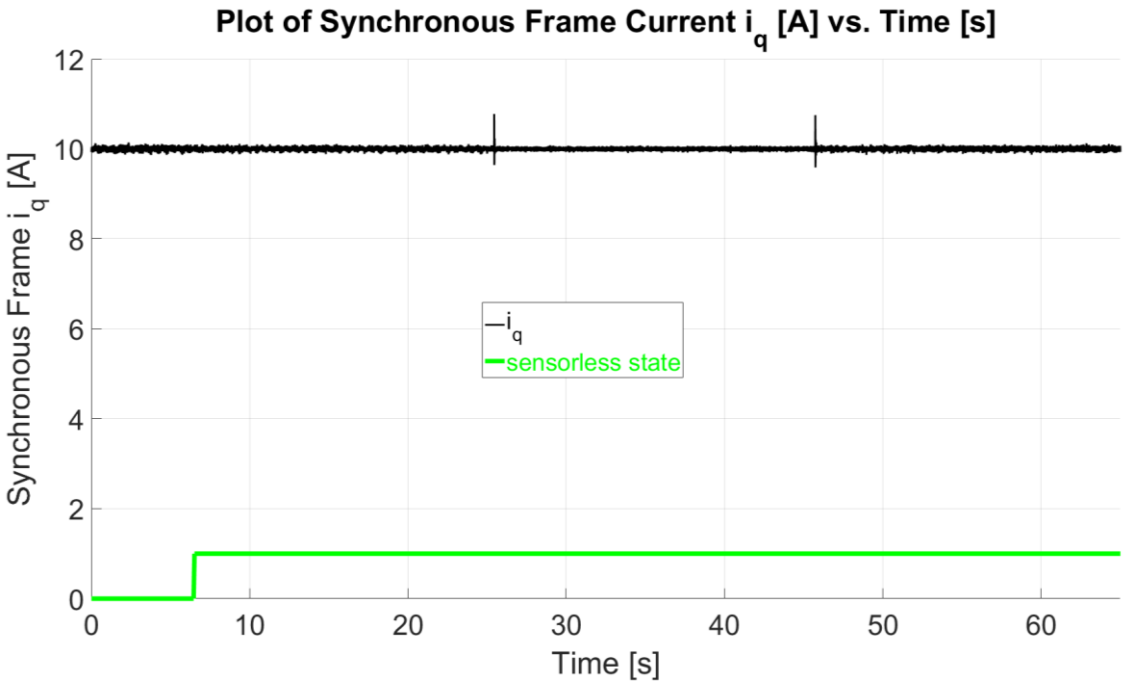

Figure 8.19 – Plot of Synchronous Frame Current i_q [°] vs. Time [s] with $\omega_{m4}^* = -1 / 0 / 1$ rad/s on M4, $i_{d3}^* = 0$ A and $i_{q3}^* = 10$ A in closed-loop sensorless current control.

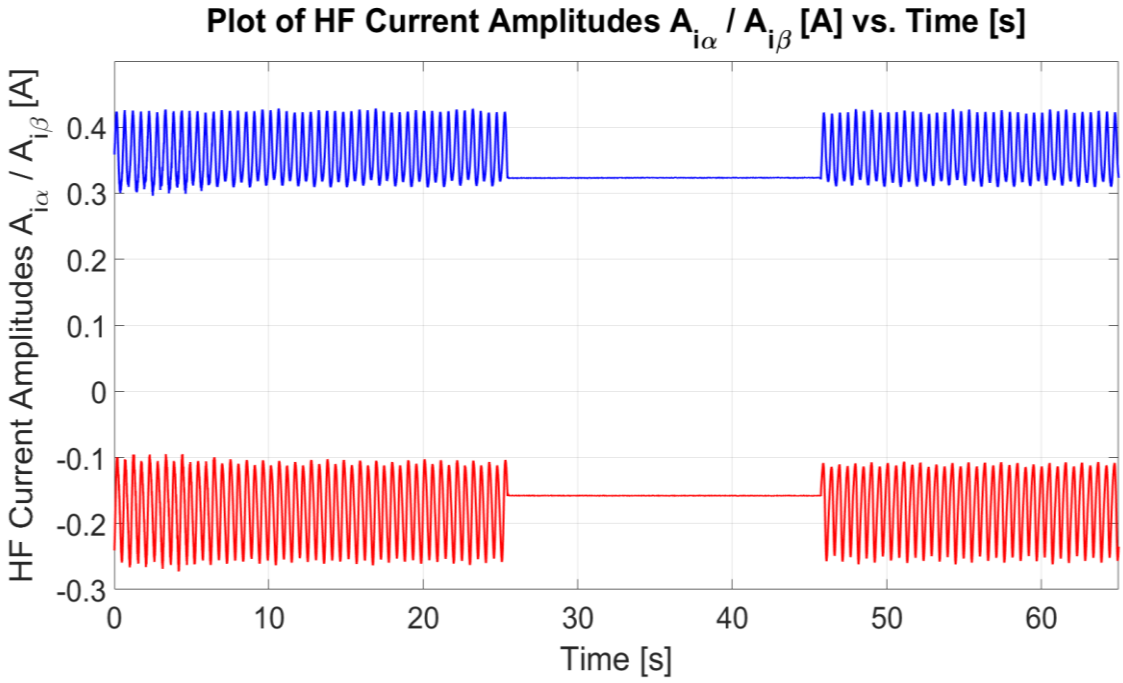

Figure 8.20 –Plot of HF Current Amplitudes $A_{i\alpha}$, $A_{i\beta}$ [A] vs. Time [s] with ω_{m4}^* = -1 / 0 / 1 rad/s on M4, i_{d3}^*= 0 A and i_{q3}^* = 10 A in closed-loop sensorless current control.

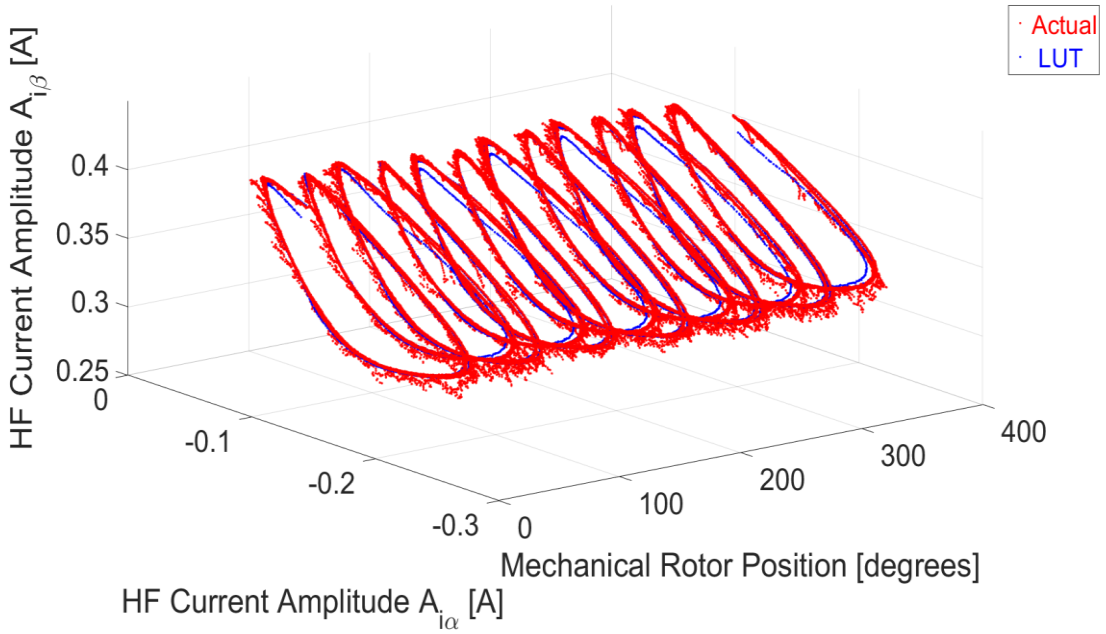

Figure 8.21 (a) – Three-Dimensional Plot of HF Current Amplitudes $A_{i\alpha}$ [A], $A_{i\beta}$ [A], θ_m [°] with ω_{m4}^* = -1 / 0 / 1 rad/s on M4, i_{d3}^*= 0 A and i_{q3}^* = 10 A in closed-loop sensorless current control.

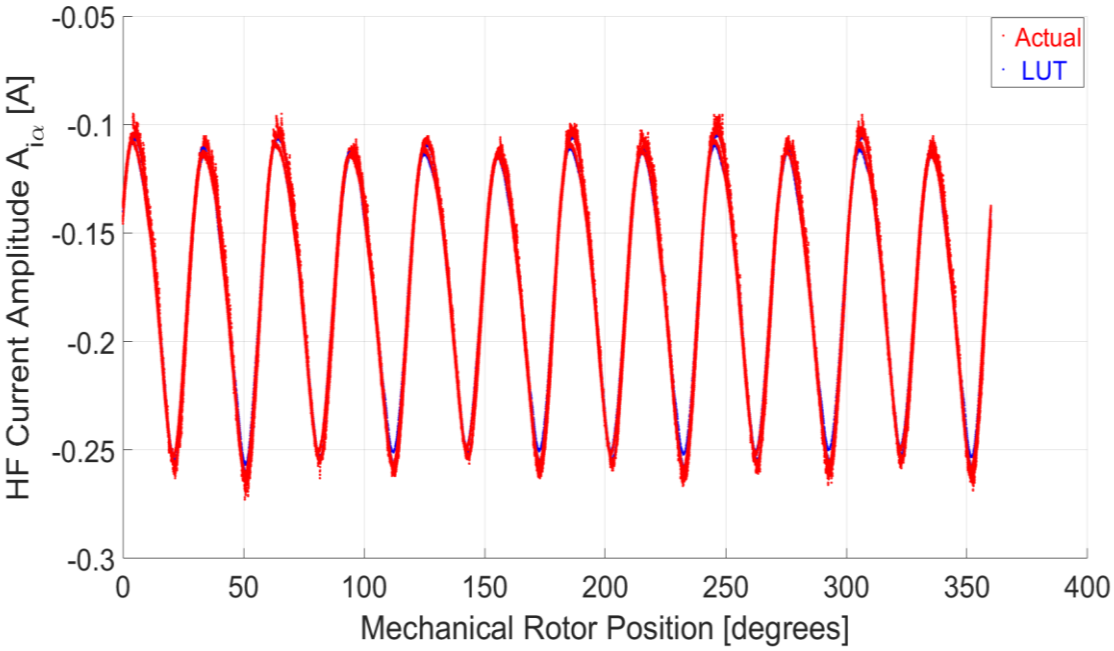

Figure 8.21 (b) –Plot of HF Current Amplitude $A_{i\alpha}$ [A] vs. θ_m [°] with ω_{m4}^* = -1 / 0 / 1 rad/s on M4, i_{d3}^*= 0 A and i_{q3}^* = 10 A in closed-loop sensorless current control.

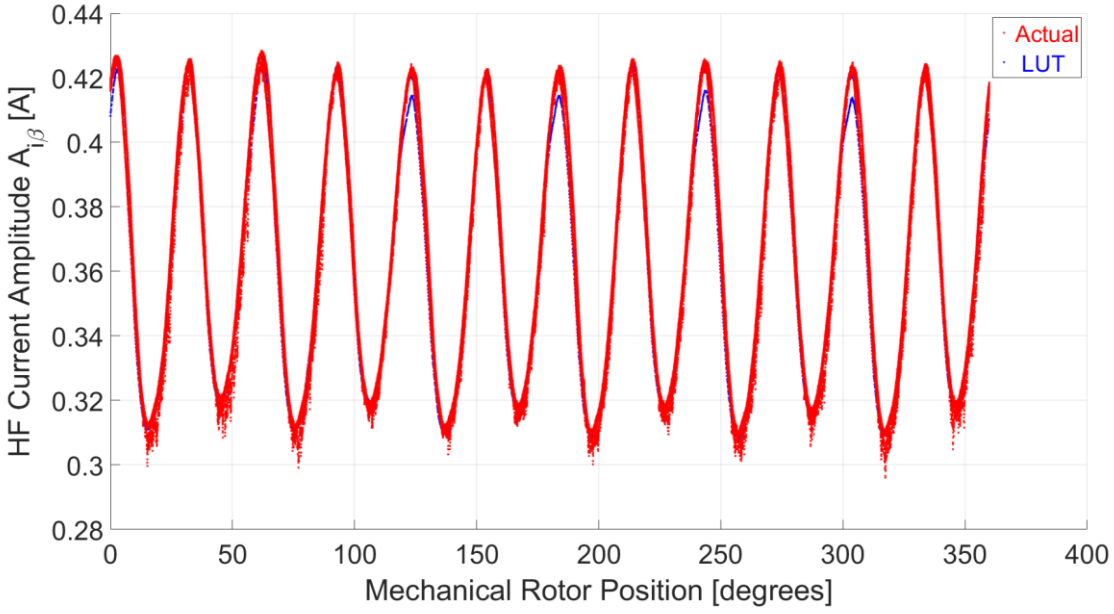

Figure 8.21 (c) –Plot of HF Current Amplitude $A_{i\alpha}$ [A] vs. θ_m [°] with ω_{m4}^* = -1 / 0 / 1 rad/s on M4, i_{d3}^*= 0 A and i_{q3}^* = 10 A in closed-loop sensorless current control.

8.5 Sensorless Current Control with Forward/Reverse Speed and Constant Reverse Torque

The SBO was tested under similar conditions to those described in Section 8.4 but with a torque in the opposite direction. The synchronous i_q-current of the sensorless machine under test, M3, was set to i_{q3}^*=10 A (100 % load). The actual/estimated ***mechanical*** rotor positions are shown in Figure 8.22 with a changeover to sensorless control at t = 5.7 s. The error in the estimated mechanical rotor position is shown in Figure 8.23, with the maximum absolute error being 2.64° and the RMSE 0.59°. The actual/estimated ***electrical*** rotor positions are shown in Figure 8.24. The speed and synchronous i_q-current of the sensorless machine are shown in Figures 8.25 – 8.26 respectively. The HF current amplitudes $A_{i\alpha}$, $A_{i\beta}$ are shown in Figure 8.27 as a function of time. The actual HF current amplitude measurements superimposed on the commissioned LUTs with respect to the mechanical rotor position can be observed in Figure 8.28 as a function of the mechanical rotor position.

Sensorless estimation was carried out in both forward and reverse directions of rotation with an intermediate zero speed region. As observed for positive values for i_{q3}^*, the sensorless estimates are more accurate when operating close to the speed operating point at which commissioning of the LUTs was carried out (ω_{m4}^* = ± 1 rad/s) as described in Section 7.4.4.

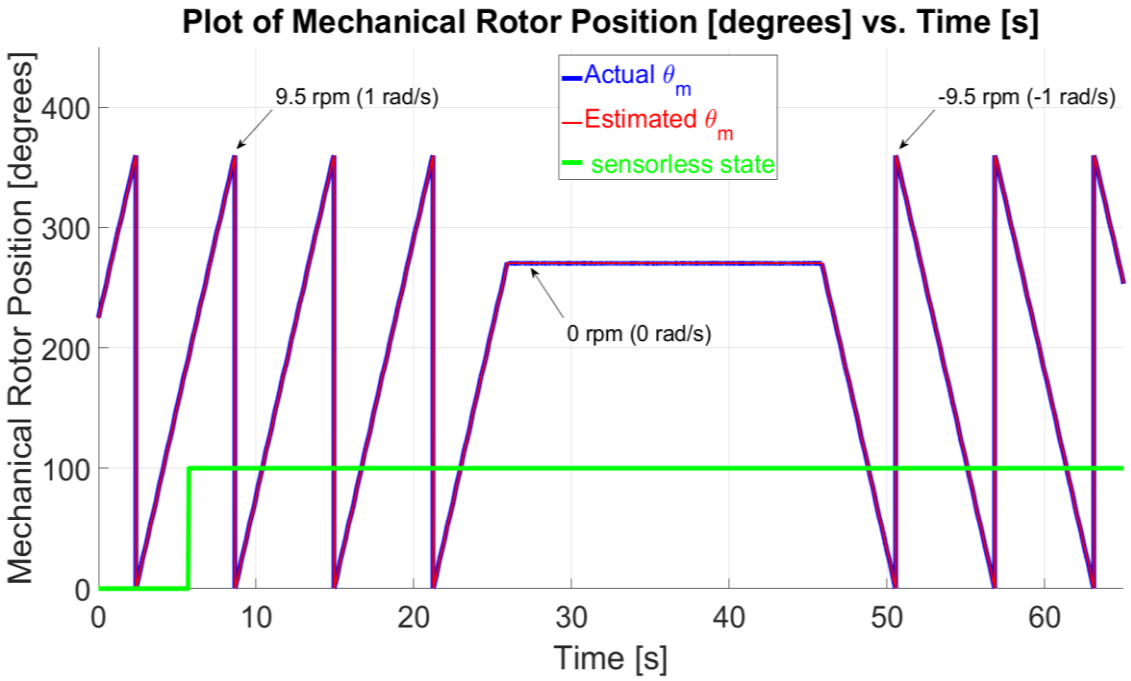

Figure 8.22 – Plot of Actual/Estimated Mechanical Rotor Position θ_m [°] vs. Time [s] with ω_{m4}^* = 1 / 0 / -1 rad/s on M4, i_{d3}^*= 0 A and i_{q3}^* = -10 A in closed-loop sensorless current control.

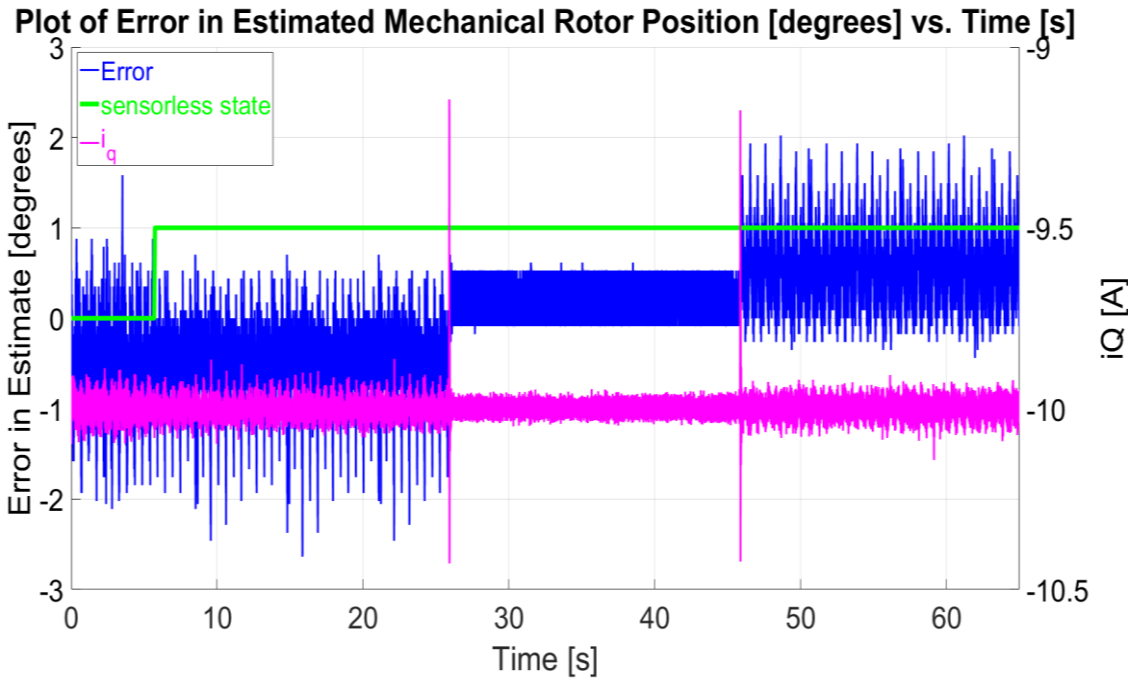

Figure 8.23 – Plot of Error in Estimated Mechanical Rotor Position θ_m [°] vs. Time [s] with $\omega_{m4}^* = 1 / 0 / -1$ rad/s on M4, $i_{d3}^* = 0$ A and $i_{q3}^* = -10$ A in closed-loop sensorless current control.

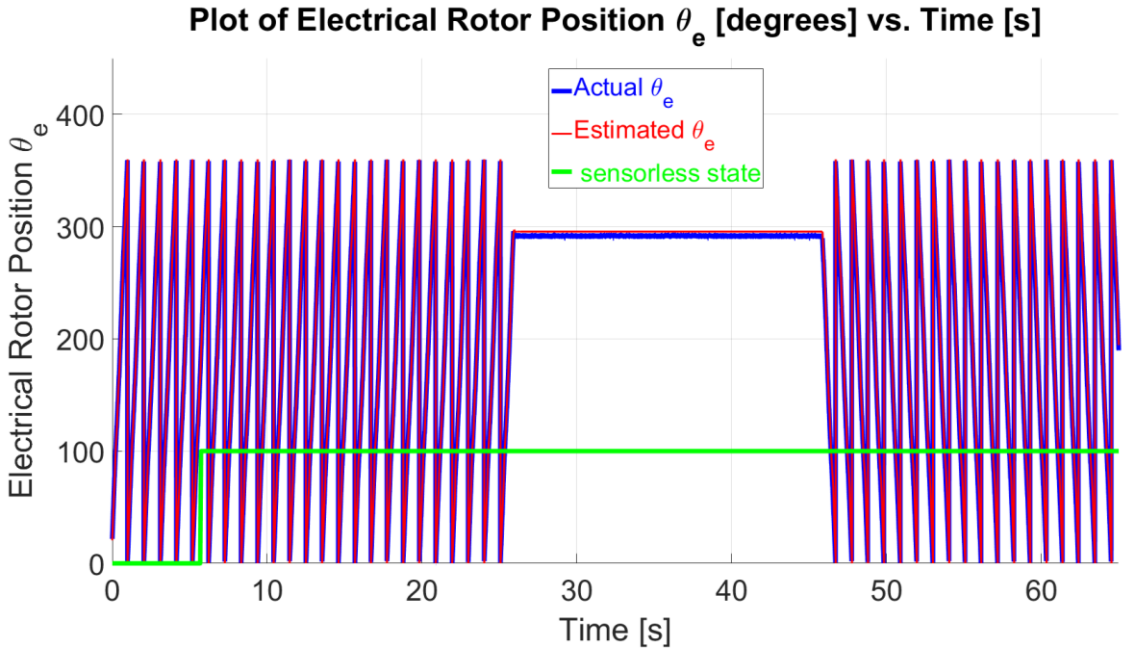

Figure 8.24 – Plot of Actual/Estimated Electrical Rotor Position θ_e [°] vs. Time [s] with $\omega_{m4}^* = 1 / 0 / -1$ rad/s on M4, $i_{d3}^* = 0$ A and $i_{q3}^* = -10$ A in closed-loop sensorless current control.

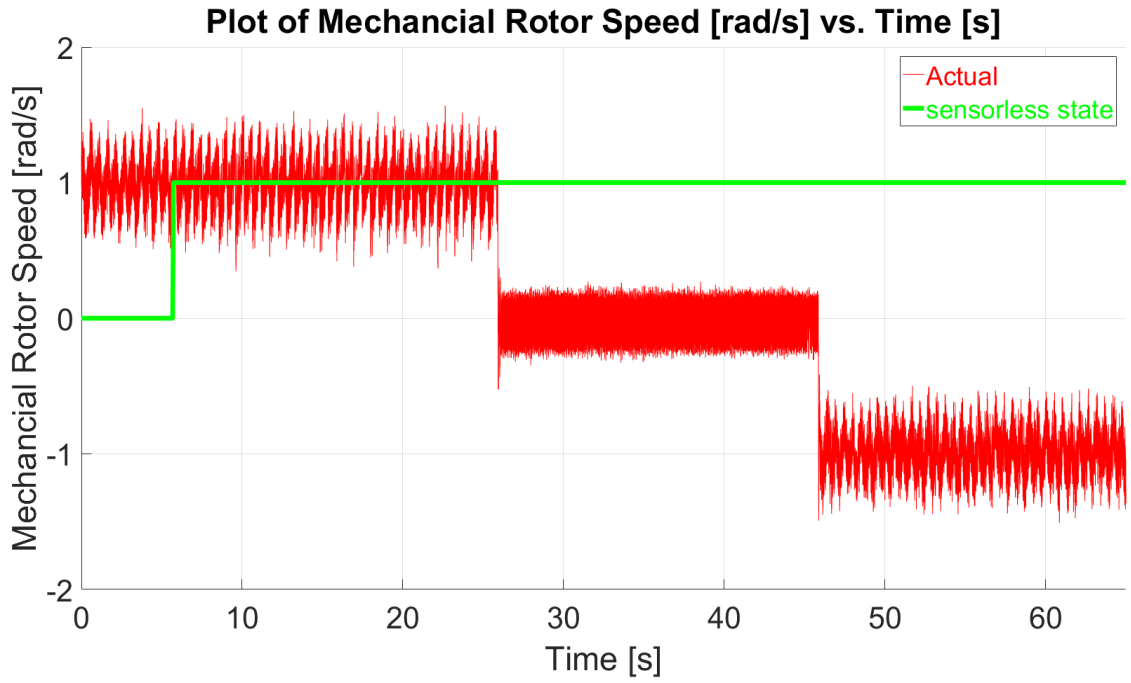

Figure 8.25 – Plot of Actual Rotor Speed ω_m [°] vs. Time [s] with $\omega_{m4}^* = 1 / 0 / -1$ rad/s on M4, $i_{d3}^* = 0$ A and $i_{q3}^* = -10$ A in closed-loop sensorless current control.

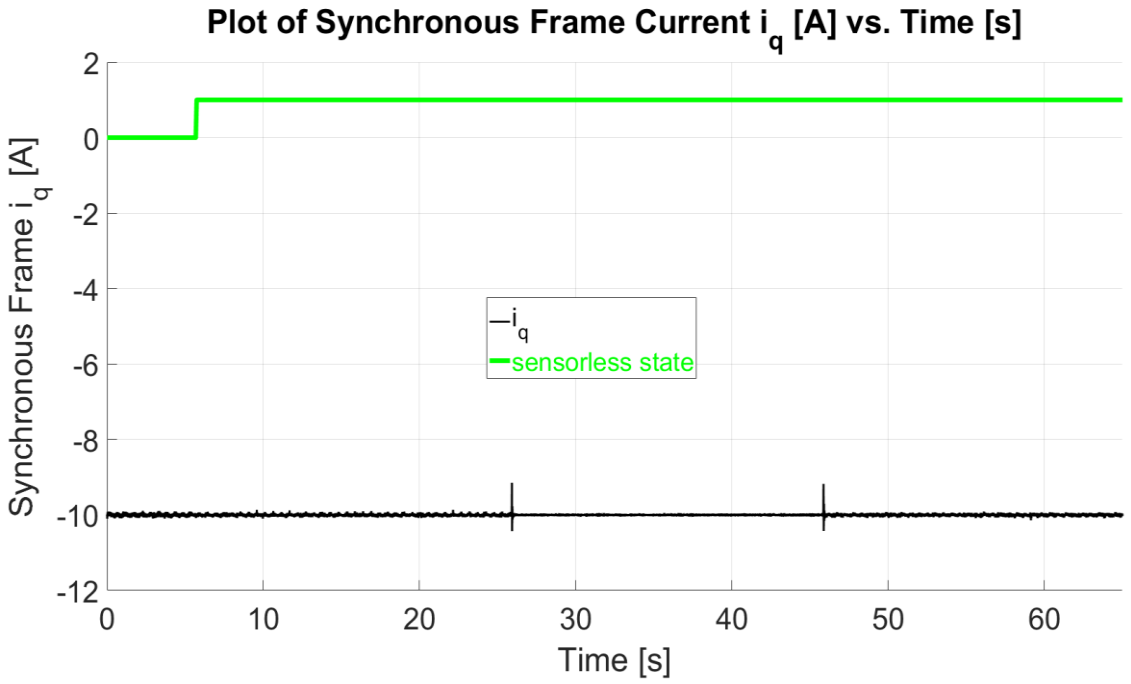

Figure 8.26 – Plot of Synchronous Frame Current i_q [°] vs. Time [s] with $\omega_{m4}^* = 1 / 0 / -1$ rad/s on M4, $i_{d3}^* = 0$ A and $i_{q3}^* = -10$ A in closed-loop sensorless current control.

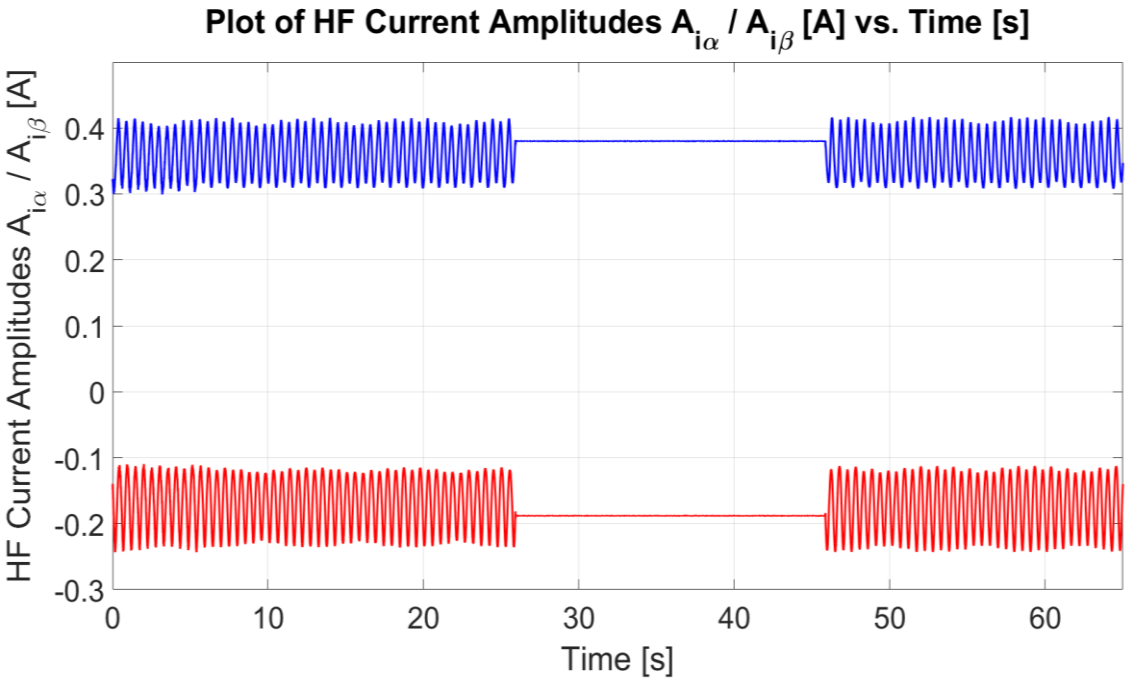

Figure 8.27 –Plot of HF Current Amplitudes $A_{i\alpha}$, $A_{i\beta}$ [A] vs. Time [s] with ω_{m4}^{*} = 1 / 0 / -1 rad/s on M4, i_{d3}^{*}= 0 A and i_{q4}^{*} = -10 A in closed-loop sensorless current control.

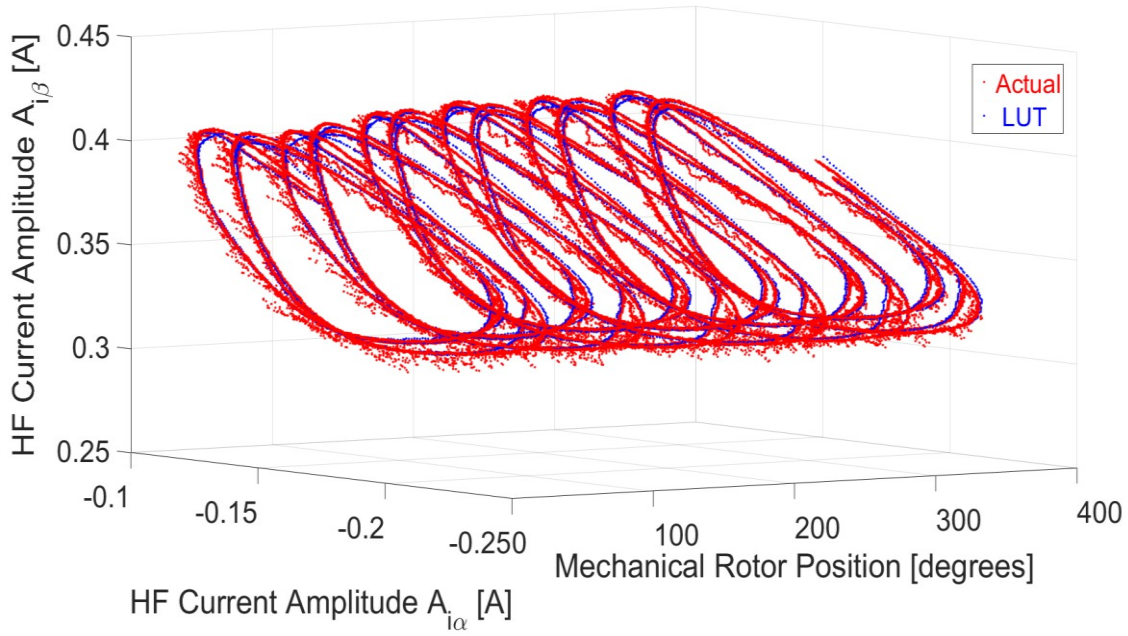

Figure 8.28 (a) – Three-Dimensional Plot of HF Current Amplitudes $A_{i\alpha}$ [A], $A_{i\beta}$ [A], θ_m [°] with ω_{m4}^{*} = 1 / 0 / -1 rad/s on M4, i_{d3}^{*}= 0 A and i_{q3}^{*} = -10 A in closed-loop sensorless current control.

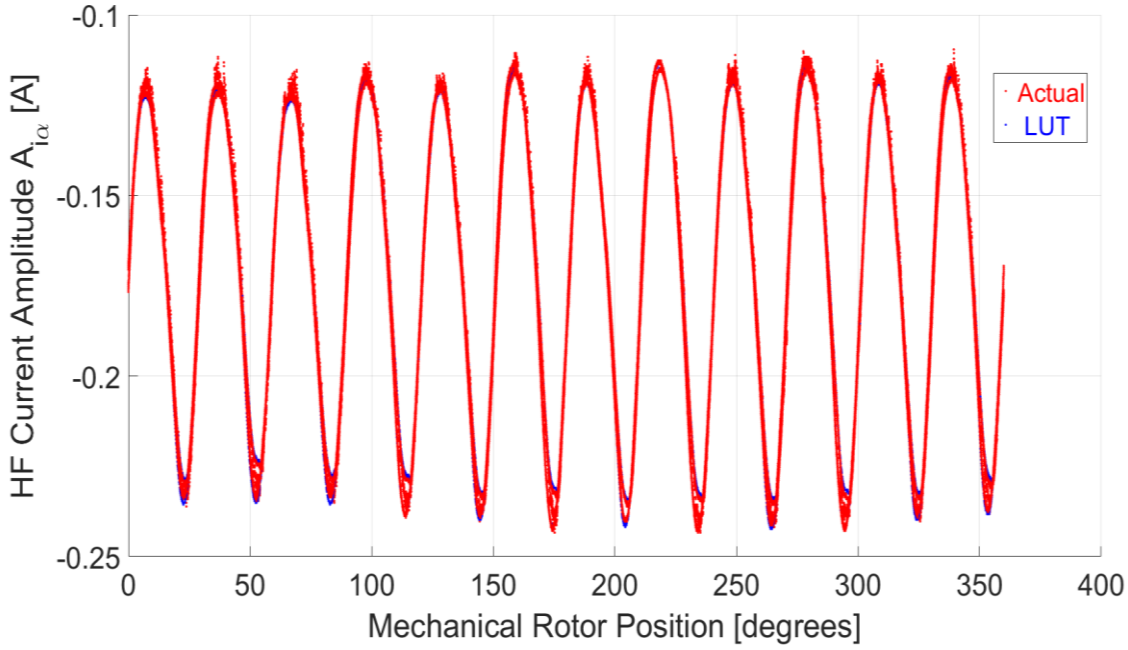

Figure 8.28 (b) –Plot of HF Current Amplitude $A_{i\alpha}$ [A] vs. θ_m [°] with ω_{m4}^* = -1 / 0 / 1 rad/s on M4, i_{d3}^*= 0 A and i_{q3}^* = -10 A in closed-loop sensorless current control.

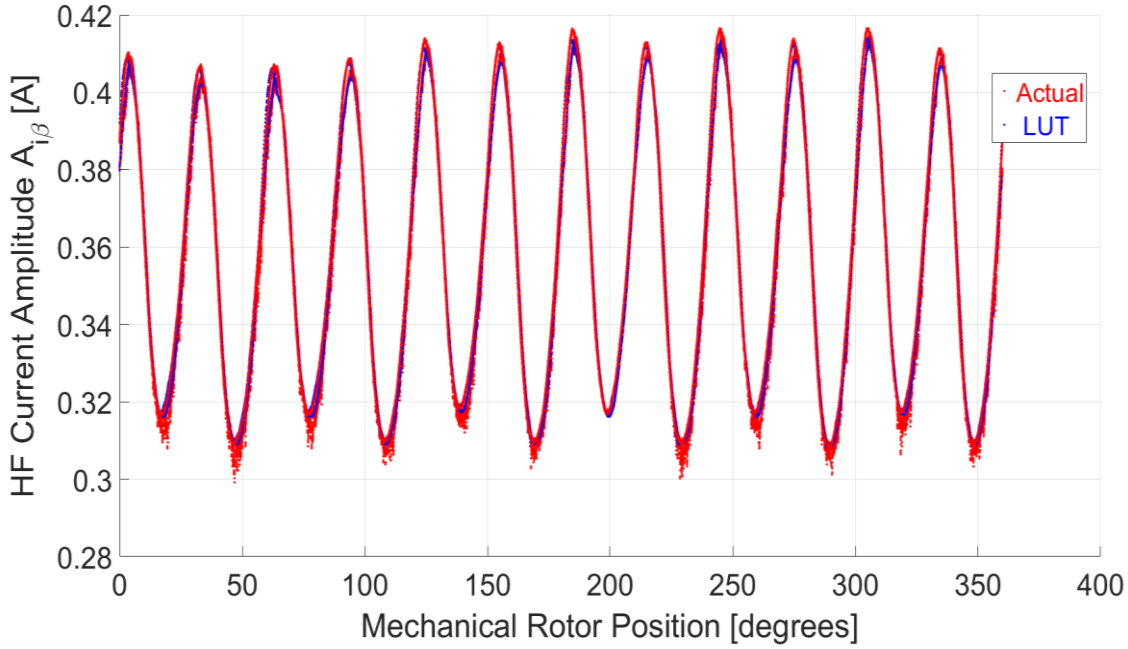

Figure 8.28 (c) –Plot of HF Current Amplitude $A_{i\alpha}$ [A] vs. θ_m [°] with ω_{m4}^* = 1 / 0 / -1 rad/s on M4, i_{d3}^*= 0 A and i_{q3}^* = -10 A in closed-loop sensorless current control.

8.6 Sensorless Current Control for Low-Speed Range and Constant Forward Torque

In Sections 8.4 – 8.5 the operation of the SBO observed was shown for low speeds of ± 1 rad/s (± 9.5 rpm, ± 1.6 % rated) with an intermediate zero speed region. While low/zero speed operation is one of the aims of this dissertation, a range of speeds is typically required for a number of industrial applications. In this section, the operation of the sensorless current control drive is shown at rated load ($i_{q3}^* = 10$ A) for a range of speeds within ± 5 rad/s (± 47.7 rpm). Given that the rated speed of the machine is 600 rpm, the results indicate a range of operation for ± 8 % of rated speed. The actual/estimated ***mechanical*** rotor positions are shown in Figure 8.29 in sensorless current control. The error in the estimated mechanical rotor position is shown in Figure 8.30, with the maximum absolute error being 3.34° and the RMSE 1.01°. The actual/estimated ***electrical*** rotor positions are shown in Figure 8.31. The shaft speed of the drive is shown in Figure 8.32. The HF current amplitudes $A_{i\alpha}$, $A_{i\beta}$ are shown in Figure 8.33.

The error in the estimated mechanical rotor position is shown to be a function of the rotor speed and increases with deviation from the calibration point at which the LUTs. are commissioned ($\omega_{m4}^* = \pm 1$ rad/s) as discussed in Section 7.4.4. The effect of speed variation on the saliency-based estimation is observed in Figure 8.33. Additional changes in the magnetic signature are observed besides the phase shift, which was observed in Section 6.3.8 for varying speed at no load when the machine is operated in full load condition. Hence, the requirement for a four-quadrant magnetic signature map as described in Section 7.4.4 which was carried out for forward and reverse rotation.

The commissioning in this dissertation was carried out for different values of the synchronous current i_q at only two speed operating points ($\omega_{m4}^* = \pm 1$ rad/s) while the sensorless machine is operated in current-controlled mode. Improved sensorless estimates would be expected if a more comprehensive magnetic signature LUT map is commissioned for different speeds rather than using LUTs for $\omega_{m4}^* = \pm 1$ rad/s only. Complete mapping of the machine would require a multi-dimensional LUT as a function of mechanical rotor position θ_m, synchronous currents i_q, i_d, and rotor speed ω_m. While such an approach is technically feasible, it would require considerably extended commissioning periods.

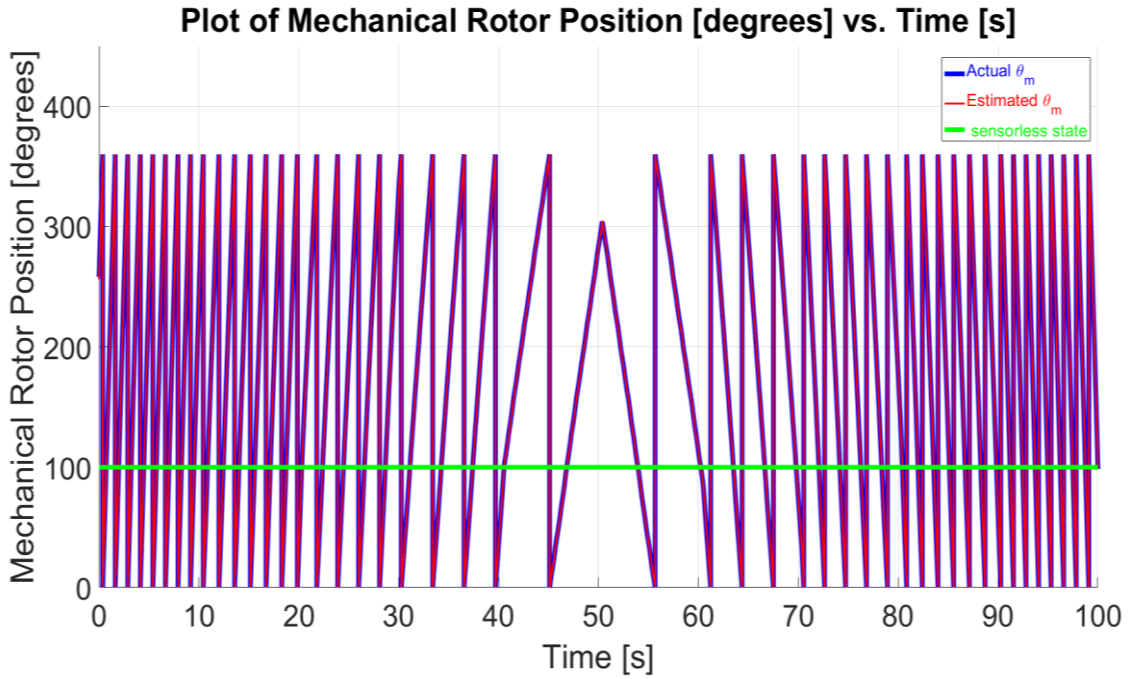

Figure 8.29 – Plot of Actual/Estimate Mechanical Rotor Position θ_m [°] vs. Time [s] with $-5 \text{ rad/s} \leq \omega_{m4}^* \leq 5 \text{ rad/s}$ on M4, $i_{d3}^* = 0$ A and $i_{q3}^* = 10$ A in closed-loop sensorless current control.

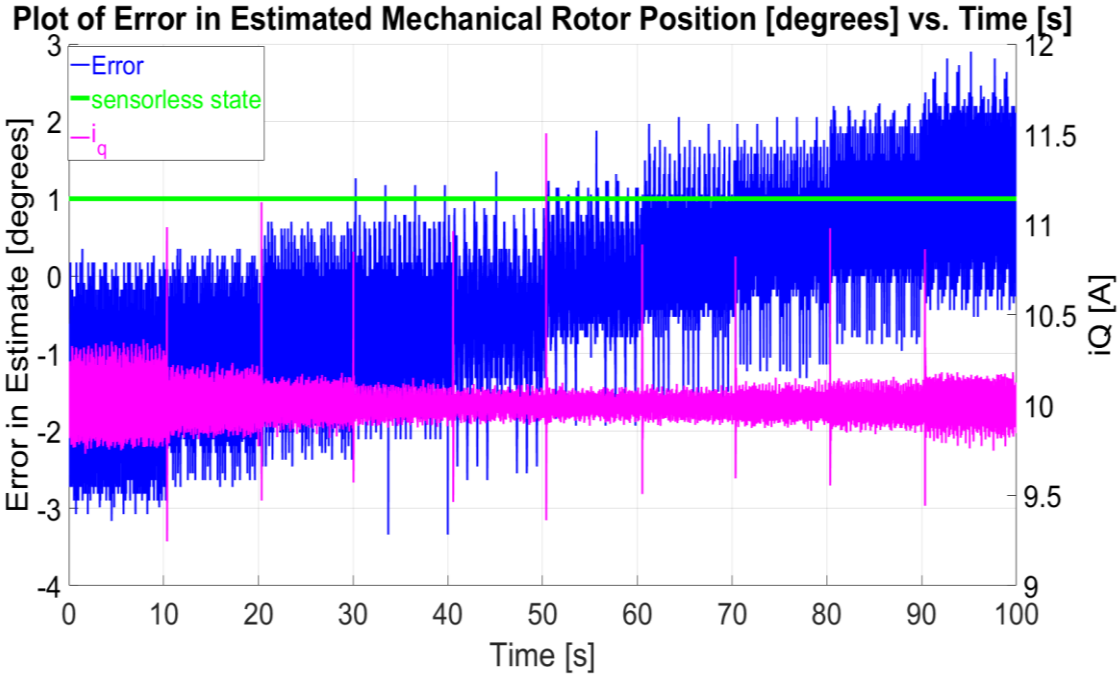

Figure 8.30 – Plot of Error in Estimated Mechanical Rotor Position θ_m [°] vs. Time [s] with $-5 \text{ rad/s} \leq \omega_{m4}^* \leq 5 \text{ rad/s}$ on M4, $i_{d3}^* = 0$ A and $i_{q3}^* = 10$ A in closed-loop sensorless current control.

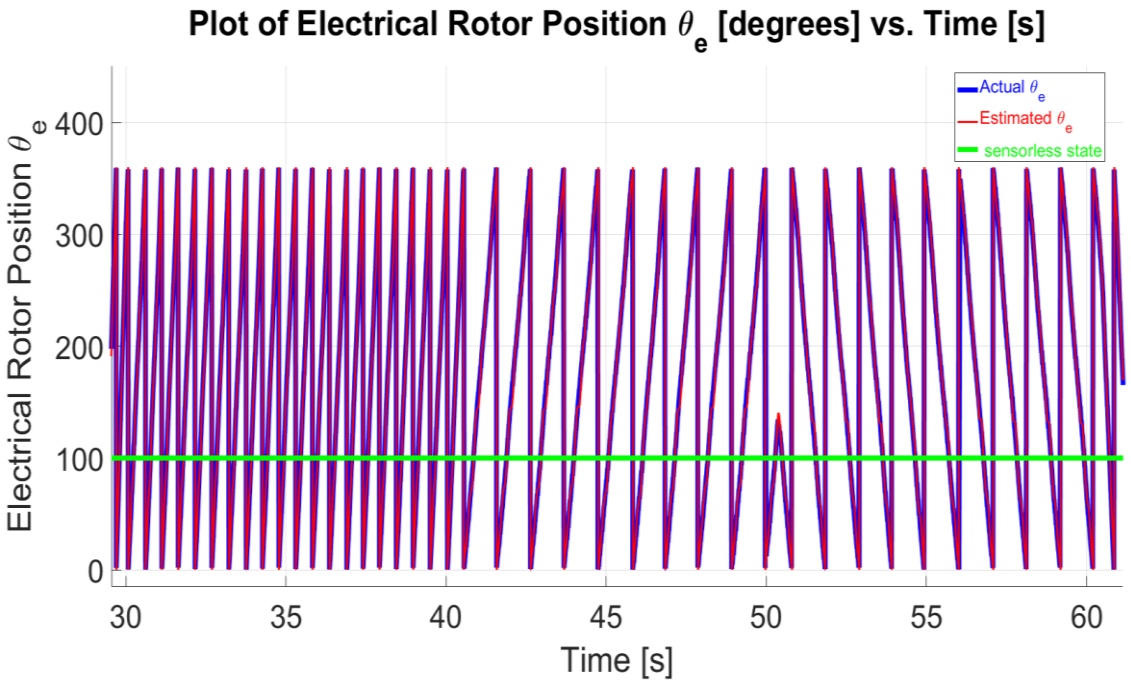

Figure 8.31 – Plot of Actual/Estimate Electrical Rotor Position θ_e [°] vs. Time [s] with -5 rad/s ≤ ω_{m4}^* ≤ 5 rad/s on M4, i_{d3}^*= 0 A and i_{q3}^* = 10 A in closed-loop sensorless current control zoomed in at 30 s ≤ t ≤ 60 s.

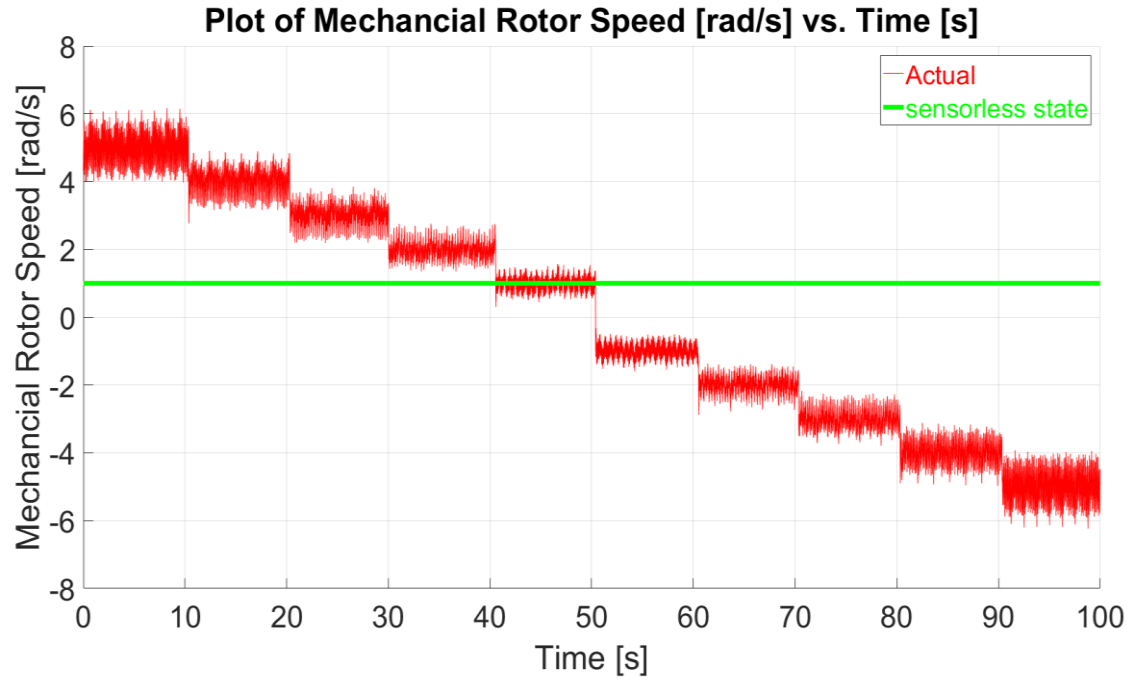

Figure 8.32 – Plot of Actual Rotor Speed ω_{m3} [°] vs. Time [s] with -5 rad/s ≤ ω_{m4}^* ≤ 5 rad/s on M4, i_{d3}^*= 0 A and i_{q3}^* = 10 A in closed-loop sensorless current control.

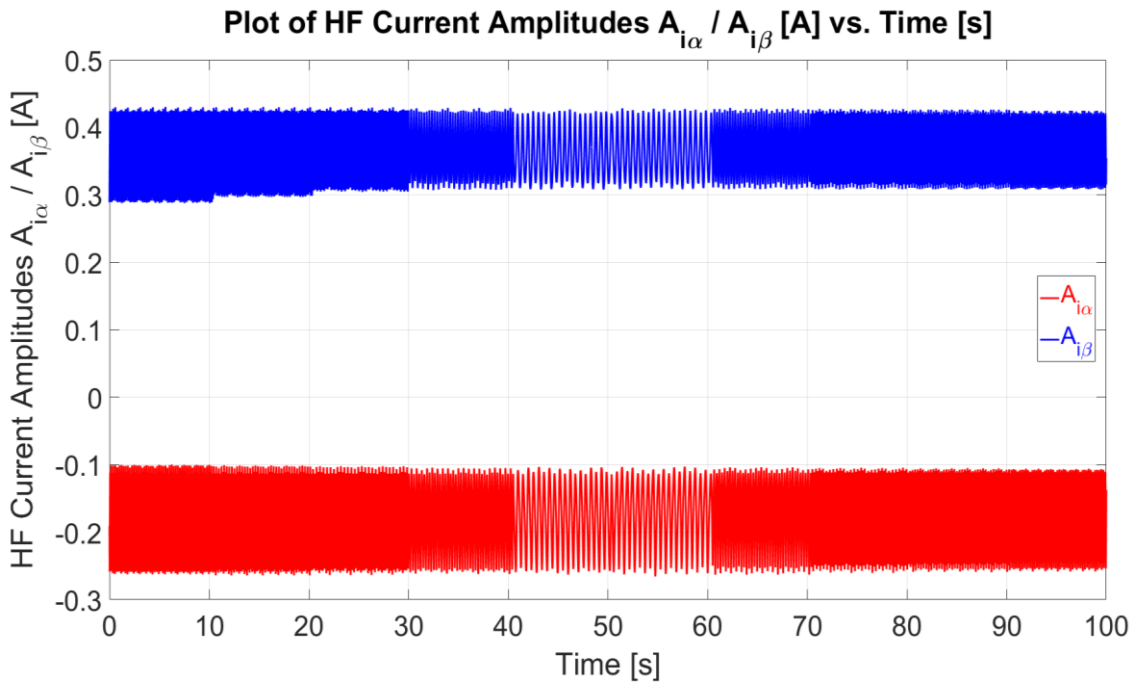

Figure 8.33 –Plot of HF Current Amplitudes $A_{i\alpha}$, $A_{i\beta}$ [A] vs. Time [s] with -5 rad/s ≤ ω_{m4}^* ≤ 5 rad/s on M4, i_{d3}^*= 0 A and i_{q3}^* = 10 A in closed-loop sensorless current control.

8.7 Sensorless Current Control for Low-Speed Range and Constant Reverse Torque

The SBO was investigated under similar conditions to those in Section 8.6 but with a negatively rated i_q-current, i_{q3}^* = -10 A (-100 % rated load). The same range of speed of ± 5 rad/s (±48 rpm, ± 8 % rated speed) was used for the results. The actual/estimated ***mechanical*** rotor positions are shown in Figure 8.34. The error in the estimated mechanical rotor position is shown in Figure 8.35, with the maximum absolute error being 4.83° and the RMSE 0.96°. The actual/estimated ***electrical*** rotor positions are shown in Figure 8.36. The shaft speed of the drive is shown in Figure 8.37 respectively. The HF current amplitudes $A_{i\alpha}$, $A_{i\beta}$ are shown in Figure 8.38 as a function of time.

The performance of the observer was similar to that observed in Section 8.6 with a positive reference for i_q^*. The results show that the error in the mechanical position estimate increases with the deviation from the calibrated speed point and that the saliency estimation is affected by the operating speed.

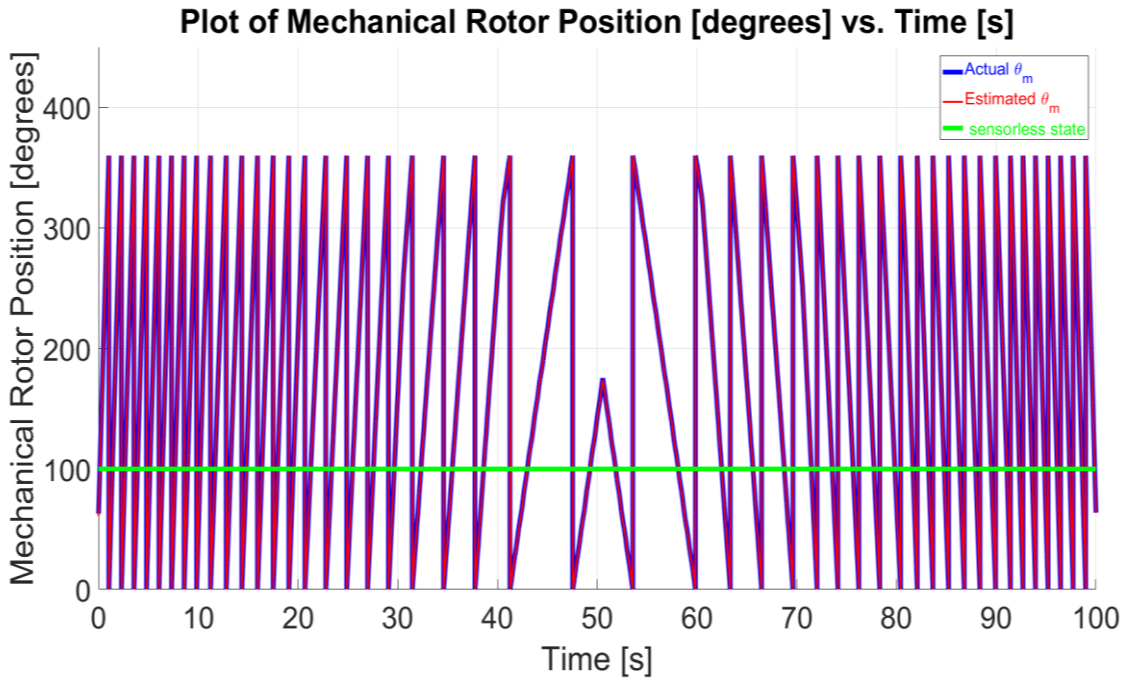

Figure 8.34 – Plot of Actual/Estimated Mechanical Rotor Position θ_m [°] vs. Time [s] with -5 rad/s ≤ ω_{m4}^* ≤ 5 rad/s on M4, i_{d3}^* = 0 A and i_{q3}^* = -10 A in closed-loop sensorless current control.

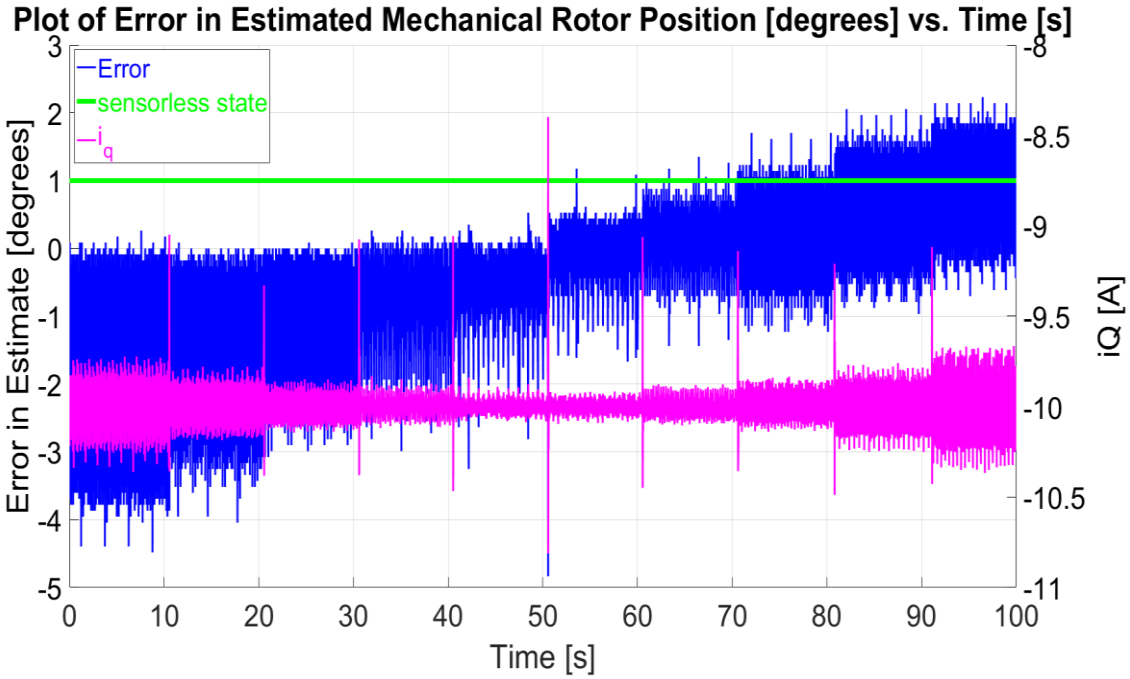

Figure 8.35 – Plot of Error in Estimated Mechanical Rotor Position θ_m [°] vs. Time [s] with -5 rad/s ≤ ω_{m4}^* ≤ 5 rad/s on M4, i_{d3}^* = 0 A and i_{q3}^* = -10 A in closed-loop sensorless current control.

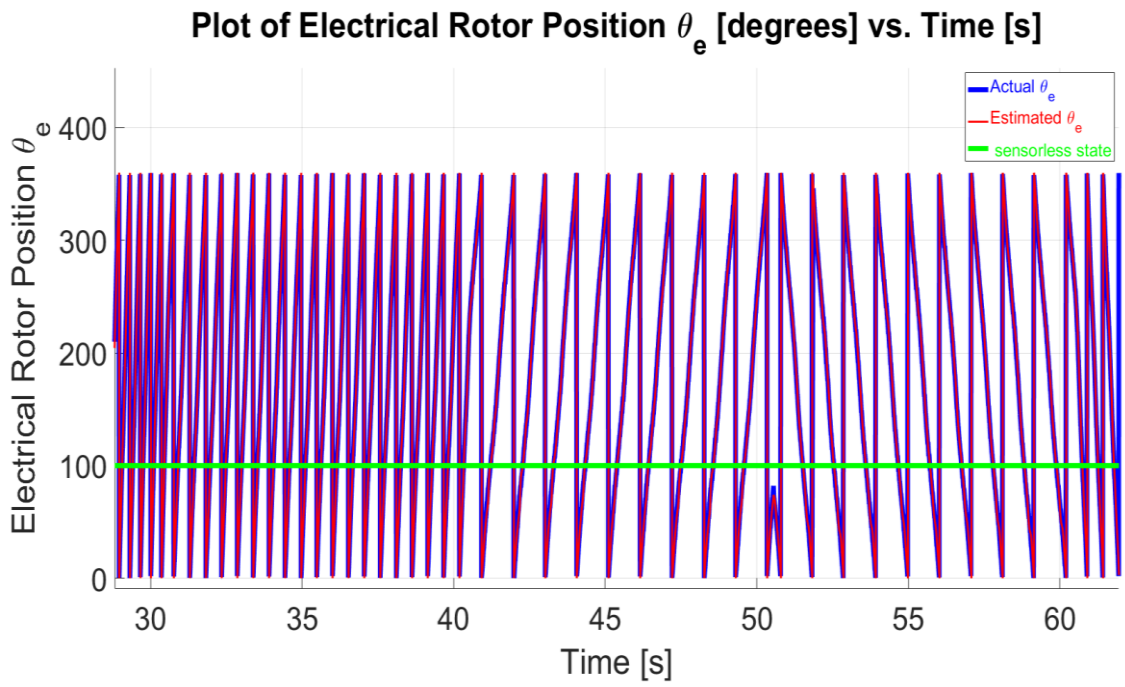

Figure 8.36 – Plot of Actual/Estimated Electrical Rotor Position θ_e [°] vs. Time [s] with -5 rad/s ≤ ω_{m4}^* ≤ 5 rad/s on M4, i_{d3}^* = 0 A and i_{q3}^* = -10 A in closed-loop sensorless current control zoomed in at 30 s ≤ t ≤ 60 s.

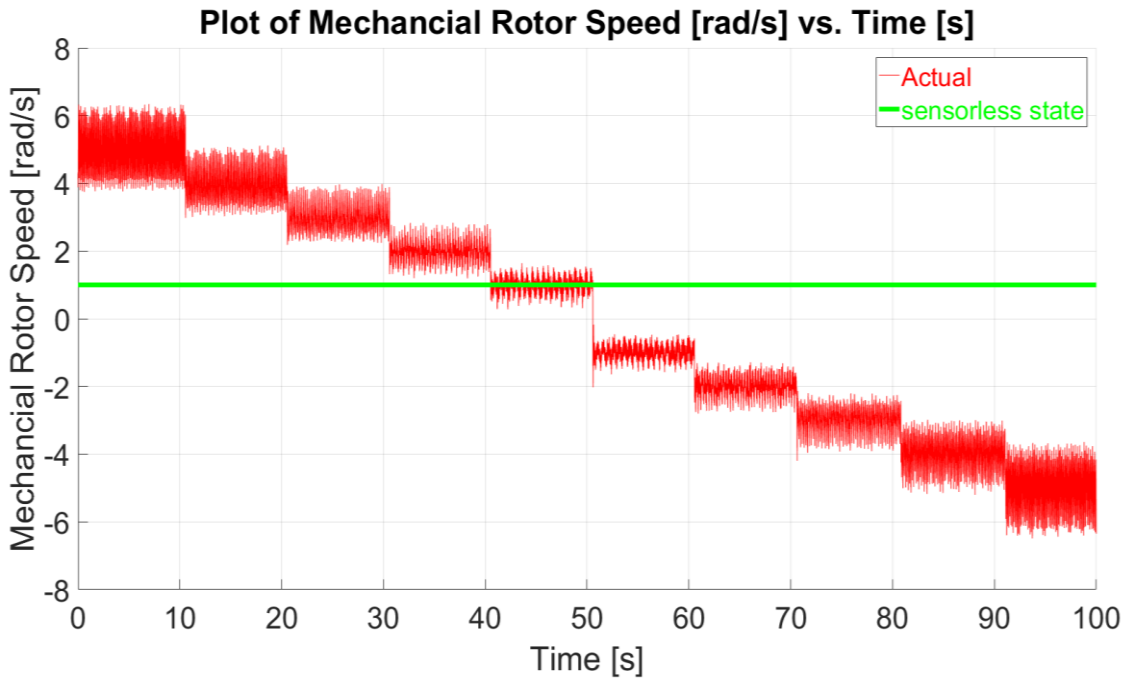

Figure 8.37 – Plot of Actual Rotor Speed ω_m [°] vs. Time [s] with -5 rad/s ≤ ω_{m4}^* ≤ 5 rad/s on M4, i_{d3}^* = 0 A and i_{q3}^* = -10 A in closed-loop sensorless current control.

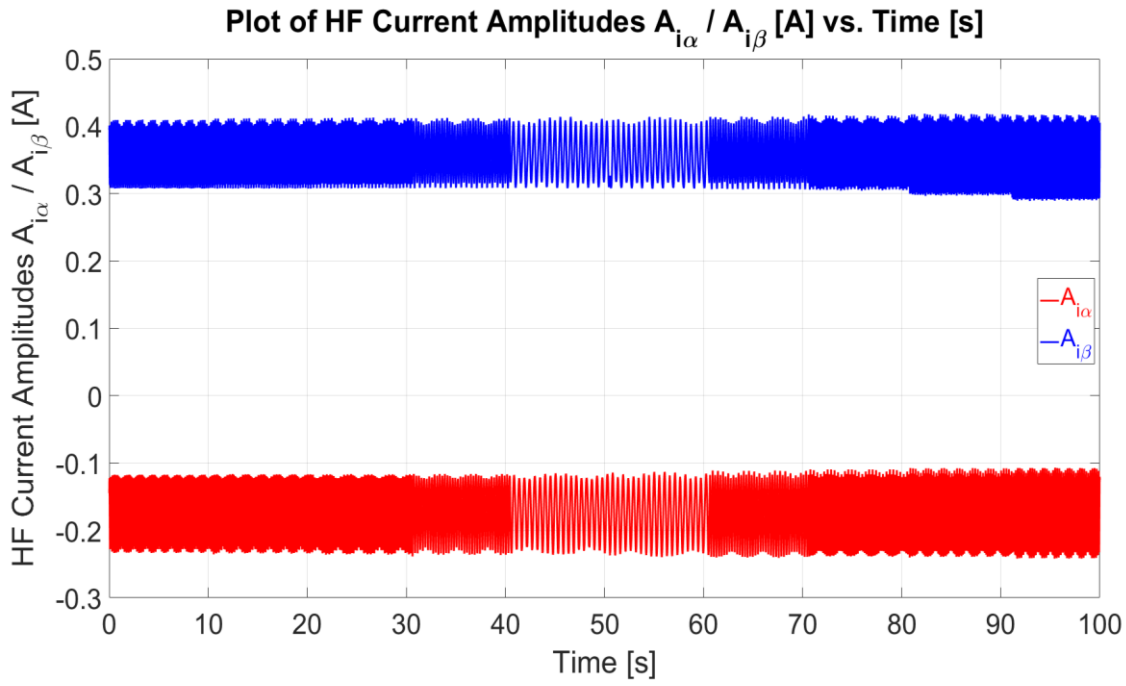

Figure 8.38 –Plot of HF Current Amplitudes $A_{i\alpha}$, $A_{i\beta}$ [A] vs. Time [s] with -5 rad/s ≤ ω_{m4}^* ≤ 5 rad/s on M4, i_{d3}^*= 0 A and i_{q3}^* = 10 A in closed-loop sensorless current control.

8.8 Summary

The sensorless operation of the machine under test, M3, in current-controlled mode was presented in this chapter. A current controller bandwidth of 85.57 Hz was set for the RFO of the sensorless drive. The reduction in bandwidth from sensored operation (281 Hz) was required in order to decouple better the HF injection from the fundamental operating frequency and limit the effects of estimation errors. In Section 8.2 the SBO achieved position estimation with a RMSE of 0.63° when tested at an average rotor speed of 1 rad/s for i_{q3} from -10 A to 10 A, in steps of 2.5 A. Tests were also carried out for reverse speed operation of -1 rad/s for the same range of currents achieving a RMSE of 0.65°. The latter results were reported in Section 8.3.

The SBO was tested for forward, zero, and reverse speed conditions at rated i_q-current in Section 8.4, yielding a RMSE of 0.66°. A similar test was carried out in Section 8.5 for rated negative i_q-current with results obtaining a RMSE of 0.59°. Variable speed operation was tested in Section 8.6 for rated positive i_q-current and in Section 8.7 for rated negative i_q-current yielding RMSE of 1.01° and 0.96°, respectively.

From Sections 8.6 and 8.7, it was noted that the estimation method is affected by both the direction of rotation also the magnitude of the speed. The magnetic signature variation with rotor speed was compensated for with a four quadrant LUT commissioning and selection through a PLL based estimation as described in Section 7.4.4. Since this research work is directed at low-speed operation, the speed was limited to ±8 % rated. This speed range caused only minimal change of the HF currents such that commissioning at ±1.6 % rated speed was sufficient. The results presented showed excellent sensorless current control of the PMSM during forward and reverse operation (± 8 % of rated speed) at positive and negative full rated current. However, for future work, it is recommended that for higher speed ranges, the LUTs used for position estimation could be further extended to include also their variation due to the speed magnitude.

Chapter 9 – Sensorless Speed and Position Control Results

9.1 Introduction

The sensorless current control performance of the Permanent Magnet Synchronous Machine (PMSM) under test was shown in Chapter 8 for a range of low to zero speed operating points up to rated load conditions. In this chapter, the performance of the drive with the Search-Based Observer (SBO) is extended to sensorless speed and position control.

The sensorless speed performance is investigated for all four quadrants of operation for a range of low-speed values. These results also include zero speed operation at rated load conditions. The effects of the frictional forces on the SBO parameters are identified and discussed. Sensorless position control with a step-reference is also presented for both no-load and loaded conditions. The settings of the controller gains within the RFO structure are discussed and the resulting bandwidths in sensorless mode are compared to those obtained for sensored operation in Chapter 3.

9.2 Sensorless Speed Control with Bidirectional Speed and No Load

The operation of the proposed SBO was tested in sensorless speed control mode where the estimated electrical rotor position and the estimated mechanical rotor speed are used for RFO speed control of the machine under test M3. The load is set by the coupled machine M4 which is in sensored current control mode. In this section, the sensorless speed operation of the machine is tested at no-load conditions. The reference of the sensorless speed control drive is varied from 2.5 rad/s (23.8 rpm) to 0 rad/s (0 rpm) and finally to -2.5 rad/s (-23.8 rpm). The speed controller gains for this test were kept the same as for sensored operation $K_{p\_W3} = 0.3$ and $K_{i\_W3} = 60$.

The reference, actual and estimated rotor speeds are shown in Figure 9.1 with a changeover from sensored to sensorless operation at t = 4.24 s. The oscillations on both the actual and estimated ***mechanical*** rotor speeds are mainly attributed to the limited resolution of the digital encoder (12-bit) being used for sensored operation and which has been used for the commissioning process in the SBO. The actual and estimated ***mechanical*** rotor positions are shown in Figure 9.2, with the error between the two shown in Figure 9.3. The absolute maximum error in the mechanical rotor position is 3.16° with a Root Mean Square Error (RMSE) of 0.97°. The actual and estimated ***electrical*** rotor positions are shown in Figure 9.4. The HF current amplitudes $A_{i\alpha}$, $A_{i\beta}$

are shown in Figure 9.5. From Figure 9.1 (b) the rise time was measured at t_r = 18.52 ms such that the bandwidth of the speed loop is 19 Hz (Bandwidth = $\frac{0.35}{t_r}$) which is similar to that observed for sensored operation.

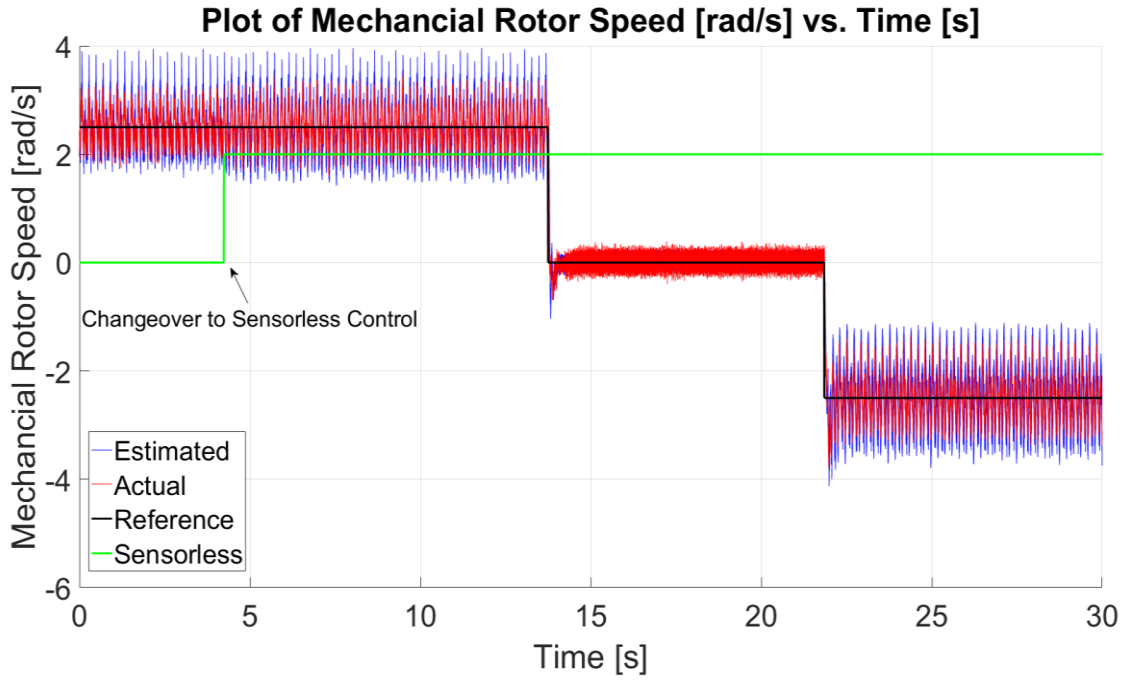

Figure 9.1 (a) – Plot of Reference/Actual/Estimated Rotor Speed ω_m [°] vs. Time [s] for sensorless speed control at no-load.

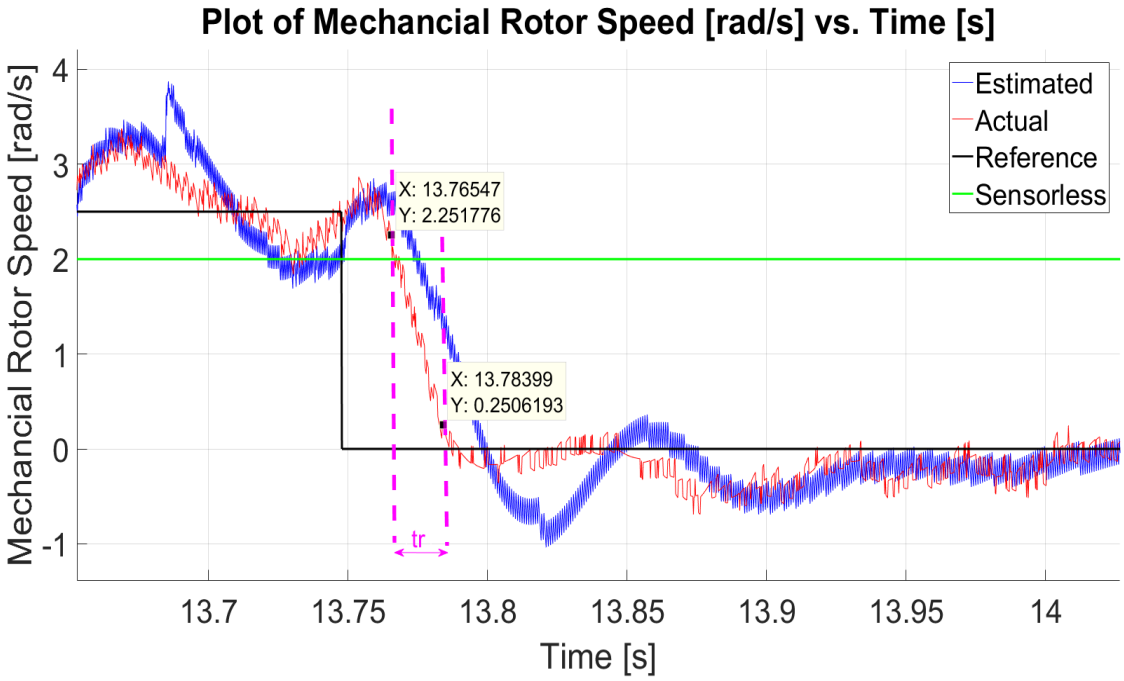

Figure 9.1 (b) – Speed Transient to Zero Speed showing Reference/Actual/Estimated Rotor Speed ω_m [rad/s] vs. Time [s] for sensorless speed control at no-load.

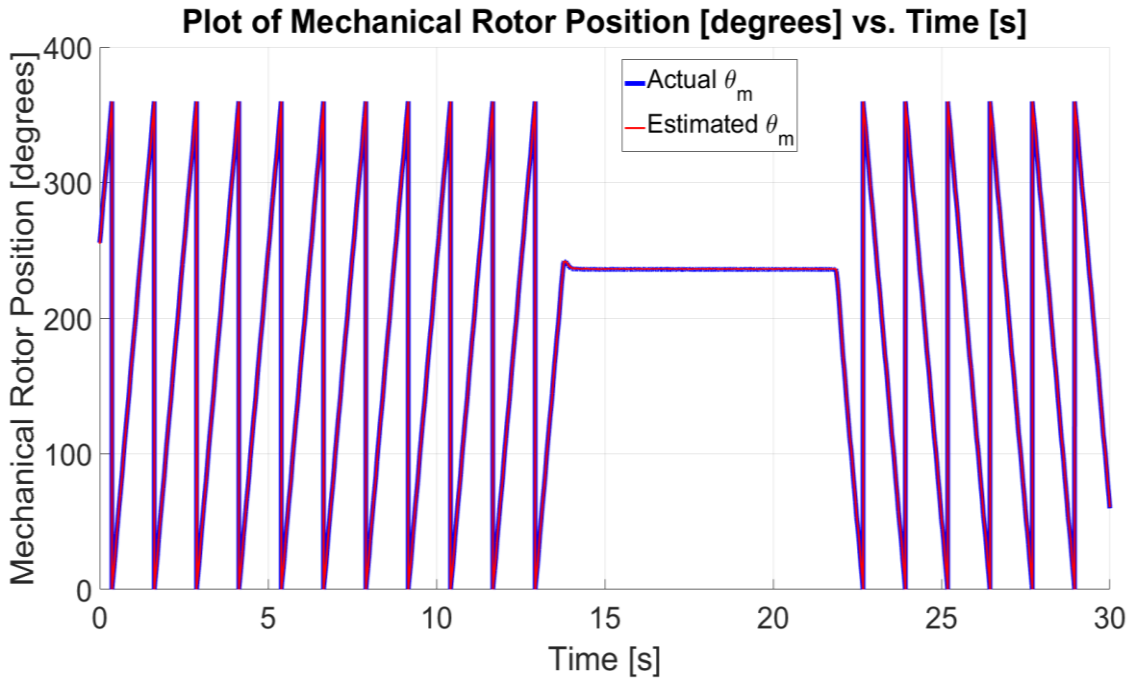

Figure 9.2 – Plot of Actual/Estimate Mechanical Rotor Position θ_m [°] vs. Time [s] for sensorless speed control at no-load.

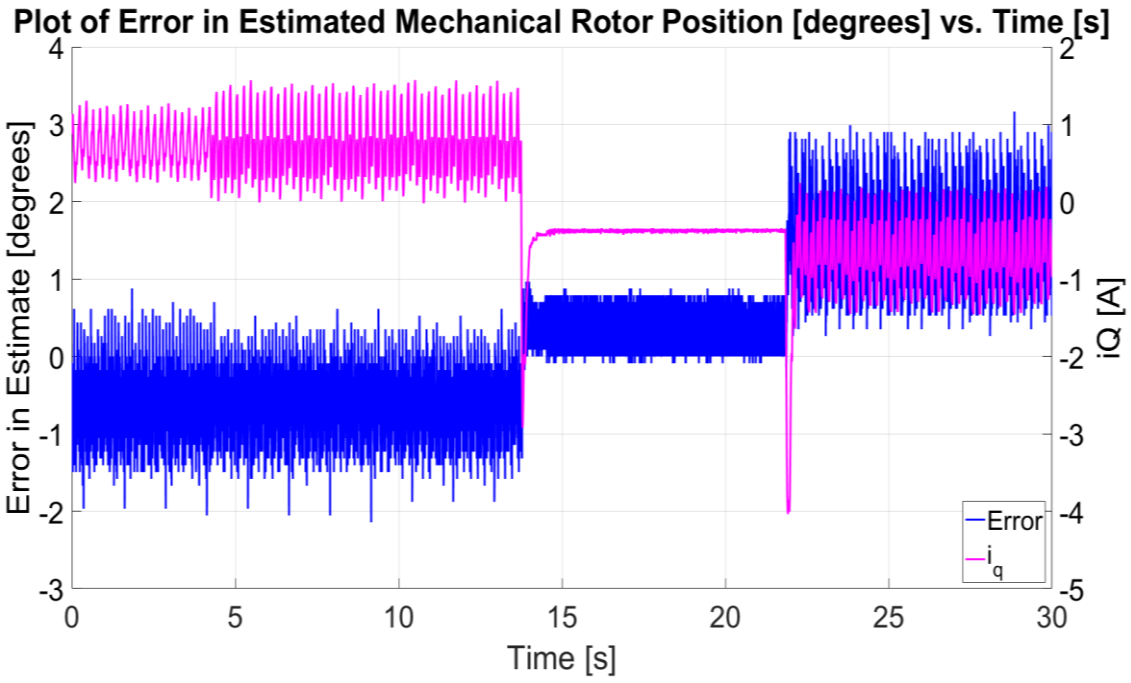

Figure 9.3 – Plot of Error in Estimated Mechanical Rotor Position θ_m [°] vs. Time [s] for sensorless speed control at no-load.

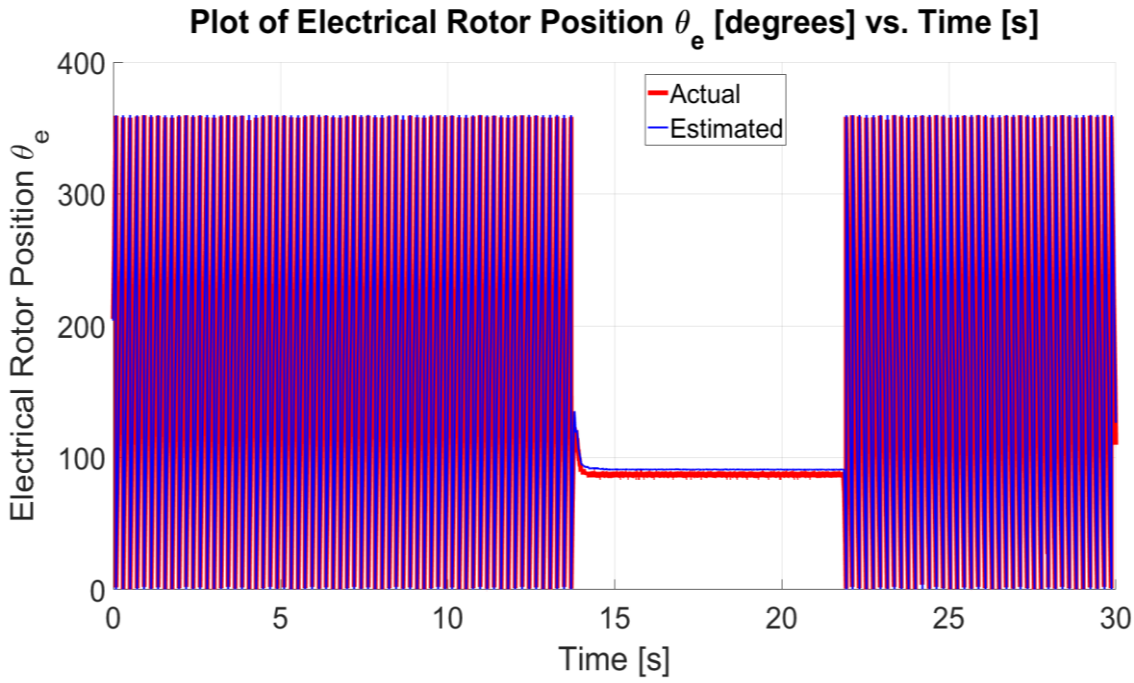

Figure 9.4 – Plot of Actual/Estimate Electrical Rotor Position θ_e [°] vs. Time [s] for sensorless speed control at no-load.

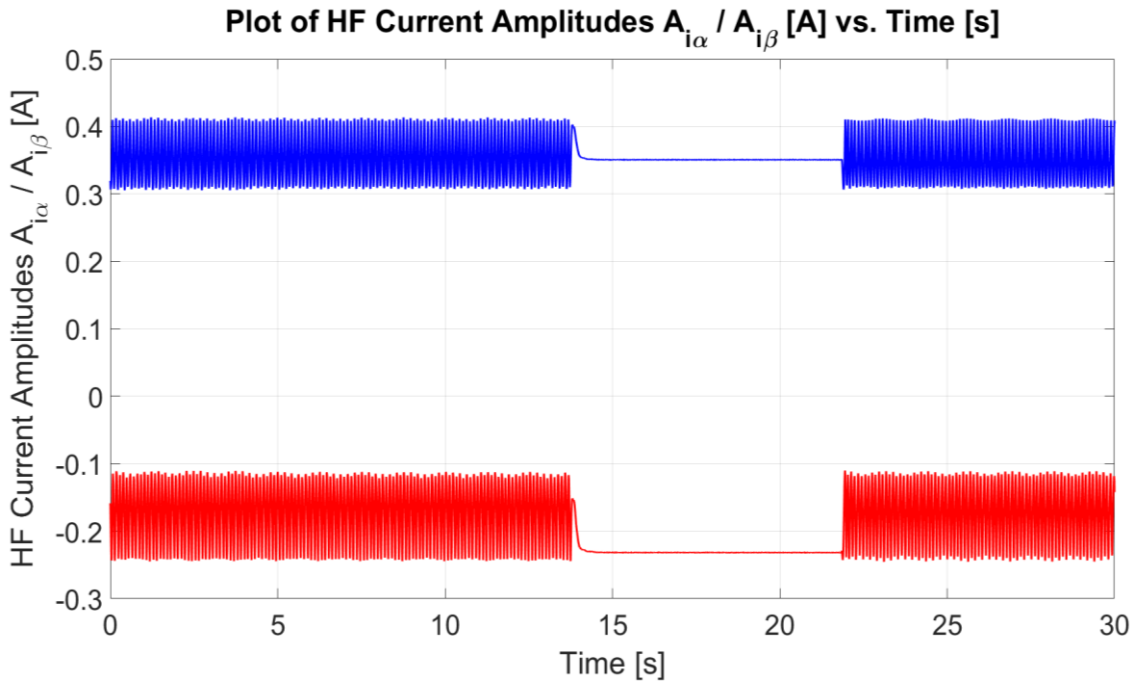

Figure 9.5 –Plot of HF Current Amplitudes $A_{i\alpha}$, $A_{i\beta}$ [A] vs. Time [s] for sensorless speed control at no-load.

9.3 Sensorless Speed Control with Bidirectional Speed and Forward Torque

This section presents the sensorless speed control operation of the machine under loaded conditions. The synchronous reference frame currents for the load machine, M4, were set as follows: $i_{d4}^* = 0$ A and i_{q4}^* was adjusted such that the maximum i_q-current on the sensorless machine M3 is approximately 10 A in steady-state. The speed reference profile is similar to that used in Section 9.2 with changes in reference speed from 2.5 rad/s (23.8 rpm) to 0 rad/s and finally to -2.5 rad/s (-23.8 rpm). The speed controller gains for this test were set in the microcontroller to $K_{p\_W3} = 0.1$ and $K_{i\_W3} = 10$ for successful sensorless control operation.

Figures 9.6 to 9.10 show the experimental results for sensorless speed control, where the changeover from sensored to sensorless operation occurs at t = 5 s. Figure 9.6 shows the reference, actual and estimated rotor speeds, whilst Figure 9.7 shows the actual and estimated ***mechanical*** rotor positions. The error between the two is shown in Figure 9.8; the absolute maximum error in the mechanical rotor position is 3.16°, with a RMSE of 0.94°. The actual and estimated ***electrical*** rotor positions are shown in Figure 9.9. The HF current amplitudes $A_{i\alpha}$, $A_{i\beta}$ are shown in Figure 9.10. The sensorless operation of the machine was observed to be stable throughout the period of operation shown with a maximum load of approximately $i_{q3\_max}^* \approx 10$ A which corresponds to 100 % rated load.

From Figure 9.6 (b) the bandwidth of the sensorless closed-loop speed control was found to be 4.48 Hz from the rise time t_r measured (Bandwidth = $\frac{0.35}{t_r}$). This is a significant reduction in bandwidth compared to the sensored speed operation (15.93 Hz) and sensorless operation at no-load conditions, as observed in Section 9.2. The reduction in bandwidth is attributed to the reduction of the speed controller gains, which was necessary to obtain robust and stable sensorless speed control operation at rated load. Increased speed controller bandwidth was obtained at lower values of i_{q3}. From the tests presented in this section, the applicability of the SBO observer for low/zero speed control is shown, albeit a reduction in dynamics compared to sensored operation. The oscillations on the estimated speed were also present in sensored operation and thus are not a direct result of sensorless control. The reduction of these oscillations through an improved experimental setup could possibly allow for a higher sensorless closed-loop speed bandwidth.

In Figure 9.8, it can be observed that the current i_{q3} for forward and reverse rotation is significantly different, although the loading machine reference currents are kept constant. Current i_{q3} is approximately 90 % of rated current in forward rotation and 70 % of rated current in reverse rotation in sensorless speed control mode. This effect was also observed in sensored operation. There was no significant difference in the current for the same operating point between sensored and sensorless modes. This variation in synchronous current i_{q3} required for obtaining the same rotational speed but in different directions is a result of practical limitations of the setup including:

1. Different frictional forces in forward and reverse rotation of the rotor shaft due to off-centric oscillations.
2. A minor misalignment due to the alignment of the shafts and coupling being carried out manually without specialized tools.
3. Minor encoder measurement errors due to the off-centric oscillations.

While this variation in the current required for rotation in forward and reverse direction shows that there are practical limitations with both the machines used and the setup; this was also found in similar work to that presented in this dissertation [95]. However, this does not affect the sensorless estimate as the LUTs used for the SBO algorithm are calibrated for different values of i_q-current.

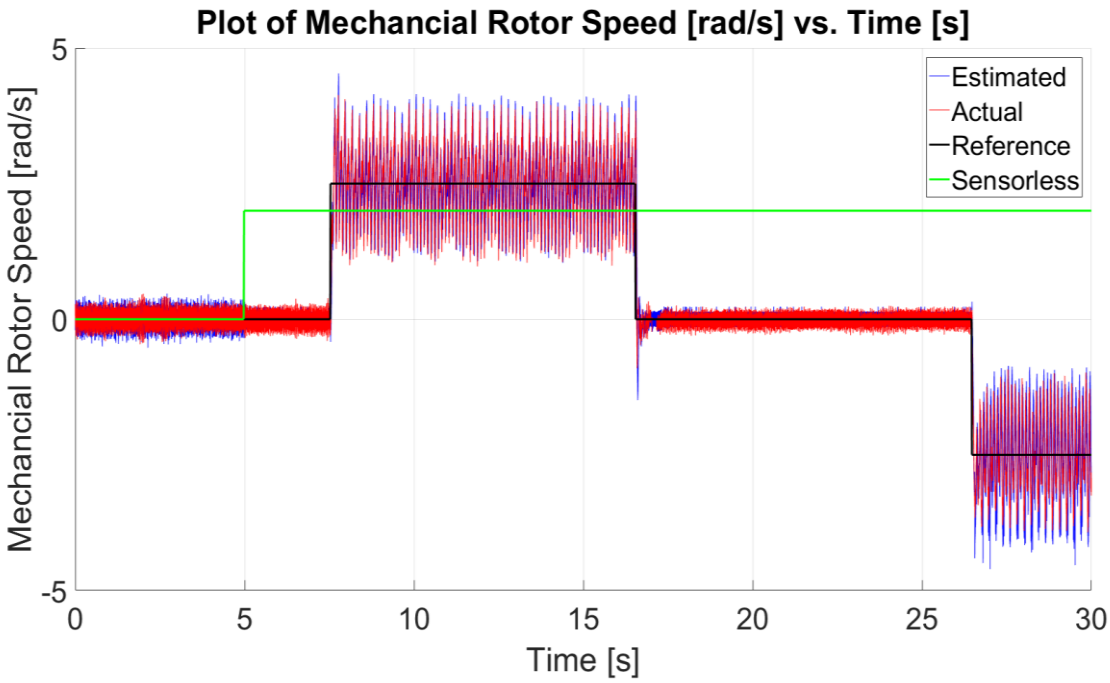

Figure 9.6 (a) – Plot of Reference/Actual/Estimated Rotor Speed ω_m [°] vs. Time [s] for sensorless speed control at $i_{q3\_max}^* \approx 10$ A on M3.

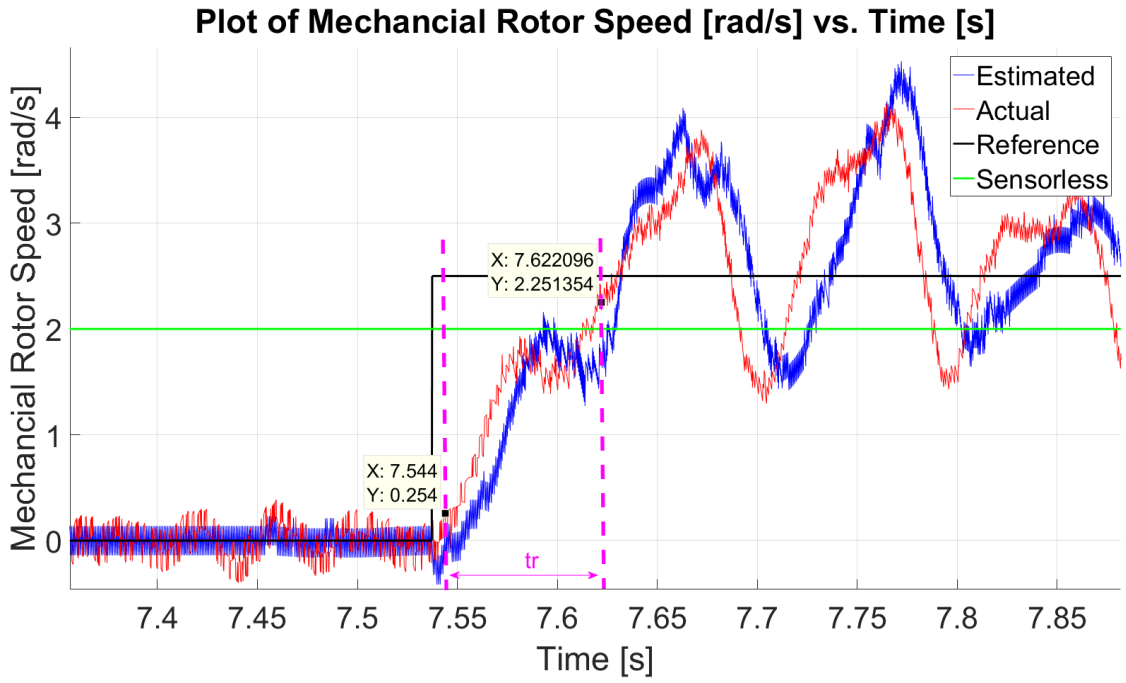

Figure 9.6 (b) – Speed Transient to Zero Speed showing Reference/Actual/Estimated Rotor Speed ω_m [rad/s] vs. Time [s] for sensorless speed control at $i_{q3\_max}^* \approx 10$ A on M3.

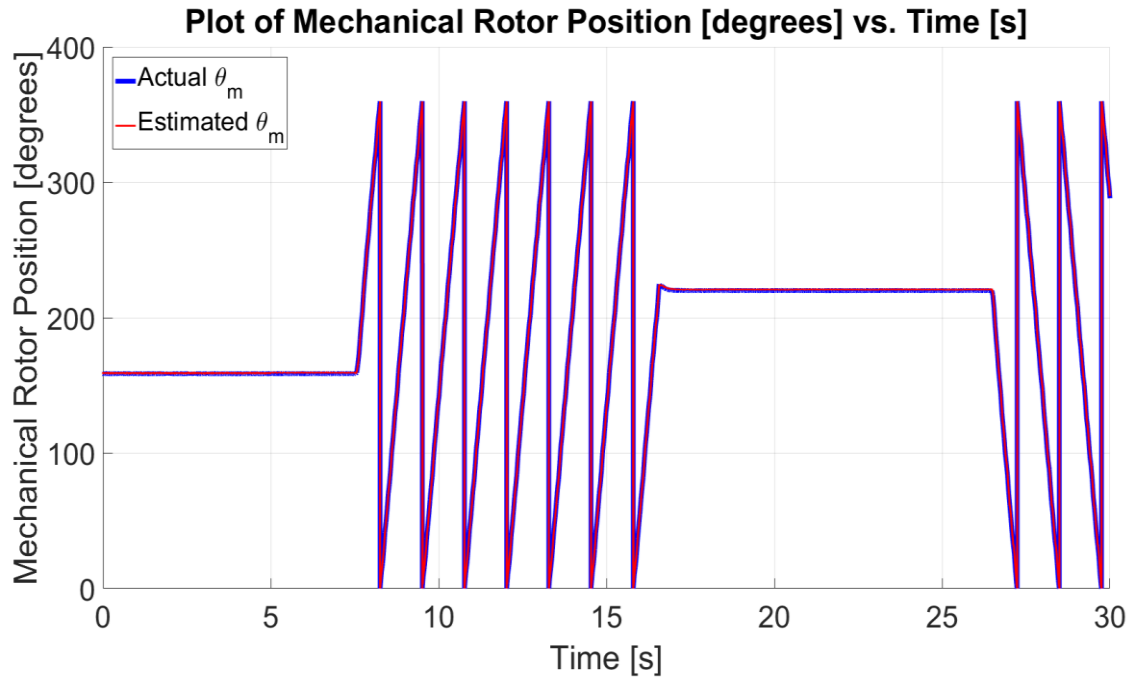

Figure 9.7 – Plot of Actual/Estimate Mechanical Rotor Position θ_m [°] vs. Time [s] for sensorless speed control at $i_{q3\_max}^* \approx 10$ A on M3.

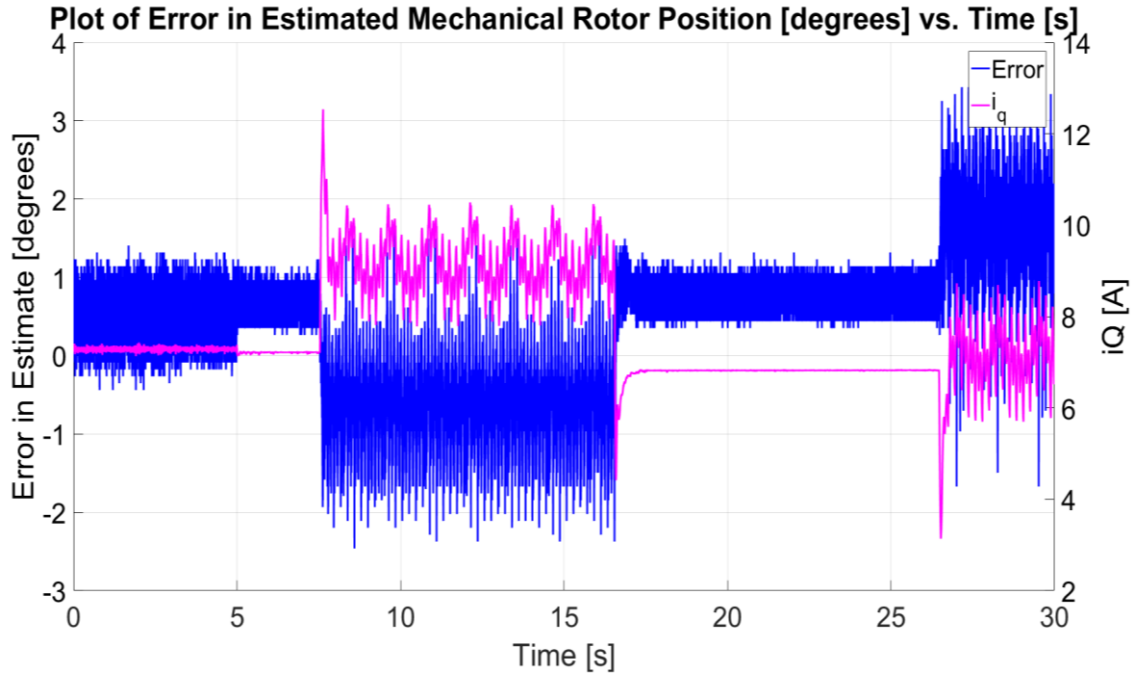

Figure 9.8 – Plot of Error in Estimated Mechanical Rotor Position θ_m [°] vs. Time [s] for sensorless speed control at $i_{q3\_max}^* \approx 10$ A on M3.

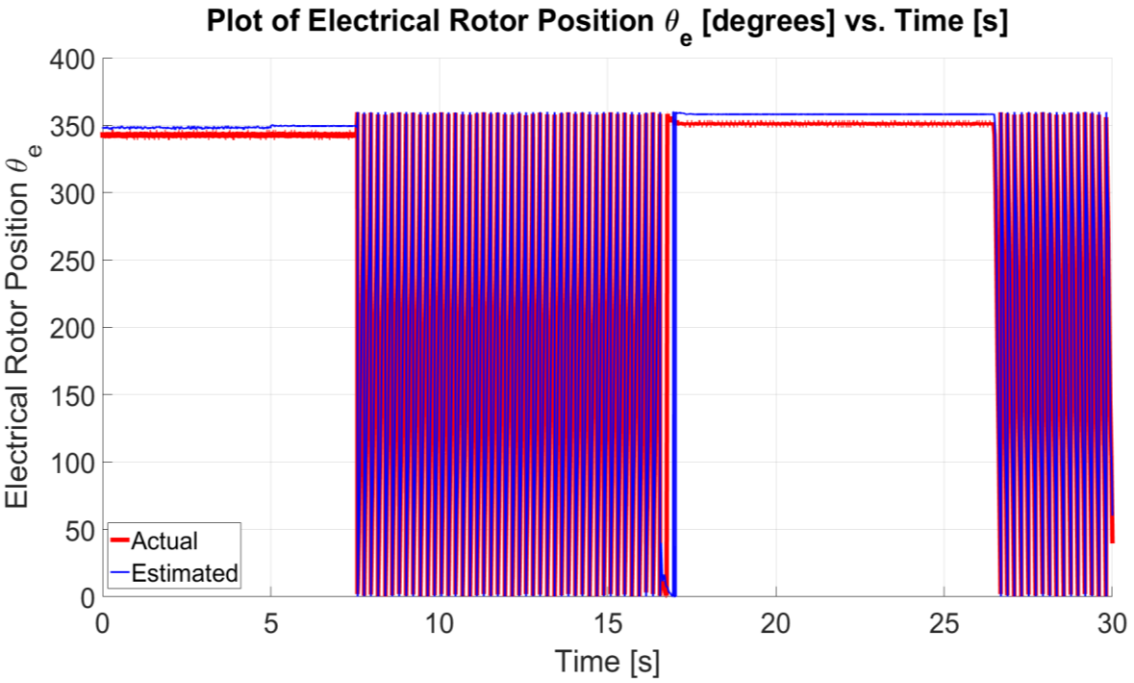

Figure 9.9 – Plot of Actual/Estimate Electrical Rotor Position θ_e [°] vs. Time [s] for sensorless speed control at $i_{q3\_max}^* \approx 10$ A on M3.

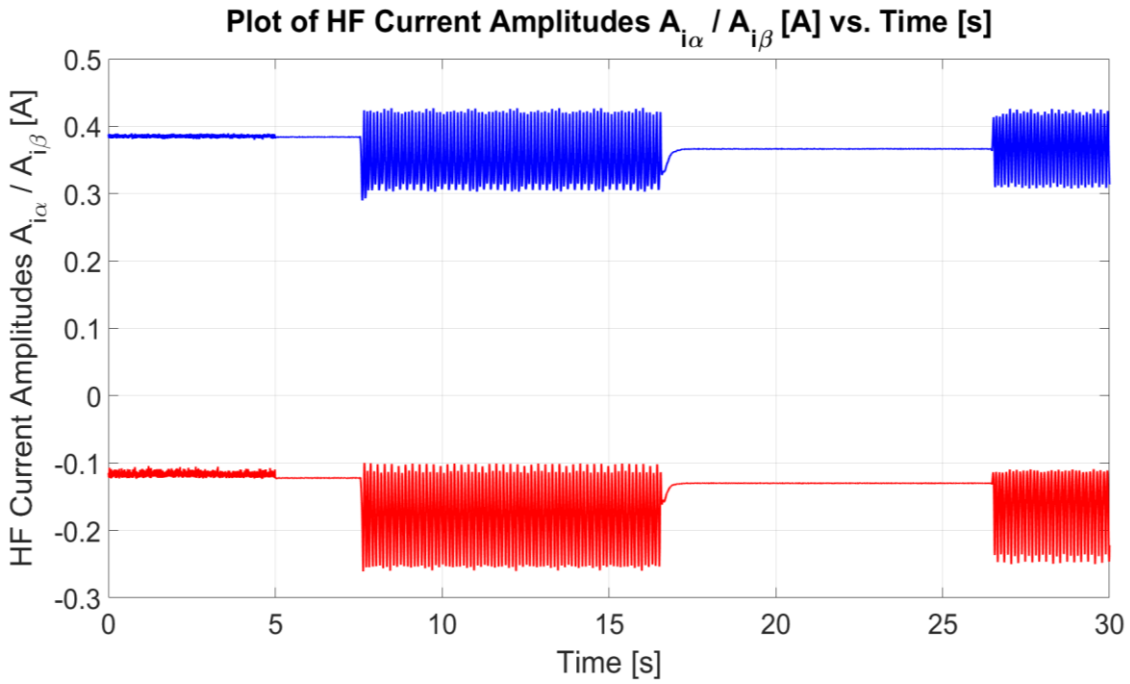

Figure 9.10 –Plot of HF Current Amplitudes $A_{i\alpha}$, $A_{i\beta}$ [A] vs. Time [s] for sensorless speed control at $i_{q3\_max}^{*} \approx 10$ A on M3.

9.4 Sensorless Speed Control with Bidirectional Speed and Reverse Torque

The sensorless speed operation of the machine was tested under loaded conditions similarly to Section 9.3 but with reverse torque applied by M4. The synchronous reference frame currents for the load machine, M4, were set as follows: $i_{d4}^{*} = 0$ A and i_{q4}^{*} was adjusted such that the maximum i_q-current on the sensorless machine M3 is approximately -10 A in steady-state. The speed reference profile is similar to that used in Sections 9.2 – 9.3 from 2.5 rad/s (23.8 rpm) to 0 rad/s and finally to -2.5 rad/s (-23.8 rpm). The speed controller gain settings are identical to those in Section 9.3.

The reference, actual and estimated rotor speeds are shown in Figure 9.11 with a changeover from sensored to sensorless operation at t = 2.58 s. The actual/estimated ***mechanical*** rotor positions are shown in Figure 9.12, with the error between the two shown in Figure 9.13. The maximum absolute error in the mechanical rotor position is 4.92° with a RMSE of 1.31°. The actual/estimated ***electrical*** rotor positions are shown in Figure 9.14. The HF current amplitudes $A_{i\alpha}$, $A_{i\beta}$ are shown in Figure 9.15. The sensorless operation of the machine was observed to be stable throughout the period of operation shown with a maximum load of approximately $i_{q3\_max}^{*} \approx -10$ A which corresponds to 100 % rated load.

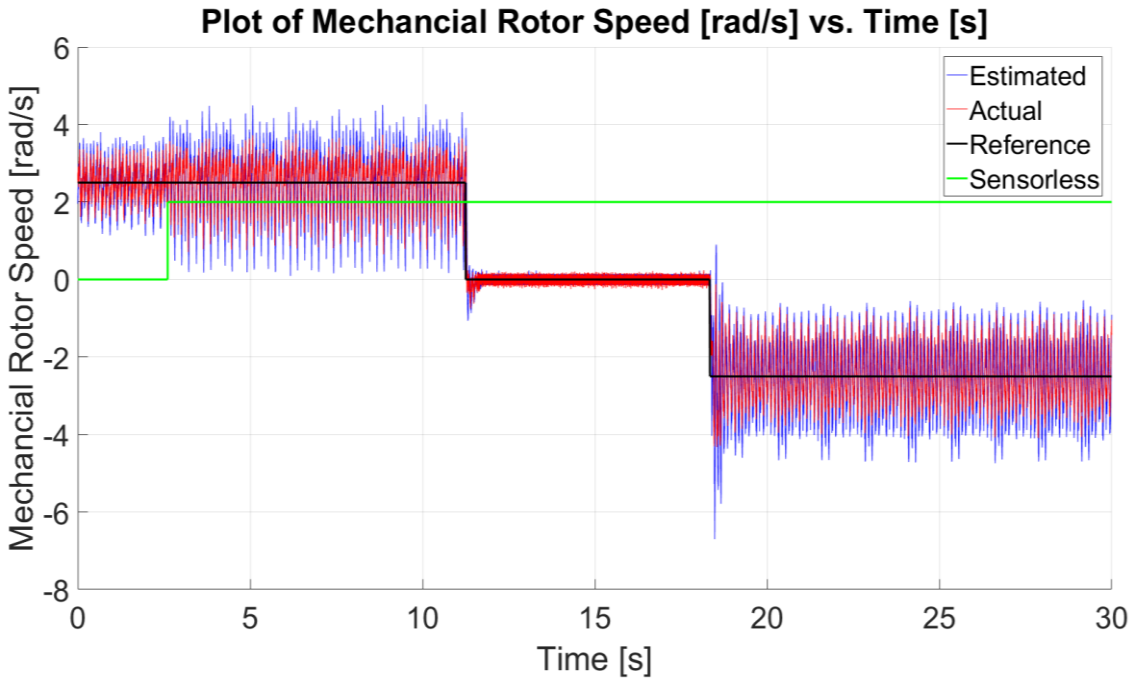

Figure 9.11 – Plot of Reference/Actual/Estimated Rotor Speed ω_m [°] vs. Time [s] for sensorless speed control at $i_{q3\_max}^* \approx$ -10 A on M3.

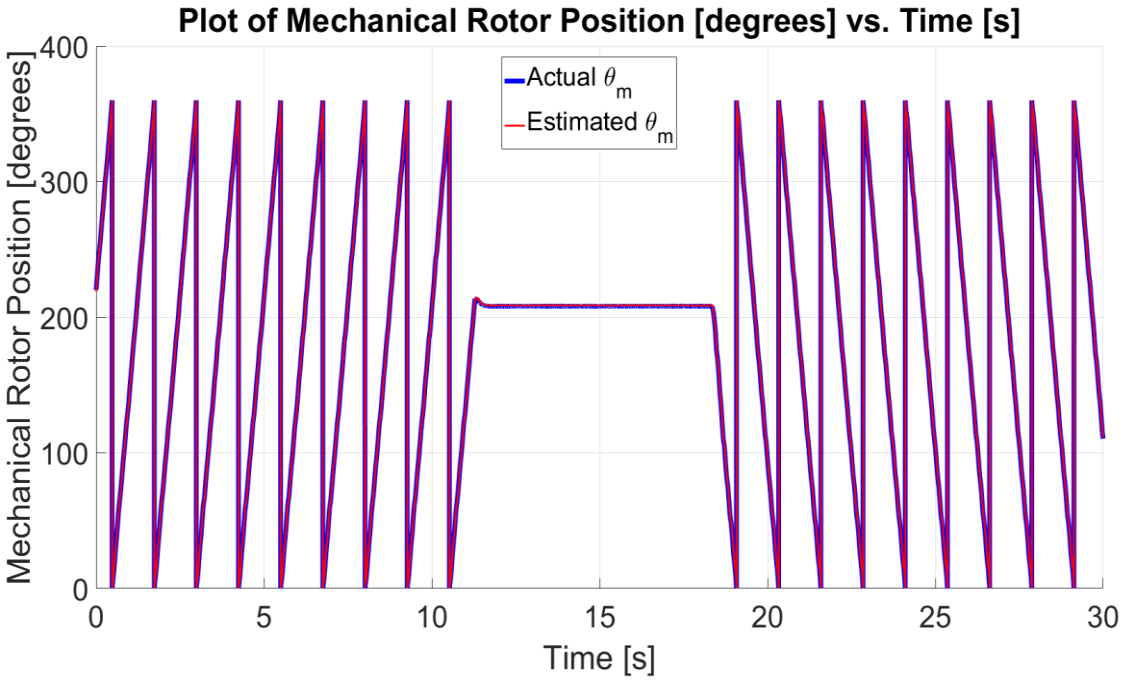

Figure 9.12 – Plot of Actual/Estimate Mechanical Rotor Position θ_m [°] vs. Time [s] for sensorless speed control at $i_{q3\_max}^* \approx$ -10 A on M3.

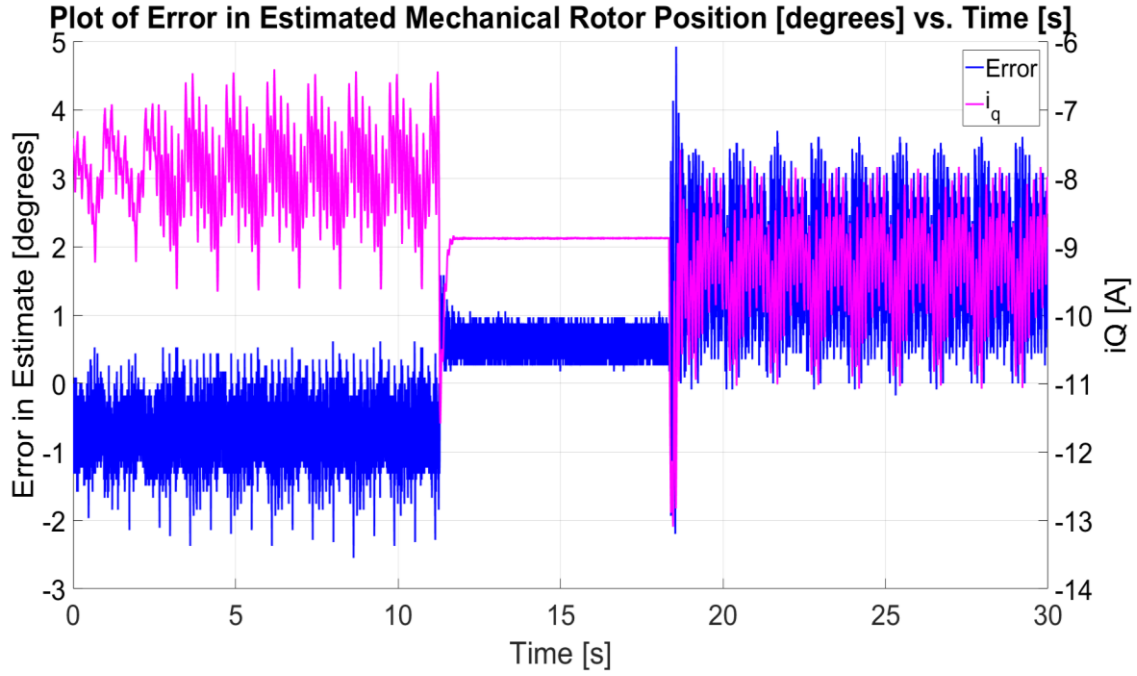

Figure 9.13 – Plot of Error in Estimated Mechanical Rotor Position θ_m [°] vs. Time [s] for sensorless speed control at $i_{q3\_max}^* \approx$ -10 A on M3.

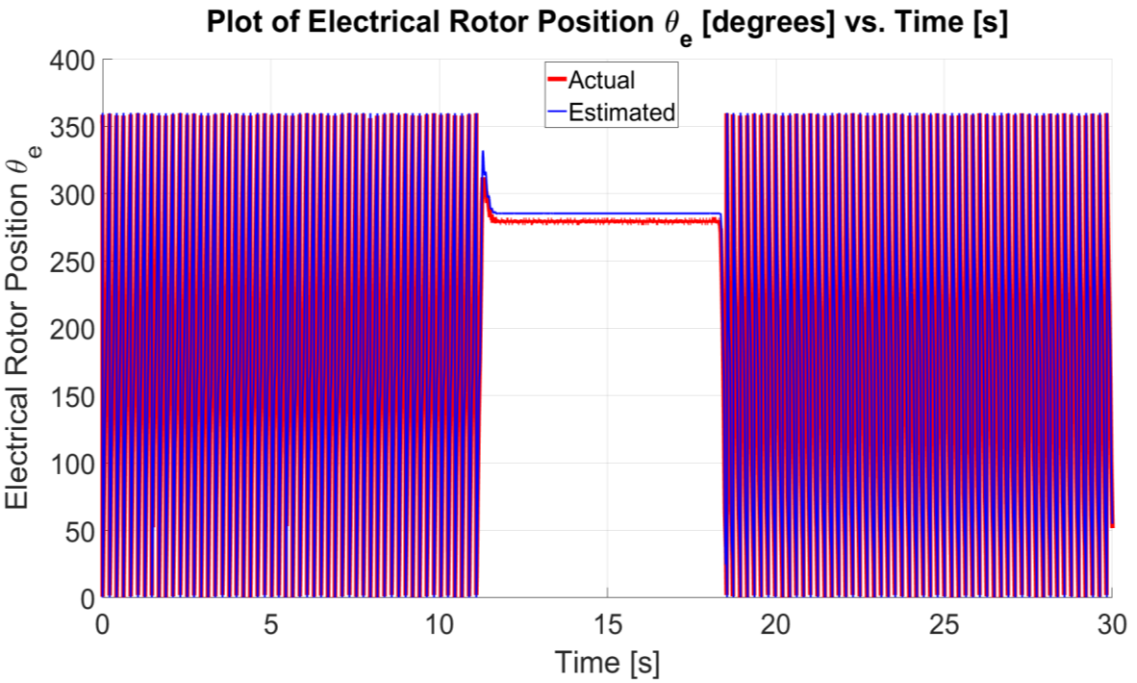

Figure 9.14 – Plot of Actual/Estimate Electrical Rotor Position θ_e [°] vs. Time [s] for sensorless speed control at $i_{q3\_max}^* \approx$ -10 A on M3.

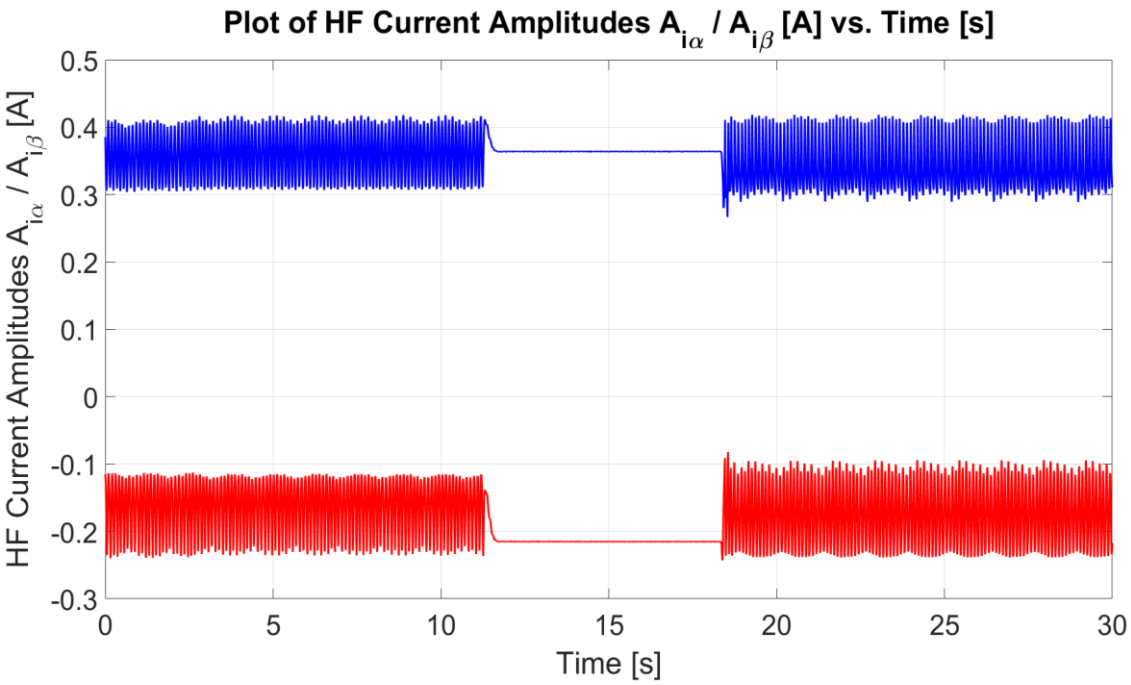

Figure 9.15 –Plot of HF Current Amplitudes $A_{i\alpha}$, $A_{i\beta}$ [A] vs. Time [s] for sensorless speed control at $i_{q3\_max}^{*} \approx$ -10 A on M3.

9.5 Sensorless Speed Control with Constant Forward Speed and Varying Torque

The sensorless speed control operation was also tested with a constant speed reference (ω_{m3}^{*} = 2 rad/s) on machine M3 with varying load. The current reference on the loading machine M4 was varied such that the i_q-current on the sensorless machine was varied between approximately -10 A $\leq i_{q3} \leq$ 10 A. The SBO and speed controller settings are identical to Sections 9.2 – 9.4. The reference, actual and estimated rotor speeds are shown in Figure 9.16 during sensorless speed control. The actual and estimated ***mechanical*** rotor positions are shown in Figure 9.17, with the error between the two shown in Figure 9.18. The absolute maximum error in the ***mechanical*** rotor position is 3.51°, with a RMSE of 0.59°. The actual and estimated ***electrical*** rotor positions are shown in Figure 9.19. The HF current amplitudes $A_{i\alpha}$ and $A_{i\beta}$ are shown in Figure 9.20.

The rotational speed estimate of the sensorless machine is shown in Figure 9.16 to be affected by the i_q-current. The transients on the estimated speed increase as the machine is operated close to full-load. The lower accuracy of the SBO can also be seen from Figure 9.18 as higher transients occur in the observer estimate as a function of the increased load. The actual rotational speed has lower transients than the estimated components since the higher frequency components are attenuated by the speed controller bandwidth.

Since the sensorless machine is operated in speed-controlled mode, the i_q-current is also dependent on the load machine. While carrying out experimental results in this dissertation, it was noticed that reduced the current controller bandwidth of the load machine M4 reduced the low-frequency oscillations on both the rotor speed and current of the sensorless machine. The magnetic signature was also observed to be predominantly a function of the i_q-current similarly to what was shown for sensorless current control in Chapter 8.

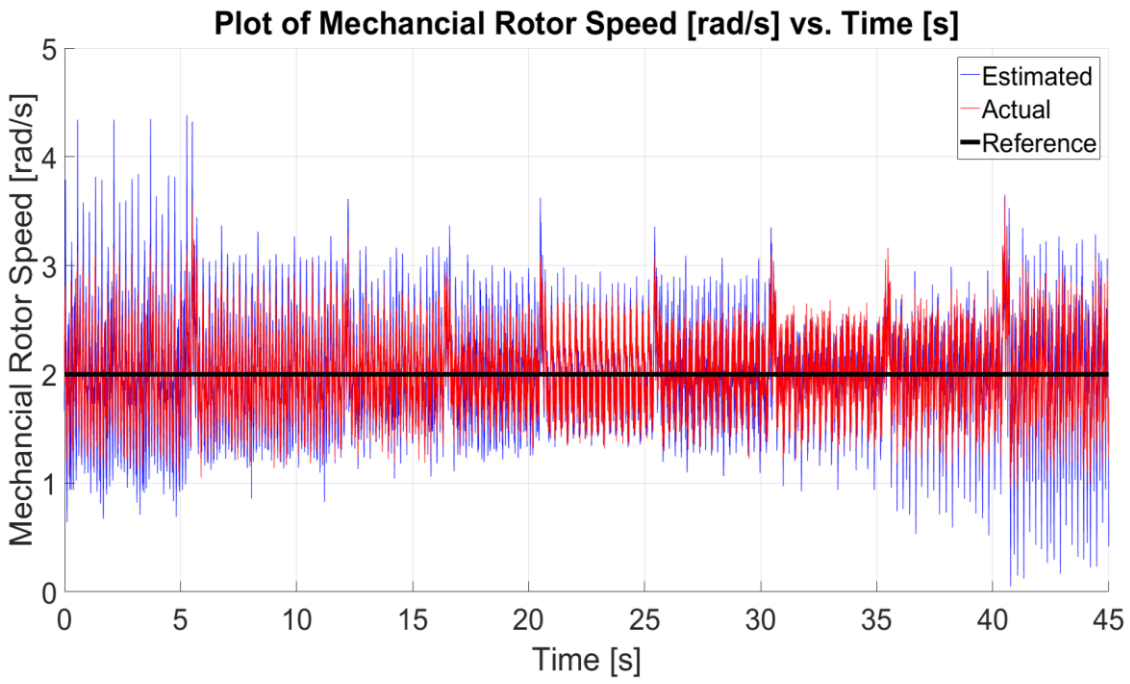

Figure 9.16 – Plot of Reference/Actual/Estimated Rotor Speed ω_m [°] vs. Time [s] for sensorless speed control at ω_{m3}^*=2 rad/s on M3, -10 A ≤ i_{q3} ≤ 10 A.

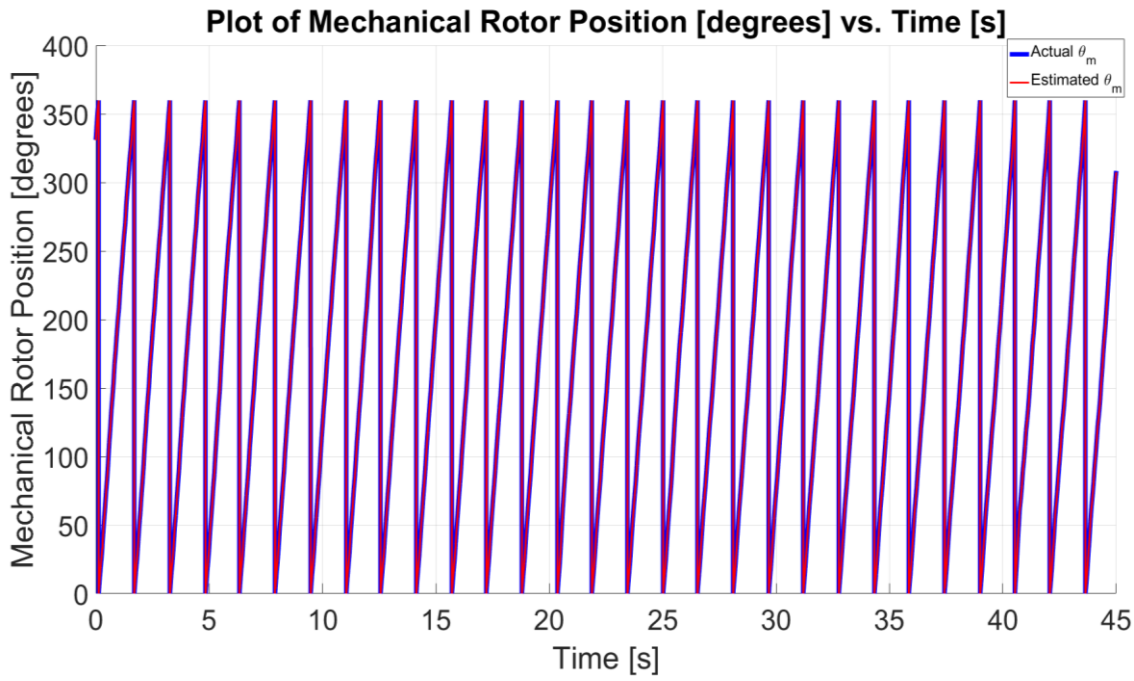

Figure 9.17 – Plot of Actual/Estimate Mechanical Rotor Position θ_m [°] vs. Time [s] for sensorless speed control at ω_{m3}^*=2 rad/s on M3, -10 A ≤ i_{q3} ≤ 10 A.

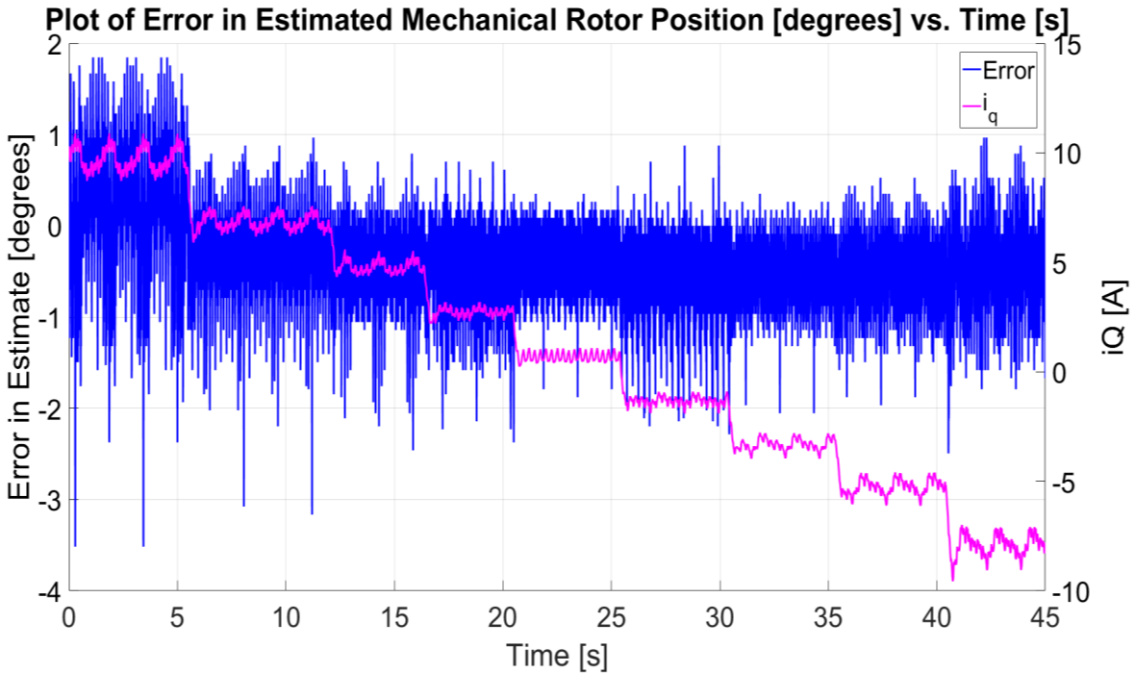

Figure 9.18 – Plot of Error in Estimated Mechanical Rotor Position θ_m [°] vs. Time [s] for sensorless speed control at ω_{m3}^*=2 rad/s on M3, -10 A ≤ i_{q3} ≤ 10 A.

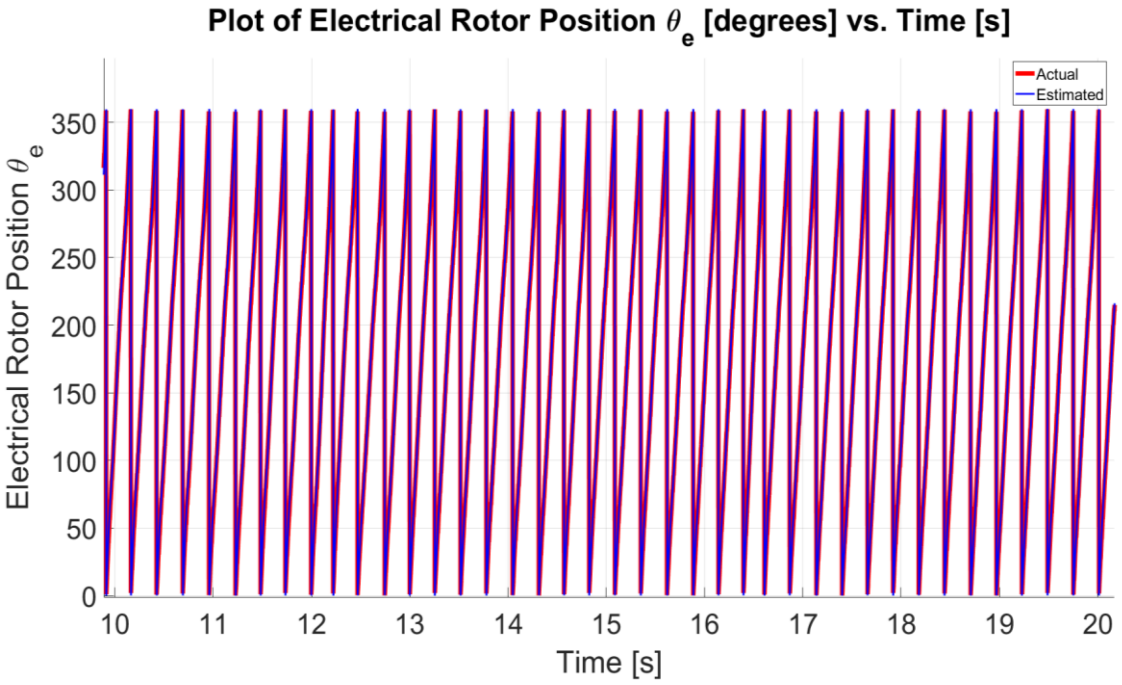

Figure 9.19 – Plot of Actual/Estimate Electrical Rotor Position θ_e [°] vs. Time [s] for sensorless speed control at ω_{m3}^*=2 rad/s on M3, -10 A ≤ i_{q3} ≤ 10 A.

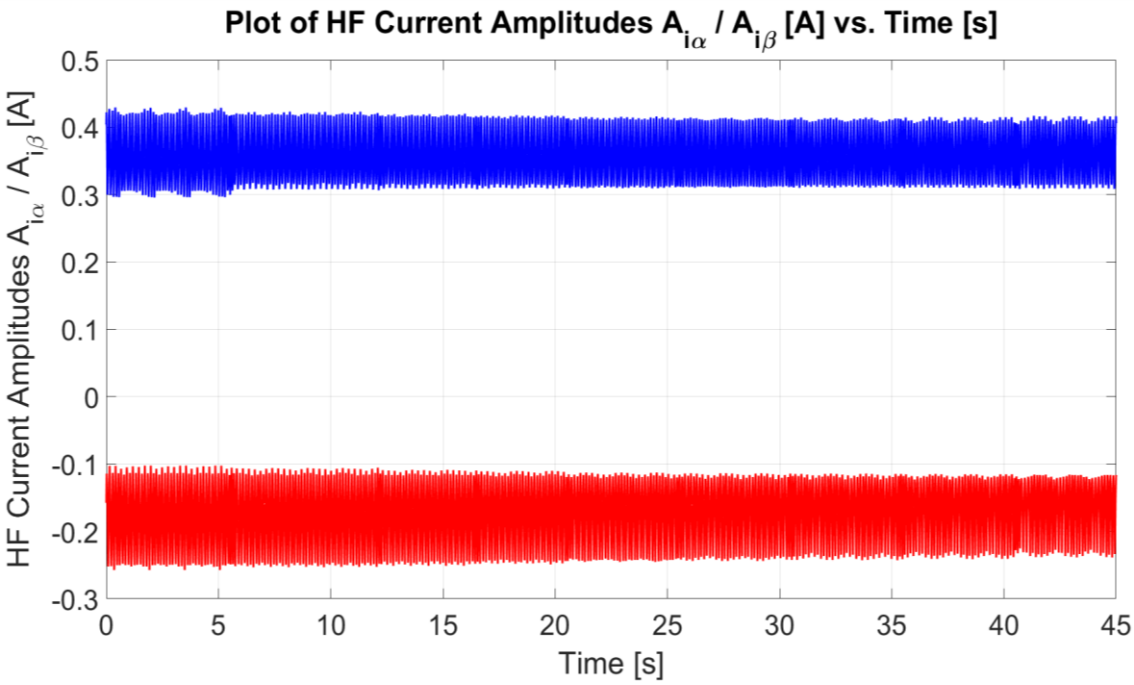

Figure 9.20 –Plot of HF Current Amplitudes $A_{i\alpha}$, $A_{i\beta}$ [A] vs. Time [s] for sensorless speed control at ω_{m3}^*=2 rad/s on M3, -10 A ≤ i_{q3} ≤ 10 A.

9.6 Sensorless Speed Control with Constant Reverse Speed and Varying Torque

The sensorless speed control operation on machine M3 was also tested at a constant speed reference ω_{m3}^* = -2.5 rad/s and varying loading conditions similarly to Section 9.5. The reference, actual and estimated rotor speeds are shown in Figure 9.21 in sensorless speed control. The actual and estimated ***mechanical*** rotor positions are shown in Figure 9.22, and the error between the two is shown in Figure 9.23. The absolute maximum error in the ***mechanical*** rotor position is 4.13°, with a RMSE of 1.59°. The actual and estimated electrical rotor positions are shown in Figure 9.24. The HF current amplitudes $A_{i\alpha}$ and $A_{i\beta}$ are shown in Figure 9.25.

The results presented in Sections 9.5 and 9.6 show stable sensorless operation at low and zero speed using the proposed SBO. For sensorless operation, the speed controller gains (K_{p_W3} = 0.1, K_{i_W3} = 10) were reduced with respect to those used in sensored operation (K_{p_W3} = 0.3, K_{i_W3} = 60). Results were shown for operation with positive and negative rated current of the machine under test. The main reason for this reduction in bandwidth was in order for the speed controller to attenuate the noise in the speed estimate.

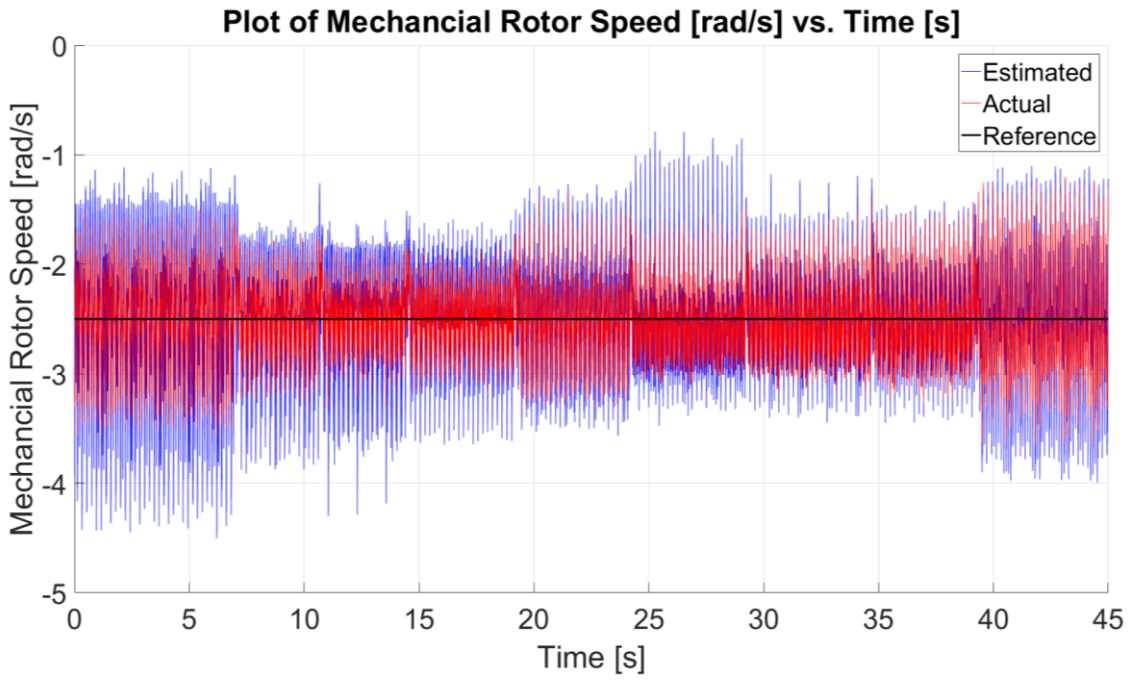

Figure 9.21 – Plot of Reference/Actual/Estimated Rotor Speed ω_m [°] vs. Time [s] for sensorless speed control at ω_{m3}^*=-2.5 rad/s on M3, -10 A ≤ i_{q3} ≤ 10 A.

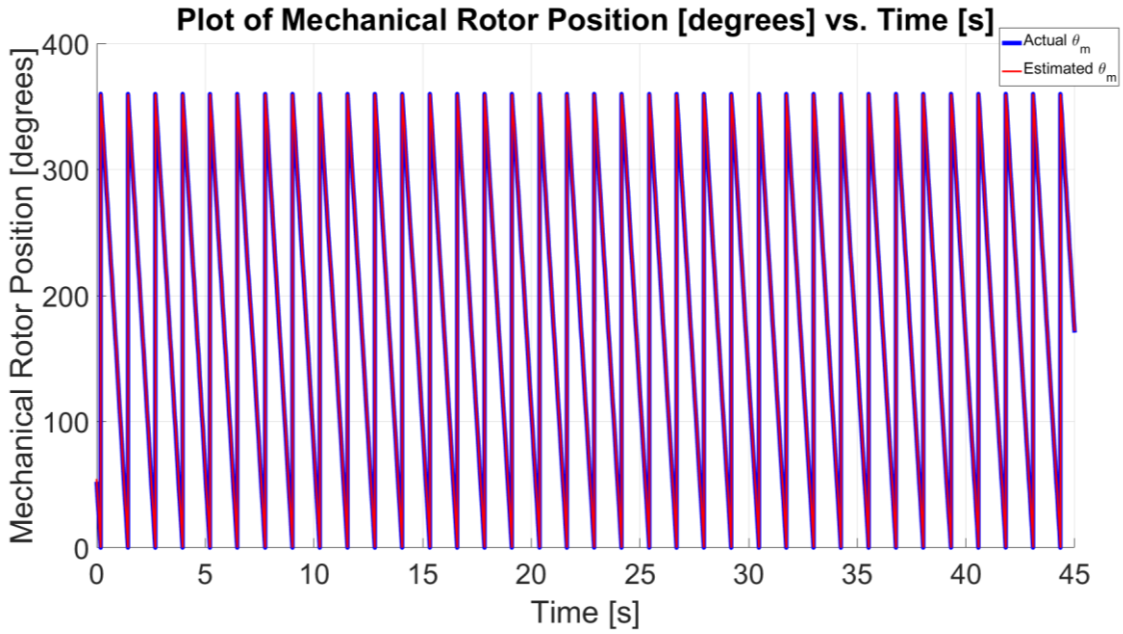

Figure 9.22 – Plot of Actual/Estimate Mechanical Rotor Position θ_m [°] vs. Time [s] for sensorless speed control at ω_{m3}^*=-2.5 rad/s on M3, -10 A ≤ i_{q3} ≤ 10 A.

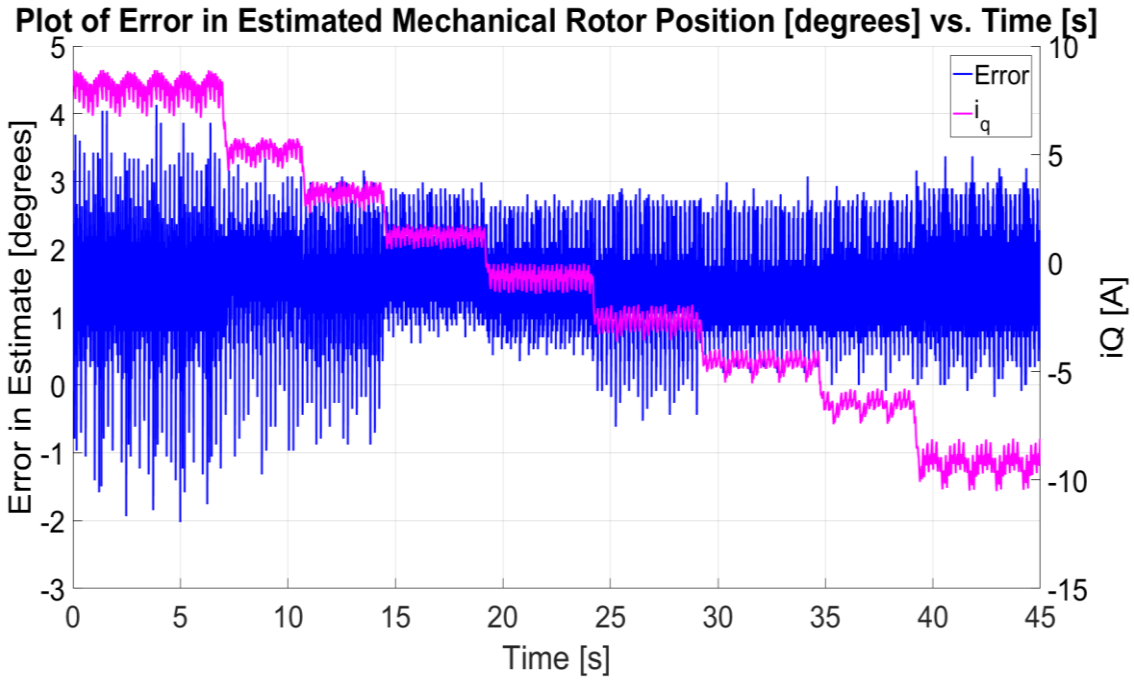

Figure 9.23 – Plot of Error in Estimated Mechanical Rotor Position θ_m [°] vs. Time [s] for sensorless speed control at ω_{m3}^*=-2.5 rad/s on M3, -10 A ≤ i_{q3} ≤ 10 A.

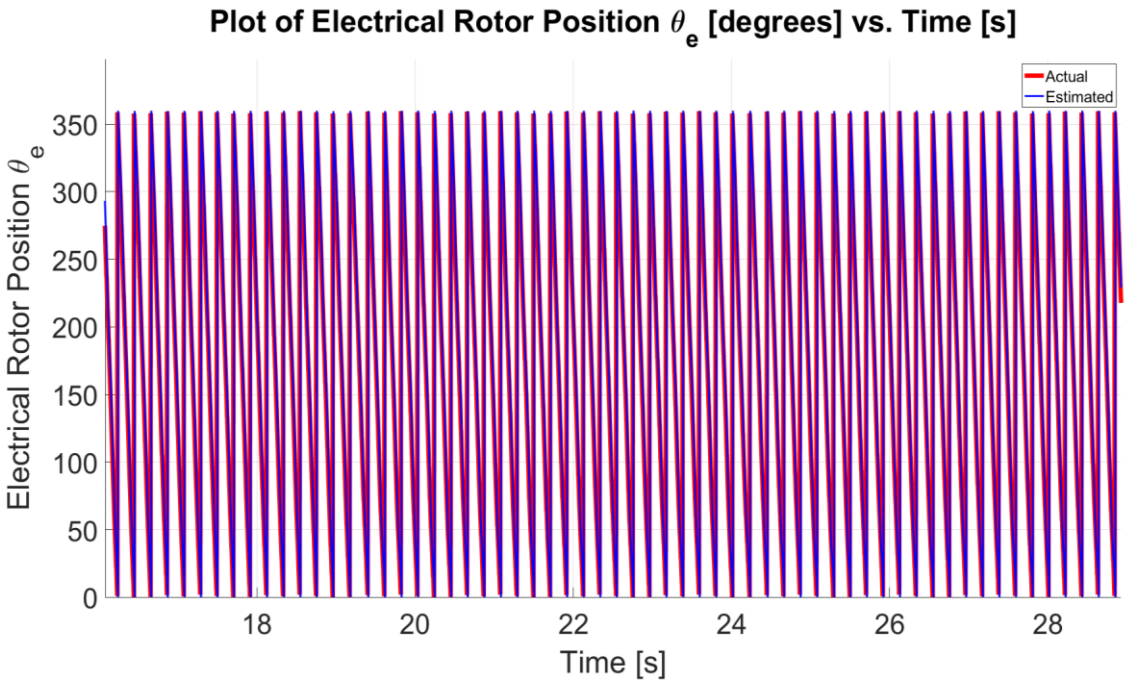

Figure 9.24 – Plot of Actual/Estimate Electrical Rotor Position θ_e [°] vs. Time [s] for sensorless speed control at ω_{m3}^*=-2.5 rad/s on M3, -10 A ≤ i_{q3} ≤ 10 A.

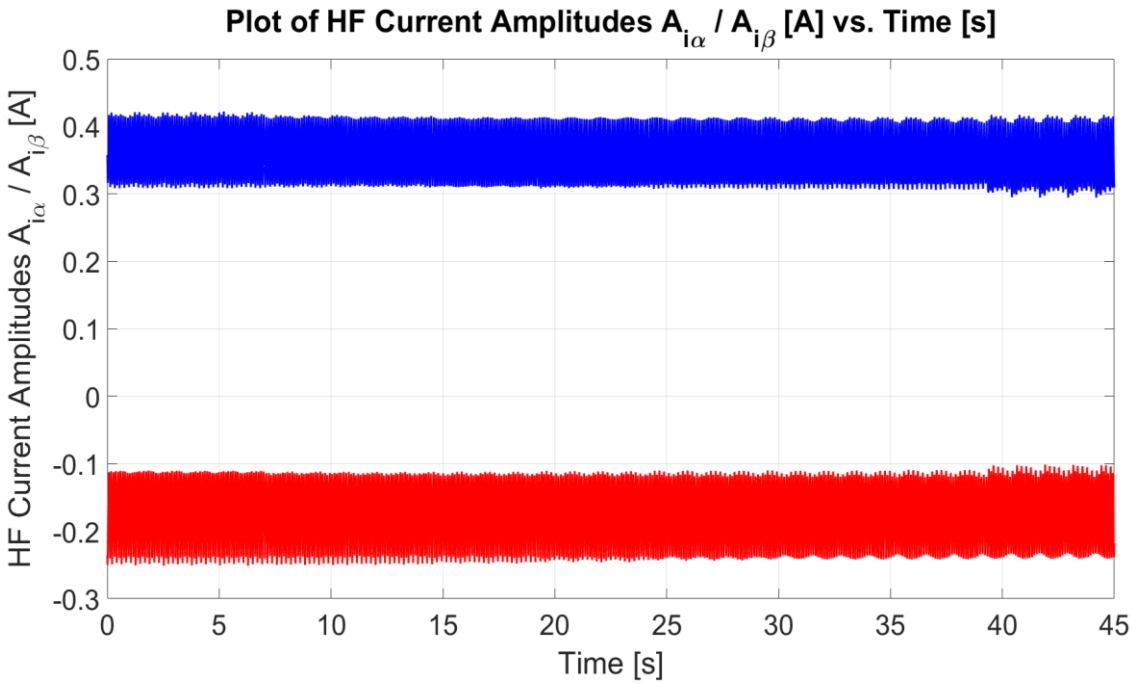

Figure 9.25 –Plot of HF Current Amplitudes $A_{i\alpha}$, $A_{i\beta}$ [A] vs. Time [s] for sensorless speed control at ω_{m3}^*=-2.5 rad/s on M3, -10 A ≤ i_{q3} ≤ 10 A.

9.7 Sensorless Position Control at No Load

One of the fundamental aims of this dissertation was to implement a position-controlled drive at the steered wheel end of the steer-by-wire application. Position control of the PMSM was investigated in sensored mode for step-inputs (Section 3.6.1) and sigmoid inputs to replicate steer-by-wire conditions (Sections 3.6.2-3.6.3). One of the requirements for steer-by-wire is the rapid positioning of the wheels in order to replicate the steering performance of what is found in a traditional steering arrangement. Therefore, the aim of the SBO in sensorless steer-by-wire is to estimate the required parameters for RFO control with a minimum reduction in dynamics. Typically a reduction in the RFO topology gains is required in sensorless control of electric drives to mitigate the effects of transient estimation errors.

The sensorless position control results were obtained for the RFO closed-loop position control system shown in Figure 3.3 (Section 3.2.3). The sensorless position performance of the SBO is shown in this section for the machine under test, M3, under no-load conditions. The load is set by machine M4 ($i_{d4}^* = 0$A, $i_{q4}^* = 0$ A). The sensorless position control system was found to be stable for a maximum proportional gain $K_{p\_P3} = 1.5$ set in the microcontroller. An unstable operation resulted for some operating points when the proportional gain was increased further. The speed and current cascaded loop controller gains are set to $K_{p\_I3} = 0.1$, $K_{i\_I3} = 100$, $K_{p\_W3} = 0.1$ $K_{i\_W3} = 10$ in the microcontroller. A step reference input $\theta_m^* = 3$ rad (172°) is applied at t = 4.95 s while in sensorless position control mode.

The reference, actual and estimated ***mechanical*** rotor positions are shown in Figure 9.26. The error between the actual and estimated ***mechanical*** rotor positions is shown in Figure 9.27, and it obtains an absolute maximum estimate error of 4.57° with a RMSE of 0.54°. The ***electrical*** rotor position is shown in Figure 9.28. The actual and estimated ***mechanical*** rotor speeds are shown in Figure 9.29, while the HF current amplitudes $A_{i\alpha}$ and $A_{i\beta}$ are shown in Figure 9.30. The experimental bandwidth of the closed-loop position system was found to be of 0.54 Hz from the rise time $t_r = 0.64$ s (Figure 9.26).

This is significantly less than what was achieved in sensored operation in Section 3.6.1, where an experimental bandwidth of 1 Hz was measured. This is a result of reducing the proportional gain from K_{p_P3}=5.75 (sensored operation) to K_{p_P3}=1.5 (sensorless

operation) due to the reasons given below. As shown in Figures 9.26 at the instant when the step reference changes are applied (t = 4.29 s and t = 7.74 s), the position controller produces a sharp transient in i_{q3} to attain the reference position similar to what was observed in sensored mode. The error in the estimate is highest during the current transients, as shown in Figure 9.27. The position controller gain K_{p_P3} can be increased further to improve the position controller bandwidth however this will increase the current transient and the observer tends to become unstable at higher loading currents since these have not been mapped onto the LUT during commissioning.

In practical case scenarios such as servo drive applications, the use of a step reference can be avoided by replacing the step with a sigmoid based transition as described in Section 3.6.2. This generally also reduces the error in sensorless mode due to a lower i_q-current transient. Experiments for sensorless position control for the loaded operation were also carried out and are reported in Sections 9.8 – 9.9.

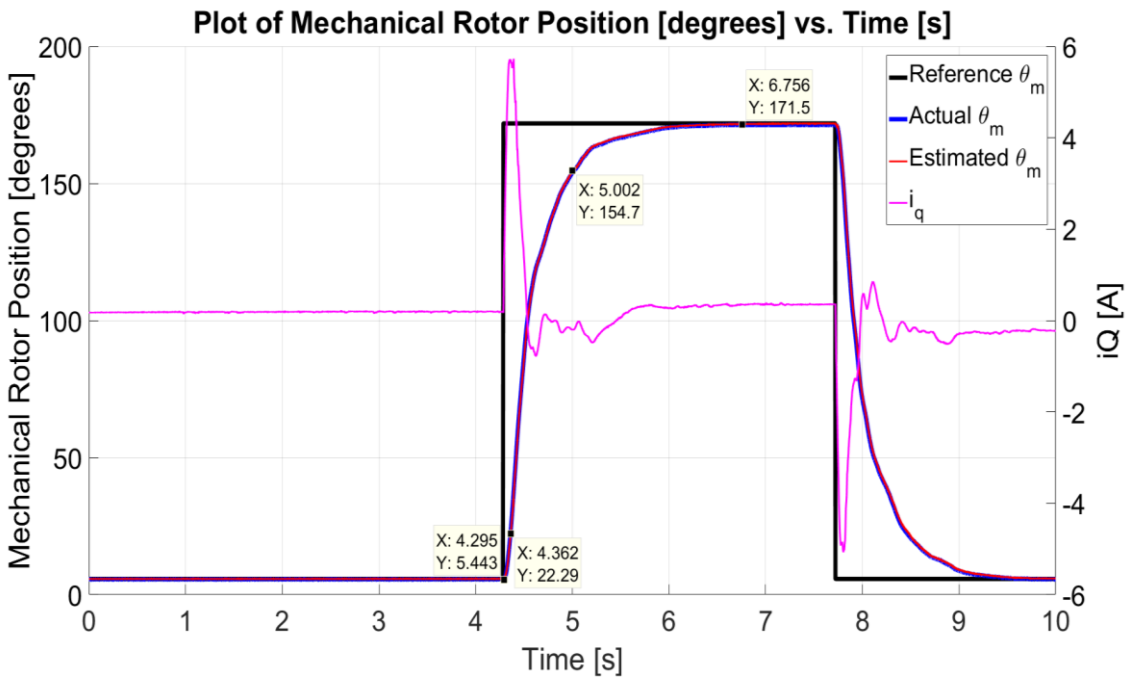

Figure 9.26 – Plot of Reference/Actual/Estimate Mechanical Rotor Position θ_m [°] vs. Time [s] for sensorless position control at no-load.

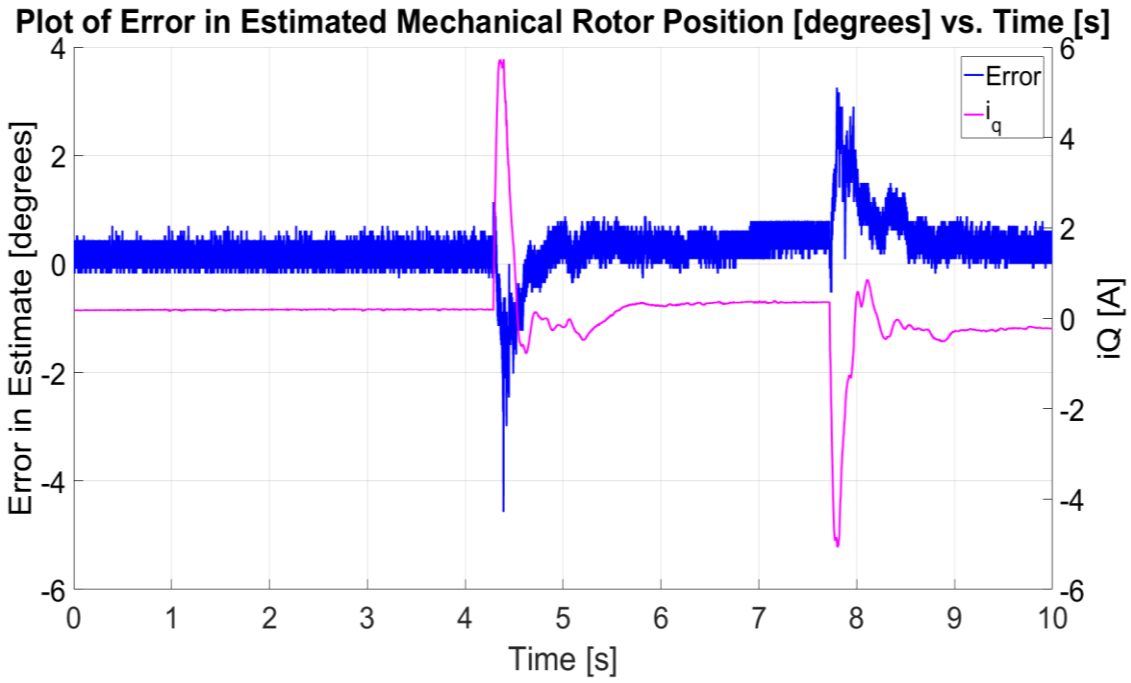

Figure 9.27 – Plot of Error in Estimated Mechanical Rotor Position θ_m [°] vs. Time [s] for sensorless position control at no-load.

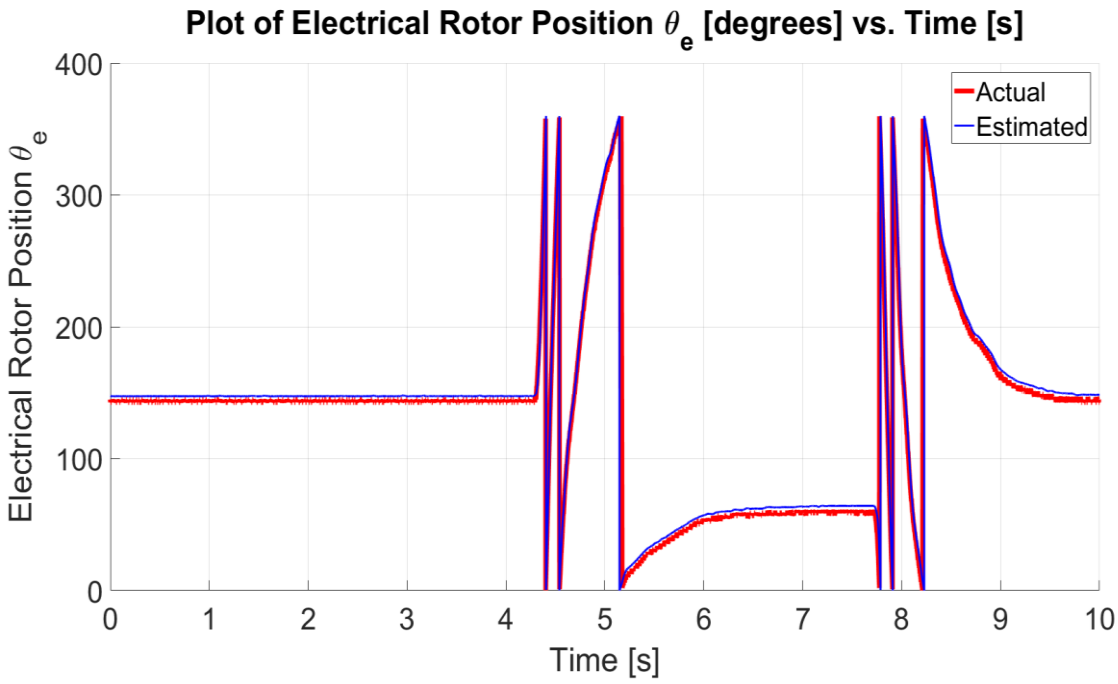

Figure 9.28 – Plot of Actual/Estimate Electrical Rotor Position θ_e [°] vs. Time [s] for sensorless position control at no-load.

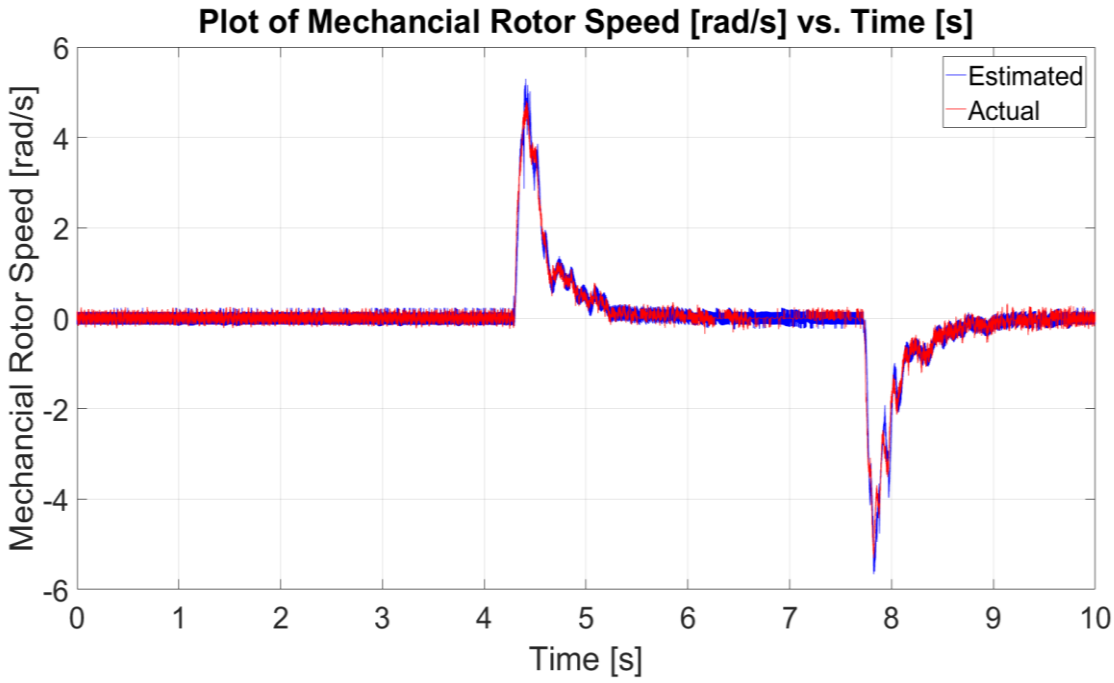

Figure 9.29 – Plot of Actual/Estimated Rotor Speed ω_m [°] vs. Time [s] for sensorless position control at no-load.

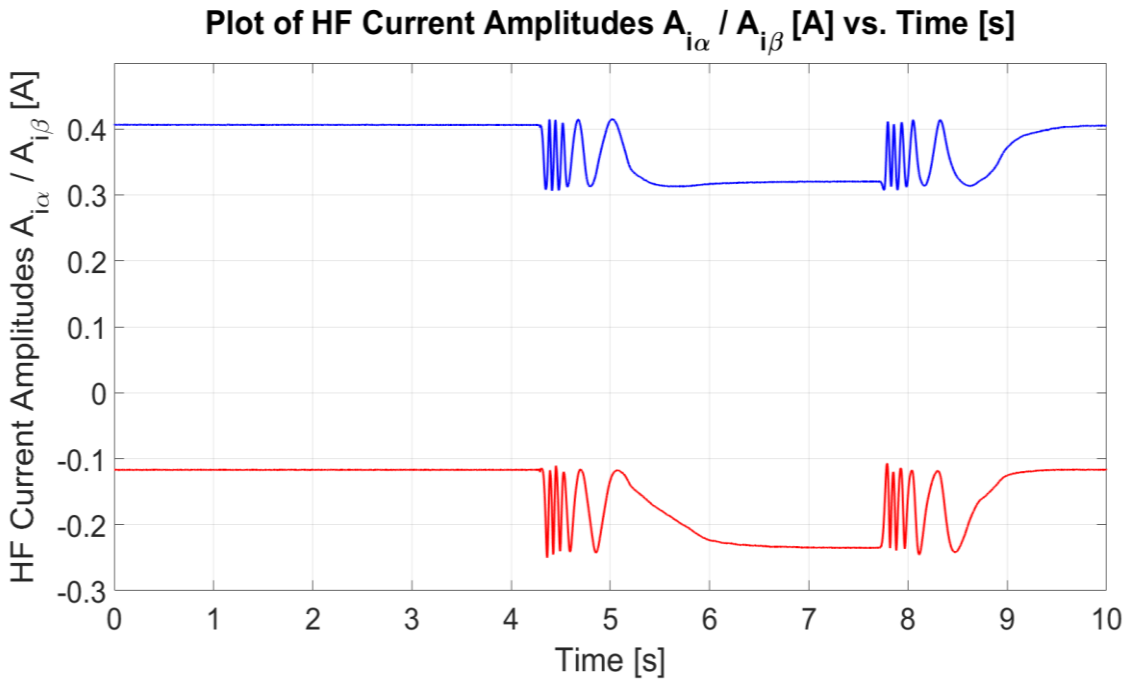

Figure 9.30 –Plot of HF Current Amplitudes $A_{i\alpha}$, $A_{i\beta}$ [A] vs. Time [s] for sensorless position control at no-load.

9.8 Sensorless Position Control with Forward Torque

This section presents the results of the performance of the SBO for sensorless position control of M3 with load set by M4 ($i_{d4}^* = 0$A, $i_{q4}^* = 5$ A). The reference, actual and estimated ***mechanical*** rotor positions are shown in Figure 9.31. The error between the actual and estimated ***mechanical*** rotor positions is shown in Figure 9.27, and it obtains an absolute maximum estimate error of 6.15° with a RMSE of 0.67°. The ***electrical*** rotor position is shown in Figure 9.33. The actual and estimated ***mechanical*** rotor speeds are shown in Figure 9.34 while the HF current amplitudes $A_{i\alpha}$ and $A_{i\beta}$ are shown in Figure 9.35.

The average load imposed on the machine was of $i_{q3} = 4.1$ A. It was not possible to increase this further, due to the fact that during a position transient the instantaneous i_q-current goes beyond 11.16 A (Figure 9.32). Since the SBO observer tables were calibrated for -10 A $\leq i_{q3} \leq$ 10 A, higher currents would be out of range for the observer. In fact, any values outside this range are limited and mapped to the ±10 A LUTs.

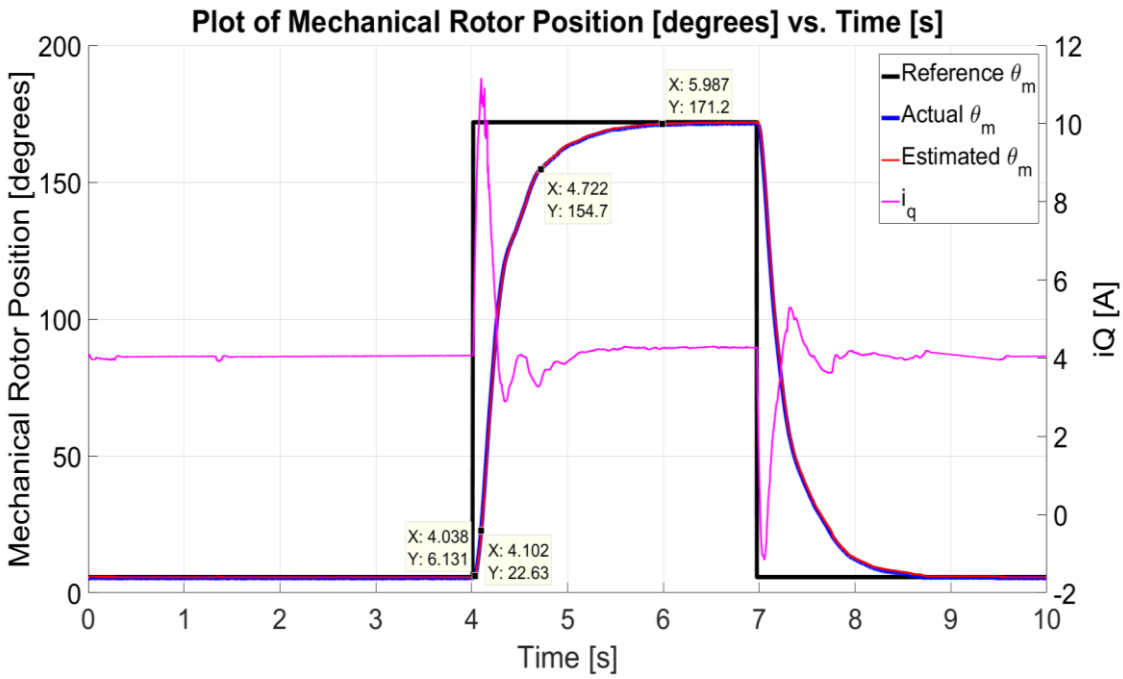

Figure 9.31 – Plot of Reference/Actual/Estimate Mechanical Rotor Position θ_m [°] vs. Time [s] for sensorless position control at $i_{q4}^* = 5$ A on M4.

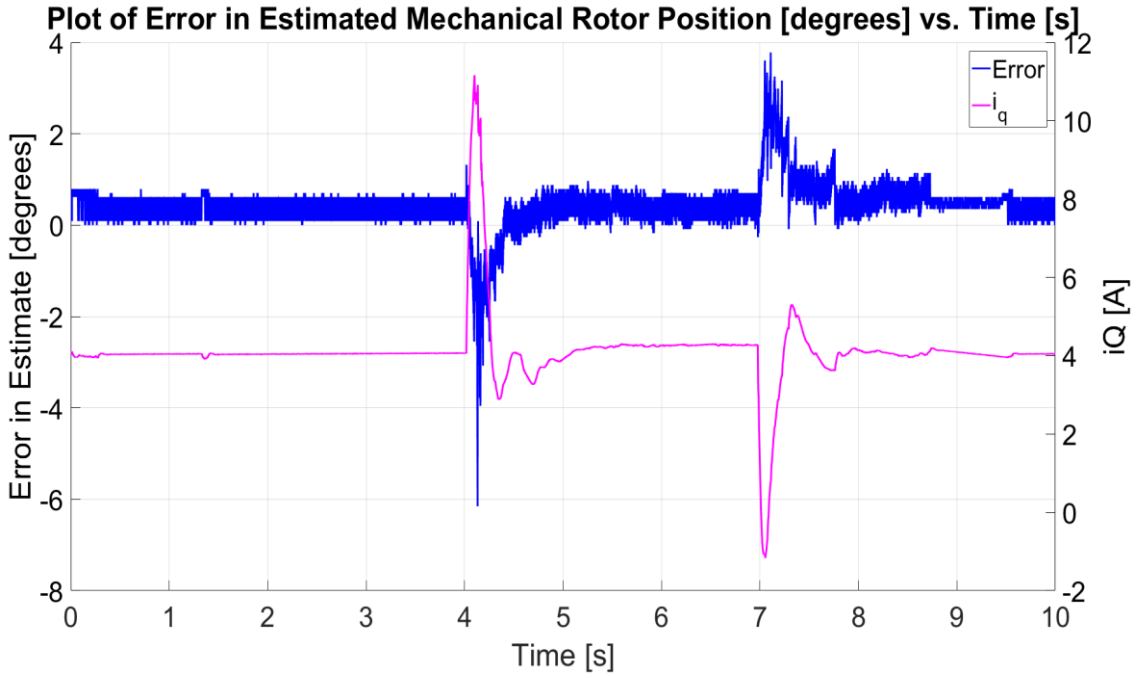

Figure 9.32 – Plot of Error in Estimated Mechanical Rotor Position θ_m [°] vs. Time [s] for sensorless position control at $i_{q4}^* = 5$ A on M4.

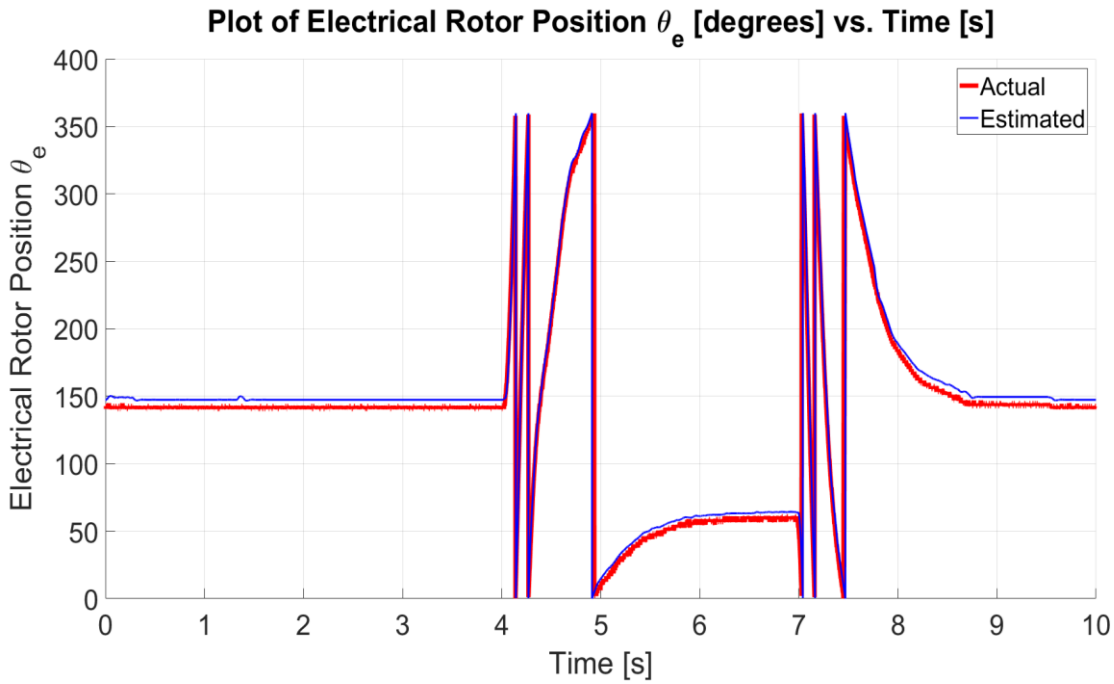

Figure 9.33 – Plot of Actual/Estimate Electrical Rotor Position θ_e [°] vs. Time [s] for sensorless position control at $i_{q4}^* = 5$ A on M4.

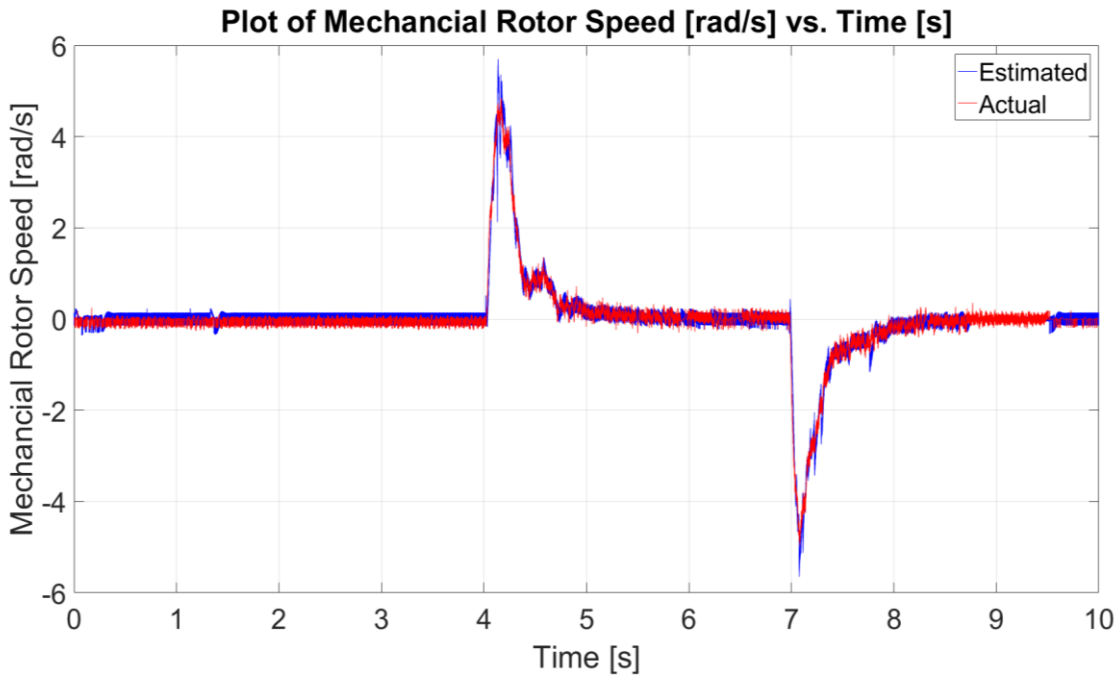

Figure 9.34 – Plot of Actual/Estimated Rotor Speed ω_m [°] vs. Time [s] for sensorless position control at $i_{q4}^* = 5$ A on M4.

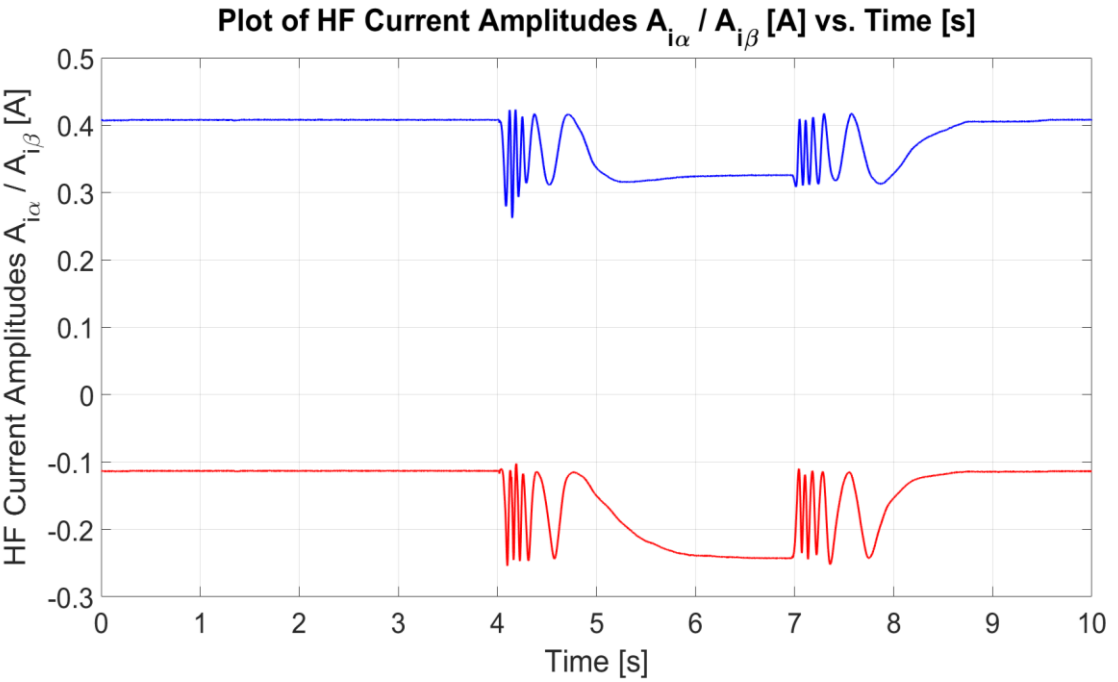

Figure 9.35 –Plot of HF Current Amplitudes $A_{i\alpha}$, $A_{i\beta}$ [A] vs. Time [s] for sensorless position control at $i_{q4}^* = 5$ A on M4.

9.9 Sensorless Position Control with Reverse Torque

This section presents the results of the performance of the SBO for sensorless position control of M3 with load set by M4 ($i_{d4}^* = 0$A, $i_{q4}^* = -5$ A). The reference, actual and

estimated ***mechanical*** rotor positions are shown in Figure 9.36. The error between the actual and estimated ***mechanical*** rotor positions is shown in Figure 9.37, and it obtains an absolute maximum estimate error of 4.84° with a RMSE of 0.43°. The ***electrical*** rotor position is shown in Figure 9.38. The actual and estimated ***mechanical*** rotor speeds are shown in Figure 9.39 while the HF current amplitudes $A_{i\alpha}$ and $A_{i\beta}$ are shown in Figure 9.40. The average load imposed on the machine was of i_{q3} = -4.1 A. In the case of reverse torque, the current during transient conditions does not exceed the -10 A value which is the maximum negative current which was calibrated for. This further confirms that the frictional forces acting upon the shaft are dependent on the quadrant of operation, as the maximum i_q-current required for the same controller gain and load current was significantly less than that for forward torque. Hence, the load imposed on the sensorless position machine could be increased further. However, it was left unchanged, so a comparison could be drawn with the results presented in Section 9.8. When comparing the maximum error in the estimated ***mechanical*** rotor position for positive/negative torque that for positive torque is slightly higher (6.15°) than that for negative torque (4.84°), the RMSE for positive torque is also higher (0.67°) when compared to that for negative torque (0.43°). This is mainly attributed to the fact that during the position transient for positive torque, the actual i_q-current exceeds the calibrated range which is not the case for negative torque.

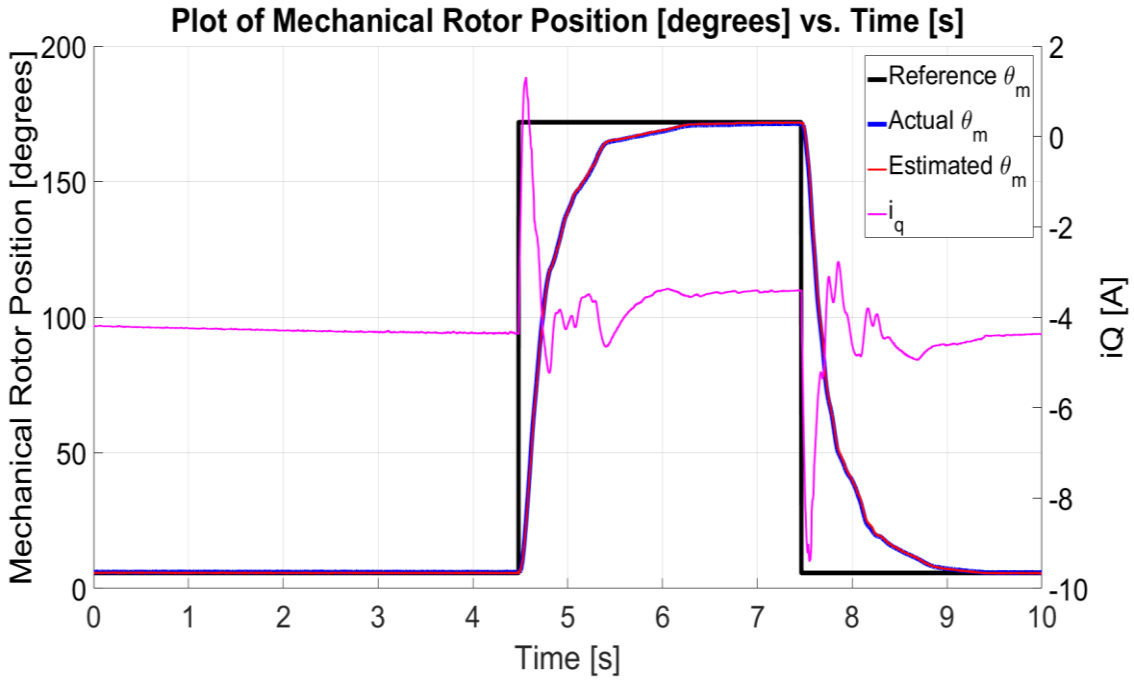

Figure 9.36 – Plot of Reference/Actual/Estimate Mechanical Rotor Position θ_m [°] vs. Time [s] for sensorless position control at i_{q4}^* = -5 A on M4.

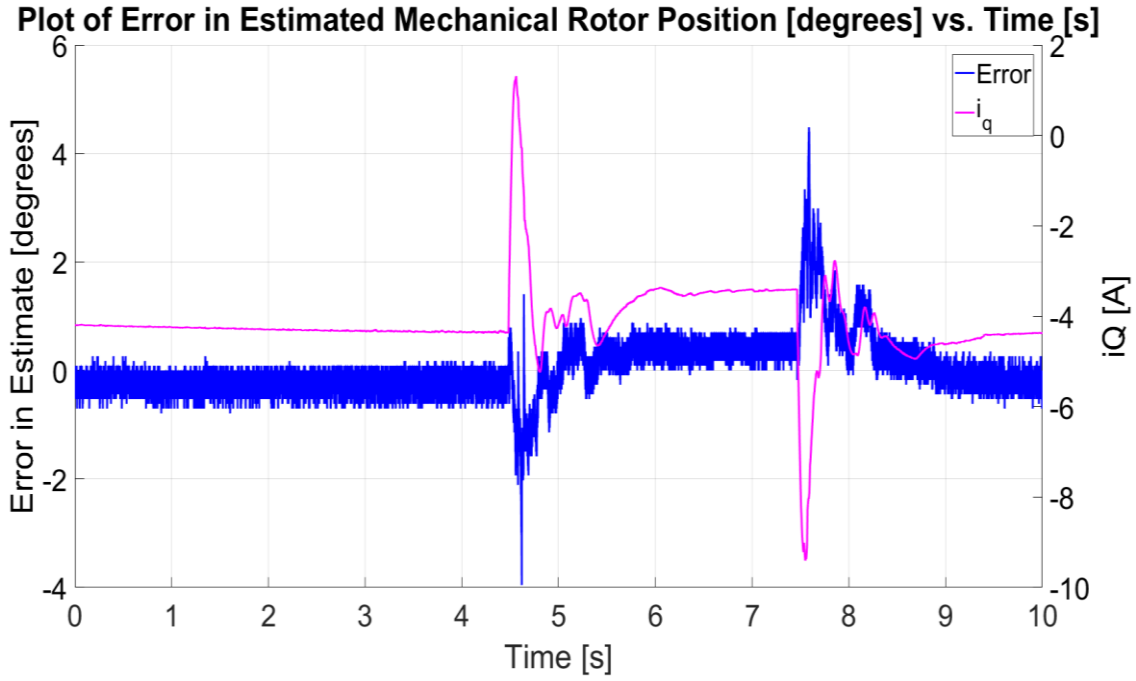

Figure 9.37 – Plot of Error in Estimated Mechanical Rotor Position θ_m [°] vs. Time [s] for sensorless position control at $i_{q4}^* = -5$ A on M4.

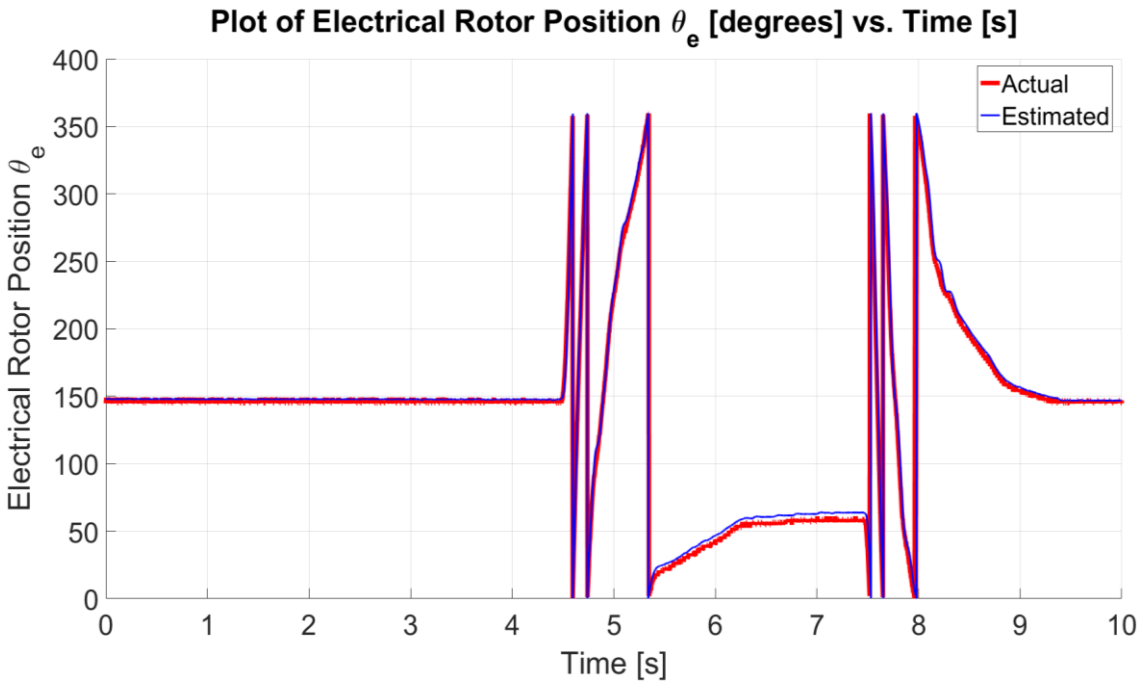

Figure 9.38 – Plot of Actual/Estimate Electrical Rotor Position θ_e [°] vs. Time [s] for sensorless position control at $i_{q4}^* = -5$ A on M4.

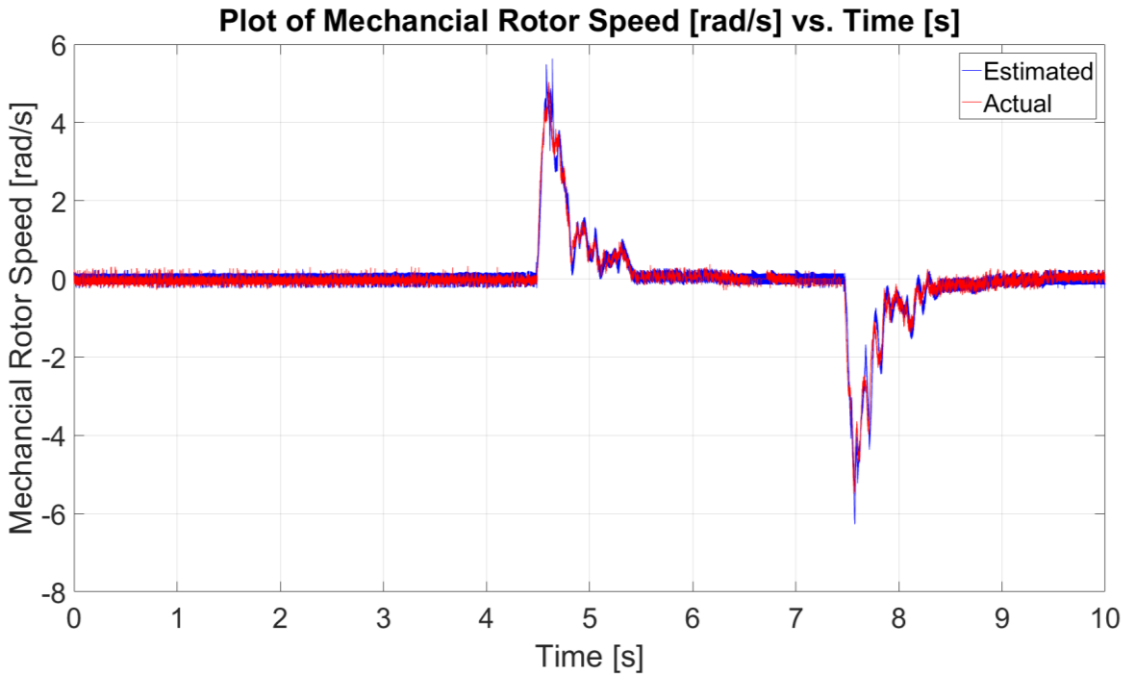

Figure 9.39 – Plot of Actual/Estimated Rotor Speed ω_m [°] vs. Time [s] for sensorless position control at $i_{q4}^* = -5$ A on M4.

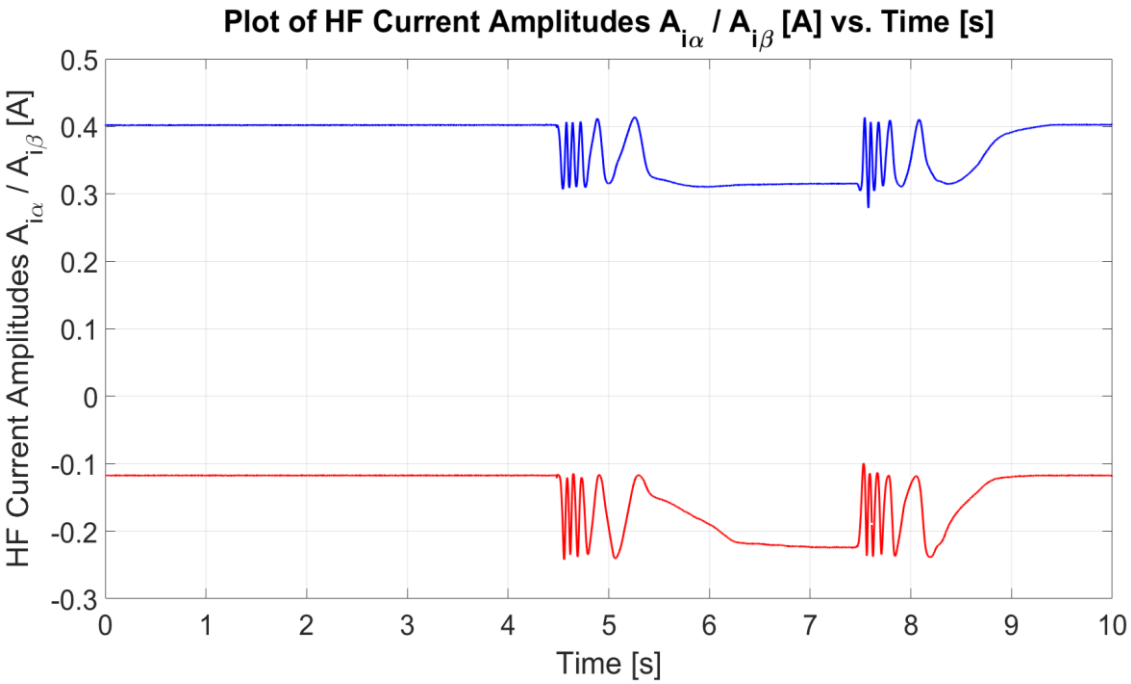

Figure 9.40 –Plot of HF Current Amplitudes $A_{i\alpha}$, $A_{i\beta}$ [A] vs. Time [s] for sensorless position control at $i_{q4}^* = -5$ A on M4.

9.10 Summary

In this chapter, the performance of the proposed SBO was investigated in sensorless speed and position control modes. For stable sensorless speed performance within the range -2.5 rad/s (-24 rpm) ≤ ω_m ≤ 2 rad/s (19 rpm) the speed controller gains were reduced from K_{p_W3} = 0.3, K_{i_W3} = 60 (closed-loop bandwidth of 15.93 Hz in sensored mode) to K_{p_W3} = 0.1, K_{i_W3} = 10 (closed-loop bandwidth of 4.48 Hz in sensorless mode. The sensorless closed-loop control system was tested for different current values with the i_q-current range ±10 A (rated current). The sensorless speed range could be possibly be extended by making use of additional LUTs commissioned at higher rotor speeds.

One of the main aims of this dissertation was to achieve suitable position control for the steered wheel side for the steer-by-wire application. For stable sensorless position performance, the position controller gain was reduced from K_{p_P3}=5.75 (closed-loop bandwidth of 1 Hz in sensored mode) to K_{p_P3}=1.5 (closed-loop bandwidth of 0.5 Hz in sensorless mode). The position controller was tested with steps in position demand for a constant positive and negative load (i_q-current of machine M4 of i_{q4}^* = ± 5 A). For the step reference, while positive torque is applied, the transient i_q-current exceeds that calibrated for in the ± 10 A. Increasing the position controller gain further could possibly result in instability due to the deviation from the last commissioned point in the LUT. The performance of the SBO observer in this chapter was shown to be stable for both sensorless speed and position control for various speed/position responses up to rated load. The performance of the SBO in current/position demands typical of steer-by-wire is investigated and presented in Chapter 10.

Chapter 10 – Sensorless Control in Steer-by-Wire

10.1 Introduction to Sensorless Control in Steer-by-Wire

This chapter presents sensorless control with test profiles typically found in the steer-by-wire application. As described in Chapter 2, the steer-by-wire system consists of two electric drives. A current-controlled machine is used at the handwheel side and a position-controlled machine at the steered wheel side. The sensorless control of the Surface Mounted Permanent Magnet Synchronous Machine (SM-PMSM) under test in this dissertation was presented in Chapters 8 and 9 with the typical step-input type references associated with generic machine control for current, speed and position control. Sensorless control was shown for all these modes of operation using the Search-Based Observer (SBO). In this chapter, the position demands are given in the form of a sigmoid-function reference as defined in Section 3.6.2. The sigmoid approximates better the steering response measured at the handwheel of the vehicle in Section 2.7. Furthermore, the curvature in the sigmoid function reduces the maximum gradient with respect to a step-type reference. This reduces the current demands during position transients which is an advantage when using the SBO with a limited range of commissioned LUTs for the i_q-current.

Sensorless current control at the handwheel side was tested by generating a torque component in the opposite direction to the rotation. The torque and the steering feel at the handwheel were adjusted through a proportional gain which is set to obtain different current demands. The resulting torque is set to be both equal to and higher to that which was determined experimentally on the test vehicle in Chapter 2. The performance of the machine was discussed with and without the torque limitation characterised in Section 2.7.2. Sensorless position control at the steered wheel side is also investigated using sigmoid position references for both no-load and loaded conditions. The performance obtained at both handwheel and steered wheel side is compared to that measured on the test vehicle fitted with an Electrically Power Assisted Steering (EPAS).

10.2 Sensorless Current Control at the Handwheel Side

10.2.1 Sensorless Current Control at the Handwheel without Torque Limit

The sensorless operation of the current control machine configured for torque feedback at the handwheel side is presented in this section. The i_q-current controller reference i_q^* for the machine under sensorless investigation is calculated as a function of the estimated

rotor position $\hat{\theta}_m$ with a current gain K_{hw} (10.1) as shown in Figure 10.1. The current gain produces a torque in the opposite direction of rotation to emulate the return to the centre position in a steering arrangement. When operating in sensorless mode the i_q-current used as feedback in the current controller for torque generation is the estimate component $\hat{i}_q$.

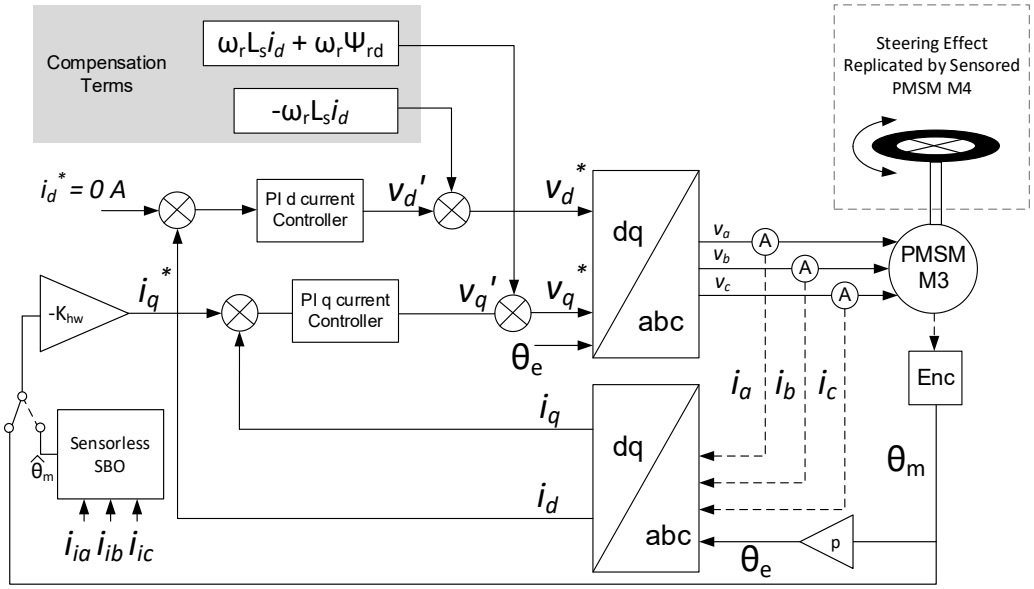

Figure 10.1 - RFO control topology for handwheel side in steer-by-wire.

$$i_q^* = -K_{hw}\hat{\theta}_m \qquad (10.1)$$

Where i_q^* is the synchronous frame q-axis current reference [A]

K_{hw} is the current gain component at the handwheel side [A/rad]

$\hat{\theta}_m$is the estimated mechanical rotor position [rad]

The performance of the SBO applied to the handwheel side of the steer-by-wire system is shown for a current gain K_{hw} = 3.5 A/rad. The sensorless current control setup is similar to that in Chapter 8, with M4 in sensored position control and M3 in sensorless current control (Figure 10.1). The current controller on M3 for this operation is tuned to K_{p_I3} = 0.1 and K_{i_I3} = 100. Figure 10.2 shows the actual and estimated ***mechanical*** rotor positions and the current i_{q3} during experimental testing. The error in the estimated ***mechanical*** rotor position is shown in Figure 10.3. The actual and estimated ***electrical*** rotor positions are shown in Figure 10.4, while the actual and estimated ***mechanical*** rotor speeds are shown in Figure 10.5. The HF current amplitudes $A_{i\alpha}$, $A_{i\beta}$ are shown in Figure 10.6. The position and speed estimated components are filtered through a

Phased-Locked Loop (PLL) architecture as discussed in Section 7.5 with a bandwidth of 8.74 Hz (K_{p_PLL2} = 50, K_{i_PLL2} = 3000).

The position references used on machine M4 were sigmoid functions to reduce the peak current required at the instant a change in position is applied. For the result shown in Figure 10.2, the observer tracks a maximum rate of change of 323.61 degrees/s in the mechanical rotor position, which is calculated as the steepest gradient between t = 4.76 s and t = 5.06 s. This is within the same order of magnitude of the steering wheel transients measured experimentally in Section 2.7, which had a maximum steering rate of change of 286 degrees/s. The peak torque for the test shown is of 3.72 Nm with an absolute maximum estimated current i_{q3} = 5.86 A. This torque value exceeds what was observed from the experimental test on the test vehicle where the torque is limited to approximately 2 Nm. The maximum error in the estimated rotor position is of 4.48°, which occurs during one of the steering transients, as shown in Figure 10.3, with a RMSE of 0.54°. For sensorless current control, only the electrical rotor position estimate is used for the RFO algorithm. The results shown in this section demonstrate that the SBO also provides accurate estimates for the mechanical rotor position and speed. The observer is shown to adequately track the mechanical rotor speed in Figure 10.5 with an actual absolute maximum rotor speed of 10.1 rad/s (96 rpm).

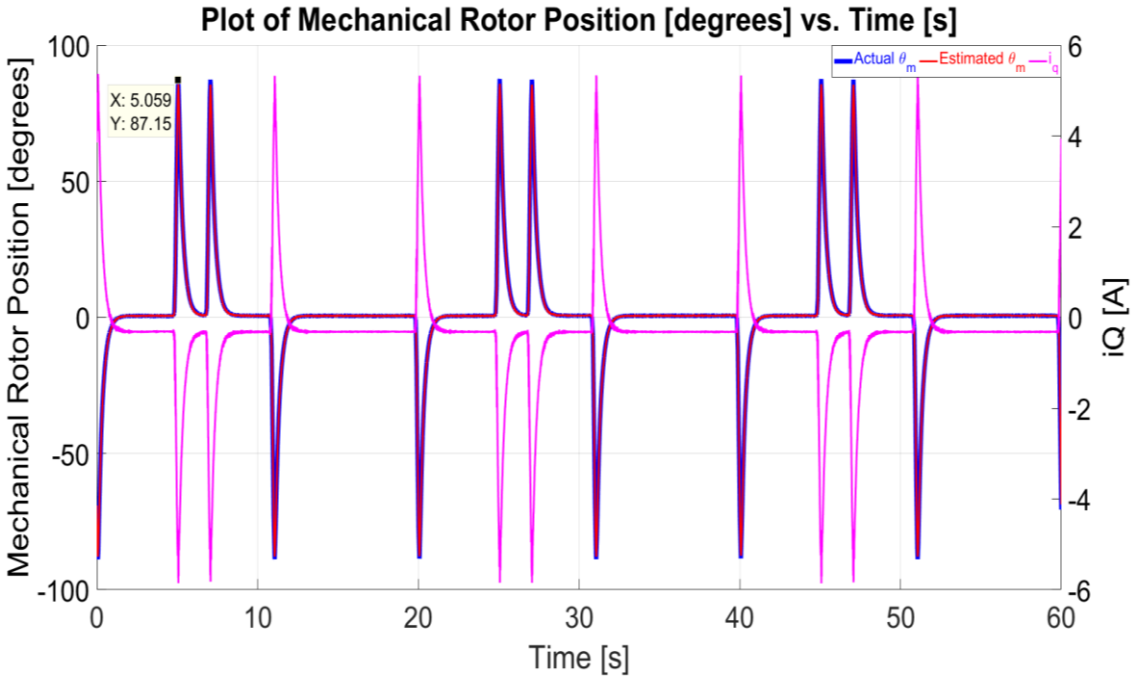

Figure 10.2 – Plot of Actual/Estimate Mechanical Rotor Position θ_m [°] vs. Time [s] for sensorless current control with K_{hw} = 3.5 and steer-by-wire profiles.

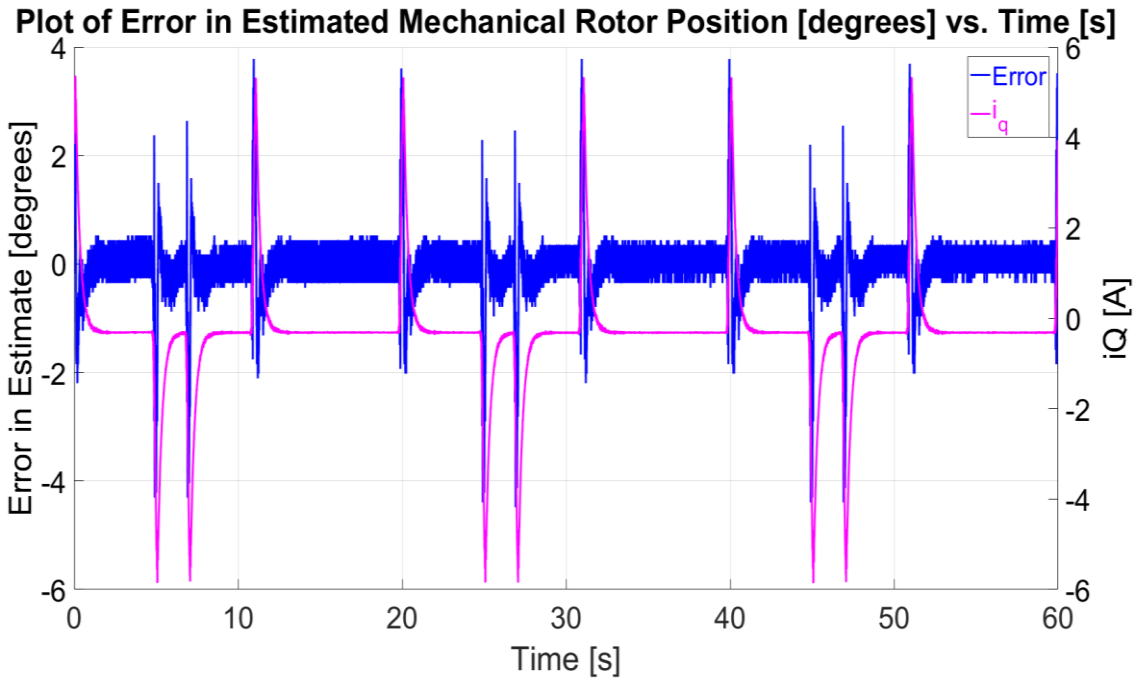

Figure 10.3– Plot of Error in Mechanical Rotor Position θ_m [°] vs. Time [s] for sensorless current control with K_{hw} = 3.5 and steer-by-wire profiles.

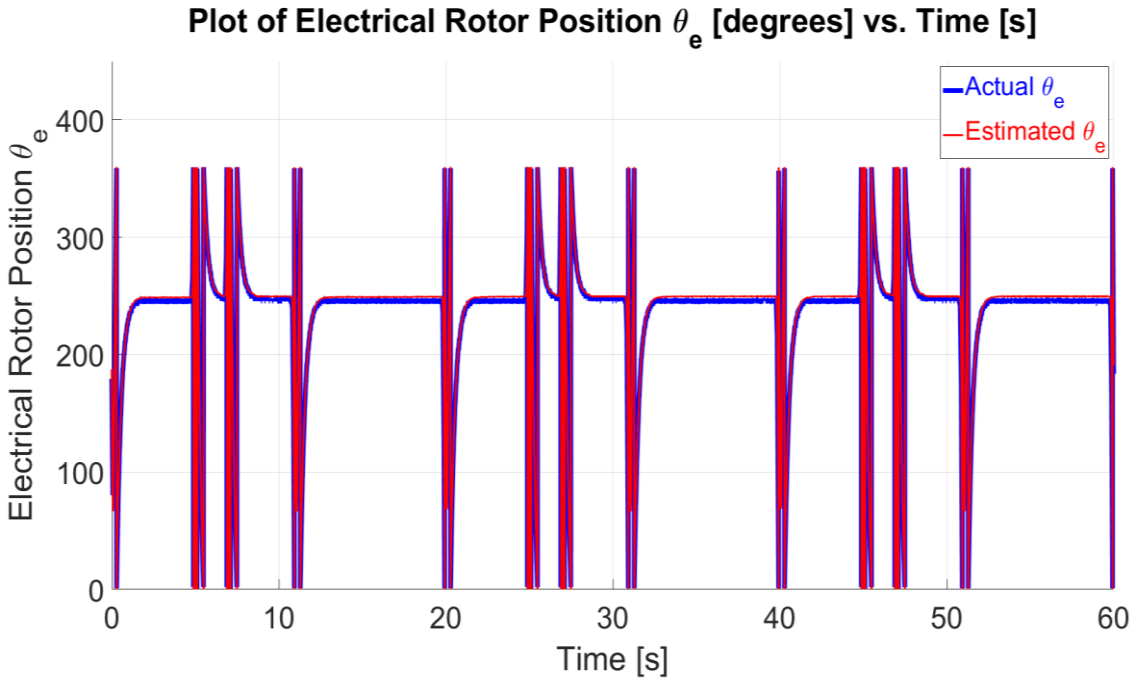

Figure 10.4 – Plot of Actual/Estimate Electrical Rotor Position θ_e [°] vs. Time [s] for sensorless current control with K_{hw} = 3.5 and steer-by-wire profiles.

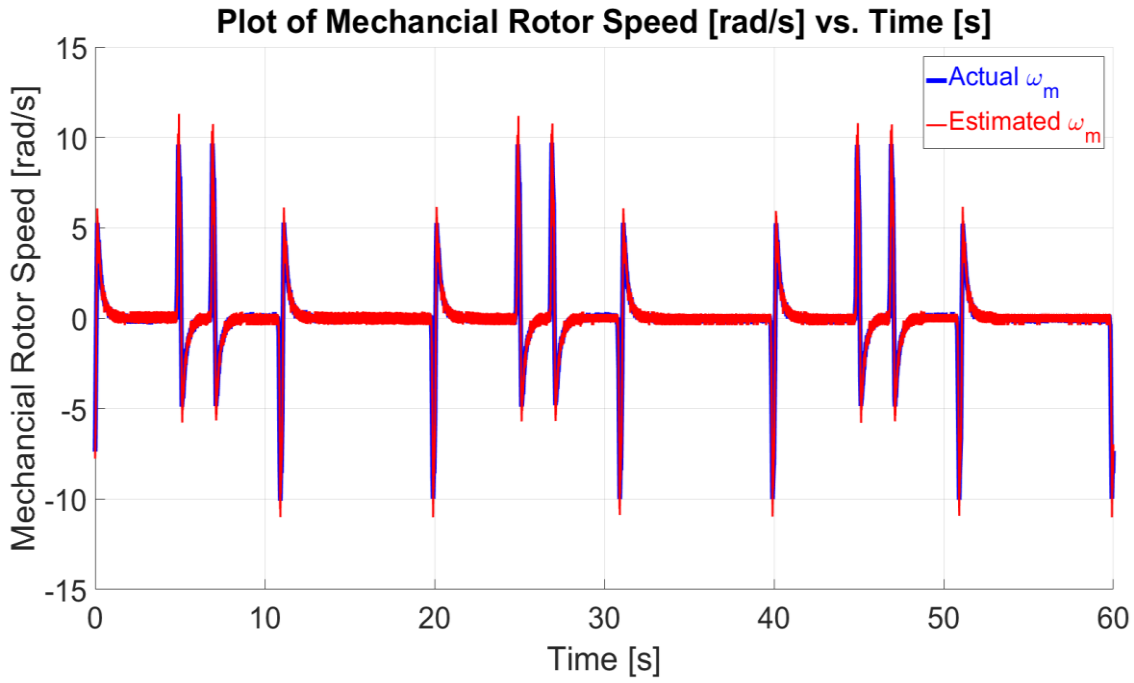

Figure 10.5 – Plot of Actual/Estimated Rotor Speed ω_m [°] vs. Time [s] for sensorless current control with K_{hw} = 3.5 and steer-by-wire profiles.

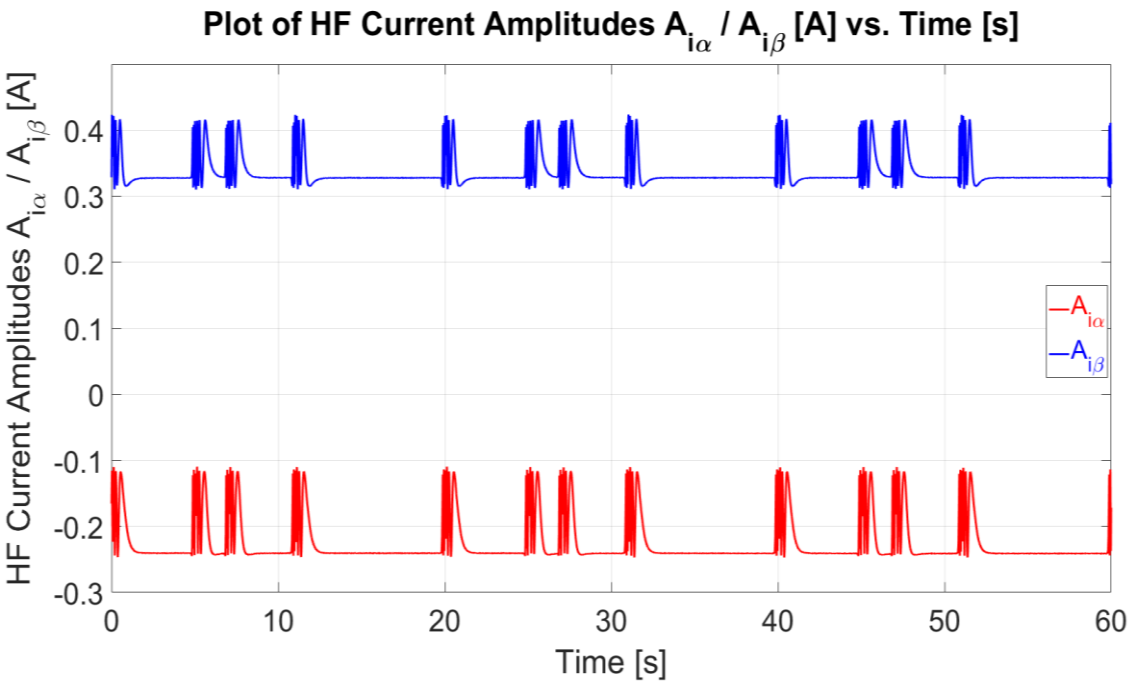

Figure 10.6 –Plot of HF Current Amplitudes $A_{i\alpha}$, $A_{i\beta}$ [A] vs. Time [s] for sensorless current control with K_{hw} = 3.5 and steer-by-wire profiles.

The gain at the handwheel side K_{hw} can be adjusted through the microcontroller to adjust the user feedback 'feel' in the steering application. Since the sensorless estimation was shown to be a function of the current $i_{q3,}$ the experiment was repeated with a higher $K_{hw} = 7$. The actual and estimated ***mechanical*** rotor positions and current i_{q3} are shown in Figure 10.7. The error in the estimated ***mechanical*** rotor position is shown in Figure 10.8 with an absolute maximum error of 3.87° and an RMSE of 0.64°. The actual and estimated ***electrical*** rotor positions are shown in Figure 10.9, while the actual and estimated ***mechanical*** rotor speeds are shown in Figure 10.10. The HF current amplitudes $A_{i\alpha}$, $A_{i\beta}$ are shown in Figure 10.11.

The increase in K_{hw} from 3.5 to 7 increases the absolute maximum i_{q3} to 10.79 A, which results in a maximum torque of 6.86 Nm. The SBO is shown to be stable even at this higher gain value. With this higher value of K_{hw} the peak current values of i_{q3} exceed the maximum calibration points used for this dissertation of ± 10 A. While such a high torque would not be used for actual steer-by-wire; it demonstrates the validity of the observer at the rated current of the machine. Traditional sensorless observers typically have reduced accuracy at rated current due to the saturation effects in the saliency which increase with i_q-current. The error in the SBO estimate is shown not to be significantly affected while operating close to or even beyond the calibrated current range for short periods.

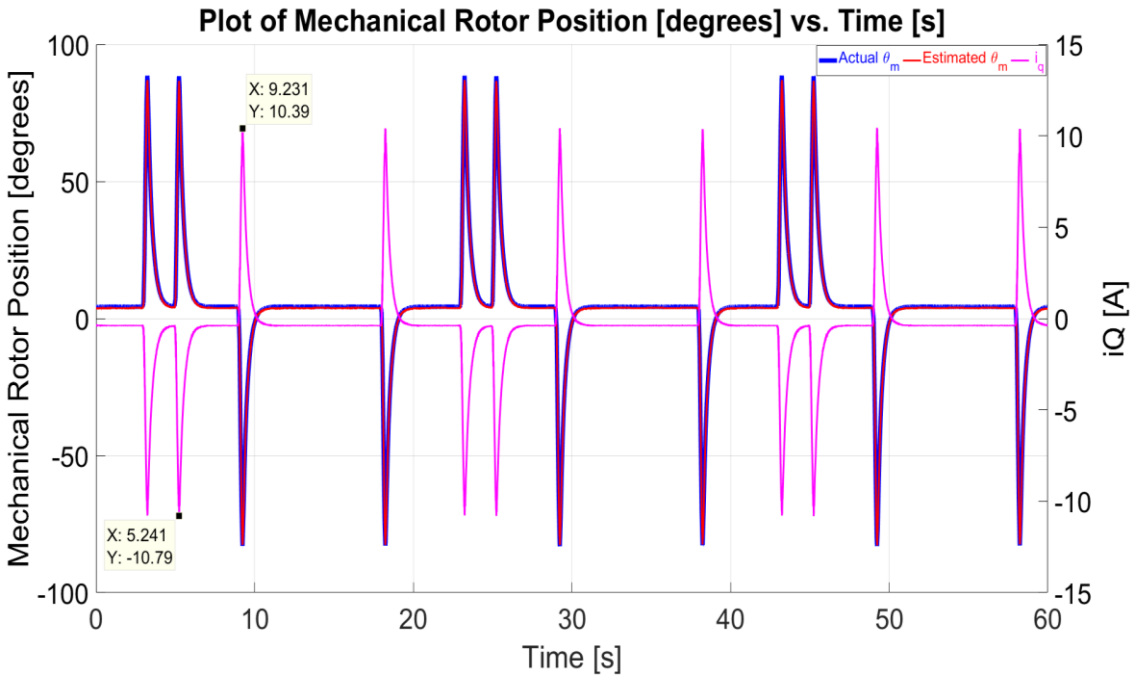

Figure 10.7 – Plot of Actual/Estimate Mechanical Rotor Position θ_m [°] vs. Time [s] for sensorless current control with $K_{hw} = 7$ and steer-by-wire profiles.

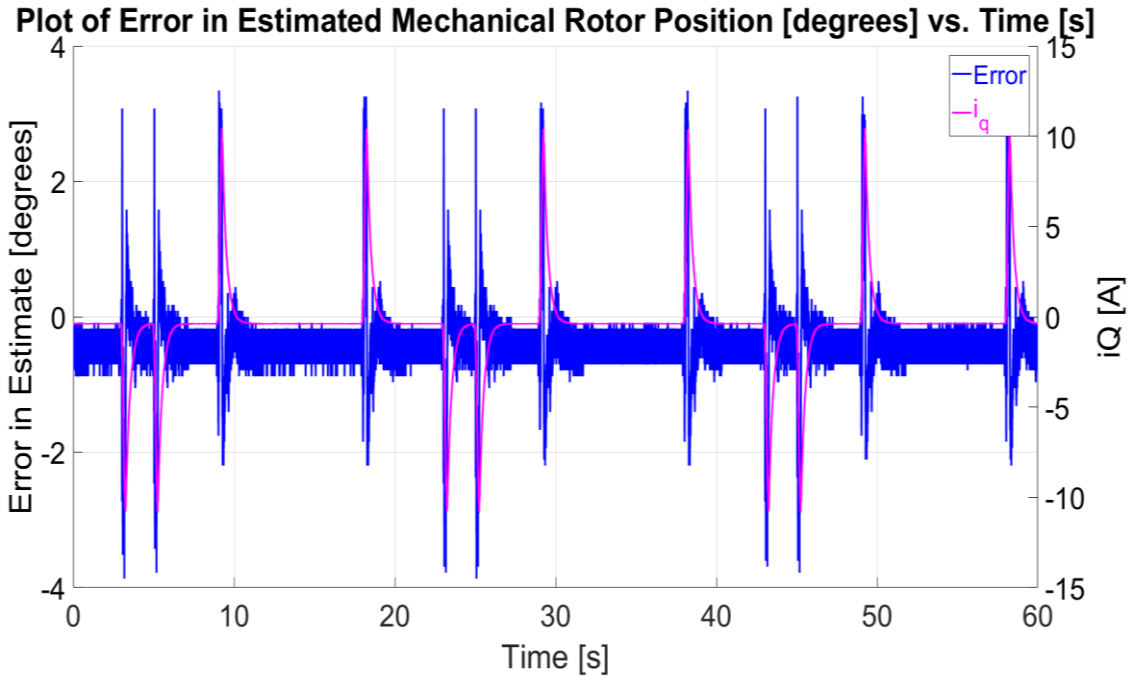

Figure 10.8 – Plot of Error in Mechanical Rotor Position θ_m [°] vs. Time [s] for sensorless current control with K_{hw} = 7 and steer-by-wire profiles.

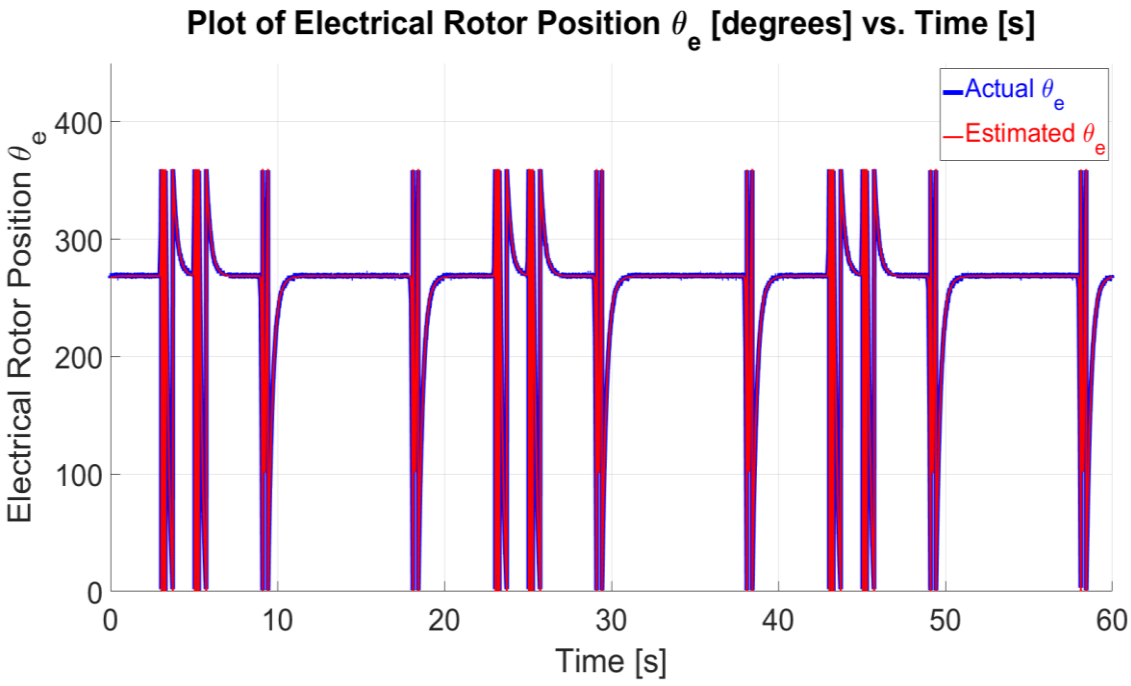

Figure 10.9 – Plot of Actual/Estimate Electrical Rotor Position θ_e [°] vs. Time [s] for sensorless current control with K_{hw} = 7 and steer-by-wire profiles.

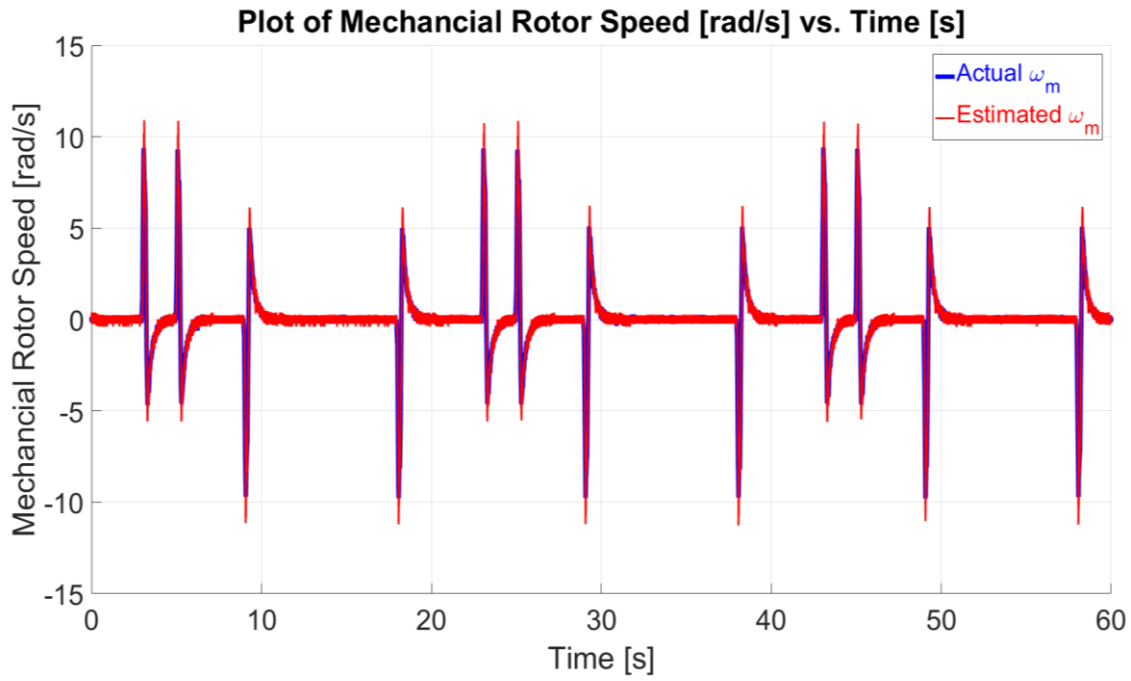

Figure 10.10 – Plot of Actual/Estimated Rotor Speed ω_m [°] vs. Time [s] for sensorless current control with K_{hw} = 7 and steer-by-wire profiles.

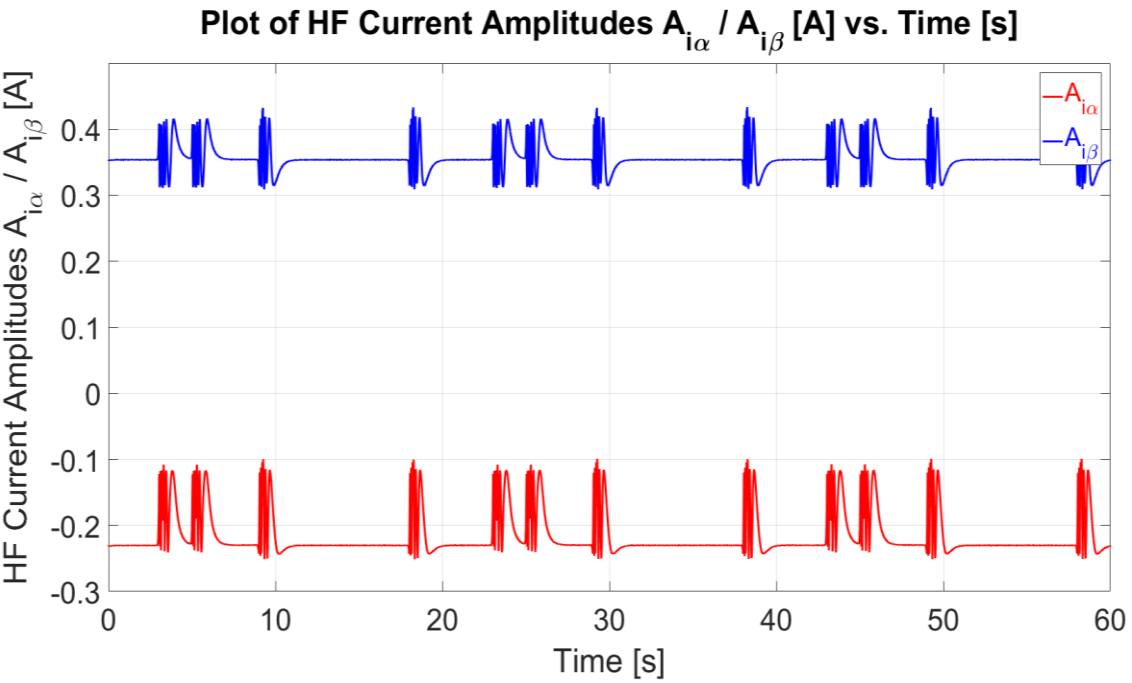

Figure 10.11 –Plot of HF Current Amplitudes $A_{i\alpha}$, $A_{i\beta}$ [A] vs. Time [s] for sensorless current control with K_{hw} = 7 and steer-by-wire profiles.

10.2.2 Sensorless Current Control at the Handwheel with Torque Limit

From the monitoring of the steering wheel parameters from the test vehicle discussed in Section 2.7, it was found that the torque at the handwheel is limited to approximately 2 Nm for a wide range of vehicle speeds. In order to replicate this effect, the reference for the synchronous current is limited to i_{q3}^{*} = ±3 A which corresponds to 2 Nm for the PMSM machine under test. The handwheel gain was set to K_{hw}=3.5.

The actual and estimated ***mechanical*** rotor positions together with the current i_{q3} are shown in Figure 10.12. The error in the estimated ***mechanical*** rotor position is shown in Figure 10.13, with an absolute maximum error of 4.31° and a RMSE of 0.45°. The actual and estimated ***electrical*** rotor positions are shown in Figure 10.14, while the actual and estimated ***mechanical*** rotor speeds are shown in Figure 10.15. The HF current amplitudes $A_{i\alpha}$, $A_{i\beta}$ are shown in Figure 10.16. From this figure, it can be observed that the HF currents do not drift as the same measurements were obtained for $A_{i\alpha}$ and $A_{i\beta}$ when the rotor returns to the initial rotor position θ_e = 245°.

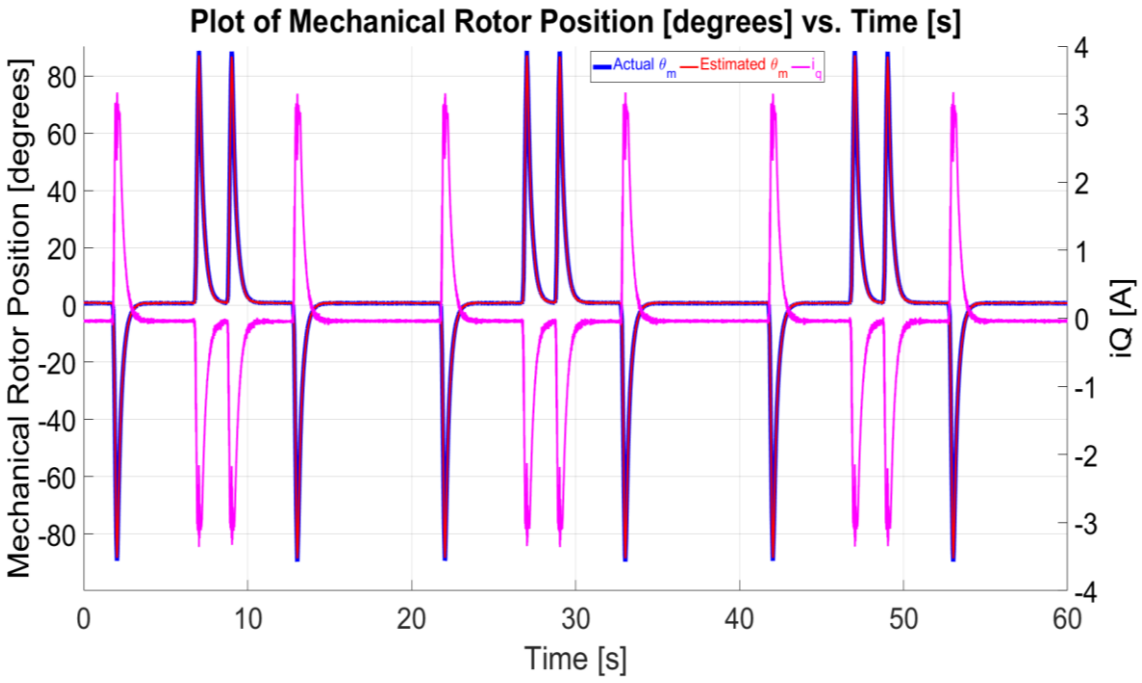

Figure 10.12 – Plot of Actual/Estimate Mechanical Rotor Position θ_m [°] vs. Time [s] for sensorless current control with K_{hw} = 3.5, $i_{q3\_limit}^{*}$ = ± 3 A and steer-by-wire profiles.

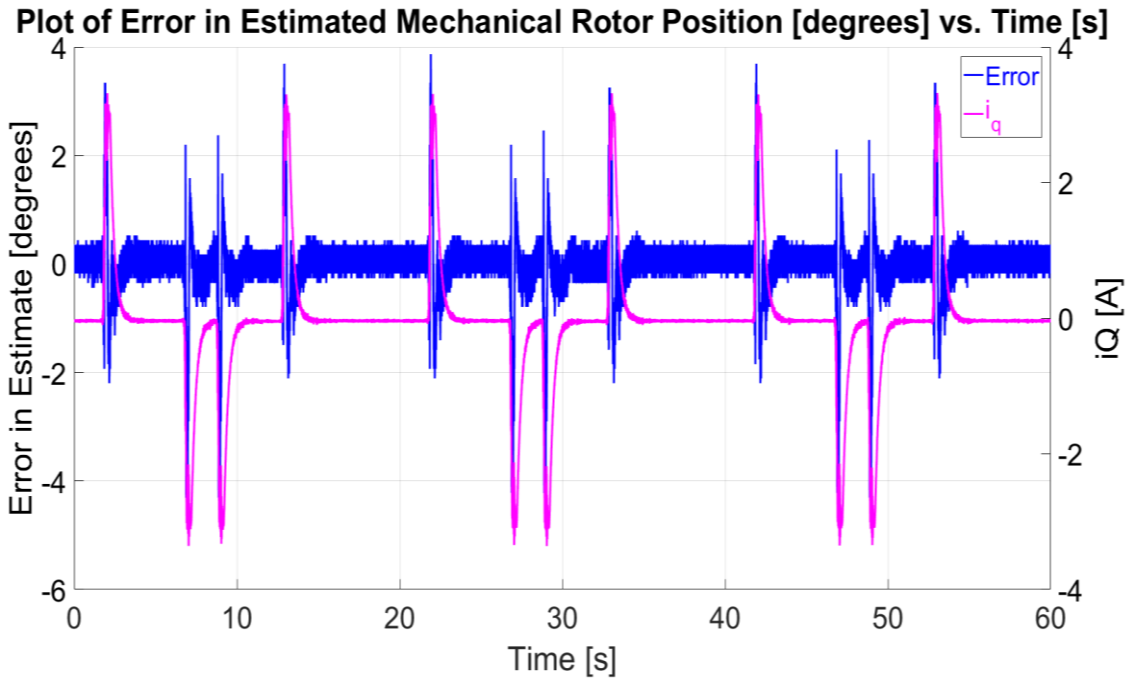

Figure 10.13 – Plot of Error in Mechanical Rotor Position θ_m [°] vs. Time [s] for sensorless current control with $K_{hw} = 3.5$, $i_{q3\_limit}^* = \pm 3$ A and steer-by-wire profiles.

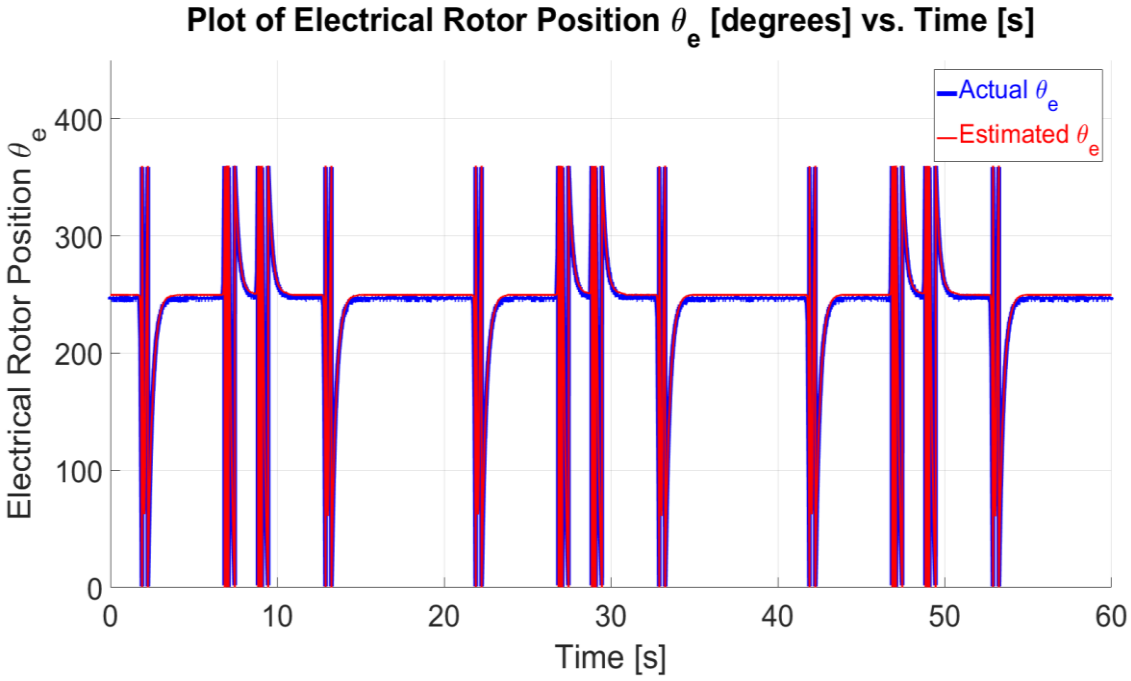

Figure 10.14 – Plot of Actual/Estimate Electrical Rotor Position θ_e [°] vs. Time [s] for sensorless current control with $K_{hw} = 3.5$, $i_{q3\_limit}^* = \pm 3$ A and steer-by-wire profiles.

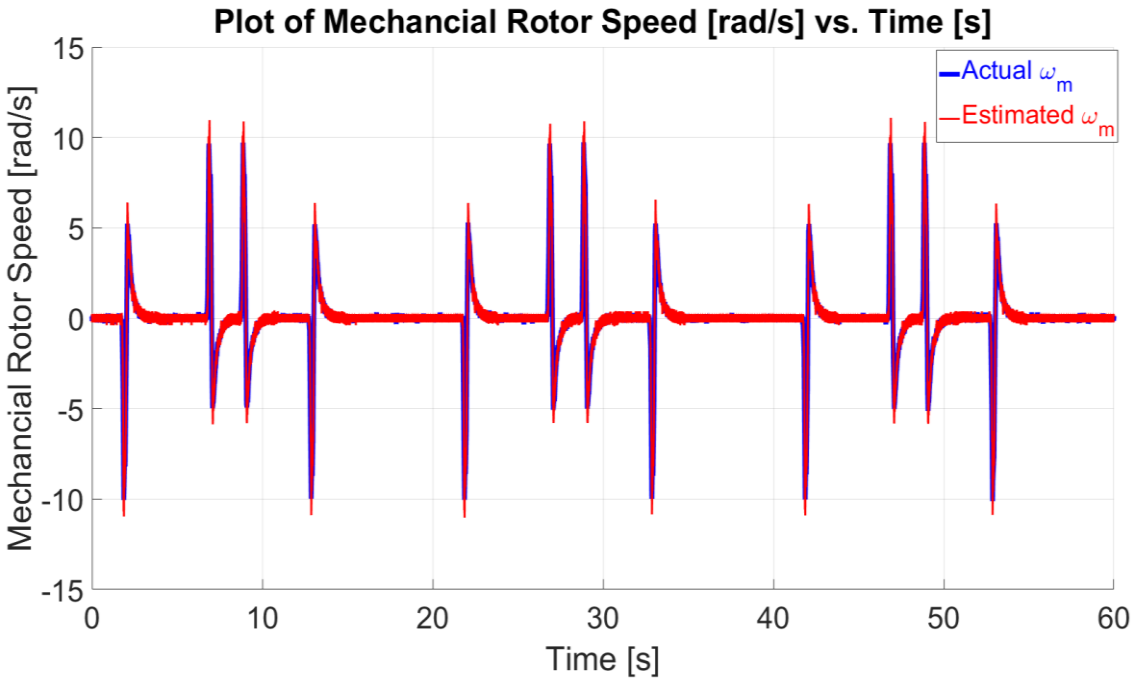

Figure 10.15 – Plot of Actual/Estimated Rotor Speed ω_m [°] vs. Time [s] for sensorless current control with K_{hw} = 3.5, $i_{q3\_limit}^*$ = ± 3 A and steer-by-wire profiles.

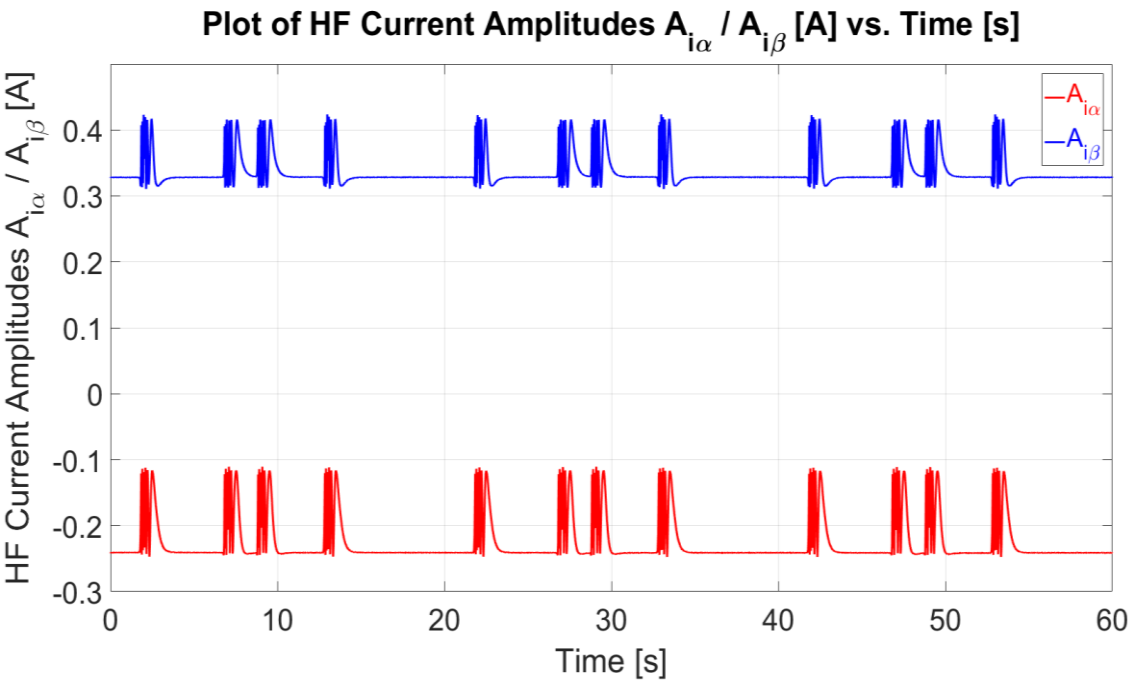

Figure 10.16 –Plot of HF Current Amplitudes $A_{i\alpha}$, $A_{i\beta}$ [A] vs. Time [s] for sensorless current control with K_{hw} = 3.5, $i_{q3\_limit}^*$ = ± 3 A and steer-by-wire profiles.

The sensorless current control experiment with torque limit was further tested with a higher value of $K_{hw} = 7$ (higher current/torque feedback with respect to steering wheel position as explained in Section 10.2.1) with the synchronous current limited to $i_{q3}^{*} = \pm 6$ A. The actual and estimated ***mechanical*** rotor positions are shown with the i_q-current in Figure 10.17. The error in the estimated ***mechanical*** rotor position is shown in Figure 10.18, with an absolute maximum error of 4.04° with an RMSE of 0.53°. The actual and estimated ***electrical*** rotor positions are shown in Figure 10.19, while the actual and estimated ***mechanical*** rotor speeds are shown in Figure 10.20. The HF current amplitudes $A_{i\alpha}$, $A_{i\beta}$ are shown in Figure 10.21. The peak torque for $i_{q3} = 6$ A is 3.81 Nm.

The SBO was shown to be a robust solution for sensorless current control at the handwheel side in Sections 10.2.1 – 10.2.2. The satisfactory sensorless current operation was shown for both cases when the torque/current are unlimited and limited. When the current was unlimited and a sufficient current gain K_{hw} was applied the sensorless observer was shown to be stable even when the synchronous current i_{q3} exceeded the rated current value of the machine ($i_{q3} = \pm 10$ A). Hence the SBO operation was shown to be stable even outside the commissioned range of current values.

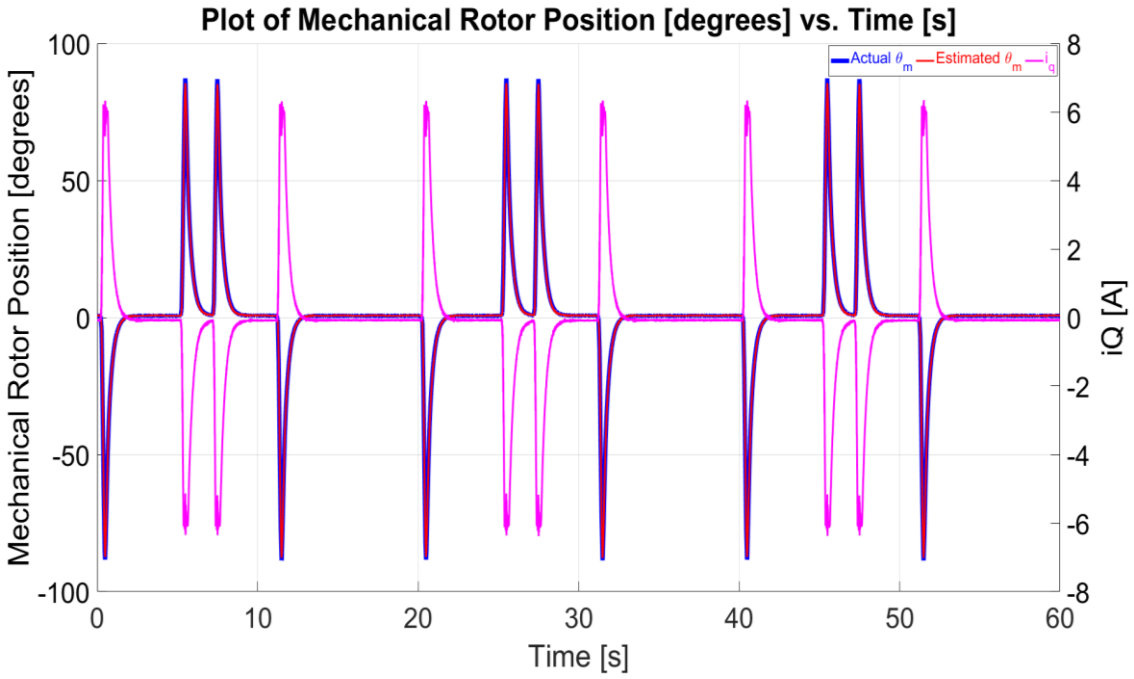

Figure 10.17– Plot of Actual/Estimate Mechanical Rotor Position θ_m [°] vs. Time [s] for sensorless current control with $K_{hw} = 7$, $i_{q3\_limit}^{*} = \pm 6$ A and steer-by-wire profiles.

.

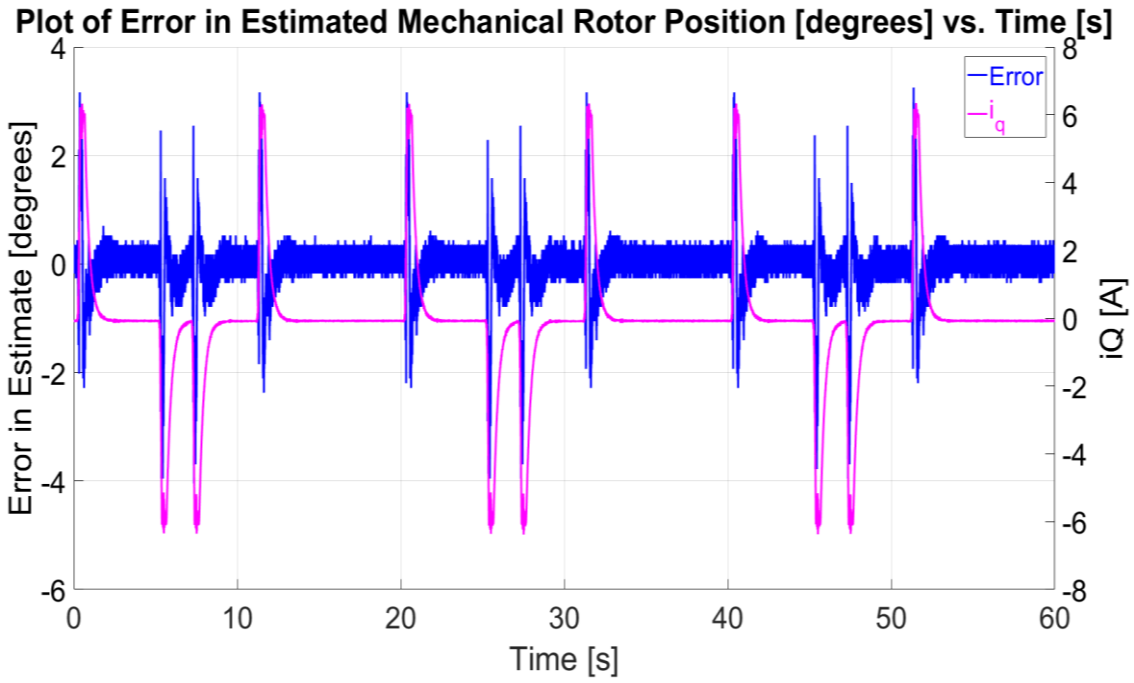

Figure 10.18– Plot of Error in Mechanical Rotor Position θ_m [°] vs. Time [s] for sensorless current control with $K_{hw} = 7$, $i_{q3\_limit}^* = \pm 6$ A and steer-by-wire profiles.

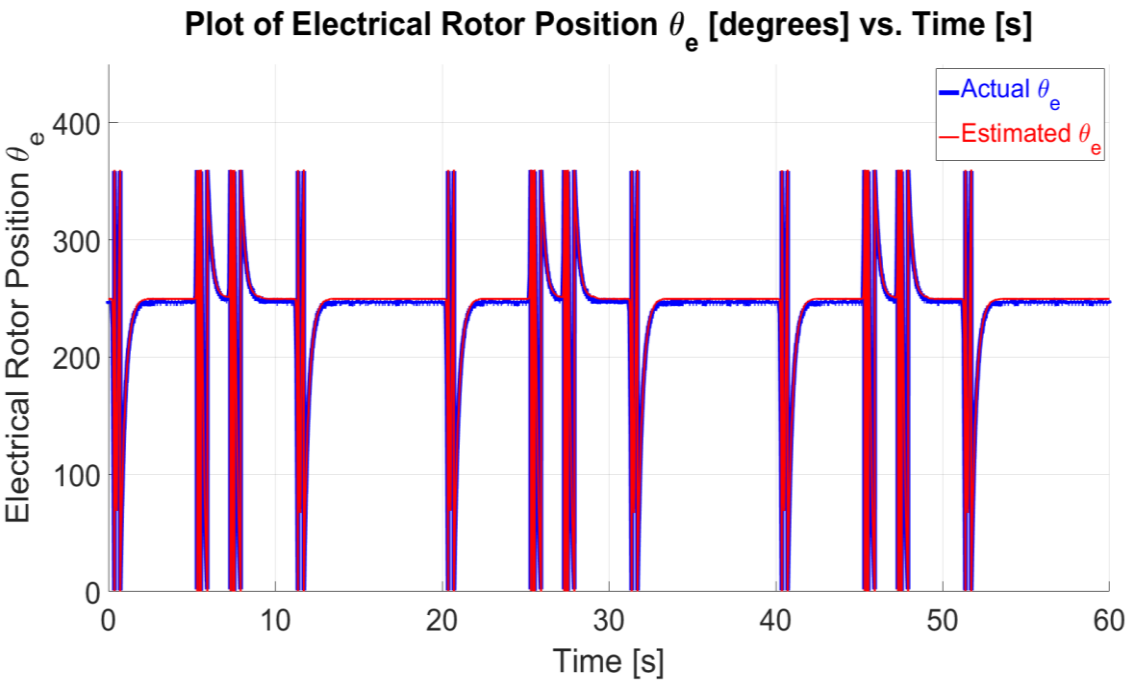

Figure 10.19 – Plot of Actual/Estimate Electrical Rotor Position θ_m [°] vs. Time [s] for sensorless current control with $K_{hw} = 7$, $i_{q3\_limit}^* = \pm 6$ A and steer-by-wire profiles.

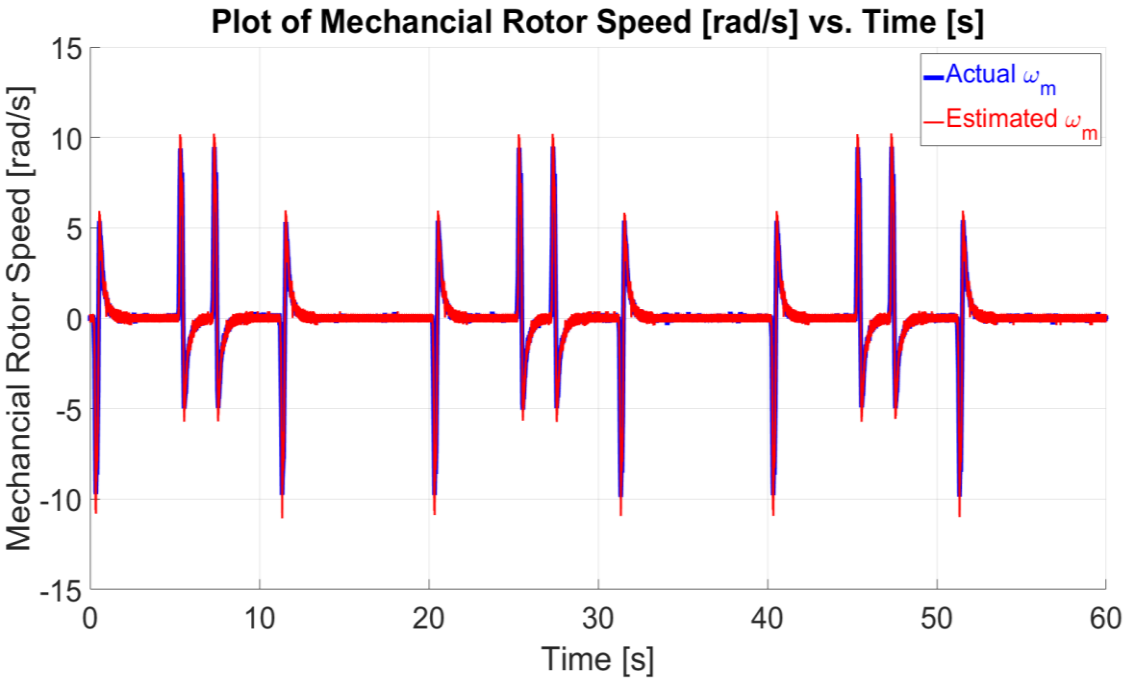

Figure 10.20 – Plot of Actual/Estimated Rotor Speed ω_m [°] vs. Time [s] for sensorless current control with $K_{hw} = 7$, $i_{q3\_limit}^* = \pm 6$ A and steer-by-wire profiles.

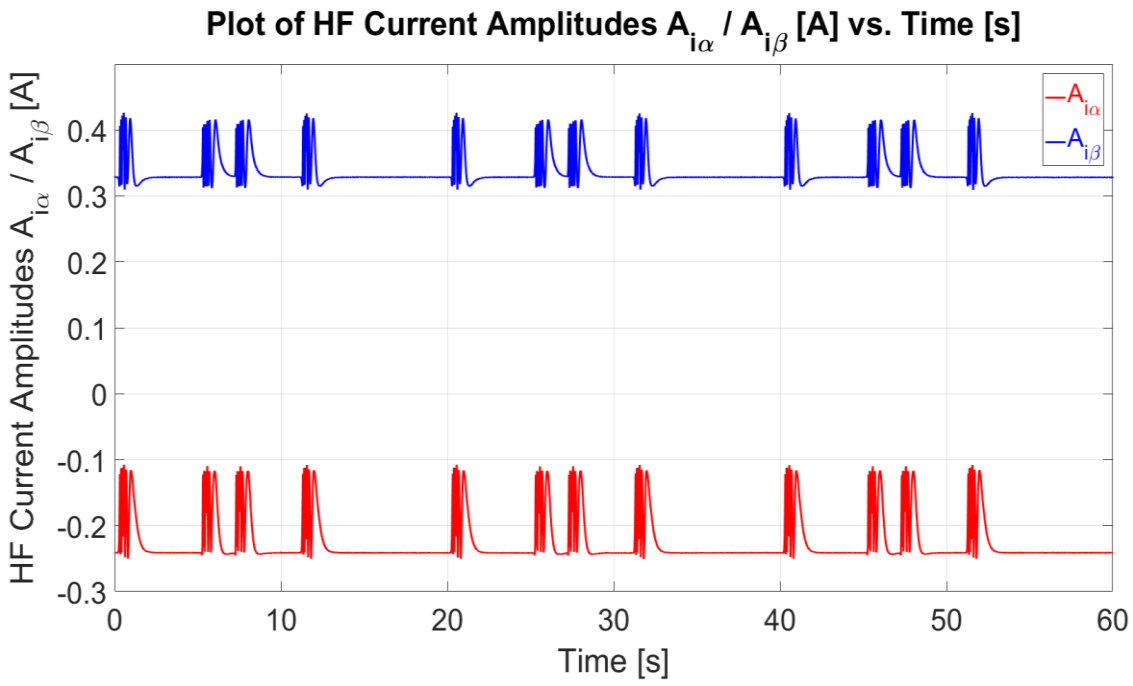

Figure 10.21 –Plot of HF Current Amplitudes $A_{i\alpha}$, $A_{i\beta}$ [A] vs. Time [s] for sensorless current control with $K_{hw} = 7$, $i_{q3\_limit}^* = \pm 6$ A and steer-by-wire profiles.

10.2.3 Sensorless Current Control at the Handwheel during 'Turning'-Operation

The sensorless current control results are discussed in Sections 10.2.1 – 10.2.2 show a transient position change with an immediate return to the initial position. In a typical driving scenario, a sustained turning condition would also be required. The sensorless current control for a 'turning' condition is presented in this section. The first test was carried out with a gain factor K_{hw} = 3.5 A/rad with a limit current i_{q3}^{*} = ± 3 A, which produces the typical limiting torque in the steering of 2 Nm. The steering reference profile in the sensored position-controlled machine still uses a sigmoid function to produce the change in position. However, the steady-state is sustained for some time before returning to the initial position.

The actual and estimated ***mechanical*** rotor positions are shown in Figure 10.22, including the i_q-current. The error in the estimated ***mechanical*** rotor position is shown in Figure 10.23 (a), with an absolute maximum error of 3.86° with an RMSE of 0.55°. The error in the estimated ***mechanical*** position at the transient is shown in Figure 10.23 (b) with the i_q-current. The oscillations observed on the i_q-current are attributed to the increased position error in the SBO estimate since the oscillations were not observed in sensored operation. The SBO LUTs for the PMSM were calibrated at ±2 rad/s and in this case the actual speed (Figure 10.25) is observed to exceed this range. The oscillations could be possibly reduced by commissioning the LUTs for a wider range of speeds. Actual and estimated ***electrical*** rotor positions are shown in Figure 10.24 while the actual and estimated ***mechanical*** rotor speeds are shown in Figure 10.25. The HF current amplitudes $A_{i\alpha}$, $A_{i\beta}$ are shown in Figure 10.26.

The sensorless control during turning condition was also tested for a higher value of the gain K_{hw} = 7 and an increased i_{q3}^{*} = 6 A. For this case the maximum torque at the handwheel is 3.81 Nm, higher than what is typically used in steering. The actual and estimated ***mechanical*** rotor positions are shown with the i_q-current in Figure 10.27. The error in the estimated ***mechanical*** rotor position is shown in Figure 10.28, with an absolute maximum error of 4.31° with an RMSE of 0.56°. The actual and estimated ***electrical*** rotor positions are shown in Figure 10.29, while the actual and estimated ***mechanical*** rotor speeds are shown in Figure 10.30. The HF current amplitudes $A_{i\alpha}$, $A_{i\beta}$ are shown in Figure 10.31. Similar performance as for the case with a low handwheel current gain setting was observed.

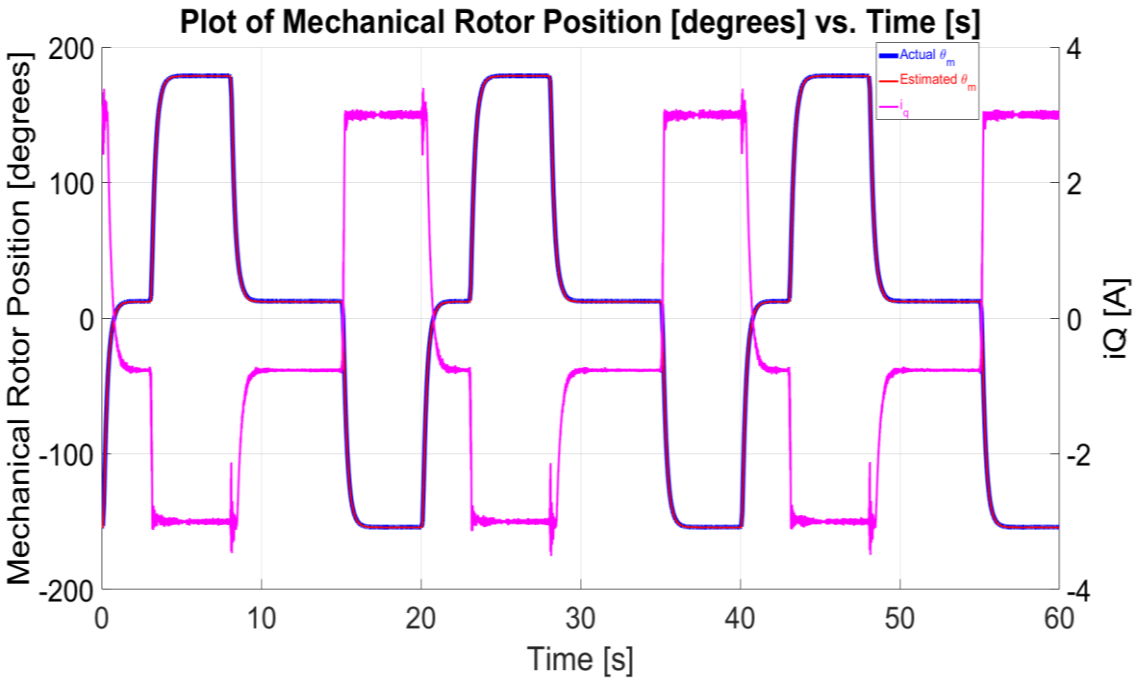

Figure 10.22 – Plot of Actual/Estimate Mechanical Rotor Position θ_m [°] vs. Time [s] for sensorless current control with K_{hw} =3.5, $i_{q3\_limit}^*$ = ± 3 A with turning condition steer-by-wire profiles.

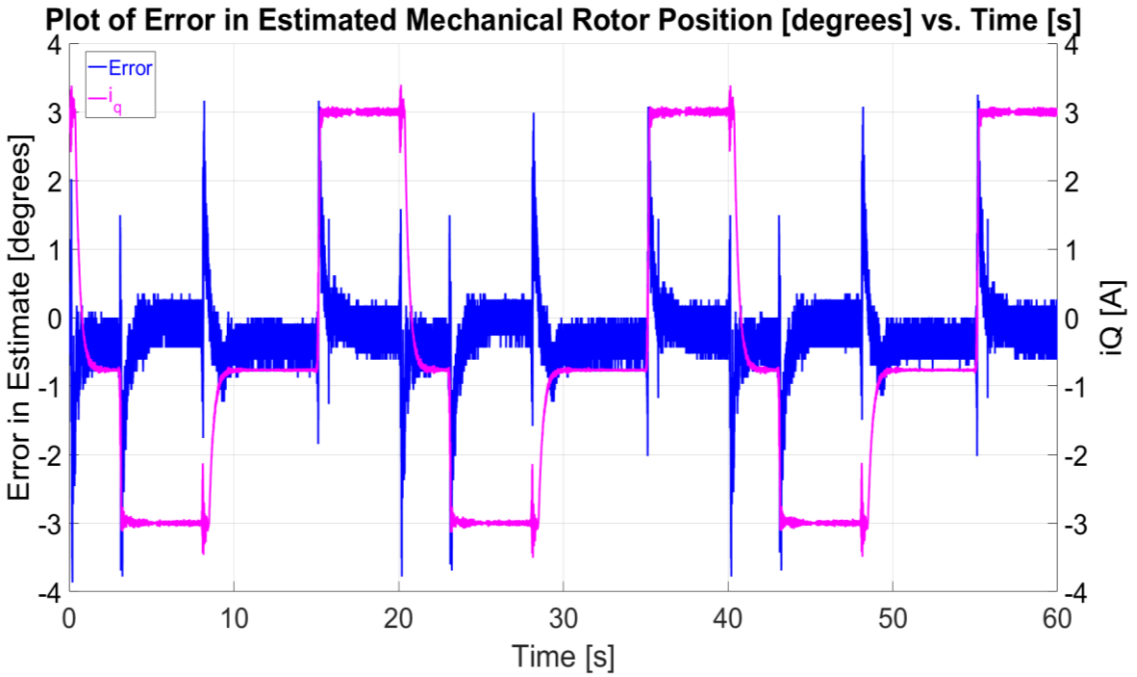

Figure 10.23 (a)– Plot of Error in Mechanical Rotor Position θ_m [°] vs. Time [s] for sensorless current control with K_{hw} =3.5, $i_{q3\_limit}^*$ = ± 3 A with turning condition steer-by-wire profiles.

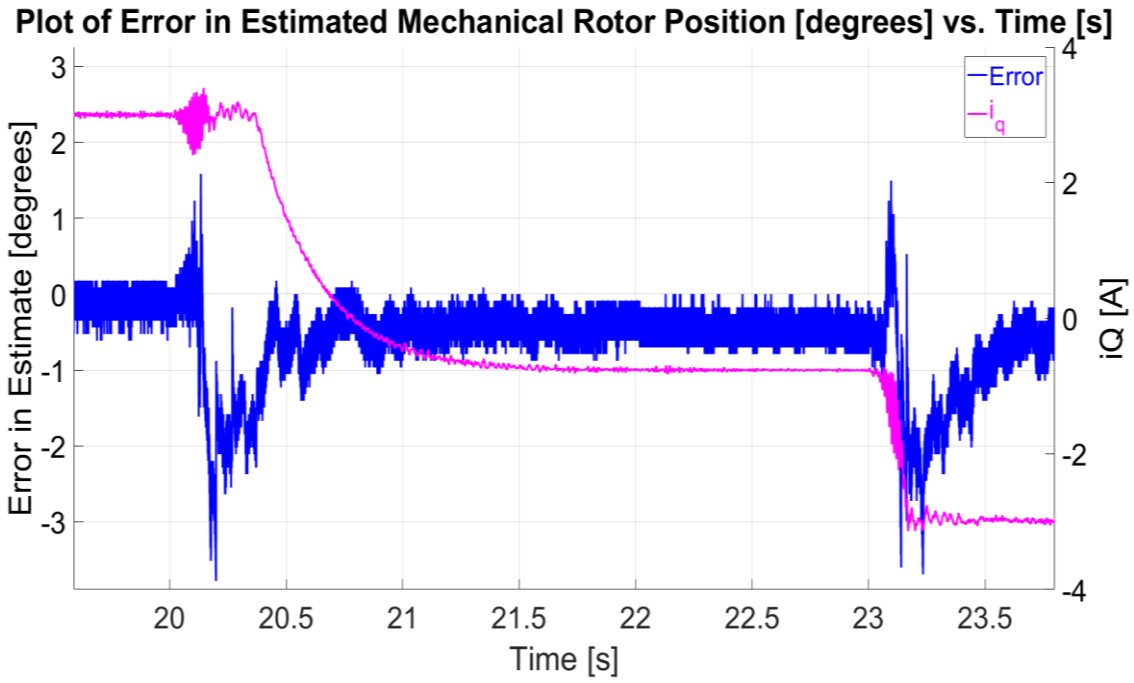

Figure 10.23 (b) – Plot of Error in Mechanical Rotor Position θ_m [°] vs. Time [s] at position transient for sensorless current control with K_{hw} =3.5, $i_{q3\_limit}^*$ = ± 3 A with turning condition steer-by-wire profiles.

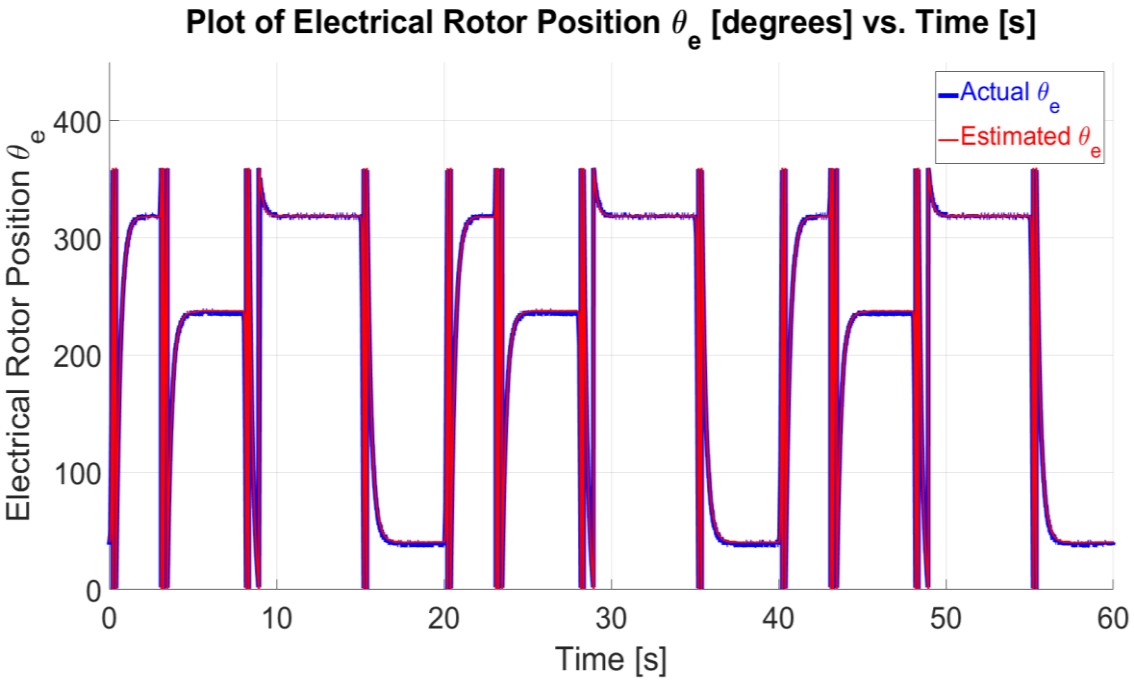

Figure 10.24 – Plot of Actual/Estimate Electrical Rotor Position θ_m [°] vs. Time [s] for sensorless current control with K_{hw} =3.5, $i_{q3\_limit}^*$ = ± 3 A with turning condition steer-by-wire profiles.

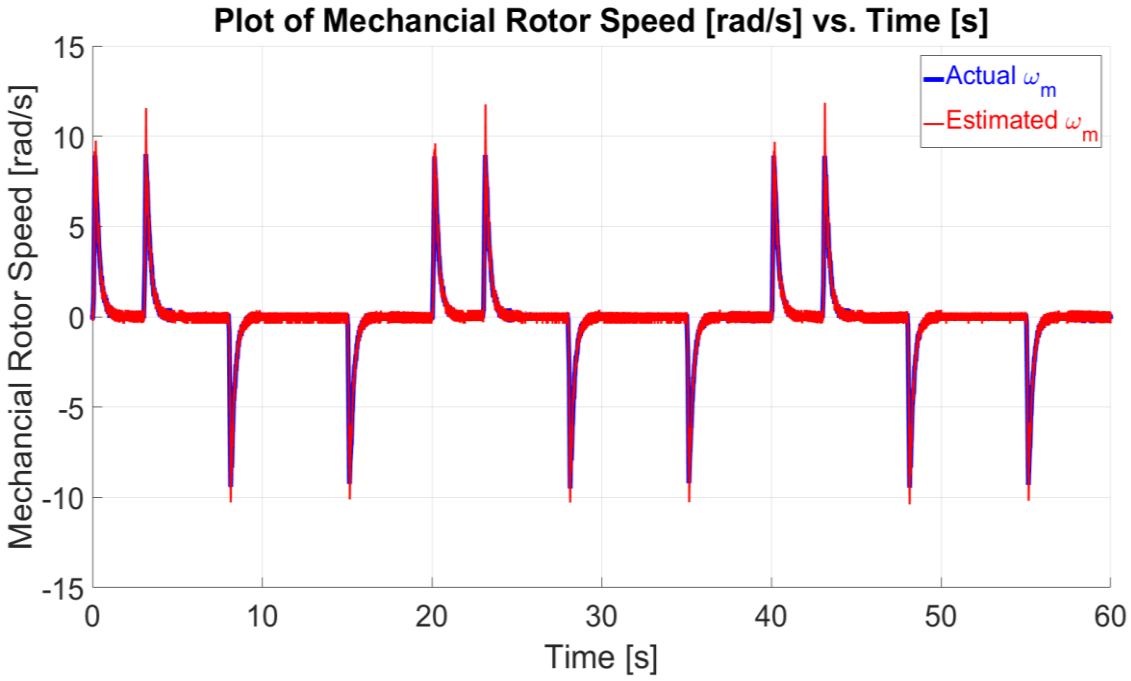

Figure 10.25 – Plot of Actual/Estimated Rotor Speed ω_m [°] vs. Time [s] for sensorless current control with K_{hw} =3.5, $i_{q3\_limit}^*$ = ± 3 A with turning condition steer-by-wire profiles.

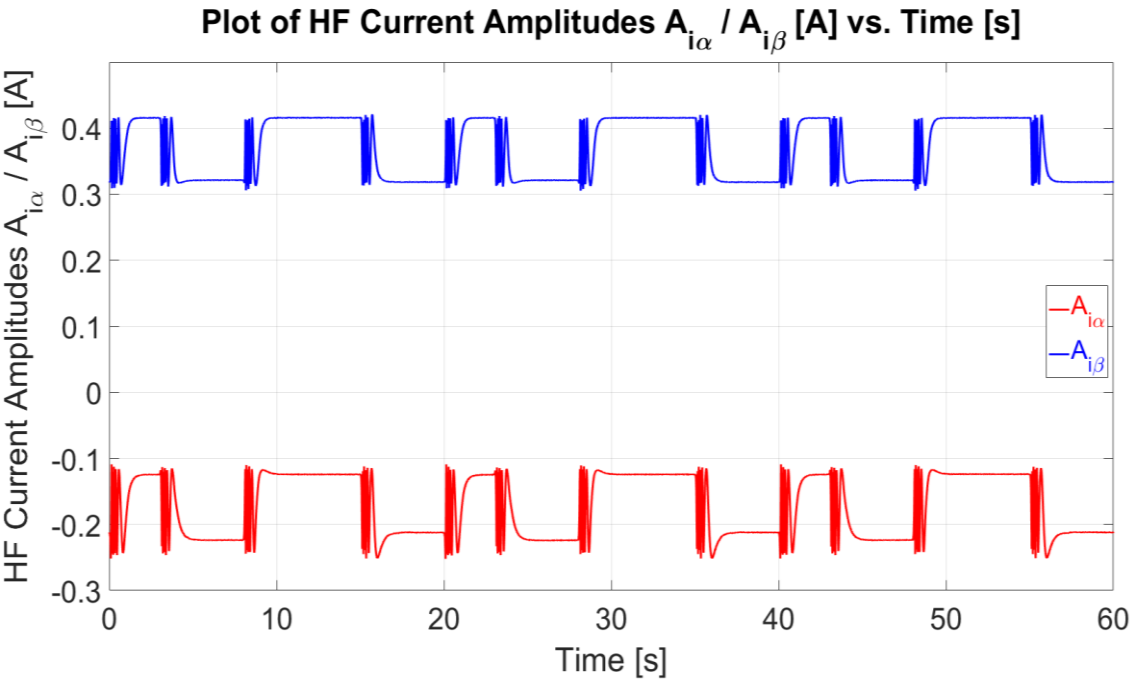

Figure 10.26 – Plot of HF Current Amplitudes $A_{i\alpha}$, $A_{i\beta}$ [A] vs. Time [s] for sensorless current control with K_{hw} =3.5, $i_{q3\_limit}^*$ = ± 3 A with turning condition steer-by-wire profiles.

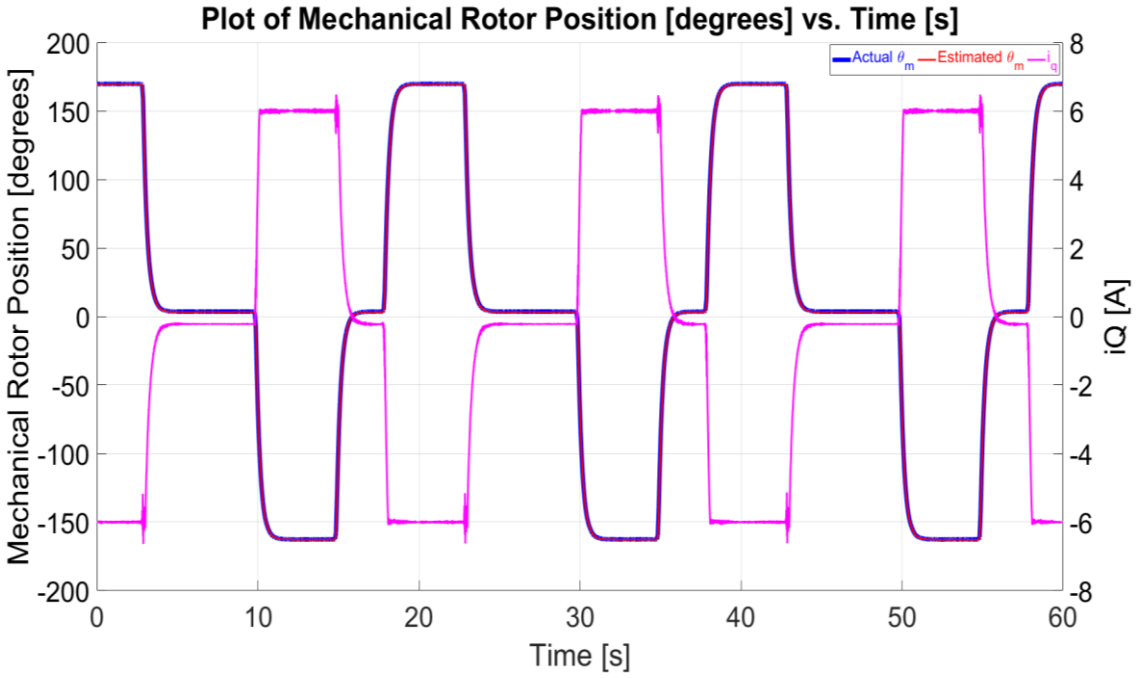

Figure 10.27 – Plot of Actual/Estimate Mechanical Rotor Position θ_m [°] vs. Time [s] for sensorless current control with K_{hw} =7, $i_{q3\_limit}^*$ = ± 6 A with turning condition steer-by-wire profiles.

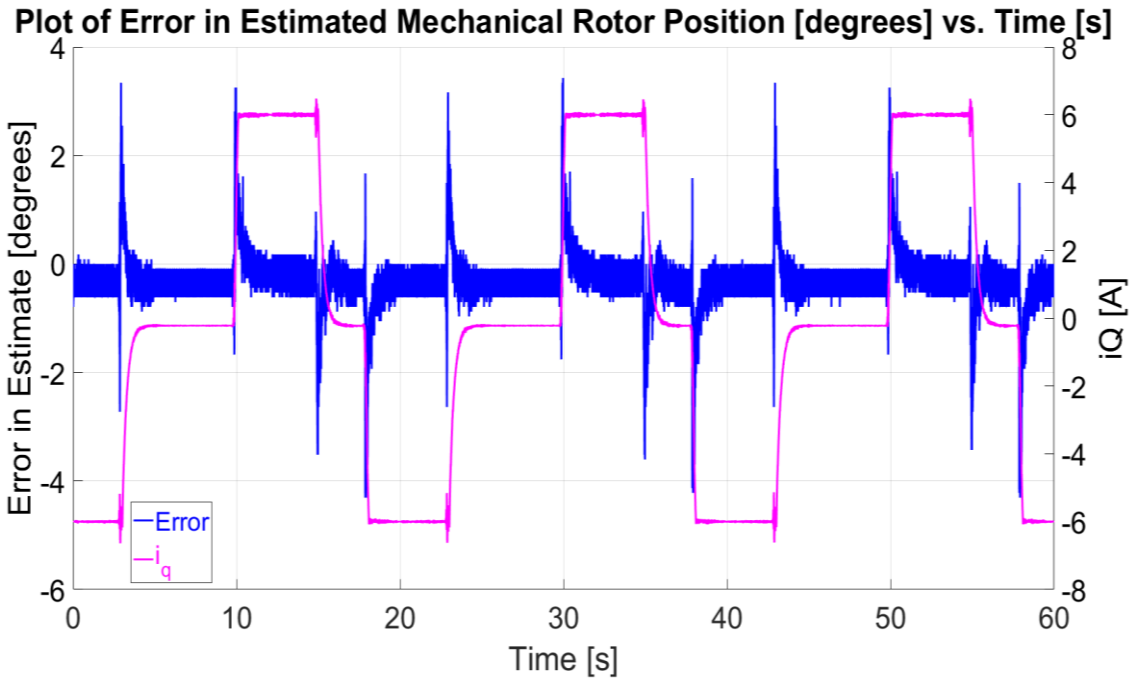

Figure 10.28– Plot of Error in Mechanical Rotor Position θ_m [°] vs. Time [s] for sensorless current control with K_{hw} =7, $i_{q3\_limit}^*$ = ± 6 A with turning condition steer-by-wire profiles.

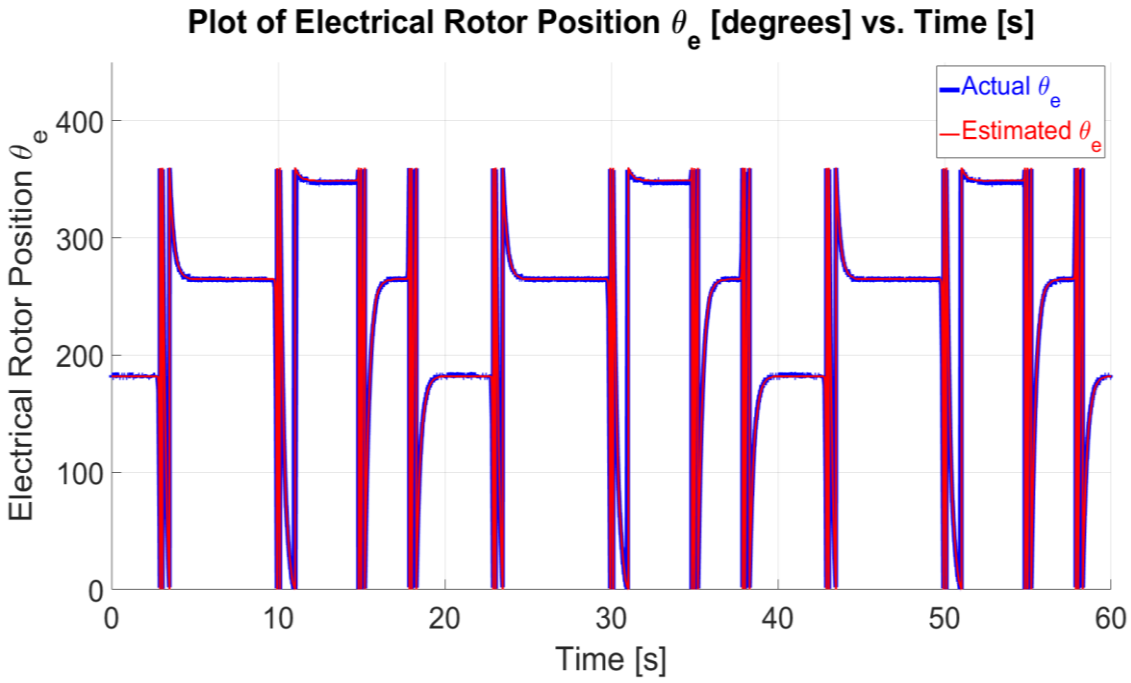

Figure 10.29 – Plot of Actual/Estimate Electrical Rotor Position θ_m [°] vs. Time [s] for sensorless current control with K_{hw} =7, $i_{q3\_limit}^*$ = ± 6 A with turning condition steer-by-wire profiles.

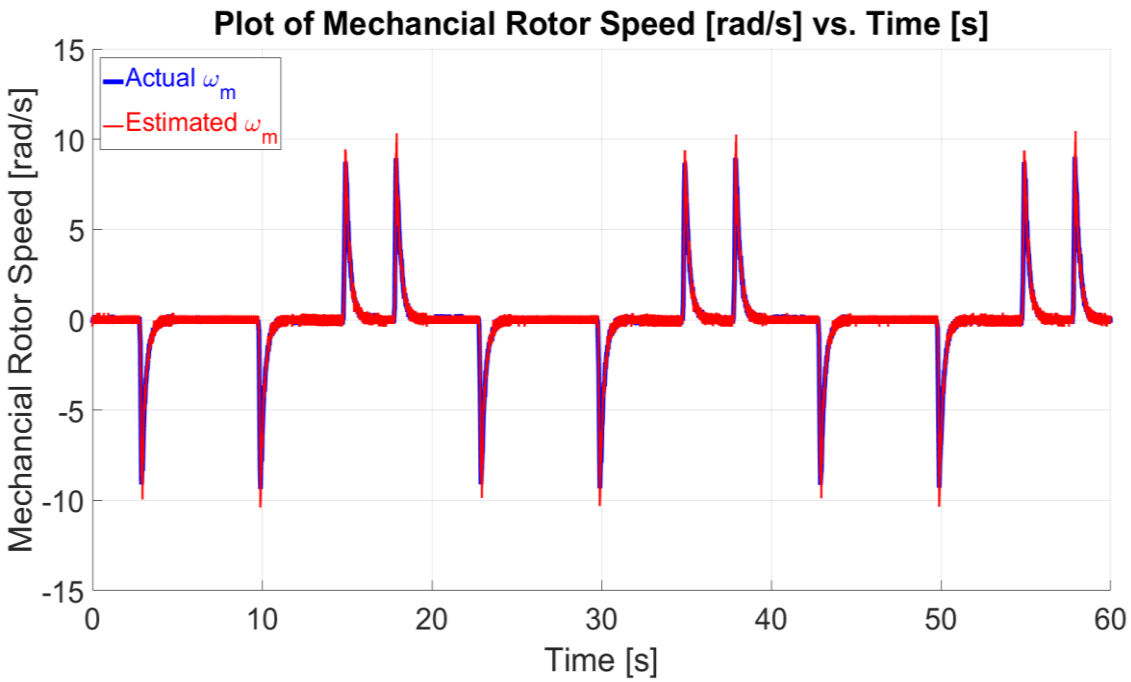

Figure 10.30 – Plot of Actual/Estimated Rotor Speed ω_m [°] vs. Time [s] for sensorless current control with K_{hw} =7, $i_{q3\_limit}^*$ = ± 6 A with turning condition steer-by-wire profiles.

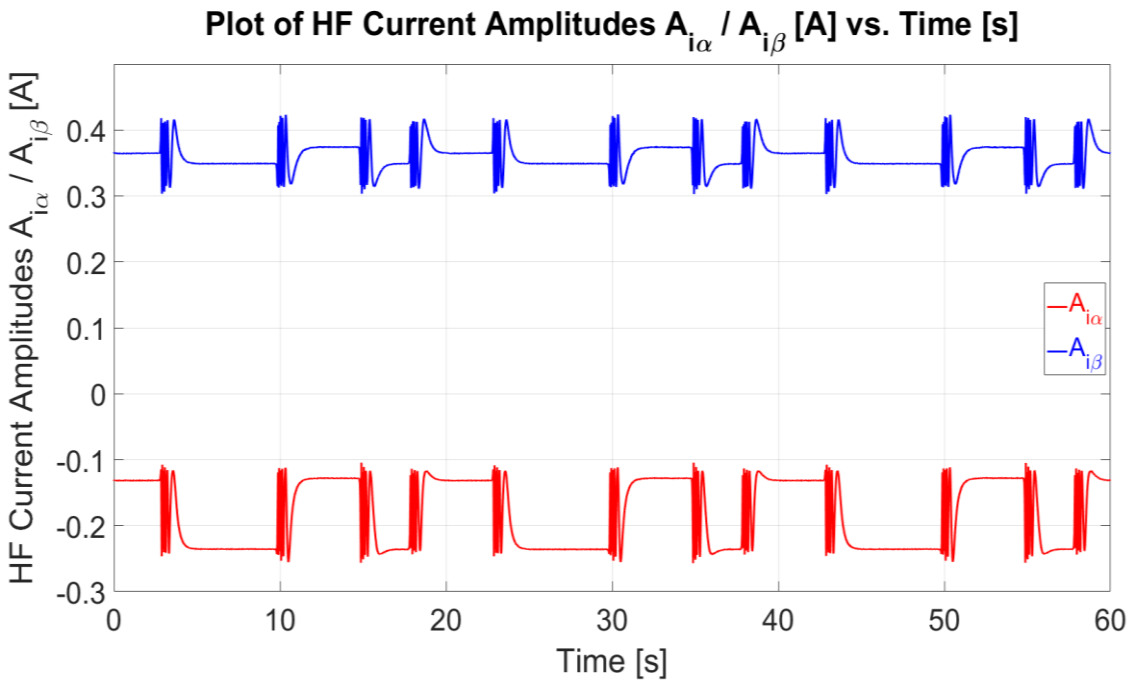

Figure 10.31 –Plot of HF Current Amplitudes $A_{i\alpha}$, $A_{i\beta}$ [A] vs. Time [s] for sensorless current control with K_{hw} =7, $i_{q3\_limit}^{*}$ = ± 6 A with turning condition steer-by-wire profiles.

10.3 Sensorless Position Control at the Steered Wheel Side

10.3.1 Sensorless Position Control at the Steered Wheel in No Load Condition

The position control of the steered wheel side in the steer-by-wire system is a critical part of the system. Sensorless position control in such a system requires a suitable dynamic response in all of the cascaded RFO control loops. Such a response is only possible through a precise and robust sensorless observer. In this sub-section, the operation of the SBO for machine M3 coupled to the sensored current control M4 is presented (Figure 10.32). The settings of the cascaded control loop system for sensorless position control are set as follows within the RFO control structure (Section 3.2.3): K_{p_I3} = 0.1, K_{i_I3} = 100, K_{p_W3} = 0.1, K_{i_W3} = 20, K_{p_P3} = 5.

Since the changes in position are applied through a sigmoid reference, the proportional gain of the position controller could be set to a higher value compared to what was implemented for step reference inputs as discussed in Sections 9.7-9.9. The actual and estimated ***mechanical*** rotor positions are shown with the i_q-current in Figure 10.33. The error in the estimated ***mechanical*** rotor position is shown in Figure 10.34, with an absolute maximum error of 4.04° and a RMSE of 0.58°. The actual

and estimated ***electrical*** rotor positions are shown in Figure 10.35, while the actual and estimated ***mechanical*** rotor speeds are shown in Figure 10.36. The HF current amplitudes $A_{i\alpha}$, $A_{i\beta}$ are shown in Figure 10.37. The sensorless position control in loaded conditions is shown in sub-sections 10.3.2 and 10.3.3 for forward and reverse torque respectively. The maximum rate of change in position to be tracked by the observer for the case shown in Figure 10.33 is 121.76 °/s.

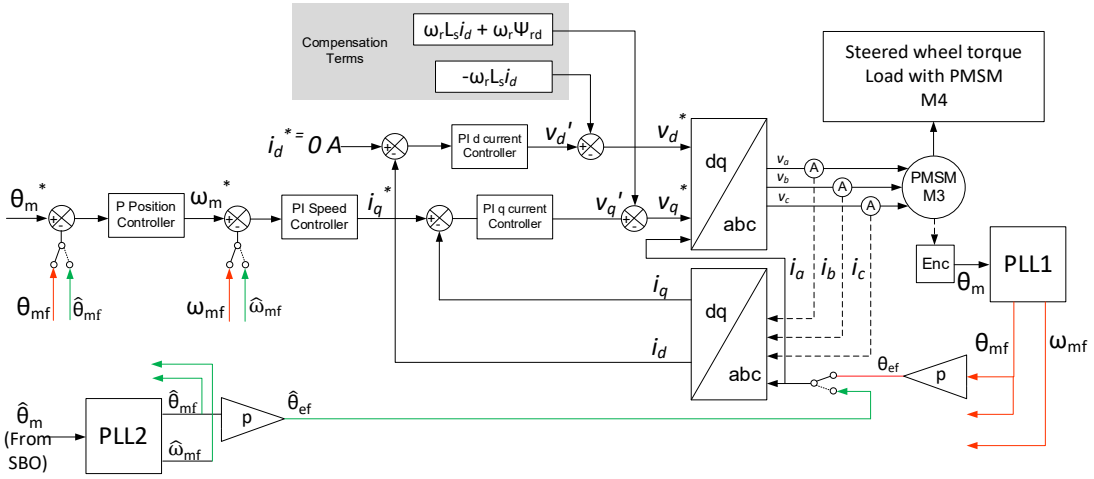

Figure 10.32 - RFO control topology for steed side in steer-by-wire.

In Section 2.7, the maximum steering angle at the handwheel side was experimentally found to be 286 °/s from the vehicle tested. Given the complexity of measuring and modelling the exact dynamics at the steered wheel side, the position demands are modelled based on the handwheel measurements with a steering ratio of 10. The steering ratio is that factor by which the handwheel position is divided to obtain the steered wheel position. In [146] an adaptive steering ratio is recommended in the range of 10 to 20. For this dissertation, a steering ratio of 10 is assumed as the position transients at the steered wheel will be faster and more challenging to track. Hence, from the practical measurements on the test vehicle, a maximum response of 28.6 °/s is expected at the steered wheel side. Since the sensorless position-controlled system was shown to track a maximum rate of 121.76 °/s (Figure 10.33), this would allow a gearbox with a ratio 4.25:1 to be used. This would also increase the sensorless system torque of 6.36 Nm at the output of the gearbox to 28.74 Nm at the steered wheel side. Since 2 Nm was observed in practice and assuming a steering ratio of 10, the resultant torque of 20 Nm is sufficient at the steered wheel side. Thus, the system proposed in this dissertation has the capability of delivering the torque required in the steer-by-wire application.

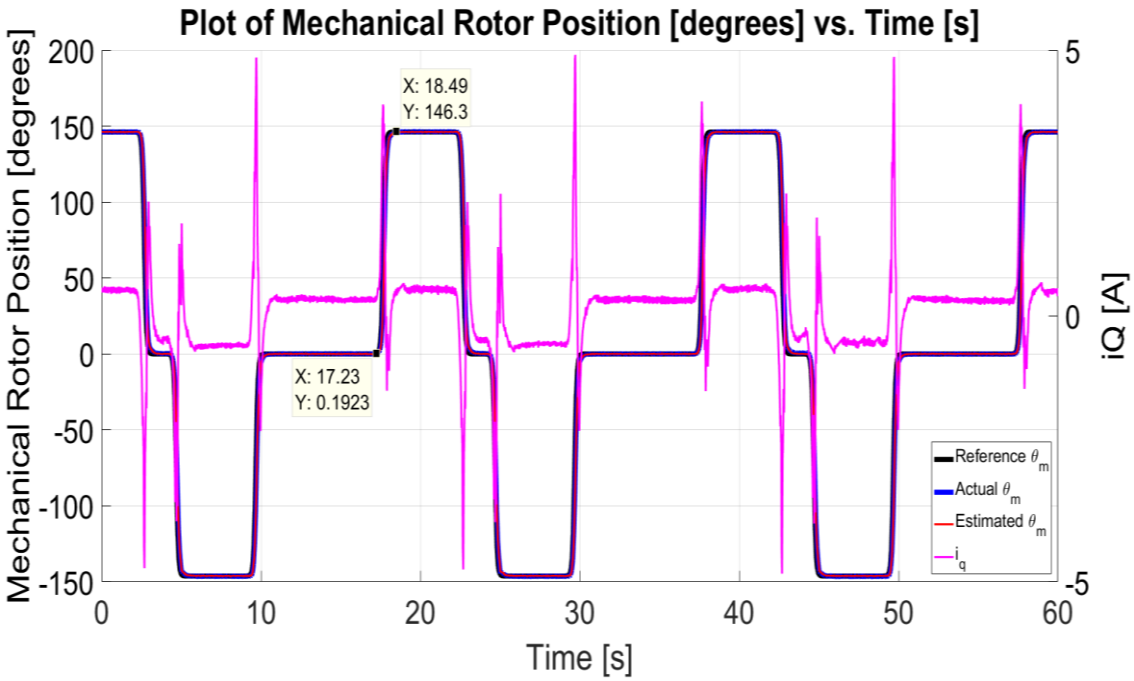

Figure 10.33 – Plot of Reference/Actual/Estimate Mechanical Rotor Position θ_m [°] vs. Time [s] for sensorless position control at no load with steer-by-wire steering profiles.

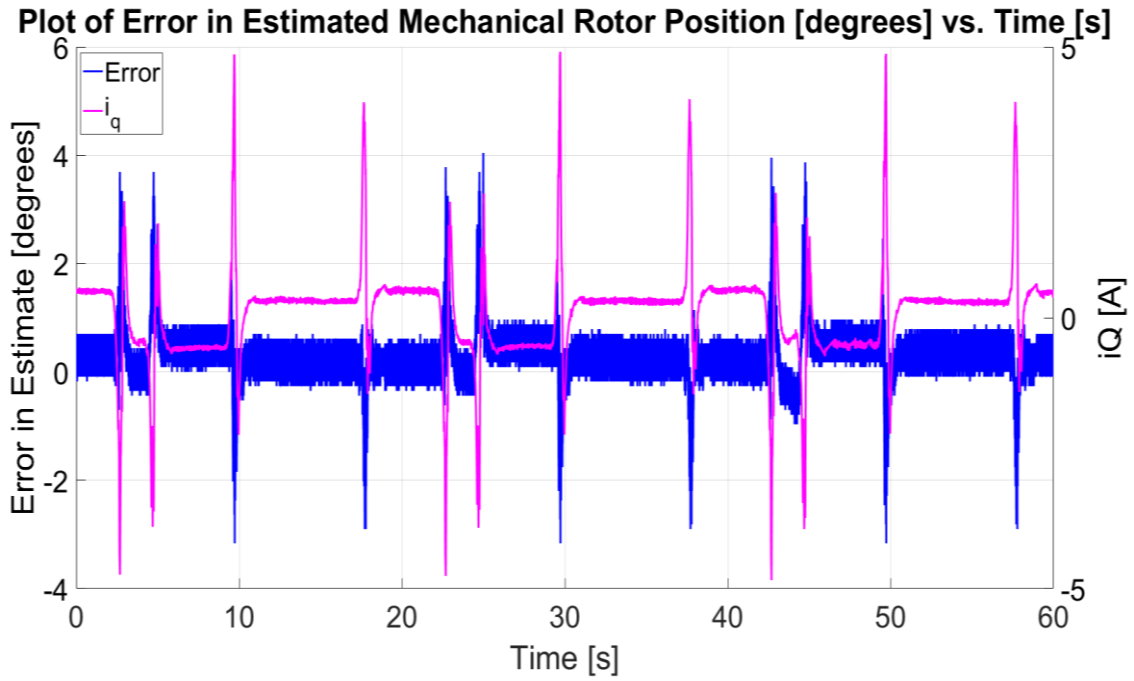

Figure 10.34– Plot of Error in Mechanical Rotor Position θ_m [°] vs. Time [s] for sensorless position control at no load with steer-by-wire steering profiles.

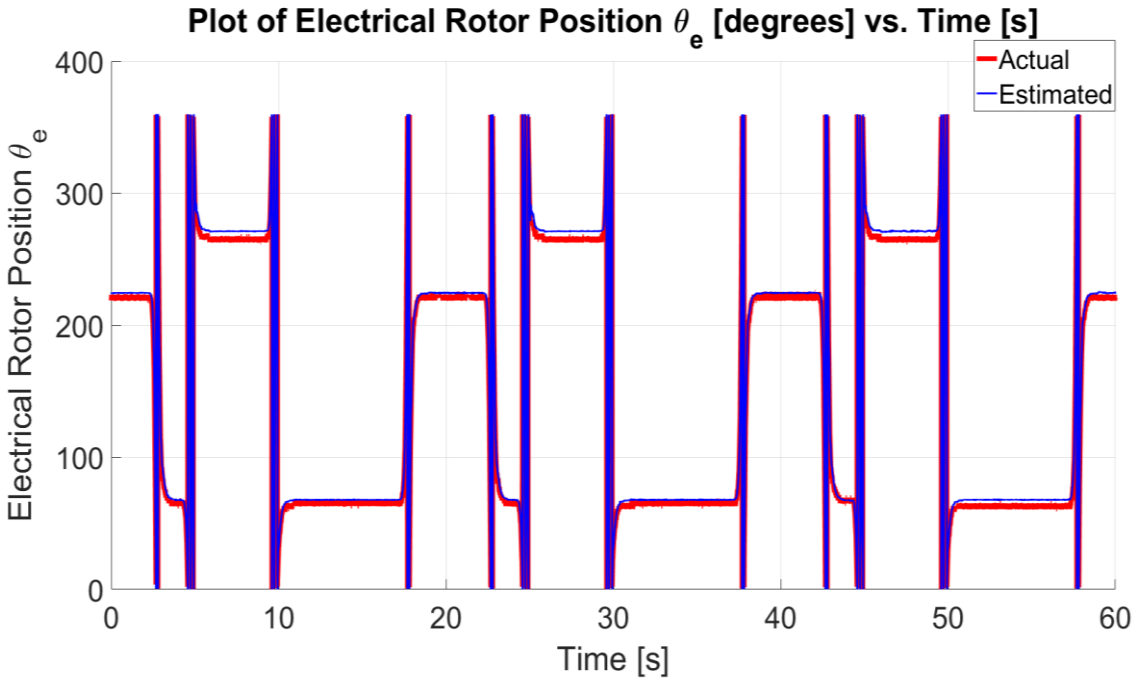

Figure 10.35 – Plot of Actual/Estimate Electrical Rotor Position θ_e [°] vs. Time [s] for sensorless position control at no load with steer-by-wire steering profiles.

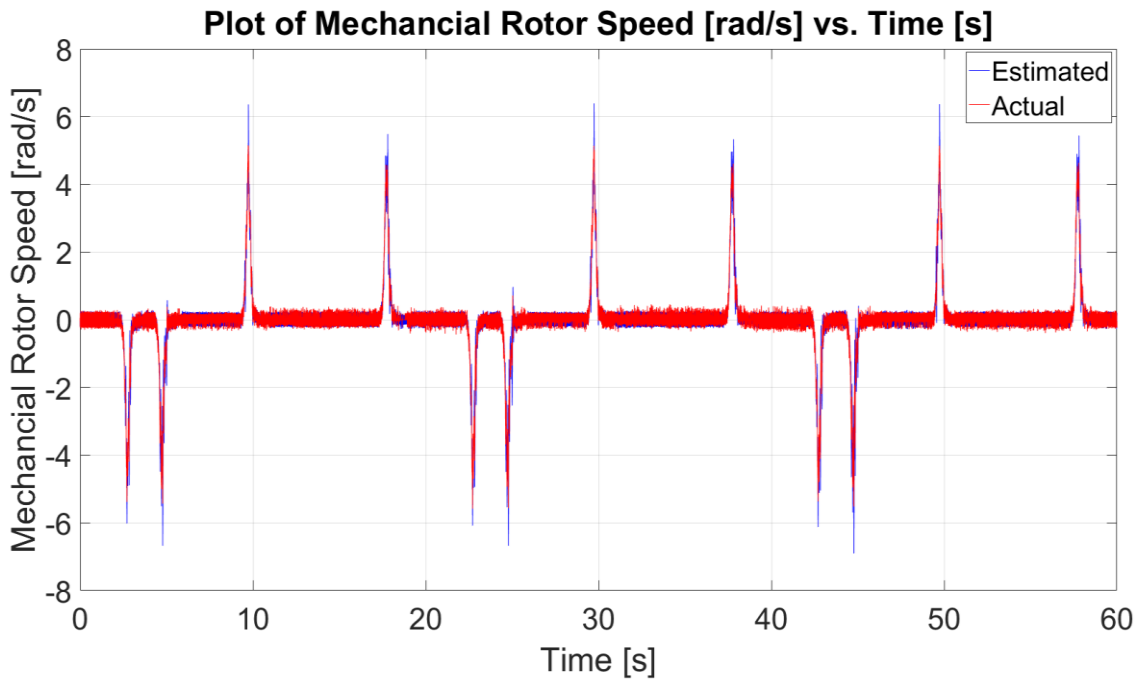

Figure 10.36 – Plot of Actual/Estimated Rotor Speed ω_m [°] vs. Time [s] for sensorless position control at no load with steer-by-wire steering profiles.

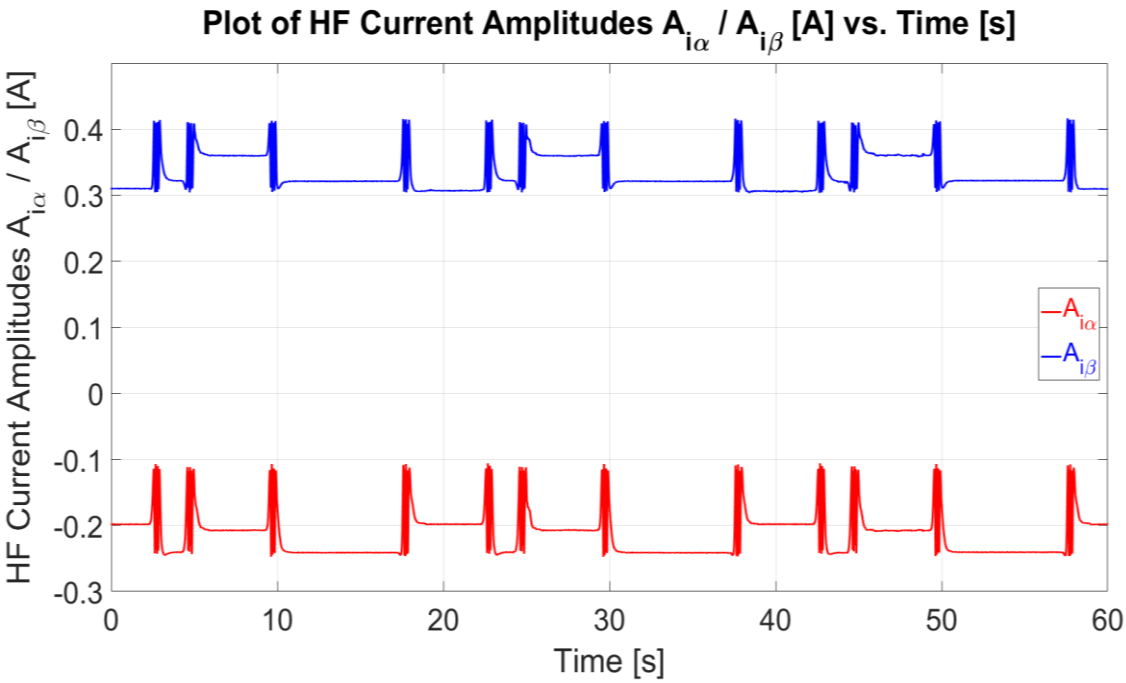

Figure 10.37 –Plot of HF Current Amplitudes $A_{i\alpha}$, $A_{i\beta}$ [A] vs. Time [s] for sensorless position control at no load with steer-by-wire steering profiles.

10.3.2 Sensorless Position Control at the Steered Wheel with Forward Torque

The sensorless position control of M3 at the steered wheel with an i_{q4}^{*} = 5 A on the sensored current-controlled machine M4 is presented in this section. The mean i_{q3} for the period shown is of 4.94 A with an absolute maximum of 9.88 A. The position references are identical to those presented in Section 10.3.1 The actual and estimated ***mechanical*** rotor positions are shown with the i_q-current in Figure 10.38. The error in the estimated ***mechanical*** rotor position is shown in Figure 10.39, with an absolute maximum error of 4.92° an RMSE of 0.74°. The actual and estimated ***electrical*** rotor positions are shown in Figure 10.40, while the actual and estimated ***mechanical*** rotor speeds are shown in Figure 10.41. The HF current amplitudes $A_{i\alpha}$, $A_{i\beta}$ are shown in Figure 10.42.

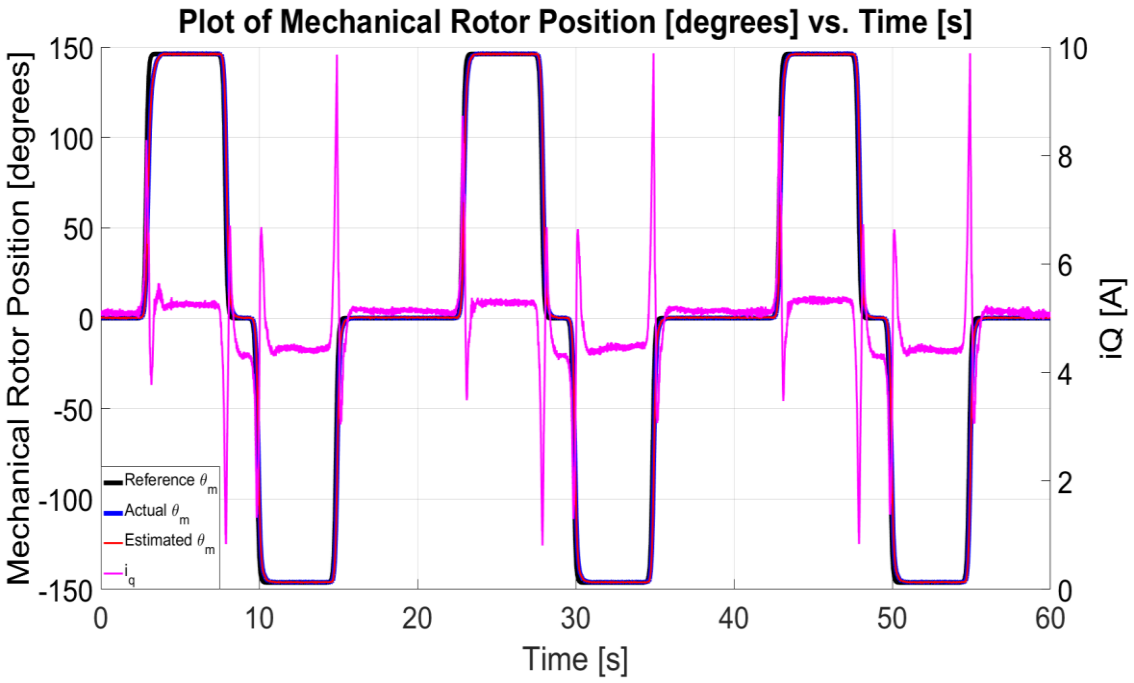

Figure 10.38 – Plot of Reference/Actual/Estimate Mechanical Rotor Position θ_m [°] vs. Time [s] for sensorless position control with $i_{q4}^* = 5$ A on M4 and steer-by-wire steering profiles.

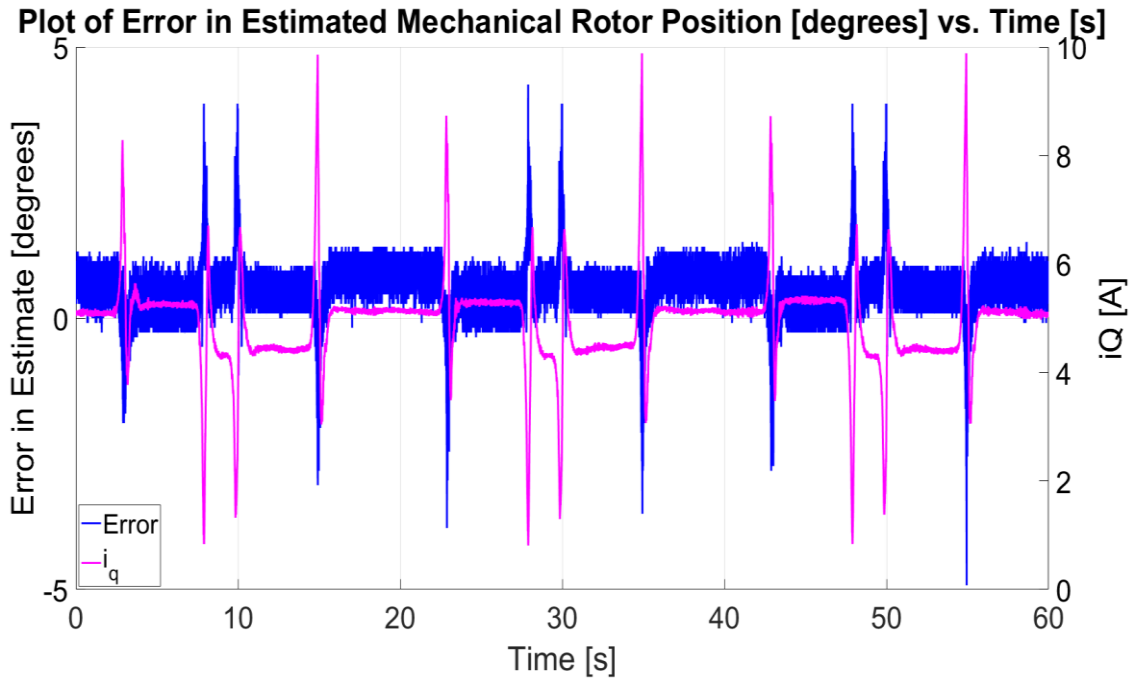

Figure 10.39– Plot of Error in Mechanical Rotor Position θ_m [°] vs. Time [s] for sensorless position control with $i_{q4}^* = 5$ A on M4 and steer-by-wire steering profiles.

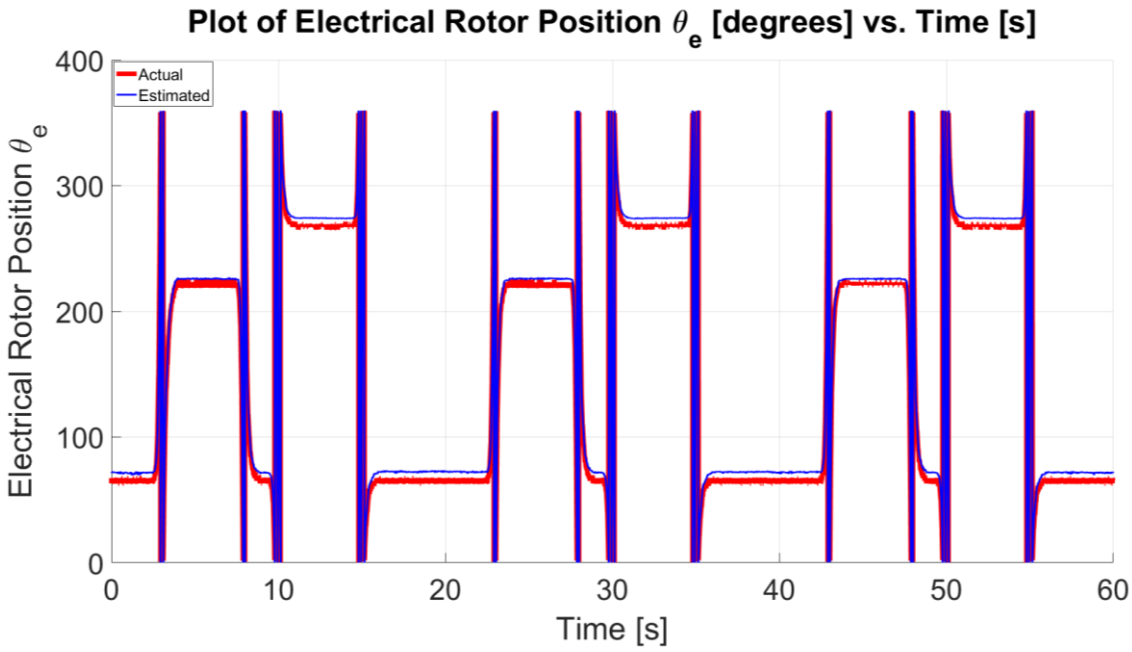

Figure 10.40 – Plot of Actual/Estimate Electrical Rotor Position θ_m [°] vs. Time [s] for sensorless position control with $i_{q4}^* = 5$ A on M4 and steer-by-wire steering profiles.

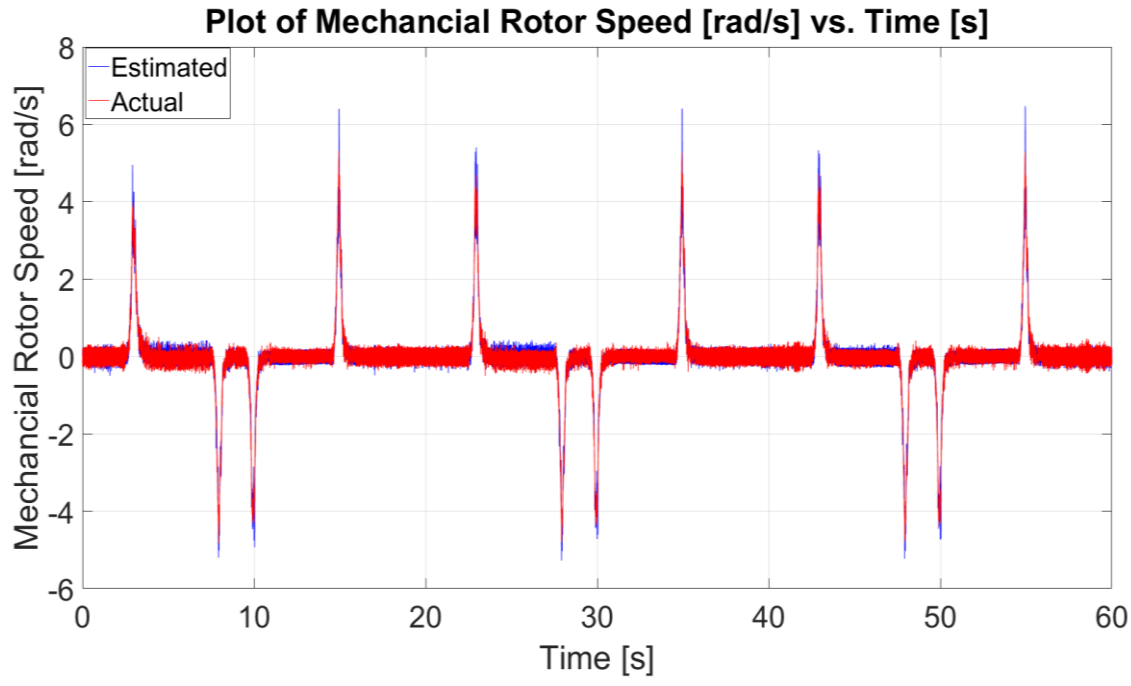

Figure 10.41 – Plot of Actual/Estimated Rotor Speed ω_m [°] vs. Time [s] for sensorless position control with $i_{q4}^* = 5$ A on M4 and steer-by-wire steering profiles.

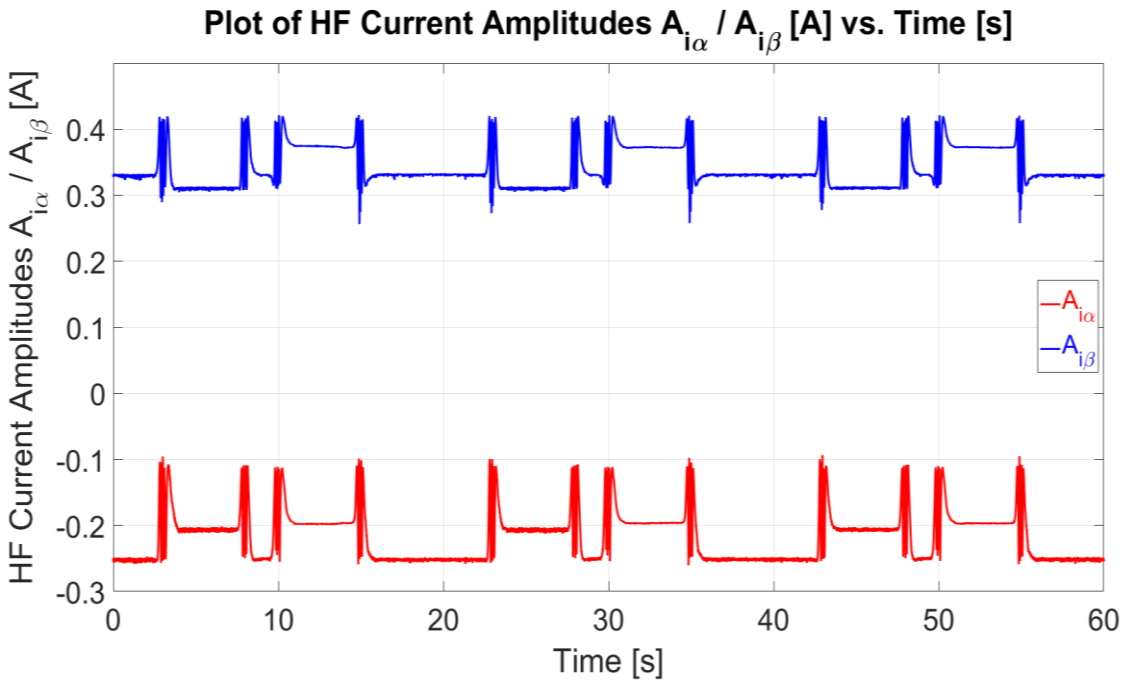

Figure 10.42 –Plot of HF Current Amplitudes $A_{i\alpha}$, $A_{i\beta}$ [A] vs. Time [s] for sensorless position control with i_{q4}^{*}= 5 A on M4 and steer-by-wire steering profiles.

10.3.3 Sensorless Position Control at the Steered Wheel with Reverse Torque

The sensorless position control of M3 at the steered wheel with an i_{q4}^{*} = -5 A on the sensored machine M4 is presented in this sub-section. The mean i_{q3} for the period shown is of -4.91 A with an absolute maximum of 9.79 A. The position references are identical to those presented in Sections 10.3.1 – 10.32. The actual and estimated ***mechanical*** rotor positions are shown with the i_q-current in Figure 10.43. The error in the estimated ***mechanical*** rotor position is shown in Figure 10.44, with an absolute maximum error of 4.74° with an RMSE of 0.65°. The actual and estimated ***electrical*** rotor positions are shown in Figure 10.45, while the actual and estimated ***mechanical*** rotor speeds are shown in Figure 10.46. The HF current amplitudes $A_{i\alpha}$, $A_{i\beta}$ are shown in Figure 10.47.

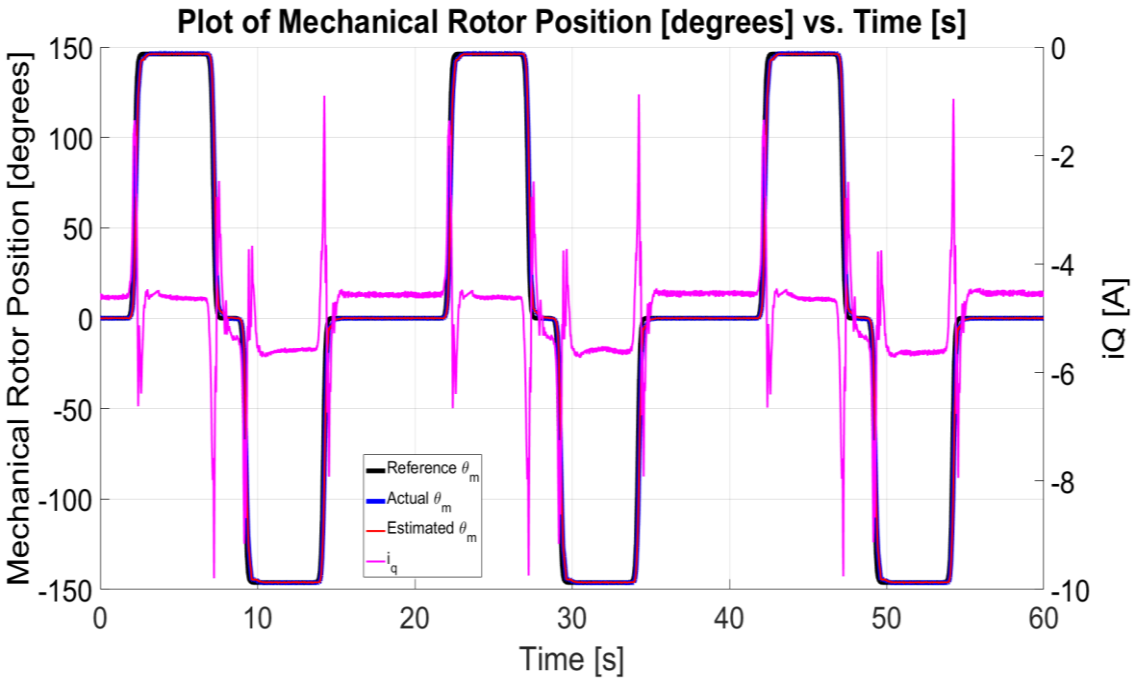

Figure 10.43 – Plot of Reference/Actual/Estimate Mechanical Rotor Position θ_m [°] vs. Time [s] for sensorless position control with i_{q4}^*= -5 A on M4 and steer-by-wire steering profiles.

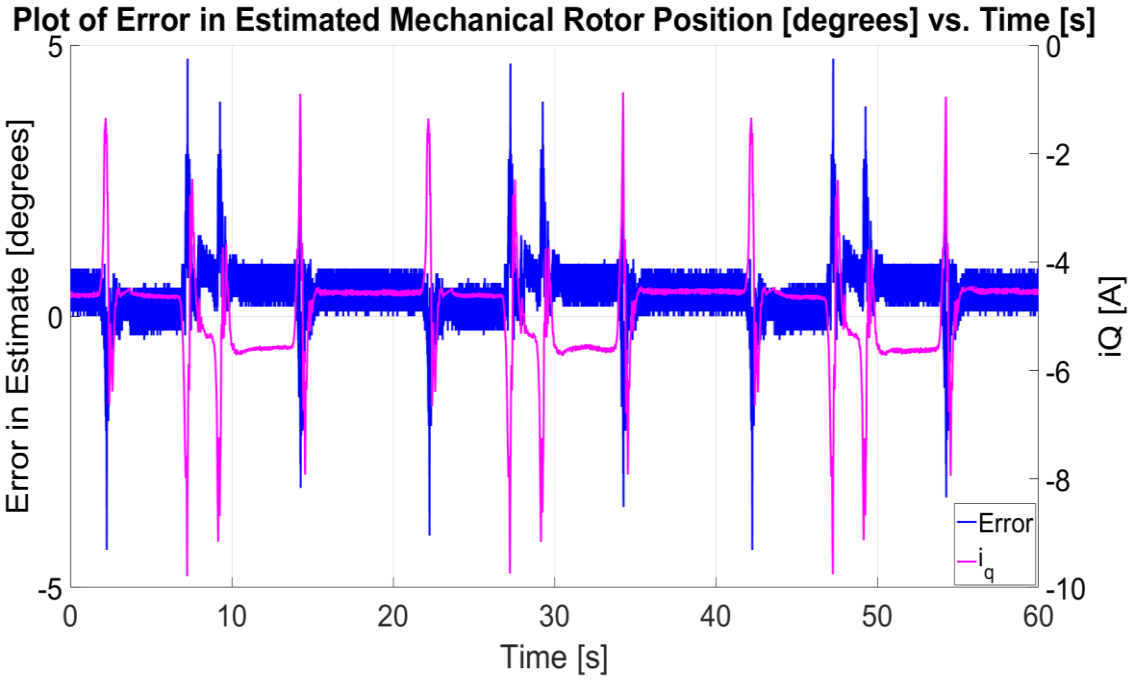

Figure 10.44– Plot of Error in Mechanical Rotor Position θ_m [°] vs. Time [s] for sensorless position control with i_{q4}^*= -5 A on M4 and steer-by-wire steering profiles.

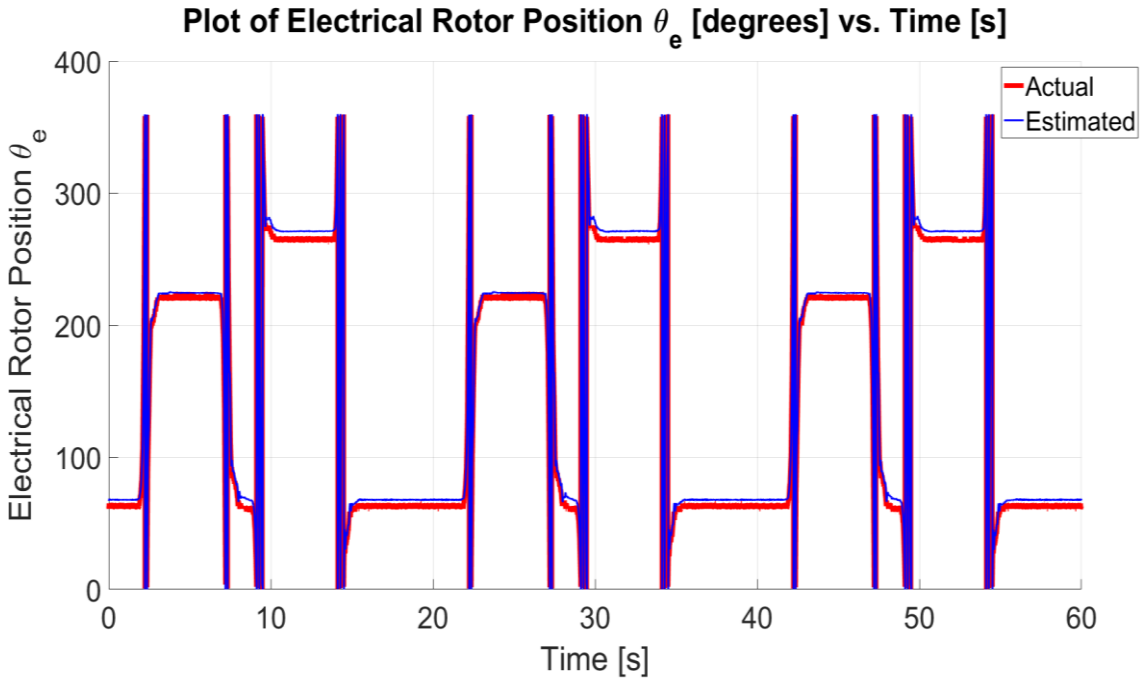

Figure 10.45 – Plot of Actual/Estimate Electrical Rotor Position θ_m [°] vs. Time [s] for sensorless position control with i_{q4}^*= -5 A on M4 and steer-by-wire steering profiles.

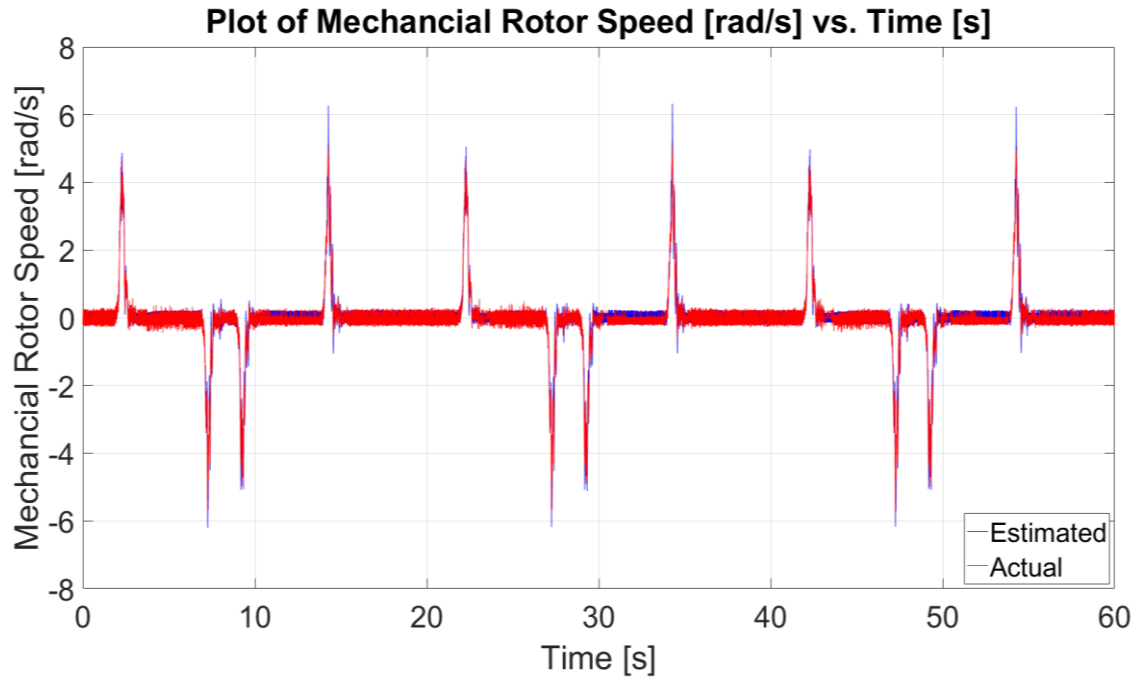

Figure 10.46 – Plot of Actual/Estimated Rotor Speed ω_m [°] vs. Time [s] for sensorless position control with i_{q4}^*= -5 A on M4 and steer-by-wire steering profiles.

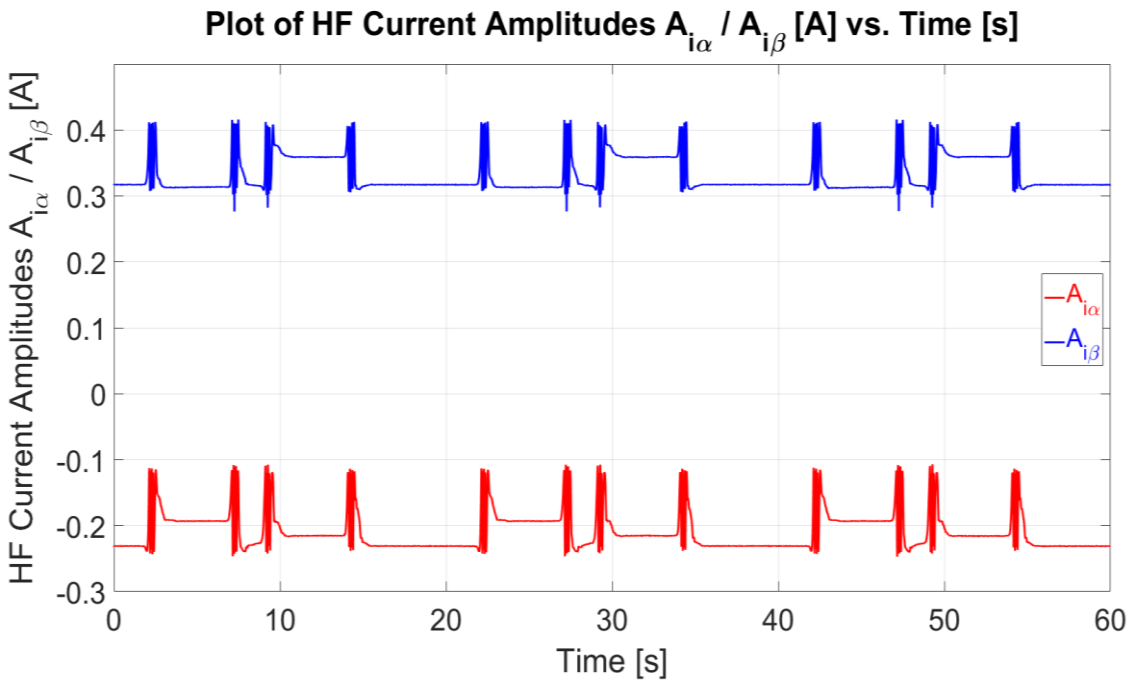

Figure 10.47 –Plot of HF Current Amplitudes $A_{i\alpha}$, $A_{i\beta}$ [A] vs. Time [s] for sensorless position control with i_{q4}^{*}= -5 A on M4 and steer-by-wire steering profiles.

10.4 Summary

In Chapter 2, position measurement at both the handwheel and the steered wheel side was identified as being safety-critical to the steer-by-wire application. In this dissertation, it was proposed to use sensorless estimation and control on the electric machines used in steer-by-wire rather than redundant hardware mechanisms such as additional encoders or mechanical linkages. In this chapter, the sensorless control using the SBO for the steer-by-wire application was presented.

The sensorless current control at the handwheel side was shown using steering position profiles set by a current-controlled sensored machine. The response of the proposed SBO was shown with and without torque limit for a wide range of torque settings equal to and above what is found in a typical steering arrangement. The torque limit was introduced to replicate the effects of the torque reference model proposed in Section 2.7.2 which replicates the torque limiting measured on the test vehicle. The maximum detection capability of the observer was found to be of 323.61 degrees/s (Section 10.2.1) in sensorless current control mode which is of the same order of magnitude as the maximum steering rate determined experimentally for the test vehicle of 286 degrees/s. The sensorless current performance was investigated for the same steering profile at

different values of gain K_{hw}, with higher values resulting in more opposing current/torque for unit values of position. With K_{hw} = 3.5 A/rad the RMSE in the mechanical rotor position estimate was of 0.54° without torque limit and 0.45° with torque limit. Similarly, for K_{hw} = 7 A/rad the RMSE in the mechanical rotor position estimate was of 0.64° without torque limit and 0.53° with torque limit. Since the i_q-current for these tests is predominantly within the ± 10 A range for which LUTs are commissioned the error in the variation in the observer estimates at different settings is negligible.

Sensorless position control at the steered wheel side was also presented with estimates in the electrical rotor position, mechanical rotor speed and mechanical rotor position from the SBO. The position-controlled machine was shown to turn at a rate of 121.76 °/s (Section 10.3.1) where the requirement at the steered vehicle wheel side is of approximately 28.6 °/s (286 degrees/s found experimental at the handwheel side divided by an assumed steering ratio of 10). The SBO was tested at no-load conditions and shown to have a RMSE in the mechanical rotor position estimate of 0.58°. The RMSE increased slightly when the load of the machine is increased to 0.74° (at a load of 5 A) and 0.65° (at a load of -5 A).

The results shown in this chapter show the robustness of the proposed SBO for the estimation and sensorless control of the observer in steer-by-wire applications, at both the handwheel and the steered wheel side. Although both current and position control loops were shown to be stable in sensorless closed-loop control, the current and speed parameters exceed the range of commissioned values. This increases the error the in estimates. Possibly, further enhancement of the current and position-controlled loops could be achieved with commissioning of additional LUTs extending the current and speed ranges investigated in this dissertation.

Chapter 11 – Dissertation Conclusions

11.1 Final Conclusions and Discussions

This dissertation has studied the improvement in functional safety for automotive steer-by-wire technology through sensorless control and estimation algorithms. In Chapter 2, the rotor position measurements at both the handwheel side and steered-wheel side were identified as being safety-critical, and thus backup is required in case of failure of the primary sensor. Since the selection of sensorless algorithms depends on the operational characteristics of the steer-by-wire system, the steering system in a Kia Sportage 2014 test vehicle was characterised in Section 2.7. From the experimental measurements logged through the vehicle's On-Board Diagnostic (OBD-II) port, it was determined that the feedback torque at the handwheel is approximately proportional to the steering angle for small displacements from the initial position. For larger steering angles the torque feedback is limited to a value in the range of 2 Nm. While the mathematical modelling of steering arrangements is complex and multi-parameter dependent, the torque reference – position generation characteristic proposed in Section 2.7.2 was considered sufficient for testing sensorless algorithms in this dissertation. This model considered a proportional characteristic in the handwheel angle in the range ± 20 degrees. Outside of this range, the torque is limited at a value of ± 2 Nm.

The sensored operation of the Permanent Magnet Synchronous Machine (PMSM) used in the experimental setup was shown in Chapter 3. The PMSM parameters were obtained from experimental tests since they were not listed on the manufacturer datasheet. Due to the limitations of the electric drive, the parameters could only be approximated. Moreover, the bandwidths of the control loops were further tuned experimentally. The current loop was designed such that current-controlled PMSM M3 (the machine on which sensorless investigation was carried out) had a bandwidth of 281 Hz with a 57.4 % overshoot. The speed control loop for the same machine was designed to have a bandwidth of 15.93 Hz with a 27.6 % overshoot. The final outer position loop was designed at a bandwidth of 1 Hz. The position controller was found to have no steady-state error with a sigmoid reference used to emulate typical steering conditions. However, a velocity error was found during the ramp part of the sigmoid. This effect is not relevant in steering as it will not be felt by the driver in the steer-by-wire application. However, the design of a lead-lag compensator was proposed to reduce the velocity error

to zero for generic servo-control applications. The operation of the lead-lag compensator was shown for sensored operation in Section 3.6.3. However, it was not considered in sensorless mode since it is not generally used for steer-by-wire.

The main objective of this dissertation was to implement a robust sensorless control scheme for the steer-by-wire application. This application operates at zero speed with high-speed transients from the initial position. Sensorless control in such conditions has been particularly challenging and requires an approach which is not model-based. In this dissertation, a High-Frequency (HF) injection-based method was used for the detection of the magnetic saliency of the machine. In Section 6.2, it was described how saliency is affected by multiple parameters, including magnetic and geometric effects. The PMSM used in this dissertation has partially-inset surface mount rotor magnets, which result in multiple saliencies besides the expected component at twice the electrical rotor frequency $2f_e$. Furthermore, the variations in the rotor magnet protrusions outside the rotor laminations result in saliency variation, which is dependent on the mechanical rotor position. When the High Frequency (HF) current amplitudes were measured with a rotating injection in the stationary frame of $V_i = 3$ V and $f_i = 2.5$ kHz it was observed that both α and β HF current amplitude components ($A_{i\alpha}$, $A_{i\beta}$) have significant harmonics. The most significant harmonic components were found at $4f_e$, with $A_{i\alpha}$ being 31 % and $A_{i\beta}$ being 11 % of the $2f_e$ components in the respective axes. Furthermore, other components were observed at even and odd harmonics of f_e.

Pulsating voltage injection in the stationary frame was also investigated in Section 6.3.5 for different injection angles. The variations in the HF current amplitudes were shown to have additional effects to that modelled in single saliency models. The variations result in saliency signatures of different shapes for the same injection voltage and different injection angles γ. As expected, the saliency signatures are affected by the loading of the machine with significant variations noted when the machine was loaded from -100 % to 100 % of rated load. Furthermore, a minor phase shift was noted with the rotor shaft speed indicating the magnetic signature mapped to the absolute rotor position is speed dependent. Given the multiple harmonic saliencies observed on the PMSM in this dissertation, a compensation mechanism would be required if the estimation was to be carried out with a trigonometric based observer. A Space Modulation Profiling (SMP) based observer as proposed in literature was successfully

implemented in Section 6.5.2 with a Root Mean Square Error (RMSE) in the estimated mechanical rotor position for the test period of 1.83°.

While the results obtained with the SMP-based observer are in line with those shown in literature, significant limitations are associated with this method when applied to the PMSM in this dissertation. In general, SMP requires the use of a zero-phase filter which cannot be computed in real-time, such that commissioning of the SMP tables can only be carried out offline. This is a significant limitation as state-of-the-art research in sensorless control has been directed towards online calibration. The SMP technique compensates for harmonics in the electrical domain such that additional post-estimation compensation was required for mechanical domain effects which were implemented in the form of a position-dependent LUT. Given these shortcomings, this dissertation aimed at obtaining a similar level of estimation accuracy as the SMP but with the possibility of online commissioning. Most techniques in literature based on HFI injection try to apply filtering techniques to obtain an isolated saliency harmonic such as the $2f_e$ or $4f_e$ as reviewed in Chapter 4. While this has been proven to obtain satisfactory results, it still does not characterise the unique profile consisting of multiple harmonics of the machine.

For this work, a novel Search-Based Observer (SBO) was developed and was presented in Chapter 7. This method consists of three processes: commissioning, searching and PLL-based speed LUT selection. The commissioning process to generate the HF current amplitude reference LUTs was carried out at V_i=3 V, f_i = 2.5 kHz, ω_{m4}^* = 1 rad/s and γ = 120°. The speed dependent LUT selects the quadrant of operation to have a similar set of LUTs being used for the current state of the machine. Position and speed measurements from both the encoder and the SBO are filtered with various PLL-based filters with different bandwidths, as presented in Section 7.5. The filtering is required to reduce quantisation.

The SBO estimation process was shown to be a robust solution such that sensorless current, speed and position control were obtained using both step and sigmoid responses. The sensorless current control of the PMSM was shown and analysed in Chapter 8. The current controller bandwidth was reduced from 281 Hz to 86 Hz in order to limit the effects of the controller on the HF injection. When in current control the PMSM was tested in a low-speed operation of ±8 % rated speed for both positive and negative

loading currents in Sections 8.6-8.7 yielding RMSEs in the estimated rotor position of 1.01° and 0.96°, respectively. Sensorless speed and position control were also shown in Chapter 9, where the bandwidths of the loops were reduced to 4.48 Hz (speed closed-loop) and 0.5 Hz (position closed-loop). This was a result of the reduction in the current loop bandwidths. The sensorless speed operation was shown between -24 rpm to 19 rpm at rated load conditions. Possibly the operating range could be extending by introducing additional LUTs commissioned at different speeds rather than having one for positive and negative rotation.

The operation of the SBO estimation method for steer-by-wire was discussed in Chapter 10 for application with both the handwheel and the steered wheel side. To replicate the steering patterns measured on the test vehicle in Chapter 2, a sigmoid-based position reference was used with a maximum rate of change of 323 degrees/s at the handwheel in sensorless current control. The system was tested with values for the handwheel gain $K_{hw} = 3.5$ A/rad and $K_{hw} = 7$ A/rad with a maximum RMSE in the estimated mechanical rotor position of 0.64°. Sensorless position control at the steered wheel side was tested with a sigmoid position reference with a maximum rate of change of 122 degrees/s with a maximum RMSE in the estimated mechanical rotor position of 0.74°.

From the results in Chapter 10, the performance of the SBO was considered as a promising solution for implementation in an actual steer-by-wire system to function as a backup to the standard encoder and allow sensorless operation in case of sensor encoder failure. Furthermore, from the results described in Chapters 8 and 9, it was shown that the proposed SBO estimation method could also be extended to generic current, speed and position control applications. The main advantage of the proposed approach is that the estimation accuracy is mainly dependent on the number of operating points considered during the commissioning stage. Since the memory of modern digital controllers continues to improve significantly, this would allow for the compilation of very detailed magnetic signature maps of each machine. These maps can also be commissioned online to cater to a wide variety of speed and load operating points.

The proposed SBO estimation process has the advantage that the LUTs which are used for comparison with real-time measurements can be adapted in real-time to compensate for minor variations in the magnetic signature. This is possible since the commissioning algorithm does no rely on computationally intensive techniques. Furthermore, the SBO

can be used on machines with saliencies which are not sinusoidal. In this dissertation the method was shown to provide a robust sensorless solutions with saliencies with significant harmonics.

11.2 Future Work

This section briefly discusses the limitations identified in the methodology used in this dissertation and proposes improvements to be carried out in future work.

- The closed-loop sensorless control implemented in this dissertation was based on the detection of HF current amplitudes resulting from a continuous HF pulsating injection. This type of injection was shown to result in current measurements modulated by the magnetic signature with a significant SNR. However, the injection results in audible noise and torque ripple. While such effects, particularly audible noise, are not generally of concern in industrial applications, they are not desirable in automotive applications. In order to keep the injection amplitudes to a minimum, the saliency measurement board shown in Section 5.5 was designed to signal condition the current sensor measurements before being sampled at the ADC. The signal conditioning circuit includes amplification stages to maintain a satisfactory SNR without increasing the injection amplitude. Alternatively, the HF components inherently present in the PWM switching frequencies could be used instead of the additional HF pulsating injection, as discussed in Section 4.8.

- The position sensors used in this dissertation for sensored control and commissioning of the SBO LUTs were 12-bit digital encoders. These encoders transmit data through a Serial Synchronous Interface (SSI) protocol of the microcontroller. The sensor integrated circuit embedded in the encoder enclosure detects the flux of a permanent magnet fitted onto the motor shaft. Such technology provides a cost-effective solution for absolute position measurement. However, a number of limitations were noticed while carrying out work on this dissertation which includes the low SNR when deriving the speed from the discretised position measurement. As a countermeasure the speed was obtained through a Phased-Locked Loop (PLL) and noise in the speed mitigated by reducing the loop bandwidth. However, the loop bandwidth cannot be reduced below that required for speed control, limiting the filtering effect.

Furthermore, it was noticed that minor misalignments between the magnet and the sensor IC result in significant differences when carrying out vector-based control. Thus, the use of a higher resolution optical encoder which has a mechanical connection rather than relying on detection of magnetic flux would result in an overall more precise speed and position control system. While the accuracy of optical encoders is superior to both magnetic encoders and sensorless algorithms, they are significantly more expensive and still require backup due to reliability issues.

- The HF current amplitudes $A_{i\alpha}$, $A_{i\beta}$ were measured with the saliency measurement circuit board presented in Section 5.5. This circuit board was initially designed to measure both HF current amplitudes and voltages so as to calculate the HF admittance of the machine. Since the pulsating injected voltage is carried out in open-loop form, it is susceptible to variations in the DC link voltage level and inverter non-linearities. The calculation of the machine admittance should theoretically result in saliency signals with improved SNR.

  However, from the experimental results obtained in this dissertation, the SNR of the HF current amplitudes was found to be better than that of the calculated admittance. This is mainly attributed to insufficient attenuation of the Pulse Width Modulation (PWM) harmonics before the Analogue to Digital (ADC) process. Since the use of the HF current amplitudes was shown to provide sufficiently robust sensorless control over the designated area in this dissertation, the admittance calculation was not considered further. However possible improvements could be obtained with this approach which would require either a higher-order low-pass filter to remove the PWM components or the use of a higher frequency PWM which would be subjected to higher attenuation.

- In this dissertation, the ADCs were oversampled at 40 kHz and averaged out over 8 samples such that a new measurement is available for every 5 kHz control loop. If the ADCs oversampling is increased such that more samples are available for each control cycle, the resultant signals used for both sensored and sensorless control would have a higher SNR. Due to the processing power available on the STM32F4 microcontroller, the sampling frequency could not be increased further. The use of a more powerful microcontroller, Digital Signal Processor

(DSP) or Field Programmable Gate Array (FPGA) is recommended for higher sampling rates.

- The HF current amplitude LUTs were calibrated for two low-speed operation points (± 1 rad/s). This was shown to produce satisfactory low-to-zero speed sensorless control in the region about zero speed. However, the saliencies were shown to have a phase shift with respect to the absolute rotor position such that commissioning at various speeds would allow for an extended speed operating region. In such a case the speed dependent LUT selection PLL proposed in Section 7.4.4 would be used to select the commissioned LUT closest to the current operating point rather than merely distinguishing between forward and reverse rotation.

- While this work was focused towards the steer-by-wire operation, the proposed SBO estimation process can be integrated within a hybrid sensorless systems with a model-based observer for intermediate to high-speed operation. Such a system would require a seamless transition between sensorless control provided by the two sensorless algorithms.

11.3 Publications

The publications [147-156] listed below were published from work carried out in this dissertation:

- K. Scicluna, C. S. Staines, and R. Raute, "High frequency injection-based sensorless position estimation in permanent magnet synchronous machines," *Mathematics and Computers in Simulation*, 2020.
- K. Scicluna, C. Spiteri-Staines, and R. Raute, "Sensorless low/zero speed Estimation for PMSM using a Search-based Real-Time Commissioning Method," *IEEE Transactions on Industrial Electronics*, pp. 1-1, 2020.
- K. Scicluna, C. S. Staines, and R. Raute, "High Frequency Injection-based Sensorless Position Estimation in Permanent Magnet Synchronous Machines," presented at the ELECTRIMACS 2019, Salerno, Italy, 2019.
- K. Scicluna, C. S. Staines, and R. Raute. (2019, Space modulation profile modelling for steer-by-wire SMPMSM. *The Journal of Engineering*. Available: https://digital-library.theiet.org/content/journals/10.1049/joe.2018.8248
- K. Scicluna, C. S. Staines, and R. Raute, "Space Modulation Profile Modelling for Steer-by-Wire SMPMSM," presented at the Power Electronics and Motor Drives (PEMD) 2018, Liverpool, UK, 2018.

- K. Scicluna, C. S. Staines, and R. Raute, "Sensorless Position Tracking in Steer-by-Wire Using the SONIC Method," in *2018 New Generation of CAS (NGCAS)*, 2018, pp. 122-125.
- K. Scicluna, C. S. Staines, and R. Raute, "Sensorless Position Estimation using a Search based Online Commissionable Method (SONIC)," in 2*018 20th European Conference on Power Electronics and Applications (EPE'18 ECCE Europe)*, 2018, pp. P.1-P.10.
- K. Scicluna, C. S. Staines, and R. Raute, "Sensorless Position Tracking for Steer-by-Wire Applications," presented at the 19th International Conference on Electrical Drives and Power Electronics (EDPE), Dubrovnic, 2017.
- K. Scicluna, C. S. Staines, and R. Raute, "Torque feedback for steer-by-wire systems with rotor flux oriented PMSM," in 2017 *19th International Conference on Electrical Drives and Power Electronics (EDPE)*, 2017, pp. 188-193.
- K. Scicluna, C. S. Staines, and R. Raute, "Sensorless position control of a PMSM for steer-by-wire applications," in *2016 International Conference on Control, Decision and Information Technologies (CoDIT)*, 2016, pp. 046-051.

References

[1] M. Bertoluzzo, G. Buja, and R. Menis, "Control schemes for steer-by-wire systems," *Industrial Electronics Magazine, IEEE,* vol. 1, pp. 20-27, 2007.

[2] R. Isermann, R. Schwarz, and S. Stolzl, "Fault-tolerant drive-by-wire systems," *IEEE Control Systems,* vol. 22, pp. 64-81, 2002.

[3] T. Kaufmann, S. Millsap, B. Murray, and J. Petrowski, "Development experience with steer-by-wire," SAE Technical Paper 0148-7191, 2001.

[4] E. A. Bretz, "By-wire cars turn the corner," *Spectrum, IEEE,* vol. 38, pp. 68-73, 2001.

[5] W. Harter, W. Pfeiffer, P. Dominke, G. Ruck, and P. Blessing, "Future electrical steering systems: Realizations with safety requirements," SAE Technical Paper 0148-7191, 2000.

[6] M. Bertoluzzo, P. Bolognesi, O. Bruno, G. Buja, A. Landi, and A. Zuccollo, "Drive-by-wire systems for ground vehicles," in *Industrial Electronics, 2004 IEEE International Symposium on*, 2004, pp. 711-716 vol. 1.

[7] G. J. Forkenbrock and D. Elsasser, "An assessment of human driver steering capability," *National Highway Traffic Safety Administration DOT HS 809,* vol. 875, 2005.

[8] A. Rodriguez-Angeles, H. Sira-Ramirez, and J. A. Garcia-Antonio, "A Vehicle Haptic Steering by Wire System Based on High Gain GPI Observers," *Mathematical Problems in Engineering,* vol. 2014, p. 14, 2014.

[9] S. M. H. Fahami, H. Zamzuri, and S. A. Mazlan, "Development of Estimation Force Feedback Torque Control Algorithm for Driver Steering Feel in Vehicle Steer by Wire System: Hardware in the Loop," *International Journal of Vehicular Technology,* vol. 2015, 2015.

[10] B.-H. Nguyen and J.-H. Ryu, "Direct current measurement based steer-by-wire systems for realistic driving feeling," in *Industrial Electronics, 2009. ISIE 2009. IEEE International Symposium on*, 2009, pp. 1023-1028.

[11] C. Kim, J. Jang, S. Yu, S. Lee, C. Han, and J. Hedrick, "Development of a control algorithm for a tie-rod-actuating steer-by-wire system," *Proceedings of the Institution of Mechanical Engineers, Part D: Journal of Automobile Engineering,* vol. 222, pp. 1543-1557, 2008.

[12] A. Bertacchini, L. Tamagnini, and P. Pavan, "Force Feedback in Steer-by-Wire Systems: Architecture and Experimental Results," in *Industrial Electronics, 2006 IEEE International Symposium on*, 2006, pp. 3050-3055.

[13] P. Yih and J. C. Gerdes, "Modification of vehicle handling characteristics via steer-by-wire," *Control Systems Technology, IEEE Transactions on,* vol. 13, pp. 965-976, 2005.

[14] Y. Yamaguchi and T. Murakami, "Adaptive Control for Virtual Steering Characteristics on Electric Vehicle Using Steer-by-Wire System," *Industrial Electronics, IEEE Transactions on,* vol. 56, pp. 1585-1594, 2009.

[15] J. J. Kenned and V. R. Patil, "Control Strategy and Simulation In Steer By Wire System," *International Journal of Scientific Engineering and Technology,* vol. 3, pp. 994-997, 1 July 2014 2014.

[16] T.-J. Park, C.-S. Han, and S.-H. Lee, "Development of the electronic control unit for the rack-actuating steer-by-wire using the hardware-in-the-loop simulation system," *Mechatronics,* vol. 15, pp. 899-918, 2005.

[17] A. Baviskar, J. R. Wagner, D. M. Dawson, D. Braganza, and P. Setlur, "An Adjustable Steer-by-Wire Haptic-Interface Tracking Controller for Ground Vehicles," *Vehicular Technology, IEEE Transactions on,* vol. 58, pp. 546-554, 2009.

[18] N. A. Kelling and P. Leteinturier, "X-by-wire: opportunities, challenges and trends," SAE Technical paper2003.

[19] A. Balachandran and J. C. Gerdes, "Designing steering feel for steer-by-wire vehicles using objective measures," *IEEE/ASME Transactions on Mechatronics,* vol. 20, pp. 373-383, 2015.

[20] A. Liu and S. Chang, "Force feedback in a stationary driving simulator," in *Systems, Man and Cybernetics, 1995. Intelligent Systems for the 21st Century., IEEE International Conference on*, 1995, pp. 1711-1716 vol.2.

[21] D. Odenthal, T. Bunte, H.-D. Heitzer, and C. Eiker, "How to make steer-by-wire feel like power steering," in *Proc. 15th IFAC World Congress on Automatic Control*, 2002.

[22] J. S. Im, F. Ozaki, M. Matsunaga, and S. Kawaji, "Design of steer-by-wire system with bilateral control method using disturbance observer," in *Advanced intelligent mechatronics, 2007 IEEE/ASME international conference on*, 2007, pp. 1-6.

[23] S. Asai, H. Kuroyanagi, and S. Takeuchi, "Development of a SBW system with force feedback using a disturbance observer," in *Steering & Suspension Technology Symposium: Steering, SAE 2004 World Congress & Exhibition, Detroit, MI, USA*, 2004.

[24] M. Segawa, "A study of reactive torque control for SBW system," in *Proceedings of 7th Symposium on Advanced Vehicle Control*, 2002.

[25] R. Cortesao and N. Bajcinca, "Model-matching control for steer-by-wire vehicles with under-actuated structure," in *IEEE/RSJ International Conference on Intelligent Robots and Systems*, 2004.

[26] J. Coudon, C. Canudas-de-Wit, and X. Claeys, "A new reference model for steer-by-wire applications with embedded vehicle dynamics," in *American Control Conference, 2006*, 2006, p. 6 pp.

[27] U. Mandhata, J. Wagner, F. Switzer, D. Dawson, and J. Summers, "A customizable steer-by-wire interface for ground vehicles," *IFAC Proceedings Volumes,* vol. 43, pp. 656-661, 2010.

[28] C. Tian, C. Zong, L. He, and X. Wang, "Fault tolerant control method for steer-by-wire system," in *Mechatronics and Automation, 2009. ICMA 2009. International Conference on*, 2009, pp. 291-295.

[29] N. Bajcinca, R. Cortesao, M. Hauschild, J. Bals, and G. Hirzinger, "Haptic control for steer-by-wire systems," in *Intelligent Robots and Systems, 2003. (IROS 2003). Proceedings. 2003 IEEE/RSJ International Conference on*, 2003, pp. 2004-2009 vol.2.

[30] J. R. Pimentel, "An architecture for a safety-critical steer-by-wire system," SAE Technical Paper 0148-7191, 2004.

[31] R. Bannatyne, "Time triggered protocol-fault tolerant serial communications for real-time embedded systems," in *Wescon/98*, 1998, pp. 86-91.

[32] S. Young Hun, K. Man Ho, L. Suk, and L. Kyung Chang, "Implementation of a fuzzy predictive redundancy system for tolerance of x-by-wire systems," in *IECON 2010 - 36th Annual Conference on IEEE Industrial Electronics Society*, 2010, pp. 3141-3145.

[33] K. Chaaban, P. Leserf, and S. Saudrais, "Steer-By-Wire system development using AUTOSAR methodology," in *Emerging Technologies & Factory Automation, 2009. ETFA 2009. IEEE Conference on*, 2009, pp. 1-8.

[34] L. Kuen-Long, W. Chin-Long, E. C. Jwu, and C. Yung-Yuan, "Robustness investigation of the FlexRay system," in *Industrial Embedded Systems, 2009. SIES '09. IEEE International Symposium on*, 2009, pp. 148-151.

[35] A. Munir and F. Koushanfar, "D2Cyber: A design automation tool for dependable cybercars," in *Design, Automation and Test in Europe Conference and Exhibition (DATE), 2014*, 2014, pp. 1-4.

[36] X. D. Xue, K. W. E. Cheng, and N. C. Cheung, "Selection of electric motor drives for electric vehicles," in *Power Engineering Conference, 2008. AUPEC '08. Australasian Universities*, 2008, pp. 1-6.

[37] S. Zhang, X. Jin, J. Junak, D. Fiederling, G. Sawczuk, M. Koch*, et al.*, "Permanent magnet technology for electric motors in automotive applications," in *Electric Drives Production Conference (EDPC), 2012 2nd International*, 2012, pp. 1-11.

[38] S. Bolognani, M. Tomasini, and M. Zigliotto, "Control Design of a Steer-by-Wire System with High Performance PM Motor Drives," in *Power Electronics Specialists Conference, 2005. PESC '05. IEEE 36th*, 2005, pp. 1839-1844.

[39] A. Benedetti, N. Bianchi, S. Bolognani, M. D. Pre, P. G. Molari, P. Morelli*, et al.*, "PM motor drives for steer-by-wire applications," in *Industry Applications Conference, 2005. Fourtieth IAS Annual Meeting. Conference Record of the 2005*, 2005, pp. 2857-2864 Vol. 4.

[40] J. Kang, "General purpose permanent magnet motor drive without speed and position sensor," *Yaskawa Electric Corp., Japan, Yaskawa Application Note WP. AFD*.

[41] M. A. M. Cheema and J. E. Fletcher, "Sensorless vector control of linear permanent magnet synchronous motor," in *ECCE Asia Downunder (ECCE Asia), 2013 IEEE*, 2013, pp. 1098-1104.

[42] T. M. Jahns, G. B. Kliman, and T. W. Neumann, "Interior Permanent-Magnet Synchronous Motors for Adjustable-Speed Drives," *Industry Applications, IEEE Transactions on,* vol. IA-22, pp. 738-747, 1986.

[43] D. W. Novotny and T. A. Lipo, *Vector control and dynamics of AC drives* vol. 1: Oxford university press, 1996.

[44] M. Rashed, P. F. A. MacConnell, A. F. Stronach, and P. Acarnley, "Sensorless Indirect-Rotor-Field-Orientation Speed Control of a Permanent-Magnet Synchronous Motor With Stator-Resistance Estimation," *Industrial Electronics, IEEE Transactions on,* vol. 54, pp. 1664-1675, 2007.

[45] Z. Shao, T. King-Jet, D. M. Vilathgamuwa, N. Trong Duy, and W. Xiao-Yu, "Design of a Robust Grid Interface System for PMSG-Based Wind Turbine Generators," *Industrial Electronics, IEEE Transactions on,* vol. 58, pp. 316-328, 2011.

[46] Y. A. R. I. Mohamed, "Design and Implementation of a Robust Current-Control Scheme for a PMSM Vector Drive With a Simple Adaptive Disturbance Observer," *Industrial Electronics, IEEE Transactions on,* vol. 54, pp. 1981-1988, 2007.

[47] K. Ogata and Y. Yang, *Modern control engineering* vol. 4: Prentice hall India, 2002.

[48] R. Bojoi, M. Pastorelli, J. Bottomley, P. Giangrande, and C. Gerada, "Sensorless control of PM motor drives—A technology status review," in *Electrical Machines Design Control and Diagnosis (WEMDCD), 2013 IEEE Workshop on*, 2013, pp. 168-182.

[49] G. Wang, M. I. Valla, and J. A. Solsona, "Position Sensorless Permanent Magnet Synchronous Machine Drives — a Review," *IEEE Transactions on Industrial Electronics,* pp. 1-1, 2019.

[50] S. Shinnaka and Y. Amano, "Elliptical Trajectory-Oriented Vector Control for Energy-Efficient/Wide-Speed-Range Drives of Sensorless PMSM," *IEEE Transactions on Industry Applications,* vol. 51, pp. 3169-3177, 2015.

[51] X. Song, B. Han, S. Zheng, and S. Chen, "A Novel Sensorless Rotor Position Detection Method for High-Speed Surface PM Motors in a Wide Speed Range," *IEEE Transactions on Power Electronics,* vol. 33, pp. 7083-7093, 2018.

[52] J. A. Benito, G. Glez-de-Rivera, J. Garrido, and R. Ponticelli, "Design considerations of a small UAV platform carrying medium payloads," in *Design of Circuits and Integrated Systems*, 2014, pp. 1-6.

[53] A. Sanchez, L. García Carrillo, E. Rondon, R. Lozano, and O. Garcia, "Hovering flight improvement of a quad-rotor mini UAV using brushless DC motors," *Journal of Intelligent & Robotic Systems,* vol. 61, pp. 85-101, 2011.

[54] T. W. Chun, Q. V. Tran, H. H. Lee, and H. G. Kim, "Sensorless Control of BLDC Motor Drive for an Automotive Fuel Pump Using a Hysteresis Comparator," *IEEE Transactions on Power Electronics,* vol. 29, pp. 1382-1391, 2014.

[55] S. Jianwen, D. Nolan, M. Teissier, and D. Swanson, "A novel microcontroller-based sensorless brushless DC (BLDC) motor drive for automotive fuel pumps," *IEEE Transactions on Industry Applications,* vol. 39, pp. 1734-1740, 2003.

[56] X. Huang, A. Goodman, C. Gerada, Y. Fang, and Q. Lu, "Design of a Five-Phase Brushless DC Motor for a Safety Critical Aerospace Application," *IEEE Transactions on Industrial Electronics,* vol. 59, pp. 3532-3541, 2012.

[57] X. Huang, A. Goodman, C. Gerada, Y. Fang, and Q. Lu, "A Single Sided Matrix Converter Drive for a Brushless DC Motor in Aerospace Applications," *IEEE Transactions on Industrial Electronics,* vol. 59, pp. 3542-3552, 2012.

[58] Y. Kang, S. B. Lee, and J. Yoo, "A microcontroller embedded AD converter based low cost sensorless technique for brushless DC motor drives," in *Industry Applications Conference, 2005. Fourtieth IAS Annual Meeting. Conference Record of the 2005*, 2005, pp. 2176-2181.

[59] H.-B. Wang and H.-P. Liu, "A novel sensorless control method for brushless DC motor," *IET electric power applications,* vol. 3, pp. 240-246, 2009.

[60] K. Iizuka, H. Uzuhashi, M. Kano, T. Endo, and K. Mohri, "Microcomputer control for sensorless brushless motor," *IEEE Transactions on Industry Applications,* pp. 595-601, 1985.

[61] P. P. Acarnley and J. F. Watson, "Review of position-sensorless operation of brushless permanent-magnet machines," *Industrial Electronics, IEEE Transactions on,* vol. 53, pp. 352-362, 2006.

[62] J.-S. Kim and S.-K. Sul, "New approach for high-performance PMSM drives without rotational position sensors," *IEEE Transactions on Power Electronics,* vol. 12, pp. 904-911, 1997.

[63] Y. Zhao, W. Qiao, and L. Wu, "Model reference adaptive system-based speed estimators for sensorless control of interior permanent magnet synchronous machines," in *Transportation Electrification Conference and Expo (ITEC), 2013 IEEE*, 2013, pp. 1-6.

[64] M. K. Hossain and S. R. Islam, "Model reference adaptive control for surface permanent magnet synchronous machine," in *Electrical Information and Communication Technology (EICT), 2017 3rd International Conference on*, 2017, pp. 1-6.

[65] S. Bolognani, R. Oboe, and M. Zigliotto, "Sensorless full-digital PMSM drive with EKF estimation of speed and rotor position," *IEEE transactions on Industrial Electronics,* vol. 46, pp. 184-191, 1999.

[66] Y.-H. Kim and Y.-S. Kook, "High performance IPMSM drives without rotational position sensors using reduced-order EKF," *IEEE Transactions on Energy Conversion,* vol. 14, pp. 868-873, 1999.

[67] X. Li and R. Kennel, "Comparison of state-of-the-art estimators for electrical parameter identification of PMSM," in *2019 IEEE International Symposium on Predictive Control of Electrical Drives and Power Electronics (PRECEDE)*, 2019, pp. 1-6.

[68] S. Singh and A. Tiwari, "Various techniques of sensorless speed control of PMSM: A review," in *Electrical, Computer and Communication Technologies (ICECCT), 2017 Second International Conference on*, 2017, pp. 1-6.

[69] Y. Feng, J. Zheng, X. Yu, and N. V. Truong, "Hybrid terminal sliding-mode observer design method for a permanent-magnet synchronous motor control system," *IEEE Transactions on Industrial Electronics,* vol. 56, pp. 3424-3431, 2009.

[70] Y.-S. Han, J.-S. Choi, and Y.-S. Kim, "Sensorless PMSM drive with a sliding mode control based adaptive speed and stator resistance estimator," *IEEE Transactions on magnetics,* vol. 36, pp. 3588-3591, 2000.

[71] H. Kim, J. Son, and J. Lee, "A High-Speed Sliding-Mode Observer for the Sensorless Speed Control of a PMSM," *IEEE Transactions on Industrial Electronics,* vol. 58, pp. 4069-4077, 2011.

[72] C. Caruana, G. M. Asher, and J. C. Clare, "Sensorless flux position estimation at low and zero frequency by measuring zero-sequence current in delta-connected cage induction machines," *Industry Applications, IEEE Transactions on,* vol. 41, pp. 609-617, 2005.

[73] N. Teske, G. M. Asher, M. Sumner, and K. J. Bradley, "Encoderless position estimation for symmetric cage induction machines under loaded conditions," *Industry Applications, IEEE Transactions on,* vol. 37, pp. 1793-1800, 2001.

[74] M. W. Degner and R. D. Lorenz, "Position estimation in induction machines utilizing rotor bar slot harmonics and carrier-frequency signal injection," *Industry Applications, IEEE Transactions on,* vol. 36, pp. 736-742, 2000.

[75] C. S. Staines, C. Caruana, G. M. Asher, and M. Sumner, "Sensorless control of induction machines at zero and low frequency using zero sequence currents," *Industrial Electronics, IEEE Transactions on,* vol. 53, pp. 195-206, 2006.

[76] Y. Hua, G. Asher, M. Sumner, and Q. Gao, "Sensorless control of surface mounted permanent magnetic machine using the standard space vector PWN," in *Industry Applications Conference, 2007. 42nd IAS Annual Meeting. Conference Record of the 2007 IEEE*, 2007, pp. 661-667.

[77] J. Holtz, "Sensorless position control of induction motors-an emerging technology," *Industrial Electronics, IEEE Transactions on,* vol. 45, pp. 840-851, 1998.

[78] P. L. Jansen and R. D. Lorenz, "Transducerless position and velocity estimation in induction and salient AC machines," *Industry Applications, IEEE Transactions on,* vol. 31, pp. 240-247, 1995.

[79] P. L. Jansen and R. D. Lorenz, "Transducerless field orientation concepts employing saturation-induced saliencies in induction machines," *Industry Applications, IEEE Transactions on,* vol. 32, pp. 1380-1393, 1996.

[80] J. Cilia, G. M. Asher, K. J. Bradley, and M. Sumner, "Sensorless position detection for vector-controlled induction motor drives using an asymmetric outer-section cage," *Industry Applications, IEEE Transactions on,* vol. 33, pp. 1162-1169, 1997.

[81] M. W. Degner and R. D. Lorenz, "Using multiple saliencies for the estimation of flux, position, and velocity in AC machines," *Industry Applications, IEEE Transactions on,* vol. 34, pp. 1097-1104, 1998.

[82] C. Silva, G. M. Asher, and M. Sumner, "Hybrid rotor position observer for wide speed-range sensorless PM motor drives including zero speed," *Industrial Electronics, IEEE Transactions on,* vol. 53, pp. 373-378, 2006.

[83] D. Paulus, P. Landsmann, and R. Kennel, "Sensorless field-oriented control for permanent magnet synchronous machines with an arbitrary injection scheme and direct angle calculation," in *Sensorless Control for Electrical Drives (SLED), 2011 Symposium on*, 2011, pp. 41-46.

[84] R. Leidhold, "Position sensorless control of PM synchronous motors based on zero-sequence carrier injection," *Industrial Electronics, IEEE Transactions on,* vol. 58, pp. 5371-5379, 2011.

[85] S. Sato, H. Iura, K. Ide, and S.-K. Sul, "Three years of industrial experience with sensorless IPMSM drive based on high frequency injection method," in *Sensorless Control for Electrical Drives (SLED), 2011 Symposium on*, 2011, pp. 74-79.

[86] S. Bolognani, S. Calligaro, R. Petrella, and M. Sterpellone, "Sensorless control for IPMSM using PWM excitation: Analytical developments and implementation issues," in *Sensorless Control for Electrical Drives (SLED), 2011 Symposium on*, 2011, pp. 64-73.

[87] M. Schroedl, "Sensorless control of AC machines at low speed and standstill based on the "INFORM" method," in *Industry Applications Conference, 1996. Thirty-First IAS Annual Meeting, IAS'96., Conference Record of the 1996 IEEE*, 1996, pp. 270-277.

[88] M. Schroedl, "Detection of the rotor position of a permanent magnet synchronous machine at standstill," in *International Conference on Electrical Machines, ICEM, Italy*, 1988, pp. 195-197.

[89] T. M. Wolbank and M. K. Metwally, "Sensorless Position and Torque Control of Induction Motors Based on Transient Signal Injection and Advanced Signal Processing," in *Applied Power Electronics Conference and Exposition, 2009. APEC 2009. Twenty-Fourth Annual IEEE*, 2009, pp. 216-222.

[90] Q. Gao, G. Asher, and M. Sumner, "Sensorless position and speed control of induction motors using high-frequency injection and without offline precommissioning," *Industrial Electronics, IEEE Transactions on,* vol. 54, pp. 2474-2481, 2007.

[91] J. Holtz and H. Pan, "Elimination of saturation effects in sensorless position controlled induction motors," in *Industry Applications Conference, 2002. 37th IAS Annual Meeting. Conference Record of the*, 2002, pp. 1695-1702.

[92] C. Caruana, G. M. Asher, K. J. Bradley, and M. Woolfson, "Flux position estimation in cage induction machines using synchronous HF injection and Kalman filtering," *Industry Applications, IEEE Transactions on,* vol. 39, pp. 1372-1378, 2003.

[93] P. Garcia, F. Briz, D. Raca, and R. D. Lorenz, "Saliency-tracking-based sensorless control of AC machines using structured neural networks," *Industry Applications, IEEE Transactions on,* vol. 43, pp. 77-86, 2007.

[94] P. Nussbaumer and T. M. Wolbank, "Saliency tracking based sensorless control of AC machines exploiting inverter switching transients," in *Sensorless Control for Electrical Drives (SLED), 2010 First Symposium on*, 2010, pp. 114-119.

[95] R. Raute, "Sensorless control of AC machines for low and zero speed operation without additional test signal injection," University of Nottingham, 2009.

[96] R. Raute, C. Caruana, J. Cilia, C. S. Staines, and M. Sumner, "A zero speed operation sensorless PMSM drive without additional test signal injection," in *Power Electronics and Applications, 2007 European Conference on*, 2007, pp. 1-10.

[97] R. Raute, C. Caruana, C. S. Staines, J. Cilia, M. Sumner, and G. Asher, "Inverter non-linearity effects on a sensorless PMSM drive without additional test signal injection and zero speed operation," in *Industrial Electronics, 2008. ISIE 2008. IEEE International Symposium on*, 2008, pp. 552-557.

[98] J.-I. Ha and S.-K. Sul, "Sensorless field-orientation control of an induction machine by high-frequency signal injection," *Industry Applications, IEEE Transactions on,* vol. 35, pp. 45-51, 1999.

[99] M. J. Corley and R. D. Lorenz, "Rotor position and velocity estimation for a salient-pole permanent magnet synchronous machine at standstill and high speeds," *Industry Applications, IEEE Transactions on,* vol. 34, pp. 784-789, 1998.

[100] C. S. Staines, C. Caruana, and R. Raute, "A Review of Saliency-based Sensorless Control Methods for Alternating Current Machines," *IEEJ Journal of Industry Applications,* vol. 3, pp. 86-96, 2014.

[101] M. P. Chaudhary, V. Patel, and J. G. Jamnani, "Sensorless vector control of PMSM drive using heterodyne technique," in *Optimization of Electrical and Electronic Equipment, 2008. OPTIM 2008. 11th International Conference on*, 2008, pp. 93-99.

[102] K. Sungmin, H. Jung-Ik, and S. Seung-Ki, "PWM Switching Frequency Signal Injection Sensorless Method in IPMSM," *Industry Applications, IEEE Transactions on,* vol. 48, pp. 1576-1587, 2012.

[103] X. Xiaodong and H. Yikang, "Sensorless vector control operation of a PMSM by rotating high-frequency voltage injection approach," in *Electrical Machines and Systems, 2007. ICEMS. International Conference on*, 2007, pp. 752-756.

[104] L. Wang, Q. Guo, and R. D. Lorenz, "Sensorless control of permanent magnet synchronous motor," in *Power Electronics and Motion Control Conference, 2000. Proceedings. IPEMC 2000. The Third International*, 2000, pp. 186-190 vol.1.

[105] C. A. Silva, "Sensorless vector control of surface mounted permanent magnet machines without restriction of zero frequency," University of Nottingham, 2003.

[106] Z. Ma, J. Gao, and R. Kennel, "FPGA implementation of a hybrid sensorless control of SMPMSM in the whole speed range," *IEEE Transactions on Industrial Informatics,* vol. 9, pp. 1253-1261, 2012.

[107] O. A. Mohammed, A. A. Khan, A. M. El-Tallawy, A. Nejadpak, and M. J. Roberts, "A wavelet filtering scheme for noise and vibration reduction in high-frequency signal injection-based sensorless control of PMSM at low speed," *IEEE Transactions on Energy Conversion,* vol. 27, pp. 250-260, 2012.

[108] S. Bolognani, S. Calligaro, R. Petrella, and M. Tursini, "Sensorless control of IPM motors in the low-speed range and at standstill by HF injection and DFT processing," *IEEE Transactions on Industry Applications,* vol. 47, pp. 96-104, 2010.

[109] W. Qian, X. Zhang, F. Jin, H. Bai, D. Lu, and B. Cheng, "Using high-control-bandwidth FPGA and SiC inverters to enhance high-frequency injection sensorless control in interior permanent magnet synchronous machine," *IEEE Access,* vol. 6, pp. 42454-42466, 2018.

[110] G. Wang, H. Zhou, N. Zhao, C. Li, and D. Xu, "Sensorless Control of IPMSM Drives Using a Pseudo-Random Phase-Switching Fixed-Frequency Signal Injection Scheme," *IEEE Transactions on Industrial Electronics,* vol. 65, pp. 7660-7671, 2018.

[111] G. Wang, L. Yang, B. Yuan, B. Wang, G. Zhang, and D. Xu, "Pseudo-random high-frequency square-wave voltage injection based sensorless control of IPMSM drives for audible noise reduction," *IEEE Transactions on Industrial Electronics,* vol. 63, pp. 7423-7433, 2016.

[112] Y. Zhang, Z. Yin, J. Liu, R. Zhang, and X. Sun, "IPMSM Sensorless Control Using High-Frequency Voltage Injection Method With Random Switching Frequency for Audible Noise Improvement," *IEEE Transactions on Industrial Electronics,* vol. 67, pp. 6019-6030, 2019.

[113] S. Ogasawara and H. Akagi, "An approach to real-time position estimation at zero and low speed for a PM motor based on saliency," *Industry Applications, IEEE Transactions on,* vol. 34, pp. 163-168, 1998.

[114] S. Ogasawara and H. Akagi, "Implementation and position control performance of a position-sensorless IPM motor drive system based on magnetic saliency," *Industry Applications, IEEE Transactions on,* vol. 34, pp. 806-812, 1998.

[115] J. Holtz and J. Juliet, "Sensorless acquisition of the rotor position angle of induction motors with arbitrary stator windings," *Industry Applications, IEEE Transactions on,* vol. 41, pp. 1675-1682, 2005.

[116] R. Raute, C. Caruana, C. S. Staines, J. Cilia, M. Sumner, and G. M. Asher, "Sensorless Control of Induction Machines at Low and Zero Speed by Using PWM Harmonics for Rotor-Bar Slotting Detection," *IEEE Transactions on Industry Applications,* vol. 46, pp. 1989-1998, 2010.

[117] F. Demmelmayr, M. Troyer, and M. Schroedl, "Advantages of PM-machines compared to induction machines in terms of efficiency and sensorless control in traction applications," in *IECON 2011-37th Annual Conference on IEEE Industrial Electronics Society*, 2011, pp. 2762-2768.

[118] E. Robeischl, M. Schrödl, and M. Krammer, "Position-sensorless biaxial position control with industrial PM motor drives based on INFORM-and back EMF model," in *IECON 02 [Industrial Electronics Society, IEEE 2002 28th Annual Conference of the]*, 2002, pp. 668-673.

[119] U.-H. Rieder, M. Schrödl, and A. Ebner, "Sensorless control of an external rotor PMSM in the whole speed range including standstill using DC-link measurements only," in *Power Electronics Specialists Conference, 2004. PESC 04. 2004 IEEE 35th Annual*, 2004, pp. 1280-1285.

[120] Q. Gao, G. M. Asher, M. Sumner, and P. Makys, "Position estimation of AC machines over a wide frequency range based on space vector PWM excitation," *IEEE Transactions on Industry Applications,* vol. 43, pp. 1001-1011, 2007.

[121] N. Teske, G. M. Asher, M. Sumner, and K. J. Bradley, "Suppression of saturation saliency effects for the sensorless position control of induction motor drives under loaded conditions," *IEEE Transactions on Industrial Electronics,* vol. 47, pp. 1142-1150, 2000.

[122] J. Holtz and P. Hangwen, "Elimination of saturation effects in sensorless position-controlled induction motors," *IEEE Transactions on Industry Applications,* vol. 40, pp. 623-631, 2004.

[123] D. Raca, P. Garcia, D. D. Reigosa, F. Briz, and R. D. Lorenz, "Carrier-Signal Selection for Sensorless Control of PM Synchronous Machines at Zero and Very Low Speeds," *IEEE Transactions on Industry Applications,* vol. 46, pp. 167-178, 2010.

[124] D. Raca, M. C. Harke, and R. D. Lorenz, "Robust Magnet Polarity Estimation for Initialization of PM Synchronous Machines With Near-Zero Saliency," *IEEE Transactions on Industry Applications,* vol. 44, pp. 1199-1209, 2008.

[125] P. Garcia, F. Briz, M. W. Degner, and D. Diaz-Reigosa, "Accuracy, Bandwidth, and Stability Limits of Carrier-Signal-Injection-Based Sensorless Control Methods," *IEEE Transactions on Industry Applications,* vol. 43, pp. 990-1000, 2007.

[126] J. Ji-Hoon, S. Seung-Ki, H. Jung-Ik, K. Ide, and M. Sawamura, "Sensorless drive of surface-mounted permanent-magnet motor by high-frequency signal injection based on magnetic saliency," *IEEE Transactions on Industry Applications,* vol. 39, pp. 1031-1039, 2003.

[127] M. Linke, R. Kennel, and J. Holtz, "Sensorless position control of permanent magnet synchronous machines without limitation at zero speed," in *IECON 02 [Industrial Electronics Society, IEEE 2002 28th Annual Conference of the]*, 2002, pp. 674-679.

[128] Y. Li, Z. Q. Zhu, D. Howe, C. M. Bingham, and D. A. Stone, "Improved Rotor-Position Estimation by Signal Injection in Brushless AC Motors, Accounting for Cross-Coupling Magnetic Saturation," *IEEE Transactions on Industry Applications,* vol. 45, pp. 1843-1850, 2009.

[129] Y.-D. Yoon, S.-K. Sul, S. Morimoto, and K. Ide, "High-bandwidth sensorless algorithm for AC machines based on square-wave-type voltage injection," *IEEE Transactions on Industry Applications,* vol. 47, pp. 1361-1370, 2011.

[130] W. Hammel and R. M. Kennel, "Position sensorless control of PMSM by synchronous injection and demodulation of alternating carrier voltage," in *Sensorless Control for Electrical Drives (SLED), 2010 First Symposium on*, 2010, pp. 56-63.

[131] X. Wu, Y. Feng, X. Liu, S. Huang, X. Yuan, J. Gao*, et al.*, "Initial Rotor Position Detection for Sensorless Interior PMSM With Square-Wave Voltage Injection," *IEEE Transactions on Magnetics,* vol. 53, pp. 1-4, 2017.

[132] H. Zhang, W. Liu, Z. Chen, G. Luo, J. Liu, and D. Zhao, "Asymmetric Space Vector Modulation for PMSM Sensorless Drives Based on Square-Wave Voltage-Injection Method," *IEEE Transactions on Industry Applications,* vol. 54, pp. 1425-1436, 2018.

[133] G. Wang, D. Xiao, G. Zhang, C. Li, Z. Xueguang, and D. G. Xu, "Sensorless Control Scheme of IPMSMs Using High-Frequency Orthogonal Square-Wave Voltage Injection into Stationary Reference Frame," *IEEE Transactions on Power Electronics,* pp. 1-1, 2018.

[134] A. Madani, J. Barbot, F. Colamartino, and C. Marchand, "Reduction of torque pulsations by inductance harmonics identification of a permanent-magnet synchronous machine," in *Control Applications, 1995., Proceedings of the 4th IEEE Conference on*, 1995, pp. 787-792.

[135] F. J. Barnard, W. T. Villet, and M. J. Kamper, "Hybrid active-flux and arbitrary injection position sensorless control of reluctance synchronous machines," *IEEE Transactions on Industry Applications,* vol. 51, pp. 3899-3906, 2015.

[136] M. Laumann, C. Weiner, and R. Kennel, "Arbitrary injection based sensorless control with a defined high frequency current ripple and reduced current and sound level harmonics," in *Sensorless Control for Electrical Drives (SLED), 2017 IEEE International Symposium on*, 2017, pp. 103-108.

[137] N. Teske, "Sensorless position control of induction machines using high frequency signal injection," University of Nottingham, 2001.

[138] Y. Zhang and J. Liu, "An improved Q-PLL to overcome the speed reversal problems in sensorless PMSM drive," in *Power Electronics and Motion Control Conference (IPEMC-ECCE Asia), 2016 IEEE 8th International*, 2016, pp. 1884-1888.

[139] J. M. Liu and Z. Q. Zhu, "A new sensorless control strategy by high-frequency pulsating signal injection into stationary reference frame," in *2013 International Electric Machines & Drives Conference*, 2013, pp. 505-512.

[140] P. Landsmann, D. Paulus, P. Stolze, and R. Kennel, "Saliency based encoderless predictive torque control without signal injection," in *Power Electronics Conference (IPEC), 2010 International*, 2010, pp. 3029-3034.

[141] R. Raute, C. Caruana, J. Cilia, C. S. Staines, M. Sumner, and G. Asher, "Impedance saliency detection for sensorless control of AC machines utilizing existing PWM switching harmonics," in *2008 4th IET Conference on Power Electronics, Machines and Drives*, 2008, pp. 557-561.

[142] W. Agius, K. Scicluna, J. Zammit, C. Seguna, and J. Scerri, "Design of an STM32F4 Microcontroller Development Board for Switching Power Converters," in *2018 New Generation of CAS (NGCAS)*, 2018, pp. 62-65.

[143] P. Brandstetter and T. Krecek, "Estimation of PMSM magnetic saliency using injection technique," *Elektronika ir Elektrotechnika,* vol. 20, pp. 22-27, 2014.

[144] S. Ovrebo, R. Nilsen, and R. Nilssen, "Saliency modeling in radial flux permanent magnet synchronous machines," in *NORPIE*, 2004.

[145] R. Lorenz, "Self-sensing methods wide bandwidth position & velocity sensing at any speed, incl. zero," in *Tutorial notes for "Sensorless control of AC machines," presented at the IEEE-IAS Annu. Meeting, San Diego, CA*, 1996.

[146] F. Li, L. Wang, C. Liao, and Y. Wu, "Active steering control strategy of steer-by-wire system based on variable steering ratio," in *Transportation Electrification Asia-Pacific (ITEC Asia-Pacific), 2014 IEEE Conference and Expo*, 2014, pp. 1-5.

[147] K. Scicluna, C. S. Staines, and R. Raute, "High frequency injection-based sensorless position estimation in permanent magnet synchronous machines," *Mathematics and Computers in Simulation,* 2020.

[148] K. Scicluna, C. Spiteri-Staines, and R. Raute, "Sensorless low/zero speed Estimation for PMSM using a Search-based Real-Time Commissioning Method," *IEEE Transactions on Industrial Electronics,* pp. 1-1, 2020.

[149] K. Scicluna, C. S. Staines, and R. Raute, "High Frequency Injection-based Sensorless Position Estimation in Permanent Magnet Synchronous Machines," presented at the ELECTRIMACS 2019, Salerno, Italy, 2019.

[150] K. Scicluna, C. S. Staines, and R. Raute. (2019, Space modulation profile modelling for steer-by-wire SMPMSM. *The Journal of Engineering*. Available: https://digital-library.theiet.org/content/journals/10.1049/joe.2018.8248

[151] K. Scicluna, C. S. Staines, and R. Raute, "Space Modulation Profile Modelling for Steer-by-Wire SMPMSM," presented at the Power Electronics and Motor Drives (PEMD) 2018, Liverpool, UK, 2018.

[152] K. Scicluna, C. S. Staines, and R. Raute, "Sensorless Position Tracking in Steer-by-Wire Using the SONIC Method," in *2018 New Generation of CAS (NGCAS)*, 2018, pp. 122-125.

[153] K. Scicluna, C. S. Staines, and R. Raute, "Sensorless Position Estimation using a Search based Online Commissionable Method (SONIC)," in *2018 20th European Conference on Power Electronics and Applications (EPE'18 ECCE Europe)*, 2018, pp. P.1-P.10.

[154] K. Scicluna, C. S. Staines, and R. Raute, "Sensorless Position Tracking for Steer-by-Wire Applications," presented at the 19th International Conference on Electrical Drives and Power Electronics (EDPE), Dubrovnic, 2017.

[155] K. Scicluna, C. S. Staines, and R. Raute, "Torque feedback for steer-by-wire systems with rotor flux oriented PMSM," in *2017 19th International Conference on Electrical Drives and Power Electronics (EDPE)*, 2017, pp. 188-193.

[156] K. Scicluna, C. S. Staines, and R. Raute, "Sensorless position control of a PMSM for steer-by-wire applications," in *2016 International Conference on Control, Decision and Information Technologies (CoDIT)*, 2016, pp. 046-051.

Appendix A – Transient Injection Angle Selection

γ	$\overline{D_\alpha}$	$D_{\alpha max}$	$\overline{D_\beta}$	$D_{\beta max}$	min_Δαβ (A/element)	$\overline{\Delta\alpha\beta}$ (A/element)
0	8.98E-04	0.0019	0.0028	0.0063	3.31E-05	0.0014
15	9.28E-04	0.0018	0.0022	0.0049	9.88E-05	0.0013
30	0.0016	0.0041	0.0015	0.0038	2.27E-05	0.0013
45	0.0056	0.012	9.13E-04	0.0019	2.47E-04	0.0014
60	0.0015	0.0035	0.0013	0.0025	4.33E-05	0.0015
75	0.0014	0.0038	0.0027	0.0051	4.88E-05	0.0016
90	0.0012	0.0033	0.0027	0.0059	7.08E-05	0.0014
105	0.0011	0.0024	0.0013	0.0027	6.62E-05	0.0014
120	0.0018	0.0037	9.00E-04	0.002	3.71E-04	0.0014
135	0.005	0.0114	8.47E-04	0.0021	2.70E-04	0.0014
150	0.0022	0.0048	0.0013	0.0038	8.07E-05	0.0015
165	0.0014	0.0036	0.0017	0.004	7.01E-05	0.0016

Table A.1 – Saliency Numerical Analysis for $0° \leq \gamma \leq 165°$, $f_i = 2.5$ kHz, $V_i = 3$ V, $i_{q3}^* = 0$ A, $\omega_{m4}^* = 1$ rad/s.

γ	$\overline{D_\alpha}$	$D_{\alpha max}$	$\overline{D_\beta}$	$D_{\beta max}$	min_Δαβ (A/element)	$\overline{\Delta\alpha\beta}$ (A/element)
0	0.0022	0.0053	0.006	0.0145	2.68E-05	0.0013
15	0.0022	0.0054	0.005	0.0152	2.66E-05	0.0012
30	0.0054	0.0176	0.0054	0.0196	5.84E-06	0.0019
45	0.1240	0.032	0.0022	0.0074	1.05E-06	0.0013
60	0.0033	0.0086	0.0022	0.0076	4.81E-06	0.0012
75	0.0043	0.013	0.0042	0.0088	2.42E-06	0.0016
90	0.0041	0.014	0.0045	0.0101	1.81E-06	0.0017
105	0.0025	0.0087	0.0024	0.0061	2.44E-06	0.0012
120	0.0037	0.0096	0.0020	0.0041	2.94E-06	0.0012
135	0.0112	0.0275	0.0021	0.0053	3.51 E-06	0.0013
150	0.0062	0.0185	0.0042	0.0123	1.08 E-06	0.0020
165	0.0040	0.0124	0.0049	0.0146	5.06 E-06	0.0018

Table A.2 – Saliency Numerical Analysis for $0° \leq \gamma \leq 165°$, $f_i = 2.5$ kHz, $V_i = 3$ V, $i_{q3}^* = 5$ A, $\omega_{m4}^* = 1$ rad/s.

γ	$\overline{D_\alpha}$	$D_{\alpha max}$	$\overline{D_\beta}$	$D_{\beta max}$	min_Δαβ (A/element)	$\overline{\Delta\alpha\beta}$ (A/element)
0	0.0027	0.0074	0.0076	0.0206	2.65 E-05	0.0014
15	0.0031	0.0065	0.0067	0.0197	4.99E-06	0.0013
30	0.0080	0.302	0.0077	0.0303	1.57 E-05	0.0020
45	0.0174	0.0466	0.0331	0.0128	1.07 E-05	0.0013
60	0.0046	0.0134	0.0029	0.0108	7.74E-06	0.0019
75	0.0061	0.0214	0.0054	0.0134	4.05 E-05	0.0018
90	0.0056	0.0177	0.0060	0.0144	3.78 E-05	0.0017
105	0.0034	0.0098	0.0032	0.0081	3.42 E-05	0.0012
120	0.0052	0.0135	0.0027	0.0066	3.21 E-05	0.0012
135	0.0150	0.0451	0.0028	0.0092	1.70 E-05	0.0013
150	0.0088	0.0267	0.0059	0.0186	1.19 E-05	0.0020
165	0.0053	0.0171	0.0062	0.0199	6.30E-06	0.0019

Table A.3 – Saliency Numerical Analysis for 0°≤ γ ≤165°, f_i = 2.5 kHz, V_i = 3 V, i_{q3}^* = -5 A, ω_{m4}^* = 1 rad/s.

γ	$\overline{D_\alpha}$	$D_{\alpha max}$	$\overline{D_\beta}$	$D_{\beta max}$	min_Δαβ (A/element)	$\overline{\Delta\alpha\beta}$ (A/element)
0	0.0011	0.0019	0.0035	0.0067	1.24E-04	0.0011
15	0.0012	0.0019	0.0028	0.0057	1.62E-04	0.0009
30	0.0020	0.0045	0.0018	0.0048	1.22E-05	0.0009
45	0.0074	0.0147	0.0012	0.0024	1.08E-04	0.0010
60	0.0019	0.0043	0.0016	0.0035	6.28E-05	0.0011
75	0.0017	0.0041	0.0034	0.0062	5.16E-06	0.011
90	0.0014	0.0035	0.0036	0.0068	4.71E-05	0.0009
105	0.0013	0.0024	0.0017	0.0034	1.66E-04	0.0011
120	0.0022	0.0042	0.0012	0.0024	2.75E-04	0.0011
135	0.0064	0.0136	0.0010	0.0019	2.65E-04	0.0011
150	0.0025	0.0064	0.0015	0.0036	3.29E-05	0.0010
165	0.0015	0.0030	0.0017	0.0039	1.75E-05	0.0011

Table A.4 – Saliency Numerical Analysis for 0°≤ γ ≤165°, f_i = 2.5 kHz, V_i = 3 V, i_{q3}^* = 0 A, ω_{m4}^* = 2 rad/s.

γ	$\overline{D_\alpha}$	$D_{\alpha max}$	$\overline{D_\beta}$	$D_{\beta max}$	min_Δαβ (A/element)	$\overline{\Delta\alpha\beta}$ (A/element)
0	0.0012	0.0024	0.0038	0.0070	2.38E-05	0.0011
15	0.0013	0.0021	0.0030	0.0063	1.72E-04	0.0009
30	0.0025	0.0066	0.0022	0.0079	3.88E-05	0.0008
45	0.0078	0.0146	0.0013	0.0025	2.13E-04	0.0010
60	0.0021	0.0042	0.0017	0.0026	7.38E-05	0.0011
75	0.0021	0.0063	0.0034	0.0060	1.40E-05	0.0011
90	0.0017	0.0052	0.0038	0.0070	5.28E-05	0.0010
105	0.0014	0.0027	0.0018	0.0032	1.97E-04	0.0011
120	0.0024	0.0047	0.0014	0.0022	3.91E-04	0.0011
135	0.0071	0.0141	0.0012	0.0021	3.52E-04	0.0010
150	0.003	0.008	0.0018	0.0052	5.18E-05	0.0010
165	0.0018	0.0048	0.0021	0.0058	6.53E-05	0.0011

Table A.5 – Saliency Numerical Analysis for $0° \leq \gamma \leq 165°$, $f_i = 2.5$ kHz, $V_i = 3$ V, $i_{q3}^* = 0$ A, $\omega_{m4}^* = 3$ rad/s.

Appendix B – Sigmoid Functions for Steering

The sigmoid function is defined mathematically as a function of time in (B.1)

$$S(t) = \frac{1}{1+e^{-t}} \tag{B.1}$$

Using Matlab/Simulink references can be generated for the standard sigmoid function using the Sigmoidal MF block, which is in the form of (B.2).

$$S_1(t) = \frac{1}{1+e^{(-a(t-c)}} \tag{B.2}$$

Where:

a sets the slope of the sigmoid function, *c* sets the point on the inflexion of the sigmoid curve.

A typical steering profile for left and right can be generated using the Product Sigmoidal MF which is in the form (B.3)

$$S_2(t) = \prod_{k=1,2} \frac{\sqrt{G}}{1+e^{(-a_k(t-c_k))}} \tag{B.3}$$

Where:

G sets the steady-state value of the sigmoid function product,

a_1 sets the slope of the first sigmoid function,

a_2 sets the slope of the second sigmoid function,

c_1 sets the point on the inflexion of the first sigmoid curve,

c_2 sets the point on the inflexion of the second sigmoid curve.

The test profile used in this section was generated with MATLAB/Simulink and can be express mathematically as in (B.4) with a period T = 20 s. The periodic function is a summation of left and right sigmoid functions defined in (B.5-B.6).

$$S_{SBW}(t) = S_{left}(t) + S_{right}(s) \tag{B.4}$$

$$S_{left}(t) = \prod_{k=1,2} \frac{\sqrt{2.54}}{1+e^{(-aleft_k(t-cleft_k))}} \tag{B.5}$$

Where $aleft_1 = 50$, $cleft_1 = 5$, $aleft_2 = -50$, $cleft_2 = 10$.

$$S_{right}(t) = \prod_{k=1,2} \frac{\sqrt{2.54}}{1+e^{(-aright_k(t-cright_k))}} \tag{B.6}$$

Where $aright_1 = -50$, $cright_1 = 13$, $aright_2 = 50$, $cright_2 = 18$.

Appendix C – Circuit Designs

C.1 – STM32 Shield Board

C.2 – Gate Driver Board

C.3 – Saliency Measurement Board

C.4 – Discrete Inverter Power Board

C.1 - STM32 Shield Board

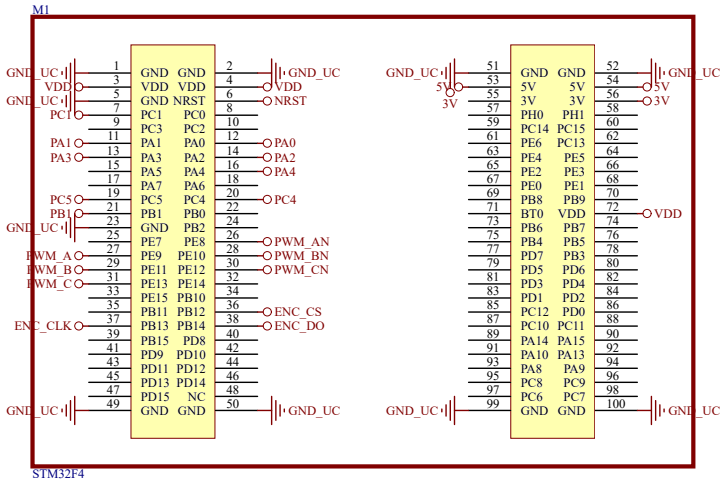

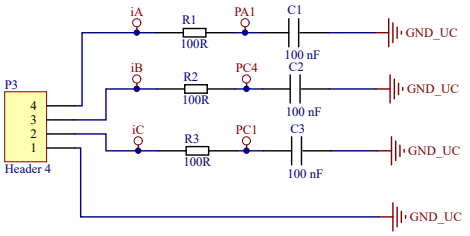

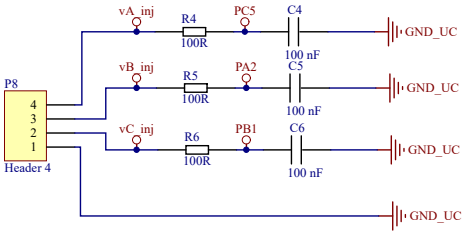

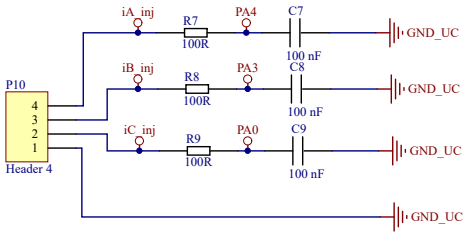

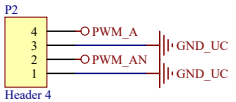

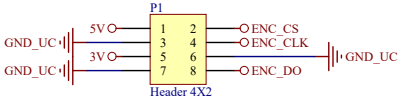

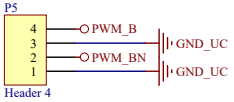

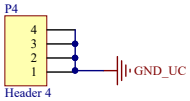

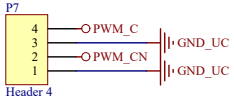

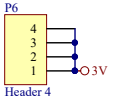

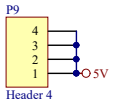

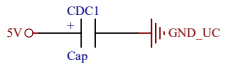

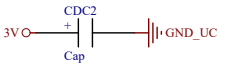

Title: STM32shield		
Size: A3	Number:	Revision: 2_0
Date: 21/08/2019		Sheet of
File: D:\Root\..\Sheet2.SchDoc		Drawn By: K. Scicluna

C.2 - Gate Driver Board

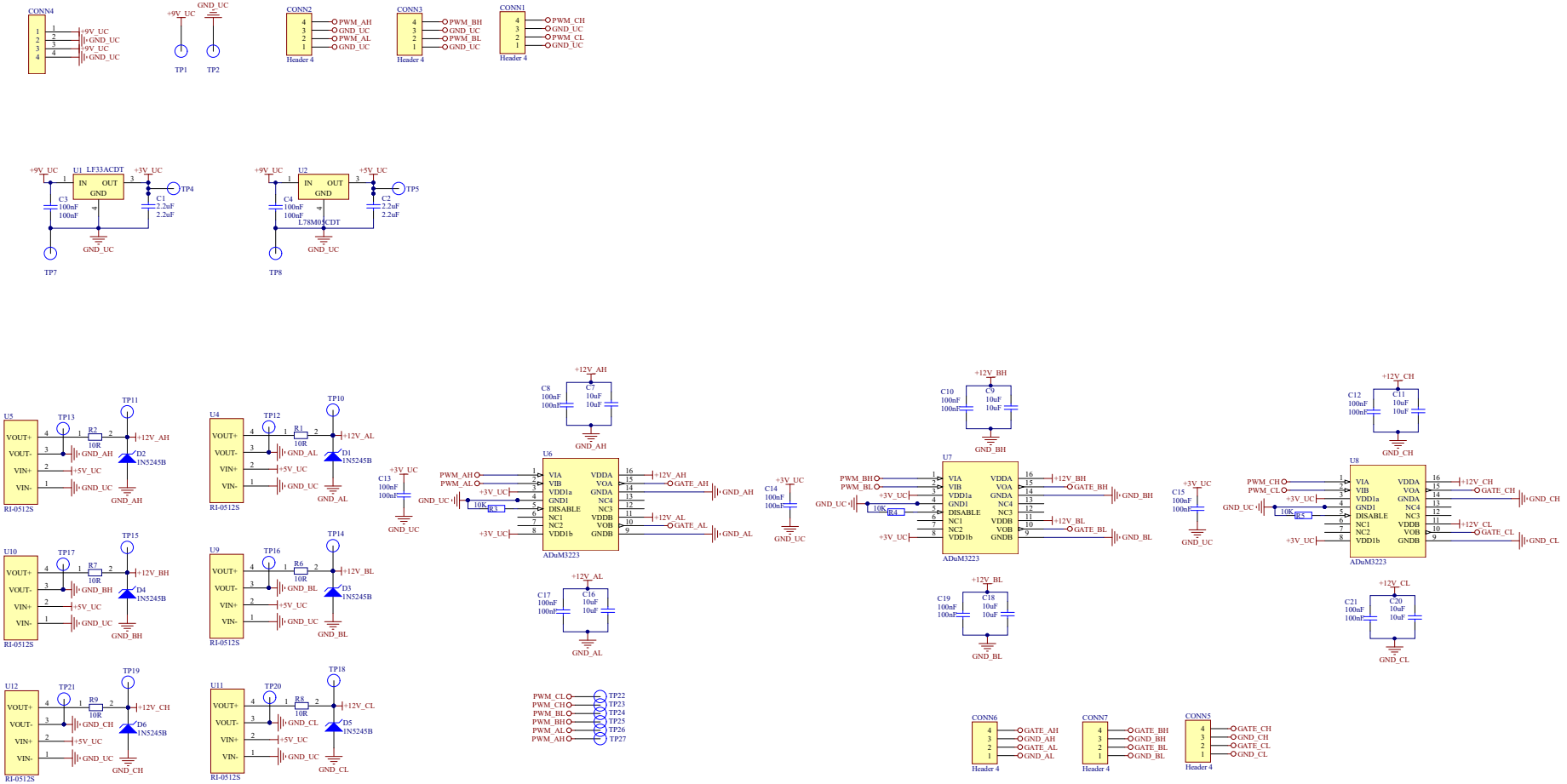

Title: DriverBoard		
Size: A2	Number:	Revision: 2_0
Date: 21/08/2019		Sheet of
File: D:\Root\..\Sheet2.SchDoc		Drawn By: K. Scicluna

Input Connectors

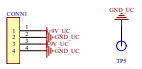

Output Connectors

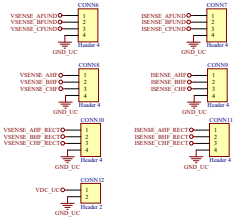

Power Supply Circuitry

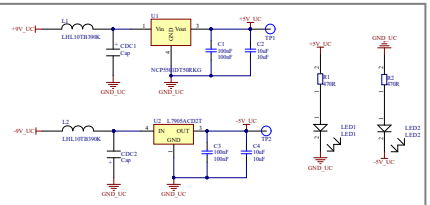

DC Link / Offset Buffers

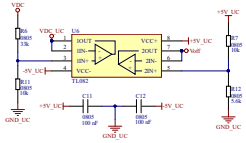

Current Sensing Circuity

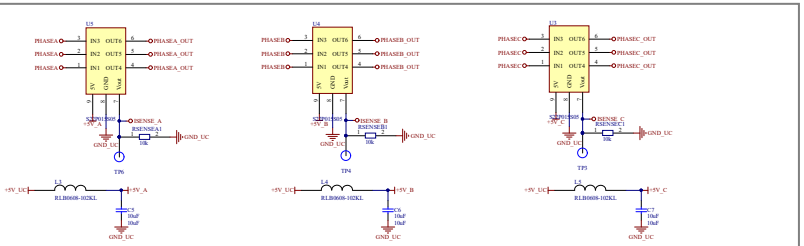

Voltage Sensing Circuitry

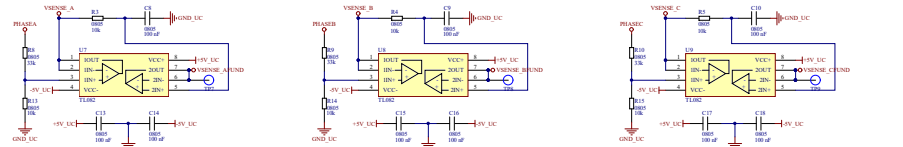

Current Measure Offset Circuitry

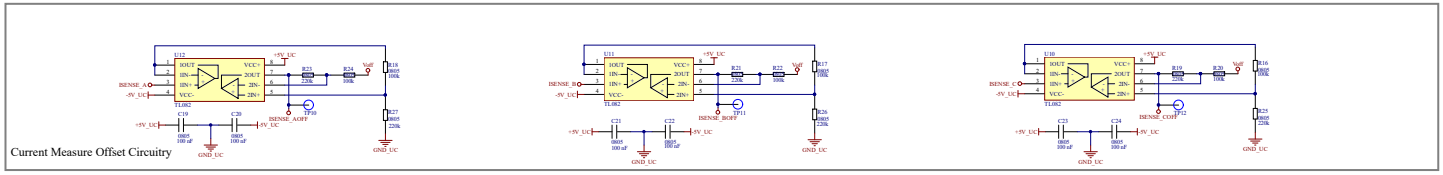

Current Fundamental Circuitry
Butterworth 4th Order fd3b = 750 Hz

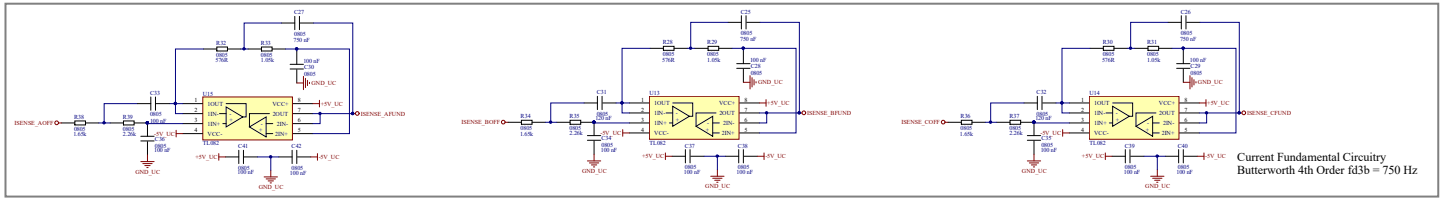

Current Injection Circuitry
Butterworth 2nd Order HPF fd3B = 500 Hz
+ 1 st Order LPF f3dB = 10 kHz

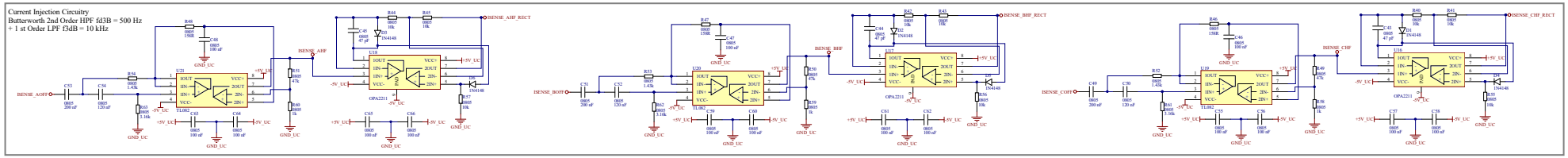

Voltage Injection Circuitry
Butterworth 2nd Order HPF fd3B = 500 Hz
+ 1 st Order LPF f3dB = 10 kHz

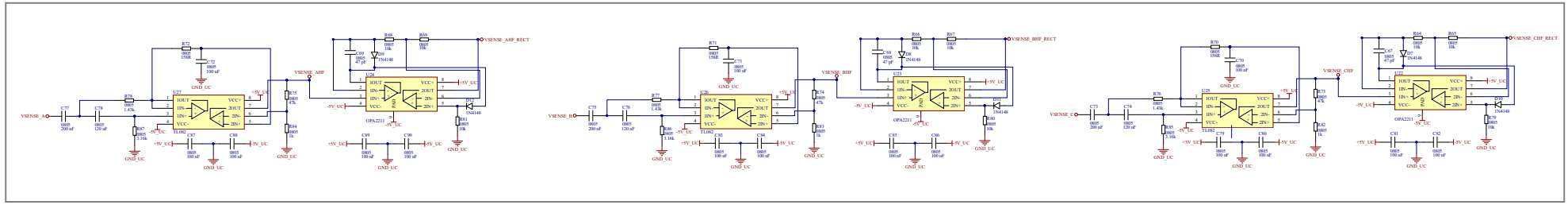

C.3 - Saliency Measurement Board

Title:	Measurement_Card	
Size: A1	Number:	Revision: 1_0
Date:	20/08/2019	Sheet of
File:	D:\Revit - Sheets\SubDoc	Drawn By: K Scicluna

C.4 - Discrete Inverter Power Board

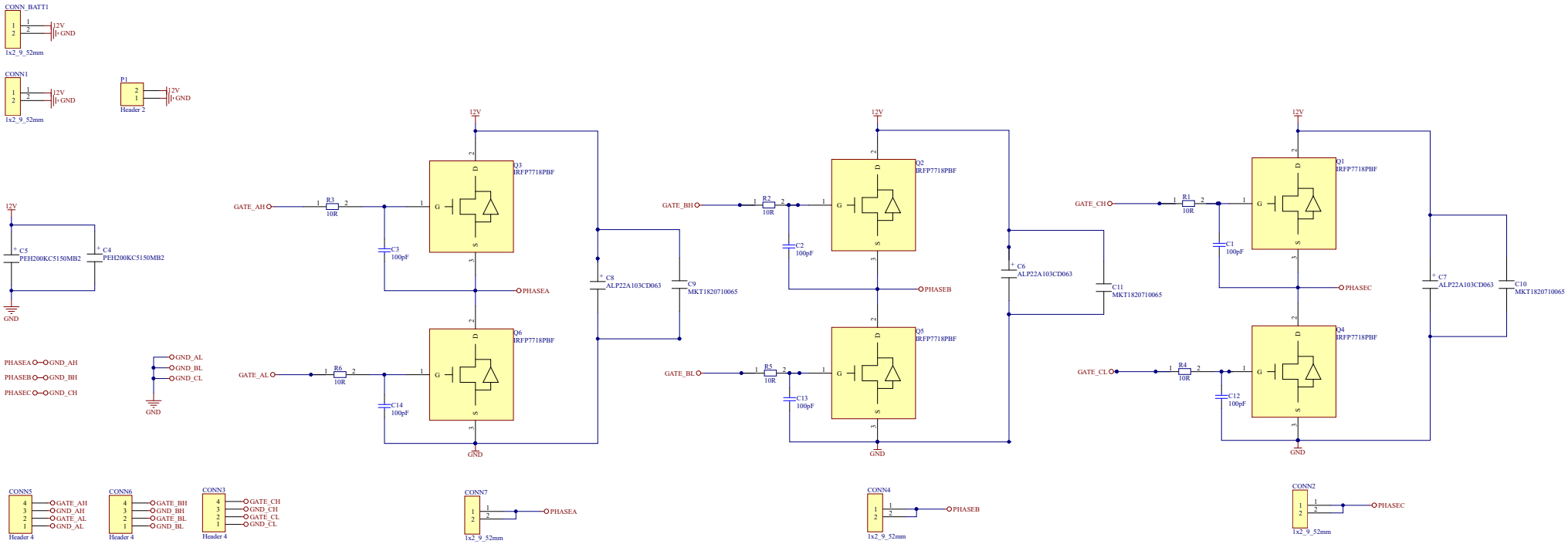

Title: PowerBoard		
Size: A2	Number:	Revision: 3_0
Date: 21/08/2019		Sheet of
File: D:\Root\...\Sheet1.SchDoc		Drawn By: K. Scicluna

C.5 - Integrated Inverter Power Board

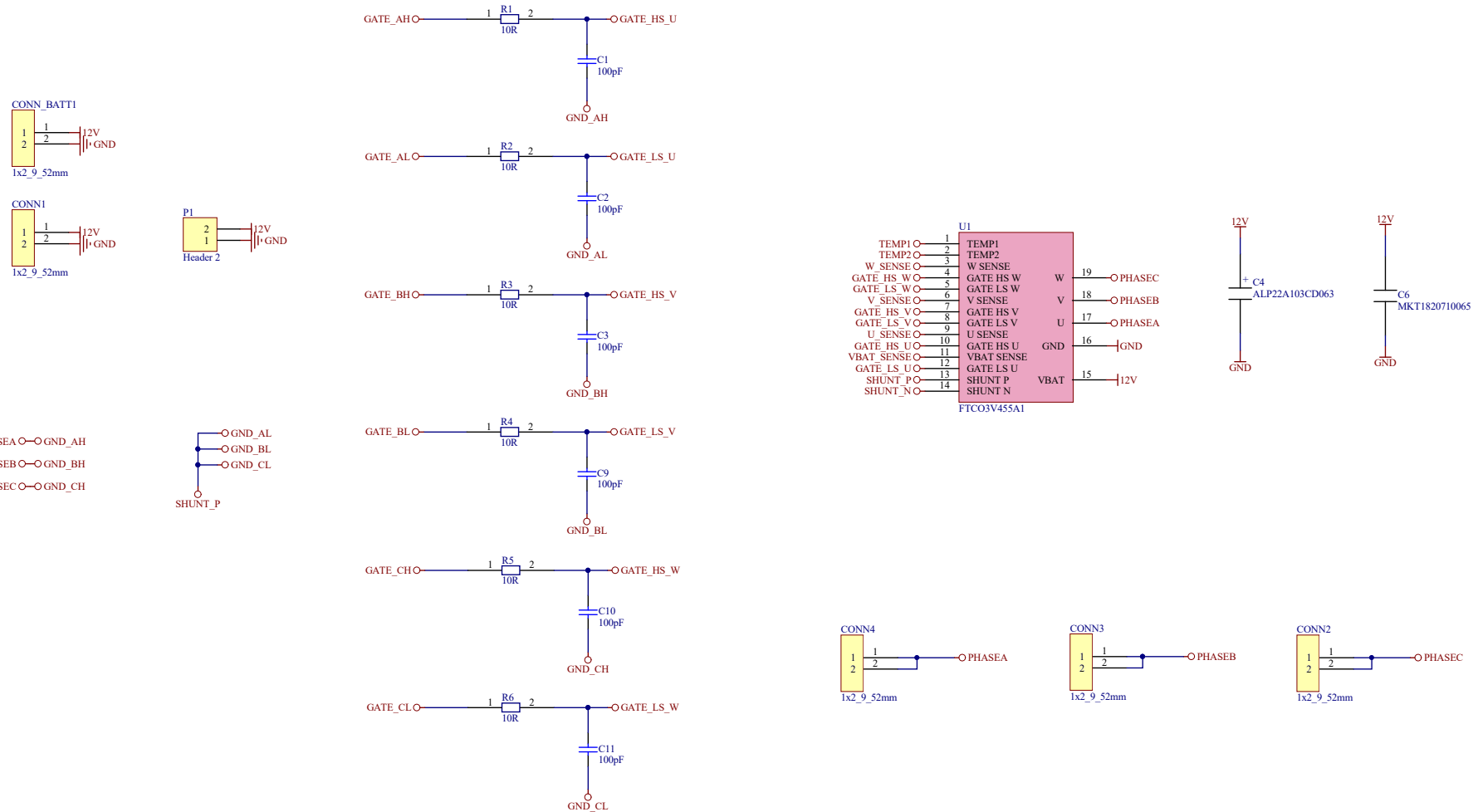

Title	PowerBoard	
Size: A3	Number	Revision: 4_0
Date: 03/03/2020		Sheet of
File: D:\Root\..\Sheet1.SchDoc		Drawn By: K. Scicluna

C.6 - Encoder Interface Board

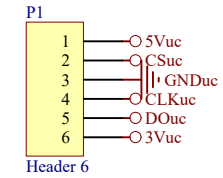

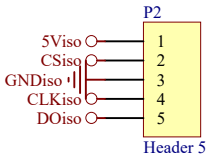

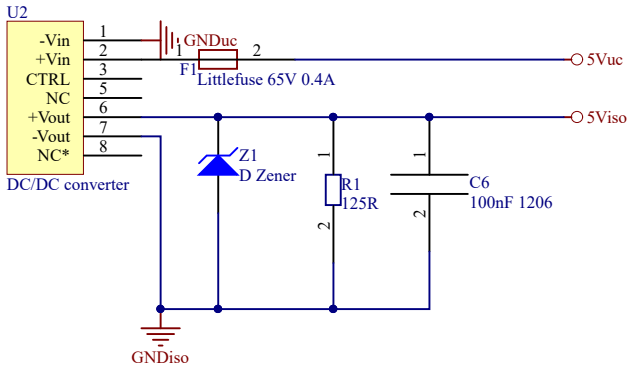

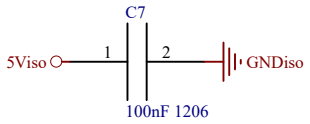

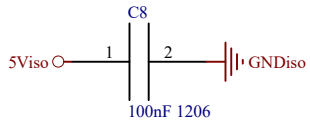

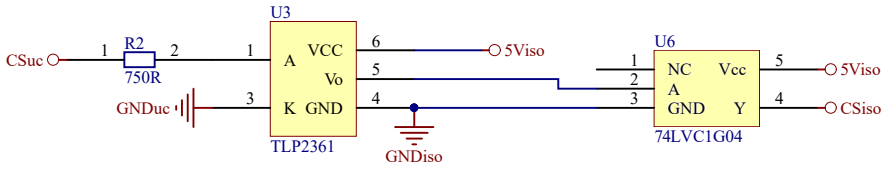

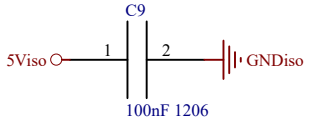

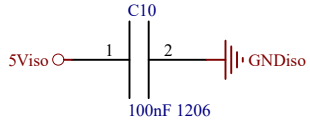

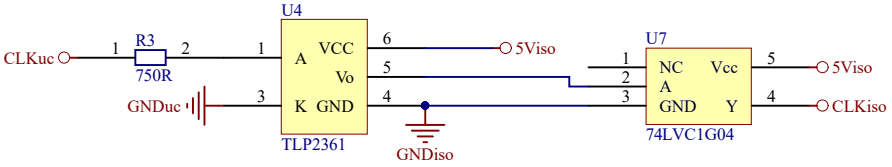

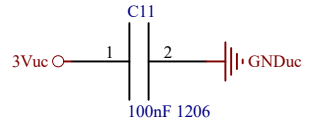

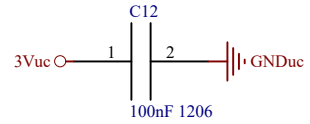

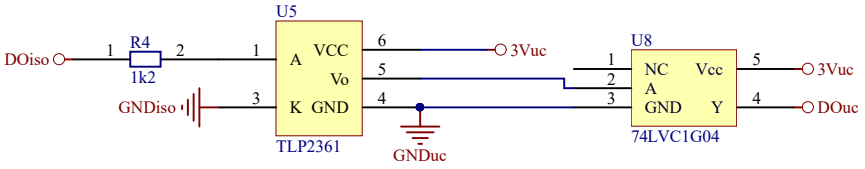

Title: ENCODER_PCB		
Size: A4	Number:	Revision: 2_0
Date: 20/08/2019		Sheet of
File: D:\Root\..\Sheet1.SchDoc		Drawn By: K. Scicluna